Fatigue & Fracture

MECHANICS

34th Volume

STP 1461

EDITORS
Steven R. Daniewicz,
James C. Newman,
and Karl-Heinz Schwalbe

ASTM INTERNATIONAL
Standards Worldwide

STP 1461

Fatigue and Fracture Mechanics, 34th Volume

Steven R. Daniewicz, James C. Newman, and Karl-Heinz Schwalbe, Editors

ASTM Stock Number: STP1461

ASTM International
100 Barr Harbor Drive
PO Box C700
West Conshohocken, PA 19428-2959

Printed in the U. S. A.

ISBN: 0-8031-3487-8
ISSN: 1040-3094

Peer Review Policy

Each paper published in this volume was evaluated by two peer reviewers and at least one editor. The authors addressed all of the reviewers' comments to the satisfaction of both the technical editor(s) and the ASTM International Committee on Publications.

To make technical information available as quickly as possible, the peer-reviewed papers in this publication were prepared "camera-ready" as submitted by the authors.

The quality of the papers in this publication reflects not only the obvious efforts of the authors and the technical editor(s), but also the work of the peer reviewers. In keeping with long-standing publication practices, ASTM International maintains the anonymity of the peer reviewers. The ASTM International Committee on Publications acknowledges with appreciation their dedication and contribution of time and effort on behalf of ASTM International.

Printed in Lancaster, PA
September 2005

Foreword

The Second International ASTM/ESIS Symposium on Fatigue and Fracture Mechanics (34th National Symposium on Fatigue and Fracture Mechanics) was held in Tampa, Florida on 19–21 November 2003. ASTM International Committee E08 on Fatigue and Fracture and the European Structural Integrity Society (ESIS) served as sponsors. Symposium chairmen and co-editors of this publication were Steven R. Daniewicz, Mississippi State University, Mississippi State, MS; James C. Newman, Mississippi State University, Mississippi State, MS; and Karl-Heinz Schwalbe, GKSS Forschungszentrum, Geesthact, Germany.

Contents

SESSION 3A: FATIGUE CRACK GROWTH THRESHOLDS II

SESSION 3B: INTEGRITY ASSESSMENT I

SESSION 4A: SMALL CRACKS I

SESSION 4B: INTEGRITY ASSESSMENT II

SESSION 5A: FATIGUE I

Overview

ASTM International Committee E08 on Fatigue and Fracture and the European Structural Integrity Society (ESIS) jointly sponsored the second International ASTM/ESIS Symposium on Fatigue and Fracture Mechanics (34th ASTM National Symposium on Fatigue and Fracture Mechanics), which was held November 19–21, 2003 in Tampa, Florida. This book represents the proceedings of that important event.

The symposium was co-chaired by S. R. Daniewicz and J. C. Newman, Jr. of Mississippi State University, USA and K.-H. Schwalbe of GKSS Research Center, Geesthacht, Germany. The 37 papers which comprise the symposium proceedings are roughly focused on two significant topics within damage tolerance: *Structural Assessment* and *Fatigue Behavior in the Threshold Regime.* Approximately 50 % of these papers were presented by researchers from outside the United States, making the symposium truly an international event.

It is noteworthy that this ASTM Special Technical Publication (STP) is the last proceedings to be published by ASTM as STP 1461, with papers from future ASTM/ESIS Symposia on Fatigue and Fracture Mechanics to be archived within the *Journal of ASTM International.* This marks the end of a tradition, in which the proceedings of each ASTM National Symposium on Fatigue and Fracture Mechanics were published as an STP. This long and proud tradition began with the publication of STP 381 in 1965, which featured papers by numerous pioneering researchers such as W. F. Brown, G. R. Irwin, F. A. McClintock, P. C. Paris, R. Pelloux, J. E. Srawley, G. Sih, and R. P. Wei. Some 40 years later, the contents of STP 1461 reveal that ASTM and ESIS symposium participants continue to perform research of superior quality and sustaining technical importance.

S. R. Daniewicz
Mississippi State University
April 2005

SESSION 1: SWEDLOW LECTURE AND KEYNOTE ADDRESSES

Journal of ASTM International, May 2005, Vol. 2, No. 5
Paper ID JAI11986
Available online at www.astm.org

Robert H. Dodds, Jr.[1] *and Sushovan Roychowdhury*[2]

Modeling of Three-Dimensional Effects on Fatigue Crack Closure Processes in Small-Scale Yielding

ABSTRACT: In ductile metals, plasticity-induced closure of fatigue cracks often retards significantly measured crack growth rates in the Paris regime and contributes strongly to the observed R-ratio effect in experimental data. This work describes a similarity scaling relationship based on the 3D small-scale yielding framework wherein the thickness, B, defines the only geometric length-scale of the model. Dimensional analysis suggests a scaling relationship for the crack opening loads relative to the maximum cyclic loads (K_{op}/K_{max}) governed by the non-dimensional load parameter $\bar{K} = K_{max}/\sigma_0\sqrt{B}$, i.e., a measure of the in-plane plastic zone size normalized by the thickness. Both K_{op} and K_{max} refer to remotely applied values of the mode I stress-intensity factor. Large-scale, 3D finite element analyses described here demonstrate that K_{op}/K_{max} values vary strongly across the crack front in thin sheets but remain unchanged when K_{max}, B, and σ_0 vary to maintain $\bar{K}$ = constant. The paper also includes results to demonstrate that the scaling relationship holds for non-zero values of the T-stress (which affect the K_{op}/K_{max} values) and for an overload interspersed in the otherwise constant amplitude cycles. The present results focus on $R = K_{min}/K_{max} = 0$ loading, although the scaling relationship has been demonstrated to hold for other $R > 0$ loadings as well. The new similarity scaling relationship makes possible more realistic estimates of crack closure loads for a very wide range of practical conditions from just a few analyses of the type described here.

KEYWORDS: fatigue, crack closure, plasticity, three dimensional, finite elements, contact, similarity scaling

Nomenclature

B	thickness
E	elastic modulus
E_T	bilinear (constant) hardening modulus
K_I	mode I stress intensity factor
K_c	fracture toughness
K_{max}	maximum applied (remote) stress intensity factor
K_{op}	applied (remote) stress intensity factor at full crack opening
K_{OL}	applied (remote) stress intensity factor during overload cycle
$\bar{K}$	normalized stress intensity factor, $\bar{K} = K_{max}/\sigma_0\sqrt{B}$
L_e	element size ahead of crack front
$\mathcal{D}_{min}$	characteristic in-plane dimension
R	K_{min}/K_{max}
$\bar{R}$	radius of cylindrical, small-scale yielding region
R_{OL}	K_{OL}/K_{max}
T	magnitude of T-stress

Manuscript received 15 December 2003; accepted for publication 15 May 2004; published May 2005. Presented at ASTM Symposium on Fatigue and Fracture Mechanics: 34th Volume on 19–21 November 2003 in Tampa, FL; S.R. Daniewicz, J.C. Newman, Jr., and K-H. Schwalbe, Guest Editors.

[1] M. T. Geoffrey Yeh Chair of Civil Engineering, University of Illinois, Urbana, IL 61801.
[2] Research Associate, Department of Civil & Environmental Engineering, University of Illinois, Urbana, IL 61801.

T_{max}	maximum value of the T-stress in a load cycle
$\overline{T}$	normalized T-stress, $\overline{T} = T/\sigma_0$
r_p	in-plane plastic zone size on crack plane
$r_{p\text{-}max}$	in-plane plastic zone size on crack plane at maximum load
(r, θ, z)	cylindrical coordinate system with origin at current crack front location
z	measures distance in the thickness direction
(X, Y, Z)	Cartesian coordinate system with origin at initial crack front location
(u, v, w)	displacement components in (X, Y, Z)
Δa	amount of crack extension
ΔK_{eff}	effective stress intensity factor range
β	non-dimensional, finite geometry factor for T-stress
μ	elastic shear modulus
θ	counterclockwise angle from crack plane
v	Poisson's ratio
σ_0	material yield stress
σ_{yy}	opening mode stress on the crack plane

Introduction

Fatigue crack growth at engineering scales in ductile metals generally exhibits a phenomenon termed plasticity induced crack closure (PICC). Elber [1] was among the first researchers to observe the contact of surfaces behind the advancing crack prior to full reversal of the applied loading, characterized accurately for small-scale yielding (SSY) conditions by $\Delta K_I = K_{max} - K_{min}$. Here, K_{max} and K_{min} denote the peak and minimum applied load in a cycle. Under mode I loading, material immediately ahead of the fatigue crack front experiences significant plastic strain normal to the crack plane, leading to unrecoverable (residual) elongation in the plastic wake once the front grows forward. This reduces the relative physical separation of the crack faces compared to that for purely elastic deformations, thereby causing the crack surfaces to contact sooner after reversal of the loading.

Plasticity induced crack closure contributes significantly to the strong effect of loading ratio (R-ratio $= K_{min}/K_{max}$) routinely observed in conventional fatigue testing for crack lengths and ΔK_I levels above those of short-crack and the near threshold behavior (see [2,3] for example test results showing the R-ratio effect). The Paris model for fatigue crack growth rate accommodates the effects of closure through the modified form

$$\frac{da}{dN} = C\left(K_{max} - K_{op}\right)^m = C\Delta K_{eff}^m \tag{1}$$

where K_{op} denotes the load level at which the crack faces become fully "open" upon reloading. Large positive R-ratios (*e.g.*, $R = 0.7 - 0.9$) generally lead to no closure such that $K_{op} = K_{min}$ and $\Delta K_{eff} = K_I$. At small positive, zero and negative R-ratios, $K_{op} > K_{min}$ and only that part of the load cycle during which the crack faces have no contact contributes to material damage (growth) in this modified model.

Realistic estimates for crack opening loads thus play a crucial role in applications of this methodology to predict fatigue growth rates in damage tolerant designs, for example, to set inspection intervals for engineering structures. Closure models based on strip-yield concepts [4,5] lead to approximate values for K_{op}/K_{max} but neglect important effects including cyclic plastic deformation-hardening in the near front material and variations of in-plane and through-thickness constraint (stress triaxiality). Beginning with the early work of Newman [6], finite element methods have enabled robust numerical solutions that simulate crack growth processes by fatigue including the effects of cyclic plasticity and physical contact conditions behind the advancing crack front. Such analyses appear capable of addressing a wide range of structural and test specimen geometries, crack sizes, crack shapes, constant amplitude loading, overload and underload events, and various types of material (cyclic) flow properties. However, the majority of investigations to date adopt (2D) plane-stress and plane-strain models and thus consider only (straight) through-thickness cracks. Recently, McClung [7] reviewed the major results of these studies and notes the reasonable agreement of K_{op}-values with available test data. The 2D models resolve in-plane effects under SSY conditions that arise primarily through T-stress differences across geometries and loading modes (tension *vs.* bending). However, the 2D models cannot resolve thickness effects on crack-front constraint or the complex interactions of in-plane and through-thickness effects.

Reported investigations of PICC using 3D finite element models remain relatively scarce. The very refined meshes and the large number of load increments necessary to resolve the history of crack face contact and plasticity over many loading cycles lead to massive computational requirements. Chermahini *et al.* [8–10] and Skinner and Daniewicz [11] use 3D models to investigate closure in M(T) and SC(T) geometries under remote cyclic tension loading but with elastic, perfectly-plastic material flow properties that exhibit no Bauschinger effect. Zhang and Bowen [12] analyze closure behavior in an SC(T) specimen with a semi-circular crack under remote tension using a plasticity model with isotropic hardening. These studies yield initial, quantitative insights into the complexity of closure behavior arising from the combined effects of in-plane (T-stress) and thickness (crack front length-curvature) constraint over a limited range of specific geometries. Systematic studies of 3D effects using more realistic plasticity models that include the Bauschinger effect seem necessary to better quantify PICC for engineering applications.

This work reviews results to-date of a systematic study of PICC effects in a practically important subset of 3D configurations characterized by structurally thin, metallic panels containing engineering-scale fatigue cracks growing under cyclic, mode I, and SSY conditions. The finite element computations advance initially straight, through-cracks in each load cycle to investigate the interacting effects on PICC of thickness, T-stress and cyclic material flow properties for constant amplitude loading and for a single overload interspersed within the constant amplitude loading. The values of K_{op}/K_{max} across the crack front for these various conditions, needed in Paris model computations of growth rates, represent the key outcomes of the analyses. Most importantly, the finite element results for K_{op}/K_{max} confirm a new, similarity scaling relationship between K_{max}, the uniaxial yield stress (σ_0), and the thickness (B) suggested by dimensional considerations of the SSY framework [13–15]. Consequently, the PICC behavior for a very wide range of practical conditions may be readily determined from a small number of key analyses of the type described here. Within a 2D analysis framework, McClung [16] explored also similarity relationship for K_{op}/K_{max} as a function of σ_0 and crack-length, a.

The paper follows this organization. The next section describes the 3D-SSY framework. Section 3 develops the non-dimensional analysis to describe crack opening loads. Section 4 summarizes the finite element model and solution procedures. Section 5 provides the key results of the computational studies and describes the various 3D effects found for PICC. The numerical results demonstrate that the proposed similarity relationship holds for constant amplitude loading, including an interspersed overload. Both negative and positive T-stress increase the amount of crack-front plastic deformation and thus increase K_{op}/K_{max} values in a similar manner. The final section lists the key conclusions for 3D effects on PICC behavior derived from this work.

3-D Small-Scale Yielding Framework

Figure 1 illustrates the construction of a model for computational studies that represents a wide range of practical conditions in a simple framework. The thin metallic panel has a thickness, B, with an initially straight (sharp) through crack. The in-plane dimensions of the panel exceed 25-50 $\times B$ (where B may be only 1-2 mm in actual structures). The combination of peak (mode I) load levels typically experienced in moderate-to-high cycle fatigue crack growth (K_{max}) and the typical values of yield stress (σ_0) for structural metals, leads to crack-front plastic zone sizes, $r_{p\text{-}max} \propto (K_{max}/\sigma_0)^2$, of at most equal to a few multiples of B and thus vanishingly small compared to the distances to nearby, traction-free boundaries. Under these conditions, the in-plane behavior remains clearly SSY at each location across the crack front.

At distances on the order of a few thicknesses at most from the crack-front, all through-thickness variations of the strain-stress fields decay to zero leaving a large, linear-elastic and plane-stress region enclosing the crack front. The crack-front region thus experiences mode I conditions characterized by KI transmitted from the remote loading (bending, tension, etc.) and the specific geometry through the surrounding linear-elastic, plane-stress material. To a good approximation under these SSY conditions, the non-singular T-stress (an additional, constant σxx stress) quantifies the near-field loading differences caused by various finite geometries, *e.g.*, M(T) *vs*. SE(B) *vs* DE(T), etc. specimens [17].

The computational model considers a semi-circular disk of thickness B and radius $\bar{R} \gg B$ centered at the crack front. Loading of this 3D, modified boundary layer (MBL) model for SSY conditions occurs through cyclically varying displacements applied on the boundary at $\bar{R}$ corresponding to specified levels of ΔK_{max} and ΔT_{max}— here T always varies in proportion to K_I as it does in finite geometries. Symmetry conditions for mode I loading and growth govern on the plane ahead of the crack front, while friction-less contact conditions hold behind the advancing front.

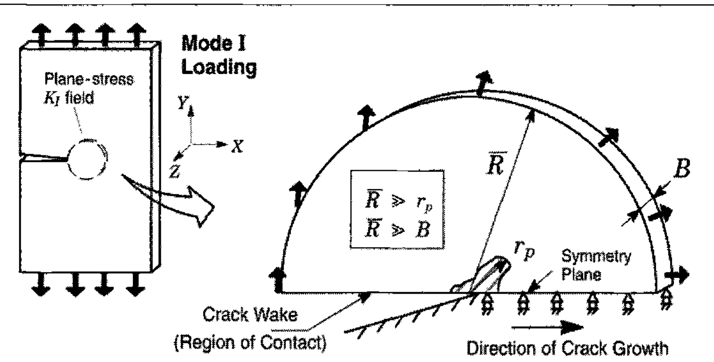

Fig. 1. 3-D small-scale yielding framework. Displacements imposed on boundary of the cylindrical disk correspond to those for the linear-elastic, mode I plane-stress solution including a T-stress.

The thickness B represents the only loading invariant, geometric length-scale in this model; $\bar{R}$ can be defined arbitrarily large compared to B without influencing the crack-front response. The in-plane size of the plastic zone and the blunting deformation at the crack tip (CTOD) define other useful, but loading dependent and closely related, length-scales. Larsson and Carlsson [18] first proposed the now extensively utilized plane-strain version of this MBL model. The plane-strain model has only the length-scale provided by the plastic zone size and the CTOD.

Only a few investigators have adopted the computational framework described above to quantify 3D features of the displacement, strain and stress fields over the near-front region under monotonically increasing load and with no crack extension. Hom and McMeeking [19-21] (HM) appear to have first proposed and used this model to study details of the crack front blunting process and the growth of discrete voids ahead of the blunting crack front. Their analyses employed a finite-strain theory and (isotropic) power-law hardening plasticity (computer limitations at the time forced the adoption of quite coarse meshes and the creative use of sub-modeling). Shortly thereafter, Nakamura and Parks [22] (NP) adopted this framework to examine details of the near-front fields for a sharp crack using a more refined mesh, small-strain theory and deformation plasticity. Both the HM and NP studies considered only T-stress = 0 loading. Yuan and Brocks [23] subsequently introduced non-zero values of the T-stress to approximate the effects of constraint variations in finite geometries. Their work, also using small-strain theory and deformation plasticity, lays out constraint effects on the fields described earlier by NP. Most recently, Kim *et al.* [24] again use small-strain theory and deformation plasticity with non-zero T-stress values to demonstrate the capability of their two-dimensional, three-term asymptotic solution (named J - A_2) to fit the 3D fields at locations across the crack front.

The NP analyses describe essential 3D features of the crack-front fields. Let r denote the distance normal to the crack front. At all load levels, consistent with the maintenance of SSY conditions ($\bar{R} \gg r_{p\text{-}max}$), NP find that: (1) for $r \lesssim 0.01B$ strain-stress fields develop over the mid-thickness region consistent with the asymptotic plane-strain solution, *i.e.* the HRR field; (2) for $r \lesssim 0.5B$, the mid-thickness stress field differs markedly from the free surface field; (3) 3D effects begin to diminish in the region $0.5B \lesssim r \lesssim 1.5B$; and (4) at $r \gtrsim 1.5B$ the linear-elastic and elastic-plastic stress fields rapidly degenerate to plane-stress conditions. In specimens with through cracks, linear-elastic, plane-stress analyses show that the K_I field gradually emerges for $r \lesssim 0.1\,\mathfrak{D}_{min}$, where $\mathfrak{D}_{min}$ denotes the minimum distance to a nearby free boundary, loading point, etc. NP use their 3D SSY results with this observation to suggest that the present 3D SSY framework applies when

$$\mathfrak{D}_{min} \geq \max[15B, 10(K_I/\sigma_0)^2]. \tag{2}$$

The second part of this requirement leads to $\mathfrak{D}_{min} \geq$ 50-60 r_p at K_{max}. These conditions readily exist for thin sheets made of typical structural metals and subjected to load levels for moderate-to-high cycle fatigue.

A Similarity Scaling Relationship for Crack Closure

A study of the Nakamura and Parks [22] results for a stationary crack subjected to monotonic loading in the same 3D SSY framework adopted here suggests the potential to normalize the near-front fields using $K_I/\sigma_0\sqrt{B}$. For fatigue crack growth, this leads naturally to developing a non-dimensional relationship for the opening load (K_{op}) relative to the maximum load (K_{max}) in each cycle of the form

$$\frac{K_{op}}{K_{max}} = F\left(\frac{K_{max}}{\sigma_0}, \frac{T_{max}}{\sigma_0\sqrt{B}}, R, R_{OL}; \frac{z}{B}, \frac{\Delta a}{B}; \frac{\sigma 0}{E}, \frac{E_T}{E}, v\right) \tag{3}$$

where F denotes a non-dimensional function of its non-dimensional parameters. The first loading parameter, $K_{max}/\sigma_0\sqrt{B}$, reflects a measure of the in-plane plastic zone size at peak load ($r_{p\text{-}max}$) scaled by the thickness, B (where again B represents the only geometric dimension of this SSY framework). The T_{max}/σ_0 term approximates constraint differences at the crack front from variations of sheet geometry (*e.g.*, M(T), SE(B), DE(T), etc.) and remote loading (*e.g.*, bending *vs*. tension). Only positive R-ratios, K_{min}/K_{max}, ≥ 0 appear relevant in the SSY framework. For negative R-ratios, much of the loading cycle occurs on a fully closed (no crack) configuration. Continued loading by a remotely applied K_I field does not seem realistic. Our ongoing studies address this issue, and the applicability of Eq 3 for finite geometries with $R < 0$. $R_{OL}=K_{OL}/K_{max}$ denotes the occasional (single) overload cycle within the otherwise constant amplitude loading.

The z/B term in Eq 3 reflects the strong variation of opening loads across the crack front that exists over the full loading history. The opening behavior exhibits an initial transient response as the crack grows through the plastic zone created by the first half cycle of loading $0 \rightarrow K_{max}$ from a previously undeformed and stress-free configuration. In the transient period, K_{op}/K_{max} values increase rapidly to reach steady-state levels. Thereafter, the $\Delta a/B$ dependence in Eq 3 vanishes (see Fig. 4 here and [13]). The last grouping of parameters describes the material properties for the bilinear stress-strain curve with kinematic hardening. Not surprisingly, our initial work [13] demonstrates that K_{op}/K_{max} values have no dependence on σ_0/E as observed in fatigue crack growth testing (growth rates for different materials can be normalized using $\Delta K_{eff}/E$). Fleck [25] and McClung [26] find this same invariance of closure behavior on σ_0/E in their plane-strain and plane-stress analyses.

In the SSY framework, the freedom exists to impose any choice of the T_{max} value to coincide with the attainment of K_{max}, where T varies proportionally with K_I in the cycle. In finite geometries under SSY conditions, T changes linearly with K_I but follows a geometry specific ratio often expressed in the form $T = \beta K_I/\sqrt{\pi\alpha}$, where β depends on the geometry and type of loading but not the load magnitude [17]. SSY solutions with prescribed K_{max} and T_{max} values thus map to a wide range of finite specimen configurations.

The significance of Eq 3 for applications becomes clear by considering a specific example. Consider the loading $\overline{K} = K_{max}/\sigma_0\sqrt{B} = 1.0$ and $\overline{T} = T_{max}/\sigma_0 = 0$, which generates a maximum in-plane plastic zone size of $r_p \approx 0.2 \times B$. Then, for constant amplitude cyclic loading and material strain hardening, the opening load levels across the crack front relative to K_{max} remain unchanged during the initial transient response and during steady-state growth as the yield stress (σ_0), thickness (B), and peak loading (K_{max}) all vary to maintain $\overline{K} = 1.0$. Consequently, one numerical solution for a set of non-dimensional parameters becomes scalable to a very wide range of practical configurations, as first shown by the authors in [13] for zero T-stress and constant amplitude, $R = 0$ loading.

A subsequent section describes additional computational results and discussion of the non-dimensional relationship for closure behavior including new results for the effects of an interspered overload cycle.

Computational Model for 3-D Small-Scale Yielding

Finite Element Mesh

Figure 2 shows the finite element model constructed to analyze the boundary-layer representation of 3-D SSY. The two-fold symmetry present for mode I loading and for subsequent fatigue crack growth reduces the required computational model to one-fourth of the cylindrical disk shown in Fig. 1. The origin of the *X-Y-Z* coordinate systems lies on the initial crack front at mid-thickness. In these exploratory studies of 3-D effects, the initially straight crack front remains straight throughout the modeling of fatigue crack growth (*i.e.*, no tunneling). The mesh covers the region $0 \le \theta \le \pi$ and $0 \le z/B \le 0.5$ and has five variable thickness layers of elements defined over $B/2$ with sizes $0.25B$ (at mid-thickness), $0.15B$, $0.05B$, $0.03B$, and $0.02B$ (at the free surface). Elements residing on the crack plane have uniform rectangular shapes in the *X-Y* plane with typical size $L_e/B = 0.01$. Ninety such elements defined ahead of the initial crack front support maximum fatigue crack growth of $\Delta A \approx B$.

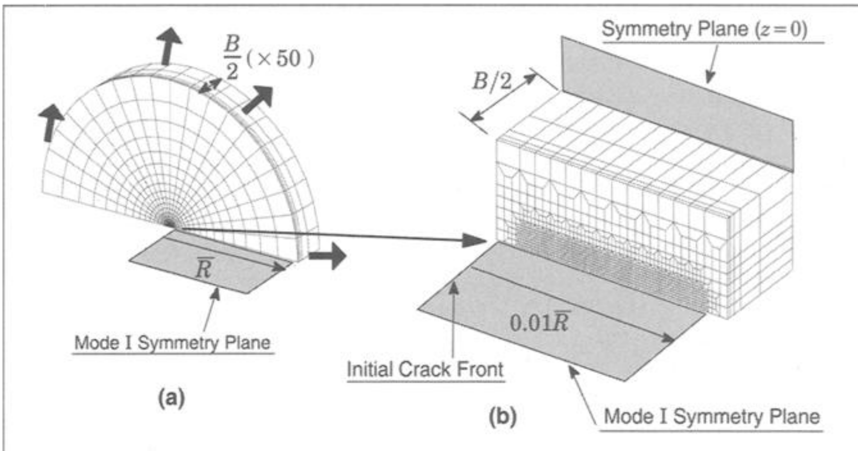

Fig. 2. SSY finite element model: (a) Thickness is scaled 50 × for illustration; (b) Near front region showing rectangular prism mesh for crack growth by node release. Elements on crack plane have size $L_e = 0.01B$.

The mesh extends outward over the cylindrical disk to a size $\overline{R} = 100B$ to ensure that a large, linear-elastic region encloses the plastically deforming crack-front material at peak load. An extensive convergence study [14] demonstrates the adequacy of this mesh refinement level, both in-plane and through-thickness, to resolve the crack-front fields and the details of contact-release events behind the advancing front at both maximum and minimum loads. Simple scaling of the mesh permits analyses of varying thickness to explore the similarity scaling concept. A typical mesh for the refinement level $L_e/B = 0.01$ has 10 000 8-node (isoparametric) brick elements with a $\overline{B}$ formulation [27] to minimize volumetric locking at large plastic deformations.

Cyclic Loading and Crack Growth

Loading of the model occurs through displacements imposed incrementally at nodes over the thickness of the remote cylindrical boundary ($r = \overline{R}$). The prescribed displacements impose a plane-stress, mode I deformation on the cylindrical disk region including an (optional) non-zero T-stress (positive or negative). The in-plane displacements follow the Williams [28] solution

$$u(\overline{R},\theta) = \frac{K_I}{2\mu}\sqrt{\frac{\overline{R}}{2\pi}}\cos\left(\frac{\theta}{2}\right)\left[\kappa - 1 + 2\sin^2\left(\frac{\theta}{2}\right)\right] + \frac{1}{2\mu(1+\nu)}T\overline{R}\cos\theta \tag{4}$$

$$v\left(\overline{R},\theta\right) = \frac{K_I}{2\mu}\sqrt{\frac{\overline{R}}{2\pi}}\sin\left(\frac{\theta}{2}\right)\left[\kappa + 1 - 2\cos^2\left(\frac{\theta}{2}\right)\right] - \frac{\nu}{2\mu\left(1+\nu\right)}T\overline{R}\sin\theta, \tag{5}$$

where K_I defines the mode I stress-intensity factor, T designates the remotely applied T-stress (in the global X-direction), and $\overline{R}$ denotes the radius of the outer circular boundary of the finite-element mesh. The material constants include the shear modulus (μ) and Poisson's ratio (ν) Here, $\kappa = \left(3-\nu\right)/\left(1+\nu\right)$ for the plane stress conditions present at distances remote from the crack front. Yuan and Brocks [23] vary the w displacements linearly over the thickness at $\overline{R}$, *i.e.* w ($r = \overline{R}, \theta, z > 0$), in accord with the plane-stress assumption, while Kim *et al.* [24] show no effects over the crack front from various treatments of the remote w displacements. The present analyses leave the w ($r = \overline{R}$, θ, $z > 0$) displacements unconstrained.

The analyses enforce symmetry conditions at all $z = 0$ nodes ($w = 0$) and ahead of the current crack front ($v = 0$ at $\theta = 0$). At nodes on the symmetry plane behind the crack front ($\theta = \pi$), the computations impose frictionless, rigid contact conditions to model the mode I closure process. The high stiffness ($1000E$) adopted in the penalty formulation for contact prevents interpenetration of these nodes through the symmetry plane, yet leads to good convergence rates of the global nonlinear solution.

The remotely applied displacements follow prescribed values of K_I and T corresponding to cyclic loading with an R-ratio = 0 (see [14] for similar analyses with R = 0.1 loading). Figure 3 illustrates the incremental loadings applied in each cycle. K_I and (optionally) T increase from zero to maximum values, denoted K_{max} and T_{max}. During each such load cycle: (1) the crack first re-opens from a closed or partially closed configuration, (2) at peak load the computational procedures execute a uniform node release across the front, which extends the fatigue crack by an amount L_e, and (3) the crack faces again make gradual contact with the symmetry plane as the remote load decreases toward zero. Convergence studies demonstrate the need to define carefully the loading increment sizes over the cycle to resolve the gradual processes of crack opening-closure and to eliminate effects of the node release process on the closure behavior. The analyses here adopt 44 variably-sized load increments per cycle, continuing for up to 90 cycles, *i.e.*, 90 increments of crack extension.

As the load increases from zero in each cycle, material behind the current location of the crack front gradually loses contact with the symmetry plane as the crack re-opens from the closed state. The discrete increments of load applied in the analysis coupled with the element size (L_e) lead to some ambiguity about the precise loading level at complete crack opening (K_{op}). This artifact of numerical modeling has been discussed extensively [14,29,30]. The present work defines K_{op} at each through-thickness location across the crack front as the remotely applied value of K_I when the second node behind a location along the (current) front loses contact with the symmetry plane.

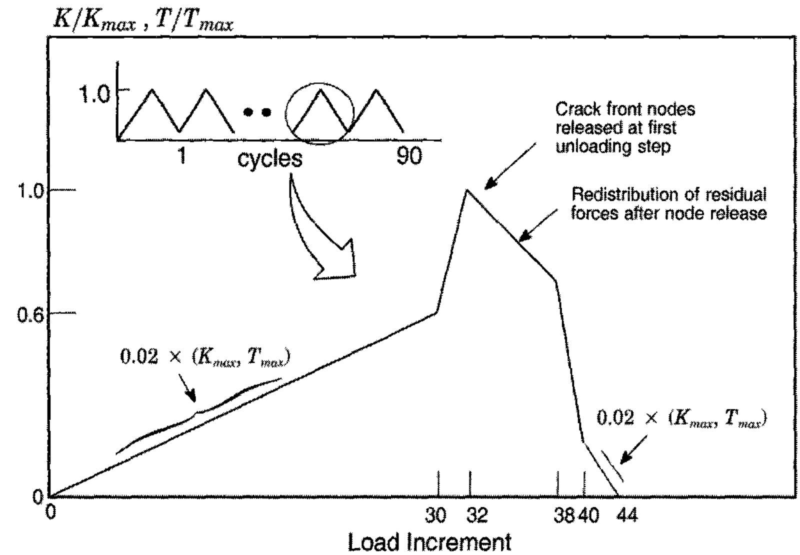

Fig. 3. Variable size load increments employed over a single load cycle for R-ratio = 0 loading.

Material Constitutive Behavior

The material response follows a Mises plasticity model with purely kinematic hardening that approximates the Bauschinger effect under load reversals. When combined with a simple bilinear representation of the uniaxial stress-strain curve, this constitutive model exhibits complete shakedown after one cycle with no effect of the mean stress. A range of values specified for the modulus (E), yield stress (σ_0), tangent modulus ($E_T = d\sigma / d\varepsilon$=constant), and Poisson's ratio (ν) describe properties for typical ferritic steel and aluminum alloys.

The element and constitutive formulations reflect a small-strain approximation. Comparative analyses using a large-strain formulation require longer computation times but reveal no significant effect on the crack opening loads [14]. Analyses with the same bilinear stress-strain curve, but with isotropic hardening, show larger crack opening load levels (K_{op}/K_{max}), especially when the plastic zone size at peak load extends less than $B/2$ ahead of the front [14]. Compared to values for the kinematic hardening model, K_{op}/K_{max} values for isotropic hardening on the centerplane increase from essentially zero→0.1, and on the free surface they increase from 0.45→0.6.

Analysis Code

The 3-D SSY analyses of fatigue crack growth have moderate size meshes (10 000 8-node brick elements) but use 3600-4000 load increments over 90 loading cycles to re-solve accurately the closure (contact) process, the discontinuity from crack extension, and the cyclic plastic deformation. Each loading increment requires 3-4 Newton iterations with a tight tolerance for convergence leading to very severe computational demands— the linearized set of 30 000+ equations must be solved some 10 000-15 000 times over the course of a single analysis.

The analyses reported here are performed with the WARP3D code [31]. This code exploits a dual level of parallel computation on shared-memory computers (message passing through MPI and threads through Open MP) coupled with advanced sparse (direct) solvers to reduce the time-to-solution. With this approach, a complete analysis requires 30 (wall clock) hours using 4-6 processors on current Unix computers (e.g., an IBM SP-3).

Key Results and Discussion

The following section describes selected key results obtained from on-going studies of closure behavior that use the 3D-SSY framework for fatigue cracks growing in thin metal sheets. The results here focus on the essential $\overline{K} = K_{max} / \sigma_0\sqrt{B}$ scaling, effects of (scaled) loading magnitudes on closure levels, *T*-stress effects, and new results that consider a single, interspersed overload event in the otherwise constant amplitude cycling. Recent papers present these and additional results in greater detail as follows: (1) the effects of E/σ_0 ratios on crack closure loads, details of the 3D closure process for $R = 0$ and zero *T*-stress loading [13]; (2) similar analyses for R = 0.1 loading, investigation of mesh convergence issues, effects of isotropic *vs.* kinematic hardening on closure loads, and a comparison of stationary and fatigue crack front fields [14]; and (3) positive and negative *T*-stress effects on closure loads and the very interesting effects on flow of plastic material in the crack front region [15].

Verification of Proposed Dimensional Scaling Model

Figure 4 demonstrates the applicability of the proposed non-dimensional scaling relationship for the crack opening loads. This figure shows the evolution of crack opening loads obtained from two analyses of the 3D SSY model using material flow properties representative of a structural aluminum. The baseline solution (solid line) employs a model with thickness $B = \underline{B}$, while the second solution (symbols) uses a model with thickness $B = 2 \times \underline{B}$. Scaling of the peak load levels (K_{max}) for the constant amplitude, $R = 0$ cycling maintains $\overline{K} = K_{max} / \sigma_0\sqrt{B} = 1.0$ in each case. A value of $\overline{K} = 1.0$ generates an in-plane plastic zone at peak load on the crack plane ($\theta = 0$) of size $r_{p\text{-}max} \approx 0.2 \times \mathrm{B}$ for the *T*-stress = 0 loading used here. The two solutions remain identical over the complete crack-growth history to within the load-step size used in the finite element computations, thus validating the non-dimensional scaling for crack opening loads. Similar computations that vary yield stress, the E/σ_0 ratio and R ratio (>0), also demonstrate the applicability of the scaling relationship [13,14].

These results illustrate key features observed in the computed behavior of the crack opening-closing process. Early in the loading history, the crack grows through the initial plastic zone of size $0.2 \times B$ established in the first half-cycle of load ($0 \rightarrow K_{max}$) from an initially unstressed configuration. This initial transient acts to retard the closure process similar to an overload later in the loading. Once the crack front extends through this initial plastic zone, the opening levels stabilize to effectively constant values (here termed steady-state). The opening load levels show a strong variation with position across the crack front from the initial transient to steady-state conditions. At the outside surface (z/B=0.48-0.5), the opening load levels of K_{op}/K_{max}=0.4-0.5 very closely match the expected values given by simple, plane-stress estimates. The opening load levels decrease very sharply at crack front locations only a small distance from the outside surfaces, reaching 0.25 at z/B=0.4. At the centerplane, the opening load slowly decreases, reaching an apparent steady-state value of 0.02, which corresponds to the load-step size used in the analysis. Thus, for R=0 and $\bar{K}=1.0$ ($r_{p\text{-}max}\approx 0.2\times$B) with T-stress = 0, these results indicate that the centerplane material experiences little or no closure at steady growth conditions. The plane-strain computations for M(T) and SE(B) specimens described by Fleck [25] show trends very similar to the present center-plane results. At this level of remote loading $\left(\left(\bar{K}=1.0\right)\right.$, the opening mode stresses at the centerplane very closely match those for idealized plane-strain conditions [14].

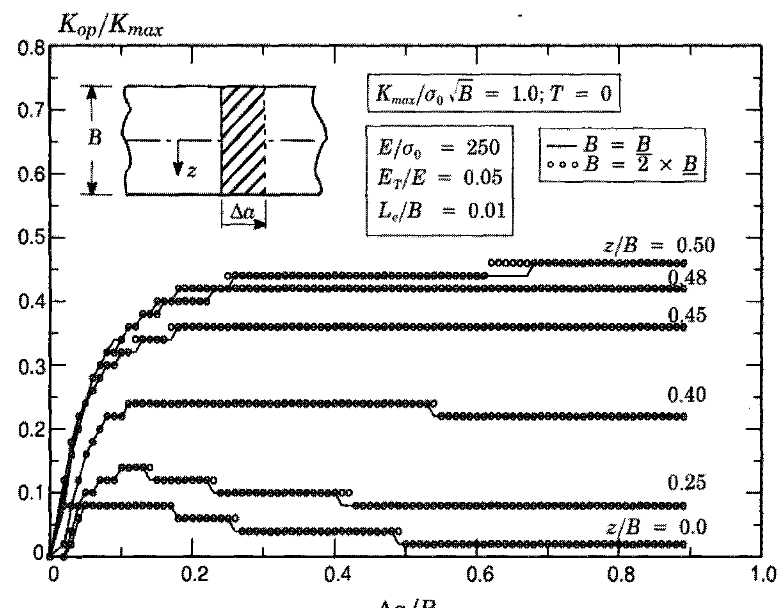

Fig. 4. Demonstration of the similarity scaling of normalized opening load at each crack front location when specimens of different thickness are subject to same normalized load.

Effects of Peak Load

The size of the in-plane plastic zone at peak load relative to the thickness causes a pronounced effect on the crack opening loads across the crack front. Figure 5 compares the opening loads for $\bar{K}=1.0$ ($r_{p\text{-}max}\approx 0.2\times B$) with those for $\bar{K}=2.0$ ($r_{p\text{-}max}\approx 0.2\times B$) for the R = 0, T-stress = 0 cycling of the material with aluminum flow properties. For the larger (relative) loading, all crack front locations show opening loads well above zero. Material near the centerplane shows clear evidence of crack closure but with some remaining 3-D effects which reduce the opening levels below those at the outside surface. At still higher $\bar{K}$ (not shown), opening loads on the interior continue to increase toward the plane-stress levels and with a gradual trend to nearly uniform opening loads along the front.

The large increase in opening loads at interior locations along the crack front for $\overline{K} = 2.0$ corresponds to extension of the plastic zone into material that undergoes essentially plane-stress or near plane-stress conditions (recall the size of the 3-D→2-D transition region discussed in Section 2). In contrast, the centerplane plastic zone for $\overline{K} = 1.0$ loading remains confined to the region of near plane-strain conditions at the crack front.

The very strong impact of plastic zone size relative to thickness on the closure process at the centerplane *does not* carry over to the opening mode stresses deep within the plastic zone at distances of $r \lesssim 0.05B$. Detailed studies of fatigue crack growth using a finite-strain formulation [14] reveal essentially no change in peak values of the centerplane opening stresses immediately ahead of the crack front $(\sigma_{yy} \approx 3.0 \times \sigma_0)$ as the remote loading increases from $\overline{K} = 1.0 \rightarrow 2.0$. These observations indicate no loss of through-thickness constraint immediately ahead of the crack front $r \lesssim 0.05B$ with increased (remote) plastic deformation.

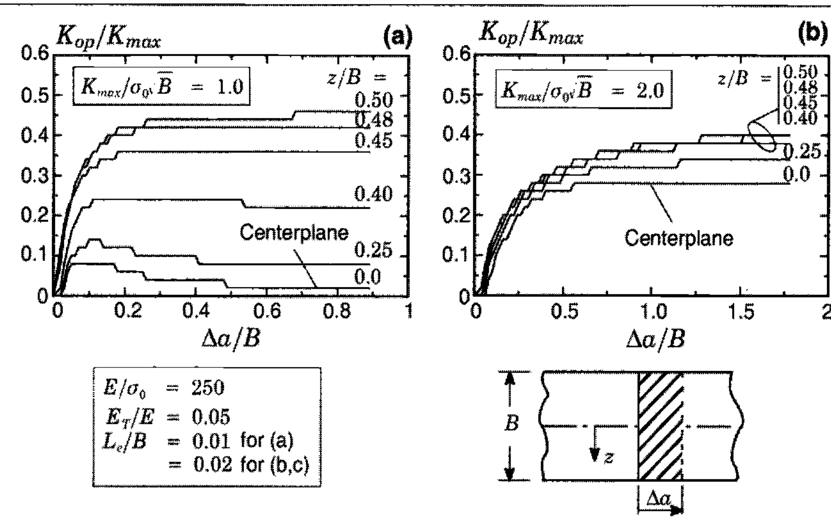

Fig. 5. Normalized opening loads for two levels of normalized peak load. Note the larger amount of fatigue crack growth required to reach steady opening loads for the larger remote load.

Effects of T-Stress on Closure

Under plane-strain conditions for a stationary crack, the *T*-stress strongly affects the size/shape of the crack front plastic zone [18,32]. Both positive and negative *T*-stress loading increase the size of the plastic zone relative to the neutral configuration ($T = 0$). A negative *T*-stress leads to much lower mean stress and opening mode stresses ahead of the crack plane, while a positive *T*-stress leads to marginal increases in opening mode stress. For plane-stress conditions, the *T*-stress has much less influence on plastic zones and opening mode stresses (the zero out-of-plane stress exerts a dominant effect). These observations for a stationary crack carry over to the crack closure phenomenon studied here for both positive and negative T-stress loadings using the 3-D SSY framework. Solanki *et al.* [33] examined T-stress effects on closure using 2D model of specific geometries.

Figure 6 demonstrates the applicability of the non-dimensional scaling relationship for crack opening loads, Eq 3, with non-zero T-stress loading. The figure shows the evolution of opening loads with crack extension for models with two different thickness, $B=\underline{B}$ and $B=2\times\underline{B}$, for two levels of T-stress $(T_{max}/\sigma_0=\pm0.8)$ when the remote mode I loading scales with B to maintain $\overline{K}=1.0$. For both of these (relatively) large values of positive and negative T-stress, the opening loads maintain the non-dimensional scaling over the complete loading history from the initial transient to steady-state conditions at crack extensions approaching the thickness. In these analyses, the T-stress increases (decreases) proportionately with K_I as illustrated in Fig. 3.

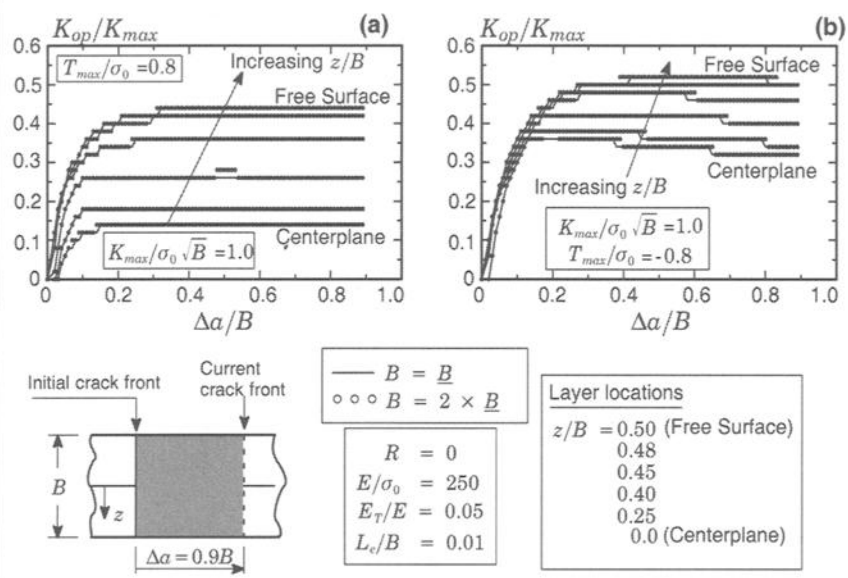

Fig. 6. Demonstration of non-dimensional scaling of crack opening loads in the presence of a strong, non-zero T-stress. (a) positive T-stress, (b) negative T-stress.

A comparison of the crack opening loads in Fig. 6 with those in Fig. 4 (T-stress = 0) readily illustrates the strong effect of T-stress. Both positive and negative T-stress increase the opening loads along the interior of the crack front— negative T-stress has the larger effect (consistent with observations for the stationary crack). The mid-plane portion of the crack front now has a non-ambiguous opening load well above that for the zero T-stress loading. Opening loads near and at the outside surface show only a marginal effect for both the positive and negative T-stress.

Figure 7 summarizes the effects for a wide range of T-stress ($-0.8\le T_{max}/\sigma_0\le 0.8$) on the steady-state opening loads, $(K_{op}/K_{max})_{ss}$, for $\overline{K}=1.0$ and 2.0.The key observations from these analyses include: (1) a less pronounced T-stress effect on closure at the free surface than at the centerplane; (2) $(K_{op}/K_{max})_{ss}$ values at the centerplane increase with deviations from zero T-stress, and the increase is more rapid with negative T-stress; and (3) at all levels of T-stress, an increase in $\overline{K}$ (from 1→2) elevates $(K_{op}/K_{max})_{ss}$ at the centerplane, but the free surface values remain relatively unchanged.

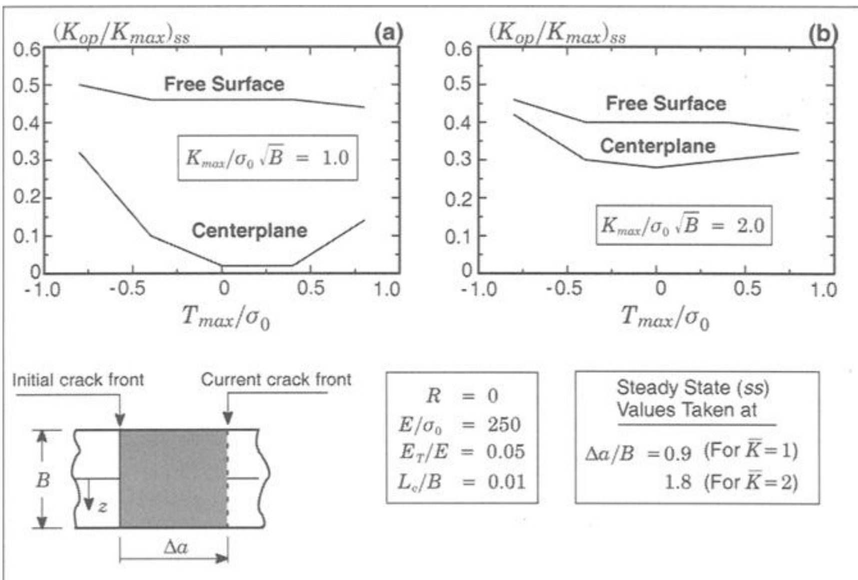

Fig. 7. Effect of T-stress on steady-state values of normalised opening load for (a) $\overline{K}=1$, (b) $\overline{K}=2$.

Overload Effects

The numerical results for crack opening loads presented to this point for the 3-D SSY model all consider constant amplitude cycling at a fixed R ratio with and without T-stress loading. Occasional overload cycles establish a larger plastic zone than exists at steady conditions for the constant amplitude cycling. The larger plastic zone size increases the crack opening loads until the crack extends beyond the influence of the overload plastic zone. The increased opening loads decrease ΔK_{eff} during the subsequent (constant amplitude) cycling and thus retard crack growth rates predicted using a Paris model. The well-known Wheeler model [34], for example, provides an empirical modification of crack-growth rate following an overload event. Newman's strip-yield model gives a numerical solution for the effect of an overlaod on ΔK_{eff} [35]. The Yisheng and Schijve [36] experimental results show clearly the effects of a single overload predicted here.

Figure 8 shows the results of modeling fatigue crack growth with the 3-D SSY framework at constant amplitude (R=0, T=0) for $\overline{K}=1.0$. The computations impose a single overload cycle once steady-state conditions exist. The overload increases K_{max} by 50 % in a single cycle. The solutions for model with two different thicknesses ($B=\underline{B}$ and $B=2\times\underline{B}$) again remain identical throughout the initial transient, the overload transient and the new steady-state conditions following the overload event. Here the loading for $B = 2 \times \underline{B}$ has K_{max} and K_{OL} both $\sqrt{2}\times$ the loading levels for $B = \underline{B}$ The non-dimensional scaling of Eq 3 thus holds for overload events.

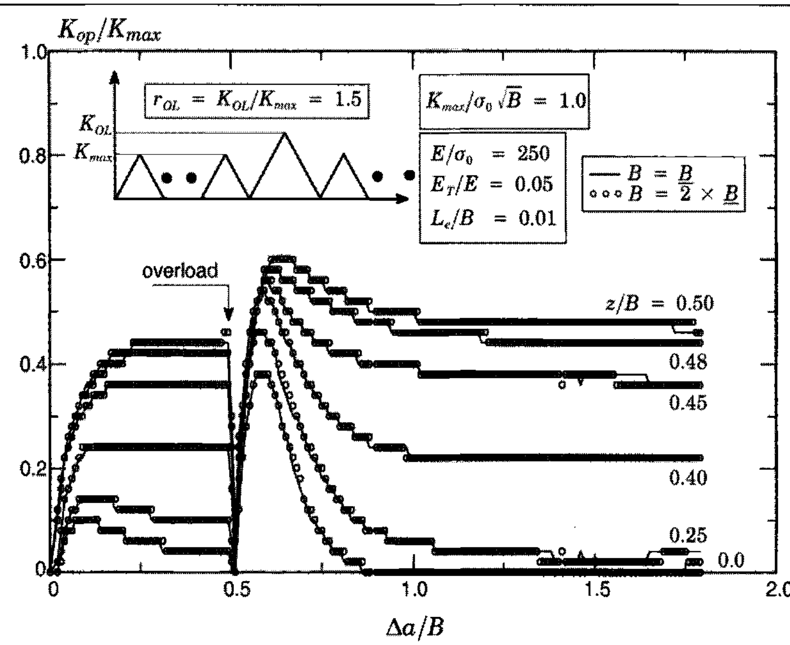

Fig. 8. Demonstration of the similarity scaling of normalized opening load for a single, 50% overload cycle (T-stress = 0).

The crack opening loads for the overload event show several expected behaviors. During the first half-cycle following the overload, the crack does not close upon reversed loading leading to the sharp "V" portion after the overload marking on the figure. Thereafter, a new transient region develops, and the opening load levels increase substantially above the previous steady-state values, including locations along the interior of the crack front. As the crack continues to extend beyond the overload point, the opening loads decrease with the most steep declines over the mid-portion of the crack front. Values over the mid-thickness region reduce to zero (no closure), while values at the outside surface approach steady-state levels marginally larger than those before the overload cycle.

Concluding Remarks

This study adopts a 3-D small-scale yielding framework with thickness, B, as the only geometric parameter to investigate plasticity effects on crack closure at engineering length-scales— long cracks loaded well above threshold levels. The computations impose constant amplitude mode I loading with and without a corresponding T-stress to provide a first-order approximation for finite geometry and loading mode (tension *vs.* bending) effects. A load cycle consists of increasing K_I and T simultaneously from zero to specified values K_{max} and T_{max}, respectively, and then decreasing them back to zero.

The finite element solutions extend the initially straight crack front uniformly forward in each load cycle by one element size on the crack plane. Rigid and frictionless contact conditions model the gradual crack closure and opening events behind the advancing front. The material follows a purely kinematic hardening behavior with a simple bilinear representation of the uniaxial stress-strain curve. The work described here supports the following conclusions and observations:

- Under SSY conditions, the computational results demonstrate that the normalized value of the stress-intensity factor, K_{op}/K_{max}, when the crack opens at each location along the front remains unchanged, provided the peak load (K_{max}), thickness (B), and material flow stress (σ_0) all vary to maintain a fixed *value* of $\overline{K} = K_{\max} / \sigma_0\sqrt{B}$. Numerical values of this similarity scaling factor, $\overline{K}$, thus provide a unique description of closure loads across all SSY configurations for a material. This similarity scaling holds both during the initial stages of growth, when opening loads vary with the amount of fatigue crack extension, and during steady-state response, when K_{op}/K_{max} values remain constant with further growth.
- The closure behavior shows the strongest 3-D effects for the lowest loading level considered, $\overline{K} = 1.0$, which causes a mid-thickness plastic zone size on the crack plane of $\approx 0.2 \times B$ at peak load. The mid-thickness region of the model shows little or no crack closure, while the outside surfaces have K_{op}/K_{max} values characteristic of a plane-stress model. At the maximum loading level considered, $\overline{K} = 2.0$ (mid-thickness plastic zone size $\approx 1 \times B$), K_{op}/K_{max} values at the center-plane increase sharply while outside surface values remain nearly unchanged.
- Under SSY with a non-zero T-stress, a two parameter characterization of crack tip fields in terms of $\overline{K} = K_{\max} / \sigma_0\sqrt{B}$. and $\overline{T} = T_{\max} / \sigma_0$ correlates successfully the normalized opening load K_{op}/K_{max} across variations of thickness, constraint level, and material flow properties. Specifically, the evolution of K_{op}/K_{max} with normalized crack growth $\Delta a/B$, at all locations along the 3-D crack front, remains unchanged when test specimens (and/or structures) experience the same normalized load $\overline{K}$ and the same normalized constraint level $\overline{T}$.
- Both positive and negative deviations in T-stress from a zero value increase the crack opening loads along the mid-thickness region and reduce the through-thickness variation of K_{op}/K_{max}. This effect is more pronounced for negative T-stress and at the lower value of $\overline{K} = 1$, where the plastic zone ahead of the crack tip spreads to a distance ~0.2×B (under zero T-stress).
- The $\overline{K}$ non-dimensional scaling for crack opening loads also describes the computed response following a single overload cycle applied once the crack extends through the initial transient. Immediately after the overload, the crack front experiences no closure with significantly increased opening loads thereafter, leading to retarded crack growth rates. With continued growth, the opening loads return to pre-overload levels with the centerplane showing no crack closure at steady-state conditions following the overload.

The 3-D effects on crack closure remain very strong throughout the overload transient and into subsequent steady-state response.

Acknowledgments

The NASA-Ames Research Center and Marshall Space Flight Center provided the support for this work through Grants NAG 2-1424 (Engineering for Complex Systems Program and the NASA-Ames Chief Engineer, Dr. Tina Panontin) and NAG 8-1751 (MSFC, Mr. Doug Wells, Technical Monitor). We also acknowledge valuable discussions with Dr. R. Craig McClung (Southwest Research Institute) and Profs. Jim Newman and Steve Daniewicz (Mississippi State University).

References

[1] Elber, W., "Fatigue Crack Closure Under Cyclic Tension," *Engineering Fracture Mechanics,* Vol. 2, 1970, pp. 37-45.
[2] Hudson, C. M., "Effect of Stress Ratio on Fatigue-Crack Growth in 7075-T6 and 2024-T3 Aluminum Alloy Specimens," NASA TN D-5390, 1969.
[3] Phillips, E. P., "The Influence of Crack Closure on Fatigue Crack Growth Thresholds in 2024-T3 Aluminum Alloy," *ASTM STP 982,* 1988, pp. 505-515.
[4] Newman, J. C., Jr., "A Crack-Closure Model for Predicting Fatigue Crack Growth Under Aircraft Spectrum Loading," *ASTM STP 748*, 1981, pp. 53-84.
[5] Newman, J. C., Jr., "An Evaluation of Plasticity-Induced Crack Closure Concept and Measurement Methods," *ASTM STP 1343,* 1999, pp. 128-144.
[6] Newman, J. C., Jr., "A Finite Element Analysis of Fatigue Crack Closure," *ASTM STP 590,* 1976, pp. 281-301.
[7] McClung, R. C., "Finite Element Analysis of Fatigue Crack Closure: A Historical and Critical Review," *Seventh International Fatigue Conference*, Beijing, China, 1999,Vol. 1, pp. 495-502.
[8] Chermahini, R. G., Shivakumar, K. N. and Newman Jr., J.C., "Three-Dimensional Finite Element Simulation of Fatigue Crack Growth and Closure," *ASTM STP 982,* 1988, pp. 398-413.
[9] Chermahini, R.G., Shivakumar, K. N., Newman Jr., J. C. and Blom, A. F., "Three-Dimensional Aspects of Plasticity Induced Fatigue Crack Closure," *Engineering Fracture Mechanics,* Vol. 34, 1989, 393-401.
[10] Chermahini, R. G., Palmberg, B., and Blom, A. F., "Fatigue Crack Growth and Closure of Semicircular and Semielliptical Surface Flaws," *International Journal of Fatigue,* Vol. 15, 1993, pp. 259-263.
[11] Skinner, J. D. and Daniewicz, S. R., "Simulation of Plasticity-Induced Fatigue Crack Closure in Part-Through Cracked Geometries Using Finite Element Analysis," *Engineering Fracture Mechanics,* Vol. 69, 2002, pp. 1-11.
[12] Zhang, J. L. and Bowen, P., "On the Finite Element Simulation of Three-Dimensional Semi-Circular Fatigue Crack Growth and Closure," *Engineering Fracture Mechanics,* Vol. 60, 1998, pp. 341-360.
[13] Roychowdhury, S. and Dodds, R., "Three Dimensional Effects on Fatigue Crack Closure in the Small-Scale Yielding Regime—A Finite Element Study," *Fatigue & Fracture of Engineering Materials & Structures,* Vol. 26, 2003, pp. 663-673.

[14] RoyChowdhury, S. and Dodds, R., "A Numerical Investigation of 3-D Small-Scale Yielding Fatigue Crack Growth," *Engineering Fracture Mechanics*, Vol. 70, 2003, pp. 2363-2383.

[15] RoyChowdhury, S. and Dodds, R., "Effect of $T_{...}$ stress on Fatigue Crack Closure in 3-D Small-Scale Yielding," *International Journal of Solids & Structures,* Vol. 41, 2004, pp. 2581-2606.

[16] McClung, R. C., "Finite Element Analysis of Specimen Geometry Effects on Fatigue Crack Closure," *Fatigue & Fracture of Engineering Materials & Structures,* Vol. 17, 1994, pp. 861-872.

[17] Sherry, A. H., France, C. C., "Goldthorpe, M.R., Compendium of $T_{...}$ Stress Solutions for Two and Three Dimensional Cracked Geometries," *Fatigue & Fracture of Engineering Materials & Structures,* Vol. 18, 1995, pp. 141-155.

[18] Larsson, S. G., Carlsson, A. J., "Influence of Non-Singular Stress Terms and Specimen Geometry on Small-Scale Yielding at Crack Tips in Elastic-Plastic Materials," *Journal of the Mechanics & Physics of Solids*, Vol. 21, 1973, pp. 263-277.

[19] Hom, C. L. and McMeeking, R. M., "Three-Dimensional Void Growth Before a Blunting Crack Tip," *Journal of the Mechanics & Physics of Solids*, Vol. 37, No. 3, 1989, pp. 395-415.

[20] Hom, C. L. and McMeeking, R.M., "Finite Element Analysis of Void Growth in Elastic-Plastic Materials," *International Journal of Fracture*, Vol. 42, 1990, pp. 1-19.

[21] McMeeking, R. M. and Hom, C. L., "Large Crack Tip Opening in Thin Elastic-Plastic Sheets," *Interna-tional Journal of Fracture*, Vol. 45, 1990, pp. 103-122.

[22] Nakamura, T. and Parks, D. M., "Three-Dimensional Crack Front Fields in a Thin Ductile Plate," *Journal of the Mechanics & Physics of Solids*, Vol. 38, No. 6, 1990, pp. 787-812.

[23] Yuan, H. and Brocks, W., "Quantification of Constraint Effects in Elastic-Plastic Crack Front Fields," *Journal of the Mechanics & Physics of Solids*, Vol. 46, No. 2, 1998, pp. 219-241.

[24] Kim, Y., Zhu, X. K., and Chao, Y. J., "Quantification of Constraint on Elastic-Plastic 3D Crack Front by the J-A_2 Three-Term Solution," *Engineering Fracture Mechanics,* Vol. 68, 2001, pp. 895-914.

[25] Fleck, N., "Finite Element Analysis of Plasticity-Induced Crack Closure Under Plane Strain Conditions," *Engineering Fracture Mechanics,* Vol. 25, 1986, pp. 441-449.

[26] McClung, R. C., and Sehitoglu, H., "On the Finite Element Modeling of Fatigue Crack Closure-2. Numerical Results," *Engineering Fracture Mechanics,* Vol. 33, 1989, pp. 253-272.

[27] Hughes, T. J., ''Generalization of Selective Integration Procedures to Anisotropic and Nonlinear Media," *International Journal for Numerical Methods in Engineering,* Vol. 15, 1980, pp. 1413-1418.

[28] Williams, M.L., "On the Stress Distribution at the Base of a Stationary Crack," *Journal of Applied Mechanics*, Vol. 24, 1957, pp. 109-114.

[29] McClung, R. C., Thacker, B. H. and Roy, S., "Finite Element Visualization of Fatigue Crack Closure In Plane Stress and Plane Strain," *International Journal of Fracture*, Vol. 50, 1991, pp. 27-49.

[30] Parry, M. R., Syngellakis, S. and Sinclair, I., "Numerical Modeling of Combined Roughness and Plasticity Induced Crack closure Effects in Fatigue," *Material Science in Engineering*, A291, 2000 , pp. 224-234.

[31] Gullerud, A. S, Koppenhoefer, K. C., Arun Roy, Y., Roychowdhury, S. and Dodds, Jr., R. H. "WARP3D—Release 14.2 Manual," Civil Engineering, Report No. UILU-ENG-95-2012, University of Illinois, 2003.

[32] Betegon, C. and Hancock, J. W., "Two Parameter Characterization of Elastic-Plastic Crack-Tip Fields," *Journal of Applied Mechanics, ASME*, Vol. 58, 1991, pp. 104-110.

[33] Solanki, K., Daniewicz, S. R., and Newman, J. C., "Finite Element Modeling of Plasticity-Induced Crack Closure with Emphasis on Geometry and Mesh Refinement Effects," *Engineering Fracture Mechanics*, Vol. 70, 2003, pp. 1475-1489.

[34] Wheeler, O.E., "Spectrum Loading and Crack Growth," *Journal of Basic Engineering, ASME*, Vol. 94, 1972, pp.181-186.

[35] Newman, J.C., "Prediction of FCG Under Variable Amplitude and Spectrum Loading Using a Closure Model," *ASTM STP 761*, 1982, pp. 255-277.

[36] Yisheng, W. and Schijve, J., "Fatigue Crack Closure Measurements on 2024-T3 Sheet Specimens," *Fatigue & Fracture of Engineering Materials & Structures*, Vol. 18, 1995, pp. 917-921.

Journal of ASTM International, June 2005, Vol. 2, No. 6
Paper ID JAI12003
Available online at www.astm.org

R. Sunder[1]

Fractographic Reassessment of the Significance of Fatigue Crack Closure

ABSTRACT: Experiments were performed on Al-alloy test coupons under specially programmed variable amplitude load sequences to assess crack closure as well as actual microscopic crack extension. Quantitative fractography of the fractures suggests that closure can account for only a fraction of observed load interaction effects. Much of the observed retardation may be attributed to the shielding effect of the overload plastic zone, which can occur even if the crack is fully open. The study also indicates that load sequence effects attributed to notch root stress-strain hysteresis can occur only if closure is absent.

KEYWORDS: fatigue crack growth mechanisms, thresholds, residual stress effect, crack closure

Introduction

Variable amplitude fatigue is influenced by a number of load interaction mechanisms including crack closure, residual stress, crack-tip blunting, and crack-front incompatibility [1]. Of these, fatigue crack closure [2] has been researched most widely. Being amenable to numerical simulation, it appears to be the natural choice for modeling variable-amplitude crack growth [3–6]. Yet, even after some thirty years of research on crack closure, there is a lack of clarity about its role in the fatigue process and, surprisingly, even about its very definition and measurement. The lack of a strict definition and standardized practice for measurement that would tie up with empirical results may explain why the phenomenon is subject to so much interpretation and associated controversy [7].

This paper describes two experiments that were specially designed to isolate closure-related effects from those that operate quite independently of it. Fractographic evidence from these experiments provides quantitative data on both crack closure as well as actual fatigue crack extension under the different cycle magnitudes. By comparing relative crack extension under different cyclic loading steps against actual effective load range, in these very steps the relative significance of closure is brought out. This study also investigates the potential connection between load sequence effects associated with stress-strain hysteresis in notch fatigue and crack closure.

Experimental Procedure

Figure 1 describes the "Closure" load sequence used in the first experiment. It consists of two sets of ten loading steps, the ACE-steps and the BDF-steps as shown in the figure. The cycle counts were selected to ensure that crack extension per step will be negligible by comparision to

Manuscript received 30 October 2003; accepted for publication 23 August 2004; published June 2005. Presented at ASTM Symposium on Fatigue and Fracture Mechanics: 34th Volume on 19–21 November 2003 in Tampa, FL; S.R. Daniewicz, J.C. Newman, Jr., and K-H. Schwalbe, Guest Editors.

[1] BiSS Research, 41A, 1stA Cross, AECS 2nd Stage, Bangalore 560 094, India.

ACE plastic zone size to ensure constant crack closure as determined by the extreme load excursions. Previous studies under constant maximum load have confirmed that as long as crack closure load exceeds applied minimum load, crack growth rate will not change with minimum load [8,9]. Thus, if S_{op} is at the level shown in Fig. 1, the four steps ACEG will cause equal crack extension, as will steps NPRT. Conversely, one can determine crack closure level from the number of equally spaced striation bands observed on a fractograph. This was the underlying concept behind the so called fractographic closure measurement technique [8].

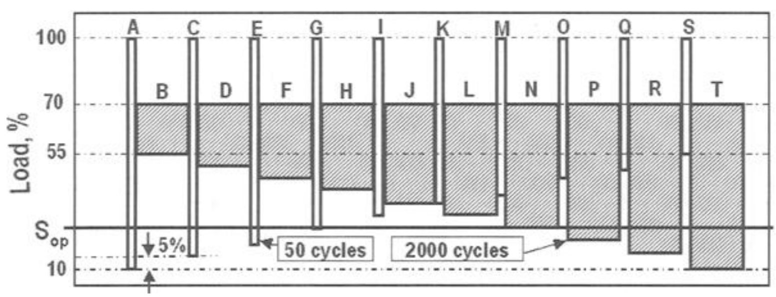

FIG. 1—*The "Closure" load sequence. Ten 50-cycle steps are applied at 100 % maximum load, with step-wise increment in minimum load from 10–55 %. These are interspersed with 2000-cycle steps applied at 70 % maximum load, with minimum load decremented as shown. If closure is constant and at the indicated level, one should observe four equally-spaced striation bands each, from the steps ACEG (100 %) and NPRT (70 %), where S_{op} >= S_{min}.and ΔK_{eff} = Const.*

A fatigue fracture surface obtained by repeated application to failure of the closure sequence will contain innumerable imprints of growth bands whose patterns can serve as quantitative references of actual local closure level. By merely counting *equally* spaced bands in a fractograph from one complete closure block, S_{op} is readily determined as the minimum stress in the step that produced the last equally spaced band. As shown in Fig. 1, the same number of equally spaced bands may be expected from both the ACE and BDF steps. Note that the measurements involved are relative and therefore do not rely on accuracy of actual growth rate estimates.

The objective of the first experiment was to investigate whether crack closure can indeed explain the difference in growth rate between steps A and T that are at different maximum load levels. The process to make this assessment is explained in the next section. The experiment was performed on a 6.4 mm thick, 25 mm wide 2024-T451 C(T) specimen that was cycled to fracture under repeated application of the closure sequence. One hundred percent load corresponds to 2 kN. In view of the substantial difference in crack driving force between alternating steps, no markers were necessary to identify striation bands. Also, direction-reversal of step-to-step minimum load change in the alternating steps precluded potential ambiguity in identifying individual striation bands.

The second experiment was on a 10 mm thick, 40 mm wide 2014-T6511 C(T) specimen with a 10 mm diameter keyhole notch aligned to a/W = 0.5. This experiment was designed in search of a tangible fracture mechanics explanation for the well-known load sequence dependency of notch root fatigue [10]. Notch fatigue analysis based on the local stress strain (LSS) relates fatigue damage to sequence-dependent, hysteretic variations in notch-root (local) mean stress. The "Embedded" load sequence as described in Fig. 2 was designed to verify this hypothesis from a fracture mechanics viewpoint. The load sequence was repeated at P_{max} = 7.5 kN until crack formation and growth to fracture, giving an opportunity to fractographically track the fatigue process from its early stages. From crack closure considerations, growth rate in Steps 1–5 should be identical if minimum load in the steps exceeds closure level. Higher closure levels were expected close to the notch root due to local tensile yield that leaves compressive notch-root residual stresses and thereby reduces local stress ratio [9].

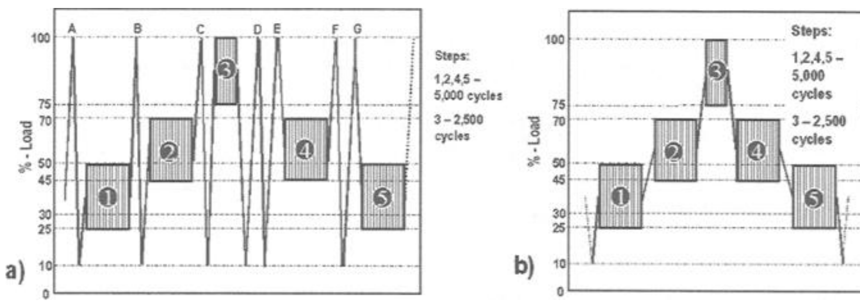

FIG. 2—*The "Embedded" load sequence. Five steps of identical range (25 %) are applied at different mean load levels. Markers A–G demarcate striation bands. They also enforce sequence sensitivity by embedding steps into the rising or falling half of the major load cycle as indicated in (b). Mean load levels were selected to cause partial long crack closure in Steps 1 and 5, while leaving 2, 3, and 4 fully open.*

For both experiments, Al-alloys were selected based on prior experience with closure measurements. Also, these alloys are suitable for quantitative fractography [11,12]. Specimen thickness was sufficient to avoid crack face rubbing from Mode III component. The test specimens were cycled to fracture under repeat application of the sequences shown in Figs. 1 and 2. The applied load level was selected to induce growth rates down to near-threshold values, which are the focus of this study. Step duration was designed to ensure clear definition of striation bands from individual steps. At the same time, sequence duration was selected to render crack extension in a single step negligible by comparison to monotonic plastic zone size. The number of steps was selected to keep crack increment small enough to neglect stress intensity variation. Thus, growth band comparison within a sequence may ignore crack size-sensitive variation in stress intensity.

Quantitative Fractography

Quantitative fractography based on striation bands rather than on the spacing of individual striations offers the advantage of vastly improved resolution because growth rate is given by the ratio of band spacing to cycle count. It is important to note that discernible band formation does not require discernible striation formation from individual cycles, but rather it relies on change in overall fracture morphology with growth rate. This permits the study of fatigue kinetics down to near-threshold growth rates using high-resolution electron fractography.

Crack extension, Δa, over cycles, n, may be expressed as follows:

$$\Delta a = n.\frac{da}{dN} = n.C\Delta K_{eff}^{m} = n.C(K_{\max} - K_{op})^{m} \tag{1}$$

where C and m are material constants in the Elber crack growth rate equation [2], K_{max} is maximum stress intensity, and K_{op} is crack opening stress intensity. If $K_{op} < K_{min}$, the latter will replace it. Then, assuming crack closure is the sole load interaction mechanism in the closure sequence, the ratio of striation bands from steps T and A (see Fig. 1) is given by

$$\frac{\Delta a_T}{\Delta a_A} = \frac{n_T}{n_A}\left(\frac{K_{\max,T} - K_{op}}{K_{\max,A} - K_{op}}\right)^{m} \tag{2}$$

Equation 2 may be used to determine K_{op} through quantitative fractography of fractures obtained under two step loading as was proposed by McGee and Pelloux [13]. In our experiment however, closure is *directly* estimated from equally spaced striation bands as described above, a process that is quite independent of constant, m. Thus, the load sequence in Fig. 1 provides the means to independently determine *both* sides of Eq 2 on the premise that 'm' does remain a constant. It would then follow that any inequality in Eq 2 may be attributed to load interaction effects other than closure, which will in turn affect the ratio on the left side of Eq 2.

The ratio $\Delta a_T/\Delta a_A$ can be affected by a change in the numerator, the denominator, or in both. Step A immediately follows Step T during the cyclic repetition of the closure sequence. As S_{max} in step T is 30 % less than in the ACE steps, the crack must grow in a plastic zone that is about two times greater than under constant amplitude conditions. On the other hand, Step A will see a transitional effect only during the first cycle, because the cyclic plastic zone will be several times larger than the cyclic plastic zone in step T. The remaining 49 cycles (98 %) of the load cycles in this step will see the same cyclic and plastic conditions as they would under constant amplitude loading. Also, they will see the same closure level. Therefore, one may assume that the denominator (Δa_A) remains unchanged and that any inequality in Eq 2 may be corrected by a retardation factor, k_{ret}, which accounts for retardation in step T *unaccounted* by closure:

$$k_{ret} = \frac{n_T}{n_A}\frac{\Delta a_A}{\Delta a_T}\left(\frac{K_{\max,T} - K_{op}}{K_{\max,A} - K_{op}}\right)^{m} \tag{3}$$

If $k_{ret} = 1$, it would follow that Eq 2 is valid with all retardation effects accounted for by closure. $k_{ret} = 4$ would indicate that real crack extension in step, T, is four times less than estimates based on closure. $k_{ret} < 1$ would indicate acceleration. All estimates in this study indicated retardation. k_{ret} estimates will be sensitive to the value of the exponent, 'm'. m = 2 is often used to correlate striation spacing in fractographic analysis of Al-alloys. A value of m = 2.65 was chosen for this study, being consistent with both fractographic as well as macroscopic growth rates for both materials studied, over the range 10^{-6} to 10^{-4} mm/cycle. Calculations were also made using m = 3.5 as an extreme possibility.

Results of Fractography and Analysis of Results

Fractographs from the two experiments appear as Figs. 3–13. Each fractograph includes a graphic imprint of the load sequence applied, along with an indication of at least one reference striation band and the corresponding step in the load sequence that caused it. This imprint can be used to cross-reference points of interest on the fractograph to actual load sequences in Figs. 1 and 2. The direction of crack growth is marked by a block arrow and is always from left to right.

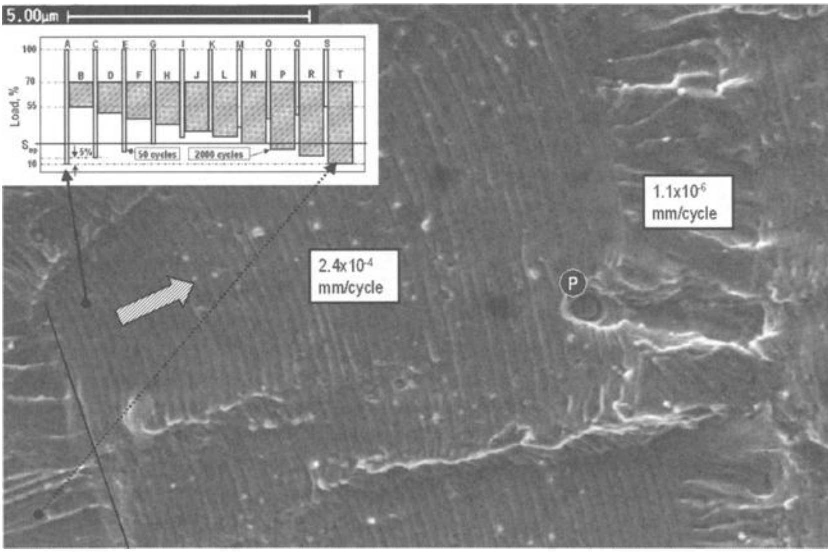

FIG. 3—*Striations in Step A of Closure sequence. The fifty striations starting from the line at left match the number of cycles applied. Note apparent lack of any transient associated with the switch from Step T to A, apart from possible jump in crack front during the first load cycle of step A. Note the faceted fracture morphology in Steps T and B at low growth rate. The banding action of A and C made it possible to track crack extension in B.*

Discernible growth bands from individual steps are seen on all the fractographs. Rare exceptions were a few R-T steps. The example shown in Fig. 5 illustrates how one may exaggerate crack extension under 'R' and 'T'. However, on closer scrutiny, the different fracture morphology associated with steps 'Q' and 'S' can be discriminated to gauge actual contribution to crack extension. Individual striations were clearly visible only at growth rates in excess of approximately 5×10^{-5} mm/cycle (see Fig. 3). The ability to observe individual striations permits detection of cycle-by-cycle transients. For example, Fig. 4*b* shows crack extension in excursion F to be twice that of the following load excursion, G, even though both peak loads are the same, and tensile half-cycle range in F is in fact much *less* than in G.

Both the 2024 as well as the 2014 Al-alloy fractures show the presence of secondary particulates on the crack path. Their location is marked by an encircled 'P'. As indicated in earlier work [14], secondary particulates do not distort local growth rates as long as the latter are much less than average particulate size, which is of the order of 0.005 mm (see for example, Figs. 6–9). All the fractographs presented in this study were obtained at low growth rates where quasi-static crack extension from particulate fracture is negligible. Actual growth rates are indicated on selected growth bands and range from 10^{-7} (as in Figs. 6 and 8) to 10^{-3} mm/cycle (as in Fig. 4b).

Closure Levels

Figure 6 shows a typical mid-thickness fractograph from the closure sequence. It indicates four equally-spaced striation bands from the ACE steps, corresponding to closure level of 25 %.

Similar fractographs were obtained over a wide range of growth rates and remain unchanged across the thickness to within 0.2 mm of either specimen surface (Figs. 7–9). Figure 10 shows a near-surface fractograph. This picture indicates an exceptionally high local S_{op}/S_{max} = 40 %. Most other surface locations indicated readouts of between 30–35 %. It is difficult to obtain near-surface fractographs with a high degree of clarity and definition. This may be due to rubbing, which is less likely to occur in the interior.

Most of the fractographs obtained from ACE steps in the mid-thickness region indicate closure level at 25 %. These estimates are consistent with previous experience using both fractography as well as near tip laser interferometry [11]. One may conclude that crack closure was of the order of 25 %, perhaps between 25 % and 30 %, given the marginal contribution of surface closure.

The number of equally-spaced striation bands from the BDF steps is strikingly inconsistent by comparison to the ones from the ACE steps. Hardly two of them appear to be equal, with the exception of Fig. 6 that indicates three and associated closure readout of 20 %. Previous investigations associated variation in closure levels with hysteresis in closure behavior, associated with the interaction of small, embedded cycles with the major cycle [11,15,16]. The sequence in Fig. 1 does not involve small embedded cycles, and yet it yields closure estimates from BDF steps that are neither self-consistent, nor comparable with those from the ACE steps. The inconsistency appears to be associated with reduced S_{max} in the BDF steps that may be causing unequal growth bands due to mechanisms other than closure. For lack of any other explanation, one may assume previous interpretation of hysteretic closure in long cracks to be flawed. Given the consistency of closure levels determined from the ACE steps, one may conclude that it indeed remains constant. The growth band spacing from the BDF steps, however, serves as a valuable input to assess actual retardation in the BDF steps given the overload effect from the ACE steps.

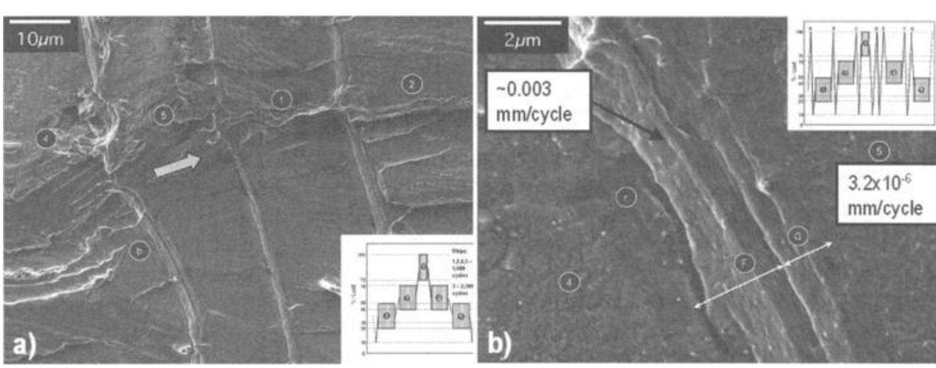

FIG. 4—(a) *Striation bands from Steps 5 and 1 of the embedded load sequence.* (b) *Zoomed-in view of area 'b' in* (a) *of striations caused by marker loads F and G between Steps 4 and 5 as seen in inset showing full load sequence. Area marked 'r' indicates signs of rubbing that may be due to Mode 2 sliding component between faces of non-propagating branched crack seen as crevice at the commencement of F.*

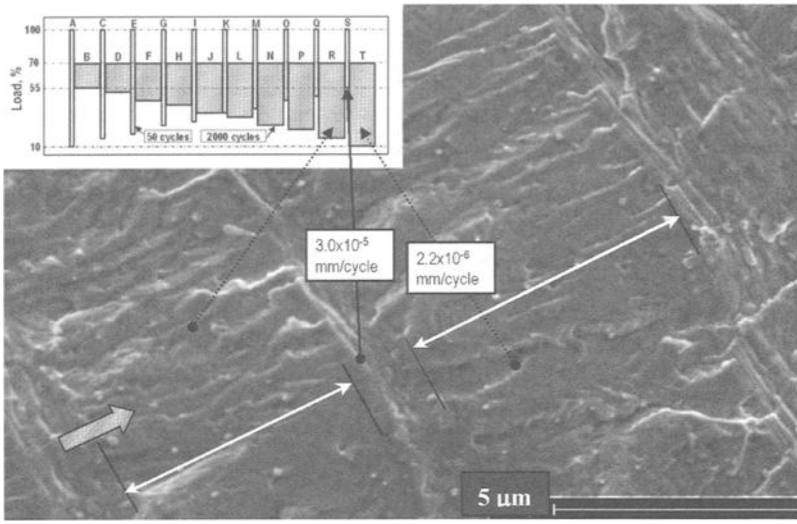

FIG. 5—*The width of striation bands from the BDF steps may sometimes seem to be larger than real as seen from the bands due to steps R and T above. The actual spacing is determined by closer comparison of neighboring bands and by discriminating between the fracture surface morphology due to the two distinctly different load levels.*

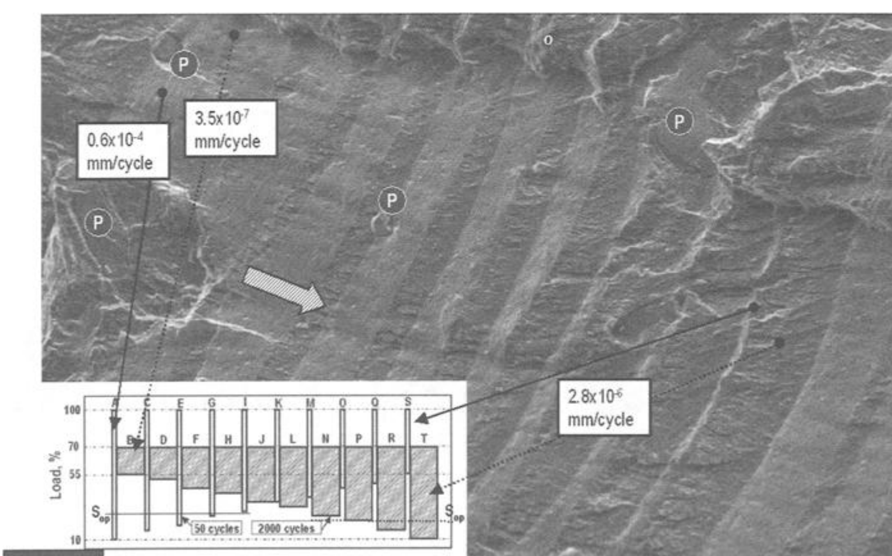

FIG. 6—*Typical fractograph from the mid-thickness area showing four equally-spaced ACE striation bands, indicative of 25 % closure level. Similar data were obtained across the thickness to within 0.2 of the specimen surface. 'P' indicates failed secondary particulates.*

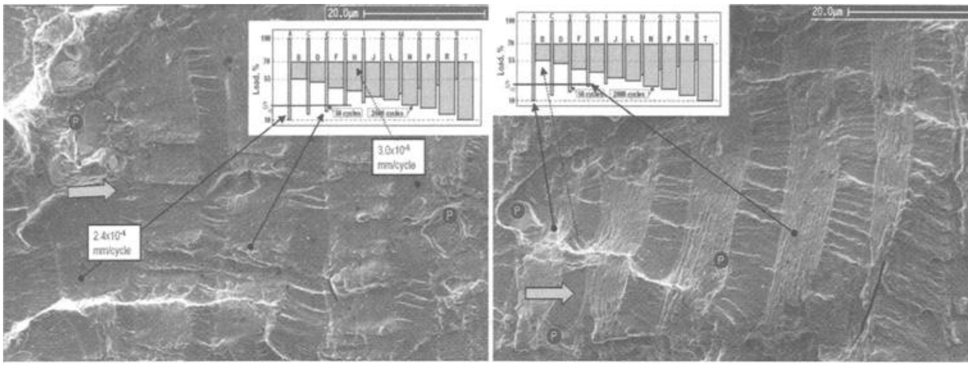

FIG. 7—*Zoomed-in fractographs from the vicinity of the location shown in Fig. 6. There appear to be four equally-spaced bands from the ACE load steps, suggesting consistency in closure level readouts of 25 %. Similar readouts were obtained in previous work [10].*

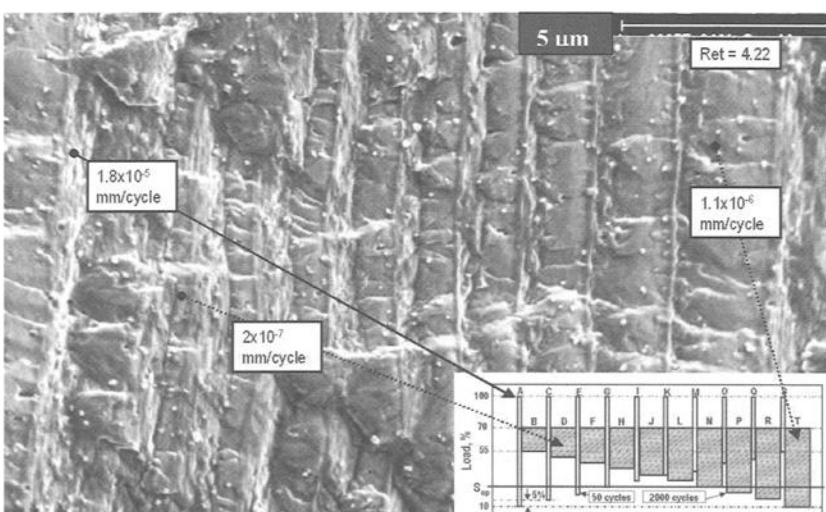

FIG. 8—*Lowest growth rate at which useful fractographs could be obtained. Four equal ACE bands are barely discernible at left. After accounting for crack closure at 25 %, growth rate in step 'T' is retarded by a factor of 4.22.*

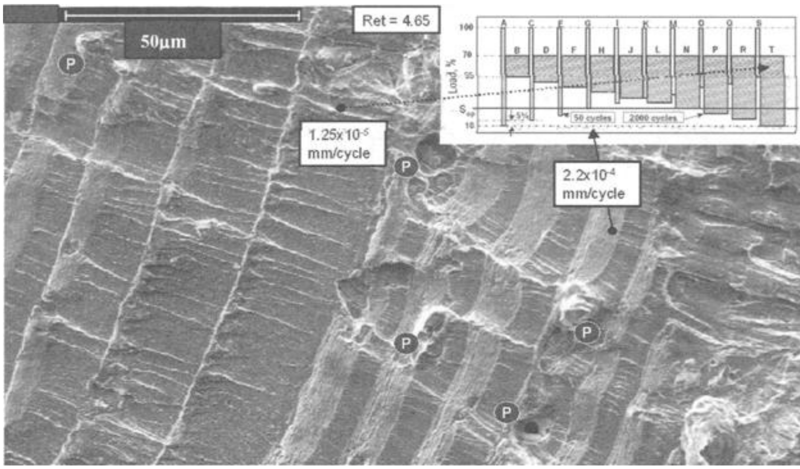

FIG. 9—*Highest growth rate at which useful fractographs could be obtained. Closure level (from ACE steps) is similar to the values in Fig. 8. Note the sizeable density of secondary particulates.*

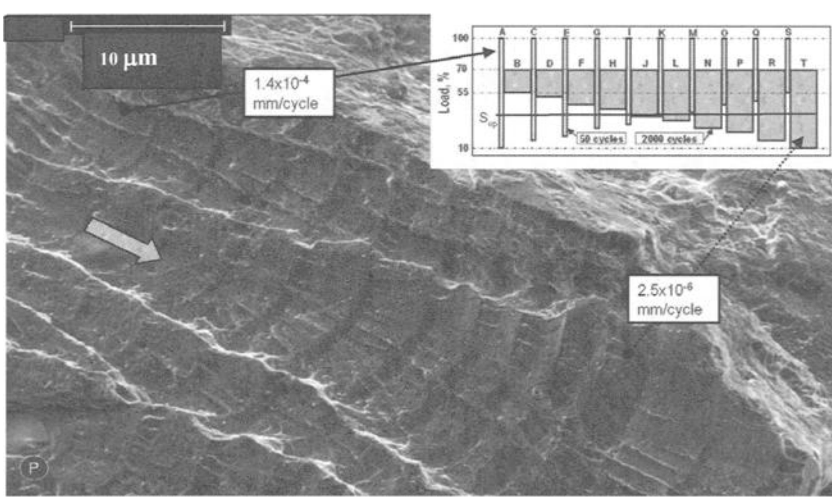

FIG. 10—*Typical near-surface fractograph indicating as many as seven equally-spaced striation bands from the ACE steps. This corresponds to* S_{op}/S_{max} *= 40 %. Such high values of closure were observed up to 0.15 mm from either surface.*

Noteworthy in all fractographs is the lack of typical ductile fatigue fracture features at near-threshold growth rates. The most visible marks under the steps 'R' and 'T' are features that run like river patterns oriented along the direction of crack growth. When near-threshold growth bands are short, the river patterns, being shorter, reveal the faceted nature of the fatigue surface, a terraced morphology associated perhaps with local preferential crystallographic orientation (see

Figs. 5 and 8). This is typical of near-threshold cracking in air. One cannot see any trace of crack extension given such morphology, but the intervening higher growth rate bands from 'Q' and 'S' confirm it was indeed fatigue.

Estimation of Closure and Retardation

Table 1 summarizes quantitative analysis of the fractographic evidence from the closure sequence using Eqs 1–3 for selected fractographs that cover the range of growth rates observed in the study.

TABLE 1—*Summary of quantitative fractographic analysis from closure sequence.*

No.	Source fract	da/dN, mm/cycle		S_{op}/S_{max}			Retardation Factor for Step T	
	Fig.	Step A	Step T	From ACE steps	Exponent, 'm' 2.65	3.5	Closure	Non-closure k_{ret}
	2	**3**	**4**	**5**	**6**	**7**	**8**	**9**
1	8	1.8×10^{-5}	1.1×10^{-6}	0.25	0.54	0.45	1.5	6.36
2	6,7	6.0×10^{-5}	2.8×10^{-6}	0.25	0.56	0.49	1.5	8.33
3	9	2.2×10^{-4}	1.3×10^{-5}	0.25	0.55	0.46	1.5	6.84
4	10	1.4×10^{-4}	2.5×10^{-6}	0.40	0.62	0.56	2.44	21.8

Column 2 in the table indicates the figure from which measurements were made. Columns 3 and 4 indicate measured crack growth rates under steps A (from ACE) and T (from BDF). These two steps being the largest at the two levels are taken as a reference. Columns 5–7 list estimated closure levels as a fraction of maximum load in the closure sequence (100 %). Column 5 lists estimates from equally-spaced striation bands in the ACE steps. One may conclude from the data in rows 1–3 that both growth rate and closure readouts remain similar across the thickness to within 0.2 mm of surface. For comparison, a single near-surface measurement is also included as row 4.

The ACE steps control both monotonic plastic zone size as well as wake compression. Therefore, it was assumed that closure from the ACE steps prevails across the BDF steps. Columns 6 and 7 list estimated closure level *required* to explain the measured ratio of growth rates in steps A and T. As this number is sensitive to the exponent, m, in the Elber equation, estimates are made for two values of 'm.'

One may note that if S_{op} estimates in columns 6 were indeed valid, *all ten* steps of the ACE and BDF steps ought to have yielded equally-spaced striation bands Ten equal bands would correspond to a closure level of 55 % (or more).

Column 8 carries estimates of closure-induced retardation in step T based on closure estimate from column 5. These values are negligible by comparison to actual retardation measured. Data in column 9 computed using Eq 3 show retardation that cannot be explained by closure. It may be argued that closure in steps A, T may not be the same. For this to be meaningful, *absolute* closure level in the BDF steps would have to be substantially greater than in the ACE steps, which appears implausible, considering that maximum load in the BDF steps is actually *less* by 30 % in comparison to the ACE steps. Conversely, assuming closure estimates from the ACE steps are valid, crack growth in step T ought to have been about eight times greater.

Finally, the analysis assumed that the ACE steps did not see any acceleration. If they did, suitable allowance would have be made to reduce estimated "closure-unrelated" retardation in the BDF steps. However, the absence of any sign of transient behavior associated with load change discounts such a possibility. This is underscored by the even striation spacing seen in Fig. 3, obtained at the high end of growth rates. Plastic zone size increases as a linear function of crack size, while growth rate increases by a larger power function. It would follow that if transients are not seen at the high end of growth rates, it is even less likely they can occur at lower rates.

The question remains as to what caused the "unaccounted" retardation listed in column 9 of Table 1. Acceleration and retardation occur due to a synergy of multiple load interaction mechanisms [1]. We now proceed to consider potential candidates.

Crack front incompatibility [1] is an unlikely factor. None of the fractographs show any sign of crack branching, blunting, or change in fracture plane. This does not come as a surprise because the closure sequence was *designed* to avoid crack front incompatibility and branching by restricting the difference in maximum load of the ACE and BDF steps to 30 % and also by restricting the study to low growth rates.

Crack tip residual stress is the other major load interaction mechanism. The ACE steps leave behind a plastic zone that is about twice the size of the monotonic plastic zone due to the BDF steps (given as square of ratio of maximum loads). The larger plastic zone may be acting as a shield of compressive residual stress to retard crack growth in the BDF steps. Fractographic evidence from the second experiment under the embedded load sequence described in Fig. 2 appears to confirm this possibility.

Crack Growth under the Embedded Load Sequence

Load levels in the Embedded load sequence used for the second experiment (Fig. 2) were designed to address unanswered questions from the first experiment. In this sequence, crack growth is primarily driven by three steps of equal range (25 % of maximum load), embedded into a major cycle at $R = 0.1$. Step 3 is "tagged" to maximum load (100 %), while the other two are embedded at distinctly different mean loads, once onto the rising major half cycle (Steps 1 and 2) and once again onto the falling half (Steps 4 and 5). Additional major cycles are applied as required to enforce the required embedding sequence (of smaller cycles into the rising or falling half of the major cycle) and also to serve as markers between steps. This is described by Fig. 2*a* and is excluded from the schematic in Fig. 2*b*. Step 3 carries 2500 cycles, while Steps 1, 2, 4, and 5 contain 5000 cycles. This was to account for potential accelerated growth at highest mean load. The other four steps were of the same duration for ready assessment of relative growth rate.

Figure 4 highlights the significance of the major half cycles and their role as markers, as well as the substantial cracking caused by them. Their overall contribution to crack extension is negligible, however, because of the much larger cycle count of embedded Steps 1–5. The markers essentially enforce sequence-sensitive hysteretic local mean stress variation within the cyclic plastic zone. Previous experiments on notched coupons had indicated closure level of up to 50 % at the notch root due to local compressive residual stress from tensile yield in the first major cycle [9,12]. Compressive residual stresses bring down *local* stress ratio, leading to increased closure when seen in terms of *applied* load. However, the tension-tension stress magnitude is not sufficient to cause notch root *reverse* yield. As the crack grows away from the notch root, closure levels drop down to long crack levels. The position of Steps 1, 2, 4, and 5 was selected to enhance sensitivity of relative growth rate to closure. Thus, in the event Steps 2 and 4 were even partially closed, Steps 1 and 5 would likely be fully closed. Finally, Step 3 is always likely to be closure-free.

Figure 11 shows the fatigue fracture surface from the failed specimen. The left extreme of Fig. 11*a* is the key-hole notch edge where the fatigue crack originated. The region encircled 'b' in Fig. 11*a* appears as a zoomed-in macro in Fig. 11*b*. Each distinct band on this picture represents crack extension over a single application of the embedded sequence. Figure 11*c* shows the zoomed-in notch root area marked as 'c' in Fig. 11*b*. This area appears to have formed by static rupture of a ligament that may have carried the crack formation site on a different plane. The initial 0.04 mm of crack growth is therefore not visible. The first visible band marked 'd' corresponds to crack size 0.05 mm and appears as Fig. 11*d*. Striation bands corresponding to individual load steps in the sequence are marked on this picture. Load Steps 1 and 5 obviously did not contribute to any crack extension. This may be either because stress intensity range fell below threshold, or, because the crack was fully closed in these steps, indicating $S_{op}/S_{max} \sim 0.5$ as suggested in earlier work [9,12]. From considerations of closure, the latter applies, because the crack *did* grow in Steps 2–4 as confirmation that $\Delta K > \Delta K_{th}$.

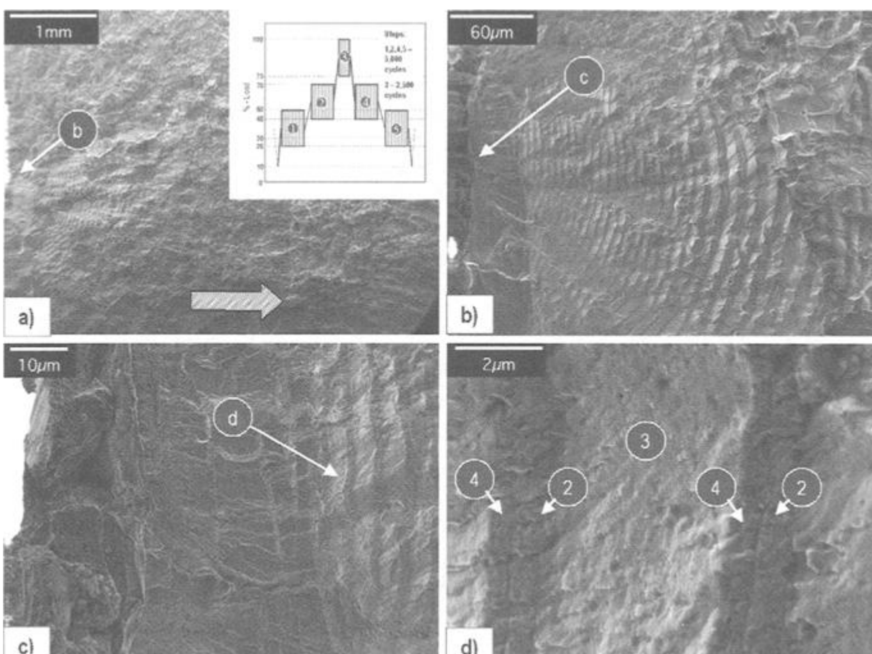

FIG. 11—(a) *Macro of fatigue failure showing origin on the notch edge at left. Inset shows schematic of load sequence.* (b) *Zoomed in view of region marked 'b' in* (a). (c) *Zoomed in view of region marked 'c' in* (b) *showing initial 0.04 mm of sheared ligament. Crack may have formed on a different plane at this location. First visible bands from Embedded sequence appear at region marked 'd'.* (d) *First visible striation band pattern from Embedded sequence. Crack was apparently fully closed in Steps 1 and 5. Equal spacing of Steps 2 and 4 appears to be proof of identical $S_{op}/S_{max} \sim 0.5$ on rising and falling half cycles. Crack depth: 0.055 mm.*

With increase in crack size, closure level progressively drops toward long crack levels. As seen in Fig. 12, two equally-spaced striation bands corresponding to Steps 1 and 5 indicate that the crack was partially closed to the *same* extent in both these steps. While Steps 2 and 4 produced equally-spaced bands in Fig. 11*d*, they are vastly different in Fig. 12. One may conclude that the crack was fully open in Steps 2 and 4 and there was also some *hysteretic* variation in *crack-tip* mean stress to cause a 3:1 retardation in Step 4 by comparison to Step 2. By implication, crack closure was much less than 40 %, which is the minimum stress in Steps 2 and 4. This effect is even more pronounced in Fig. 13, showing a fractograph at larger crack size that indicates 5:1 retardation in Step 4 by comparison to Step 2. This is the opposite of what one may expect from both closure as well as notch fatigue considerations. If this hysteretic effect was due to closure, it should have been more pronounced at the notch root due to increased local yield. For the same reason, the effect would have been more pronounced if it were related to *notch-root* stress-strain hysteresis, which again would be greatest at the notch root. The apparent paradox may instead be attributed to *crack-tip* stress-strain hysteresis as explained by the schematic in Fig. 14.

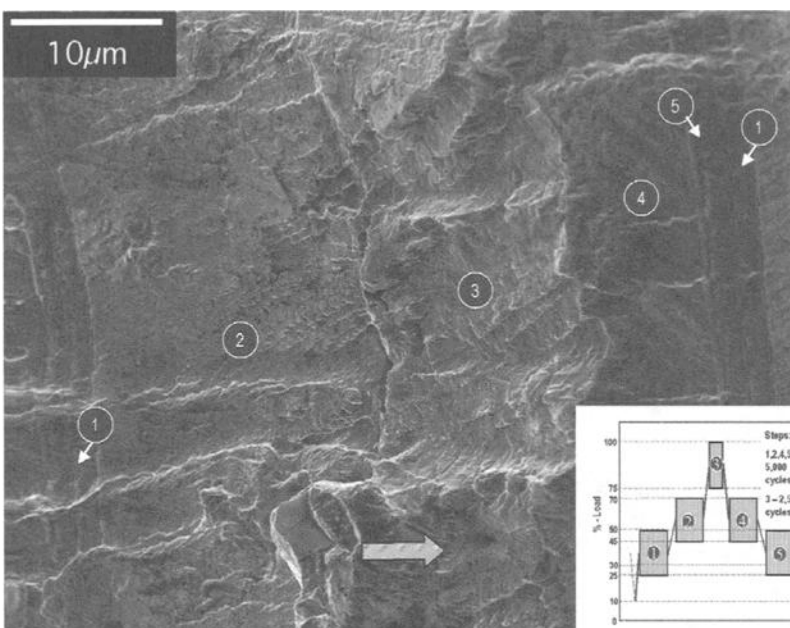

FIG. 12—*Fractograph at crack depth 0.47 mm showing crack extension from all five steps. Crack closure level has dropped at this point to leave Steps 1 and 5 partially open. Note equal spacing of 1 and 5 and retarded growth in Step 4 by comparison to Step 2. Growth rate in Step 3 exceeds that in Steps 1, 2, 4, and 5.*

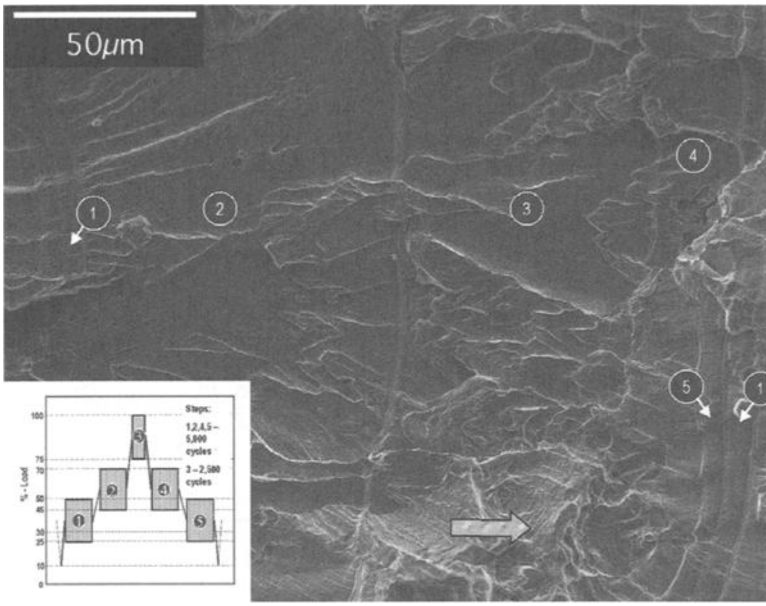

FIG. 13—*Full load block at crack depth 1.15 mm. 5:1 retardation in Step 4 by comparison to Step 2. Crack closure at this crack size may be close to long crack levels, but still in excess of 25 % judging from equally-spaced striation bands from Steps 1 and 5. Direct growth rate comparison is still possible, as striation bands 1 and 5 at left and right are of similar spacing.*

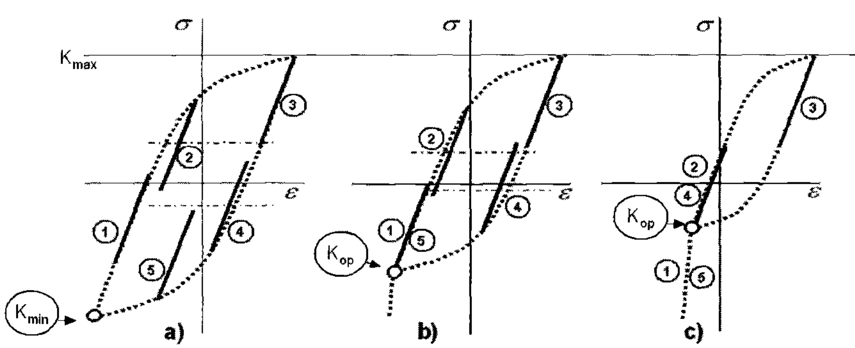

FIG. 14—*Schematic of near-tip stress-strain response to embedded load sequence with varying degree of crack closure. Numbers denote individual steps in the sequence. Closure truncates near-tip stress-strain loop from below. Partial closure of Steps 1 and 5 in (b) makes these two steps cease to be sequence sensitive unlike (a), where Step 1 is at a higher mean stress. Likewise, Steps 2 and 4 cease to be sequence sensitive in (c) due to the onset of closure. Note also that in (c), crack is closed in Steps 1 and 5 and therefore is arrested.*

Figure 14 represents a schematic of *near-tip* stress-strain response to an applied stress intensity range corresponding to the major cycle in the embedded sequence, but given different levels of closure. It is assumed that at a hypothetical point ahead of the crack tip, local stress and strain at a given K_{max} will be identical and independent of the extent of closure in the cycle. Then, local stress-strain hysteresis loop size will be determined by that portion of the load cycle, over which the crack is open. In this regard, Fig. 14*a* depicts the case of a fully open crack. Figure 14*b* shows the case of a crack that is partially closed in Steps 1 and 5 (as in Figs. 12 and 13), and Fig. 14*c* shows the case of partial closure in Steps 2 and 4 (as in Fig. 11*d*). Figures 14*b* and *c* illustrate a significant consequence of closure that has not been recognized thus far. Closure *forces* the lower tip of stress-strain hysteresis loops from *all* cycles that are partially (or fully) closed to coincide. Thus, if closure does occur, partially closed load cycles will no longer be sequence sensitive in terms of crack tip mean stress. Therefore, loops 1 and 5 coinciding in Fig. 14*b* may explain why striation bands from Steps 1 and 5 are equal in Figs. 12 and 13. Likewise, coincidence of loops 2 and 4 in Fig. 14*c* explains why bands due to Steps 2 and 4 are equally-spaced in Fig. 11*d*.

TABLE 2—*Summary of crack growth retardation in Steps 1, 2, 4, and 5 with respect to Step 3 of the embedded load sequence*

No.	Crack size	Step 3 da/dN	Retardation factor by comparison to Step 3 Ratio of da/dN in step to that in Step 3			Relative retardation in Step 4
	mm	mm/cycle	Step 1, 5	Step 2	Step 4	Step 4 / Step 2
	1	**2**	**3**	**4**	**5**	**6**
1	0.055	1.62×10^{-6}	No growth	12.93	10.59	0.818
2	0.193	4.47×10^{-6}	118.42	4.08	5.15	1.26
3	0.463	5.29×10^{-6}	19.94	1.41	2.94	2.08
4	0.778	9.53×10^{-6}	16.04	1.13	5.87	5.19
5	1.147	2.85×10^{-5}	25.09	1.63	6.57	4.02
6	1.515	2.69×10^{-5}	16.51	1.37	3.02	2.21

Table 2 summarizes fractographic estimates of crack growth rates and retardation factors, up to crack depth of 1.5 mm from the notch root and over an order of magnitude variation in growth rates. Column 3 in Table 2 is the ratio of growth rate in Steps 1 and 5 (deemed equal) to that in Step 3. Columns 3 and 4 represent similar estimates for Steps 2 and 4. Note that all retardation factors in columns 3–5 are estimated as ratio of growth band to that from Step 3. This factor includes potential retardation from closure as was obviously the case in column 3. As Steps 2 and 4 are identical, but embedded on opposite halves of the major load cycle, their striation spacing ratio appears in column 6 to indicate relative retardation in Step 4 with respect to Step 2.

Steps 1 and 5 were partially closed, leading to substantial retardation in them. For the same reason, retardation in Steps 2 and 4 is also substantial (see row 1). In the other rows, relative retardation in Step 4 with respect to Step 2 (column 6) provides a measure of the stress-strain hysteresis effect. If this ratio is large, it indicates that crack growth in embedded cycles is highly sequence sensitive. Note the trend for the ratio to increase up to a crack depth of 0.78 mm, followed by a decrease. Initial near-unity estimates are readily explained by high level of closure that kept these steps partially closed. Hysteretic variation in near-tip mean stress will be zero at the tips of the major hysteresis loop and maximum when the steps are embedded mid-way on the loop. This has been analytically shown through notch root stress-strain simulation [17]. It is indeed possible that closure levels had diminished at 0.78 mm to an extent that brought Steps 2 and 4 mid-way in the stress-strain hysteresis loop as illustrated in Fig. 14*b*.

Decrease in the ratio of growth rate in Step 4 to Step 2 with subsequent increase in crack size may be explained by decreasing sensitivity to hysteretic effects with increasing growth rate. Early fractographic studies under programmed loading confirm this trend at higher growth rates where individual striations are visible [18]. It was shown in these studies that striations before and after periodically applied cycles of higher magnitude appear identical, though the very first cycle of higher magnitude appears to be at a higher growth rate.

The crack closure phenomenon cannot explain retardation of fully open cracks. As indicated by estimates of retardation in Steps 2 and 4 for crack size over 0.4 mm, it would appear that a crack can see substantial retardation even if it is fully open. While retardation in Step 2 is not dramatic, it is substantial in the case of Step 4. Since Step 2 cycles are embedded on the rising half of the major load cycle, they will cause higher crack tip mean stress than those on the falling half.

The absence of striation bands due to Steps 1 and 5 in Fig. 11*d* and the extent of retardation at small crack size (column 3, rows 1 and 2 in Table 2) highlight the significance of fatigue crack closure. Unless a fatigue crack is open, it cannot grow, quite independent of applied stress intensity range, ΔK. While residual stress effects can significantly retard crack growth, closure can totally arrest the crack. This reflects a qualitative difference between the operative mechanisms of closure and residual stress.

Recent research demonstrated the potential connection between residual stress and environmental action [19]. Tests under programmed loading revealed retardation effects in steps at reduced load that disappeared when the test was performed in vacuum. A model to describe this behavior as a consequence of environment-induced crack tip cyclic embrittlement is the subject of another study [20].

A common thread running through all the fractographs presented is the shade of individual striation bands. A cursory scan of the fractographs presented would indicate that retarded crack growth is marked by darker shades. Unlike optical microscopy, scanning electron microscopy (SEM) is sensitive to the chemical composition of the surface being scanned. Indeed, less conducting media such as oxide layers tend to produce brighter shades on an SEM. It may follow that residual compressive stresses (or reduced tensile crack-tip stresses) induced by prior overloads (the ACE steps in the closure sequence) or near-tip stress-strain hysteresis (as in the embedded load sequence) control crack-tip surface chemistry and through it, determine instantaneous crack extension. The darker shades associated with retarded growth may then indicate inducement of near-vacuum conditions, due to which crack growth rate would be appropriately reduced.

While the residual stress effect in fatigue has been well characterized and used for over 130 years now, its operative mechanism has not altogether been understood. Early models of retardation, such as the Wheeler and Willenborg models, were based on this effect, but may have lacked conviction due to lack of a viable operative mechanism [21,22]. In contrast, Elber's closure model is amenable to analytical modeling apart from carrying a convincing operating mechanism that is backed by hard empirical evidence of closure. This may have been responsible for the attention and importance attached to the phenomenon. However, unlike other stress parameters, such as modulus or yield stress, closure lacks tangible and reproducible laboratory techniques for its measurement that could be implemented as standard practice. A combination of the above may have led to observed effects being attributed solely to closure, followed by the use of such inflated references for modeling purposes.

Conclusions

1. Quantitative electron fractography was used to assess correlation of measured crack closure under specially programmed load sequences with actual growth rates.
2. Fractographic evidence confirms the existence of crack closure and provides measurements that are consistent with other localized techniques such as laser indentation interferometry. However, closure appears to account for as low as 15% of the total retardation observed in programmed load experiments.
3. Fractographs show that load interaction associated with load-sequence sensitive crack-tip mean stress variation can occur only in those cycles where the crack is fully open. It follows that well-known hysteretic mean stress effects from notch root fatigue are conceptually incompatible with crack closure, unless it can be shown that closure is hysteretic.
4. The apparent absence of hysteresis in closure indicates that crack closure and crack opening load are synonymous. Conclusions made in previous studies (including work by this author) about the existence of sequence-sensitive hysteresis in long crack closure may be a case of misinterpretation associated with the wrong assumption that closure is the dominant load interaction mechanism.

Acknowledgments

This work was supported by the Materials & Manufacturing Directorate, Air Force Research Laboratory (AFRL/MLLN), Wright-Patterson AFB, OH 45433-7817 and BiSS Research, Bangalore, India. The assistance of Raghu Prakash in setting up the embedded load sequence test is deeply appreciated. SEM fractography at Air Force Research Laboratory (AFRL), WPAFB, OH was facilitated by Luanne Piazza. The author is grateful for discussions and support of colleagues at University of Dayton Research Institute and AFRL.

References

[1] Schijve, J., "Observations on the Prediction of Fatigue Crack Growth Propagation under Variable Amplitude Loading," *ASTM STP 595*, ASTM International, West Conshohocken, PA, 1976, pp. 3–23.

[2] Elber, W., "The Significance of Fatigue Crack Closure," *Damage Tolerance in Aircraft Structures, ASTM STP 486*, ASTM International, West Conshohocken, PA, 1971, pp. 230–242.

[3] Elber, W., "Equivalent Constant-Amplitude Concept for Crack Growth Under Spectrum Loading," *Fatigue Crack Growth under Spectrum Loads, ASTM STP 595*, ASTM International, West Conshohocken, PA, 1976, pp. 236–250.

[4] Newman, J. C., "A Crack-Closure Model for Predicting Fatigue Crack Growth under Aircraft Spectrum Loading," *Methods and Models for Predicting Fatigue Crack Growth under Random Loading, ASTM STP 748*, J. B. Chang and C. M. Hudson, Eds., ASTM International, West Conshohocken, PA, 1981 pp. 53–84.

[5] Aliaga, D., Davy, A., and Schaff, H., "A Simple Crack Closure Model for Predicting Fatigue Crack Growth under Flight Simulation Loading," *Durability and Damage*

Tolerance in Aircraft Design, A. Salvetti and G. Cavallini, Eds., EMAS, Warley, 1985, pp. 605–630.

[6] de Koning, A. U., "A Simple Crack Closure Model for Prediction of Fatigue Crack Growth Rates under Variable Amplitude Loading," *Fracture Mechanics, ASTM STP 743*, R. Roberts, Ed., ASTM International, West Conshohocken, PA, 1981, pp. 63–85.

[7] Vasudevan, A. K., Sadananda, K., and Loust, N., "A Review of Crack Closure, Fatigue Crack Threshold and Related Phenomena," *Materials Science and Engineering*, A188, 1994, pp. 1–22.

[8] Sunder, R. and Dash, P. K., "Measurement of Fatigue Crack Closure Through Electron Microscopy," *Int. J. Fatigue*, Vol. 4, April 1982, pp. 97–105.

[9] Anandan, K. and Sunder, R., "Closure of Part-Through Cracks at the Notch Root," *Int. J. Fatigue*, Vol. 9, pp. 217–222

[10] Morrow, J., "Fatigue Properties of Metals," *Fatigue Design Handbook*, Section 3.2, *Soc. of Automotive Engg.*, 1968.

[11] Ashbaugh, N. E., Dattaguru, B., Khobaib, M., Nicholas, T., Prakash, R. V., Ramamurthy, T. S., et al., "Experimental and Analytical Estimates of Fatigue Crack Closure in an Aluminum-Copper Alloy. Part I: Laser Interferometry and Electron Fractography," *Fatigue Fract. Engg. Mater. Struct*, Vol. 20, No. 7, 1997, pp. 951–961.

[12] Sunder, R., "An Explanation for the Residual Stress Effect in Metal Fatigue," *Fatigue 2002 – Proc. 8th International Fatigue Congress*, Stockholm, 2002, EMAS, pp. 3339–3350.

[13] Pelloux, R. M. N., Faral, M., and McGee, W. M., *ASTM STP 700*, ASTM International, West Conshohocken, PA, 1980, pp. 35–48.

[14] Sunder, R., Porter, W. J., and Ashbaugh, N. E., *Fatigue Fract Engng Mater Struct*, Vol. 25, 2002, pp. 1015–1024. [C

[15] Sunder, R., "Notch Root Crack Closure under Cyclic Inelasticity," *Fatigue Fract. Engng. Mater. Struct.*, Vol. 16, 1993, pp. 677–692.

[16] Sunder, R., Prakash, R. V., and Mitchenko, E. I., "Fractographic Study of Notch Fatigue Crack Closure and Growth Rates," *ASTM STP 1203*, ASTM International, West Conshohocken, PA, 1993, pp. 113–131.

[17] Sunder, R., "Rainflow Applications in Accelerated Cumulative Fatigue Analysis," *The Rainflow Method in Fatigue*, Y. Murakami, Ed., Butterworth-Heinemann, Oxford, 1992, pp. 67–76

[18] McMillan, J. C. and Pelloux, R. M. N., "Fatigue Crack Propagation under Program and Random Loads," *ASTM STP 415*, ASTM International, West Conshohocken, PA, 1967, pp. 505–535.

[19] Sunder, R., Porter, W. J., and Ashbaugh, N. E., "The Role of Air in Fatigue Load Interaction," *Fatigue Fract Engng Mater Struct*, Vol. 26, 2003, pp. 1–16.

[20] Sunder, R., "Fatigue as a Process of Brittle Micro-Fracture," *Fatigue Fract. Engng. Mater. Struct.*, accepted for publication, 2004

[21] Wheeler, O. E., *Journal of Basic Engineering, Trans. ASME*, March 1972, pp. 181–186.

[22] Willenborg, J. D., Engle, R. M., and Wood, H. A., "A Crack Growth Retardation Model Using an Effective Stress Concept," AFFDL-TM-FBR-71-1, Air Force Flight Dynamics Laboratory, WP-AFB, OH, 1971.

SESSION 2A: FATIGUE CRACK GROWTH THRESHOLDS I

Journal of ASTM International, September 2005, Vol. 2, No. 8
Paper ID JAI12025
Available online at www.astm.org

Mark A. James,[1] *Scott C. Forth,*[2] *and John A. Newman*[3]

Load History Effects Resulting from Compression Precracking

ABSTRACT: Compression precracking (CPC) has seen renewed interest as a possible alternative procedure for generating fatigue crack growth threshold data with minimal load history effects, but recent testing confirms results from the literature that compression precracking does induce load history effects through residual stresses that influence subsequent fatigue crack growth test data. Using the CPC method, specimens are precracked with both maximum and minimum compressive loads. Compressive yielding occurs at the crack-starter notch, resulting in a local tensile residual stress field through which the fatigue crack must propagate. Although the tensile residual stress field contributes to the driving force for precracking, it also introduces the possibility of history effects that may affect subsequent fatigue crack growth. The tensile residual stress field elevates the local driving force at the crack tip, promoting higher crack growth rates than would be expected from the applied loading. This paper presents three-dimensional finite element results and experimental data for compact tension specimens that characterize the load history effects induced by compression precracking. The analysis results indicate that for low tensile loading levels near the threshold region, the residual stresses cause the calculated crack tip driving force to increase from the applied driving force by 25 % or more. In addition, significant crack growth of about two times the estimated plastic zone size is needed to grow away from the residual stress field and reduce the calculated crack tip driving force to within 5 % of the applied driving force. Experimental results show that growth of about two to three times the estimated plastic zone size is necessary to establish steady growth rates under constant ΔK loading for the materials and loading levels evaluated. Constant ΔK testing following compression precracking will demonstrate when residual stress effects are no longer significant and will ensure consistent growth rates.

KEYWORDS: compression precracking, residual stress, threshold, finite element analysis

Nomenclature

a	crack length, mm
a_n	initial notch length, mm
B	specimen thickness, mm
C	normalized K gradient, $(1/K)\cdot(dK/da)$, mm^{-1}
E	Young's modulus, MPa
K	stress intensity factor, $MPa\sqrt{m}$
$K_{max\text{-}tip}$	maximum stress intensity factor at the crack tip, $MPa\sqrt{m}$
P	applied load, kN
P_{max}	maximum applied load, kN
P_{min}	minimum applied load, kN
r_n	notch radius, mm

Manuscript received 12 February 2004; accepted for publication 24 September 2004; published September 2005. Presented at ASTM Symposium on Fatigue and Fracture Mechanics: 34th Volume on 19–21 November 2003 in Tampa, FL; S.R. Daniewicz, J.C. Newman, Jr., and K-H. Schwalbe, Guest Editors.
[1] Staff Scientist, National Institute of Aerospace, 144 Research Dr, Hampton, VA 23666.
[2] Research Engineer, NASA Langley Research Center, Hampton, VA 23681.
[3] Research Engineer, U.S. Army Research Laboratory, Vehicle Technology Directorate, Hampton, VA 23681.

r_p plastic zone size, mm
R load ratio (minimum to maximum applied load)
S applied remote stress, MPa
W specimen width, mm
Δa crack growth, mm
ν Poisson's ratio
σ_o flow stress (average of yield and ultimate stresses)
σ_y yield stress, MPa

Introduction

Industry and regulatory agencies are developing damage tolerance methodologies for high-cycle fatigue components, such as the transmission system of a helicopter. The damage tolerance methodologies rely on fatigue crack growth (FCG) rate data to predict service life and inspection intervals. In the case of high-cycle fatigue, where many thousands of loading cycles are applied per flight hour, accurate FCG threshold data are essential because large numbers of cycles can accumulate in a very short time, causing significant crack growth even for cracks with a driving force very near the material threshold.

Fatigue crack growth threshold data are typically generated using a load reduction procedure, where the driving force is methodically reduced to a threshold while monitoring the crack growth rates. ASTM "Standard Test method for Measurement of Fatigue Crack Growth Rates," (E 647) contains two load reduction procedures for generating the FCG data: the constant K_{max} procedure and the constant load ratio procedure. The constant K_{max} procedure is not applicable for generating low load ratio threshold data and will not be discussed. The constant load ratio procedure holds the ratio of minimum to maximum load constant as the driving force is reduced to threshold. Recent experimental data and analytical results indicate that the constant load ratio procedure can produce non-conservative, high FCG thresholds [1] that could lead to the unsafe design of structures that experience high-cycle fatigue loading. Possible causes for these high thresholds are load history effects caused by the test procedure [1] and specimen size and configuration effects [2,3]. Load history effects can be caused by fatigue precracking at loads above the recommended level. For example, high precracking loads can cause remote crack closure, resulting in a plasticity-induced crack-tip shielding effect that reduces the crack driving force.

Forth, et al. [4] proposed using compression precracking (CPC) followed by constant load amplitude testing to generate FCG data, thus using a procedure that does not contain a load reduction component. During compression precracking, both maximum and minimum loads are compressive. The compressive loading causes yielding at the notch, which results in a tensile residual stress field [5,6]. The cyclic nature of the compressive loading leads to crack formation in the residual stress field and drives cracking through the residual stress field until the residual stresses relax and the crack arrests [5,7,8,9]. After precracking, the constant load amplitude testing allows the crack to grow using a monotonically increasing driving force starting at near threshold growth rates. However, recent test results on single edge notch bend specimens indicate that the residual stress field affects crack growth rates during the test following compression precracking [9].

The objective of this study was to further the understanding of the effects of the precracking induced residual stress state on the subsequent fatigue crack growth rate data. This understanding will lead to guidelines for using CPC to generate fatigue crack growth threshold data. Elastic-plastic finite element analyses with crack growth for a compact tension specimen were used to model the compression precracking process and to estimate the residual stress effects. Experimental procedures for a compact tension specimen were used to quantify the amount of crack growth necessary to minimize the residual stress effects under constant ΔK loading.

Background

Compression precracking (CPC) originated as a means of precracking materials that have low fracture toughness and would otherwise fail in fracture at typical tensile precracking loads [5]. The first precracking load cycle causes the material in the region of the notch to yield in compression, resulting in a tensile notch-tip residual stress field when unloaded [5]. Subsequent cyclic loading causes fatigue crack formation and growth from the notch-tip region. Figure 1 is a schematic of this yielding and growth process that occurs during compression precracking (CPC). Cyclic compressive loads are applied to the pins, as shown in Figs. 1*a* and 1*b*. The inset in Fig. 1*b* is a schematic of the stress-strain response during the cyclic loading. States (1) and (2) on the loading diagram correspond to states (1) and (2) on the stress-strain diagram and on the others schematics of Fig. 1. Figure 1*c* is a schematic of the yielding zones at the notch during the first load cycle, and Fig. 1*d* is a schematic of the associated stress distributions in front of the notch. At minimum load, indicated as loading state (1) in Fig. 1*b*, 1*c*, and 1*d*, the material yields in compression in front of the notch. As the load relaxes to unloaded state (2) the material at the notch reverse yields in tension to establish the forward monotonic tensile plastic zone. As the loading continues to state (3) the cyclic plastic zone is established inside the monotonic plastic zone, which through continued cycling causes fatigue crack formation and growth from the notch. Other than inside the monotonic tensile plastic zone, the cyclic behavior is essentially elastic after the first loading cycle. That is, after the first load cycle, cyclic plasticity occurs only inside the monotonic tensile plastic zone (2) and is adequately described with small scale yielding concepts [10]. The small scale yielding assumption can simplify analysis procedures.

As a crack starts to propagate through the residual stress field, the residual stresses relax, which in turn reduces the size of the cyclic plastic zone (Figs. 1*e* and 1*f*). As the residual stress field associated with the compressive plastic zone diminishes, the local driving force diminishes until the crack arrests at the crack growth threshold, even though the compressive cyclic loading continues [5,7]. Thus, when the crack arrests there is still a residual stress field operating on the crack, i.e., the driving force is greater than zero. This residual stress field will continue to affect any subsequent crack growth. The effect of the residual stress field may have significant implications when generating fatigue crack growth rate data immediately after compression precracking is stopped.

Aswath, et al. [11] showed through both experimental results and two-dimensional finite element analyses that the minimum load during compression precracking establishes the size of the compressive plastic zone. When the crack tip approaches the edge of their estimated compressive plastic zone, crack growth slows and arrests; that is, the amount of growth to crack arrest in compression is a function of the size of the compressive plastic zone. Aswath, et al. also showed that there are two components to the plasticity providing the driving force. First, they directly showed that the minimum compressive load determines the size of the compressive plastic zone extending in front of the crack. They demonstrated this by restarting a crack after crack-arrest using a single spike under-load with twice the cyclic compressive magnitude and

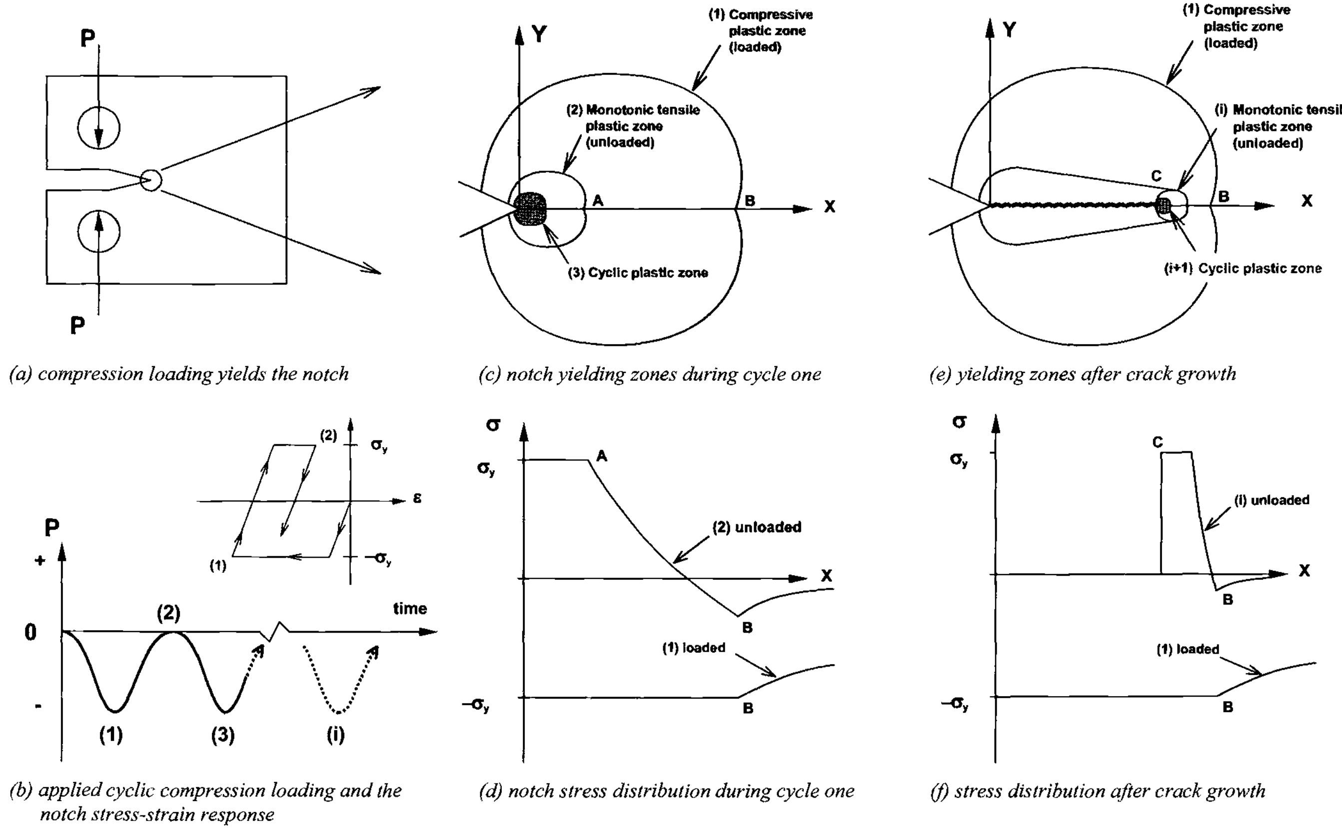

FIG. 1—*Yielding zones and stresses for compression precracking (after [8]).*

then returning to the (previously arrested) cyclic loading. The crack grew to the edge of the new, larger compressive plastic zone and again arrested. Second, they showed that the crack driving force is related to the magnitude of the residual stress field established during the first compressive load cycle. They accomplished this by showing that the crack growth rates are a direct function of the magnitude of the compressive loading.

Finite Element Analysis Procedure

Finite element analysis (FEA) was used to model the elastic-plastic deformation process around the notch for a typical compact tension specimen subjected to compression precracking. The FEA was also used to model the subsequent crack growth through the residual stress field caused by the compressively yielded material. This section gives details of the FEA model and analysis procedure.

The compression precracking fatigue crack growth process is modeled using elastic-plastic FEA, similar to analyses performed by other researchers [12,13,14,15]. The finite element code WARP3D [16,17] is used for all of the analyses herein. The model uses the eight-noded brick element with the Hughes $\bar{B}$ reduced integration scheme [18] to prevent locking. Analyses were performed for compact tension, C(T), specimens with two different thicknesses, B = 12.7 mm and B = 6.35 mm, each with a width of W = 76.2 mm, notch length of a_{notch} = 19.1 mm, and notch root radius of 0.191 mm. Nominal 2025-T6 aluminum alloy properties were used: Young's modulus, E = 68.95 GPa, Poison's ratio, ν = 0.3, yield stress, and σ_y = 386 MPa.

Two compression precracking (CPC) loading levels were analyzed: moderate loading at P_{min} = -13.3 N (K_{CPC} = -18.7 MPa$\sqrt{m}$) and high loading at P_{min} = -26.6 N (K_{CPC} = -37.4 MPa$\sqrt{m}$). Both cases had P_{max} = 0 during precracking. The stress intensities presented throughout this paper with the CPC subscript represent the compression precracking loading level assuming that the notch is a crack. Tensile loading followed compression precracking for both precracking load levels. For both cases, tensile loading levels were equivalent to threshold for an aluminum alloy, with K_{max} = 1.83 MPa$\sqrt{m}$ and R = 0.1.

Crack growth was modeled using a node release algorithm at the maximum load after each cycle [19], and crack closure was modeled using a rigid plane algorithm at the crack symmetry plane. Local crack tip stress-intensity factors (SIF) were calculated using the modified crack closure integral method [20,21,22]. All analyses used the same in-plane finite element mesh, shown in Fig. 2, and were scaled through the thickness for the different material thicknesses. All analyses used ¼ symmetry with 10 elements through the half thickness. The crack plane element size in the X direction (direction of growth) is L_e = 0.0127 mm (as shown in the inset of Fig. 2). These elements are sufficiently small to accurately predict yielding during compression precracking. Fifty to one hundred elements yielded in the crack plane in front of the notch, which provides a highly refined mesh for resolving the residual stresses during tensile loading. However, this analysis does not attempt to resolve crack closure for the tensile case at near threshold loading levels because approximately 1 or 2 orders of magnitude more mesh refinement would be required. The von Mises material model with a simple Ziegler kinematic hardening model was used for material behavior. For comparison, a single limited case was run using isotropic hardening.

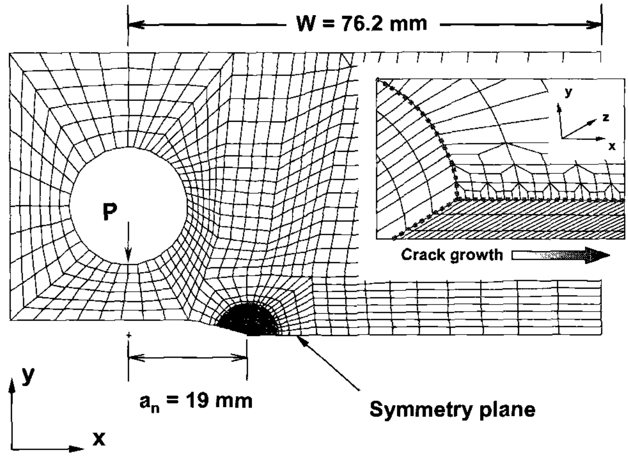

FIG. 2—*FEA mesh used for all analyses (scaled only for different thicknesses). Inset shows mesh detail near the notch including the notch root.*

Test Specimens and Experimental Procedure

This section describes the test specimens and experimental procedure used to support the FEA results and used to quantify the amount of crack growth necessary to establish steady-state growth rates under constant ΔK loading conditions after compression precracking. A secondary objective of the experimental results is to quantify the effects of precracking procedure on subsequent threshold test data.

All testing was performed on C(T) specimens. Two specimen sizes were tested: width, W = 50.8 mm with thickness, B = 6.35 mm and width, W = 76.2 mm with thickness, B = 12.7 mm. All specimens were machined from a 7050-T7451 aluminum alloy. Specimen notches were created using electro discharge machining (EDM). The smaller specimens have a simple EDM plunge cut notch with a diameter of 0.38 mm. The larger specimens have a notch angle of 30° and a notch root diameter of 0.38 mm, per ASTM E 647. In addition to compression precracking, baseline data were also generated using standard ASTM E 647 procedures, including standard tensile precracking, constant R load reduction to threshold, and constant K_{max} load reduction to threshold. All constant R load reduction tests used a normalized K gradient of C = -0.08 mm^{-1}, per ASTM E 647.

Procedure for Compression Precrack Specimens

Compression precracking was performed on the C(T) specimens at several load levels. First, compression loading at K_{CPC} = -38.5 MPa$\sqrt{m}$ was applied using standard clevises and pins for approximately 30 000 cycles, which produced crack growth slightly less than the estimated compressive plastic zone size. Cracking at the pin holes was not observed for this number of precracking cycles, but in a separate case, continued loading until near crack arrest caused crack initiation at the pin holes, thus rendering the specimen unusable for further testing. A lower load magnitude level of K_{CPC} = -18.7 MPa√m produced two cracks at the notch, as shown in Fig. 3. The two cracks grew from the notch at angles of approximately ±20° from the anticipated symmetry crack path. During subsequent tensile loading one crack eventually dominated to become the primary crack, and the other arrested. At slightly higher load magnitudes two cracks formed during precracking, but one dominated before precracking ended. At K_{CPC} = -28 MPa√m only one crack was visible from precracking. All data reported here were generated using clevises and pins for approximately 30 000 cycles. Compression precracking load levels were selected as the lowest load magnitude that still produced a single crack at the specimen notch. Constant amplitude loading was used for all compression precracking.

The occurrence of multiple cracks is likely associated with the distribution of plasticity in front of the notch and is likely a function of the notch radius. Tabernig and Pippan [9] developed a procedure to create a very sharp notch and were able to promote cracking at very low loads, and thus with minimal residual stress history.

After precracking, tensile loads were applied using constant ΔK and R = 0.1. Test load applied to the specimen was computer controlled, with either front-face clip gauges or back-face strain gauges used for compliance-based crack length measurements. Five to ten visual crack length measurements were recorded and used to calibrate the compliance-based data according to ASTM E 647. These data were used to ensure that the notch tip residual stresses did not influence the compliance based crack length measurements. After demonstrating stable constant ΔK growth rates, the smaller specimens were used for constant R load reduction tests, starting from the constant ΔK value.

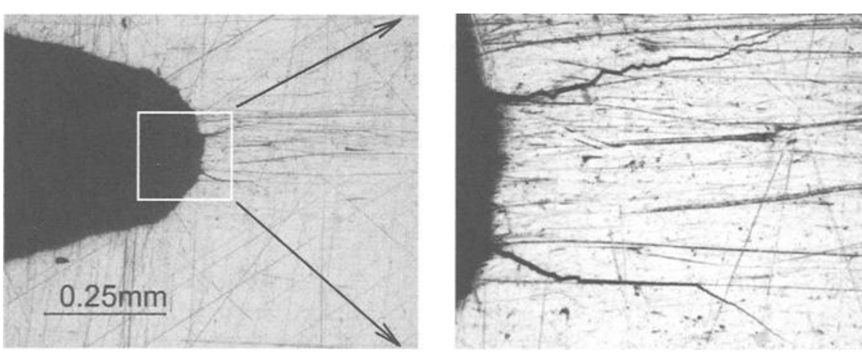

FIG. 3—*Image of multiple precracks caused by interaction between low magnitude compression precracking loads and the notch root geometry (K_{CPC} = -18.7 MPa√m with pin loading).*

Finite Element Analysis Results

Several compression precracking load magnitudes were analyzed to evaluate the size and shape of the compressive plastic zone and to evaluate the effects of the plastic zone on crack tip driving force. Figure 4 is a contour plot of von Mises stresses on the crack plane at the minimum load (K_{CPC} = -28.2 MPa√m, P_{min} = -10 KN) prior to crack initiation for the B = 6.35 mm case. Also included are lines showing the shape of the yielded region for four other lower load magnitudes. Table 1 shows load magnitudes, stress-intensity, and normalized stress-intensity for each of the five yield zones noted in Fig. 4. The stress intensities presented here assume that the notch is a crack. At low loads (Cases 1 and 2) the plastic zone is essentially uniform through the thickness. As the load magnitude increases, plasticity develops more rapidly near the surface, as indicated by the extended plastic zone size just below the surface in Fig. 4.

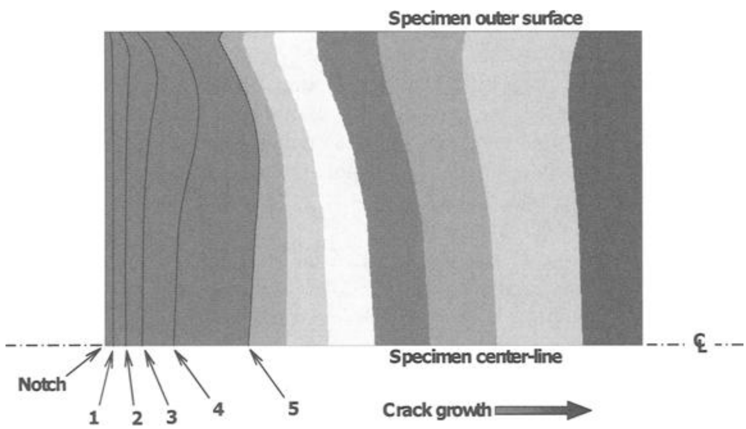

FIG. 4—*Von Mises stresses showing plastic zone size and shape on the crack plane for load level 5 and plastic zone size for four lower load levels (see Table 1).*

TABLE 1—*Loading levels for plastic zones in Fig. 4.*

Case	P_{min}	K_{min}
1	-2.7	-7.7
2	-4.5	-12.8
3	-6.3	-17.9
4	-8.1	-23.0
5	-10.0	-28.2

The FEA code WARP3D has a simple von Mises-Ziegler kinematic hardening model to approximate the cyclic material behavior commonly called the Bauschinger effect [6]. The model has two parameters: the hardening modulus and the hardening ratio. The hardening modulus is approximated here from a uniaxial stress-strain curve. The hardening ratio, β, varies from zero to one and allows a linear mix of isotropic and kinematic hardening [16]. Figure 5 shows analysis results of the crack tip opening load (fully open) versus crack growth for three levels of the hardening ratio. The open circles are for pure isotropic hardening (β = 1.0), and the upward pointing triangles are for pure kinematic hardening (β = 0.0). The two show markedly different results for the shortest amounts of crack growth, but after about Δa = 0.51 mm they converge to the same opening level. An intermediate value of β shows some sensitivity for the initial growth steps, but quickly merges with the isotropic (β = 1) opening levels. All subsequent results here assume kinematic hardening with β = 0.0, with the understanding that beyond a certain amount of crack growth, which is small relative to the compressive plastic zone size (r_p = 2.2 mm for this case), the isotropic and kinematic models produce the same opening results. Therefore, all subsequent results omit the initial transient for simplicity.

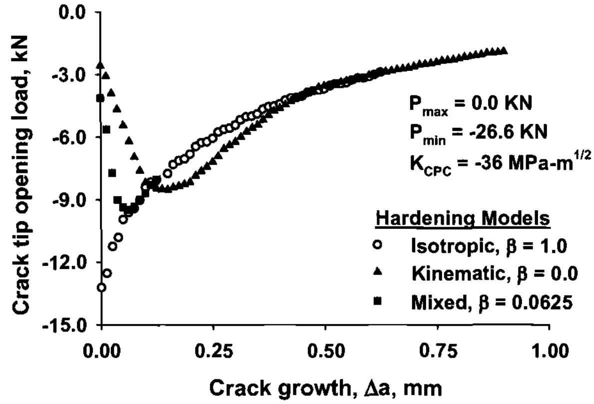

FIG. 5—*The effect of the kinematic hardening ratio, β, on the crack tip opening load.*

There are many ways to show the effects of the tensile residual stress field caused by the compressive loading. One way is to express the elevated loading as a mean stress effect, where the crack tip ΔK is consistent with the applied ΔK, but the residual stress field elevates both K_{min} and K_{max}, essentially altering the load ratio at the crack tip. A simpler and somewhat more objective way is to show the effects on the maximum stress intensity at the tip ($K_{max\text{-}tip}$). Figure 6 shows results for the high compression precracking load case where K_{CPC} = -37.4 MPa$\sqrt{m}$ (P_{min} = -26.6 N). First, cyclic compression was applied for about 1.27 mm. Then a constant tensile load amplitude was applied with the initial K_{max} = 1.83 MPa$\sqrt{m}$ at R = 0.1. The line in the constant amplitude section of Fig. 6 shows the calculated crack tip driving force caused by the combination of applied loading and residual stress effects from the compression precracking for the finite element analysis using node release at each crack growth step at maximum load. The filled circles in Fig. 6 show results for a superposition analysis, where the tensile loading stress-intensity factor was superimposed on the residual stress field results to obtain the superposition results. The problem is modeled using initial strains to provide the residual stresses and to allow load redistribution as the crack grows through the residual stress field (to determine the SIF due to only the residual stress field). The argument for using superposition is that the crack growth process is still essentially small-scale yielding inside the residual stress field [8]. But the problem must be modeled using initial strains to correctly capture the load redistribution with crack growth. The results in Fig. 6 support this argument and show that the superposition approach taken here captures the load redistribution that takes place as the crack grows through the residual stress field. Therefore, this simplified approach to modeling the fatigue crack growth through the residual stress field can be used while maintaining reasonable accuracy.

The results in Fig. 6 also show that there can be a significant difference in the maximum stress intensity caused by the residual stress field, compared with the applied loading, at least for the high compressive loading case. Figures 7 and 8 show similar analysis results for a more moderate loading case, K_{CPC} = -18.7 MPa$\sqrt{m}$ (P_{min} = -13.3 kN). Compared to the previous case, this case has compressive loads of one-half the magnitude and a plastic zone of one-quarter the size. Figure 7 shows the stress intensity at the crack tip caused by the residual stress field verses crack growth normalized by the calculated plastic zone size, r_p, at the centerline of the specimen

(r_p=0.432 mm). Even for this moderate precracking level, the residual stress field has noticeable effects.

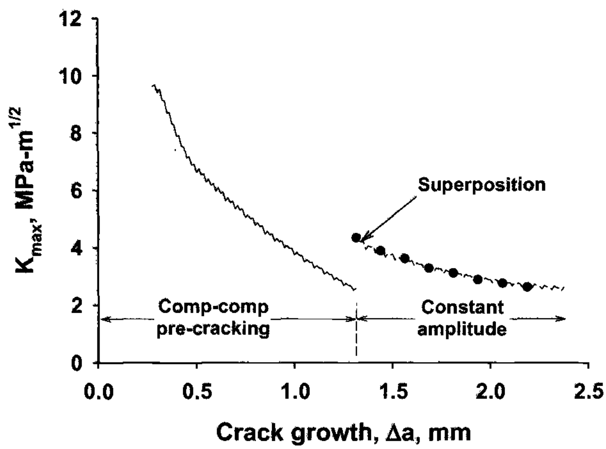

FIG. 6—*Calculated crack tip driving force during compression precracking (K_{CPC} = -38.4 MPa$\sqrt{m}$) and subsequent constant amplitude loading (K_{max} = 1.83 MPa$\sqrt{m}$, R = 0.1).*

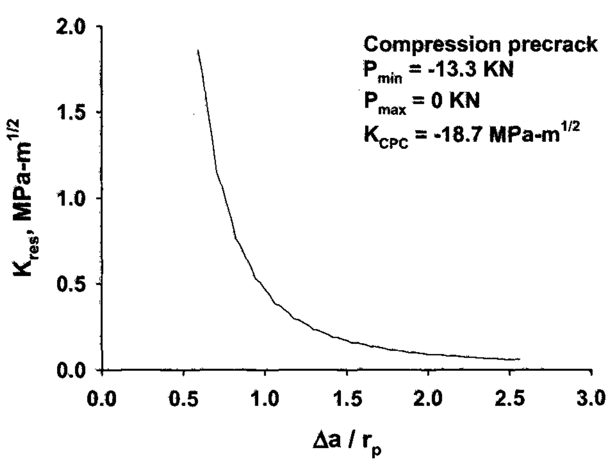

FIG. 7—*Calculated crack tip driving force caused by the residual stress field (P_{max} = 0).*

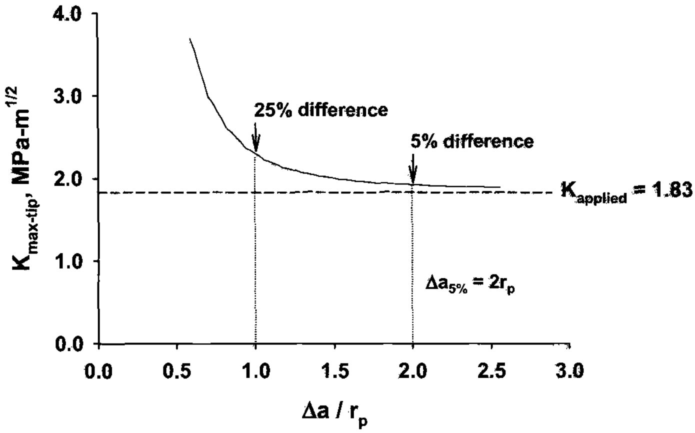

FIG. 8—*Total superimposed driving force of the residual stress component* (K_{CPC} = *-18.7 MPa√m) and the applied tensile load of* K_{max} = *1.83 MPa√m, R = 0.1.*

An essential component of fatigue crack growth testing is that the applied K_{max} be known to within a small tolerance. ASTM E 647 places tolerances on measured quantities (load, 2 %; crack length, 0.1 mm or 0.002 W, whichever is greater, etc.). However, the standard does not place tolerances on calculated quantities such as K_{max}. The residual stress field causes a difference between the actual and applied driving force. Based on the ASTM E 647 tolerances on load and crack length, it is not unreasonable to set a tolerance on K_{max} of 5 %. Based on this level of acceptable difference, the example in Fig. 7 is further investigated to determine the point where the K_{max} value with residual stress effects included is within acceptable limits of the applied value. Figure 8 shows the superposition results for the total K_{max} at the tip (K_{tip}) versus crack growth normalized calculated plastic zone size, r_p. The dotted line shows the applied K_{max} = 1.83 MPa√m.

The crack tip SIF differs from the applied value by about 25 % at the edge of the plastic zone. The vertical dashed line at $\Delta a/r_p = 2.0$ shows the crack growth required for 5 % difference in K_{tip} from the applied load. At this loading level, crack growth equal to about two times the compressive plastic zone size is needed to reduce the difference to the 5 % level. The residual stress field provides a non-proportional loading case to the applied tensile load, and thus does not scale with applied tensile load. In other words, the amount of normalized crack growth ($\Delta a/r_p$) necessary to reduce the K_{tip} to within 5 % of the applied level will be shorter for higher applied tensile loads. Figure 9 shows normalized crack growth necessary for a 5 % difference between K_{tip} versus applied K_{max}. The line shows the result for a range of applied loads, and the open circle shows the specific result from Fig. 8. As the applied tensile load increases, the effect of the residual stresses diminishes. However, at low values of driving force, which are necessary for threshold determination, the effects are significant.

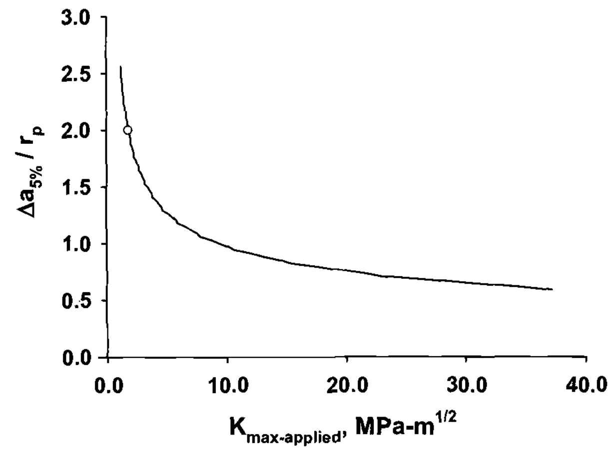

FIG. 9—*Amount of crack growth necessary to reduce the difference between $K_{max\text{-}applied}$ and K_{tip} to within 5 % for the precracking case of Figs. 7 and 8.*

Experimental Results

This section first describes the experimental results that were run to verify the finite element analyses. Then, experimental results are presented to compare the effect that the two precracking procedures have on the crack growth rate data. Figure 10 is a plot of experimental crack growth versus cycle count results for a loading case similar to the finite element analysis of the high loading case presented in Fig. 6. The specimens dimensions are W = 76.2 mm and B = 12.7 mm. The specimens were compression precracked at K_{CPC} = -38.5 MPa$\sqrt{m}$ and R = 20 (that is, both K_{max} and K_{min} negative) for approximately 400 cycles, which resulted in approximately 0.5 mm of crack growth. Then, tensile loading was applied at constant ΔK = 3.33 MPa$\sqrt{m}$, R = 0.1. Under constant ΔK loading, crack growth rates are expected to be a constant steady-state value, which is a straight line on a plot of crack length versus cycles. Figure 10 shows the results of two tests run with these conditions. (Note that the second test ended prematurely at about 500 000 cycles due to a computer problem.) The final seven data points of the first test were fit with a straight line to determine the average crack growth rate (slope of the data) as 7.6E-5 mm/cycle. The extended line shows that the initial growth rates are higher than steady state (data has a steeper slope), but gradually decrease. Here, steady state crack growth occurs at about Δa = 4.3 mm, which is more than two times the FEA estimated plastic zone size for this precrack condition. Thus, these test results agree quite well with the analysis results presented in Figs. 8 and 9, where crack growth of about twice the plastic zone size is required to reduce the difference in total K_{tip} to about 5 %.

Figure 11 is a plot of experimental crack growth versus cycle count results for a third test. In this case the smaller, thinner specimen was used (W = 50.8 mm, B = 6.35 mm). As depicted in Fig. 11, about 3.5 times the plastic zone size is needed to stabilized crack growth rates. The tensile loading level is lower than that for the case presented in Fig. 10 confirming the trends defined using the finite element analyses. A lower applied tensile load will require more crack growth to achieve steady-state.

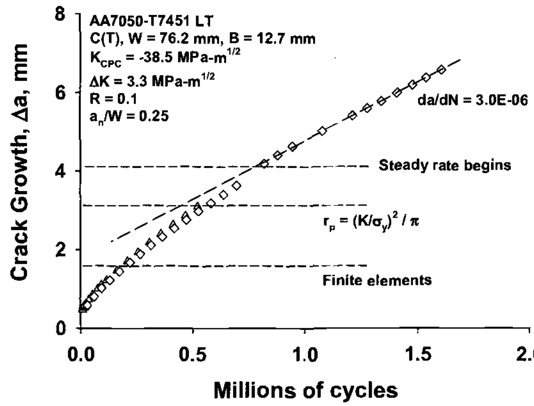

FIG. 10—*Crack length versus cycles showing the elevated growth rates caused by the residual stress field.*

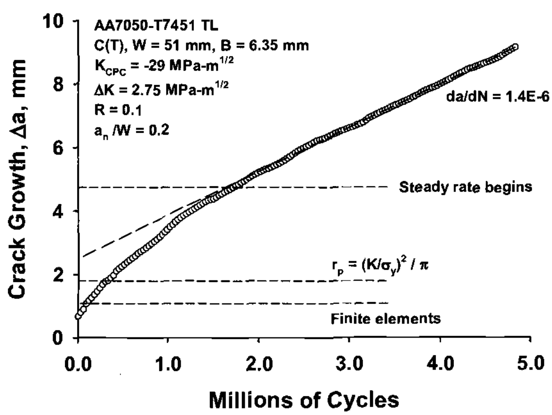

FIG. 11—*Crack length versus cycles showing the elevated growth rates caused by the residual stress field.*

Figure 12 is a plot of growth rate data that compares standard tensile precracking with the effects of compression precracking (CPC). The figure includes baseline data for reference purposes and includes data for crack growth parallel (LT) and transverse (TL) to the material rolling direction. The baseline data, which include a constant K_{max} test and a constant R test, form the basis for a ΔK_{eff} relationship used by Newman [1]. The ΔK_{eff} relationship models the crack as fully open, and all load ratio effects are modeled using plasticity induced closure [1]. The dashed line shows the predicted R = 0.1 curve based on plasticity induced closure. The open symbols are data for material in the LT orientation, and the dotted symbols are data for material in the TL orientation. The dotted triangle and dotted circle are data for compression precracking specimens that were run for significant constant ΔK to establish steady state, then had a standard load reduction test from the constant ΔK end point. The dotted square data are for traditional precracking.

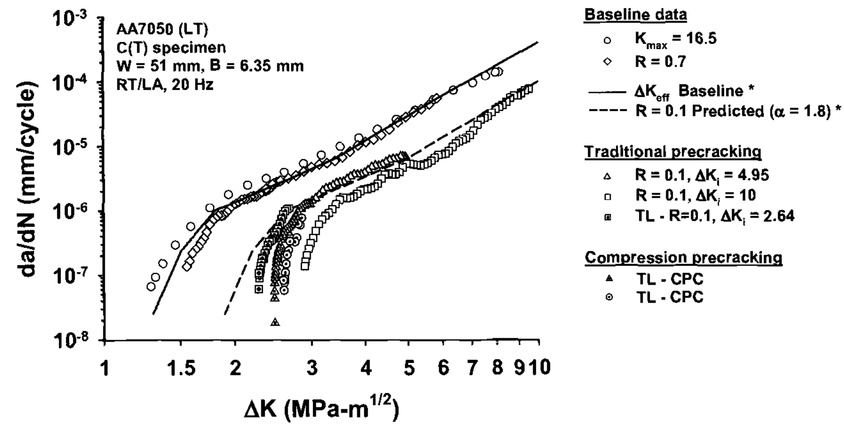

FIG. 12—*Crack growth rate data. (*Provided by Jim Newman using FASTRAN [2].)*

The results show that for this material there is essentially no difference in crack growth rates between data from traditional precracking and from compression precracking, as long as the CPC residual stress effects have been minimized, and as long as the testing procedure is the same. That is, the only major difference between the dotted traditional precracking data and the dotted compression precracking data is the precracking procedure. The open squares are data started at a higher initial ΔK level, and these data appear to show a higher threshold that may be attributable to starting level. Note that the initial growth rates are nearly an order of magnitude greater than suggested by ASTM E 647. More testing is required to characterize a relationship between starting level and threshold.

Discussion

The results in Figs. 6–11 show that compression precracking does introduce residual stresses. These residual stresses can cause crack growth rates that are significantly greater than the expected steady-state value for the applied loads. One might think that the effects of residual stresses would be limited to the yielded material in the plastic zone, because some stress relief is expected to occur as the crack propagates through this region. However, a significant volume of material yields above the crack plane, and this yielded material continues to influence crack growth well beyond the edge of the plastic zone. The experimental constant ΔK results show that the residual stresses affect the crack-tip driving force until the crack propagates nearly three times the notch-tip estimated plastic zone size.

In Fig. 8 the difference between the applied K_{max} and the tip K_{max} at the edge of the plastic zone is about 25 %. Experimental results from the literature [11] show that the amount of crack growth during precracking until crack arrest can be less than the estimated plastic zone size. This is because crack arrest is both a function of the residual stress field and the material threshold [7]. As a result, simply precracking until crack arrest occurs will minimize the effect of the residual stresses on subsequent testing, but it will not eliminate these effects.

Other factors such as K_{max} effects and closure development can affect crack growth rates following compression precracking. Tabernig and Pippan [8–10,23,24,25,26] have extensively studied transient effects for crack growth that begins with a fully open crack (created using either CPC or another technique). They have expended significant effort to exclude or minimize residual stress effects by annealing specimens after compression precracking and by creating extraordinarily sharp cracks. Their experimental results showed that cracks that initially grew at ΔK values below the threshold eventually arrested, and for ΔK values above the threshold cracks eventually achieved steady state growth rates consistent with long crack data. The primary conclusion of their work was that for initially-fully-open cracks a significant amount of crack growth is required to achieve steady state crack growth rates, even in the absence of notch-tip residual stresses, presumably due to the fact that crack closure development affects the crack driving force.

Summary

Compression precracking provides a means of creating a fully open sharp crack. The absence of crack closure allows subsequent crack growth at very low applied ΔK levels significantly below those normally possible from standard tensile precracking. This is possible because the compressive loading yields the crack starter notch, creating a tensile residual stress field at the notch root. However, the residual stresses caused by the compression precracking continue to affect crack growth rates even after the fatigue crack propagates beyond the edge of the compressive plastic zone. In addition, results from the literature show that steady-state crack closure can take a significant amount of crack growth to develop (on the order of 5 mm). Because of the combined effects of residual stresses and closure development, crack growth rate data generated after compression precracking must be interpreted carefully. Both of these effects, decreasing residual stresses and increasing crack closure, likely contributed to the transient decreasing growth rates observed under constant ΔK loading. Local closure measurements were not performed, so it is unclear which effect dominated the observed results. In this study about three times the plane stress plastic zone size is adequate to ensure steady state growth rate conditions. However, the duration of the transient is dependent on the compressive loading level, the subsequent tensile loading level, and on material characteristics such as yield behavior. Constant ΔK testing following compression precracking will demonstrate when residual stress effects are no longer significant and will ensure consistent growth rates.

References

[1] Newman, J.C., Jr., "Analyses of Fatigue Crack Growth and Closure Near Threshold Conditions for Large-Crack Behavior," *Fatigue Crack Growth Thresholds, Endurance Limits, and Design, ASTM STP 1372*, J.C. Newman, Jr. and R.S. Piascik, Eds., ASTM International, West Conshohocken, PA, 2000, pp. 227–251.

[2] Garr, K.R. and Hresko, G.C., III, "A Size Effect on the Fatigue Crack Growth Rate Threshold of Alloy 718," *Fatigue Crack Growth Thresholds, Endurance Limits, and Design, ASTM STP 1372*, J.C. Newman, Jr. and R.S. Piascik, Eds., ASTM International, West Conshohocken, PA, 2000, pp. 155–174.

[3] Haakon, O. L. and Stephens, R. R., "Effect of Geometry and Load History on Fatigue

Crack Growth in Ti-62222," *Fatigue Crack Growth Thresholds, Endurance Limits, and Design, ASTM STP 1372*, J.C. Newman, Jr. and R.S. Piascik, Eds., ASTM International, West Conshohocken, PA, 2000, pp. 175–191.
[4] Forth, S.C., Newman, J.C., Jr., and Forman, R.G., "On Generating Fatigue Crack Growth Thresholds," *International Journal of Fatigue*, Vol. 25, 2003.
[5] Hubbard, R. P., "Crack Growth under Cyclic Compression," *J. Basic Engineering*, Trans ASME 91, 1969, pp. 625–631.
[6] Hill, R., *The Mathematical Theory of Plasticity*, Oxford University Press, London, 1950.
[7] Suresh, S., "Crack Initiation In Cyclic Compression and Its Applications," *Engineering Fracture Mechanics*, Vol. 21, No. 3, 1985, pp. 452–463.
[8] Tabernig, B. and Pippan, R., "Resistance Curves For The Threshold Of Fatigue Propagation: The Influence Of Microstructure," *Proceedings*, *Fatigue-99*, X.R. Wu and Z.G. Wang, Eds., Beijing, P. R. China, 1999, pp. 1477–1482.
[9] Tabernig, B. and Pippan, R., "Determination Of The Length Dependence of the Threshold for Fatigue Crack Propagation," *Engineering Fracture Mechanics*, 69, 2002, pp. 899–907.
[10] Pippan, R., "The Growth of Short Cracks under Cyclic Compression," *Fat Fract. of Eng Mater Struct*, Vol. 9, No. 5, 1987, pp. 319–328.
[11] Aswath, P. B., Suresh, S., Holm, D. K., and Blom A. F., "Load Interaction Effects on Compression Fatigue Crack Growth in Ductile Solids," *Journal of Engineering Materials and Technology*, Vol. 110, July 1988, pp. 278–285.
[12] Newman, J.C., Jr, "Finite Element Analysis of Fatigue Crack Propagation – Including the Effects of Crack Closure," Ph.D. Thesis, Virginia Polytechnic Institute and State University, Blacksburg, VA, 1974.
[13] Newman, J.C., Jr, *Mechanics of Crack Growth, ASTM STP 590*, ASTM International, West Conshohocken, PA, 1976, pp. 281–301.
[14] McClung, R.C., "Finite Element Modeling of Crack Closure During Simulated Fatigue Threshold Testing," *International Journal of Fracture*, Vol. 52, 1991, pp. 145–157.
[15] McClung, R.C., "Finite Element Analysis Of Fatigue Crack Closure: A Historical And Critical Review," Fatigue '99: Seventh International Fatigue Congress, Beijing; China, 8–12 June 1999, pp. 2655–2660.
[16] Gullerud, A. S., Koppenhoefer, Roy, A., Roychowdhury, S., Walters, M., and Dodds, R. H., Jr., *WARP3D -- Release 14.0 Users Manual*, Department Of Civil Engineering, University of Illinois at Urbana-Champaign, Urbana, IL, 2002.
[17] Gullerud, A. S., Dodds, R. H., Jr., Hampton, R. W., and Dawicke, D. S., "Three-Dimensional Modeling of Ductile Crack Growth in Thin Sheet Metals: Computational Aspects and Validation," *Engineering Fracture Mechanics* 63, 1999, pp. 347–374.
[18] Hughes, T. J., "Generalization of Selective Integration Procedures to Anisotropic and Nonlinear Media," *International Journal for Numerical Methods in Engineering*, Vol. 15, 1980, pp. 1413–1421.
[19] McClung, R.C., "Analysis of Fatigue Crack Closure During Simulated Threshold Testing," *Fatigue Crack Growth Thresholds, Endurance Limits, and Design, ASTM*

STP 1372, J.C. Newman, Jr. and R.S. Piascik, Eds., ASTM International, West Conshohocken, PA, 2000, pp. 209–226.

[20] Rybicki, E.F. and Kanninen, M.F., "A Finite-Element Calculation of Stress-Intensity Factors by a Modified Crack Closure Integral," *Engineering Fracture Mechanics*, Vol. 9, 1977, pp. 931–938.

[21] Krueger, R., "The Virtual Crack Closure Technique: History, Approach and Applications," NASA/CR-2002-211628, ICASE Report No. 2002-10, May 2002. ASME, *Applied Mechanics Reviews*, in press.

[22] Smith S.A. and Raju I.S., "Evaluation of Stress-Intensity Factors Using General Finite-Element Analysis," *Fatigue and Fracture Mechanics: 29th Volume ASTM STP 1321*, T.L. Panontin and S.D. Sheppard, Eds., ASTM International, West Conshohocken, PA, 1998.

[23] Pippan, R., Berger, M., and Stuwe, H.P., "The Influence of Crack Length on Fatigue Crack Growth in Deep Sharp Notches," *Metallurgical Transactions*, Vol. 18A, 1987, pp. 429–435.

[24] Pippan, R., Stüwe, H.P., and Galos, K., "A Comparison of Different Methods to Determine the Threshold of Fatigue Crack Propagation," *Fatigue*, Vol. 16, 1994, pp. 579–582.

[25] Pippan, R., Plochl, L., Dlanner, F., and Stuwe, H.P., "The Use of Fatigue Specimens Precracked in Compression for Measuring Threshold Values and Crack Growth," *Journal of Testing and Evaluation, JTEVA*, Vol. 22, 1994, pp. 98–103.

[26] Tabernig, B., Powell, P., and Pippan, R., "Resistance Curves for the Threshold of Fatigue Crack Propagation in Particle Reinforced Aluminum Alloys," *Fatigue Crack Growth Thresholds, Endurance Limits, and Design, ASTM STP 1372*, J.C. Newman, Jr. and R.S. Piascik, Eds., ASTM International, West Conshohocken, PA, 2000, pp. 96–108.

Journal of ASTM International, July/August 2005, Vol. 2, No. 7
Paper ID JAI12023
Available online at www.astm.org

H. R. Zonker,[1] *G. H. Bray,*[1] *K. George,*[2] *and M. D. Garratt*[1]

Use of ACR Method to Estimate Closure and Residual Stress Free Small Crack Growth Data

ABSTRACT: Life predictions for small cracks emanating from material inhomogeneities or small flaws caused by manufacturing or corrosion damage are becoming increasingly important for several reasons, including: concerns over widespread fatigue damage; a shift in philosophy for fatigue initiation design from stress-life (S-N) to the equivalent initial flaw size (EIFS) approach; and the greater usage of unitized structure. For these reasons, development of accurate fatigue crack growth rate (FCGR) data in the near threshold region is needed, which is not influenced by closure or residual stress. Threshold data ARE often generated from long crack specimens by load shedding as outlined in ASTM E 647. However, this data can be non-conservative and variable due to load history effects caused by crack closure. Generating closure-free short crack FCGR data requires much more sophisticated instrumentation and testing techniques than long crack testing, making it prohibitively expensive to perform on a routine basis. Small crack tests also sample only a small volume of material and typically exhibit large scatter, so multiple tests must be performed in order to determine the typical or average behavior of the material. As a result of these disadvantages, use of long crack tests to estimate short crack behavior is the preferred approach.

The objective of this study was to evaluate the adjusted compliance ratio (ACR) method for obtaining residual stress and closure-free data from long crack tests and to compare the ACR method against the current ASTM opening load method. The ACR method was developed by Donald for estimating the closure-free ΔK_{eff} FCGR curve from standard long crack tests. To evaluate the method's ability to estimate closure-free data, standard ASTM long crack tests and short corner crack tests were conducted on 7075-T651 and 2324-T39 alloys. The ΔK_{eff} FCGR data resulting from the application of the ACR method to the ASTM long crack test results were then compared with the closure-free short corner crack data. Additionally, to assess the method's ability to account for residual stresses, long crack tests using ASTM standard middle crack and compact tension specimens, prepared from alloy 7055-T74511, were conducted, and the resulting $\Delta K_{applied}$ and ΔK_{eff} FCGR data were compared.

KEYWORDS: fatigue, fatigue threshold, crack propagation, effective stress intensity, crack closure, residual stress, adjusted compliance ratio

Introduction

Material trade studies are becoming increasingly advanced, necessitating fatigue crack growth data, free from the influences of closure and residual stresses, to reliably predict the fatigue life of structures. This is particularly important when considering widespread fatigue damage (WFD) and the desire to use an integral structure, which removes some redundancies associated with built-up structure.

To obtain closure free fatigue crack growth rate (FCGR) curves, typically one of the following three methods has been used: (1) measuring the fatigue crack growth rates of small cracks (e.g., ASTM E 647, Appendix X3); (2) performing long crack tests at high stress ratio, R,

Manuscript received 13 December 2003; accepted for publication 5 April 2005; published July 2005. Presented at ASTM Symposium on Fatigue and Fracture Mechanics: 34th Volume on 19–21 November 2003 in Tampa, FL; S.R. Daniewicz, J.C. Newman, Jr., and K-H. Schwalbe, Guest Editors.

[1] Sr. Staff Eng., Tech. Specialist, Sr. Eng., respectively, Alcoa Technical Center, Alcoa Center, PA 15069.
[2] Ph.D. Candidate, Lehigh University, Bethlehem, PA 18018.

or performing a constant K_{max} test, variable R, at a sufficiently high K_{max} such that crack closure does not occur [1]; or (3) performing long crack, constant R tests at the relevant stress ratio and measuring crack closure levels (K_{op}) in accordance with ASTM E 647, Appendix X2 (Recommended Practice for Determination of Fatigue Crack Opening Load from Compliance), in order to obtain an FCGR curve versus ΔK_{eff} (K_{max}-K_{op}) [2]. Each of these methods has disadvantages as currently practiced which have previously been discussed in detail elsewhere [3,4]. The primary issues associated with the above practices are accounting for the influence of K_{max} [5] and accounting for the additional crack driving force below K_{op} [6], which play an increasingly significant role near threshold.

To address the K_{op} issue, Donald [7] introduced the adjusted compliance ratio technique (ACR) for estimating ΔK_{eff}, which is designed to account for the additional crack driving force below K_{op}. The ACR technique is determined by subtracting the compliance prior to the initiation of a crack (C_i) from both the secant compliance (C_s) and the compliance above the opening load (C_o) as follows:

$$ACR = \frac{C_s - C_i}{C_o - C_i} \tag{1}$$

To compensate for possible bias in the secant compliance or slope compliance, which may occur due to signal conditioning noise or non-linearity, the ACR may be normalized as follows:

$$ACR_n = \frac{C_{oi}}{C_{si}} \bullet \frac{C_s - C_i}{C_o - C_i} \tag{2}$$

where

C_{oi} = inverse slope of the load displacement curve above the opening load prior to crack initiation, and

C_{si} = inverse slope of the secant drawn between the minimum and maximum load-displacement prior to crack initiation.

Since its introduction, the ACR method has been evaluated in several experimental programs. The ACR method was used by Donald [8] to re-analyze data from the second ASTM round robin program on opening-load measurement. The technique was shown to produce a higher mean value of ΔK_{eff} than the ASTM procedure and demonstrated a stronger correlation with crack growth data, having a slope more comparable to typical fatigue crack growth curves. Additionally, use of the ACR method reduced scatter between data sets and proved to be relatively insensitive to measurement location, unlike the ASTM method. McClung [9] compared the suitability of ACR and ASTM methods for describing closure and deformation behavior at the crack tip. It was concluded that the ACR method may be more appropriate for roughness-induced closure. The effectiveness of the ACR method in describing the near crack tip plasticity-induced closure was reduced in the Paris regime of the FCGR curve. Increased analytical understanding of the ACR method was achieved through the development of the Crack Wake Influence (CWI) theory [10]. CWI linked the interpretation of remote load displacement curves to crack tip strain behavior. From this it was shown that the ACR method was an improvement over opening load for predicting the true strain range near the crack tip but was less effective than the CWI closed form solution.

The relative improvement of the ACR method over the ASTM opening load method was further demonstrated by Brockenbrough et al. [4]. Stress-life S-N fatigue curves were predicted using a small crack growth model and ΔK_{eff} curves determined by the ACR and ASTM techniques, and compared with experimental S-N fatigue data. It was found that the ΔK_{eff} curves obtained by the ACR method at the same stress ratio as the fatigue tests produced the best and most consistent predictions. By making predictions at the same stress ratio as the generated experimental data, the K_{max} for a given ΔK_{eff} was the same in both cases.

As an alternative to estimating short crack closure-free crack growth behavior from long crack data, George et al. [11] has developed a corner-notched open hole fatigue crack growth test. The specimen used had a thickness of 3.18 mm, width of 38.1 mm, and a centrally located 6.35 mm diameter hole. A notch was introduced in the open hole by drawing a serrated razor across one edge at a 45° angle to the specimen face, positioned within 0.5 mm of the hole's centerline. Direct Current Potential Difference (DCPD) method was then used for measurement of crack extension. Overall, the results of the test were shown to have good agreement with existing closure corrected long crack data. It was also observed that 2xxx alloys demonstrated increased variability compared to 7xxx alloys, which was attributed to grain structure differences. More detailed description of the test method and K-solution development for the open hole specimen can be found in Ref. [11].

The influence of residual stress on fatigue crack growth rates has been known since 1981 [12]. The presence of residual stress in test coupons causes an additional internal loading component to be added to the applied load that is not accounted for during data analysis. Residual stress effects have been more commonly shown to occur with use of the compact tension specimen, however they also can occur in the middle crack specimens. An example of residual stress bias is shown in Fig. 1 [12]. This shows test results for an aluminum alloy using an existing and modified processing practice. Initially it was concluded that the modified practice had increased the FCGR threshold, however it was later found that the alloy had not been stress relieved. Subsequent testing of the stress-relieved modified product demonstrated similar performance.

Unrelieved residual stresses from quenching operations have also been recognized to cause increased variability in the crack growth response of thick aluminum forgings. Quenching of thick products can result in cooling variations, which may leave surfaces in residual compression and interiors in residual tension. To assess the influence of residual stress on crack growth response of a thick forged product, constant amplitude FCG tests were conducted on S-L oriented CT specimens extracted from hand forgings, and the results were compared with FCG data for plate product [13]. A significant variation in the $\Delta K_{applied}$ data was observed between the separate hand forging specimens and between the hand forging and plate product (Fig. 2). To account for the presence of residual stress, the ASTM opening load method was used by Bush et al. to estimate the ΔK_{eff} FCGR curves (Fig. 3). The results indicated that the intrinsic FCG performance of the hand forging and plate products were comparable; however, use of the ASTM method resulted in estimated ΔK_{eff} thresholds, which may have been artificially low.

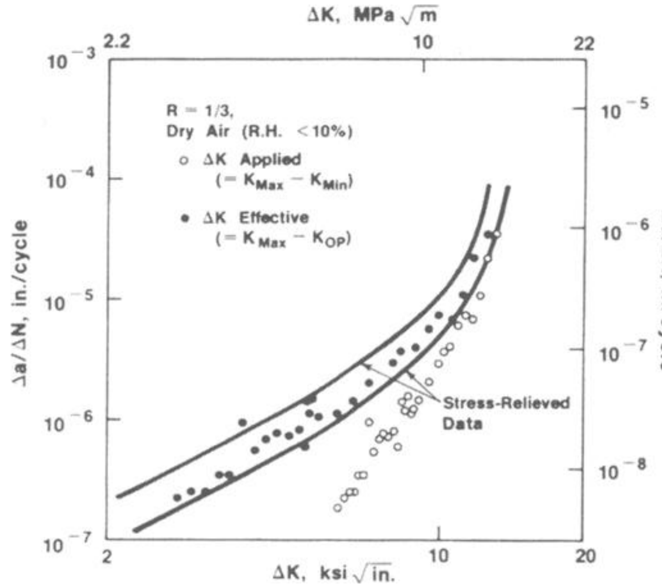

FIG. 1—*Comparison of valid and anomalous fatigue crack growth rate measurements for specimens with and without residual stress [12].*

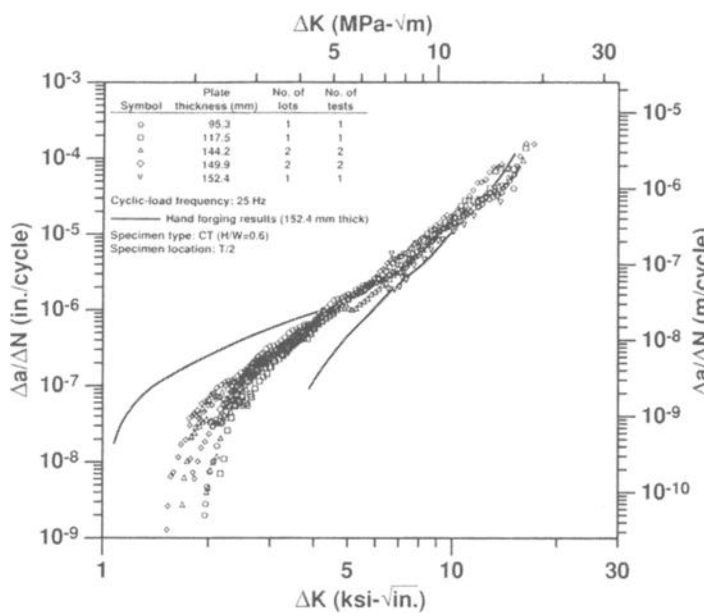

FIG. 2—*FCGR response for 7050-T7451 plate and 7050-T7452 hand forgings: S-L orientation, R-ratio = 0.33, high humidity (RH > 90 %) air [13].*

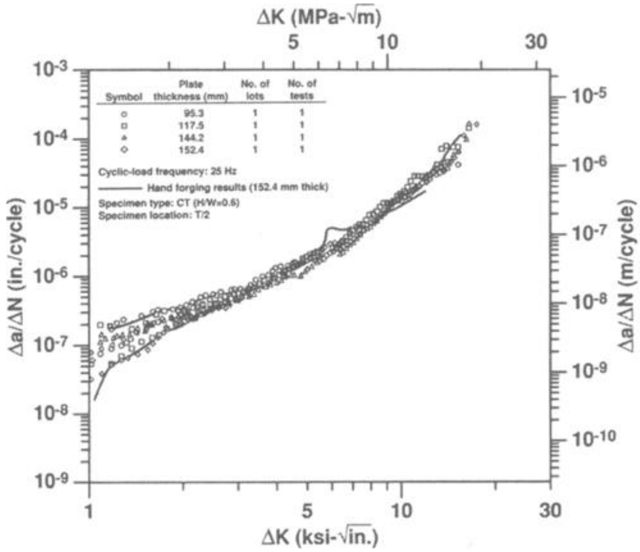

FIG. 3—*ASTM opening load closure corrected FCGR response for 7050-T7451 plate and 7050-T7452 hand forgings: S-L orientation, R-ratio = 0.33, high humidity (RH > 90 %) air [13].*

Experimental Procedure

Fatigue crack growth testing was conducted on aluminum alloys 7075-T651, 2324-T39, 7055-T74511 using middle crack tension specimen according to ASTM E 647. In addition, a compact tension FCGR test was conducted on alloy 7055-T74511. For all tests, the ACR and ASTM opening load methods were used to estimate ΔK_{eff}. For alloys 7075-T651 and 2324-T39, the resulting curves were then compared with the corner-notched $\Delta K_{applied}$ curves developed by George et al. [11]. The dimensions of the middle crack and compact tension test specimens and corresponding test conditions for the conducted evaluation are summarized in Tables 1 and 2. The geometry of the corner notched open hole specimen is provided in Fig. 4.

The experiments were conducted on a servo-hydraulic closed loop mechanical test machine interfaced to a computer for control and data acquisition. Clip-on strain gage transducers were used for displacement measurements. Subsequent to testing, the collected M(T) FCGR data was reduced using the incremental polynomial method as outlined in ASTM E647, Appendix X1. To ensure a good comparison between the long crack and corner-notch tests, all middle crack tension specimens were prepared from the same material lots used for the corner-notch open hole tests. Uniaxial tensile properties for the two alloys are provided in Table 3.

TABLE 1—*7075-T651 and 2324-T39 specimen and testing details.*

M(T) Specimen	Testing
Thickness: 3.175 mm	Pre-crack $\Delta K_{ini} = 4.9$ MPa$\sqrt{m}$
Width: 101.6 mm	Pre-crack $K_{grad} = -0.12$/mm
2ao: 5.08 mm	Testing $K_{grad} = 0.08$/mm
Test Orientation: L-T	R-Ratio: 0.1
	Test Frequency: 25 Hz
	Environment: RH > 90 %

TABLE 2—*7055-T74511 specimen and testing details.*

C(T) Specimen	M(T) Specimen	Testing
Thickness: 6.35 mm	Thickness: 6.35 mm	Pre-crack $\Delta K_{ini} = 3.8$ MPa$\sqrt{m}$
Width: 76.2 mm	Width: 101.6 mm	Pre-crack $K_{grad} = -0.08$/mm
ao: 19.05 mm	2ao: 5.08 mm	Testing $K_{grad} = 0.08$/mm
Test Orientation: L-T	Test Orientation: L-T	R-Ratio: 0.1
		Test Frequency: 25 Hz
		Environment: RH > 90 %

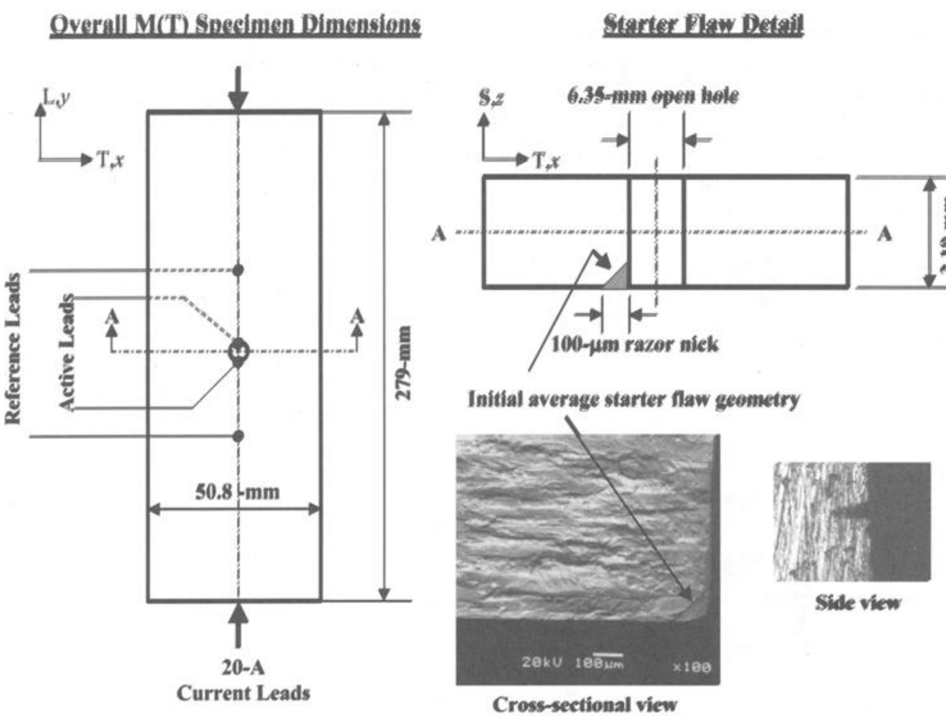

FIG. 4—*Schematic of M(T) open hole specimen with initial starter flaw geometry.*

TABLE 3—*Longitudinal uniaxial tensile properties.*

Alloy-Temper	Plate Thickness (mm)	Yield Strength (MPa)	Tensile Strength (MPa)	Elongation (%)
7075-T651	12.7	564	607	12.5
2324-T39	19.1	452	482	15.7
7055-T74511	16.5	612	572	12.9

Results and Discussion

The fatigue crack growth curves showing both the $\Delta K_{applied}$ and ΔK_{eff} curves, with ΔK_{eff} based on the ACR and ASTM opening load method for alloy 7075-T7651 and 2324-T39, are illustrated in Figs. 5 and 6, respectively. Similar to previous studies [5,8], the ASTM opening load method produced a decreased ΔK_{eff} value compared to the ΔK_{eff} value estimated using the ACR method. Additionally, threshold values determined from the ACR method are more consistent with the FCGR curve than those estimated from the ASTM method. For both alloys, the ASTM method would estimate threshold values near or less than 1 $MPa\sqrt{m}$. This would seem to be an unrealistically low value, particularly for 2324-T39 when compared against a threshold value previously determined of ~2.8 $MPa\sqrt{m}$ when using an R-ratio of 0.5 ($Kmax_{ini}$ = 6.6 $MPa\sqrt{m}$) [5]. Such discrepancies are very important to understand since they would significantly impact material trade study results. This is due to the fact that threshold values represent a limit for damage tolerant design and that stress intensity factors for cracks below the threshold are assumed to be non-propagating. Additionally, a larger portion of a structure's life is spent in the low crack growth regime, at or near threshold. Therefore, to improve life prediction, accurate threshold estimates are a necessity.

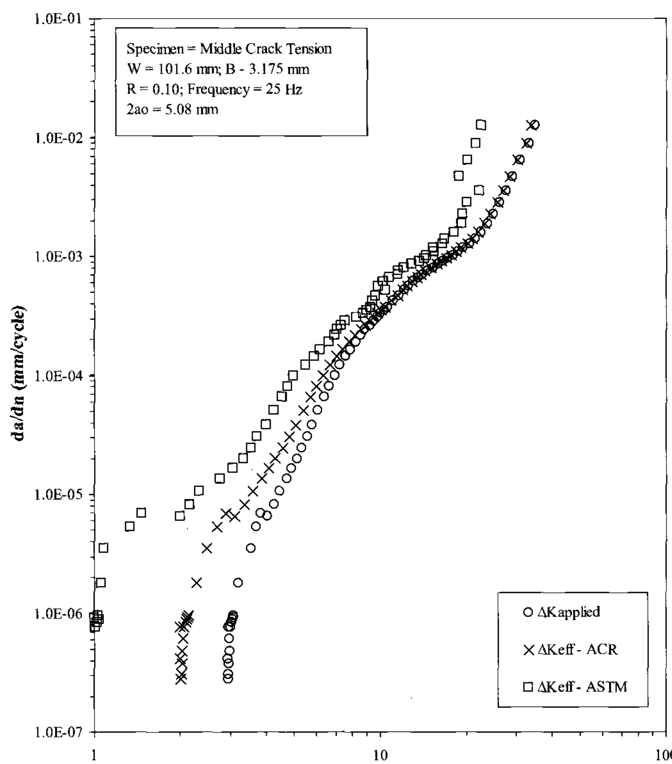

FIG. 5—*FCGR response of alloy 7075-T651.*

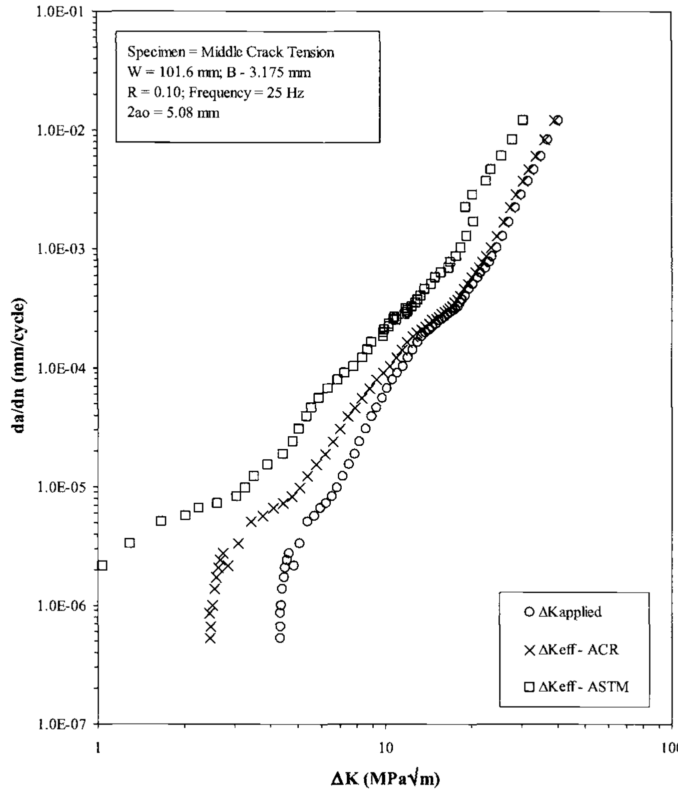

FIG. 6—*FCGR response of alloy 2324-T39.*

It has been long recognized that small surface cracks will propagate at stress intensity values below the threshold value determined by long crack data [14]. This is potentially due to corner crack data being closure-free. To determine small crack growth behavior, a corner notched open hole specimen has been developed [11] to enable a direct measurement of closure-free small crack FCGR data. Data developed in this manner can potentially provide a better representation of the actual structure when considering that a large number of cracks emanate from fastener holes. However, as previously mentioned, one disadvantage of short crack data is that only a very small amount of the material is tested, which can lead to increased variability in results. To overcome this issue, multiple tests might be needed. As an alternative, it would be desirable to estimate short crack behavior with long crack data since long cracks provide a microstructructural averaging effect over the thickness of the material being tested. Also, use of long crack data would be beneficial due to the well-established testing practices for this type of crack growth data.

To determine the effectiveness of the ACR method to estimate short crack behavior, the ACR ΔK_{eff} curves for the 7075-T651 and 2324-T39 alloys were compared with the corresponding small crack $\Delta K_{applied}$ curve from the corner notch open hole specimen (Fig. 7). For the two alloys evaluated in this study, the ACR adjusted M(T) curves show excellent agreement with the corner flaw curves, which provides additional evidence of the ACR method's ability to correct for closure in the threshold regime. However, despite the excellent agreement, caution may need to be exercised since long crack data average the alloy's response across the entire thickness, while the corner crack data, especially in the near threshold regime, represent a very localized area of a material's microstructure. As a result, corrected long crack data may not always match short crack data, but should represent an average condition. Therefore, the decision to use short crack or corrected long crack data will depend on the application or desired end use of the information.

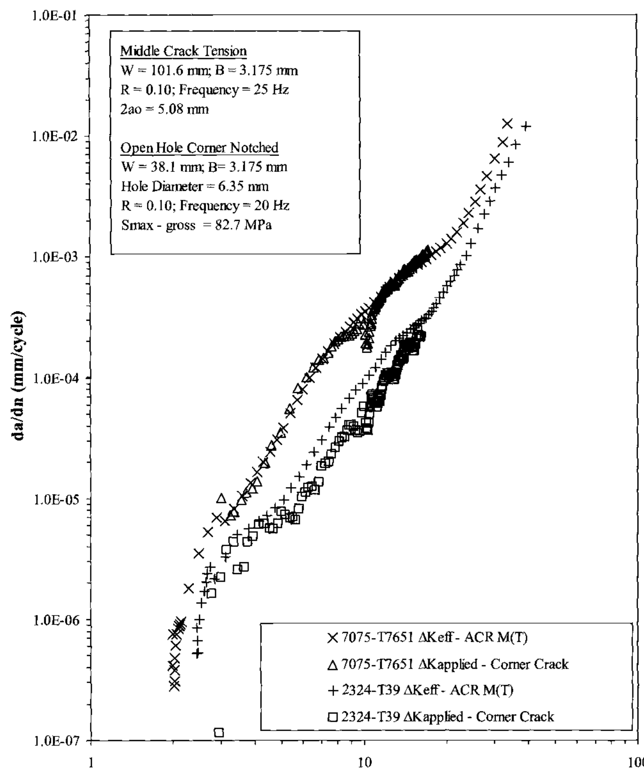

FIG. 7—*Comparison of M(T) ACR adjusted* ΔK_{eff} *FCGR curves and* $\Delta K_{applied}$ *FCGR curves developed from a Corner Notch Open Hole specimen.*

In addition to closure, residual stresses contained in test specimens can have a dramatic influence on the measured fatigue crack growth rate, particularly near threshold. Fatigue crack growth rate curves were generated on extrusion alloy, 7055-T74511, using both C(T) and M(T) specimen geometries as part of a routine alloy evaluation. Although the testing parameters were identical, the resulting $\Delta K_{applied}$ FCGR curves were significantly different (Fig. 8). For the C(T) specimen, a growth rate of 3.0E-06 mm/cycle was obtained at a $\Delta K_{applied}$ value of 3.0 $MPa\sqrt{m}$, while for the M(T) specimen the same growth rate occurred at 5.2 $MPa\sqrt{m}$. Due to the observed differences, the M(T) specimen growth rates became suspect. The M(T) panel was extracted from the mid-thickness and mid-width location of a rectangular extrusion cross-section. Due to the cross-section geometry, it was known that strength differences from edge to center could exist, which would potentially create residual stress variations after stretching. To determine if this had occurred, residual stress measurements were taken from the center of the panel toward the edge by placing five longitudinal strain gages, as shown in Fig. 9, and sawing the specimen along the dashed line just above the gages. The residual stresses were then calculated and are shown in Fig. 10. A compressive residual stress of approximately 17 MPa was found near the center of the M(T) panel, and was concluded to be the source of the higher $\Delta K_{applied}$ threshold value.

ACR and ASTM opening load methods were applied to the data set to determine the ΔK_{eff} curves. It was found that the ACR method effectively corrected for the presence of residual stress in the M(T) specimen producing similar ΔK_{eff} curves for the M(T) and C(T) specimens (Fig. 8). Use of the ASTM opening load method corrected the M(T) data to a reduced ΔK_{eff} compared to the C(T) specimen, and produced an increased difference between the M(T) and C(T) ΔK_{eff} curves compared to the ACR method.

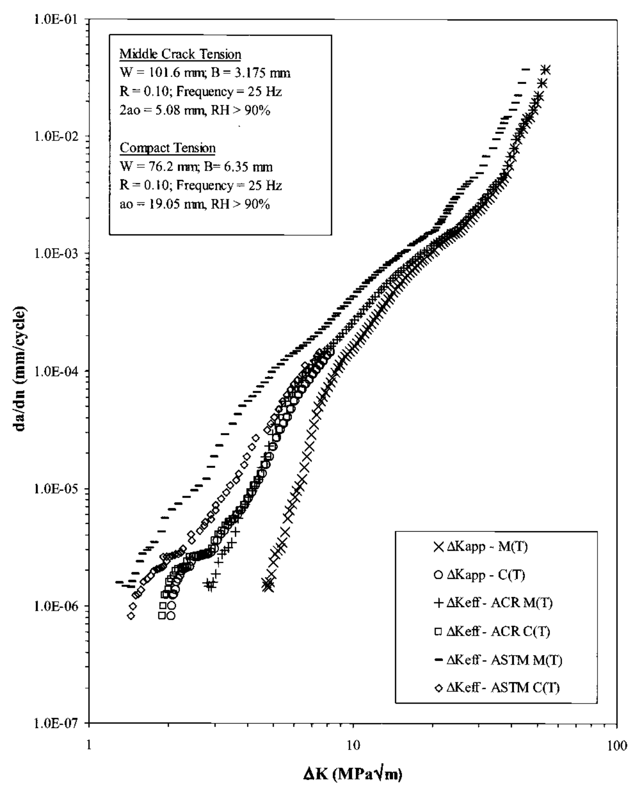

FIG. 8—*Crack growth response of alloy 7055-T74511 illustrating that reduced differences between M(T) and C(T) curves are observed with the ACR corrected curves.*

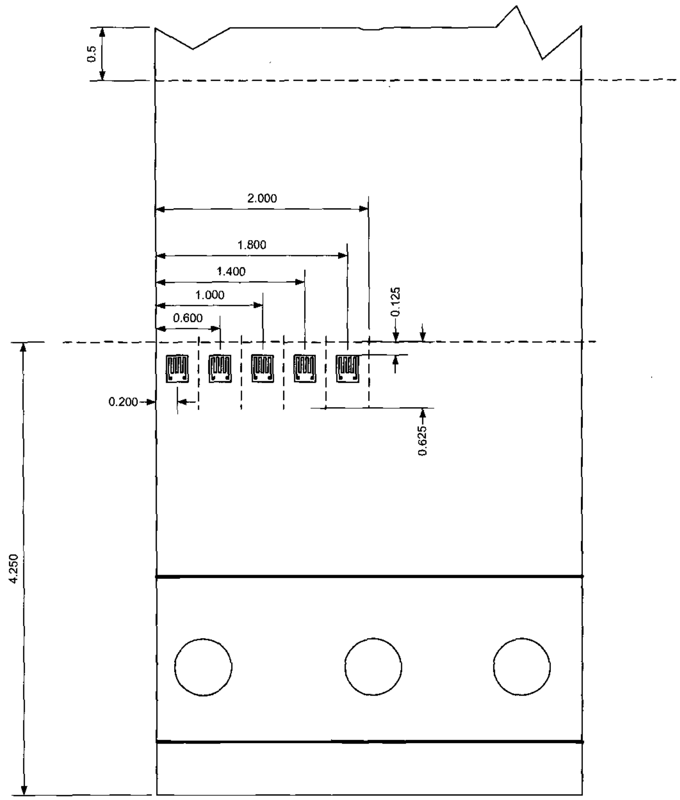

FIG. 9—*Strain gage location and saw path for measuring residual stress in M(T) panel.*

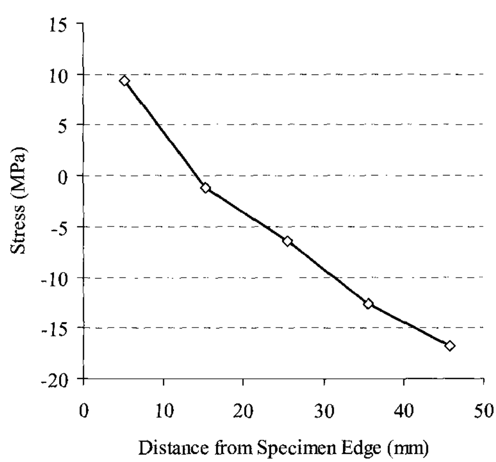

FIG. 10—*Residual stress as a function of position across M(T) specimen width.*

Summary

The adjusted compliance ratio (ACR) method was demonstrated to accurately estimate short crack growth response from long crack data for alloys 7075-T651 and 2324-T39, while use of the ASTM method under-estimated threshold values which could lead to very conservative life predictions. Long crack data average the alloy's response across the entire thickness, while the corner crack data, especially in the near threshold regime, represent a very localized area of a material's microstructure. As a result, corrected long crack data may not always match short crack data, but should represent an average condition. Therefore, the decision to use short crack or corrected long crack data will depend on the application or desired end use of the information.

The ACR method was also found to effectively account for the presence of residual stress in test coupons. Differing applied crack growth responses were experimentally observed for extrusion alloy 7055-T74511 when tested with standard ASTM C(T) and M(T) type specimens. The differences were found to be due to residual stresses in the M(T) specimen. Despite the presence of residual stresses, the ACR method estimated similar ΔK_{eff} curves for both specimen geometries.

References

[1] Hertzberg, R., Herman, W. A., Clark, T., and Jacard, R., "Simulation of Short Crack and Other Low Closure Loading Conditions Utilizing Constant K_{max} ΔK-Decreasing Fatigue Crack Growth Procedures," *Small-Crack Test Methods, ASTM STP 1149*, J. M. Larsen and J. E. Allison, Eds., ASTM International, West Conshohocken, PA, 1992, pp. 197–200.

[2] Donald, J. K., "A Procedure for Standardizing Crack Closure Levels," *Mechanics of Fatigue Crack Closure, ASTM STP 982*, J. C. Newman, Jr. and W. Elber, Eds., ASTM International, West Conshohocken, PA, 1988, pp. 222–229.

[3] Donald, J. K., Bray, G. H., and Bush, R. W., "An Evaluation of the Adjusted Compliance Ratio Technique for Determining the Effective Stress Intensity Factor," *29th National Symposium on Fatigue and Fracture Mechanics, ASTM STP 1332*, T. L. Panontin and S. D. Sheppard, Eds., ASTM International, West Conshohocken, PA, 1997.

[4] Brockenbrough, J. R. and Bray, G. H., "Prediction of S-N Fatigue Curves Using Various Long-Crack Derived ΔK_{eff} Fatigue Crack Growth Curves and a Small Crack Life Prediction Model," *Fatigue and Fracture Mechanics, 30th Volume, ASTM STP 1360*, P. C. Paris and K. L. Jerina, Eds., ASTM International, West Conshohocken, PA, West Conshohocken, PA, 1999, pp. 388–402.

[5] Bray, G. H. and Donald, J. K., "Separating the Influence of K_{max} from Closure-Related Stress Ratio Effects Using the Adjusted Compliance Ratio Technique," *Advances in Fatigue Crack Closure Measurements and Analysis: Second Volume, ASTM STP 1343*, R. C. McClung and J. C. Newman, Jr., Eds., ASTM International, West Conshohocken, PA, 1999, pp. 57–78

[6] Chen, D. L., Weiss, B., and Stickler, R., "Contribution of the Cyclic Loading Portion Below the Opening Load to Fatigue Crack Growth," *Materials Science and Engineering*, Vol. A208, 1996, pp. 181–187.

[7] Donald, J. K., "Introducing the Compliance Ratio Concept for Determining Effective Stress Intensity," *International Journal of Fatigue*, Vol. 19, Suppl. No. 1, 1997, pp. 191–195.

[8] Donald, J. K. and Phillips, E. P., "Analysis of Second ASTM Round Robin Program on Opening Load Measurement Using the Adjusted Compliance Ratio Technique," *Advances*

in Fatigue Crack Closure Measurement and Analysis: Second Volume, ASTM STP 1343, R. C. McClung and J. C. Newman, Jr., Eds., ASTM International, West Conshohocken, PA, 1997.
[9] McClung, R. C., Davidson, D. L., "Near Tip and Remote Characterization of Plasticity Induced Fatigue Crack Closure," *Advances in Fatigue Crack Closure Measurement and Analysis, ASTM STP 1343*, R. C. McClung and J. C. Newman, Jr., Eds., ASTM International, West Conshohocken, PA, 1999, pp. 106–127.
[10] Donald, J. K., Connelly, G. M., Paris, P. C., and Tada, H., "Crack Wake Influence Theory and Crack Closure Measurement," *National Symposium on Fatigue and Fracture Mechanics: 30th Volume, ASTM STP 1360*, K. L. Jerina and P. C. Paris, Eds., ASTM International, West Conshohocken, PA, 1999.
[11] George, K., Reemsynder, H. S., Donald, J. K., and Bucci, R. J., "Development of a Corner-Notched, Open Hole Specimen for Material Evaluation," *Fatigue Testing and Analysis Under Variable Amplitude Loading Conditions, ASTM STP 1439*, P. C. McKeighan and N. Ranganathan, Eds., ASTM International, West Conshohocken, PA, 2002.
[12] Bucci, R. J., "Effect of Residual Stress on Fatigue Crack Growth Rate Measurement," *Fracture Mechanics (13th Conference), ASTM STP 743*, ASTM International, West Conshohocken, PA, 1981, pp. 28–47.
[13] Bush, R. W., Bucci, R. J., Magnusen, P. E., and Kuhlman, G. W., "Fatigue Crack Growth Rate Measurements in Aluminum Alloy Forgings: Effects of Residual Stress and Grain Flow," *Fracture Mechanics: Twenty-Third Symposium, ASTM STP 1189*, Ravinder Chona, Ed., ASTM International, West Conshohocken, PA, 1993, pp. 568–589.
[14] Pearson, S., "Initiation of Fatigue Cracks in Commercial Aluminum Alloys and the Subsequent Propagation of Very Short Cracks," *Engineering Fracture Mechanics*, Vol. 7, No. 2, 1975, pp. 235–247.

Guocai Chai[1] *and Sofia Hansson*[2]

Influence of Temperature and Microstructure on the Fatigue Behaviour in the Threshold Regime for a Super Duplex Stainless Steel

REFERENCE: Chai, G. and Hansson, S., "Influence of temperature and microstructure on the fatigue behaviour in the threshold regime for a super duplex stainless steel," *Fatigue and Fracture Mechanics: 34th Volume, ASTM STP 1461*, S. R. Daniewicz, J. C. Newman and K. H. Schwalbe, Eds., ASTM International, West Conshohocken, PA, 2004.

ABSTRACT: The fatigue crack propagation behaviour of a super duplex stainless steel in the near threshold regime at -50°C, 20°C (RT) and 150°C has been studied. The fatigue threshold values of the stress intensity factor range and the effective threshold value of this material are higher at –50°C and 150°C than at RT. The closure threshold value is also smaller at RT than at -50°C, but comparable with that at 150°C. The material aged at 475°C for 3 hours shows similar effective threshold value, but a smaller closure threshold value. Crack propagation mismatch at the interface of the two phases and brittle to ductile fracture transition in the material at -50°C or in the aged material at RT were observed, and possible mechanisms were discussed.

KEYWORDS: super duplex stainless steel, fatigue threshold, temperature, closure

Introduction

Super duplex stainless steels are a family of steels consisting of an austenite-ferrite two phase microstructure with a pitting resistance equivalent (PRE) greater than 40 [1]. These materials combine an attractive match of excellent corrosion resistance and high mechanical properties in the temperature range -50°C to 250°C, and have now been widely used in many marine and petrochemical applications.

The fatigue crack propagation behaviour of duplex stainless steels in the near threshold regime was first studied by Wasén et al. [2]. It was found that the fatigue crack growth threshold, ΔK_{th}, depends strongly on the microstructures and the stress ratio, R. Similar results have also been obtained by Murakami et al. in a cast duplex stainless steel [3]. Nyström et al. [4] have performed an extensive investigation on the influence of amount of ferrite phase and cold working on the near threshold fatigue crack propagation behaviour of duplex stainless steels. The results were also compared with that of ferritic and austenitic single-phase materials. Since duplex stainless steels can suffer from embrittlement due to the spinodal decomposition in the ferrite phase in the temperature range from 275°C to 500°C, the influence of the spinodal decomposition has also been widely investigated, but different results have been reported [4, 5].

The temperature has a great influence on the fatigue crack propagation behaviour in the near threshold range [6-9]. An increase in temperature increases the fatigue crack growth (FCG) rate. However, the situation near the threshold range depends on the material and the environments. In

[1] Senior Specialist, R&D, Sandvik Materials Technology, S-811 81 Sandviken Sweden.
[2] Ph D Student, Dalarna University, Forskargatan 3, S-781 88 Borlänge, Sweden.

vacuum, the threshold value, ΔK_{th}, of 9%Cr1%Mo steel decreases with increasing temperature [8]. For SUS 403, the effective ΔK_{th} is independent of temperature [7]. At low temperature, the FCG rate generally decreases while the threshold value, ΔK_{th}, increases in stable austenitic stainless steels [6]. In ferritic steels, the FCG rate can be raised again at temperatures where the fatigue ductile-brittle transition (FDBT) occurs [10]. The aim of this study is to investigate the fatigue crack propagation behaviour of a super duplex stainless steel in the near threshold regime in the temperature range (-50°C to 150°C) where they are used since not much work has been done in this area for duplex stainless steel.

Experimental

Material and Specimen

The material used in the present work is a super duplex stainless steel SAF 2507[3] (equivalent to UNS S32750) with the nominal chemical composition as shown in Table 1.

TABLE 1—*Nominal chemical composition of SAF 2507(wt%).*

C	Si	Mn	Cr	Ni	Mo	N
0.03	0.80	1.2	25	7	4	0.3

CT-specimens with thickness B= 18mm and width W= 36mm and crack plane orientation code T-S were used in this test. They were taken from a round bar (80 mm in diameter) produced by hot rolling and containing a microstructure with elongated austenite phase in a matrix of ferrite (Figure 1). Some specimens were aged in air at 475°C for 3 hours.

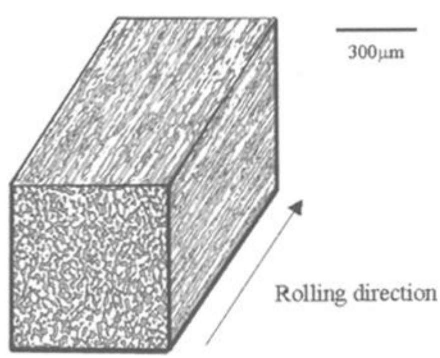

FIG. 1—*Microstructure of the hot rolled duplex SAF 2507 bar material.*

The tensile properties were determined using the samples from the longitudinal direction or rolling direction (Fig. 1). Table 2 shows the tensile properties of SAF 2507 bar material at different temperatures.

[3] SAF 2507 is a registered trade mark of Sandvik AB.

TABLE 2—*Tensile properties.*

Material	Temperature (°C)	σ_y (MPa)	σ_{TS} (MPa)	Elongation (%)
As received	RT	625	820	41.7
	150	484	719	41.0
	-50	738	944	41.9
475°C/3h	RT	659	946	41.6

Testing Procedure

The FCG tests were performed using an MTS servo-hydraulic machine (50kN) equipped with Instron 8500+ digital electronics, and controlled by the Fast Track Program-da/dN. The physical crack length was determined by the compliance method with a clip gage. The following relationship was used.

$$a/W = C_0 + C_1U + C_2U^2 + C_3U^3 + C_4U^4 + C_5U^5 \quad (1)$$

where a = crack length, W = width of specimen, C_0-C_5 = compliance coefficients (table 3) and U = specimen compliance.

TABLE 3—*Compliance coefficients*

C_0	C_1	C_2	C_3	C_4	C_5
1.00112	-4.81493	21.15587	-287.867	1556.555	-2944.9

The CT-specimen was first pre-cracked using a K-decreasing process. The terminal value of the maximum stress intensity factor, K_{max} was lower than the initial K_{max} for the main tests. The pre-crack length was grown to the range of 0.5-0.6W.

The main tests were performed using also the K-decreasing method. The test procedure was continued until the fatigue crack growth rate had slowed down to 10^{-8} mm/cycle. Two normalised K-gradient constant values (Cg=-0.08 and –0.13 mm^{-1}) were used.

Testing was performed in air at -50°C, RT and 150°C. The various temperatures were obtained in an MTS environmental chamber with temperatures ranging from -130°C to 300°C with a variation of ±1°C. Liquid nitrogen is the cooling medium. The tests were performed under R= 0.1 and a frequency of about 10 Hz.

Crack closure was evaluated by analysing the load versus crack opening displacement (COD) curves. The closure load P_{cl} was defined as the load corresponding to the point where the curve changed its slope.

Fractography

The fracture surface and fatigue crack paths were investigated using a JEOL 840 scanning electron microscope. The emphasis was put on the fracture near the threshold fatigue crack propagation range. The crack length was also measured on the fracture surface and compared with the crack length calculated by the compliance method.

Results and Discussion

Influence of Temperature and K-Gradient Constant Cg on the Fatigue Crack Growth

Figure 2 shows the fatigue crack growth (FCG) rate (da/dN) versus stress intensity factor range (ΔK) curves from this study. A summary of the results is shown in Table 4. A decrease in temperature increases the threshold of the stress intensity factor range, ΔK_{th}. This result is similar to the observations made in some single phase alloys [6, 9, 11]. At 150°C, however, the ΔK_{th} seems to be higher than that at RT. This is an interesting result that will be discussed below. It seems that the Paris law's constant n is larger at −50°C or 150°C than at RT. This indicates that there is a tendency that the FCG rate at high ΔK is higher at −50°C or 150°C than at RT.

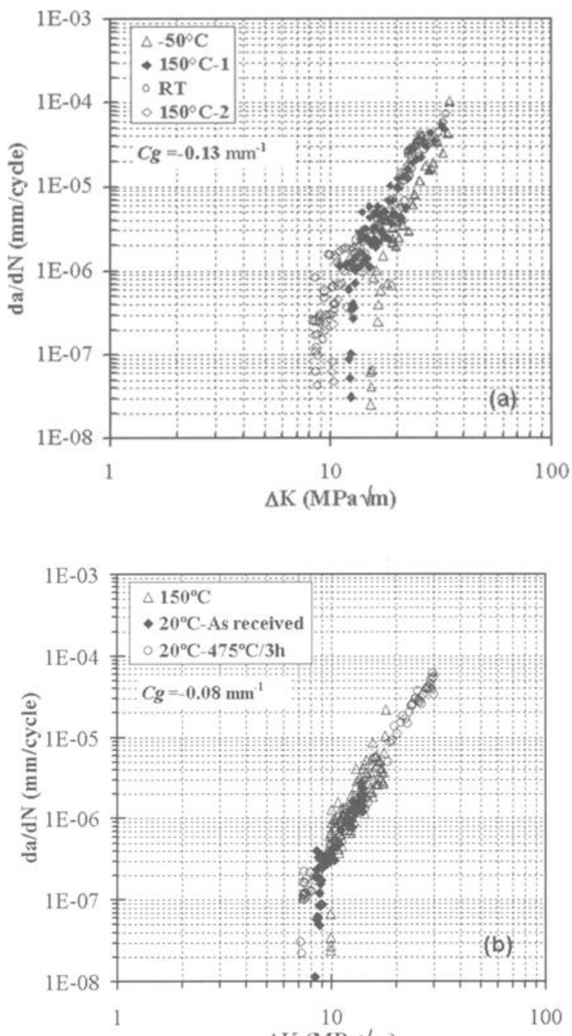

FIG. 2—*Crack growth rate versus stress intensity factor range for SAF 2507 tested at given temperatures and K-gradient constants Cg.*

The ageing at 475°C seems to influence the fatigue behaviour near the threshold range. The ΔK_{th} of the aged material is lower than that of the as received material. This phenomenon can be compared with the results by Nyström et al [4]. However, the fatigue crack growth rates in the Paris law regime of the unaged and aged materials are comparable. In this investigation, a decrease in K-gradient constant Cg from 0.13 to 0.08 shows only a slight decrease in the ΔK_{th}.

TABLE 4—*Influence of temperature on the Paris law's constants and the threshold stress intensity factor range.*

Cg (mm^{-1})	Material	Temperature (°C)	C_m (mm/cycle)	n	$\Delta K_{th\,exp}$ (MPa√m)
-0.13	As received	-50	2.96x10^{-12}	4.69	14.85
		20	5.35x10^{-10}	3.52	8.64
		150	1.10x10^{-10}	3.79	12.01
		150	1.70x10^{-11}	4.24	10.09
-0,08	As received	20	6.88x10^{-12}	4.73	8.43
		150	6.22x10^{-12}	4.83	9.85
	475°C/3h	20	1.68x10^{-11}	4.42	7.44

$da/dN=C_m(\Delta K)^n$ – the Paris law, C_m and n are the Paris law's constants.
$\Delta K_{th\,exp} = \Delta K_{th}$ evaluated from the da/dN versus ΔK curves.

Influence of Temperature on the Intrinsic and Extrinsic Threshold

It is known that fatigue crack growth behaviour near the threshold range is affected by various factors, which are categorised into the intrinsic and extrinsic mechanisms [12]. The intrinsic threshold determines the inherent resistance of a material against fatigue crack propagation. The extrinsic threshold causes a reduction in crack driving force at the crack tip. In experiments, the extrinsic part is coupled to the contribution of the crack closure effect. The threshold of the stress intensity factor range, ΔK_{th}, is divided into the threshold of the effective stress intensity factor range, $\Delta K_{eff\,th}$, and the threshold of the closure stress intensity factor range, $\Delta K_{cl\,th}$, as follows:

$$\Delta K_{th} = \Delta K_{eff\,th} + \Delta K_{cl\,th} \tag{2}$$

Table 5 shows the influence of temperature, material and C_g on the intrinsic and extrinsic threshold. The influences of the ageing at 475°C and the K-gradient constant C_g on the $\Delta K_{eff\,th}$ are small. However, a high C_g value leads to a high $\Delta K_{cl\,th}$ value. This is due to the fact that a quick decrease in ΔK from a high C_g value will cause an overload effect that may cause an arrest or retardation of the crack growth [13].

TABLE 5—*Influence of temperature on the closure and effective threshold of the stress intensity factor range of SAF 2507.*

Cg (mm^{-1})	Material	Temperature (°C)	ΔK_{th_exp} (MPa√m)	ΔK_{clth} (MPa√m)	$\Delta K_{eff\,th}$ (MPa√m)	$\Delta K_{eff\,th}+\Delta K_{cl\,th}$ (MPa√m)
-0.13	As received	-50	14.85	8.97	5.84	14.81
		20	8.64	5.35	3.90	9.25
		150	12.01	5.91	4.92	10.83
		150	10.09	6.26	5.83	12.09
-0.08	As received	20	8.43	4.74	3.73	8.47
		150	9.85	4.57	5.38	9.95
-0.08	475°C/3h	20	7.44	3.74	3.88	7.42

The results in Table 5 show that the $\Delta K_{eff\ th}$ is temperature dependent, and is higher at either –50°C or 150°C than at RT. As known, the $\Delta K_{eff\ th}$ is usually considered as a function of the modulus of elasticity, E, the tensile strength, σ_{TS}, and the fracture ductility, ε_f, of the material as follows [17].

$$\Delta K_{eff\ th} = 0{,}32\sqrt{\pi E\ \sigma_{TS}\ \varepsilon_f\ \rho_o} \tag{3}$$

where ρ_o is the maximum critical radius of the crack tip. This equation may give some explanation for the high $\Delta K_{eff\ th}$ value at –50°C due to the higher tensile properties (Table 2). However, it can not explain the high $\Delta K_{eff\ th}$ value at 150°C since the tensile properties are lower and the ductility is similar to that at RT. However, this alloy shows a higher fatigue limit at 150°C than at RT. The explanation for this disparity is the effect of dynamic strain ageing [14]. Since SAF 2507 contains a high amount of nitrogen, an interaction between the nitrogen atom and moving dislocations (the Portevin-LeChatelier effect-PLC effect) will occur during cyclic loading at intermediate temperature, which can hinder the movement of dislocations and lead to a strengthening. During the fatigue crack propagation test at this high temperature, the PLC effect can also occur in the plastic zone at the crack tip during cyclic straining. This may increase the intrinsic threshold that is correlated to the high cycle fatigue limit.

It seems that the $\Delta K_{cl\ th}$ is dependent on both temperature and material conditions. The $\Delta K_{cl\ th}$ of the aged material is slightly lower than that of the as received material. This may be due to its low plasticity. In the temperature range between RT and 150°C, the temperature has a little effect on the $\Delta K_{cl\ th}$. In the low temperature range, however, the temperature shows a great influence on $\Delta K_{cl\ th}$. As known, there are many factors that affect closure behaviour [13]. At the threshold range, however, fracture surface roughness or oxidation-induced closure is considered to be the most important mechanisms [2, 4]. Since the temperatures used in this test are comparatively low (<150°C), roughness induced closure is therefore of most interest. Figure 3 shows the influence of temperature and material on the fatigue crack paths of SAF 2507. For the aged material (Figure 3b), the crack path is rather smooth, but closure in austenite phase (dash line area), which is soft, occurred. For as received material, the fracture surfaces are much rougher, and large kinks occurred at the interfaces between austenite and ferrite (Figure 3a, c and d).

A rougher fracture surface has been shown to correlate to higher closure. The parameters such as mean standard deviation of height and deflection angles have been used to describe the crack closure [2, 4]. This concept is used to describe the $\Delta K_{eff\ th}$ using the maximum heights of the fracture profile in this investigation. Table 6 shows a comparison between the values from the fatigue testing and from the fracture investigation, which again shows that the roughness induced closure may be an important mechanism for the closure of duplex stainless steels in this threshold range.

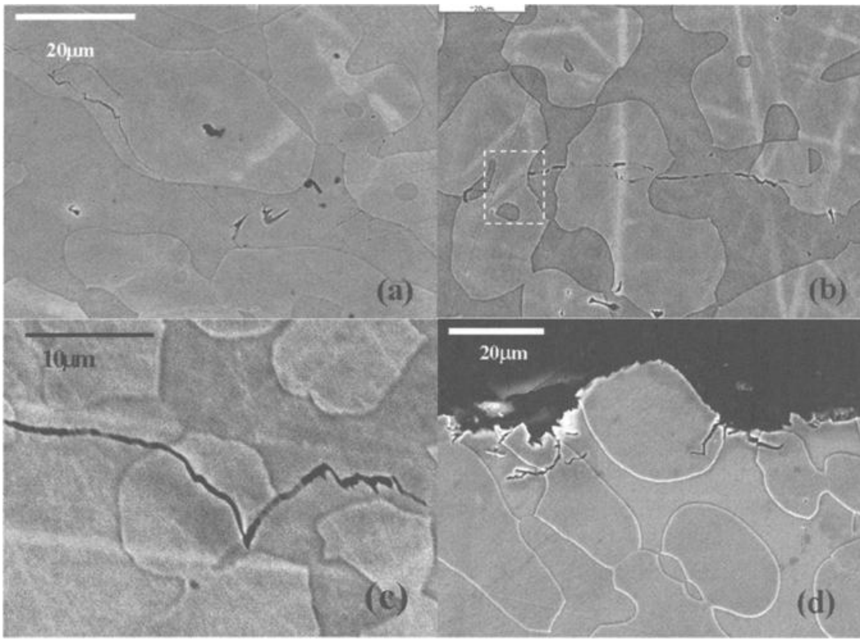

FIG. 3—*Influence of temperature on the fatigue crack path near the threshold range, (a). As received material at RT, (b). Aged material at RT, (c). As received material at 150°C, (d). As received material at -50°C.*

TABLE 6—*Influence of temperature on the closure threshold of the stress intensity factor range.*

Material	Temperature (°C)	Maximum height (μm)	$\Delta K_{cl\,th}$ (MPa√m)	$\Delta K_{th\text{-}cal}$* (MPa√m)
As received	-50	19.4	8.97	6.39
	20	6	4.74	4.33
	150	7.4	4.57	4.66
475°C/3h	20	2.2	3.74	3.12

$\Delta K_{th\text{-}cal}{}^{*}=2,4(H_{max})^{1/3}$, H_{max} is the maximum height. This is a modified relation as mentioned in [2].

Fractographic Investigation

Strain or Crack Propagation Mismatch—Fatigue crack propagation behaviour at the interface in austenite and ferrite bimaterial has recently been investigated [15]. This work shows that when a crack approaches the interface, the crack propagation behaviour can change. In this investigation, the fatigue behaviour at the interface of the austenite and ferrite phases in duplex stainless steel has been studied. The results show that the phase boundaries are of less importance when ΔK is high (Figure 4a). However, in the threshold range, crack propagation mismatch can be observed at the interfaces of these two phases. The crack propagation from one phase to another changed its pattern and even the rate (Figure 4b-c). It was observed that the crack propagation mismatch is strongly effected by temperature. At -50°C, a cleavage crack even initiated at the interface. This crack propagation mismatch may cause a deflection of the crack propagation path, which is beneficial to crack closure or fatigue life.

As mentioned previously, crack closure in softer phases can be observed (Figure 5). This is a type of plasticity induced micro crack closure, which may be caused by the residual stresses. During cyclic straining, high residual stresses can be introduced in the softer phase of the duplex stainless steels [16].

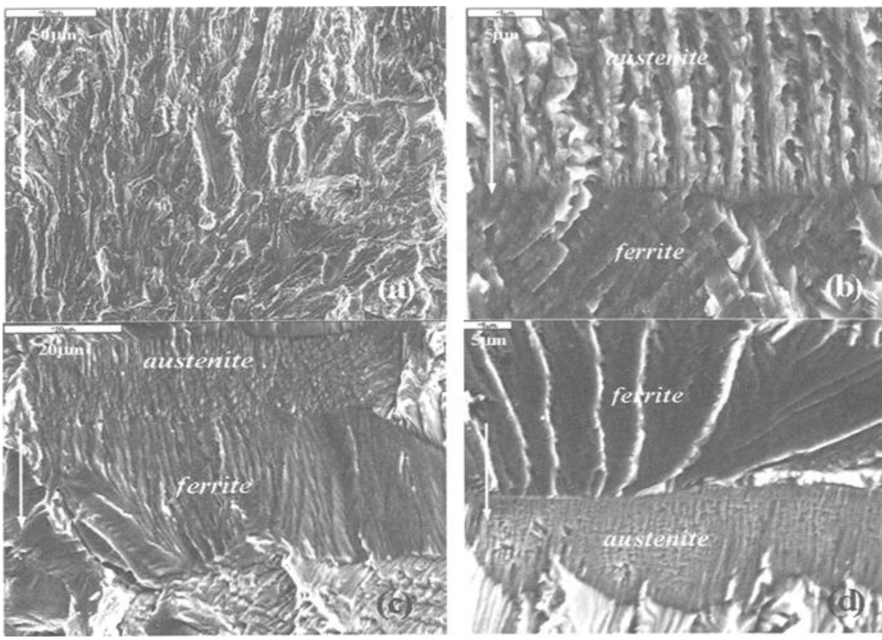

FIG. 4—*SEM fractographs showing propagation mismatch at the interface of the austenite and ferrite phases, (a). RT, ΔK=27 MPa$\sqrt{m}$, (b). RT, ΔK=9.7 MPa$\sqrt{m}$, (c). 150°C, ΔK=9.7 MPa$\sqrt{m}$, (d). -50 ℃, ΔK=15.2MPa*$\sqrt{\text{m}}$.

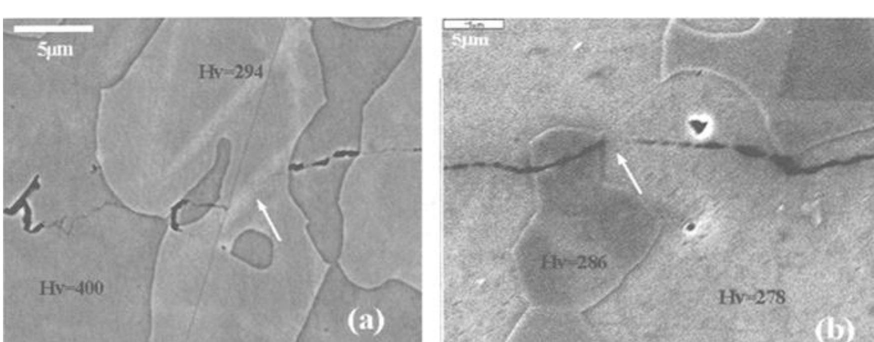

FIG. 5—*SEM fractographs showing crack closure, (a). RT, Aged material, (b). 150°C, As received material.*

An Observation of Transition from Brittle to Ductile near the Threshold Range—For ferritic steels, the FDBT may occur when a certain temperature is reached, leading to a rise in the FCG rate. In this investigation, cleavage in some ferritic areas has been observed on the sample tested at -50°C, but this occurred only in the high ΔK range (Figure 6a). No cleavage fracture was observed in the near threshold range, and the fracture is mainly ductile (Figure 6b). A similar phenomenon has been reported in one ferritic steel [11], but the mechanism for this mixture mode is not quite understood. As known, however, there is a critical stress needed to initiate cleavage fracture. No cleavage can be observed when the stress is below this critical stress.

For the aged material, the cleavage in the ferrite phase is usually observed during cyclic loading in the high ΔK range (Figure 7a) and the amount of cleavage area increases with increasing ΔK. However, it was found in this investigation that the fracture character was different, mainly transgranular facet, in the near threshold range. Little or no cleavage can be observed (Figure 7b). This is similar to that at low temperature. Actually, we can also use the critical shear stress to explain this phenomenon.

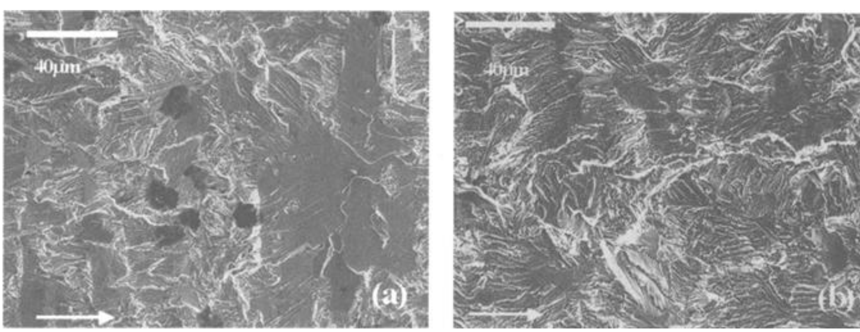

FIG. 6—*Fracture of the as received material at -50°C; the allows are the FCG directions; (a). ΔK=15.9 MPa$\sqrt{m}$, (b). ΔK=14.9 MPa$\sqrt{m}$.*

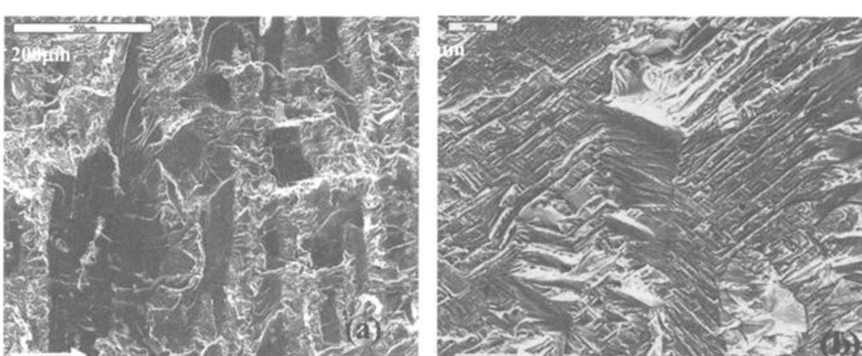

FIG. 7—*Fracture of the aged material at RT; the allows are the FCG directions; (a). ΔK=9.47MPa$\sqrt{m}$, (b). ΔK=7.42MPa$\sqrt{m}$.*

Conclusions

The fatigue threshold value of the stress intensity factor range and the effective threshold value of super duplex stainless steel SAF 2507 are higher at –50°C and 150°C than at RT. The closure threshold value is smaller at RT than at -50°C, but comparable with that at 150°C.

The effective threshold value of the material aged at 475°C is comparable to that of the as received material, but the closure threshold value of the as received material is higher than that of the aged material.

Strain mismatch at the interface of the austenite and ferrite phases can cause crack propagation mismatch and crack closure in the softer phase.

There is a brittle to ductile fracture transition in the near threshold regime for the material at low temperature and for the aged material at RT.

Acknowledgments

This paper is published with permission of AB Sandvik Materials Technology. The support of Dr T. Thorvaldsson, Prof. J. O. Nilsson, and Mr M. Lundström and the technical assistance of Mr G. Svensk are gratefully acknowledged.

References

[1]. Nilsson, J-O, "Super duplex stainless steels", *J. of Material Science and Technology,* Vol. 8, 1992, pp. 685-700.

[2]. Wasen, J., Engström, E. U., and Karlsson, B., "Near-Threshold Fatigue Growth in a Micro duplex Stainless Steel" *Stainless Steels '87,* York, UK, 1987, The Institute of Metals, 1988, pp. 357-362,

[3]. Murakami, R. I., Kim, Y. H., and Ferguson, W. G., The Effects of Microstructure and Fracture Surface Roughness on Near Threshold Fatigue Crack Propagation Characteristics of a Two-Phase Cast Stainless Steel", *Fatigue and Fracture of Engineering Materials and Structures,* Vol. 14, no. 7, 1991, pp. 741-748.

[4]. Nyström, M., "Plastic deformation of duplex stainless steel", *PhD thesis,* Charmers University of Technology, Sweden, 1995.

[5]. Iturgoyen, L. and Anglada, M., "The influence of ageing at intermediate temperatures on the mechanical behaviour of a duplex stainless steel. II. Fatigue life and fatigue crack growth", *Fatigue and Fracture of Engineering Materials and Structures,* Vol. 20, no. 6, 1997, pp. 917-928

[6]. Stephens, R. L., "Fatigue at low temperature", *ASTM STP 857,* 1985.

[7]. Matsuoka, S, et al., "Near-threshold fatigue crack growth properties at elevated temperature for 1Cr-1Mo-0,25V steel and stainless steel", *Metall. Trans. A,* Vol 20A, 1989, pp. 741-749

[8]. Cotterill, P. J. and Knott J. F., "Effect of temperature and environment on fatigue crack growth mechanisms in a 9%chromium 1%molybdenum steel", *Acta Metall. Mater.,* Vol. 40, 1992, pp. 2753-2764.

[9]. Liaw, P. K. and Logsdon W. A., "Near-threshold fatigue crack growth properties at cryogenic temperature", *Fatigue'87,* Vol II, 1987, pp. 899-908.

[10]. Moody, N. R. and Gerberich, W. W., "Fatigue Crack Propagation in Iron and Two Iron Binary Alloys at Low Temperatures," *Mater, Sci. Eng.,* Vol. 41, 1979, pp, 271-280.

[11]. Tschegg, E. and Stanzl, S., "Fatigue Crack Propagation and Threshold in B.C.C. and F.C.C. Metals at 77 and 293 deg K," *Acta Metall.*, vol. 29, 1981, pp. 33-40.
[12]. Ritchie, R. O, "Mechanisms of Fatigue Crack Propagation in Metals, Ceramics and Composites: Role of Crack Tip Shielding, " *Mater. Sci. Eng.*, Vol. 103, 1988, pp, 15-28.
[13]. Suresh, S., Fatigue of Materials, 2nd edition, Cambridge, UK, 2001
[14]. Unpublished results.
[15]. Suresh, S., Sugimura, Y., and Tschegg, E. K., "The Growth of a Fatigue Crack Approaching a Perpendicularly-Oriented, Bimaterial Interface," *Scripta Metallurgica et Materialia (USA),* vol. 27, no. 9, pp. 1189-1194, 1 Nov. 1992.
[16]. Moverare, J. J., "Microstresses and anisotropic mechanical behaviour of duplex stainless steels" *PhD thesis,* Linköping Institute of Technology, Sweden, 2001.
[17]. Lü, B. and Zheng, X., Predicting fatigue crack growth rates and thresholds at low temperatures," Mater. Sci. Eng. A, Vol. 148, 1991, pp. 178-188.

SESSION 2B: FRACTURE FUNDAMENTALS

Journal of ASTM International, January 2005, Vol. 2, No. 1
Paper ID JAI11991
Available online at www.astm.org

James A. Joyce[1]

Evaluation of the Effect of Crack Tip Constraint on Fatigue Crack Growth Rate in Inconel 718

ABSTRACT: The objective of this work has been to characterize the fatigue crack growth rate of Inconel 718 in the elastic and elastic-plastic regimes. The major new contribution here is to develop fatigue crack growth rate data on this alloy using shallow crack specimens subjected to cyclic loadings that involve material plasticity exceeding what is allowed by the standard Linear Elastic Fracture Mechanics (LEFM) procedures of ASTM E 647.

Compact (C(T)) and three point bend (SE(B)) specimen geometries were used in this investigation. The SE(B) specimens were used to obtain shallow crack data using crack to depth ratios (a/W) as small as 0.08 in standard bend specimens with W = 50.8 mm. Compliance methods were used to estimate the crack length during the cyclic testing. The C(T) specimens were used to investigate the effect of fully reversed loading, i.e., R = –1.0. These specimens were tested only in deep crack configurations with a/W > 0.3. Both C(T) and SE(B) specimens were used to obtain high cycle fatigue crack growth data as well as some component of the low cycle fatigue crack growth rate data. The cyclic elastic stress intensity range was used to characterize the crack growth driving "force" in the high cycle regime as defined in ASTM E 647. A cyclic J integral range, as originally utilized by Dowling and Begley [1], was used in the elastic-plastic regime.

High cycle and low cycle fatigue crack growth data were successfully obtained from tests on shallow crack SE(B) specimens. High cycle fatigue crack growth was not affected by specimen geometry or by crack length ratio, even for a/W ratios as low as 0.08. The low cycle fatigue crack growth rate was similar, but not identical, to what one would get by extrapolating the high cycle fatigue crack growth rate, as proposed by Dowling and Begley [1]. Under conditions of increasing J range, the crack growth rate under elastic-plastic conditions was accelerated, while under decreasing J range conditions the crack growth rate was decelerated in comparison to the extrapolated high cycle fatigue crack growth rate measurements. The R ratio did not affect the crack growth rate for the two cases tested here, namely R = 0.1 and R = –1.0. More rapidly increasing J range conditions resulted in greater crack growth rate acceleration. In the elastic-plastic fatigue regime, shallow crack specimens demonstrated slower crack growth rates than deep crack specimens

KEYWORDS: high cycle fatigue crack growth, elastic-plastic fatigue crack growth, cyclic J-integral, shallow cracks, low cycle fatigue crack growth

Introduction

The objective of this work has been to characterize the elastic-plastic fatigue crack growth rate behavior of Inconel 718 and to relate the results to high cycle fatigue crack growth data. It was also a goal to determine the effect that constraint has on the elastic-plastic fatigue crack growth rate and to incorporate this information into computational codes used to design and evaluate complex components of the NASA space shuttle launch system. Constraint effects of the fatigue crack growth rate will be measured using shallow crack three point bend specimens.

Manuscript received 22 October 2003; accepted for publication 15 April 2004; published January 2005. Presented at ASTM Symposium on Fatigue and Fracture Mechanics: 34th Volume on 19–21 November 2003 in Tampa, FL; S.R. Daniewicz, J.C. Newman, Jr., and K-H. Schwalbe, Guest Editors.

[1] Professor of Mechanical Engineering, U.S. Naval Academy, Annapolis, MD 21402.

In the work completed to date, the basic tensile properties of the Inconel 718 plate have been evaluated, the static J integral resistance curve has been measured on C(T) and shallow and deep crack SE(B) specimen geometries, and the high cycle fatigue crack growth properties of the material have been evaluated using shallow and deep crack SE(B) geometries. Deep crack specimens were tested with load ratios of $R = 0.1$ and -1.0, and shallow crack specimens with $R = 0.1$. Elastic-plastic, low-cycle fatigue crack growth data have been measured for shallow and deep crack SE(B) specimens with a load ratio of $R = 0.1$ and for deep crack C(T) specimens with $R = 0.1$ and -1.0.

Description of the Experiments

Tensile Properties

The Inconel 718, corresponding to the SAE Aerospace Material Specification AMS 5597E, was purchased in the form of a 13 mm thick plate 305 mm × 610 mm in dimension. Round tensile specimens having a diameter of 6.35 mm and a test gauge length of 25 mm were machined from this material in the as-received condition. The specimens were then heat treated as required by the AMS 5597E standard and tested at 22°C at a quasi-static loading rate in a standard servohydraulic test machine. The measured tensile mechanical properties are presented in Table 1 with two typical engineering stress-strain curves as shown in Fig. 1. These tensile mechanical properties are well within the requirements of AMS 5597E.

Fracture Toughness

Fracture toughness and fatigue crack growth properties were measured using C(T) and SE(B) specimens machined according to ASTM E 1820. A 1T plan size was used with $W = 50.8$ mm and a thickness of $B = 12.5$ mm. Specimens were machined and heat-treated according to AMS 5597E, side grooved using a standard Charpy cutter notch configuration to a total reduction of 20 %, and then fatigue precracked before testing. Specimens were all tested at ambient temperature, approximately 22°C, in a standard 100 kN servohydraulic test machine using a PC computer as a test controller and 16 bit digital resolution data acquisition system. Software was written in Visual Basic to control the various tests described below. A summary of all fracture and fatigue specimens is presented in Table 2.

The unloading compliance method, according to ASTM E 1820, was used to evaluate the J_{Ic} and J integral resistance curve toughness for this material. A typical load displacement curve is shown in Fig. 2, and the resulting J-R curves are shown in Fig. 3. The measured J_{Ic} of this material was estimated as 110–120 kJ/m^2, as shown in Fig. 3.

TABLE 1—*Tensile mechanical properties of Inconel 718.*

Specimen ID	Yield Strength MPa	Ultimate Strength MPa	% Elongation	% Reduction of Area
T2	1226	1459	27	37
T4	1200	1425	25	46

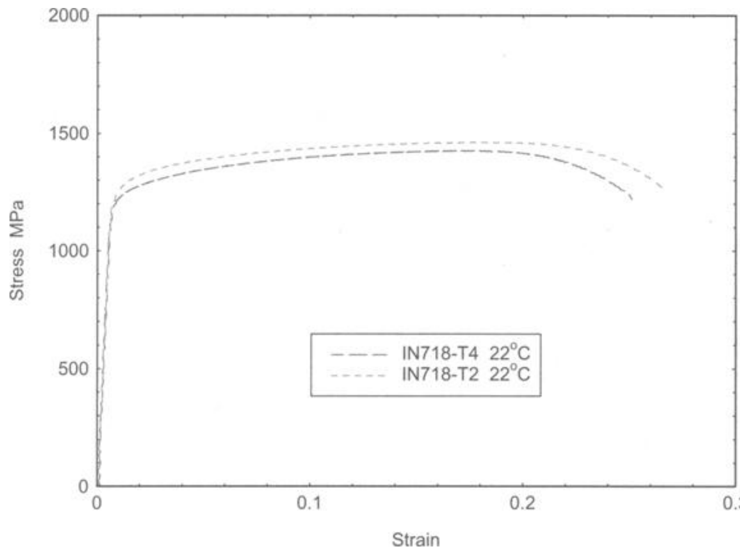

FIG. 1—*Tensile engineering stress-strain curves for Inconel 718.*

TABLE 2—*Inventory of fracture toughness and fatigue specimens.*

Specimen ID	Specimen Type	Crack Size	R	Description
CT1	C(T)	Deep	...	Not Tested
CT2	C(T)	Deep	...	Not Tested
CT3	C(T)	Deep	R = 0.1	Low Cycle
CT4	C(T)	Deep	R = 0.1	Low Cycle
CT5	C(T)	Deep	...	J-R curve
CT6	C(T)	Deep	...	Not tested
CT7	C(T)	Deep	R = -1.0	Low Cycle
CT8	C(T)	Deep	R = -1.0	Low Cycle
CT9	C(T)	Deep	R = 0.1	High Cycle
SB1	SE(B)	Deep	R = 0.1	Broken in setup
SB2	SE(B)	Deep	R = 0.1	High Cycle
SB3	SE(B)	Shallow	R = 0.1	Low Cycle
SB4	SE(B)	Deep	R = 0.1	Low Cycle
SB5	SE(B)	Shallow	R = 0.1	Low Cycle
SB6	SE(B)	Deep	...	J-R curve
SB7	SE(B)	Deep	R = 0.1	Shallow/Deep High Cycle
SB8	SE(B)	Shallow	R = 0.1	Low Cycle/Large COD Step
SB9	SE(B)	Shallow	...	J-R curve
SB10	SE(B)	Deep	R = 0.1	Low Cycle
SB11	SE(B)	Shallow	R = 0.1	Low Cycle

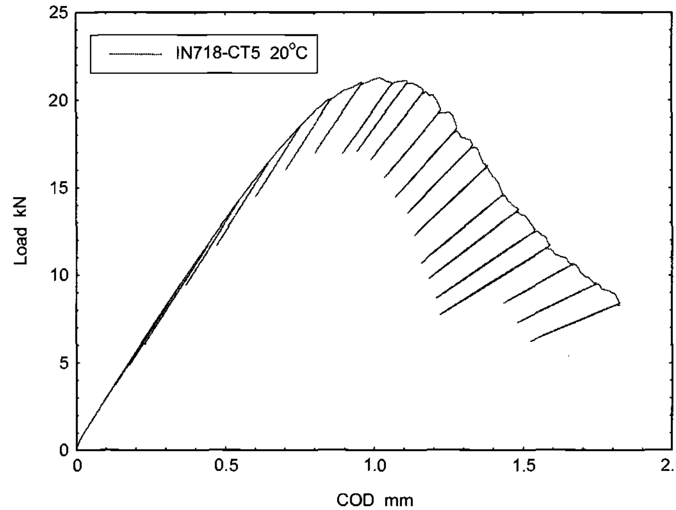

FIG. 2—*Unloading compliance load-COD record.*

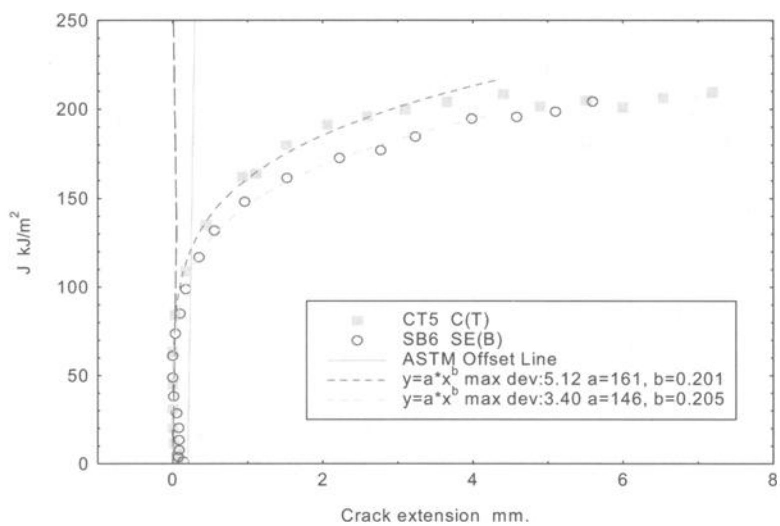

FIG. 3—*J-R curves for the IN718 alloy.*

A shallow crack SE(B) specimen was also tested to evaluate the effect of crack tip constraint on the J-R curve of this alloy. Results presented in an earlier NASA report by McClung et al. [2] show a distinct elevation of the J-R curve for a surface crack test geometry, but much scatter and uncertainty were demonstrated in the earlier results. The measured shallow crack J-R curve is compared to the deep crack results in Fig. 4. Both the J_{Ic} and the J-R curve slope are strongly elevated in the J-R curve of the shallow crack specimen.

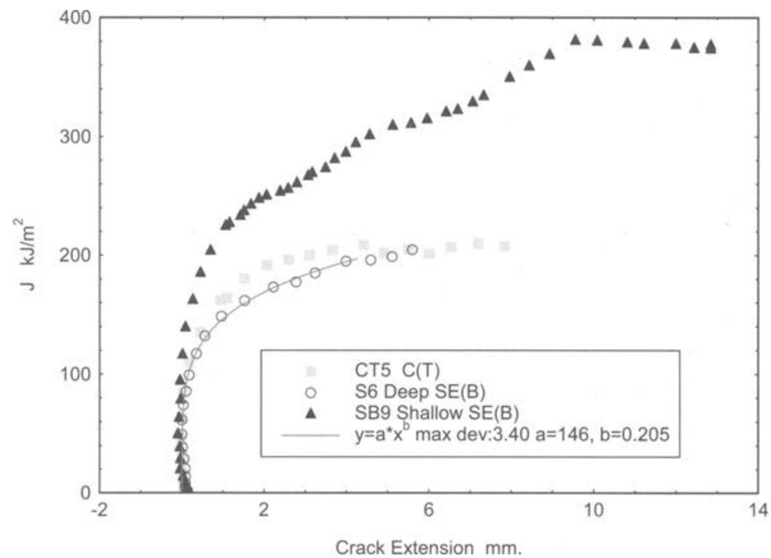

FIG. 4—*Comparison of shallow and deep crack J-R curves for Inconel 718.*

High Cycle Fatigue Crack Growth

High cycle fatigue crack growth data were measured on both C(T) and SE(B) specimen geometries using the procedure of ASTM E 647. Testing was done at 22°C in lab air at a frequency of 30 Hz. The same 20 % reduction side grooves were used on these specimens to keep the crack in the desired central plane. The results obtained from one C(T) specimen, showing both ΔK increasing and ΔK decreasing data, are presented in Fig. 5. A standard Paris [3] curve fit of the form:

$$\frac{da}{dN} = C\left(\Delta K\right)^m \tag{1}$$

is included on this plot. Figure 6 shows high cycle fatigue crack growth results for a deep SE(B) specimen of the same IN718 alloy and also includes fatigue crack growth data obtained from a shallow crack SE(B) specimen. Deep crack specimens were those with a/W > 0.28. The shallow crack specimen initially had a/W = 0.08 and was tested with an increasing K range and R = 0.1, starting with a K range of about 20 MPa $m^{0.5}$, and increasing the K range slowly until the K range reached 25 MPa $m^{0.5}$. The K range was then shed, falling to a low value of 15 MPa $m^{0.5}$. The crack length had increased at this point to 13 mm, corresponding to a/W = 0.256. The crack was then not considered "shallow," and cycling was continued under increasing ΔK conditions until the K range approached 40 MPa $m^{0.5}$. The COD gauge calibration was then changed, the test frequency was reduced, and this same specimen was tested until the applied K range approached 88 MPa $m^{0.5}$, as shown in Fig. 7, at which point the specimen failed with a final a/W = 0.875. The comparison demonstrated between deep and shallow high cycle fatigue crack growth rates is excellent, as can be seen in Figs. 6 and 7.

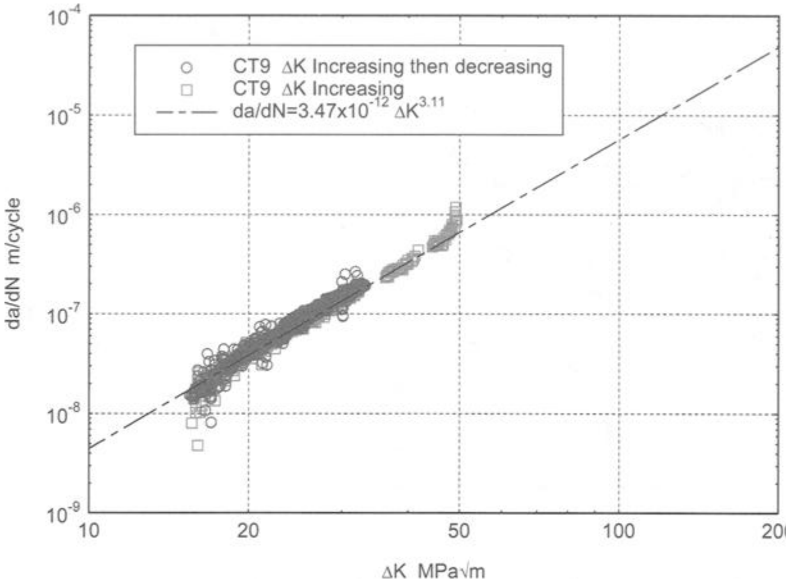

FIG. 5—*High cycle fatigue crack growth resistance of the IN718 alloy, C(T) specimen geometry.*

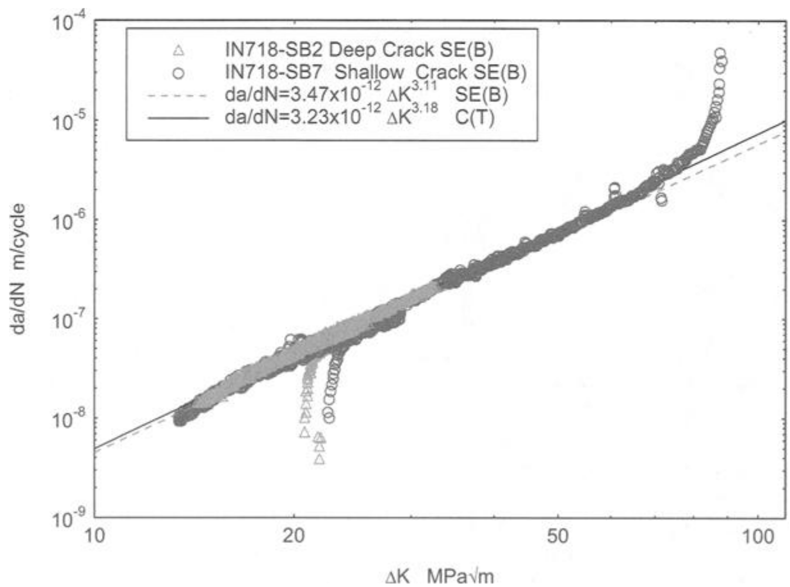

FIG. 6—*Comparison of high cycle fatigue crack growth rates for deep and shallow SE(B) specimens of IN718.*

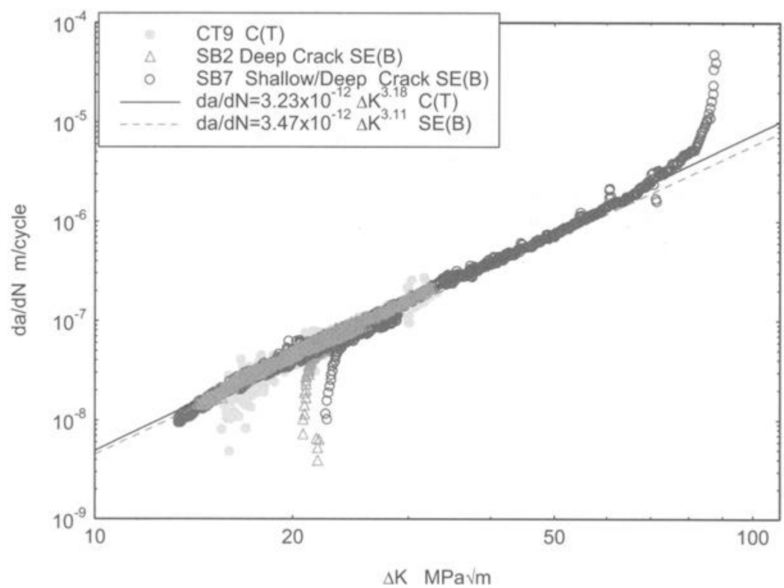

FIG. 7—*Comparison of C(T) and SE(B) geometry high cycle fatigue crack growth rate data showing, again, very similar crack growth rates.*

Nothing exceptional was done to obtain the fatigue crack growth data from shallow crack specimens. The PC used a readily available 16 bit A/D-D/A PCI bus data acquisition card capable of 100 000 readings per second. The specimen notches were machined using a wire EDM system with a wire diameter of 0.3 mm. A ring gauge, shown in Fig. 8, was mounted directly on the surface of the specimen using 90° mounting corners with an initial opening of about 0.75 mm. The ring gauge was conditioned by a standard transducer conditioner with a sensitivity of approximately 0.05 mm/volt. The crack length is calculated from a stiffness estimate based on approximately 2000 data points taken over one to two load cycles. Data near crack closure are discarded in the basic crack length estimation scheme. For the shallow crack compliance based crack length measurement, the COD value is smaller, but at the same time the load range is much larger, and the resulting compliance system is only somewhat less sensitive and precise. With a quality transducer calibrated tightly to the signal range, a good signal conditioner amplifier, and a 16 bit or better data acquisition system, precise and repeatable shallow crack length estimates can be made for the a/W ~ 0.08 crack length and greater.

The Paris relationship taken from the C(T) specimen data of Fig. 5 and superimposed on Fig. 6 shows that the C(T) and SE(B) specimens generate nearly identical fatigue crack growth rates in this alloy in the high cycle fatigue crack growth regime. This is further shown in Fig. 7 where deep and shallow SE(B) and C(T) geometry data are combined for comparison. Figure 9 shows the crack length versus cycle histories for the shallow and deep SE(B) specimens, showing the full history of specimen SB7 from the initial a/W = 0.08 to the final a/W = 0.875.

Using the standard plane stress equation for plastic zone size from Irwin's plastic zone size estimation [4] that:

$$r_p = \frac{1}{2\pi}\left(\frac{K_I}{\sigma_y}\right)^2 \tag{2}$$

gives a plastic zone size for this alloy of only about 0.2 mm at the highest stress intensity applied to the shallow crack, which was approximately 5 mm in depth at that time. Clearly the plastic zone is surrounded and dominated by a large elastic annular region at all times during the high cycle fatigue crack growth test of the shallow crack configuration, and it is not surprising that the crack length did not affect the measured crack growth rate in these tests. The principal conclusions to this point are that the high cycle fatigue crack growth behavior of IN718 at an R ratio of 0.1 is not affected by a/W ratios as low as 0.1, specimen type (C(T) versus SE(B)), or whether the K range applied is increasing or decreasing.

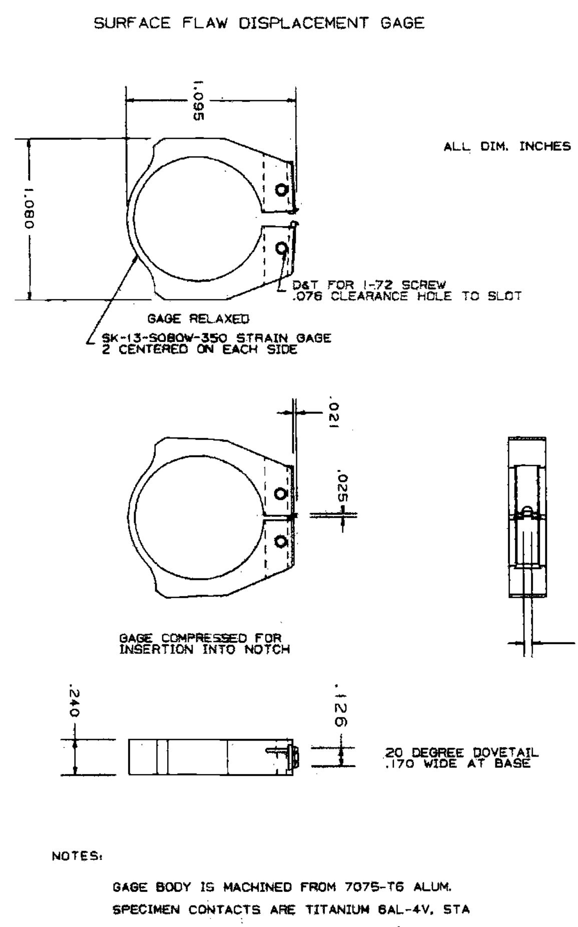

FIG. 8—*Ring gauge used for shallow crack COD measurements.*

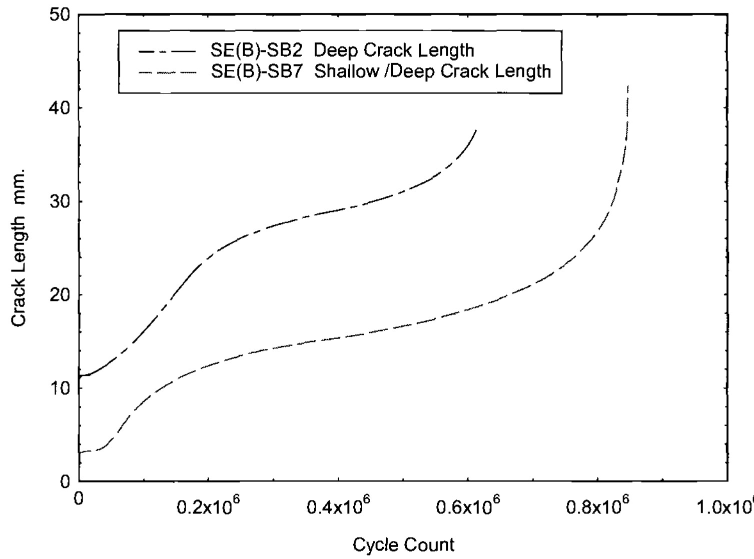

FIG. 9—*Crack length shown versus cycle count for two SE(B) high cycle fatigue crack growth specimens.*

Low Cycle Fatigue Crack Growth

Standard procedures do not exist for measuring low cycle fatigue crack growth properties on engineering alloys. Work was begun in this area by Dowling and Begley [1] in the 1980s and was extended by the work of Kaiser [5] and others [6–8], including this author, at that time. Tests conducted here used the techniques developed in Joyce and Culafic [9]. Basically the J integral is taken as the crack driving force parameter, and crack length is measured by compliance techniques. The C(T) and SE(B) geometries described above are used as the test specimens. J increasing conditions are achieved by applying a loading cycle to a prescribed load line COD value, then cycling with a slowly increasing final COD value. Holding the maximum COD cycle limit constant results in falling cyclic J (ΔJ) conditions as the crack extends with the applied cycles.

In this work, a cycle-to-cycle COD increment of 0.0025 mm was used in most cases. The desired R ratio was used to set the lower bound of the cycling, using either R = 0.1 or R = −1.0. R ratio effects are investigated using the C(T) specimen, while shallow crack effects are investigated using the SE(B) specimen geometry. Cycling frequencies are slow, approximately 20 s per cycle, or 0.05 Hz, and crack growth rates investigated are generally on the order of 2×10^{-5} m/cycle or higher.

Following the work of Dowling and Begley [1], the cyclic J integral is evaluated above the crack opening load, defined here using a compliance technique. The cyclic J is converted to the equivalent cyclic K using the relationship that:

$$\Delta K = \sqrt{E'\Delta J} \tag{3}$$

where $E' = E/(1-\nu^2)$.

C(T) Specimen Results

The C(T) specimen geometry was tested under R = 0.1 and R = –1.0 conditions with $0.4 \leq a/W \leq 0.85$. The R = –1.0 loading was achieved by using specimen caps which were installed on top and bottom of the C(T) specimen as shown in Fig. 10. The specimen was loaded in tension using the standard pin/clevis fixtures of ASTM E 1820 and in compression by having the clevises apply load line forces to the specimen through the end caps. All compliance based crack length estimations were done using tension data so that accurate crack length estimates were assured.

Typical load versus COD cycling history plots for R = –1.0 and R = 0.1 are shown in Figs. 11 and 12. In each case these correspond to approximately 200 cycles of increasing cyclic J followed by 400–600 cycles of falling cyclic J. All data were taken digitally and stored to allow full data re-analysis as necessary. Some data files were up to 70 MB in size, but having the complete data file for reanalysis was considered worth the cost of file storage, given the cost of present day disk space.

The resulting low cycle fatigue crack growth data are compared in Fig. 13 to the high cycle measurements obtained above. These specimens were precracked with constant ΔK cycling at $\Delta K = 20$ MPa $m^{0.5}$. The applied ΔK was then increased dramatically to $\Delta K = 40$ MPa $m^{0.5}$ at the start of the low cycle fatigue crack growth testing. Not surprisingly, this resulted in a larger acceleration in the fatigue crack growth rate that took several cycles to dissipate. When it did dissipate, the resulting crack growth rate remained elevated above the extrapolated high cycle fatigue crack growth rate by about a factor of 2. The R = –1.0 crack growth rate appears to be elevated above the R = 0.1 data throughout the tests. When the COD was held constant, the driving ΔK conditions started to fall, and the crack growth rate fell approaching the extrapolated high cycle fatigue crack growth rate curve.

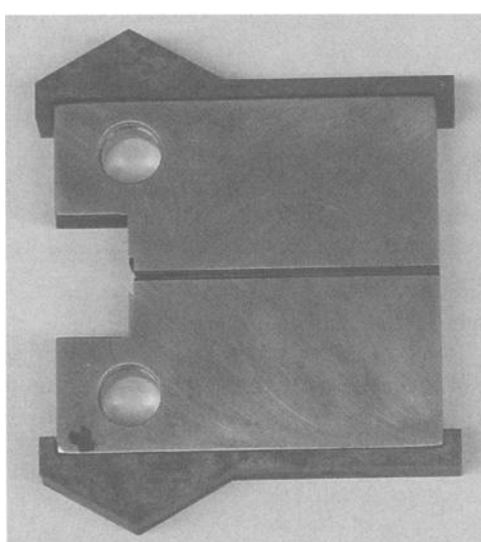

FIG. 10—*C(T) specimen with compression end caps in place.*

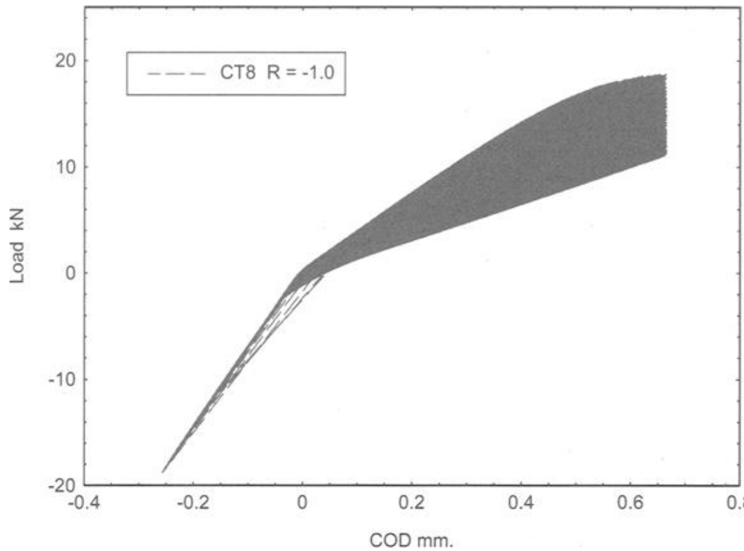

FIG. 11—*Cyclic load versus COD history for an IN718 specimen with R = –1.0.*

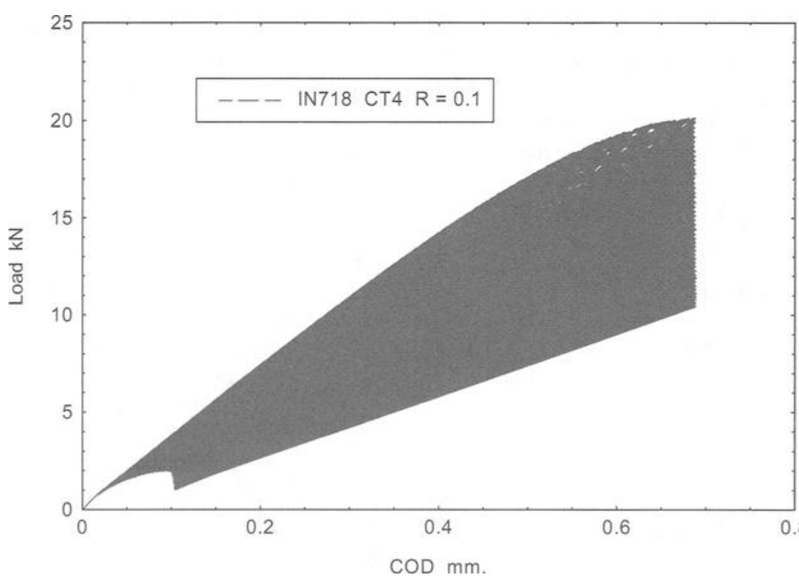

FIG. 12—*Cyclic load versus COD history for an IN718 sample with R = 0.1.*

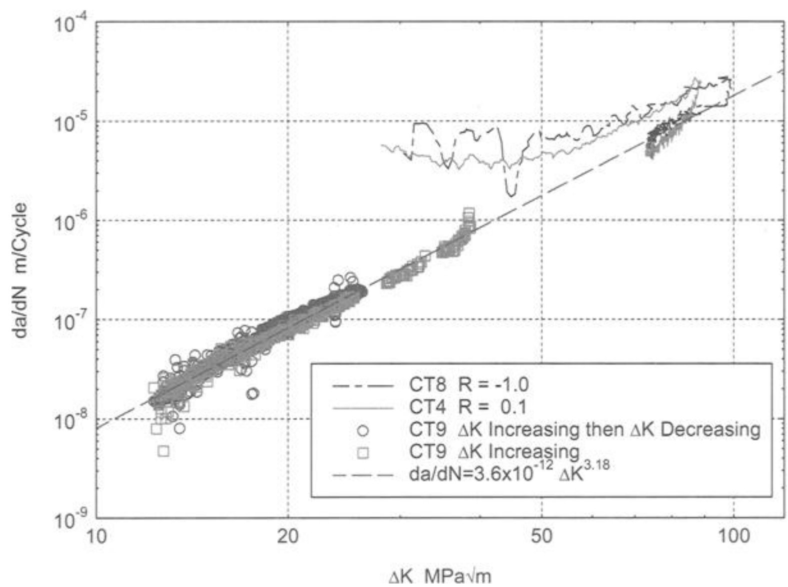

FIG. 13—*Comparison of low cycle and high cycle fatigue crack growth rate data on a cyclic K range scale.*

The two low cycle fatigue crack growth specimens presented in Fig. 13 demonstrate an elevated crack growth rate in comparison with the high cycle growth behavior while the cyclic ΔK (from ΔJ) is increasing and a return to the extrapolated high cycle fatigue crack growth rate when the ΔK is decreasing. The applied R ratio of -1.0 seems to correspond to a slightly higher crack growth rate for both ΔK increasing and decreasing conditions.

Bend Specimen Data

Single edge notched bend specimens were tested in both high and low cycle fatigue crack growth using deep crack (a/W = 0.4–0.7) and shallow crack (a/W = 0.1–0.3) configurations. All tests were conducted with R = 0.1. Load versus COD displacement records for two typical specimens are shown in Fig.14.

These tests were run in COD control with small increments in COD added with each cycle, giving increasing ΔK, and then after a crack growth rate of approximately 2.5×10^{-2} mm/cycle was reached, the maximum COD was held constant, resulting in decreasing ΔK cycling conditions. The test control software utilized ΔJ for all calculations, with the conversion to equivalent ΔK done using Eq 3 for plotting and comparison following Dowling and Begley [1]. Each specimen shown in Fig. 14 was subjected to approximately 200 cycles of increasing K range followed by 2000 cycles of decreasing K range. The resulting crack growth rate measurements are presented in Fig. 15. Clearly the crack growth rate is distinctly greater, about a factor of 2, during the increasing J range cycles than during the decreasing J range cycles. It is also apparent that the deep crack specimen has a higher crack growth rate than the shallow crack specimen for both the increasing K range cycles and the decreasing J range cycles.

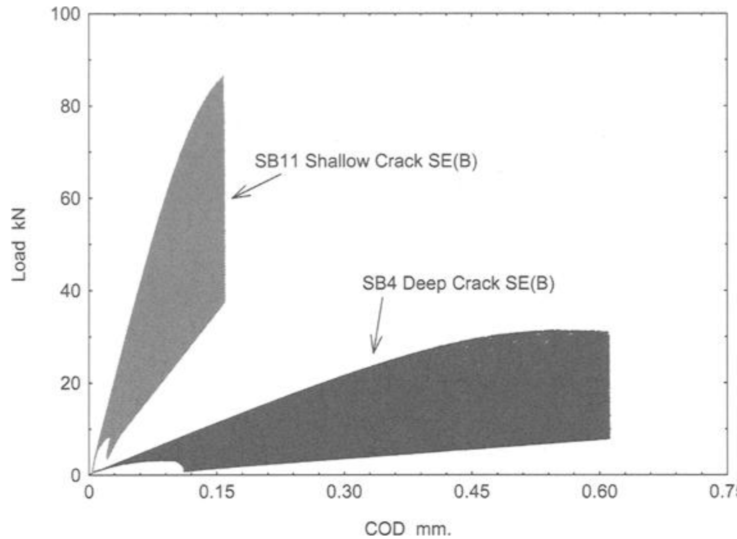

FIG. 14—*Load versus COD displacement records for typical deep and shallow bend specimens with R = 0.1.*

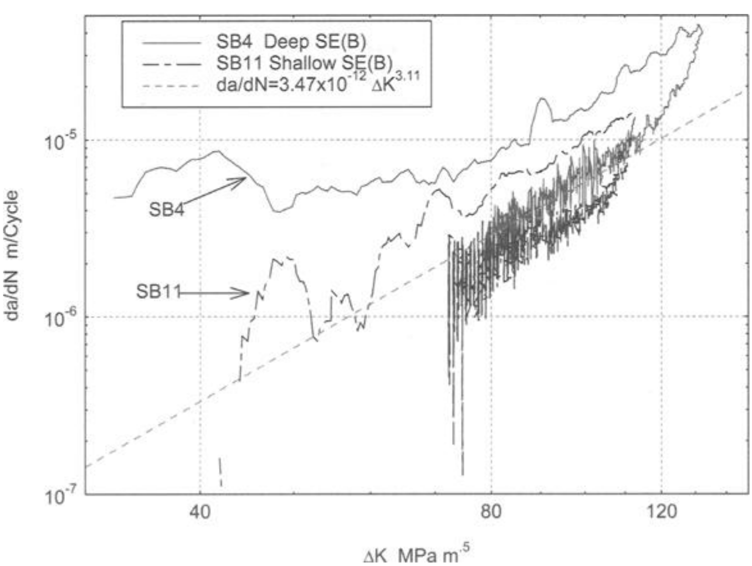

FIG. 15—*Comparison of deep and shallow low cycle fatigue crack growth rates during increasing and decreasing K range cycles.*

Figure 16 shows the application of two separate K increasing/decreasing cycling steps that were applied to SE(B) specimen SB3. Figure 17 shows that the high and low crack growth rates were established for the first K increasing then decreasing cycles, then re-established for the second K increasing/decreasing cycles. Figure 18 shows the a/W ratio versus cycle count for the shallow crack SE(B) specimens SB3 and SB11. The "shallow" crack size is varying from a/W = 0.1 to a/W = 0.3 through the course of these tests.

The low cycle fatigue crack growth rate is approximately equivalent to an extrapolation of the high cycle fatigue crack growth rate data, but under low cycle conditions, ΔK increasing conditions result in slightly higher crack growth rates, while ΔK decreasing conditions result in somewhat lower crack growth rates, in comparison to the extrapolation of the high cycle data. Shallow crack specimens demonstrate the same basic behavior except that under both ΔK increasing and ΔK decreasing loading conditions, the crack growth rate in the shallow crack specimen is about a factor of 2 slower than that of the deep crack specimen subjected to the same ΔK conditions. The crack growth rate appears to be slightly higher in C(T) specimens with R = –1.0 in comparison with the same geometry tested with R = 0.1. No difference was measured between the C(T) and SE(B) test piece geometries.

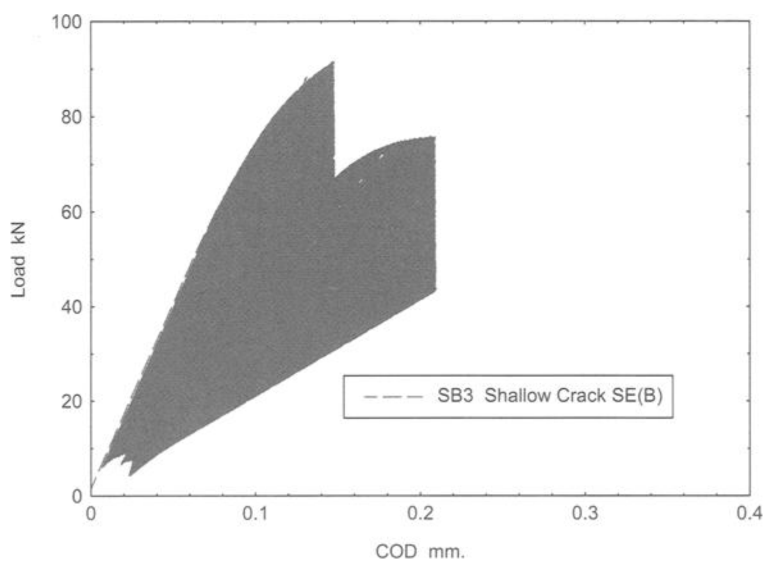

FIG. 16—*Loading history applied to specimen SB3 showing two loading blocks with K range increasing, then decreasing.*

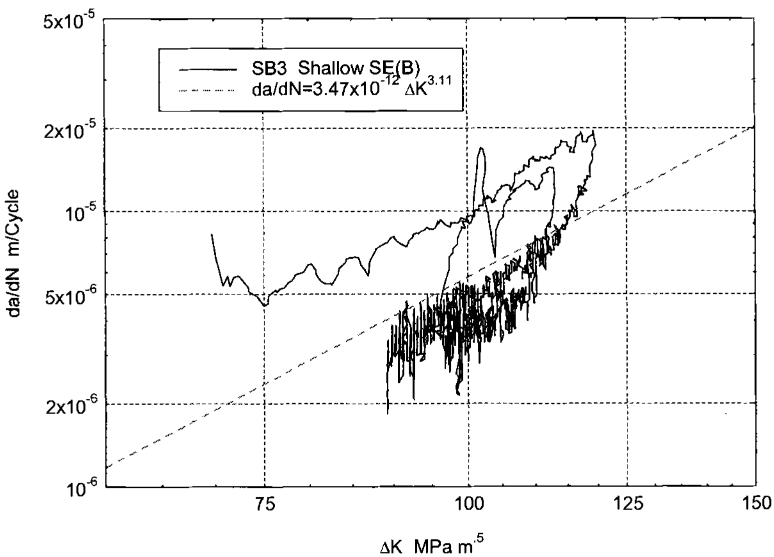

FIG. 17—*Crack growth rate resulting from cycling history of Fig. 16 showing the clearly defined high and low rates corresponding to increasing and decreasing applied K range.*

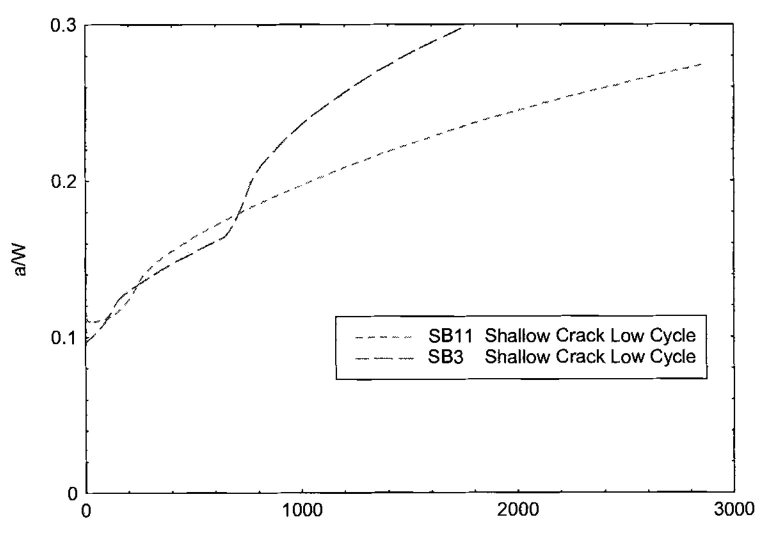

FIG. 18—*Crack length versus cycle count for the two shallow crack low cycle SE(B) specimens.*

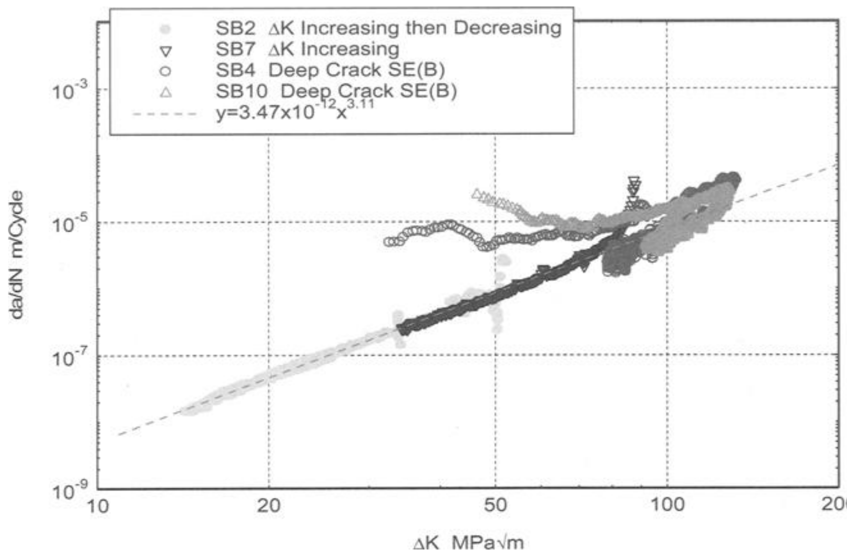

FIG. 19—*Low cycle data for a deep crack SE(B) specimen compared with the high cycle data and the extrapolation curve.*

Step Size Effect

To investigate the effect of the COD step size on the crack growth rate during low cycle fatigue crack growth conditions, SE(B) specimen SB8 was tested with a COD step of 0.005 mm, which was a factor of two larger than that used on other specimens. Three steps of increasing and then decreasing ΔK were applied to specimen SB8 as shown in the load versus COD plot in Fig. 20. Figure 21 shows that increasing the COD step size during the ΔK increasing part of the cyclic loading results in a higher crack growth rate, which is then followed by a lower crack growth rate when the COD step is set to zero.

Conclusions

Under high cycle fatigue conditions, the fatigue crack growth rate for Inconel 718 is insensitive to the specimen geometry, whether the ΔK applied is decreasing, and to crack length ratio over the range $0.08 \leq a/W \leq 0.8$ tested in this program.

Low cycle fatigue is approximately equivalent to an extrapolation of the high cycle fatigue crack growth rate data, but under low cycle conditions ΔK/ΔJ increasing conditions result in slightly higher crack growth rates, while ΔK/ΔJ decreasing conditions result in somewhat lower crack growth rates, in comparison to the extrapolation of the high cycle data. More rapidly increasing ΔK/ΔJ loading conditions result in a higher crack growth rate under low cycle fatigue crack growth conditions.

Shallow crack specimens demonstrate the same basic behavior except that under both ΔK/ΔJ increasing and ΔK/ΔJ decreasing loading conditions, the crack growth rate in the shallow crack specimen is about a factor of 2 slower than that of the deep crack specimen subjected to the same

ΔK conditions. The crack growth rate appears to be slightly higher in C(T) specimens with R = −1.0 in comparison with the same geometry tested with R = 0.1.

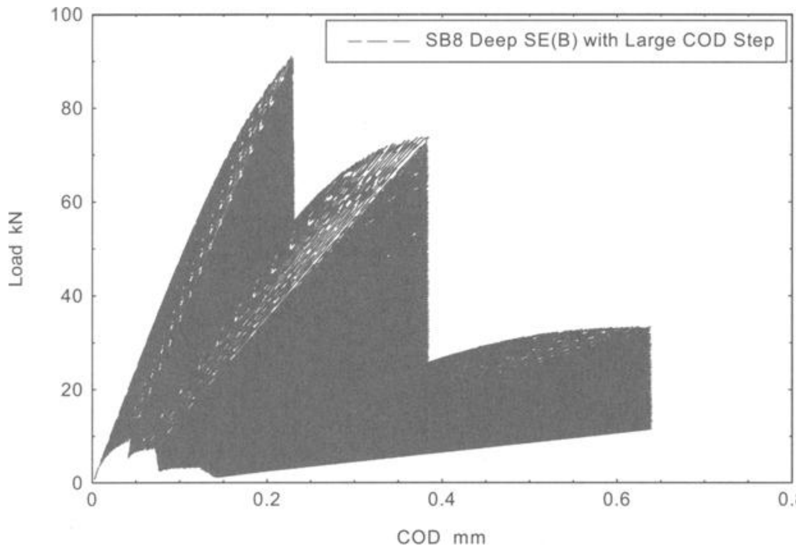

FIG. 20—*Cyclic load-COD record for specimen SB8.*

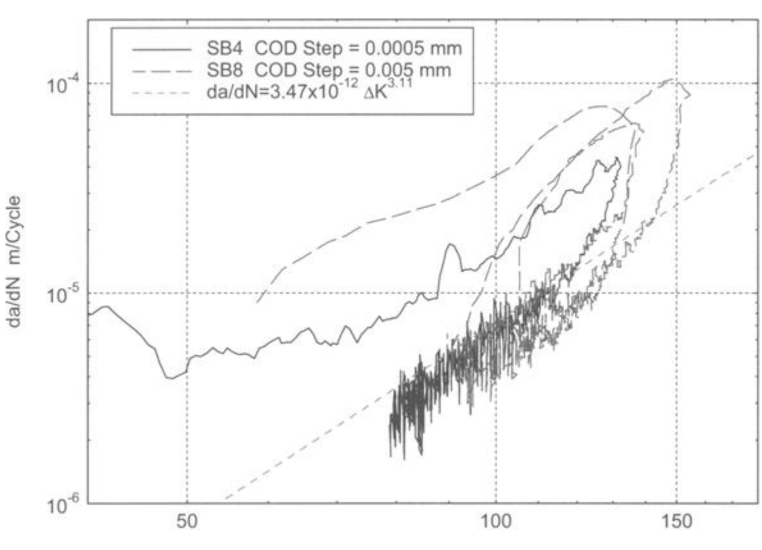

FIG. 21—*Effect of COD step size on the crack growth rate in two deep crack SE(B) specimens.*

Acknowledgments

This work was funded by a grant from Marshall Space Flight Center, Huntsville AL. I would like to acknowledge the support of Doug Wells and Preston McGill of NASA Marshall for their support and assistance during the course of this work. I would also like to thank Professor Robert Dodds, Jr. of the University of Illinois, Urbana, IL, for his invaluable assistance in the initiation of this project. The assistance of technical support personnel at the U.S. Naval Academy, especially Derek Baker, is also greatly appreciated.

References

[1] Dowling, N. E. and Begley, J. A., "Fatigue Crack Growth During Gross Plasticity and the J-Integral," *Mechanics of Crack Growth, ASTM STP 590*, ASTM International, West Conshohocken, PA, 1976, pp. 82–103.

[2] McClung, R. C., et al., "A Comparison of Single-Cycle Versus Multiple-Cycle Proof Testing Strategies," NASA/CR-1999-209426, Marshall Space Flight Center, 1999.

[3] Paris, P. C. and Erdogan, F., "A Critical Analysis of Crack Propagation Laws," *Journal of Basic Engineering*, Vol. 85, 1960, pp. 528–534.

[4] Anderson, T. L., *Fracture Mechanics: Fundamentals and Applications*, 2nd ed., CRC Press, 1995, p. 73.

[5] Kaiser, S., "On the Relation Between Stable Crack Growth and Fatigue," *Fatigue of Engineering Materials and Structures*, Vol. 6, No. 1, 1983.

[6] El Haddad and Mukherjee, B., In *Elastic-Plastic Fracture: Second Symposium, ASTM STP 803*, ASTM International, West Conshohocken, PA, 1983, pp. II689–II707.

[7] Tanaka, K., Hoshide, T., and Nakata, M., In *Elastic-Plastic Fracture: Second Symposium, ASTM STP 803*, ASTM International, West Conshohocken, PA, 1983, pp. II708–II722.

[8] Joyce, J. A. and Sutton, G. E., "An Automated Method of Computer-Controlled Low-Cycle Fatigue Crack Growth Testing Using the Elastic-Plastic Parameter Cyclic J," *ASTM STP 877*, ASTM International, West Conshohocken, PA, 1985, pp. 227–247.

[9] Joyce J. A. and Culafic, V., "Characterization of Interaction Effects Between Ductile Tearing and Intense Fatigue Cycling," *Int. J. Fract.*, Vol. 36, 1988, pp. 89–100.

SESSION 3A: FATIGUE CRACK GROWTH THRESHOLDS II

Journal of ASTM International, May 2005, Vol. 2, No. 5
Paper ID JAI12042
Available online at www.astm.org

Patrick J. Golden[1] *and Theodore Nicholas*[2]

The Effect of Negative Stress Ratio Load History on High Cycle Fatigue Threshold

ABTRACT: The objective of this research was to measure the load history effects of negative stress ratio loading on the high cycle fatigue (HCF) crack growth threshold of Ti-6Al-4V. Previous work has shown an increase in the HCF threshold that is dependent on the K_{max} during the low cycle fatigue loading that nucleated a crack. The increase in fatigue limit was attributed to an overload effect from the LCF loading and was quantified through the use of a simple overload model. On the contrary, evidence from R = –1 testing suggests that negative overloads, referred to as underloads, may reduce this K_{max} load history effect and even lower the threshold below long crack values. To investigate this further, smooth and notched Ti-6Al-4V specimens were pre-loaded in fatigue below their endurance limit at stresses expected to nucleate cracks in approximately 10 million and 100 000 cycles, respectively, and at stress ratios of –3.5 and –3, respectively. Although the smooth specimens could not be monitored for crack nucleation, the notched specimens allowed the use of an infrared damage detection system to monitor the localized region at the notch root for indications of crack nucleation. These cracked specimens were then heat tinted, and several were also stress relieved to remove load history effects. All of the preloaded specimens were then HCF step tested to determine the fatigue limit stress or threshold. Although the smooth bars showed little effect due to the preloading at negative R, the threshold results on the notched specimens that developed measurable cracks seem to show competing effects of underloading and K_{max} overloading, dependent somewhat on precrack length. The specimens with smaller cracks nucleated at R = –3 tend to have a reduced HCF threshold compared to the conventional long crack threshold. Short crack effects and load-history effects are quantitatively explained with the aid of a Kitagawa diagram with an El Haddad short crack correction.

KEYWORDS: high cycle fatigue, threshold, load history, small cracks, Ti-6Al-4V, overload, fracture mechanics

Introduction

The conventional approach to damage tolerance in structural design involves the assumption of the existence of either initial or service induced damage, usually in the form of fatigue cracks. Initial or in-service inspection procedures must be available to ensure that any crack whose size is below the inspection limit will not grow to a catastrophic size before the next inspection or for the life of the part. This approach has been highly successful in avoiding low cycle fatigue (LCF) failures in U.S. Air Force gas turbine engines since the inception of damage tolerance specifications in the 1980s. However, a similar approach is not practical for use in high cycle fatigue (HCF) design because of the very high frequencies and large numbers of cycles that can be accumulated under HCF in a very short time period. This, combined with the very large fraction of life consumed in crack nucleation, makes it impractical to inspect for cracks and to apply damage tolerance principles. Rather, the approach to HCF needs to be based on threshold

Manuscript received 24 January 2004; accepted for publication 16 June 2004; published May 2005. Presented at ASTM Symposium on Fatigue and Fracture Mechanics: 34th Volume on 19–21 November 2003 in Tampa, FL; S.R. Daniewicz, J.C. Newman, Jr., and K-H. Schwalbe, Guest Editors.
[1] Materials Research Engineer, Air Force Research Laboratory, AFRL/MLLMN, Wright-Patterson AFB, OH 45433-7817, telephone: 937-255-5438, Fax: 937-656-4840, e-mail: patrick.golden@wpafb.af.mil.
[2] Visiting Professor, Air Force Institute of Technology, AFIT/ENY, Wright-Patterson AFB, OH 45433-7817.

or endurance limit concepts that involve determining stress levels below which failures due to HCF will not occur. Such an approach requires an extensive database, simple models for interpolating among mean stresses, and statistical considerations that address a realistic yet conservative probability of failure. Issues such as load sequencing and history of loading effects make such predictions even more difficult. Another aspect that must be addressed is the degradation of the fatigue strength with time in service due to damage accumulation. Such damage may be gradually accumulated such as from LCF where cracks might form and continue to grow due to repeated loading during service. This paper addresses some issues with respect to fatigue limit stresses in both smooth bars and notched specimens that are subject to prior LCF loading histories under negative values of stress ratio, R.

Background

Recent work by Nicholas and Maxwell [1] has shown that a modified version of the constant energy density range theory of Jasper [2] can represent fatigue strength at 10^7 cycles in a Ti-6Al-4V titanium alloy over a wide range of stress ratios (or mean stresses) including data in the negative mean stress region. Their fit to the data involves an empirical constant to account for the observation that compressive stresses contribute less than tensile stresses in fatigue. This is neither a new nor a surprising finding, whose roots can be traced back to some of the earliest work in fatigue. In 1930, Haigh [3], in referring to Bauschinger's results from 1915 and 1917, noted that "this series of tests...was probably the first that ever revealed any difference between the actions of pull and push in relation to fatigue." Referring to data on naval brass, he indicated "In this metal, as in many others, pull tends to reduce the fatigue limit, while push increases the resistance to fatigue." Following this idea, Nicholas and Maxwell [1] postulated that stored energy density per cycle does not contribute toward the fatigue process as much when the stresses are compressive as when they are in tension. Thus, when testing in a stress state where the bar is in compression for a majority of the fatigue cycle, fatigue failure can still be expected to occur. However, if one subscribes to the postulate that cracks initiate over the entire stress range, but propagate only under a positive stress range (positive value of stress intensity factor, K), then one might expect to find evidence of cracks forming at a lower peak stress under negative R testing and propagating only when the positive range of stress reaches some higher critical (threshold) value. Complicating this hypothesis even more, the negative stress cycling might have a history effect associated with it once cracks form, similar to what negative overloads produce during crack growth under aircraft spectrum loading.

In another parallel investigation, Moshier et al. [4] studied the application of fracture mechanics to prediction of HCF thresholds or fatigue limit stresses. There, notched specimens were precracked in LCF, including tests at negative R, and subsequently retested in HCF to determine the fatigue limit stress. Fracture mechanics were used to relate the observed stresses to stress intensity factors including corrections for small crack behavior using the approach suggested by El Haddad [5]. Specimens having a notch with $K_t = 2.25$ were subjected to LCF at either $R = -1$ or $R = 0.1$ until a crack was detected using an infrared detection system. Surface flaws at the notch root having depths under 20 μm were detected and subsequently heat tinted in order to be able to detect them on the fracture surface. All of the cracked specimens were then tested under HCF in order to establish the fatigue limit stress using step loading. K analysis of the surface flaw at a notch root, combined with a small crack correction, was plotted on a

Kitagawa[3] diagram [6]. The Kitagawa diagram for this geometry showed that the endurance limit and the value of a_0 for the short crack correction are not material constants but, rather, material parameters for the particular geometry and stress ratio, R, being investigated. Further, the load levels and stress ratios used in the precracking were found to produce a history effect, which influenced the value of the subsequent threshold. In their work, the maximum stress levels for LCF precracking at $R = -1$ and $R = 0.1$ were below and above the respective endurance stresses for undamaged material. In the formation of a crack under LCF and the subsequent propagation under HCF, these conditions would be referred to as an underload (negative overload) and overload, respectively. For the overload condition, a simple model was developed in [7], which modified the threshold K. The modified K and the small crack correction were found to provide a very good representation of the data. Similarly, the data representing LCF precracking at $R = -1$ were well represented by an uncorrected threshold K with a small crack correction. In that case, no underload model was needed to correct for the effective threshold. They also found that, at either value of R where stress relief annealing (SRA) was performed after the LCF precracking, the SRA process removes any history effects, and the resulting precracks follow the prediction of the long crack threshold with the a_0 short crack correction. While no history effect seems to be present when precracking at $R = -1$, the reason for this is not apparent. Perhaps the combination of overload for the positive portion of the cycle, combined with an underload due to the negative portion, cancel each other out. To explore this further, the present series of tests were conducted where the underload portion of the cycle is emphasized by precracking at values of $R = -3.5$.

Specimens with cracks formed under fretting fatigue have also been tested to determine the effect of the fretting fatigue loading history on the fatigue limit stress. In two separate investigations [8,9], the crack sizes in the fretted samples and corresponding fatigue limit stresses were plotted on a Kitagawa diagram for the specific crack specimen geometry. In both cases, the data followed the curve connecting the endurance limit stress with the threshold stress intensity factor using a small crack correction. The cracks formed under fretting fatigue are subjected to a nominal stress condition of fully reversed loading, and no apparent history effect appeared to be present in the two studies cited.

A final consideration in evaluating the effects of prior fatigue loading at negative R on the subsequently measured fatigue limit stress of a material is an observation on the number of cycles for the last block in the step-loading procedure developed by Maxwell and Nicholas [10] and the implications on crack development. The step-loading procedure was used for the determination of a crack growth threshold in two recent investigations [4,9]. In the first, surface flaws were produced under LCF loading in notched specimens. When cracks were detected, the specimens were tested under HCF at a frequency of 600 Hz using the step-loading procedure until crack growth occurred. At this high frequency, and because of the large number of cycles in the step-loading block (10^7), onset of growth and total specimen failure could be considered to be nearly simultaneous events. The number of cycles in the last block of loading in the step testing showed that failure occurred very early in the test block of 10^7 cycles, typically under 10^6 cycles. This indicated that the crack growth threshold is a well-defined quantity, or that the

[3] The terminology for the diagram with log stress plotted against log crack length for any crack geometry and stress ratio is referred to variously as a Kitagawa-Takahashi diagram, a Kitagawa type diagram, or most commonly, a Kitagawa diagram. In this paper, the common terminology "Kitagawa diagram" will be used to refer to that type of plot. In a similar manner, the terminology "El Haddad short crack correction" will be used to represent the contribution of El Haddad et al. [5].

"initiation" phase in a specimen that already has some damage has already taken place. By comparison, uncracked (smooth) specimens were observed to have a number of cycles in the last block, which are randomly distributed from 1 to 10^7 cycles, indicating the initiation phase of the fatigue process is both random and dominant [11].

A similar procedure was applied to C-shaped specimens, which were cut out of fretting pads in which cracks developed under fretting fatigue testing [9]. From the experience gained in the earlier work, the cycle count of the step-loading block was reduced from 10^7 to 2×10^6 cycles to save time. The results showed that the number of cycles to failure in the last loading block was less than 10^6 cycles, indicating again that the threshold for crack extension is very well defined.

The present investigation explored the nature of the crack initiation, threshold crack propagation, and any associated load history effects when a specimen is initially subjected to loading at negative stress ratios. Two types of experiments were conducted. In the first series of tests, smooth bars were loaded at $R = -3.5$ in order to see if this would initiate cracks which might affect the subsequent threshold at a higher value of R. In the second series of tests, LCF cracks were deliberately introduced with loading at $R = -3$, and the subsequent threshold was determined experimentally. The effect of loading history is assessed for both test procedures.

Experimental Procedures

The material used for this study was taken from forged Ti-6Al-4V plates. This material has been widely used by researchers throughout the National Turbine Engine High Cycle Fatigue Program [12]. It has an alpha-beta microstructure with approximately 60 % primarily alpha, and the remainder is transformed beta. Tensile properties of the material are $\sigma_y = 930$ MPa and $\sigma_{UTS} = 980$ MPa.

For the first series of tests, smooth hourglass fatigue specimens were machined with the loading axis in the longitudinal direction of the forged plate. These specimens conform to the fatigue specimen guidelines in ASTM Standard Practice for Conducting Force Controlled Constant Amplitude Axial Fatigue Tests of Metallic Materials (E 466-96). They have a gage section diameter of 5.6 mm and blending radius of 74 mm. The grip end diameter is 12.7 mm. This specimen geometry was chosen to avoid buckling at the high compressive forces in the negative R tests. After machining and prior to testing, the specimens were stress relief annealed for 1 h at 704°C in vacuum in order to remove any residual stresses from machining. This has been a standard practice for this material [4,12] to achieve stress relief without altering the microstructural features.

For the second set of tests, double notched fatigue specimens as shown in Fig. 1 were machined from the Ti-6Al-4V plate with the loading axis in the longitudinal direction of the plate and the crack growth in the transverse direction of the plate. As with the hourglass specimens, all specimens were stress relief annealed at 704°C for 1 h in vacuum after machining. Following stress relief, the specimens were electro-polished in the notch region to create a very smooth surface finish at the root of the notch, which was important for the crack detection method described later in this section. The specimens have two notches with the same depth to reduce the in-plane bending stresses in the fairly short specimen. One notch, however, was slightly sharper, resulting in a higher stress concentration factor, Kt, or 2.25 versus 1.96 as shown in Fig. 1. As a result, cracks nucleated in the sharp notch during precracking in virtually every test, allowing them to be observed by the method described in the following paragraphs. An anti-buckling guide was clamped onto the faces of the specimen for the tests with negative stress ratios. This guide was very stiff in the lateral direction to prevent buckling but was very flexible in the axial direction to minimize load transfer from the specimen.

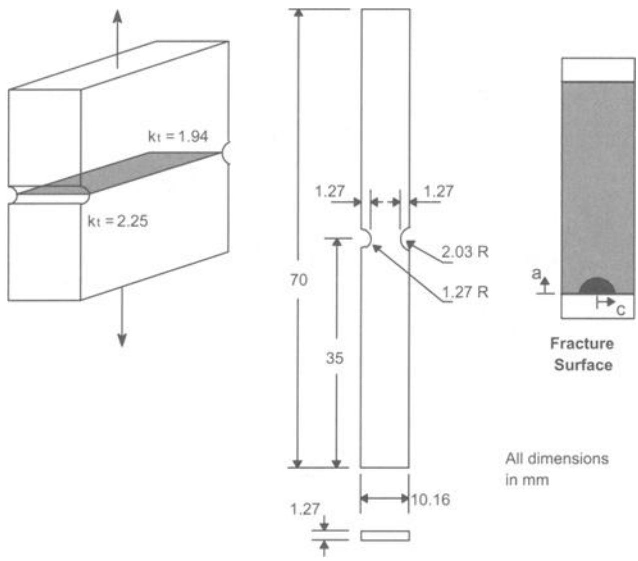

FIG. 1—*Drawing of the double notch specimen showing the stress concentration factors and the surface crack geometry at the sharpest notch.*

Fatigue testing of both specimen types was performed under load control using MTS servo-hydraulic test frames for most testing, but an Unholz-Dickie electromagnetic shaker based high frequency test system was used for the high cycle fatigue portion of the notched specimen testing. Each test, whether an hourglass or notched specimen, consisted of two phases, a preloading or precracking phase and a threshold step test [10] phase. In some of the reporting, this is referred to as LCF/HCF testing because of the different frequencies involved. In the case of the hourglass specimens, the objective was to determine if damage formed below the 10^7 cycle fatigue limit stress at negative R would affect the HCF threshold stress. In this case the preloading is not LCF, however, there may be an interaction due to the changing stress ratio. Figure 2 is a schematic of the applied loading for the hourglass specimens. In the first block of cycles, the specimens were pre-loaded for 10^7 cycles at R = –3.5 with a maximum stress of 240 MPa, which was below the endurance limit stress of 265 MPa. The specimens were then either heat tinted at 420°C for 4 h in air or heat tinted and stress relieved at 704°C for 1 h. Heat tinting has been shown to mark cracks accurately for subsequent identification and measurement on the fracture surface [4,9]. Stress relief annealing in Ti-6Al-4V has been shown to completely remove the effects of load history on subsequent fatigue crack growth [7]. The second block of cycles was the R = 0.1 HCF step test in which a constant stress was applied in blocks of cycles and increased until failure.

As described in the previous section, the objective of the notched specimen tests was different than the hourglass tests. In this case, a controlled crack initiation was desired so that the effect of a negative R load history on the HCF threshold could be determined. To that end, the loading described by Fig. 3 was applied. Here the initial block of loading was intended to precrack the specimens to a small size in approximately 100 000 cycles. The maximum applied net section stress was 150 MPa at R = –3, while the endurance stress was approximately 135 MPa. Again, after precracking and prior to the threshold step test, the specimens were either heat tinted at 420°C for 4 h in air or heat tinted and stress relieved at 704°C for 1 h.

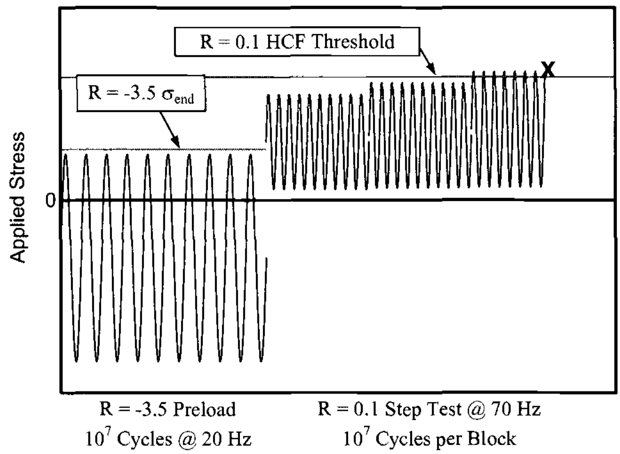

FIG. 2—*Tension-compression preloading and tension-tension step test loading of the hourglass specimens.*

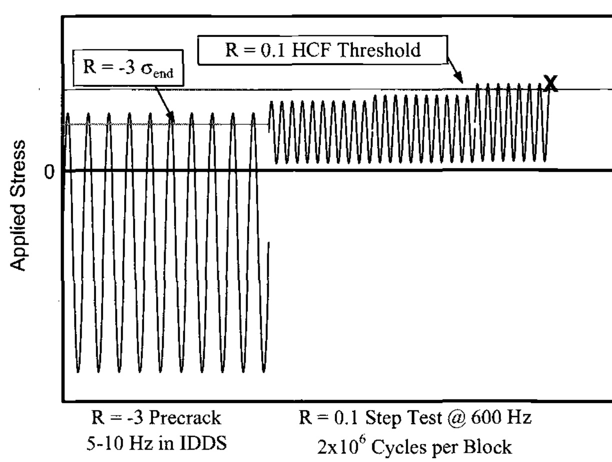

FIG. 3—*Tension-compression precracking and tension-tension step test loading of the notched specimens.*

The precracking was performed with the aid of an infrared damage detection system (IDDS) [13]. In this procedure, an infrared camera captures images at the area of interest, i.e., the notch root, at the maximum and minimum applied loads while cycling the load at 5–10 Hz. For illustration, these images are named image A and B, respectively. Software is then used to create a differential image in real time as the difference, C = A – B. Once software adjustments are complete and the images have stabilized, usually after a few thousand cycles, a reference differential image is saved, D = C(t = t_{ref}). Finally, a composite image is created, also in real time, as the difference, E = C – D. This composite image, E, is then monitored for anomalies that might be cracks. Figure 4 is an example of a composite image with a 120 μm surface crack indication (note the anomaly only measures approximately 60 μm in the image, but post test inspection revealed the actual crack size). After precracking, the specimen notches were examined in an SEM using backscatter imaging to confirm the presence of cracks. Figure 5 is an example of a small precrack located on the notch face.

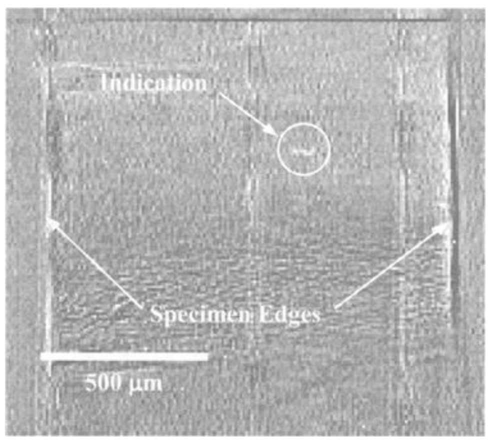

FIG. 4—*Image from the infrared damage detection system (IDDS) showing a 120 μm surface crack indication in the notch face. The loading axis is vertical.*

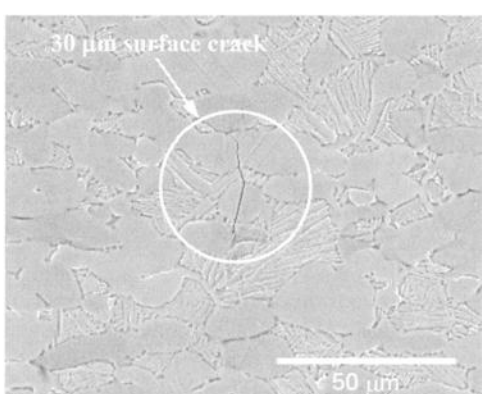

FIG. 5—*SEM image of a small crack detected in the notch face with the aid of the IDDS. The loading axis is horizontal.*

The step test method [10] was used for the second phase of testing to determine if the prior load affected the threshold stress of the specimens due to the initiation of a crack or some damage. Schematics of the R = 0.1 step tests are plotted in Figs. 2 and 3. The initial stress amplitude is applied below the expected failure stress for a block of cycles. The stress is then increased, and the process is repeated until failure. The threshold stress is interpolated between the failure step and the prior step based on the number of cycles to failure in the final step. The resulting maximum threshold stress could be less than or greater than the maximum precracking stress depending on the crack size. This will be an important factor when analyzing load history effects. For example, a specimen with a relatively large crack would have a precracking K_{max} significantly higher than the long crack threshold K_{max} possibly leading to a load history effect. For the hourglass specimens, the threshold stress was measured at R = 0.1 and R = 0.5. In the case of the notched specimens, only the R = 0.1 threshold stress was measured in this study. Following the step test failures, the fracture surfaces were examined for heat tint markings that would indicate the presence of a crack that had initiated during pre-loading or precracking. These cracks could then be measured directly in the optical microscope. Figure 6 is an example of a heat tinted surface crack from a notched specimen.

Additional precracked notched specimen tests were conducted with values of the precrack R of −1 and 0.1 with maximum net-section stresses of 265 MPa and 430 MPa, respectively. These were used for comparison with previous work [4] and to provide additional test data. The R = 0.1 step-test portion of these tests was performed identically to those precracked at R = −3. Also, several notched specimens that were not precracked were threshold step-tested to determine the fatigue endurance limit in the notched geometry. The measured endurance limit at R = 0.1 was approximately 310 MPa maximum net section stress. Prior research has shown that Ti-6Al-4V does not exhibit coaxing[4] at these test temperatures or frequencies [14].

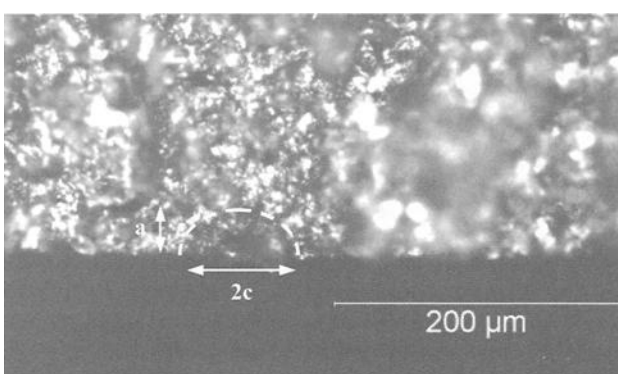

FIG. 6—*An optical micrograph of the fracture surface showing a semi-elliptical surface crack located on the notch face detected by heat tinting.*

[4] Coaxing is defined as an increase in fatigue limit stress due to cycling below the fatigue limit. It has been demonstrated not to exist in the material used in this investigation [14] and, further, to be a phenomenon that has "uselessly haunted people's minds for decades" [15].

Results and Discussion

Figure 7 is a schematic of a Kitagawa diagram [6] that has been shown to represent short crack growth threshold data quite well, as described earlier. Fatigue crack growth or no growth is predicted using two bounds, either the endurance stress or by the linear elastic fracture mechanics (LEFM) stress intensity factor threshold, ΔK_{th}. The LEFM threshold stress range, $\Delta\sigma_{th}$, is calculated by Eq 1, where Y is a generic geometry factor that is dependent on the geometry of the problem, and it is a function of the crack length a. ΔK_{th} is the long crack threshold stress intensity factor range. A third curve, the short crack threshold curve developed by El Haddad et al. [5], is used to transition the endurance stress to the LEFM prediction of threshold stress. The primary feature of this model is the short crack parameter a_0, which is determined either by the intersection of the endurance stress with the LEFM prediction or by solving Eq 2 below. Here, $\Delta\sigma_{end}$ is the endurance stress range. Equations 1 and 2 are a general form of the stress intensity factor equation. In this study, as in several previous studies [4,8,9], a_0 is shown to be dependent not just on material properties but also on the crack and specimen geometries as well as the stress ratio, R. Equation 3 describes the short crack threshold curve showing how a crack of length a behaves as a crack with length $a + a_0$.

$$\Delta K_{th} = \Delta\sigma_{th}\sqrt{\pi a}\,Y(a) \quad (1)$$

$$\Delta K_{th} = \Delta\sigma_{end}\sqrt{\pi a_0}\,Y(a_0) \quad (2)$$

$$\Delta\sigma_{th} = \frac{\Delta K_{th}}{\sqrt{\pi(a + a_0)}\,Y(a + a_0)} \quad (3)$$

The smooth bar specimens were tested under three conditions: 1) a baseline condition with no preloading; 2) preloaded and then heat tinted prior to threshold step test; and 3) preloaded, heat tinted, and stress relieved prior to threshold step test. The 10^7 cycle fatigue strength for each of these three test conditions are reported in Fig. 8 for R = 0.1 and R = 0.5 step tests. At least two tests per condition were conducted. The results show that the pre-loading reduces the 10^7 cycle fatigue strength of the Ti-6Al-4V material by approximately 5 %. Given the small difference in fatigue strength and the small number of specimens, this difference is not very significant in a statistical sense. Also, the stress relief did not seem to have a consistent or significant effect on the results. Examination of the fracture surfaces of these specimens showed no obvious heat tint markings. A threshold stress analysis, however, reveals that the calculated a0 for this material and geometry would be approximately 60 μm. According to the Kitagawa diagram, the small reduction of strength observed from these tests would indicate cracks approximately 10 μm deep, which is too small to typically detect using the optical microscope. A scanning electron microscope (SEM) examination of the fracture surface revealed some possible initial flaws. Examples are shown in Fig. 9. Here, the lines indicate the possible initial crack boundaries. These markings were considered an upper bound to the crack sizes that may have been present after preloading. This is consistent with the Kitagawa diagram analysis. Additionally, the number of cycles to failure in the last block of loading in the R = 0.1 or R = 0.5 step tests provides further evidence supporting the existence of damage or cracking caused by the R = –3.5 preloading. In all but one test, there were less than one million cycles to failure in the last step. As discussed previously, this indicates that a crack or some damage was formed during the preloading.

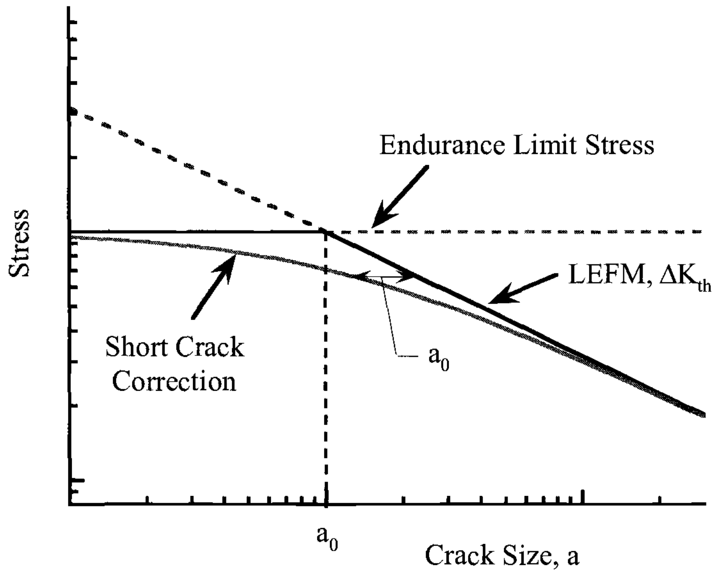

FIG. 7—*Schematic of a Kitagawa diagram used to represent the data in this study.*

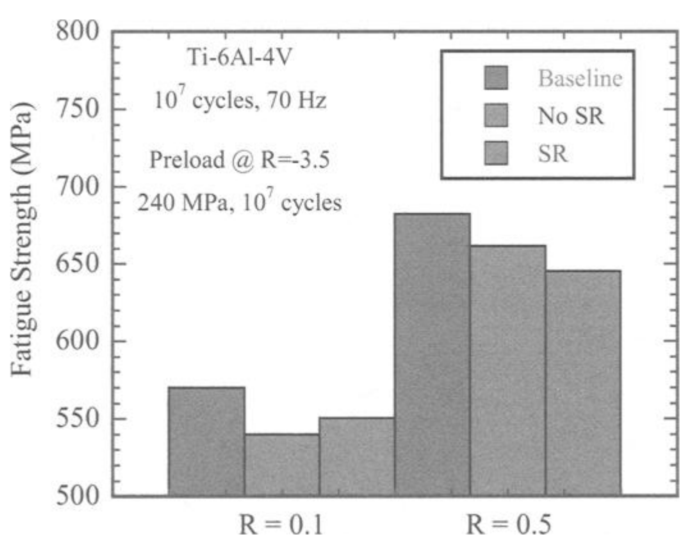

FIG. 8—*Average HCF threshold results for smooth bars with and without $R = -3.5$ preloading and with and without stress relief (SR).*

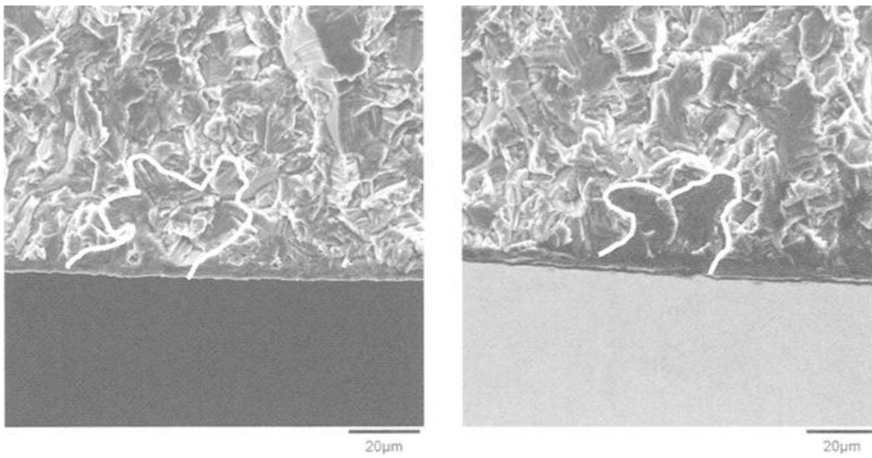

FIG. 9—*Fracture surfaces of round bar specimens showing possible indications of cracks (outlined in white) nucleated during the R = –3.5 preloading.*

In the notched specimens, the precrack test phase was run until cracks were generated and observed as described in the experimental procedures section. Therefore, nearly all specimens had a measurable heat tinted crack on the fracture surface, and several had multiple cracks. Some tests had false IDDS indications, and therefore no cracks were found. Figure 10 is a plot of the surface crack measurements made in the current study, where *a* and *c* are the depth and half surface length of a semi-elliptical crack as defined in Fig. 1. In two specimens the crack that led to failure in the threshold portion of the test was a corner crack, and in a third specimen an 800 μm through crack was found. These three cracks are not plotted in Fig. 10. The crack aspect ratio, *a*/*c*, varies from about 0.4–1.0. Most of the cracks have an aspect ratio near 0.6, and this value was chosen for purposes of LEFM analysis on the Kitagawa diagram.

The threshold stress and crack depths have been plotted on a Kitagawa diagram in Fig. 11. The lines on the plot represent the predicted crack growth or no growth boundaries. The endurance stress (maximum net section stress) at R = 0.1 was 310 MPa, and ΔK_{th} was 4.6 MPa-m$^{1/2}$. Two stress intensity factor solutions were needed for the LEFM threshold prediction. The first was for semi-elliptical surface cracks, and the other accounted for larger through-the-thickness cracks. The stress intensity factor solutions for this specimen were developed in Moshier [16] using finite element analysis. The dashed line is the prediction for the short crack threshold as described earlier. The El Haddad short crack parameter, a_0, was determined to be 25 μm. This value is not a material property but is dependent on the crack geometry, which was assumed to be a semi-elliptical crack in a plate with an aspect ratio of 0.6.

All of the data for the notch specimens precracked in LCF at R = –3 and R = –1 followed or fell slightly below the short crack and/or LEFM R = 0.1 threshold predictions as shown in Fig. 11. The stress relief (SR) did not seem to have a consistent or significant effect on the results. The specimens that were precracked in LCF at R = 0.1, both from this study and from multiple tests by Moshier et al. [4], had significantly higher R = 0.1 thresholds than the negative R results. It was found that this increase in the threshold stress is due to a tension overload in the R = 0.1 load history. In this case, stress relief eliminates the load history effect. In the negative R tests, however, a tension overload effect does not seem to be present, and it seems that the compressive loading may contribute to the removal of the load history effect much like stress relief.

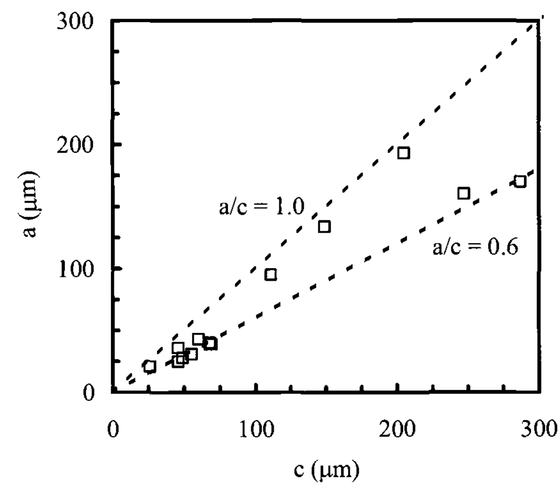

FIG. 10—*Measured crack sizes showing most crack shapes between a/c = 0.6 and 1.0.*

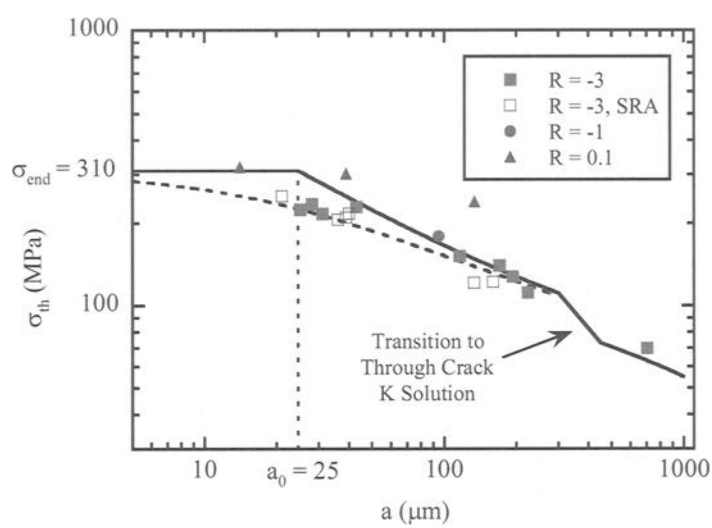

FIG. 11—*R = 0.1 HCF threshold data plotted on a Kitagawa diagram.*

To compare the results from the smooth bar tests and the precracked notched specimens, a normalized Kitagawa diagram is introduced. Crack length on the x-axis is normalized with respect to a_0, while stress on the y-axis is normalized with respect to the fatigue limit stress for the specific geometry and value of R. This diagram can be used to compare results from two (or more) entirely separate geometries. Such a plot is presented as Fig. 12, where the smooth (circular) bar and the notched specimen are represented by their respective long crack (solid) and El Haddad short crack corrected (dashed) curves for R = 0.1. Curves for the two geometries for R = 0.5 lay nearly on top of the R = 0.1 curves in both cases and are not plotted. Nearly identical normalized curves on a Kitagawa diagram at different stress ratios were also observed and documented in Golden [17] for arch specimens from a fretting fatigue study.

In Fig. 12, for R = 0.1, maximum endurance limit stresses used were 310 MPa and 570 MPa for the notched and smooth specimens, respectively. The long crack ΔK_{th} used in the analysis was 4.6 MPa-m$^{1/2}$. For the notched specimen, a_0 = 25 μm for surface crack with a/c = 0.6, and a_0 = 15 μm for a through crack, while for the smooth specimen a_0 = 58 μm. Experimental data points from the notched tests at R = 0.1 are also shown on the curve. Horizontal and vertical dashed lines represent the predicted a/a_0 crack sizes for 95 % and 80 % of fatigue strength, which covers the range of the data shown in Fig. 8 for specimens preloaded at R = –3.5. This leads to predicted crack sizes in the smooth bars of approximately 7–35 μm. As noted earlier, no indications of such cracks were observed, and, further, no load history effects were observed in the notched specimens precracked at R = –3.

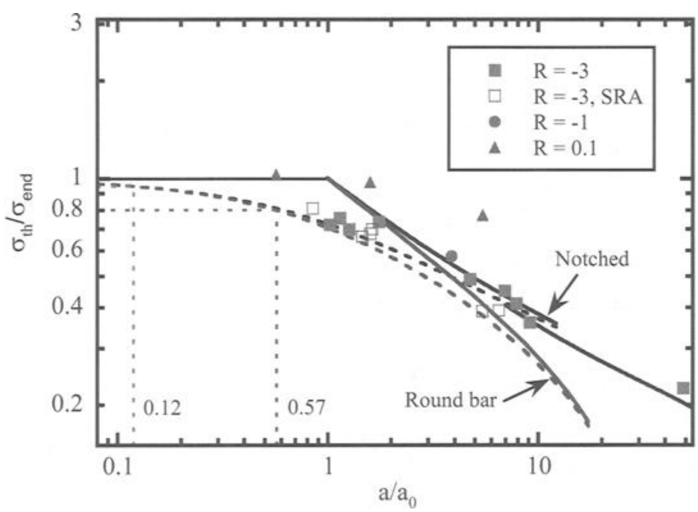

FIG. 12—*Normalized Kitagawa diagram showing curves for circular bar and notched specimens.*

Another plot used to represent the data was the measured threshold stress intensity factor, K_{max} threshold, versus the applied K_{max} precrack. K_{max} precrack is the stress intensity factor of the final crack size during precracking with the precracking stress applied while K_{max} threshold was calculated using the same crack size, but with the threshold stress applied. The plot shown in Fig. 13 contains all of the data collected in this study. All of the data on this plot have threshold values measured at R = 0.1, however, LCF precracking R values are labeled in the legend. Several curves have been added to this plot that represent the predicted or measured threshold behavior for long cracks with and without load history effects and also for short cracks. The horizontal line is simply the long crack threshold K_{max} of 5.1 MPa-m$^{1/2}$ measured by the load shedding method from ASTM Standard Test Method for Measurement of Fatigue Crack Growth Rates (E647-00). The endurance stress, σ_{end}, boundary for growth or no growth was included for material with very short cracks in which failure is controlled by stress rather than LEFM. This boundary was calculated using Eqs 4 and 5, where σ_{pc} is the R = –3 precrack maximum stress of 150 MPa, and σ_{end} is the R = 0.1 endurance stress of 310 MPa. The short crack threshold curve is a transition between the endurance stress and LEFM criteria much like that used in the Kitagawa diagram. Here, K_{pc} was calculated by Eq 4, and the small crack threshold stress intensity factor, $K_{th,sc}$, was calculated according to Eq 6. Finally, Eq 7 was plotted showing the effect of tension overload on the threshold. This line was fit to R = 0.1 fatigue crack growth threshold tests performed by Moshier et al. [7], where the crack growth thresholds were measured after different levels of R = 0.1 precracking.

$$K_{pc} = \sigma_{pc}\sqrt{\pi a}\,Y(a) \tag{4}$$

$$K_{th,end} = \sigma_{end}\sqrt{\pi a}\,Y(a) \tag{5}$$

$$K_{th,sc} = K_{th,lc}\sqrt{\frac{a}{a+a_0}}\,\frac{Y(a)}{Y(a+a_0)} \tag{6}$$

$$K_{th} = 0.303K_{pc} + 3.33 \tag{7}$$

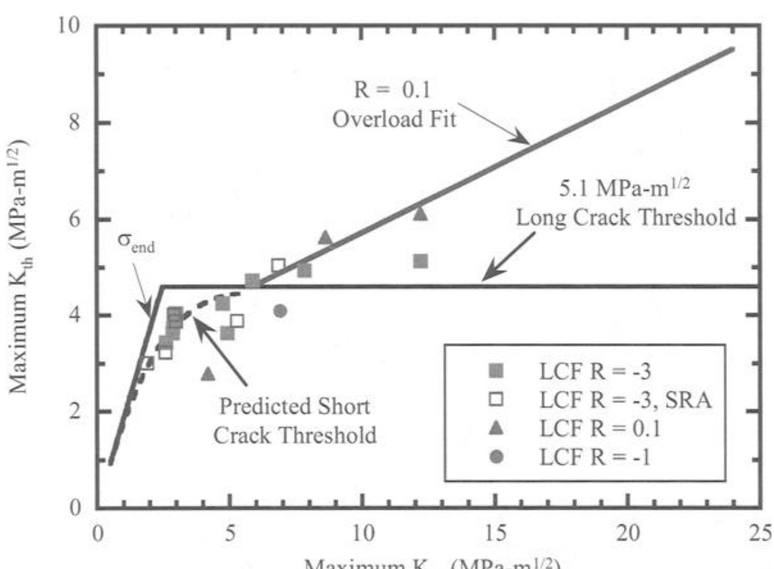

FIG. 13—*Summary of calculated R = 0.1 K_{max} threshold of cracks measured in the precracked notched specimens. The precracking K_{max} for the endurance stress and short crack threshold predictions were based on the R = –3 precracking stress of 150 MPa.*

The results plotted in Fig. 13 are very consistent with the predictive curves. Starting from the lower precracking K_{max}, the R = –3 precracked data all seem to have R = 0.1 thresholds that match the short crack curve very well. In the K_{max} precrack range of 5–10 MPa-$m^{1/2}$, the data precracked at R = –3 and R = –1 seem to follow the long crack R = 0.1 threshold as expected with some scatter. Two points from this study precracked at R = 0.1 seemed to follow the load history fit quite well, which was consistent with similar notch data generated by Moshier et al. [4]. What was interesting to note was the data point precracked at R = –3 and K_{max} = 12 MPa-$m^{1/2}$ has an R = 0.1 threshold much lower than predicted using the K_{max} overload fit and much lower than the data precracked at R = 0.1 with the same precracking K_{max}. Although this result was from only one test, it could only be due to the compression portion of the cycle during the precracking. This result was also consistent with the R = –1 precracking data presented by Moshier et al. [4]. In summary, it seemed that at higher levels of precracking, the compressive "overload" (sometimes referred to as an underload) has the effect of eliminating or canceling the effect of the tensile "overload" load history effect. At lower levels of precracking K_{max} where a tensile "overload" load history effect was not expected, the compressive precracking appeared to have very little effect.

The question arises whether it could be possible that the negative stress ratio precracking had an undetected "underload" effect on the crack growth threshold of many of the tests that did not appear to show an effect. Single or multiple underload cycles have been shown to accelerate crack growth for a short period of crack extension in constant amplitude crack growth tests [18]. During the threshold step test it was possible that a stress level was encountered that grew the crack at a ΔK less than the threshold level (either long crack or short crack) due to the "underload" load history. The crack could have grown a short distance out of the reduced ΔKth effect and then arrested until the next step increase in stress. This could repeat until a stress was reached that would grow the crack to failure. In the analysis, only this final stress would be considered; therefore, the "true" reduced crack growth threshold stress would not be known and could be lower than had been measured. This scenario, however, is speculative, and the current experimental procedures cannot prove or disprove this possibility.

Conclusions

The effect of negative stress ratio loading on the subsequent HCF threshold in Ti-6Al-4V was investigated. It was found that preloading a smooth specimen below the endurance limit at R = –3.5 caused only a marginal reduction in the R = 0.1 and R = 0.5 HCF strengths of smooth bars. No conclusive evidence of cracks forming under the preloading was found. HCF threshold testing of R = –3 precracked notched specimens revealed that at high precracking K_{max}, the compressive "overload" seemed to cancel the beneficial effect of the well-documented tensile "overload" effect. At lower values of precracking K, the compressive "overload" seemed to have very little effect on the measured value of crack growth threshold, and the threshold results were close to the predictions made using LEFM with a short crack correction. In summary, the implications of this study are twofold. First, these results show that for HCF design, it should not be necessary to use a crack growth threshold that is significantly lower than the long crack threshold with a short crack correction. Second, the results of this and previous studies show that the beneficial effect of an elevated ΔK_{th} due to tensile overloads cannot be counted on if compressive overloads are also within the loading spectrum.

Acknowledgments

The authors would like to acknowledge Mr. David Maxwell of UDRI for his support with the smooth bar specimen testing and Mr. John Porter of UDRI for his fractography support. This work was supported by the U.S. Air Force National Turbine Engine High Cycle Fatigue (HCF) Program.

References

[1] Nicholas, T. and Maxwell, D. C., "Mean Stress Effects on the High Cycle Fatigue Limit Stress in Ti-6Al-4V," *Fatigue and Fracture Mechanics: 33rd Volume, ASTM STP 1417*, W. G. Reuter and R. S. Piascik, Eds., ASTM International, West Conshohocken, PA, 2002, pp. 476–492.

[2] Jasper, T. M., "The Value of the Energy Relation in the Testing of Ferrous Metals at Varying Ranges of Stress and at Intermediate and High Temperatures," *Philosophical Magazine*, Series 6, Vol. 46, Oct. 1923, pp. 609–627.

[3] Haigh, B. P., "The Relative Safety of Mild and High-Tensile Alloy Steels Under Alternating and Pulsating Stresses," *Proceedings of the Institution of Automotive Engineers*, Vol. 24, 1930, pp. 320–347.

[4] Moshier, M. A., Nicholas T., and Hillberry, B. M., "High Cycle Fatigue Threshold in the Presence of Naturally Initiated Small Surface Cracks," *Fatigue and Fracture Mechanics: 33rd Volume, ASTM STP 1417*, W. G. Reuter and R. S. Piascik, Eds., ASTM International, West Conshohocken, PA, 2002, pp. 129–146.

[5] El Haddad, M. H., Smith, K. N., and Topper, T. H., "Fatigue Crack Propagation of Short Cracks," *Journal of Engineering Materials and Technology*, Vol. 101, 1979, pp. 42–46.

[6] Kitagawa, H. and Takahashi, S., "Application of Fracture Mechanics to Very Small Cracks or the Cracks in the Early Stage," *2nd International Conference on Mechanical Behaviour of Materials*, 1976, pp. 627–630.

[7] Moshier, M. A., Nicholas, T., and Hillberry, B. M., "Load History Effects on Fatigue Crack Growth Threshold for Ti-6Al-4V and Ti-17 Alloys," *International Journal of Fatigue*, Vol. 23, 2001, pp. S253–S258.

[8] Hutson, A. L., Neslen, C., and Nicholas, T., "Characterization of Fretting Fatigue Crack Initiation Processes in Ti-6Al-4V," *Tribology International*, Vol. 36, 2003, pp. 133–143.

[9] Golden, P. J., Bartha, B. B., Grandt, Jr., A. F., and Nicholas, T., "Measurement of the Fatigue Crack Propagation Threshold of Fretting Cracks in Ti-6Al-4V," *International Journal of Fatigue*, Vol. 26, 2004, pp. 281–288.

[10] Maxwell, D. C. and Nicholas, T., "A Rapid Method for Generation of a Haigh Diagram for High Cycle Fatigue," *Fatigue and Fracture Mechanics: 29th Volume, ASTM STP 1321*, T. L. Panontin and S. D. Sheppard, Eds., ASTM International, West Conshohocken, PA, 1999, pp. 626–641.

[11] Moshier, M. A., Nicholas, T., and Hillberry, B. M., "The Effect of Low Cycle Fatigue Cracks and Loading History on High Cycle Fatigue Threshold," *Fatigue and Fracture Mechanics: 31st Volume, ASTM STP 1389*, G. R. Halford and J. P. Gallagher, Eds., ASTM International, West Conshohocken, PA, 2000, pp. 427–444.

[12] Gallagher J. P., et al., *AFRL-ML-TR-2001-4159, Improved High-Cycle Fatigue (HCF) Life Prediction,* Wright-Patterson Air Force Base, OH, January 2001.

[13] Hartman, G. A., "Infrared Damage Detection System (IDDS) for Real-Time, Small-Scale Damage Monitoring," *Proceedings of SEM Annual Conference on Experimental Mechanics*, Charlotte, NC, 2003, in press.

[14] Nicholas, T., "Step Loading, Coaxing and Small Crack Thresholds in Ti-6Al-4V under High Cycle Fatigue," *Fatigue – David L Davidson Symposium*, K. S. Chan, P. K. Liaw, R. S. Bellows, T. C. Zogas, and W. O. Soboyejo, Eds., Cleveland: TMS (The Minerals, Metals & Materials Society), 2002, pp. 91–106.

[15] Schütz, W., "A History of Fatigue," *Engineering Fracture Mechanics*, Vol. 54, 1996, pp. 263–300.

[16] Moshier, M. A., "The Effect of Low Cycle Fatigue Cracks and Loading History on High Cycle Fatigue Threshold," Ph.D. Dissertation, Purdue University, 2000.

[17] Golden, P. J., "High Cycle Fatigue of Fretting Induced Cracks," Ph.D. dissertation, Purdue University, 2001.

[18] Russ, S. M., "Effect of Underloads on Fatigue Crack Growth of Ti-17," Ph.D. Dissertation, Georgia Institute of Technology, October 2003.

Journal of ASTM International, January 2005, Vol. 2, No. 1
Paper ID JAI12026
Available online at www.astm.org

S.C. Forth,[1] *D.J. Herman,*[2] *M.A. James,*[3] *and W.M. Johnston*[4]

Fatigue Crack Growth Rate and Stress-Intensity Factor Corrections for Out-of-Plane Crack Growth

ABSTRACT: Fatigue crack growth rate testing is performed using automated data collection systems that assume straight crack growth in the plane of symmetry and that use standard polynomial solutions to compute crack length and stress-intensity factors from compliance or potential drop measurements. Visual measurements used to correct the collected data typically include only the horizontal crack length, which underestimates the crack growth rates for cracks that propagate out-of-plane. The authors have devised an approach for correcting both the crack growth rates and stress-intensity factors based on two-dimensional mixed mode-I/II finite element analysis (FEA). The approach is used to correct out-of-plane data for 7050-T7451 and 2025-T6 aluminum alloys. Results indicate the correction process works well for high ΔK levels, but it fails to capture the mixed-mode effects at ΔK levels approaching threshold (da/dN ~ 10^{-10} meter/cycle). Based on the results presented in this paper, the authors propose modifications to ASTM E 647: to be more restrictive on the limits for out-of-plane cracking (15°); to add a requirement for a minimum of two visual measurements (one at test start and one at test completion); and to include a note on crack twisting angles, with a limit of 10° being acceptable.

KEYWORDS: fatigue crack growth, mixed-mode, stress-intensity factor, aluminum, out-of-plane

Nomenclature

$\dot{a}$	Corrected crack length
a_c	Compliance crack length
a_n	Notch length
β	Out-of-plane angle
B	Specimen thickness
da/dN	Crack growth rate
Δa	Projected crack length
$\Delta a'$	Actual crack length
ΔK	Stress intensity factor range
f	Out-of-plane angle fraction
K_I	Mode-I stress intensity factor
K_{max}	Maximum stress intensity factor
R	Stress ratio (minimum/maximum)
W	Specimen width

Manuscript received 8 December 2003; accepted for publication 15 April 2004; published January 2005. Presented at ASTM Symposium on Fatigue and Fracture Mechanics: 34th Volume on 19–21 November 2003 in Tampa, FL; S.R. Daniewicz, J.C. Newman, Jr., and K-H. Schwalbe, Guest Editors.
[1] Materials Research Engineer, NASA Langley Research Center, MS 188E, 2 W. Reid St., Hampton, VA 23681.
[2] Student, Washington University in St. Louis, One Brookings Drive, St. Louis, MO 63130.
[3] Staff Scientist, National Institute for Aerospace, NASA Langley Research Center, MS 188E, 2 W. Reid St., Hampton, VA 23681.
[4] Research Engineer, Lockheed Martin Corporation, NASA Langley Research Center, MS 188E, 2 W. Reid St., Hampton, VA 23681.

Introduction

Experimental testing for baseline fatigue crack growth rate properties has traditionally been performed on laboratory coupons designed to promote mode-I crack growth, where cracking is perpendicular to the applied load. However, material microstructure, residual stresses, and other factors can cause the crack to turn out-of-plane and propagate in a mixed-mode manner. The ASTM Standard Test Method for Fatigue Crack Growth Rates (E 647), the testing standard used to develop fatigue crack growth rate data, limits the out-of-plane crack growth to within 20° of the specimen symmetry plane for any growth increment over one-tenth the specimen width to maintain a reasonable accuracy of the mode-I equations. Additionally, any out-of-plane cracking exceeding 10° must be reported with the data. However, in some circumstances significant numbers of specimens may be invalid because of out-of-plane cracking, or they may be invalid by a small amount, directly impacting the value of a test program. For example, during a recent testing effort at NASA Langley Research Center on aluminum alloy 2025-T6 forgings, significant out-of-plane cracking was observed [1]. Nearly half of the test specimens had out-of-plane angles outside the ASTM E 647 limit of 20°. The authors have devised an approach for correcting both the crack growth rates and stress-intensity factors based on two-dimensional mixed mode-I/II finite element analysis (FEA). The approach is used to correct out-of-plane data for 7050-T7451 obtained from the literature [2] and recent test results [1] from 2025-T6 aluminum alloys.

Mixed-Mode Crack Growth Data Correction

A correction procedure can take more than one form, depending on the format in which the data are collected. For this study, the driving force and the crack growth rate will be considered separately because the testing was controlled by an automated computer-based K-control system that used compliance to determine crack length. All crack lengths obtained during the test were computed from measured compliance. Visual measurements, taken during the test with microscopes on traveling stages, were used to correct the compliance-based crack length values after completion of the test, prior to data reporting per ASTM E 647. The visual measurements are taken along the symmetry plane of the specimen and represent the projected crack growth, Δa, defined in Fig. 1. To assess the effect of mixed-mode crack growth on measured compliance values and computed stress intensity factors, finite element analyses were performed for several out-of-plane crack configurations.

Stress Intensity Factors

The finite element analysis (FEA) software FRANC2D/L [3–5] was used to calculate mode-I/II stress intensity factors (SIFs) for straight and angled crack configurations. A typical compact tension specimen, C(T), was considered with out-of-plane cracking. Figure 1 shows the configuration and nomenclature for the C(T) specimen studied herein, where the specimen dimensions for this study are: width, W = 76.2 mm; thickness, B = 12.7 mm; and notch length, a_n = 19.05 mm. The out-of-plane angle β was varied from 0° to 40°. We assumed that the precrack and subsequent crack growth was in a straight line at an angle β from the symmetry plane. In each case the projected crack growth, Δa, was kept constant at Δa = 12.7 mm, and the actual crack growth $\Delta a'$ varied as

$$\Delta a' = \Delta a / \cos(\beta) \tag{1}$$

The finite element analysis was used to determine straight-crack and mixed-mode stress-intensity factors. Figure 2 shows mixed-mode K_I SIFs normalized by the straight-crack ($\beta = 0$) SIFs as a solid line. Error bounds of ± 2 % were placed on the finite element analyses (denoted as dashed lines) for the purpose of evaluating the accuracy of the correction method to be presented. It is presumed in this paper that the K_I from the mixed-mode FEA is the most accurate representation of the SIFs at the crack tip.

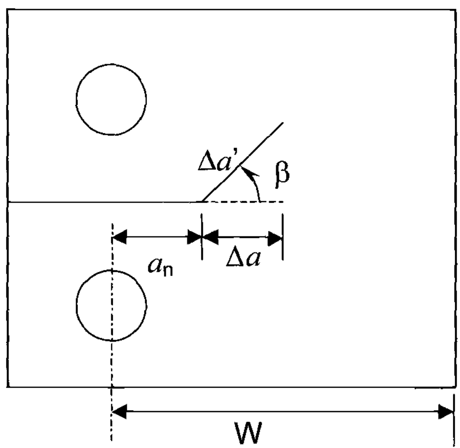

FIG. 1—*Out-of-plane crack growth configuration for a C(T) specimen.*

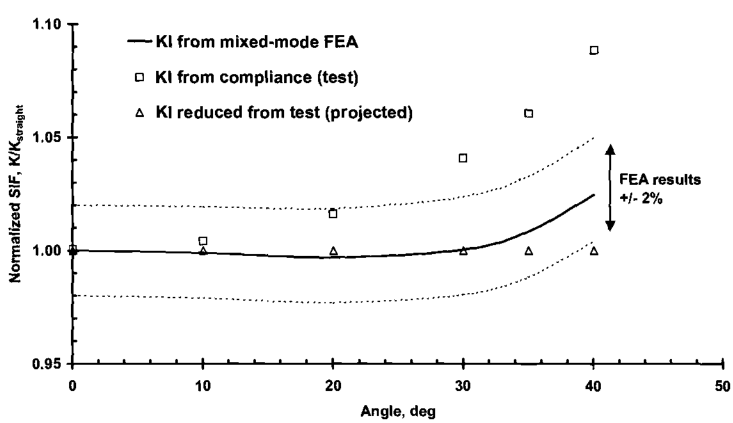

FIG. 2—*Stress-intensity factor as a function of out-of-plane cracking angle.*

Crack-mouth-opening displacements (CMOD) from the FEA results were used to calculate the compliance crack length and SIF values for each angle. The open squares in Fig. 2 show compliance K_I calculated from the analysis CMOD using the ASTM E 647 polynomial solutions for crack length and stress-intensity factor. The K_I from compliance is representative of the uncorrected SIF computed during a test. The compliance solution overestimates the actual out-of-plane crack length, $a_n + \Delta a'$, resulting in a high K_I with +2 % error when the crack is about 20° out-of-plane and +10 % error when the crack is about 40° out-of-plane. The open triangles in Fig. 2 show the K_I using the projected crack length, $a_n + \Delta a$. The projected crack length SIFs are comparable to the SIFs obtained from reducing compliance data from an experiment using visual measurements. The projected crack growth underestimates the actual out-of-plane crack growth, $\Delta a'$, resulting in a reduced K_I with –2 % error when the crack is about 40° out-of-plane.

Using the projected crack growth to compute SIF is reasonably accurate to an angle of 40°. However, the correct SIF will not be known until after the test is complete, since that is when the visual measurements will be used to reduce the compliance data. For example, when conducting an experiment contained within ASTM E 647, a constant K_{max} test could no longer be valid when out-of-plane cracking occurs, as the K_{max} will vary with out-of-plane angle. However, when conducting a constant stress-ratio test, the data generated will still be at the same constant stress ratio, as both K_{max} and K_{min} vary with out-of-plane angle.

Crack Growth Rate

The crack growth rate, da/dN, should be corrected after the test is complete. Assuming the compliance data are reduced using at least two visual measurements, the projected crack growth, Δa, is known (see Fig. 1). Equation 1 must then used to determine the actual crack growth, $\Delta a'$, for computation of crack growth rate.

Correction Procedure

The stress intensity factors and crack growth rates for out-of-plane data must be corrected independently. Assuming at least two visual measurements are used to reduce the compliance data, then the SIF computed using the projected crack length, $a_n + \Delta a$, is accurate for a crack with an out-of-plane angle less than 40°.

An accurate crack growth rate, da/dN, must then be computed from the projected crack growth, Δa, using Eq 1.

7050-T7451 Mixed-Mode Data

Donald [2] performed tests on 7050-T7451 in the S-L orientation using compact tension, C(T), specimens. The specimens were machined such that the S-L orientation was at specific out-of-plane angles with respect to the specimen configuration, i.e., all crack growth was in the S-L orientation, but at different angles on the C(T) specimen, as shown in the inset of Fig. 3. Results were presented for cracking angles of 1, 10, 17, and 26° and are reproduced in Fig. 3. Tests were performed at a stress ratio, R, of 0.7 and a constant ΔK of 3.3 MPa $m^{1/2}$. The results support the ASTM E 647 guidelines for out-of-plane cracking, showing that crack growth rates are affected by the out-of-plane angle.

Donald described the applied K and the projected crack length ($a_n + \Delta a$) as would be expected from the reporting requirements of ASTM E 647. The FEA results presented in Fig. 2 show that for K control based on compliance crack length, the applied K can differ significantly from the actual K at the crack tip. To apply a correction to the data, the compliance crack length must be known. An estimate of the compliance crack length can be computed from the projected crack length, since the projected crack length gives an accurate representation of the SIF for the out-of-plane angles investigated. Using the compliance crack length, we can estimate the applied load for a given ΔK and calculate the correct crack length and, subsequently, a corrected ΔK. The growth rate is then corrected using Eq 1 since the projected crack length is known.

Donald also provided baseline fatigue crack growth rate data over a range of ΔK values from about 2–5 MPa $m^{1/2}$, as shown in Fig. 3. A comparison of the average values of growth rate for uncorrected and corrected data sets with the baseline data is also presented in Fig. 3. The uppermost closed circle symbol shows the average for the 1° specimens. This data point is in excellent agreement with the baseline data and is not corrected. The remaining closed circles show average values for the uncorrected data. As the out-of-plane angle increases, the growth rates deviate more from the baseline data. The closed triangles show average values for the corrected data. The corrected values agree very well with the baseline data. For instance, the uncorrected, average crack growth rate for the 26° case is in error by 37 % compared to the baseline data. The ΔK was in error by 4 %. The correction of this data yielded good agreement with the baseline data; the resulting error in crack growth rate and ΔK were each less than 2 %.

Figure 4 shows the full data set for the 26° case. The open circles show the baseline data, and the closed circles show the uncorrected out-of-plane data. The closed triangles show the data using a corrected ΔK only, i.e., da/dN has not been corrected. Finally, the closed squares show the corrected data. The horizontal shift in the data are the correction of SIF, and the vertical shift is the correction of growth rate. The scatter in crack growth rate and ΔK is depicted in Fig. 4 to illustrate that the uncorrected constant ΔK data masks the actual variability in the mixed-mode data. The data presented in Figs. 3 and 4 show the importance of correcting both the growth rates and driving force and the validity of this approach.

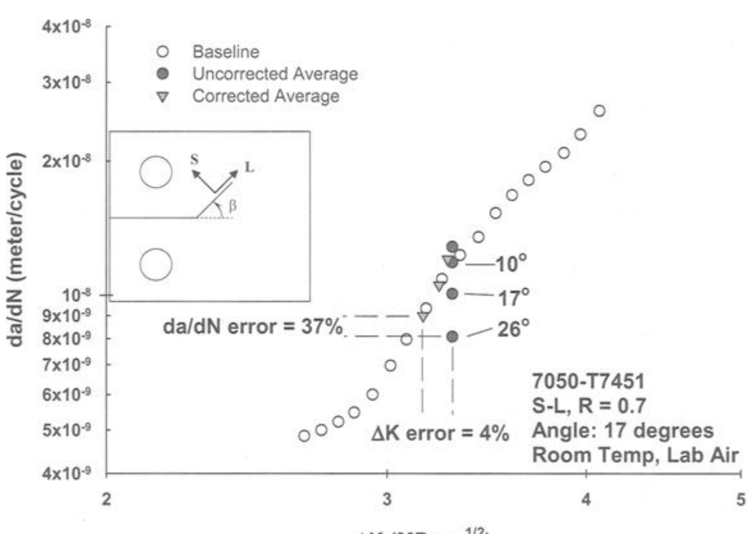

FIG. 3—*Comparison of corrected data with original and baseline data.*

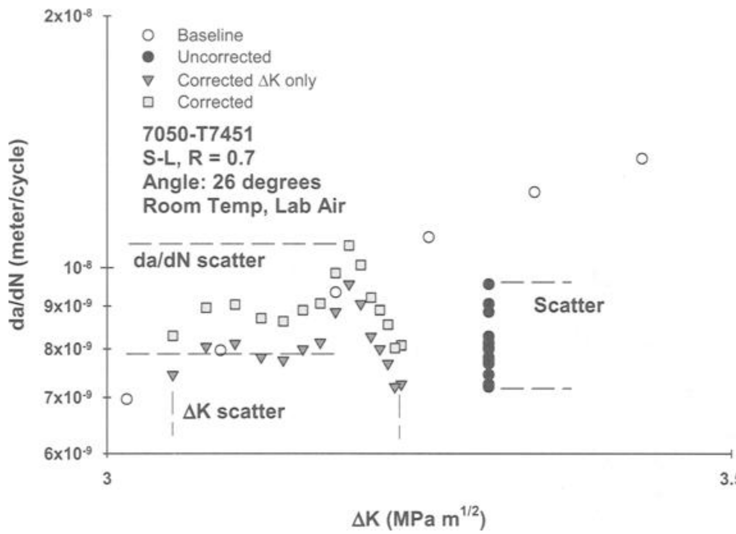

FIG. 4—*Comparison of corrected data with original and baseline data for the 26° case.*

2025-T6 Mixed-Mode Data

Test specimens were machined from near-net-shape forged aluminum alloy 2025-T6 propeller spars, shown in Fig. 5, which were provided by a propeller manufacturer. Each propeller spar is forged from cylindrical billets, so the material is substantially deformed during the forging process. The mechanical work of the forging process resulted in weak microstructural planes that promoted out-of-plane cracking, i.e., the microstructure directed the crack path more than the primary loading, similar to what Donald reported [2]. More information can be found in Forth et al. [1].

Out-of-Plane Angle

The out-of-plane angle for each specimen was determined by: 1) measuring the distance from the point at which the crack deviated from the specimen centerline to the crack tip ($\Delta a'$ from Fig. 1); 2) measuring the crack growth along the specimen centerline (Δa from Fig. 1); and 3) computing out-of-plane angle, β, using the cosine of the two crack growth lengths measured, $\Delta a'$ and Δa. An average out-of-plane angle was then computed by averaging the out-of-plane angle measured on each side of the specimen. Figure 6 shows the average out-of-plane angle for each of the specimens tested, and the front-to-back out-of-plane angles are presented in Table 1. For the 60 specimens, there were 16 straight cracks and 24 cracks outside the ASTM E 647 limit of 20°. The remaining specimens were not straight but were within the 20° limit for crack path straightness.

The specimens were numbered sequentially from the tip of the blade (1) to the hub (20) (see Fig. 5) to identify trends. Two specimens were extracted across the width of the blade, such that specimens 1-b1 and 2-b1 were taken from the tip of Blade 1. High numbered specimens from Blades 1 and 3 appear to have a larger number of straight cracks, but Blade 2 did not produce any straight cracks. The specimens extracted from the hub region, which have higher specimen numbers, have less mechanical work performed on the material during the forging process, because the hub is geometrically similar to the original product form, a cylindrical billet. This led to a more uniform, orthotropic microstructure [1], decreasing the probability of a weak microstructural plane being out-of-plane with the specimen centerline, leading to more straight cracks than the tip region.

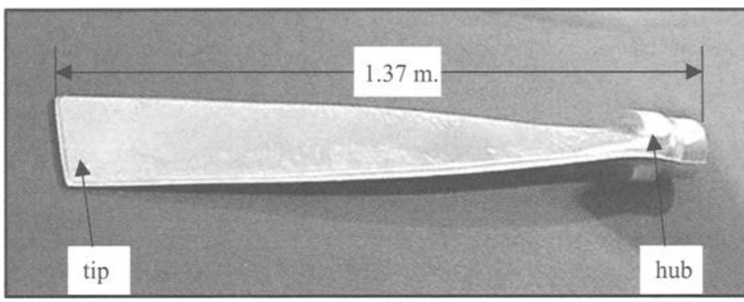

FIG. 5— *Photograph of propeller spar forging made of aluminum alloy 2025-T6.*

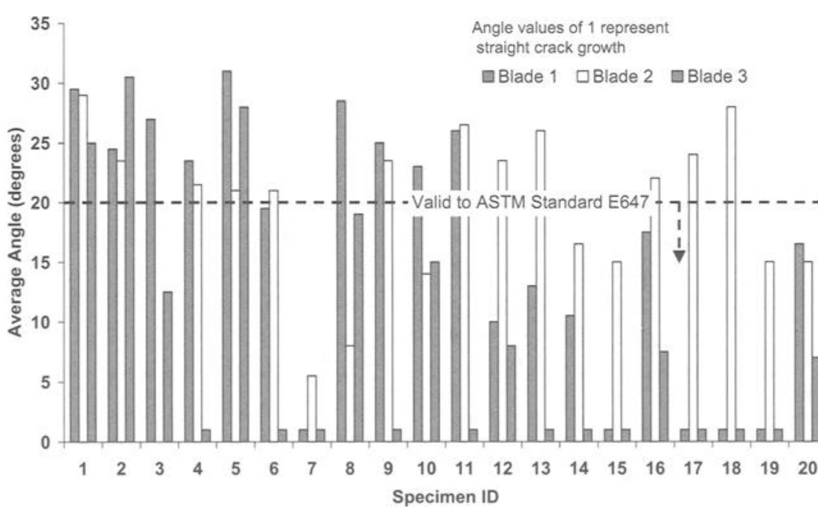

FIG. 6—*Average out-of-plane angle from centerline for fatigue crack growth tests.*

TABLE 1—*Out-of-plane angle (front/back) from centerline for fatigue crack growth tests.*

Specimen ID	Blade 1 Out-of-Plane Angle (front/back)	Blade 2 Out-of-Plane Angle (front/back)	Blade 3 Out-of-Plane Angle (front/back)
Tip 1	31/28	26/32	25/25 Tip
2	27/22	25/22	31/30
3	25/29	untested	10/15
4	25/22	21/22	0/0
5	29/33	18/24	30/26
6	22/17	17/37	0/0
7	0/0	0/11	0/0
8	30/27	8/8	16/22
9	28/22	23/24	0/0
10	23/23	13/15	13/17
11	22/30	30/23	0/0
12	12/8	29/18	9/7
13	17/9	26/26	0/0
14	11/10	19/14	0/0
15	0/0	15/15	0/0
16	16/19	24/20	7/8
17	0/0	28/20	0/0
18	0/0	28/28	0/0
19	0/0	12/18	0/0
Hub 20	9/24	12/18	12/2 Hub

Fatigue Crack Growth Rate Data

Fatigue crack growth rate data were generated using fixed stress ratios of 0.05, 0.1, and 0.7 and using constant K_{max} values of 11, 13.7, 16.4, 22, and 33 MPa $m^{1/2}$ per ASTM E 647. The specimen test data presented are grouped and plotted based on high and low stress ratio in Figs. 7 and 8, respectively. Specimens presented in these plots were tested using the constant R and K_{max} load reduction methods to determine threshold, da/dN ~ 10^{-10} meter/cycle and using the constant R load increasing method to determine the upper portion of the crack growth rate curve, as indicated by the figure legends. The constant R load reduction and load increasing tests are denoted with "LR" and "LI," respectively. The specimen number is denoted in the figure legend to correlate test data to out-of-plane angle. The majority of the constant R load increasing tests were performed following load reduction tests on the same specimen, resulting in duplicate specimen numbers in the figure legends.

All of the out-of-plane data were corrected using the previously described procedure, except that specimens 2-b3 and 5-b1 were not analyzed because significant crack branching occurred, which is not in the realm of this correction procedure. An example of the effect that the correction procedure has on the data is presented in Fig. 9. Specimen number 18 from blade number 2 (18-b2) was chosen for examination because the average out-of-plane angle was approximately 28°. The original data obtained during the test is labeled "uncorrected." The uncorrected data are in error with the baseline data (14-b1) by 50 % in crack growth rate at a ΔK of 3.8 MPa $m^{1/2}$. The data were then adjusted for ΔK using the projected crack length. Finally, the fatigue crack growth rate was corrected to the actual crack length using Eq 1, and this data set is labeled "corrected." The correction procedure yielded slightly better agreement with the baseline data (14-b1), with an error in crack growth rate of 44 % at a ΔK of 3.7 MPa $m^{1/2}$. The reduced benefit of the correction procedure at this ΔK, in comparison to Donald's data, is discussed in the next section.

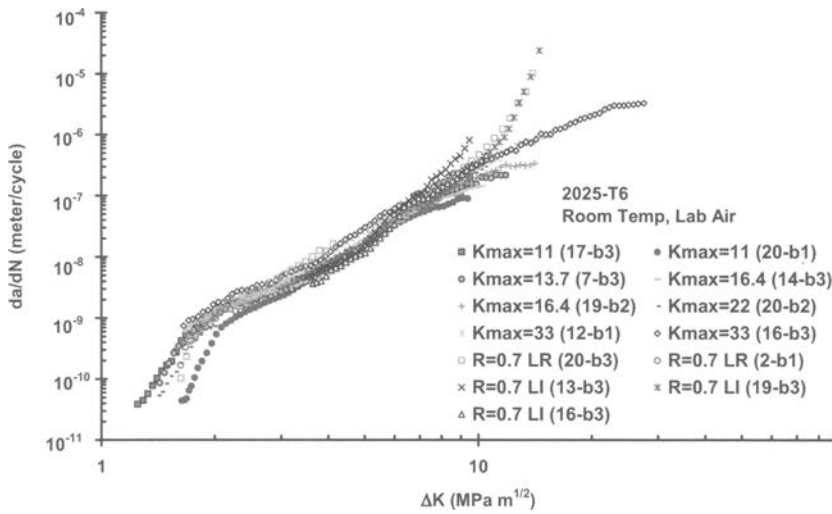

FIG. 7—*High stress ratio fatigue crack growth rate data for aluminum alloy 2025-T6. (All data are corrected for out-of-plane angle.)*

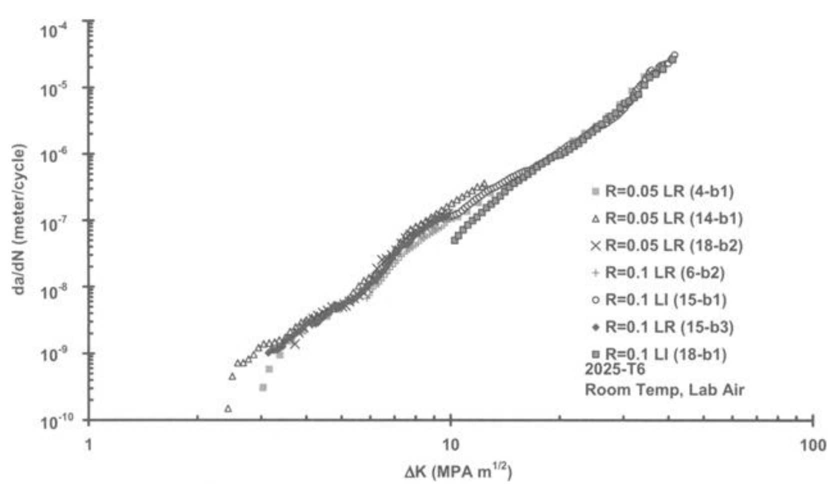

FIG. 8—*Low stress ratio fatigue-crack-growth-rate data for alloy 2025-T6. (All data are corrected for out-of-plane angle.)*

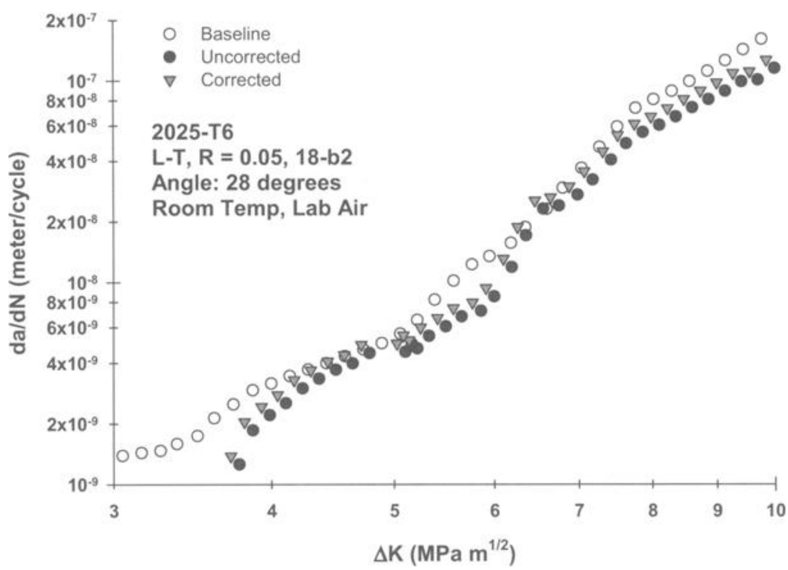

FIG. 9—*Effect of corrections on the fatigue crack growth rate data of specimen 18, blade 2 (R = 0.05 LR).*

Effect of Mode-Mixity on Crack Growth Rate

Much research has shown experimental evidence that mixed-mode behavior at the crack tip can influence the crack growth rate [6,7]. Based on this, Donald [2] generated the presented data for 7050-T7451 at a stress ratio of 0.7 and a crack growth rate above 10^{-9} meters/cycle. The combination of high stress ratio and crack growth rate above threshold minimizes energy dissipation due to roughness- and plasticity-induced crack closure or other mechanisms that may influence growth rates in mixed-mode. The 2025-T6 data were generated at both high and low stress ratios and over a wide range of crack growth rates. Both the high and low stress ratio data are investigated to asses the effect mode-mixity has on fatigue crack growth. The high R data will isolate the ranges of crack growth rate that are affected, while minimizing the effects of roughness- and plasticity-induced crack closure [8]. The low R data will likely be more influenced by plasticity- or roughness-induced closure and other mechanisms that can reduce the driving force in mixed-mode situations [7].

Focusing first on the low stress ratio data (Fig. 8), specimens 15-b1, 15-b3, and 18-b1 had out-of-plane angles of essentially zero. Specimen 14-b1 had an angle greater than 10° but less than 20°. These specimens comprise the data set that meets ASTM E 647 and forms the basis for a low stress ratio baseline data set. The remaining three specimens are outside the 20° requirement. The data in Fig. 8 show that for this data set there appears to be very little effect of out-of-plane angle for the Paris regime (da/dN > 10^{-8} m/cycle for this discussion). Only two specimens approached threshold: 14-b1 and 4-b1. Specimen 14-b1 is part of the baseline set, and specimen 4-b1 had an average out-of-plane angle of about 24°. Near-threshold, the out-of-plane cracking data had significantly slower crack growth. For instance, at a ΔK of approximately 3.2 MPa $m^{1/2}$, the crack growth rate of specimen 4-b1 was 6.4 × 10^{-10} m/cycle, whereas the baseline specimen 14-b1 had a crack growth rate of 1.4 × 10^{-9} m/cycle, more than a factor of two faster. Therefore, the out-of-plane angle of 24° is significant near-threshold.

To investigate the high stress ratio data, constant K_{max} and constant R = 0.7 load reduction test specimens were chosen. The crack growth rate versus stress intensity for the constant K_{max} tests is plotted in Fig. 10. Comparing the constant K_{max} = 11 MPa $m^{1/2}$ tests, specimen 17-b3 propagated straight, whereas specimen 20-b1 propagated an average of 16.5° out-of-plane (front/back = 9/24). At higher ΔK levels (ΔK > 5 MPa $m^{1/2}$), there is little difference in the tests. However, as the ΔK reduces below 4 MPa $m^{1/2}$, the data sets diverge with the higher out-of-plane angles having lower crack growth rates.

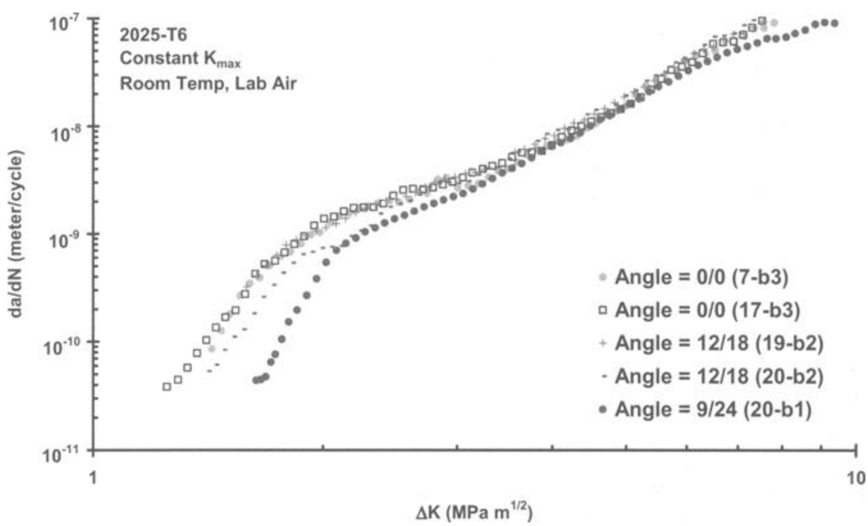

FIG. 10—*Constant K_{max} data near threshold for different out-of-plane angles. (All data are corrected for out-of-plane angle.)*

As a crack twists out-of-plane through-thickness for a compact tension specimen (twisting is defined as front-to-back out-of-plane angle variation), mode-III behavior is observed at the crack tip [9]. The difference in crack growth data from specimen 20-b1 to specimens 19-b2 and 20-b2 could be indicative of mode-III behavior. Each test propagated out-of-plane at approximately the same average angle, however specimen 20-b1 had significant twisting. Near threshold, the twisting exhibited in specimen 20-b1 translated into an order of magnitude decrease in the crack growth rate, whereas specimen 19-b2 nearly matched the straight data. Specimen 20-b2 fell between the other data and suggests that the out-of-plane angle may introduce significant variability in the crack growth rates, more than specimen 19-b2 suggests.

The constant R = 0.7 data are presented in Fig. 11 as crack growth rate versus stress intensity. Specimen 2-b1 propagated an average of 24.5° out-of-plane. Unfortunately, there is no overlap of specimen 2-b1 data with the straight tests. However, extrapolating the data from specimen 2-b1, it would appear to have the same crack growth rates at ΔK values exceeding 5 MPa $m^{1/2}$, similar to the constant K_{max} data presented in Fig. 10. Specimen 20-b3 exhibited significant twisting, much like specimen 20-b1 discussed previously, and it does overlap the straight data. Once again, the crack growth rates from specimen 20-b3 do not coincide with the straight data until ΔK exceeds 5 MPa $m^{1/2}$. A comparison of specimens 20-b3 and 2-b1 near threshold ($\Delta K <$ 2 MPa $m^{1/2}$) show similar crack growth behavior. It appears the effect of the high out-of-plane angle of specimen 2-b1 and the lower angle plus the twisting of specimen 20-b3 have coincidentally generated the same crack growth rates, demonstrating the significance of twisting in a low angle test.

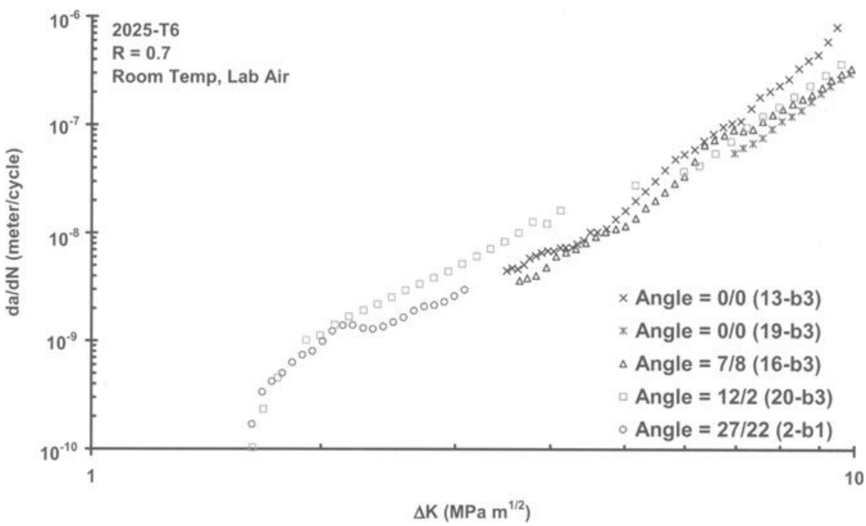

FIG. 11—*Constant R = 0.7 data near threshold for different out-of-plane angles. (All data are corrected for out-of-plane angle.)*

Discussion

When out-of-plane cracking occurs, the polynomial equations defined in ASTM E 647 underestimate the actual crack length and overestimate the projected crack length. This, in turn, overestimates the stress intensity factor (SIF) and underestimates the crack growth rates. The use of projected crack length to correct this data will correct the SIF but still underestimate the crack growth rates. These high-level continuum descriptions are only simple approximations to the true behavior along a crack front, where the crack path is not straight but is locally influenced by microstructure. The local stress intensity factor (SIF) is only a convenient approximation to the cyclic deformations that drive the growth. When compared to a straight crack, the out of plane crack likely has a more tortuous path, and the local SIFs are consequently influenced both by the global mixed-mode behavior as well as by the local crack path deviations [9].

The authors have presented a very simple procedure for correcting out-of-plane crack growth data that are within 40° of straight. The correction procedure was initially validated using 7050-T7451 aluminum alloy data available in the literature [2]. In that work, the out-of-plane cracking was encouraged by machining specimens with the S-L material axis rotated with respect to the crack symmetry plane of the C(T) specimen (see Fig. 3). As a result, in each case the cracking was essentially in the S-L material plane, resulting in a relatively smooth and consistent fracture surface. Further, the data were generated at a high stress ratio and ΔK level to minimize crack face interaction effects. The correction procedure worked well to conform the out-of-plane data with the baseline data.

The correction procedure was also applied to out-of-plane data generated in 2025-T6 aluminum alloy from a weak microstructural plane established during the forging process. The correction procedure was applied to this data at both high and low stress ratios with some success. However, if the average out-of-plane angles exceeded 15°, the data could not be reliably corrected near threshold, da/dN $\sim 10^{-10}$ meter/cycle, because mixed-mode effects became dominant [10]. Furthermore, specimens that displayed significant twisting (i.e., the difference in out-of-plane angle measured on the specimen front and back exceeded 10°) could not be reliably corrected near threshold. The authors believe that the mixed-mode behavior in the threshold regime is dominant, and a simple correction procedure is inadequate.

Conclusion

In conclusion, a simple procedure has been developed to correct out-of-plane data to account for mixed-mode effects. Application of this procedure to test data that experience significant, unexpected out-of-plane cracking may aid in generating usable data. However, this procedure cannot be reliably used for crack growth rates approaching the fatigue crack growth threshold (da/dN $\sim 10^{-10}$ meter/cycle) when the out-of-plane angle exceeds 15°. Furthermore, this procedure is inappropriate for correcting data that have significant variation in the through-thickness out-of-plane angle, i.e., twisting or mode-III type behavior. The mixed-mode phenomenon of both of these cases is beyond the scope of a simple continuum-based approach to recover out-of-plane data. Finally, the ASTM E 647 standard allows for out-of-plane cracking angles to 20°. Near threshold, this will lead to inaccurate data, as shown in this paper. Therefore, the standard should be more restrictive on the limits for out-of-plane cracking (15°) and add a requirement for a minimum of two visual measurements (one at test start and one at test completion) to correct for out-of-plane angles. Additionally, the standard does not address crack twisting. A note on crack twisting angles should be included, with a limit of 10° being acceptable based on the data in this paper.

References

[1] Forth, S. C., James, M. A., and Johnston, W. M., "Development and Validation of Advanced Test Methods to Generate Fatigue Crack Growth and Threshold Data for Use in Damage Tolerance Analyses," *DOT/FAA/AR-xxx*, 2003.

[2] Donald, J. K., "The Effect of Out-of-Plane Cracking on FCGR Behavior," ASTM Research Report #E8-1001, 12 December 1995.

[3] James, M. and Swenson, D., "FRANC2D/L: A Crack Propagation Simulator for Plane Layered Structures," 2002, available online at: http://www.mne.ksu.edu/~franc2d/.

[4] Wawrzynek, P. A. and Ingraffea, A. R., "Integrated Finite Element Analysis of Fracture Processes: An Integrated Approach," *Theoretical and Applied Mechanics*, No. 8, 1987, pp. 137–150.

[5] James, M. A. and Swenson, D. V., "A Software Framework for Two Dimensional Mixed Mode-I/II Elastic-Plastic Fracture," *Mixed-Mode Crack Behavior, ASTM STP 1359*, K. J. Miller and D. L. McDowell, Eds., ASTM International, West Conshohocken, PA, 1999.

[6] Lam, Y. C., "Mixed Mode Fatigue Crack Growth with a Sudden Change in Loading Direction," *Theoretical and Applied Fracture Mechanics*, Vol. 19, 1993, pp. 69–74.
[7] Newman, Jr., J. C. and Piascik, R. S., Eds., *Fatigue Crack Growth Thresholds, Endurance Limits, and Design, ASTM STP 1372*, ASTM International, West Conshohocken, PA, 2000.
[8] Smith, S. W. and Piascik, R. S., "An Indirect Technique for Determining Closure-Free Fatigue Crack Growth Behavior," *Fatigue Crack Growth Thresholds, Endurance Limits, and Design, ASTM STP 1372*, J. C. Newman, Jr. and R. S. Piascik, Eds., ASTM International, West Conshohocken, PA, 2000, pp. 109–122.
[9] Buchholz, F. G., Chergui, A., and Richard, H. A., "Fracture Analyses and Experimental Results of Crack Growth under General Mixed Mode Loading Conditions," *Engineering Fracture Mechanics*, Vol. 71, 2004, pp. 455–468.
[10] Zheng, Y. S., Wang, Z. G., and Ai, S. H., "Mixed-Mode I and II Fatigue Threshold and Crack Closure in Dual-Phase Steels," *Metall. Mater. Trans. A*, Vol. 25A, No. 8, 1994, pp. 1713–1723.

Journal of ASTM International, June 2005, Vol. 2, No. 6
Paper ID JAI12027
Available online at www.astm.org

Toshiyuki Meshii,[1] *Kenichi Ishihara,*[2] *and Katsuhiko Watanabe*[3]

Assessment for Decrease in Threshold Stress Intensity Factor (SIF) Range Due to High Maximum SIF

ABSTRACT: In this paper, we consider the decrease in threshold stress intensity factor (SIF) range ΔK_{th} due to high maximum SIF K, which is observed for several materials in the tests with the K_{max} constant method when closure-free conditions are realized. We proposed an assessment criterion to predict this phenomenon from the past data for Al and Ti and showed that the criterion is valid also for steels. Finally, we proposed a simplified model to explain the phenomenon, considering the fact that marks of static fracture are observed on the fracture surface.

KEYWORDS: fracture mechanics, fatigue crack growth, threshold stress intensity factor range, static fracture mode

Introduction

Since the pioneering work of Paris and Erdogan [1], the applied stress intensity factor (SIF) range ΔK has been known to be a major controlling parameter in fatigue crack growth (FCG) rate da/dN under small scale yielding conditions. At low FCG rates, da/dN - ΔK curve in log-log scale generally becomes steep and appears to approach a vertical asymptote that corresponds to the FCG threshold. ΔK corresponding to this asymptote is named as the threshold SIF range ΔK_{th}. Almost without exception, existing data show that the ΔK_{th} tends to decrease with increasing load ratio R [2]. One example of the variation in the ΔK_{th} with R by Boyce and Ritchie [2] is shown in Fig. 1*a*. Schmidt and Paris [3] rationalized this behavior solely on the basis of the crack closure concept. Assuming that both the closure-corrected effective fatigue threshold, $\Delta K_{eff,th}$ and the closure stress intensity, K_{cl}, are not affected by load ratio, there exists some critical load ratio, R_c at which $K_{min} = K_{cl}$, such that:

$$\Delta K_{eff,\,th} = \begin{cases} K_{max,\,th} - K_{cl} < \Delta K_{th}, & if\ R < R_c\ (K_{min,\,th} < K_{cl}) \\ K_{max,\,th} - K_{min,th} = \Delta K_{th}, & if\ R > R_c\ (K_{min,\,th} > K_{cl}) \end{cases} \quad (1)$$

Under these conditions, the maximum SIF at threshold, $K_{max,th}$, is independent of R below R_c, and the ΔK_{th} is independent of R above R_c. Plotted as $K_{max,th}$ versus ΔK_{th}, this is manifest by a distinct 'L' shape, as shown in Fig. 1*b*. This illustrates that the value of ΔK_{th} is independent of K_{max} when $R > R_c$, where global closure is no longer effective.

However, this behavior is not universal, and the existence of materials that show characteristics illustrated in Fig. 1*c* and *d* has been reported [2]. Since this decrease in ΔK_{th} was

Manuscript received 3 November 2003; accepted for publication 4 August 2004; published June 2005. Presented at ASTM Symposium on Fatigue and Fracture Mechanics: 34th Volume on 19–21 November 2003 in Tampa, FL; S.R. Daniewicz, J.C. Newman, Jr., and K-H. Schwalbe, Guest Editors.
[1] Professor, Faculty of Graduate School of Engineering, University of Fukui, 3-9-1 Bunkyo, Fukui, Fukui, JAPAN.
[2] Graduate Student, Graduate School of Engineering, University of Fukui, 3-9-1 Bunkyo, Fukui, Fukui, JAPAN.
[3] Professor, Institute of Industrial Science, University of Tokyo, 4-6-1 Komaba, Meguro-ku, Tokyo, JAPAN.

observed in the range of $R > R_c$, this behavior is apparently independent of crack closure. One example is the case shown in Marci's report [4]. The FCG threshold ceased to exist for a Ti-6Al-2Sn-4Zr-6Mo alloy under high maximum stress intensity K_{max} (Marci effect), though their tests were the K_{max}-constant tests that ensure closure free conditions. Lang [5] et al.'s report should have encouraged engineers because their report concluded that the Marci effect is not caused by an abnormal or unknown phenomena; i.e., the effect is caused by time-dependent crack growth (hydrogen-assisted sustained load cracking), well known for Ti alloys for a long time. On the other hand, Newman et al.'s near threshold data by K_{max}-constant method on Al7050-T6 alloy [6] and Ritchie et al.'s data for Ti-6Al-4V alloy [2] show the decrease in ΔK_{th} with the increase in K_{max} without time-dependent crack growth. The mechanism for these phenomena is not necessarily clear.

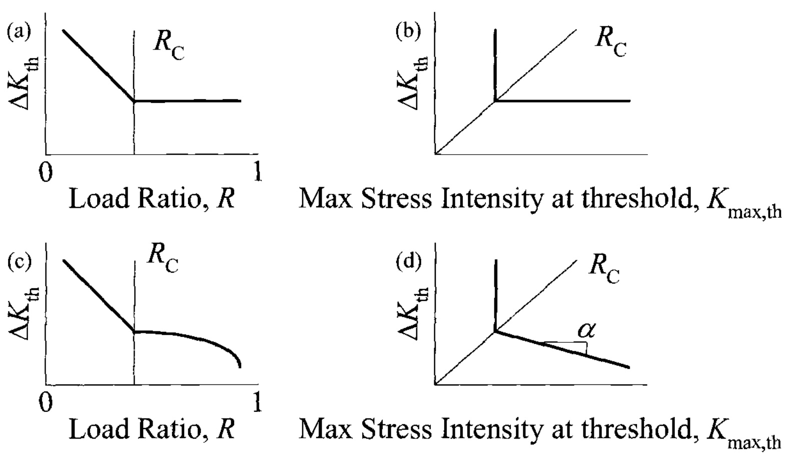

FIG. 1—*Conceptual representations of the influence of the load ratio, R, on the fatigue threshold, ΔK_{th} [2].*

Besides the lack of full understanding of the decrease in ΔK_{th} due to high K_{max}, there are instances where the medium range FCG rate data for a material is linearly extrapolated to the near threshold range on the log-log scale (*linear extrapolation*) [7] when the near threshold FCG rate data for a specific material are not given. This *linear extrapolation* is a natural engineering approach and is considered safe, assuming that a FCG threshold exists. Thus, we thought it important as a first step to be able to assess whether a material will show a tendency toward the decrease in ΔK_{th} due to high K_{max}. In the following, we first compiled the existing data for Al [6,8] and Ti [2] that showed the decrease in ΔK_{th} due to high K_{max} under closure-free and proposed an assessment criterion to predict the phenomena. Then we applied our assessment criterion to carbon steels (JIS S55C, HT60, and SS400) and type 304 stainless steel and showed its validity with constant-K_{max} FCG tests. Finally, by examining the S55C's fractography taken with scanning electron microscope, which showed the decrease in ΔK_{th} due to high K_{max}, we considered possible mechanistic explanations.

Proposal of Assessment Criterion for the Decrease in ΔK_{th} Due to High K_{max} from Existing Data of Al and Ti

We first examined the existing data for Al and Ti that showed the decrease in ΔK_{th} due to high K_{max}, expecting to find something in common. We chose data for CT specimens under K_{max}-controlled load in a laboratory air environment. We considered the fact that there is an implicit upper limit on K_{max} to satisfy the small scale yielding condition. For example, the ASTM E 647 guideline for CT test specimens [9] can be read so as to choose the test K_{max} not larger than the K_{maxSSY} defined as follows:

$$K_{maxSSY} = \sigma_{YS}\sqrt{\pi(W-a)/4} \tag{2}$$

where σ_{YS} is the yield stress of the material, and W and a are the width and the final crack length of the CT test specimen, respectively. Considering the fact that static fracture should be avoided at this K_{maxSSY}, we assessed the safety margin for static failure under K_{maxSSY} on the Failure Assessment Diagram (FAD) [10]. For this purpose, we first calculated the static load P_{maxSSY} corresponding to K_{maxSSY} with the final crack length a. Then, we calculated the limit load equivalent stress for a CT specimen with the following equation [11]:

$$\sigma_{cqSSY} = \frac{P_{maxSSY}}{BW}\frac{1}{-(1+\xi)+\sqrt{2+2\xi^2}}, \quad \xi = a/W \tag{3}$$

which is the closed form equation for plane stress under Tresca's yielding criterion (B is the thickness of the test specimen). We chose this equation from the various equations given for a combination of plane stress/strain conditions and yielding criterions, because Eq 3 formally gives the maximum value.

$(K_r, S_r)_{SSY} = (K_{maxSSY}/K_{IC}, \sigma_{eqSSY}/\sigma_f)$ of Ti-6Al-4V [2], Al7050-T6 [6], Al2024-T3[6], Al6013-T651 [8] plotted on the FAD is shown as Fig. 2. Here, K_{IC} is the fracture toughness, and $\sigma_f = (\sigma_{YS} + \sigma_B)/2$ is the flow stress used in limit load analysis, where σ_B is the tensile strength of the material. FAD is a failure assessment tool that combines the SIF criterion under small scaling yield conditions ($K = K_{IC}$) and the stress criterion under full scale yielding conditions ($\sigma = \sigma_f$). On the FAD, failure under arbitrary crack tip yielding condition is assessed by the Failure Assessment Curve (FAC) expressed as the following:

$$K_{rFAC} = \left[\frac{8}{(\pi S_{rFAC})^2}\ln\left\{\sec\left(\frac{\pi}{2}S_{rFAC}\right)\right\}\right]^{-1/2} \tag{4}$$

Since we could not directly find the final crack length a from the manuscripts for each test, we first asked for the data from the authors. In cases where we could not get the details, we estimated the a by the following procedures: i) assume the initial crack length as $a_0 = 0.3W + 3$ mm (same as our tests given later), ii) read the initial and the final SIF ranges ΔK_0 and ΔK, respectively, from the da/dN-ΔK curves from the manuscripts, and iii) finally evaluate the desired a from the specified normalized K-gradient $C = (d(\Delta K)/da)/\Delta K$ and the following ASTM loading curve [9].

$$\Delta K = \Delta K_0 e^{C(a-a_0)} \tag{5}$$

Detailed data used in the plots on Fig. 2 are summarized as Table 1.

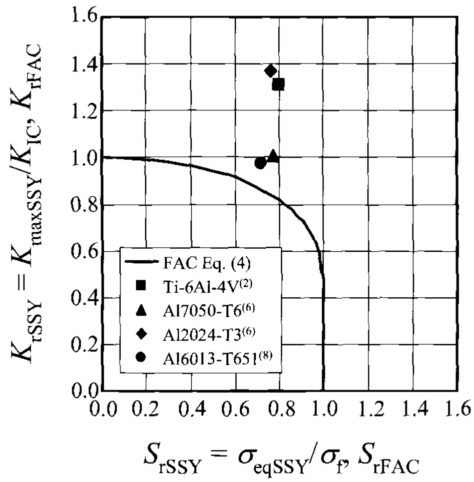

$S_{rSSY} = \sigma_{eqSSY}/\sigma_f, S_{rFAC}$

FIG. 2—*Comparison of K_{max} constant test conditions.*

TABLE 1—*$(K_r, S_r)_{SSY}$ for Al and Ti.*

	W	B	a	K_{IC}	K_{maxSSY}	K_{rSSY}	σ_{YS}	σ_B	σ_f	σ_{eqSSY}	S_{rSSY}
	mm	mm	mm	$MPam^{1/2}$	$MPam^{1/2}$		MPa	MPa	MPa	MPa	
Ti-6Al-4V[2]	25	8	13.7	67.0	87.6	1.31	930	970	950	760	0.80
7050-T6[6]	30.5	2.5	12.9*	34.0	29.2	1.01	248	248*	248	192	0.77
2024-T3[6]	38.1	2.3	14.9*	29.0	46.6	1.37	345	345*	345	263	0.76
6013-T651[8]	76.2	9.52	26.2*	70.7*	68.8	0.97	347	379	363	261	0.72

* estimated value.

We see from Fig. 2 that all the plotted materials considered are on or outside of the FAC, which represent the locus of predicted failure points. We thought this was a peculiar characteristic of materials that experience the decrease in ΔK_{th} due to high K_{max}. Though the plots are results for Al and Ti, and though some estimated data were used for the plots, we considered that $(K_r, S_r)_{SSY}$, which is determined from material strength (σ_{YS}, σ_B, K_{IC}) and the specimen configuration (a, W), might be a candidate to assess the decrease in ΔK_{th} due to high K_{max}. In the following, we apply the process to plot $(K_r, S_r)_{SSY}$ on FAD for steels and examine whether the process is valid to assess the decrease in ΔK_{th} due to high K_{max}.

Test Conditions and Results: Case for Steels

Test Conditions

We made tests fundamentally in accordance with the ΔK-decreasing threshold test procedure specified in ASTM E 647 [9] in association with a constant maximum stress intensity level K_{max} [12]. The dimensions of the CT test specimen are shown in Fig. 3. The cyclic stress intensity range was varied according to Eq 5, as specified in ASTM E 647 [9]. Here a_0 (= initial machine notch length of 15 mm + fatigue pre-cracking of 3 mm = 18 mm) and a are initial and current values of the crack length, respectively. ΔK_0 is the initial value of ΔK set to 12 MPam$^{1/2}$ for all the materials and regardless of K_{max}. This value of ΔK_0 was chosen to make ΔK = 3 MPam$^{1/2}$ at a = 20 mm, considering the fact that the threshold ΔK of various ferritic alloys is approximately 3 MPam$^{1/2}$. C is the normalized K-gradient $(d(\Delta K)/da)/\Delta K$ set to a value of $C = -0.7$ mm^{-1}, which is a deviation from the ASTM E 647 specification of $C > -0.08$ mm^{-1} based on the R-constant test method. This deviation is validated in the case of the K_{max}-constant test method for a value of C as small as $C = -1.2$ mm^{-1}. This is based on the work by Hertzberg et al. [13], who explained that this is true because the crack tip plastic zone size is held constant for K_{max}-constant tests. Under the above conditions, we selected S55C as the material whose $(K_r, S_r)_{SSY}$ might exceed FAC, and SS400, HT60, and SUS304 as the material whose $(K_r, S_r)_{SSY}$ are below FAC (Table 2). Chemical compositions of the tested materials are given in Table 3. S55C-1, 2 in this table distinguishes the heats. Fracture toughness K_{IC} in Table 2 was estimated from the Charpy test results and the following equation [14] (S55C-1, 2, SS400, HT60), and estimated from J_Q in J_Q test (SUS304).

$$\left(K_{IC}/\sigma_{YS}\right)^2 = 0.6478\left(C_V/\sigma_{YS} - 0.0098\right) \tag{6}$$

where the quantities in the equation above are all in SI units, and C_V is the absorbed energy (J) obtained from the Charpy impact test.

For each material, tests were conducted for several values of K_{max}, which were chosen to satisfy the small scale yielding condition. In concrete, S55C-1: K_{max} = 50, 46, 42, 36, 18 MPam$^{1/2}$ (K_{max}/K_{maxSSY} = 0.87, 0.80, 0.73, 0.63, 0.31); S55C-2: K_{max} = 70, 50, 18 MPam$^{1/2}$ (K_{max}/K_{maxSSY} = 0.95, 0.68, 0.24); HT60: K_{max} = 80, 70, 50, 30 MPam$^{1/2}$ (K_{max}/K_{maxSSY} = 1.00, 0.88, 0.63, 0.38); SS400: K_{max} = 42, 32, 18 MPam$^{1/2}$ (K_{max}/K_{maxSSY} = 1.00, 0.76, 0.43); SUS304: K_{max} = 31, 25, 18 MPam$^{1/2}$ (K_{max}/K_{maxSSY} = 0.90, 0.72, 0.52).

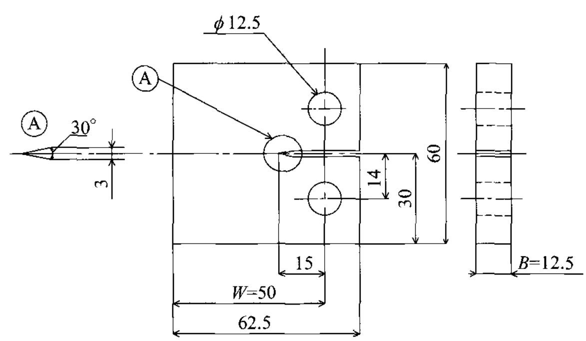

FIG. 3—*Geometry of CT test specimen (Dimensions in mm).*

TABLE 2—*$(K_r, S_r)_{SSY}$ for tested materials.*

	W	B	a	K_{IC}	K_{maxSSY}	K_{rSSY}	σ_{YS}	σ_B	σ_f	σ_{eqSSY}	S_{rSSY}
	mm	mm	mm	MPam$^{1/2}$	MPam$^{1/2}$		MPa	MPa	MPa	MPa	
S55C-1	50	12.5	20	65	57.6	0.89	375	724	550	287	0.52
S55C-2	50	12.5	20	72	73.8	1.02	481	808	644	368	0.57
HT60	50	12.5	20	304	79.8	0.26	520	631	576	398	0.69
SS400	50	12.5	20	151	42.2	0.28	275	438	357	211	0.59
SUS304	50	12.5	20	533	34.5	0.06	225	608	417	172	0.41

TABLE 3—*Chemical composition of test specimens.*

	C	Si	Mn	P	S	Cu	Ni	Cr	Nb	B	Fe
S55C-1	0.53	0.20	0.66	0.007	0.003	0.01	0.02	0.02	...	...	Bal.
S55C-2	0.56	0.20	0.84	0.015	0.010	0.01	0.03	0.15	...	...	Bal.
HT60	0.12	0.25	1.45	0.008	0.003	0.01	0.02	0.03	0.02	0.0001	Bal.
SS400	0.12	0.22	0.58	0.021	0.017	...	...	...	...	...	Bal.
SUS304	0.05	0.59	1.02	0.028	0.008	...	9.11	18.35	...	0.0001	Bal.

Test Results

Tests were conducted in a laboratory air environment, and the loading frequency was 30 Hz. The maximum difference in ΔK for the planned and measured was less than 5 %. For all tests, the closure free condition was confirmed by measuring back surface strain.

The da/dN data we obtained for HT60, SS400, SUS304, and S55C are summarized in Figs. 4–7, respectively. We measured the crack length with an optical micrometer with a resolution of 1/100 mm and evaluated da/dN by the incremental polynomial method given in ASTM E 647 [9].

We see from Figs. 4–6 that though the tests for HT60, SS400, and SUS304 were conducted for several K_{max} levels smaller than K_{maxSSY}, the da/dN data within the measured range showed little variance and a clear threshold ΔK existed.

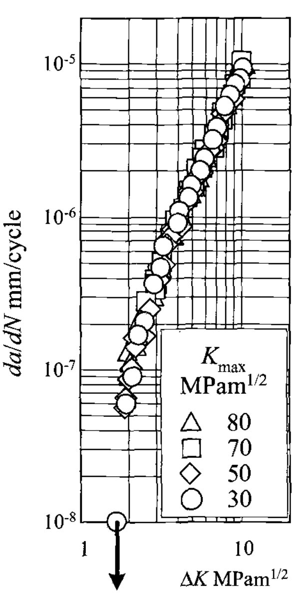

FIG. 4—K_{max}-*const. test results (HT60).*

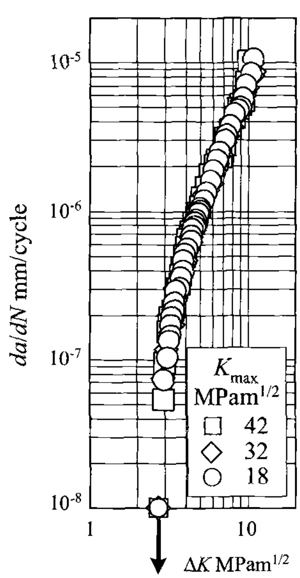

FIG. 5—K_{max}-*const. test results (SS400).*

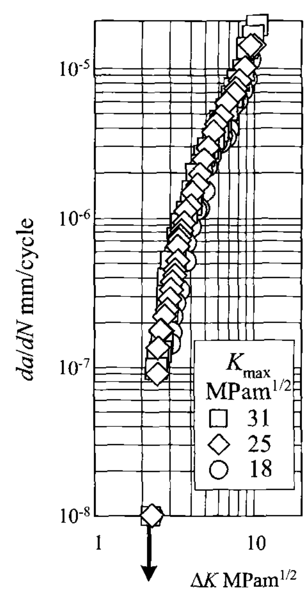

FIG. 6—K_{max}-*const. test results (SUS304).*

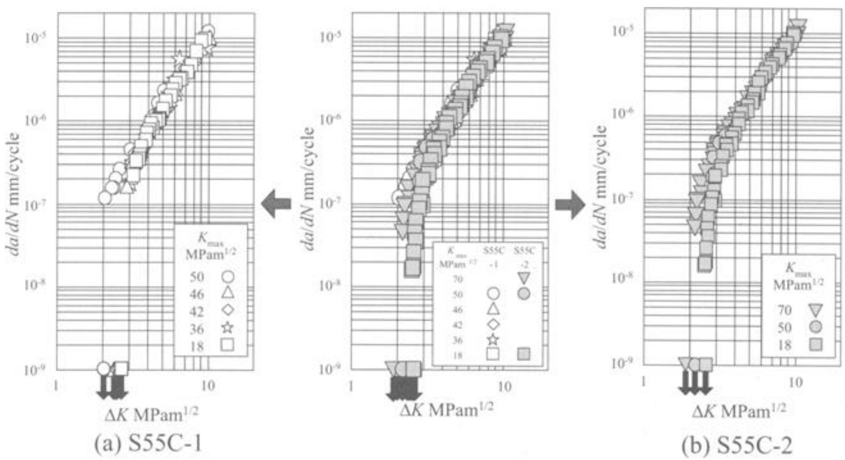

FIG. 7—K_{max}-*const. test results (S55C).*

On the other hand, we see in Figs. 7*a* and *b* that the trend observed for the S55C was somewhat different from the other materials. Though the *da/dN* data show little variance for *da/dN* > 10^{-6} mm/cycle, the *da/dN* seemed to increase according to the increase in K_{max} in the range of $1 \times 10^{-7} \leq da/dN \leq 1 \times 10^{-6}$ mm/cycle, and the decrease in ΔK_{th} due to high K_{max} was observed. This is similar to what Ritchie et al. reported for Ti alloy [2] and what Newman et al. reported for Al alloy [6].

Thus, as we expected from the assessment by $(K_r, S_r)_{SSY}$ and FAC, HT60, SS400, and SUS304 did not experience the decrease in ΔK_{th} due to high K_{max}, while S55C did. In summary, the validity of our proposal to assess decrease in ΔK_{th} due to high K_{max} by $(K_r, S_r)_{SSY}$ and FAC, which was originally based on compiled data of Al and Ti alloys, was shown also for steels.

Fractography

Since S55C showed the decrease in ΔK_{th} due to high K_{max}, we compared fractographs obtained from scanning electron microscopy (SEM) corresponding to $da/dN \approx 1 \times 10^{-5}$ mm/cycle (a = 18 mm; *Paris region*) and $da/dN \approx 1 \times 10^{-7}$ mm/cycle (a = 20 mm; ΔK_{th} *region*) at K_{max} = 50 and 18 MPam$^{1/2}$ for S55C-1 and K_{max} 70, 50, and 18 MPam$^{1/2}$ for S55C-2. Fractographs for S55C-1, K_{max} = 50 MPam$^{1/2}$ at a magnification of ×1000 are shown as Figs. 8–10. No apparent differences in fractography due to heat difference (S55C-1 and 2) or K_{max} level were found; thus other cases were omitted on account of limited space.

Figure 8, which is difficult to characterize, is a typical fractograph observed regardless of K_{max} or *da/dN* (*Paris region* or ΔK_{th} *region*). This was not surprising considering the fact that striations are not easy to observe for carbon steels like S55C, and considering the magnification rate. Besides the fracture shown in Fig. 8, though area ratios were small, striation-like marks shown in Fig. 9 (though the direction of the mark does not necessarily coincide with the FCG direction) and river pattern-like marks shown in Fig. 10 were observed. The area size of the striation-like or river pattern-like mark was close to 30 microns, which seemed to correspond to the grain size. The total area of the cleavage-like marks was not larger than 10 % of the total fractured area.

We also observed that neither marks of corrosion pits nor sustained load cracking were found from a fractograph for $K_{\max}$ = 50 MPam$^{1/2}$ (as shown in Figs. 8–10), though the decrease in ΔK_{th} due to high $K_{\max}$ was observed. Considering the fact that our tests were not conducted in an inert gas environment, we do not deny the possible effect of environment as a cause of the decrease in ΔK_{th} due to high $K_{\max}$. However, we consider the phenomena we observed for S55C seem to be similar to those that Newman et al. [6] reported for Al7050-T6 alloy, on the standpoint that some static fracture modes affected the decrease in the ΔK_{th} due to high $K_{\max}$. The marks of static fracture mode for Al7050-T6 alloy were dimples, which we could not observe in the S55C fractographs. Instead, we observed river pattern-like marks in the ΔK_{th} *region*. Thus, though the mechanism represented by the term "static fracture mode" for S55C and Al7050-T6 is different, we consider the possibility of some static fracture mode affecting the decrease in ΔK_{th} due to high $K_{\max}$ for S55C steel.

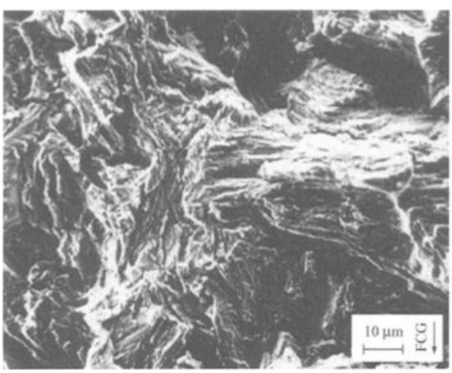

FIG. 8—*Typical fractured surface in the Paris region (S55C-1, K_{max} = 50 MPam$^{1/2}$, da/dN ≈ 1 × 10^{-5} mm/cycle).*

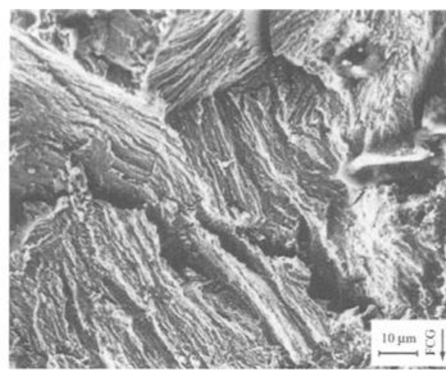

FIG. 9—*Striation-like marks in the Paris region (S55C-1, K_{max} = 50 MPam$^{1/2}$, da/dN ≈ 1 × 10^{-5} mm/cycle).*

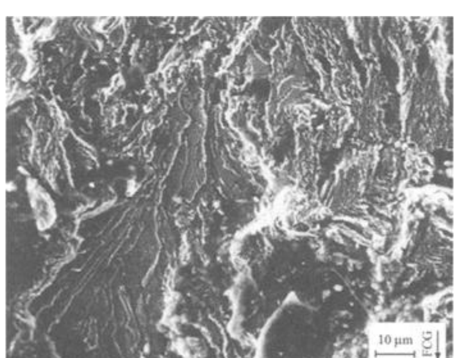

FIG. 10—*River pattern-like marks in the near threshold region (S55C-1, K_{max} = 50 MPam$^{1/2}$, da/dN ≈ 1 × 10^{-7} mm/cycle).*

As another possibility, the striation-like mark may be caused by a pearlite structure in the case of a carbon steel like S55C. Thus, we observed typical monotonically fractured surfaces by a SEM (×1000) from a CT specimen, which was monotonically fractured after fatigue testing (Figs. 11 and 12). Figure 11 shows the river pattern observed at the specimen thickness center and Fig. 12 the dimples observed near the specimen surface. The fractured surface clearly could be classified into two categories; river pattern and dimples. The area of dimples was small compared with that of the river pattern. No striation-like marks were found from the monotonically fractured surface. In addition, striation-like marks were not found from the virgin CT specimen, though the photographs are not shown here. Thus, we conclude at least that the striation-like marks found in Figs. 8 and 9 are not caused by pearlite structure but by the damage due to cyclic load.

Thus, though further validation studies may be necessary, from the examination of fractographs shown above, we conclude that the decrease in ΔK_{th} due to high K_{max} observed for S55C is due to a static fracture mode accelerating fatigue crack growth.

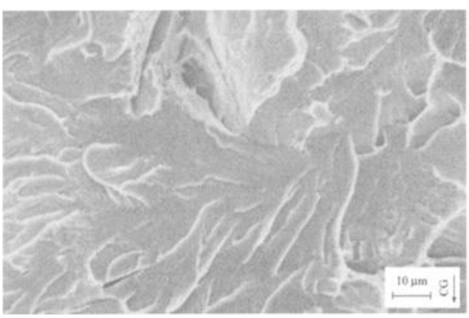

FIG. 11—*River pattern in the monotonically fractured region (S55C-2).*

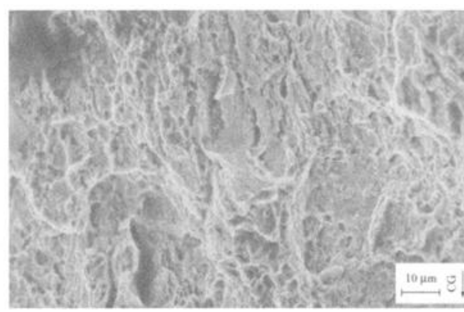

FIG. 12—*Dimples in the monotonically fractured region (S55C-2).*

Discussion

We concluded that the decrease in ΔK_{th} due to high K_{max} observed for S55C is a result of the fact that some static fracture mode accelerates fatigue crack growth. This mechanism is similar to the one that Ritchie et al. [15] pointed out in 1973. However, though the two parties use the common term "static mode fracture," the FCG rate Ritchie et al. focused on was in the range of $da/dN = 10^{-5} \sim 5 \times 10^{-3}$ mm/cycle, where the Paris law is applied. In addition, the phenomenon that Ritchie et al. considered was the increase in the power of the Paris law due to high K_{max}. On the other hand, the phenomenon we focused on was in the range of $da/dN < 10^{-6}$ mm/cycle. In fact, though the decrease in ΔK_{th} due to high K_{max} was observed for S55C, the change in FCG rate in the range of $da/dN = 10^{-6} \sim 10^{-5}$ mm/cycle was not observed. Thus, when we consider the effect of high K_{max}, we distinguish the phenomena for near threshold and for $da/dN = 10^{-5} \sim 5 \times 10^{-3}$ mm/cycle. In the following, we consider only the decrease in ΔK_{th} due to high K_{max}.

In our present study, we proposed a criterion to assess the decrease in ΔK_{th} due to high K_{max} by $(K_r, S_r)_{SSY}$ and FAC, which was originally based on compiled data of Al and Ti alloys, and which showed it is also valid for steels. On the other hand, Ritchie et al. [15] insist that the K_{max} effect on FCG rate of $da/dN = 10^{-5} \sim 5 \times 10^{-3}$ mm/cycle appears for materials of $K_{IC} < 60$

$\mathrm{MPam}^{1/2}$ and for thick test specimens. Newman et al.'s test result [6] that shows the decrease in ΔK_{th} due to high K_{max} observed for thin Al test specimens (Table 1, $B/W = 2.3/30.5$) seems to support our idea to distinguish "the effect of high K_{max} on FCG rate" by whether the da/dN is in the range of $< 10^{-5}$ mm/cycle or $10^{-5} \sim 5 \times 10^{-3}$ mm/cycle. Our criterion considers also the test specimen configuration.

We see in Fig. 2 that K_{rSSY} of 2024-T3, for example, is as high as 1.61, and thus significantly exceeds the FAC. Since the maximum K_r for the actual tests was 0.76 [6], no static fracture is expected. However, considering the report that FCG tests were conducted for $K_r > 1$ without static fracture [15], there is a possibility that FCG tests might be conducted at $(K_r, S_r)_{SSY}$ exceeding FAC without experiencing static fracture, so exceeding the FAC is necessary but not sufficient.

We concluded that the decrease in ΔK_{th} due to high K_{max} observed for S55C is a result of the fact that some static fracture mode accelerates fatigue crack growth (*cyclic mode failure*). This is based on the examination of fractographs such as Fig. 10. We considered the river pattern-like mark as evidence of static load damage (*static mode failure*). We suspect cleavage fracture as one possible *static failure mode* that occurs when a grain is strongly restrained and the local load on the grain effectively works on its cleavage plane. We consider that the damages due to both modes are transgranular and that they occur selectively from a combination of load direction, slip plane, and cleavage plane. The fact that unstable fracture did not occur for FCG tests for $K_{max} > K_{IC}$ seems to suggest that the *cyclic mode failure* preferentially appears in FCG tests, if the preference for both modes is equivalent.

From the observation of SEM fractographs and the assumptions we have made, we consider that the FCG mechanism is the same regardless of the FCG rate, based on the standpoint that microscopic cracks grow locally (such as in a single crystal) due to a *cyclic* or *static* failure mode and the macroscopic crack front growth is observed as coalescence of microscopic cracks. In this case, the microscopic crack growth in any direction will contribute to macroscopic crack growth, because the crystal is separated. Figure 13 is a simplified model showing this mechanism.

In Fig. 13, each square (hereafter called cell) corresponds to a grain. In our model, we assume that the microscopic crack growth mechanism is selectively determined as *cyclic* or *static* failure mode, due to the direction of the slip plane of the grain. Another simplification is that the microscopic crack growth direction coincides with the FCG direction. Here we specify material resistances for *cyclic* and *static* failure modes as ΔR_S and R_C, respectively. These resistance values are functions of location of the cell. Here, to describe FCG it is assumed, in the initial state whether for Paris region or ΔK_{th} region, that the macroscopic crack front is even, and nominal crack driving force (controlled in FCG tests) F and range ΔF work uniformly for each cell along the crack front line.

Paris Region

1. The microscopic cracks grow in the cells, and the macroscopic crack front becomes as shown in Fig. 13*a*.
2. Once the macroscopic crack front becomes uneven, crack tip cell load is redistributed. The cells with crack tip left behind will share more load, and thus, there appears a cell where $F_{local} > R_C$ or $\Delta F_{local} > \Delta R_S$ is satisfied. In these cells, a microscopic crack will restart. As a result, the macroscopic crack front proceeds as shown in Fig. 13*b*.

ΔK_{th} Region

- When conditions $\Delta F < \Delta R_S$ and $F_{local} < R_C$ are satisfied for all cells, the macroscopic crack growth stops (the SIF range corresponding to this ΔF is the ΔK_{th}).
- However, though $\Delta F < \Delta R_S$, there is a case in which $\Delta F_{local} > \Delta R_S$ is satisfied for some cells. If so, the microscopic cracks will grow in these cells, as shown in Fig. 13*c*.
- As a result, there appear cells where $F_{local} > R_C$ are satisfied. In these cells, microscopic crack growth occurs due to *static* failure mode. In addition, microscopic crack growth by *cyclic* failure mode continues, and due to the continuous load redistribution, microscopic crack growth continues due to *static* failure mode as shown in Fig. 13*d*.
- This microscopic crack growth continues until conditions $\Delta F_{local} < \Delta R_S$ and $F_{local} < R_C$ are satisfied for all cells. In this process, there is a chance that the microscopic crack coalescence propagates to the test specimen thickness surface, and finally, a crack growth is observed (Fig. 13*e*) on the specimen surface.
- To increase the test condition K_{max} in the K_{max}-constant tests means that there is a possibility that $F_{local} > R_C$ will increase. Thus, there is a possibility that continuous crack growth is observed, which means that ΔK_{th} decreases due to the effect of high K_{max}.

In the preceding model, R_C and ΔR_S seem intuitively related to K_{IC} and σ_{YS}(CTOD$\propto \sigma_{YS}$), due to the failure modes, respectively. In summary, in a material whose K_{max}/K_{IC} can be selected high under small scale yielding condition, local fracture due to *static* failure mode tends to happen. We consider that this tendency is the cause of the decrease in ΔK_{th} due to high K_{max}.

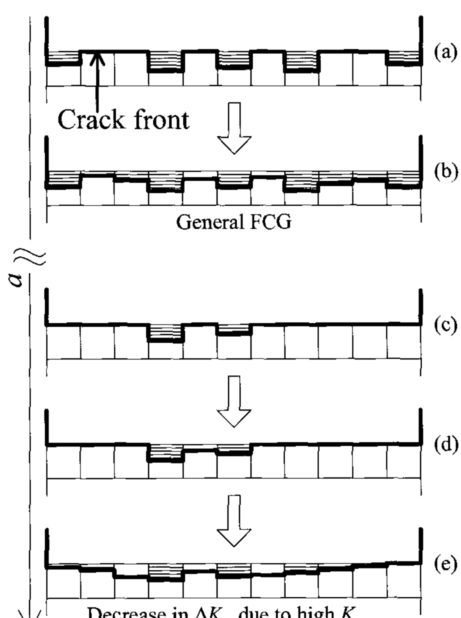

FIG. 13—*Simplified FCG model.*

In addition, striation spacing of approximately 2 × 10^{-4} mm was observed in the near threshold region (Fig. 14; da/dN = 1.8 × 10^{-7} mm/cycle). Our observation does not contradict with Davidson et al. [16], who insist that, if a striation is observed, the minimum striation spacing is in the range of 1~4 × 10^{-4} mm regardless of material. If a striation mark is produced also in the near threshold region in accordance with the Laird's model [17], the large striation spacing of 2 × 10^{-4} mm might be considered as being produced in one cycle due to a high local stress, as explained in the model of Fig. 13. Another possibility is that minimum striation spacing due to the intrinsic fatigue mechanism exists, as Davidson et al. [16] point out. If so, striation spacing might be a mark which appears with multiple load cycles. Our model in Fig. 13 can handle both possibilities if we treat the damage due to *cyclic* mode failure appropriately. In addition, the main theme of our study, that is, the decrease in ΔK_{th} due to high K_{max}, is well explained whether a striation mark is produced in one cycle or more.

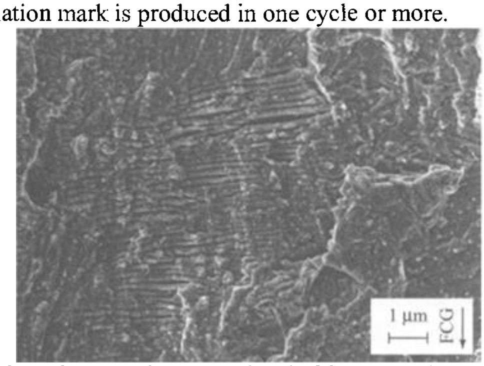

FIG. 14—*Fractured surface in the near threshold region (S55C-2, K_{max} = 50 MPam$^{1/2}$, $da/dN \approx 1.8 \times 10^{-7}$ mm/cycle).*

Conclusion

In this paper, we first compiled the existing data for Al and Ti that showed the decrease in ΔK_{th} due to high K_{max} under closure-free conditions and proposed an assessment criterion to predict the phenomena. Then we applied our assessment criterion to carbon steels (JIS S55C, HT60, and SS400) and type 304 stainless steel and showed its validity by constant-K_{max} FCG tests. Finally, by examining the S55C's fractography from the scanning electron microscope, which showed the decrease in ΔK_{th} due to high K_{max}, we considered possible mechanistic explanations.

Acknowledgments

The authors thank Prof. R. O. Ritchie, Drs. B. L. Boyce, G. H. Bray, and J. K. Donald's cooperation for compiling their detailed data in Table 1. The authors also thank Dr. Kitsunai for discussion on Fig. 14.

References

[1] Paris, P. C. and Erdogan, F., "A Critical Analysis of Crack Propagation Laws," *Transactions of ASME, Ser. D*, Vol. 85, 1963, pp. 528–534.

[2] Boyce, B. L. and Ritchie, R. O., "Effect of Load Ratio and Maximum Stress Intensity on the Fatigue Threshold in Ti-6Al-4V," *Engineering Fracture Mechanics*, Vol. 68, No. 2, 2001, pp. 129–147.

[3] Schmidt, R. A. and Paris, P. C., "Thresholds for Fatigue Crack Propagation and the Effects of Load Ratio and Frequency," *Progress in Flaw Growth and Fracture Toughness Testing, ASTM STP 536*, ASTM International, West Conshohocken, PA, 1973, pp. 79–94.

[4] Marci, G., "Failure Mode Below 390 K with IMI 834," *Fatigue '96. Proceedings of the Sixth International Fatigue Conference, Vol. 1*, G. Lütjering and H. Newack, Eds., Pergamon, Oxford, 1996, pp. 493–498.

[5] Lang, M., Hartman, G. A., and Larsen, J. M., "Investigation of an Abnormality in Fatigue Crack Growth Curves-the Marci Effect," *Scripta Materialia*, Vol. 38, No. 12, 1998, pp. 1803–1810.

[6] Newman, J. A., Riddell, W. T., and Piascik, R. S., "Effects of K_{max} on Fatigue Crack Growth Thresholds in Aluminum Alloys," *Fatigue Crack Growth Thresholds, Endurance Limits, and Design, ASTM STP 1372*, J. A. Newman, W. T. Riddell, and R. S. Piascik, Eds., ASTM International, West Conshohocken, PA, 2000, pp. 63–77.

[7] JSME, JSME S NA1-2000, Codes for Nuclear Power Generation facilities – Rules on Fitness-for-Service for Nuclear Power Plants, Japan Society of Mechanical Engineers, Tokyo, 2000.

[8] Bray, G. H. and Donald, J. K., "Separating the Influence of K_{max} from Closure-Related Stress Ratio Effects Using the Adjusted Compliance Ratio Technique," *Advances in Fatigue Crack Closure Measurements and Analysis: Second Volume, ASTM STP 1343*, ASTM International, West Conshohocken, PA, 1999, pp. 57–78.

[9] ASTM Standard E 647-95a, "Standard Test Method for Measurement of Fatigue Crack Growth Rates," *Annual Books of ASTM Standards*, Section 3, Vol. 03.01, ASTM International, West Conshohocken, PA.

[10] British Energy, *Assessment of the Integrity of Structures Containing Defects, R6-Revision 4*, British Energy, 2001.

[11] Miller, A. G., "Review of Limit Loads of Structures Containing Defects," *International Journal of Pressure Vessels and Piping*, Vol. 32, Nos. 1–4, 1988, pp. 197–327.

[12] Döker, H., "Fatigue Crack Growth Threshold: Implications, Determination and Data Evaluation," *International Journal of Fatigue*, Vol. 19, No. 93, 1997, pp. S145–S149.

[13] Clark, T. R., Herman, W. A., Hertzberg, R. W., and Jaccard, R., "The Influence of the K Gradient and K_{cmax} Level on Fatigue Response During the K_{cmax} Threshold Testing of Van 80 Steel and Astroloy," *International Journal of Fatigue*, Vol. 19, No. 2, 1997, pp. 177–182.

[14] Barsom, J. M. and Rolfe, S. T., "The Correlations Between K_{IC} and Charpy V-Notch Test Results in the Transition-Temperature Range" *Impact Testing of Metals, ASTM STP 466*, ASTM International, West Conshohocken, PA, 1970, pp. 281–302.

[15] Ritchie, R. O. and Knott, J. F., "Mechanisms of Fatigue Crack Growth in Low Alloy Steels," *Acta Metallurgica*, Vol. 21, No. 5, 1973, pp. 639–648.

[16] Davidson, D. L. and Lankford, J., "Fatigue Crack Growth in Metals and Alloys: Mechanisms and Micromechanics," *International Materials Reviews*, Vol. 37, No. 2, 1992, pp. 45–76.

[17] Laird, C., "The Influence of Metallurgical Structure on the Mechanisms of Fatigue Crack Propagation," *Fatigue Crack Propagation, ASTM STP 415*, ASTM International, West Conshohocken, PA, 1967, pp. 131–168.

Journal of ASTM International, March 2005, Vol. 2, No. 3
Paper ID JAI12044
Available online at www.astm.org

E. U. Lee[1] *and A. K. Vasudevan*[2]

Environmentally Influenced Fatigue in High Strength Steels

ABSTRACT: A study was conducted to identify the environmental influence on fatigue crack growth behavior of three high strength steels: AerMet 100, 300M, and 4340. These steels were subjected to fatigue tests under constant amplitude loading of frequency 10 Hz and stress ratios R = 0.1 and 0.9, in vacuum, air, and 3.5 % NaCl solution. The fatigue crack growth was characterized with two driving force parameters, stress intensity range, ΔK, and maximum stress intensity, K_{max}. Especially, the variation of fatigue crack growth per time, da/dt, with K_{max} in 3.5 % NaCl solution was evaluated with respect to R, environment, and threshold stress intensity for environmentally assisted cracking (EAC), K_{IEAC}. In addition, the environmental influence on fatigue crack growth was examined with the fractographic features and trajectory path, drawn with the limiting values of ΔK and K_{max}, ΔK^* and K_{max}^*.

KEYWORDS: fatigue, environment, constant amplitude loading, frequency, stress ratio, environmentally assisted cracking (EAC), fractographic features, trajectory path

Introduction

Fatigue crack growth in a metallic material arises from a combination of stress, environment, and microstructure of the material. There have been a number of empirical models proposed for fatigue crack growth life prediction However, the reliable one is still lacking, because the load-load interaction and the role of environment have not been fully understood and quantified. To resolve such uncertainties, Vasudevan and Sadananda [1–9] have developed a Unified Approach. According to this approach, ΔK and K_{max} are two intrinsic parameters, and their thresholds must be exceeded for a fatigue crack to grow. Environmental interactions, being time and stress-dependent processes, affect fatigue crack growth through K_{max} parameter. For each fatigue crack growth rate, two limiting values of ΔK and K_{max}, ΔK^* and K_{max}^*, are necessary to enforce the growth rate. Their magnitudes depend on the material resistance to fatigue crack growth. A fatigue crack growth trajectory path is defined by plotting ΔK^* against K_{max}^* as a function of da/dN [7–9]. For a pure fatigue crack growth, the trajectory path falls on the reference line of $\Delta K^* = K_{max}^*$. Deviation from this line occurs when monotonic fracture mode and environmental effect are superimposed on fatigue. In this study, the Unified Approach is employed for the analysis of the fatigue crack growth behaviors of three high strength steels, AerMet 100, 300M, and 4340, in three environments, vacuum, air, and 3.5 % NaCl solution.

Manuscript received 30 October 2003; accepted for publication 26 April 2004; published March 2005. Presented at ASTM Symposium on Fatigue and Fracture Mechanics: 34th Volume on 19–21 November 2003 in Tampa, FL; S.R. Daniewicz, J.C. Newman, Jr., and K-H. Schwalbe, Guest Editors.
[1] Materials Engineer, Naval Air Warfare Center Aircraft Division, Aerospace Materials Division, Code 4.3.4.2, Patuxent River, MD 20670.
[2] Scientific Officer, Office of Naval Research, Arlington, VA 22217.

Experimental Procedure

Material and Specimen

Heat-treated slabs of AerMet 100, 300M, and 4340 steels were used as the specimen materials. The microstructures are tempered martensite with prior austenite grain diameters of 6 μm for the AerMet 100 steel, 20 μm for the 300M steel, and 14 μm for the 4340 steel. The mechanical properties are shown in Table 1. From the slabs, compact tension, C(T), specimens, 4.8 mm thick and 38 mm wide, were prepared in the L-T orientation. Prior to the fatigue and EAC tests, the specimen was pre-cracked under constant amplitude loading of frequency 10 Hz at test stress ratio, R = 0.1 or 0.9, in the test environment.

TABLE 1—*Mechanical properties of AerMet 100, 300M, and 4340 steels.*

Property	AerMet	300M	4340
YS (MPa)	1,724	1,703	1,669
UTS (MPa)	1,979	2,000	1,944
K_{IC} (MPa$\sqrt{m}$)	126	57	53

Fatigue Test

Two closed-loop servo-hydraulic mechanical test machines were used. One was a 490 KN vertical MTS machine for the fatigue test in vacuum and air, and the other was a 45 KN horizontal test machine for the fatigue test in liquid. The fatigue test was conducted under constant amplitude loading of frequency 10 Hz and R = 0.1 and 0.9 at ambient temperature. The test environments were vacuum of 2×10^{-8} torr, air of 50 % relative humidity, and 3.5 % NaCl solution of pH 7.3. The crack length was monitored with a computer system, employing compliance technique. The fatigue loading procedure was K-decreasing with K-gradient parameter $C = -0.08\ mm^{-1}$ in the near-threshold crack growth regime and K-increasing with $C = 0.08\ mm^{-1}$ in the other regimes.

Environmentally Assisted Cracking Test

Before the test, a C(T) specimen was pre-cracked in 3.5 % NaCl solution of pH 7.3, and a wedge was inserted into the specimen notch to make a deflection, measured with a clip-on displacement gage. Then, the lower portion of the specimen, including the crack tip, was put under the 3.5 % NaCl solution of pH 7.3 in a container throughout the test. During the test, the upper portion of the specimen, including most of the notch, was in air above the 3.5 % NaCl solution. The crack length was measured with a binocular microscope, less frequently as the crack grew. The test was continued with crack length increasing and stress intensity decreasing, and the K_{IEAC} was defined as the stress intensity, K_I, at crack arrest. K_I was calculated from the following relations [10,11].

$$K_I = (P/B\sqrt{W})[(2+\alpha)/(1-\alpha)^{3/2}](0.886 + 4.64\alpha - 13.32\alpha^2 + 14.72\alpha^3 - 5.6\alpha^4) \quad (1)$$

$$P = BEV_o/F(\alpha) \quad (2)$$

$$F(\alpha) = [1 + (0.25/\alpha)][(1+\alpha)/(1-\alpha)]^2[1.61369 + 12.6778\alpha - 14.2311\alpha^2 - 16.6102\alpha^3 + 35.0499\alpha^4 - 14.4943\alpha^5] \quad (3)$$

where P is the load, B the specimen thickness, W the specimen width, α = a/W, a the crack length, E the modulus of elasticity, and V_o the displacement at front face of specimen. The data were reduced to crack length, a, versus time, t, and crack growth rate, da/dt, versus K_I plots.

Fractography

After the fatigue and EAC tests, the crack surface morphology was examined at several spots, corresponding to various crack growth rates, with a scanning electron microscope, JEOL JSM-5800LV, operating at an accelerating voltage of 20 kV.

Results

Variation of Fatigue Crack Growth Rate, da/dN, with Stress Intensity Range, ΔK

Raising R from 0.1 to 0.9 moves the da/dN versus ΔK curve to the left, increasing the da/dN in the near-threshold crack growth and Paris regimes (Regimes A and B), and reducing the threshold stress intensity range for fatigue crack growth, ΔK_{th} (Fig. 1). For the test in 3.5 % NaCl solution, the da/dN versus ΔK curve levels off in the Regime B for a given ΔK region at R = 0.9. Figure 2 shows the environmental effect on da/dN variation with ΔK.

(1) AerMet 100 Steel—At R = 0.1, in Regime A, da/dN is greater in air than in 3.5 % NaCl solution and vacuum, and it is similar in 3.5 % NaCl solution and vacuum. In Regime B, da/dN is still greater in air, intermediate in 3.5 % NaCl solution, and least in vacuum. In the high da/dN and ΔK regime (Regime C), da/dN is similar in air and 3.5 % NaCl solution, but it is less in vacuum. At R = 0.9, in Regime A, da/dN is greatest in 3.5 % NaCl solution, intermediate in air, and smallest in vacuum. In Regime B, the da/dN curve levels off in 3.5 % NaCl solution and crosses over the da/dN curve in air, and da/dN is lower in vacuum. In Regime C, the three da/dN versus ΔK curves tend to converge.

(2) 300M Steel—At R = 0.1, in Regime A, da/dN is slightly greater in 3.5 % NaCl solution than in air. However, it is similar in Regimes B and C in air and 3.5 % NaCl solution. da/dN is lowest in vacuum in Regimes A and B. The three da/dN versus ΔK curves merge in Regime C. At R = 0.9, da/dN is greatest in 3.5 % NaCl solution, intermediate in air, and least in vacuum in Regimes A and B. The da/dN versus ΔK curve levels off in 3.5 % NaCl solution, and they merge in Regime C in air and vacuum.

(3) 4340 Steel—The main features of da/dN variation with ΔK are similar to those for 300M steel in the respective environments.

Figure 3 compares the resistances of the three steels to fatigue crack growth, indicated by da/dN, in the three environments.

(1) Vacuum—At R = 0.1, in Regime A, da/dN is greatest for 300M steel, intermediate for AerMet 100 steel, and least for 4340 steel. In Regime B, da/dN is similar for 300M and AerMet 100 steel and lowest for 4340 steel, and in Regime C, the three curves tend to merge. At R = 0.9, in Regime A, the three da/dN versus ΔK curves overlap each other. In Regimes B and C, da/dN is similar for 300M and 4340 steels, whereas that of the AerMet 100 steel is least.

(2) Air—At R = 0.1, in Regime A, da/dN is greatest for 4340 steel, intermediate for 300M steel, and least for AerMet 100 steel. However, in Regimes B and C, the three da/dN versus ΔK

curves overlap each other, indicating similar da/dN. At R = 0.9, in Regime A, the three da/dN versus ΔK curves nearly overlap each other. In Regimes B and C, the da/dN versus ΔK curves of the 300M and 4340 steels nearly overlap each other, and da/dN is lowest for AerMet 100 steel.

(3) 3.5 % NaCl Solution—Throughout the three regimes, da/dN is greatest for 4340 steel, intermediate for 300M steel, and least for AerMet 100 steel, except the da/dN for the 300M steel is close to those for the 4340 and AerMet 100 steels. At R = 0.9, the three da/dN versus ΔK curves level off, and the level is highest for the 4340 steel, intermediate for the 300M steel, and lowest for the AerMet 100 steel. This observation evidences that the resistance to corrosion fatigue crack growth is greatest for the AerMet 100 steel, intermediate for the 300M steel, and least for the 4340 steel in 3.5 % NaCl solution.

Variation of Fatigue Crack Growth/Time, da/dt, with Maximum Stress Intensity, K_{max}

The fatigue crack growth per cycle, da/dN, was converted to the corresponding crack growth per time, da/dt, for the test in 3.5 % NaCl solution, following the relationship of da/dt = f (da/dN), where f is the loading frequency. The da/dt is plotted against K_{max} in Fig. 4. Also, the environmentally assisted crack growth rate, da/dt, in 3.5 % NaCl solution is plotted against the applied stress intensity factor, K_I, in this figure. (The EAC plots of 300M and 4340 steels were determined in this study, and that of AerMet 100 steel is Oehlert's [12].) The upper portion or whole of the da/dt versus K_{max} curve is in the region of K_{max} > K_{IEAC} for both of the stress ratios 0.1 and 0.9.

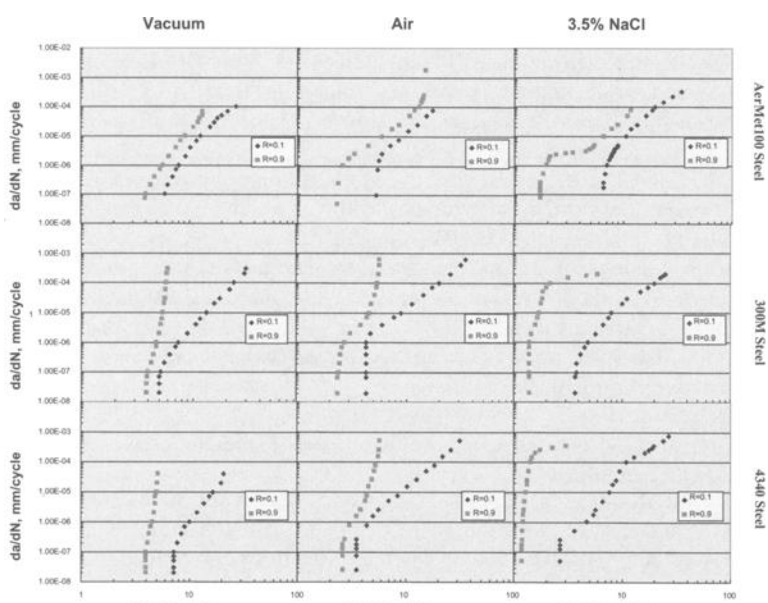

FIG. 1—*Curves of da/dN versus ΔK, showing stress ratio effect.*

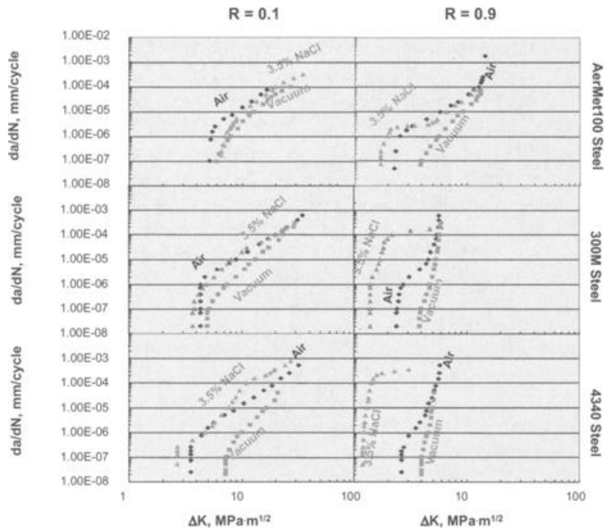

FIG. 2—*Curves of da/dN versus ΔK, showing environmental effects.*

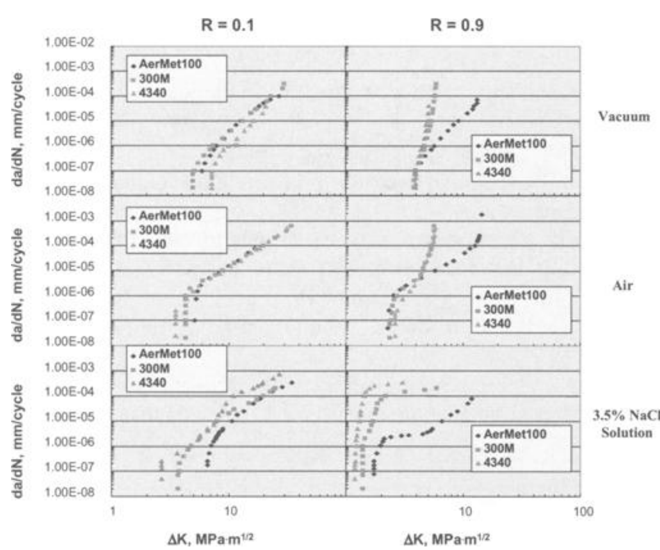

FIG. 3—*Curves of da/dN versus ΔK, showing relative fatigue resistance.*

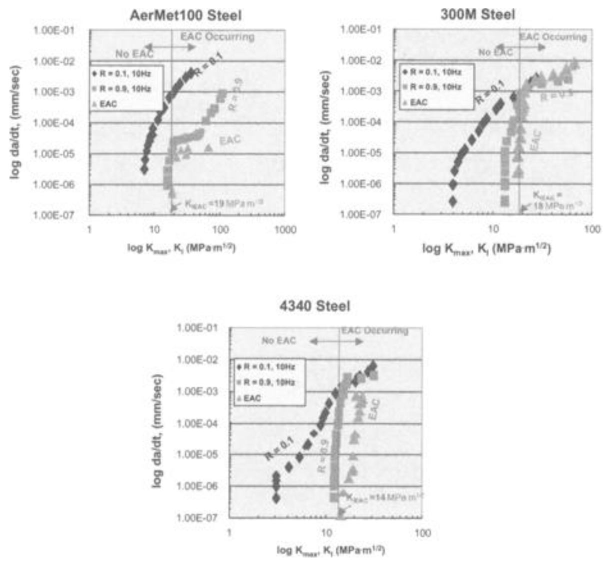

FIG. 4—*Variation of da/dt with K_{max} or K_I.*

Trajectory Path of Fatigue Crack Growth

To find the trajectory path [7–9], the limiting value of ΔK at R = 0.9, $(\Delta K)_{R = 0.9} \cong \Delta K^*$, is plotted against that of K_{max} at R = 0.1, $(K_{max})_{R = 0.1} \cong K_{max}^*$, in Fig. 5.

(1) AerMet 100 Steel—The trajectory paths for the fatigue in vacuum and air deviate slightly from the pure fatigue line of $\Delta K^* = K_{max}^*$ and they nearly overlap each other. That for the fatigue in 3.5 % NaCl solution moves toward the pure fatigue line from a separated starting point of the lowest ΔK* and K_{max}^*, indicative of Type I [6], and eventually converges to those for the fatigue in vacuum and air.

(2) 300M Steel—The trajectory paths for the fatigue in vacuum and air deviate from the pure fatigue line considerably, and become nearly parallel to the K_{max}^*-axis, overlapping each other and indicating a type between Types III and IV [7]. The one for the fatigue in 3.5 % NaCl solution is initially Type IV [7] at low ΔK*, and then moves upward almost parallel to the pure fatigue line, Type II [7].

(3) 4340 Steel—The features of trajectory paths are similar to those for the 300M steel, except the paths deviating slightly more toward the K_{max}^*-axis than those for the 300M steel.

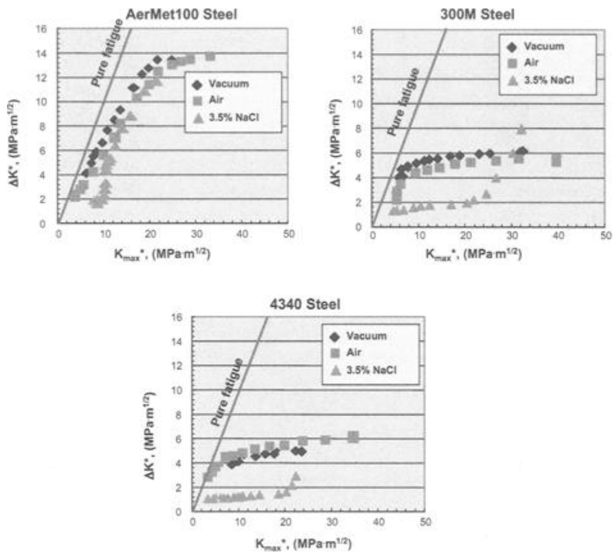

FIG. 5—*Trajectory path.*

Fractographic Features

(1) AerMet 100 Steel—In vacuum and air, cleavage-like facets are visible at lower da/dN, and larger cleavage-like facets and some dimples at higher da/dN for R = 0.1, Fig. 6. Faint striations are seen in the cleavage-like facets, and the number and size of the dimple increase with greater da/dN for R = 0.9. In 3.5 % NaCl solution, cleavage-like facets with striations and some dimples are seen for $K_{max} < K_{ISCC}$ at R = 0.1. However, mixed cleavage-like and intergranular facets are visible at low da/dN (or da/dt) and mostly dimples at high da/dN for R = 0.9. At the initial stage of EAC, mixture of intergranular and cleavage-like facets are noticeable, and at the later stage of EAC, intergranular facets and dimples.

(2) 300M Steel—In vacuum and air, cleavage-like facets are visible at lower da/dN and dimples at higher da/dN for R = 0.1 and 0.9. At lower da/dN, the cleavage-like facets are larger for R = 0.9 than those for R = 0.1. In 3.5 % NaCl solution, at R = 0.1, cleavage-like facets and some dimples are visible at lower da/dN and $K_{max} < K_{ISCC}$, but larger cleavage-like facets, striations, secondary cracks, and intergranular facets at higher da/dN and $K_{max} > K_{ISCC}$. At R = 0.9, mixed cleavage-like and intergranular facets are visible at lower da/dN and $K_{max} < K_{IEAC}$, and mostly intergranular facets and secondary cracks at higher da/dN and $K_{max} > K_{IEAC}$. The crack surface of EAC-tested specimen shows intergranular facet and secondary cracks.

(3) 4340 Steel—In vacuum and air, the fractographic features are similar to those of 300M steel. In 3.5 % NaCl solution, at R = 0.1, mostly intergranular facets and patches of dimples are seen at low and high da/dN and K_{max} below and above K_{IEAC}, Fig. 7. More dimples are visible at greater da/dN. At R = 0.9, intergranular facets and secondary cracks are mostly seen at low and high da/dN. The crack surface of EAC-tested specimen shows intergranular facets and secondary cracks.

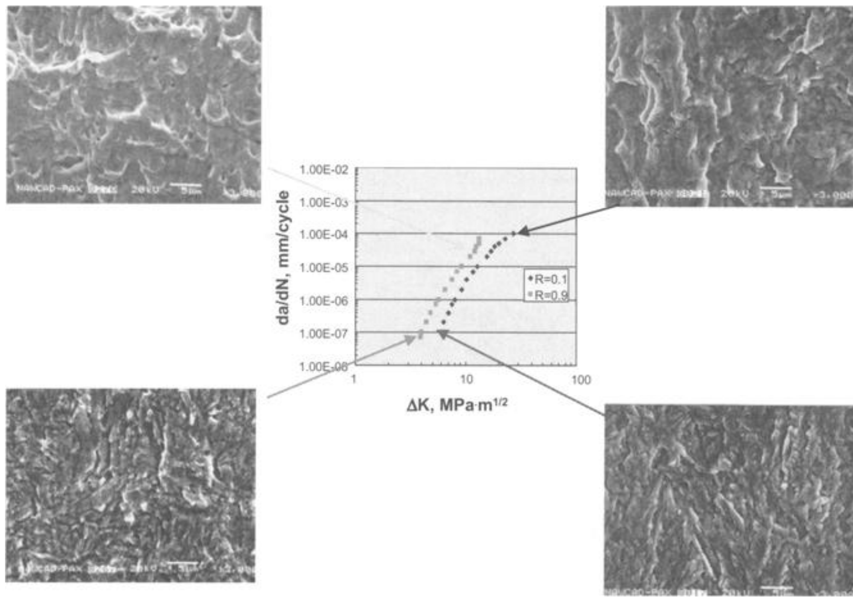

FIG. 6—*SEM fractographs of AerMet 100 steel, fatigue tested at R = 0.1 and 0.9 in vacuum.*

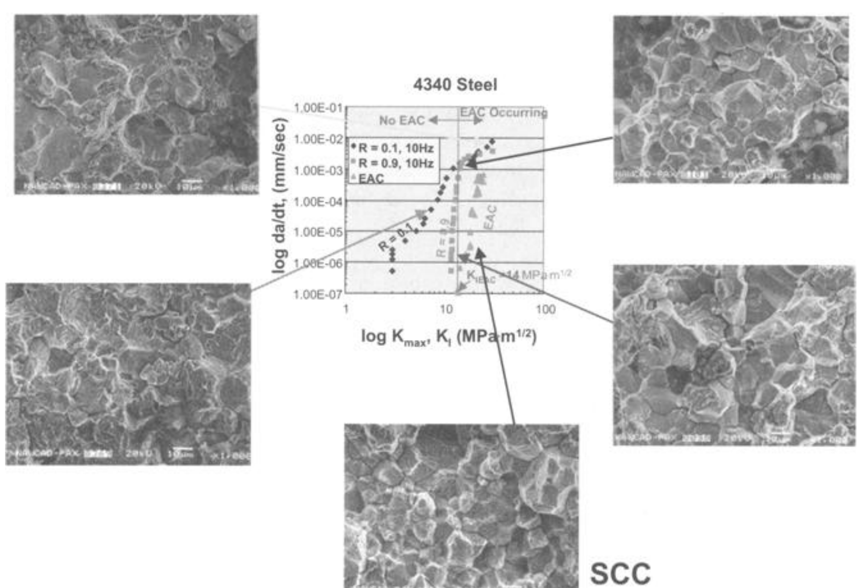

FIG. 7—*SEM fractographs of 4340 Steel, fatigue tested at R = 0.1 and 0.9 in 3.5 % NaCl solution.*

Discussion

Stress Ratio Effect

It was observed that da/dN increased and ΔK_{th} decreased with increasing stress ratio from 0.1 to 0.9 in the three environments for the three steels, Fig. 1. This observation is similar to those reported for various steels and alloys by a number of investigators [13–27].

Environmental Effect

Compared to air, 3.5 % NaCl solution enhanced the fatigue crack growth in AerMet 100 steel at R = 0.9 but retarded it at R = 0.1 in the near-threshold crack growth regime, Fig. 2. Similar observations were reported for 2 ¼ Cr-1 Mo, rotor, and 4340 steels, and attributed to oxide-induced crack closure [16,17,19,28,29]. But such a crack growth retardation by 3.5 % NaCl solution was not observed for 300M and 4340 steels at R = 0.1.

As Fig. 4 shows, the lower portion of the da/dt versus K_{max} curve for the fatigue test at R = 0.1 in 3.5 % NaCl solution is in the region of $K_{max} < K_{IEAC}$, and no EAC is expected to occur under cyclic loading in this region. Yet 3.5 % NaCl solution can still influence the fatigue crack growth process and induce the true or environmental corrosion fatigue [6]. On the other hand, in the region of $K_{max} > K_{IEAC}$, the environmentally assisted crack growth is superimposed over the fatigue crack growth, resulting in environmentally assisted fatigue [6]. Such an EAC contribution to fatigue crack growth has also been discussed by other investigators [30–33]. Wei and Landes [30] considered the fatigue crack growth in high-strength steels in an aggressive environment to be composed of two components, mechanical and environmental. They proposed that the da/dN in an aggressive environment, $(da/dN)_c$, could be expressed in terms of the da/dN in an inert reference environment, $(da/dN)_r$, and an environment component computed from sustained-load crack growth data. Gerberich, Birat, and Zackay [31] proposed that the da/dN in a corrosive environment consisted of a fatigue contribution, $(da/dN)_f$, and an EAC contribution, $(da/dN)_{EAC}$. Wei [32] re-defined his previous model [30] as the da/dN in an aggressive environment, $(da/dN)_e$, composed of three components, $(da/dN)_r$ for pure fatigue in inert or reference environment, $(da/dN)_{cf}$ for environmental contribution due to the synergistic interaction of fatigue and environmental attack, and $(da/dN)_{EAC}$ for EAC at $K > K_{IEAC}$. Pao, Wei, and Wei [33] studied the fatigue crack growth behavior of 4340 steel in water vapor, and pointed out the environmental contribution arising from EAC for $K_{max} > K_{IEAC}$ and from synergistic action of fatigue and environmental attack for $K_{max} < K_{IEAC}$.

Grain Size Effect

It has been known that in the near-threshold regime of fatigue crack growth, an increase in the grain size generally results in a marked reduction in da/dN and an increase in ΔK_{th} [34]. However, such a grain size effect on fatigue crack growth is not noticeable in this study, especially in 3.5 % NaCl solution. As Fig. 3 shows, the AerMet 100 steel has the lowest da/dN and the greatest ΔK_{th} in 3.5 % NaCl solution, though it has the smallest grain diameter (6 μm) of prior austenite, compared to those (20 and 14 μm) of 300M and 4340 steels. Apparently, the highest inherent resistance of AerMet 100 steel to corrosion fatigue crack growth overwhelms the unfavorable grain size effect.

Trajectory Path

When a crack is grown by cyclic strain alone, the trajectory path follows the pure fatigue line of $\Delta K^* = K_{max}^*$ [7–9]. However, the trajectory path is deviated by superimposing K_{max}-dependent monotonic fracture mode and/or environmental effect on fatigue. The monotonic fracture is indicated by fractographic features of crystallographic facet and/or dimple. The environmental effect is evidenced predominantly by intergranular facets.

Considering the fractographic features, cleavage-like facets and dimples observed at lower da/dN of the AerMet 100 and 300M steels and fatigue-tested in the three environments, the trajectory path deviation is partly attributable to the cleavage-like facet and dimple modes of crack growth. In 4340 steel, the cleavage-like facet and dimple are observable only for the fatigue tests in vacuum and air at lower da/dN.

The trajectory path deviation is least for the AerMet 100 steel, much greater for the 300M steel, and greatest for the 4340 steel in the three environments, Fig. 5. In 3.5 % NaCl solution, the deviation is drastic for the 4340 steel and somewhat less for the 300M steel, compared to the AerMet 100 steel. This appears to be associated with the K_{IEAC} value, least for the 4340 steel, intermediate for the 300M steel, and greatest for the AerMet 100 steel; and the susceptibility to intergranualr cracking, greatest for the 4340 steel, intermediate for the 300M steel, and least for the AerMet 100 steel.

Fractographic Features

In vacuum and air, at $R = 1$, the fractographic features are similar for the three steels, finer cleavage-like facets at lower da/dN, and larger cleavage-like facets and some dimples at higher da/dN. At $R = 0.9$, the number and size of dimple increase with increasing da/dN. This observation evidences that in vacuum and air:

- The cleavage-like facet becomes larger with increasing da/dN and R.
- The number and size of dimple increase with increasing da/dN and R.
- The larger cleavage-like facet is replaced by dimples at higher da/dN and R.

In 3.5 % NaCl solution, at $R = 0.1$, cleavage-like facets and some finer dimples are seen at lower da/dN (or da/dt) and larger cleavage-like facets at higher da/dN for the AerMet 100 steel. However, at $R = 0.9$, mixed cleavage-like and intergranular facets are visible at lower da/dN and mostly dimples at higher da/dN. At $R = 0.1$, cleavage-like facets are mostly visible with some scattered dimples at lower da/dN, and mixture of cleavage-like and intergranular facets at higher da/dN for the 300M steel. At $R = 0.9$, a mixture of cleavage-like and intergranular facets is visible at lower da/dN, and mostly intergranular facets at higher da/dN for the steel. On the other hand, mostly intergranluar facets are present at low and high da/dN and $R = 0.1$ and 0.9 for the 4340 steel. This observation evidences that in 3.5 % NaCl solution:

- Cleavage-like facets and dimples are still seen at lower R and da/dN in more corrosion fatigue resistant steel, such as AerMet 100 steel. However, these fractographic features are replaced by mixed cleavage-like and intergranular facets at higher R and lower da/dN, and they are replaced mostly by dimples at higher da/dN.
- In lower corrosion fatigue resistant steels, such as 300M and 4340 steels, more intergranular facets cover the crack surface at low and high da/dN and R.

At the initial stage of EAC, mixture of intergranular and cleavage facets are seen, and at the later stage of EAC, intergranular facets and dimples for the AerMet 100 steel are seen. On the other hand, the crack surface of EAC-tested specimen shows intergranular facets and secondary cracks for 300M and 4340 steels. These observations suggest that the susceptibility to intergranular cracking or grain boundary de-cohesion is greatest for 4340 steel, somewhat less for 300M steel, and least for AerMet 100 steel during fatigue and EAC in 3.5 % NaCl solution. Considering the relative values of K_{IEAC} of the three steels, the least for 4340 steel, the intermediate for 300M steel, and the greatest for AerMet 100 steel, the greater susceptibility to intergranular cracking corresponds to smaller K_{IEAC} or smaller EAC resistance.

Conclusions

- da/dN increases and ΔK_{th} decreases with increasing R in vacuum, air, and 3.5 % NaCl solution.
- Crack growth is retarded at R=0.1 in the near-threshold regime for AerMet 100 steel in 3.5 % NaCl solution. This is attributable to corrosion product induced crack closure.
- The main fractographic features of fatigue in vacuum and air are cleavage-like facets and some dimples at lower da/dN and R. The cleavage-like facets are enlarged and replaced by an increasing number of dimples with increasing da/dN and R.
- The main fractographic features of fatigue in 3.5 % NaCl solution are mixed cleavage-like and intergranular facets at lower da/dN and R for AerMet 100 steel. On the other hand, intergranular facets and secondary cracks are predominant features for the fatigue of 300M and 4340 steels in 3.5 % NaCl solution. These fractographic features of fatigue are similar to those of EAC in 3.5 % NaCl solution.
- The resistance to fatigue and intergranular cracking in 3.5 % NaCl solution is greatest for AerMet 100 steel, intermediate for 300M steel, and least for 4340 steel.
- Trajectory path deviates due to superimposition of cleavage-like and dimple fracture and EAC on fatigue in 3.5 % NaCl solution.

References

[1] Vasudevan, A. K., Sadananda, K., and Louat, N., "A Review of Crack Closure, Fatigue Crack Threshold and Related Phenomena," *Materials Science and Engineering*, Vol. A188, 1994, pp. 1–22.

[2] Vasudevan, A. K. and Sadananda, K., "Classification of Fatigue Crack Growth Behavior," *Metall Trans A*, Vol. 26A, 1995, pp. 1221–1234.

[3] Sadananda, K. and Vasudevan, A. K., "Short Crack Growth and Internal Stresses," *International Journal of Fatigue*, Vol. 19, 1997, pp. S99–S108.

[4] Sadananda, K. and Vasudevan, A. K., "Short Crack Growth Behavior," *ASTM STP 1296, Fatigue and Fracture Mechanics*, R. S. Piascik, J. C. Newman, and N. E. Dowling, Eds., ASTM International, West Conshohocken, PA, 1997, pp. 301–316.

[5] Sadananda, K., Vasudevan, A. K., Holtz, R. L., and Lee, E. U., "Analysis of Overload Effects and Related Phenomena," *International Journal of Fatigue*, Vol. 21, 1999, pp. S233–S246.

[6] Vasudevan, A. K., Sadananda, K., and Glinka, G., "Critical Parameters for Fatigue Damage," *International Journal of Fatigue*, Vol. 23, 2001, pp. S39–S53.

[7] Sadananda, K., Vasudevan, A. K., and Holtz, R. L., "Extension of the Unified Approach to Fatigue Crack Growth to Environmental Interactions," *International Journal of Fatigue*, Vol. 23, 2001, pp. S277–S286.
[8] Sadananda, K. and Vaudevan, A. K., "Fatigue Crack Growth Mechanisms in Steels," Submitted for Publication in *International Journal of Fatigue*.
[9] Sadananda, K., Vasudevan, A. K., and Kang, I. W., "Effect of Superimposed Monotonic Fracture Modes on the ΔK and K_{max} Parameters of Fatigue Crack Propagation," *Acta Materialia*, Vol. 51, 2003, pp. 3399–3414.
[10] Saxena, Ashok, and Hudak, S. J., Jr., "Review and Extension of Compliance Information for Common Crack Growth Specimens," *International Journal of Fracture*, Vol. 14, 1978, pp. 453–468.
[11] ASTM Standard E 399-90, "Standard Test Method for Plane-Strain Fracture Toughness of Metallic Materials," *Annual Book of ASTM Standards*, Vol. 03.01, 2003, pp. 451–482.
[12] Oehlert, A. and Atrens, A., "Stress Corrosion Crack Propagation in AerMet 100," *Journal of Materials Science*, Vol. 33, 1998, pp. 775–781.
[13] Schmidt, R. A. and Paris, P. C., "Threshold for Fatigue Crack Propagation and the Effects of Load Ratio and Frequency," *Progress in Flaw Growth and Fracture Toughness Testing, ASTM STP 536*, ASTM International, West Conshohocken, PA, 1973, pp. 79–94.
[14] Kirby, B. R. and Beevers, C. J., "Slow Fatigue Crack Growth and Threshold Behaviour in Air and Vacuum of Commercial Aluminum Alloys," *Fatigue of Engineering Materials and Structures*, Vol. 1, 1979, pp. 203–215.
[15] Ritchie, R. O., "Near-Threshold Fatigue-Crack Propagation in Steels," *International Metals Reviews*, Nos. 5 and 6, 1979, pp. 205–230.
[16] Stewart, A. T., "The Influence of Environment and Stress Ratio on Fatigue Crack Growth at Near Threshold Stress Intensities in Low-Alloy Steels," *Engineering Fracture Mechanics*, Vol. 13, 1980, pp. 463–478.
[17] Ritchie, R. O., Suresh, S., and Moss, C. M., "Near-Threshold Fatigue Crack Growth in 2¼ Cr-1 Mo Pressure Vessel Steel in Air and Hydrogen," *Journal of Engineering Materials and Technology*, Vol. 102, 1980, pp. 293–299.
[18] Nakai, Y., Tanaka, K., and Nakanishi, T., "The Effects of Stress Ratio and Grain Size on Near-Threshold Fatigue Crack Propagation in Low-Carbon Steel," *Engineering Fracture Mechanics*, Vol. 15, 1981, pp. 291–302.
[19] Suresh, S., Zamiski, G. F., and Ritchie, R. O., "Oxide-Induced Crack Closure: An Explanation for Near-Threshold Corrosion Fatigue Crack Growth Behavior," *Metall Trans A*, Vol. 12A, 1981, pp. 435–1443.
[20] Lafarie-Frenot, M. C. and Gasc, C., "The Influence of Age-Hardening on Fatigue Crack Propagation Behaviour in 7075 Aluminum Alloy in Vacuum," *Fatigue of Engineering Materials and Structures*, Vol. 6, 1983, pp. 329–344.
[21] Gray, G. T., III., Williams, J. C., and Thompson, A. W., "Roughness-Induced Crack Closure: An Explanation for Microstructurally Sensitive Fatigue Crack Growth," *Metall Trans A*, Vol. 14A, 1983, pp. 421–433.
[22] Doker, H. and Marci, G., "Threshold Range and Opening Stress Intensity Factor in Fatigue," *International Journal of Fatigue*, Vol. 5, 1983, pp. 187–191.
[23] Suresh, S., Vasudevan, A. K., and Bretz, P. E., "Mechanisms of Slow Fatigue Crack Growth in High Strength Aluminum Alloys: Role of Microstructure and Environment," *Metall. Trans. A*, Vol. 15A, 1984, pp. 369–379.

[24] Liaw, P. K., Saxena, A., Swaminathan, V. P., and Shin, T. T., "Influence of Temperature and Load Ratio on Near-Threshold Fatigue Crack Growth Behavior of CrMoV Steel," *Fatigue Crack Growth Threshold Concepts*, D. L. Davidson and S. Suresh, Eds., The Metallurgical Society of AIME, 1984, pp. 205–223.

[25] Blom, A. F., "Near-Threshold Fatigue Crack Growth and Crack Closure in 17-4 PH Steel and 2024-T3 Aluminum Alloy," *ibid*, pp. 263–279.

[26] Cadman, A. J., Nicholson, C. E., and Brook, R., " Influence of R Ratio and Orientation on the Fatigue Crack Threshold and Subsequent Crack Growth of a Low-Alloy Steel," *ibid*, pp. 281–298.

[27] Esaklul, K. A., Wright, A. G., and Gerberich, W. W., "An Assessment of Internal Hydrogen Versus Closure Effects on Near-Threshold Fatigue Crack Propagation," *Ibid*, pp. 299–326.

[28] Liaw, P. K., Leax, T. R., and Donald, J. K., "Fatigue Crack Growth Behavior of 4340 Steels," *Acta Metall*, Vol. 35, 1987, pp. 1415–1432.

[29] Tu, L. K. L. and Seth, B. B., "Threshold Corrosion Fatigue Crack Growth in Steels," *Journal of Testing and Evaluation*, Vol. 6, 1978, ASTM International, West Conshohocken, PA, pp. 66–74.

[30] Wei, R. P. and Landes, J. D., "Correlation Between Sustained-Load and Fatigue Crack Growth in High-Strength Steels," *Materials Research and Standards*, Vol. 9, 1969, pp. 25–46.

[31] Gerberich, W. W., Birat, J. P., and Zackay, V. F., "On the Superposition Model for Environmentally Assisted Fatigue Crack Propagation," *Corrosion Fatigue: Chemistry, Mechanics and Microstructure, NACE-2*, O. F. Devereux, A. J. McEvily, and R. W. Stehle, Eds., National Association of Corrosion Engineers, 1972, pp. 396–408.

[32] Wei, R. P., "On Understanding Environment-Enhanced Fatigue Crack Growth – A Fundamental Approach," *Fatigue Mechanisms, ASTM STP 675*, J. T. Fong, Ed., ASTM International, West Conshohocken, PA, 1979, pp. 816–840.

[33] Pao, P. S., Wei, W., and Wei, R. P., "Effect of Frequency on Fatigue Crack Growth Response of AISI 4340 Steel in Water Vapor," *Environment-Sensitive Fracture of Engineering Materials,* Z. A. Foroulis, Ed., The Metallurgical Society of AIME, 1979, pp. 565–580.

[34] Suresh, S., *Fatigue of Materials*, Cambridge University Press, Cambridge, UK, 1991, p. 211.

SESSION 3B: INTEGRITY ASSESSMENT I

Journal of ASTM International, June 2005, Vol. 2, No. 6
Paper ID JAI11999
Available online at www.astm.org

Susanne Höhler[1] *and Gerhard Sedlacek*[2]

Selection of Material for Welded Steel Structures Based on Fracture Mechanics

ABSTRACT: The European technical rules for the design of steel structures (Eurocode 3) offer a method to select steels to avoid brittle fracture. This concept is available for members subject to fatigue loads and is based on a safety assessment using fracture mechanics, applying stress intensity factors (K-concept). In order to extend these rules to members with predominant static loads, investigations have been carried out for typical details as used in buildings, both experimentally and theoretically. The details investigated were welded connections of solid bars or I-profiles with slotted gusset plates. The experimental studies included large scale tests using test specimens with initial cracks at locations of high stress concentrations. For the theoretical studies, the K-concept was applied. Formulae for K-requirements were developed for such details with numerical simulations using BE- (Boundary Element-) methods. The results allow an extension of the rules in Eurocode 3.

KEYWORDS: brittle fracture, steel structures, toughness requirements, boundary element methods, crack growth

Nomenclature

a_d:	Crack size at "hot spot" of structural detail [m]
b_{eff}:	Length of crack front to include crack shape [m]
$f_y(t)$	Yield strength in dependence on the member thickness t [MPa]
$K^*_{appl,d}$:	Toughness requirement expressed as stress intensity factor [MPa $m^{1/2}$]
$K_{mat,d}$:	Fracture toughness expressed as stress intensity factor [MPa $m^{1/2}$]
k_{R6}:	Plasticity factor of R6-Failure Assessment Diagram [-]
T_{Ed}:	Lowest ambient temperature [°C]
T_{Rd}:	Lowest permissible temperature to fulfill safety assessment [°C]
T_{27J}:	Charpy energy test temperature where the charpy energy 27 J is achieved [°C]
T_{K100}:	Temperature where K reaches the value of 100 MPa $m^{1/2}$ [°C]
ΔT_R:	Safety element derived by statistical evaluation of large scale tests [°C]
ΔT_σ:	Temperature effect including stress intensity of geometry and stresses [°C]
ρ:	Correction factor including local residual stresses at critical detail [-]
σ_{Ed}:	Tensile stress at critical structural detail [MPa]
σ_S:	Global residual stress influencing toughness requirement $K^*_{appl,d}$ [MPa]

Manuscript received 31 October 2003; accepted for publication 25 October 2004; published June 2005. Presented at ASTM Symposium on Fatigue and Fracture Mechanics: 34th Volume on 19–21 November 2003 in Tampa, FL; S.R. Daniewicz, J.C. Newman, Jr., and K-H. Schwalbe, Guest Editors.
[1] Scientific Researcher, Institute of Steel Construction, University of Technology Aachen (RWTH), 52074 Aachen, Germany.
[2] Professor, Institute of Steel Construction, University of Technology Aachen (RWTH), 52074 Aachen, Germany.

Introduction

In the frame of the unification of the European technical rules for the design of steel structures (Eurocode 3), a method has been developed to select steels to avoid brittle fracture. This concept is implemented in EN 1993-1-10 [1] and is applicable to structural members subject to fatigue loads (e.g., bridges) with details covered by EN 1993-1-9 [2]. It is based on a safety assessment using fracture mechanics and assumes initial surface cracks grown to design values by fatigue. In the assessment, the K-concept is applied using stress intensity factors.

The objective of a recent research project was the extension of these rules to members with predominant static loads as in buildings, for which the details in general are not designed for fatigue. For buildings, critical details are connections of members made of solid bars or I-profiles welded to slotted gusset plates. Investigations have been carried out for these details, both experimentally and theoretically, to define toughness requirements to provide simple rules which allow the selection of material. The investigations included tests with large scale test specimens with initial cracks at locations of high stress concentrations. For numerical calculations of the crack growth, the BE-method was applied.

Selection of Materials for Fracture Toughness in Eurocode 3

The choice of material according to EN 1993-1-10 is based on a safety assessment using fracture mechanics

$$K^*_{appl,d} \leq K_{mat,d} \tag{1}$$

In this equation $K^*_{appl,d}$ (stress intensity factor) is the design value of the action effect which gives the toughness requirement for a certain flaw size, modelled by a surface crack including a correction for plastic strains according to the R6-Failure Assessment Diagram (FAD) [3]. $K_{mat,d}$ is the design value of the toughness resistance of the material. The toughness resistance includes a modified Sanz-correlation [4] correlating the temperature T_{K100}, where the K-factor achieves the value 100MPa $m^{1/2}$, and the temperature T_{27J} for charpy energy tests, and the Wallin-Master-curve [5]. It also includes the reference temperature T of the structural component and an additive safety element ΔT_R to be determined from test evaluations. Figure 1 demonstrates the various components of the safety assessment.

The assessment format in terms of K-values as given in Fig. 1 has been transferred to a temperature format for implementation in EN 1993-1-10 (Eurocode 3 - Part 1.10: Selection of Materials for Fracture Toughness) where all relevant input parameters from actions and from the structure are included in T_{Ed}, whereas T_{Rd} contains the material properties from tests only. This transformation is necessary because product standards provide standardized toughness values as T_{27J}- and T_{40J}- values where the charpy energy is 27 J or 40 J, respectively.

To make this concept applicable for preparing a table for permissible plate thicknesses, the following steps have been performed:

- The safety element ΔT_R was derived from large scale tests with cracks by statistical evaluations.
- A standard fracture mechanical requirement curve ΔT_σ was determined with a critical surface crack of the size a_d at the hot spot of a critical standardized welded detail. The design crack may have developed from an initial flaw (of size a_0) that propagated under

fatigue load during a time interval between inspections or the full service time. The values ΔT_σ should cover all detail classes in EN 1993-1-9.

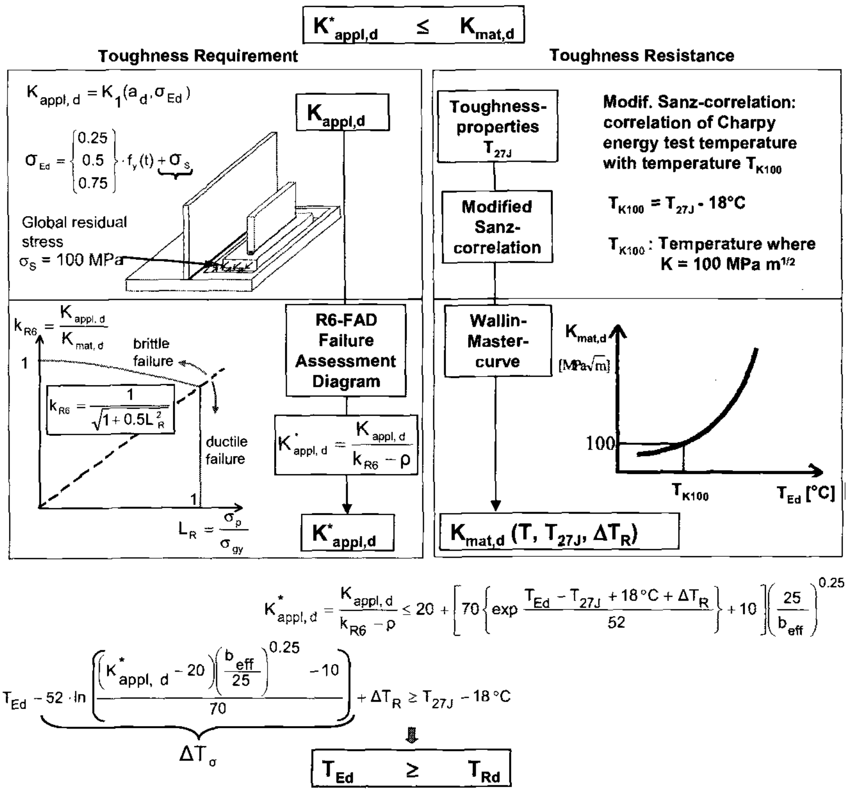

FIG. 1—*Safety assessment for limit state "brittle fracture" in EN 1993-1-10.*

Figure 2 shows this standard toughness requirement curve ΔT_σ and also a comparison with individual requirement values calculated numerically with BE-methods for members of practical sizes with various fatigue classes. As the standardized values ΔT_σ reach higher toughness requirements than the individual ones calculated with more precise (numerical) methods, the safe sidedness of the assessment procedure is proved.

The table for permissible plate thicknesses as given in Fig. 3 results from this requirement curve. The requirement curve in Fig. 2 covers only details according to the fatigue classes with semi-elliptical surface cracks. For details not listed in the fatigue class catalog [2], e.g., for details with through-thickness-cracks, a solution had still to be found. Also, guidance was necessary in cases like building structures, where fatigue is not as relevant as for bridges or gantry girders.

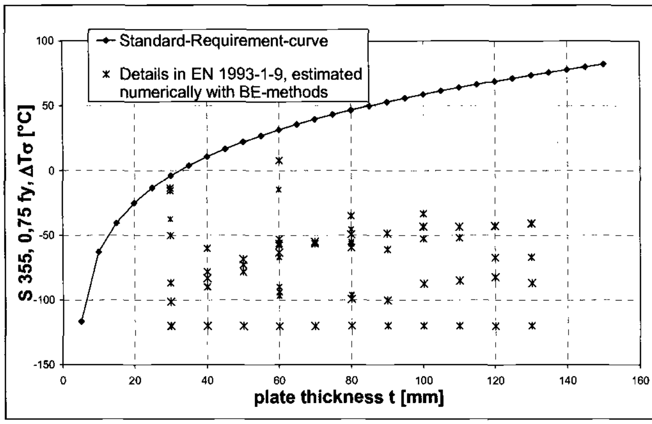

FIG. 2—*Standard requirement curve compared to results for details in EN 1993-1-9.*

The Approach for the Extension of the Existing Rules

General Considerations

For the extension of the concept for buildings and details with through-thickness-cracks the safety assessment format used in EN 1993-1-10 was kept. Two problems had to be solved:

1. Determination of the fracture mechanical requirement $K^*_{appl,d}$ for typical structural details with through-thickness-cracks
2. Definition of design values of cracks a_d for such structural details compatible with the fabrication- and service-conditions for members and buildings.

Typical details for members in buildings and frames were used that are made of solid bars or I-profiles and are welded to slotted gusset plates. For such details no hand formulae for K-values exist. Therefore, a numerical solution had to be developed suitable for parametric studies. For that purpose the BE- method was chosen, which had to be compared to test results in order to guarantee realistic simulations. Since this type of large scale test specimens did not allow a direct measurement of stress intensity factors or the J-integral, instead crack growth tests were performed under cyclic loading to measure the crack growth rate and to use this crack growth for comparison. Knowing the crack growth rate, the correlation to K-factors can be established by Paris-law [6]. The investigations included the following steps:

1. Identify the test specimens
2. Perform large scale tests (accompanied by small scale tests) for measuring crack growth
3. Perform BE-modelling and simulation of crack growth by application of Paris-law:

$$\frac{da}{dN} = C \cdot \Delta K^m \qquad (2)$$

where da/dN = crack growth rate; C,m = material parameters; and ΔK = range of stress intensity factors.

Steel grade	Sub-grade	Charpy energy CVN		Reference temperature T_{Ed} in °C																				
				$\sigma_{Ed}=0,25 \times f_y(t)$							$\sigma_{Ed}=0,50 \times f_y(t)$							$\sigma_{Ed}=0,75 \times f_y(t)$						
		at T °C	$J_{min.}$	10	0	-10	-20	-30	-40	-50	10	0	-10	-20	-30	-40	-50	10	0	-10	-20	-30	-40	-50
S235	JR	20	27	135	115	100	85	75	65	60	90	75	65	55	45	40	35	60	50	40	35	30	25	20
	J0	0	27	175	155	135	115	100	85	75	125	105	90	75	65	55	45	90	75	60	50	40	35	30
	J2	-20	27	200	200	175	155	135	115	100	170	145	125	105	90	75	65	125	105	90	75	60	50	40
S275	JR	20	27	125	110	95	80	70	60	55	80	70	55	50	40	35	30	55	45	35	30	25	20	15
	J0	0	27	165	145	125	110	95	80	70	115	95	80	70	55	50	40	75	65	55	45	35	30	25
	J2	-20	27	200	190	165	145	125	110	95	155	130	115	95	80	70	55	110	95	75	65	55	45	35
	M, N	-20	40	200	200	190	165	145	125	110	180	155	130	115	95	80	70	135	110	95	75	65	55	45
	ML, NL	-50	27	230	200	200	200	190	165	145	200	200	180	155	130	115	95	185	160	135	110	95	75	65
S355	JR	20	27	110	95	80	70	60	55	45	65	55	45	40	30	25	25	40	35	25	20	15	15	10
	J0	0	27	150	130	110	95	80	70	60	95	80	65	55	45	40	30	60	50	40	35	25	20	15
	J2	-20	27	200	175	150	130	110	95	80	135	110	95	80	65	55	45	90	75	60	50	40	35	25
	K2, M, N	-20	40	200	200	175	150	130	110	95	155	135	110	95	80	65	55	110	90	75	60	50	40	35
	ML, NL	-50	27	210	200	200	200	175	150	130	200	180	155	135	110	95	80	155	130	110	90	75	60	50
S420	M, N	-20	40	200	185	160	140	120	100	85	140	120	100	85	70	60	50	95	80	65	55	45	35	30
	ML, NL	-50	27	200	200	200	185	160	140	120	190	165	140	120	100	85	70	135	115	95	80	65	55	45
S460	Q	-20	30	175	155	130	115	95	80	70	110	95	75	65	55	45	35	70	60	50	40	30	25	20
	M, N	-20	40	200	175	155	130	115	95	80	130	110	95	75	65	55	45	90	70	60	50	40	30	25
	QL	-40	30	200	200	175	155	130	115	95	155	130	110	95	75	65	55	105	90	70	60	50	40	30
	ML, NL	-50	27	200	200	200	175	155	130	115	180	155	130	110	95	75	65	125	105	90	70	60	50	40
	QL1	-60	30	215	200	200	200	175	155	130	200	180	155	130	110	95	75	150	125	105	90	70	60	50
S690	Q	0	40	120	100	85	75	60	50	45	65	55	45	35	30	20	20	40	30	25	20	15	10	10
	Q	-20	30	140	120	100	85	75	60	50	80	65	55	45	35	30	20	50	40	30	25	20	15	10
	QL	-20	40	165	140	120	100	85	75	60	95	80	65	55	45	35	30	60	50	40	30	25	20	15
	QL	-40	30	190	165	140	120	100	85	75	115	95	80	65	55	45	35	75	60	50	40	30	25	20
	QL1	-40	40	200	190	165	140	120	100	85	135	115	95	80	65	55	45	90	75	60	50	40	30	25
	QL1	-60	30	200	200	190	165	140	120	100	160	135	115	95	80	65	55	110	90	75	60	50	40	30

FIG. 3—*Table of permissible plate thicknesses in EN 1993-1-10.*

4. Check the BE-calculations by comparing numerical results of crack growth with experimental results. In case of good matching, a realistic simulation of the fracture mechanical behavior and thus the K-values can be assumed.
5. Perform parametric studies with varied geometric dimensions to develop a general function for K-values.
6. Perform fracture tests with the same test specimens as used for crack propagation to determine the resistance to brittle fracture at low temperatures. These tests include the "worst case" scenario comprising "lowest temperature" plus "large cracks at points of high stress concentrations" plus "high strains."
7. Check of the assessment method for the safety assessment to avoid brittle fracture by comparison with fracture tests and derivation of standardized requirement curves and simplified rules for the choice of material.

Identification of Test Specimens

For the typical details chosen, i.e., welded connections of diagonal components with slotted gusset plates, high stress concentrations occur at the gap at the weld ends (Fig. 4).

From inquiries at various steel fabricators, the following common features could be determined for the components [7]: Common profiles connected are I-profiles (HEA, HEB, IPE) and solid circular bars. The gusset plates have thicknesses ranging from 10–120 mm. Steel grades are S235JRG2, S355J0, and S355J2G3. The test program was defined following these investigations. The test plates were dimensioned so that fracture would occur at the location of the gap next to the weld end. The variation of plate dimensions was reduced to two thicknesses, taking the common thickness of 20 mm and a greater thickness of 40 mm to include the more brittle and critical case. Figure 5 shows the test program.

Experimental Investigations with Large Scale Tests

All experimental works have been carried out at the Institute of Ferrous Metallurgy (IEHK) of University of Technology Aachen (RWTH) [8]. Small scale tests were performed to determine the material properties including metallographic tests, chemical analysis, tensile tests, Charpy energy tests, fracture mechanical tests, and crack growth tests. The steels were S235J2G3 and S355J2G3 with thicknesses of 20 mm or 40 mm. Large scale tests were carried out with welded test specimens. Beams representing diagonal components were welded into the slotted gusset plates leaving a gap at the weld ends. Figure 5 gives the test program and a sketch of the test specimens with initial flaws according to the test program.

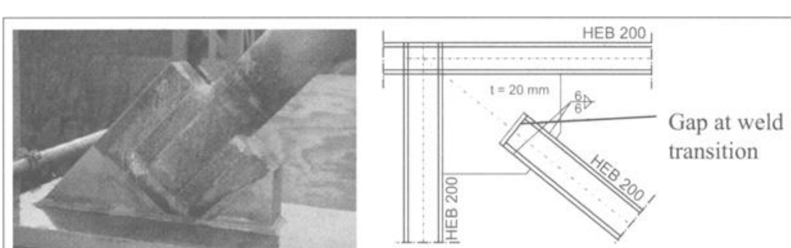

FIG. 4—*Examples for welded connections of components in building frames.*

Specimen	Beam	Gusset plate thickness t	Steelgrade
1	Solid circular bar	40mm	S235J2G3
2	D=100mm		S355J2G3
3	Solid circular bar	40mm	S235J2G3
4	D=140mm		S355J2G3
5	HEB 200	20mm	S235J2G3
6			S355J2G3
7	HEA 200	20mm	S235J2G3
8			
9		20mm	S355J2G3
10			

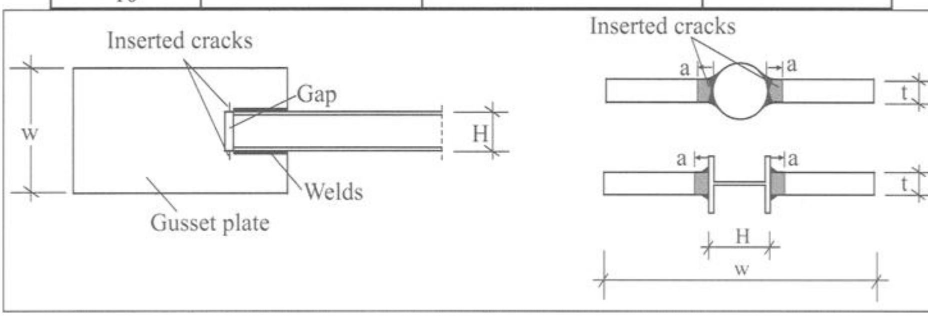

FIG. 5—*Test program and sketch of test specimens and location of initial flaws.*

After inserting artificial flaws into the test specimens at points of high stress concentrations (at weld ends), each large scale test was conducted in two parts: At first the specimens were subjected to cyclic loading to create a sharp crack and to induce crack propagation This crack propagation part was needed to check the numerical results. As the test specimens resembled structural details from buildings that are plastically designed, high stress ratios of ~0.8 and low stress ranges between 30 and 60 MPa were used. By reducing the cyclic loading at several times for a small number of load cycles, rest lines were received at the crack surfaces that could be observed after the fracture test and allowed a better understanding of the crack growth (see Fig. 7 later). The second test part included a fracture test under low temperature to examine the load bearing capacity under brittle fracture circumstances.

Numerical Investigations with BE-Methods

The fracture mechanical calculations were carried out using stress intensity factors (K-concept). The numerical BE- method was applied for three-dimensional simulation of the crack behavior.

Check of the Simulation Program—The first step was to determine the accuracy of the simulation program for calculating stress intensity factors. For this reason the crack growth tests (part 1 of large scale tests) were simulated to compare the numerical results to experimental results.

The modelling of the test specimens was three-dimensional. The commercial BE-program BEASY [9] was applied. As the BE-method only requires modelling of the outer surface (boundaries) of the detail, the complex geometry with initial cracks could be modelled with surface boundary elements (Fig. 6).

For the details considered, the initial crack configuration was modeled according to Fig. 5 with through-thickness cracks with straight crack front lines. The loading of the model was equivalent to the stress ranges used in the crack growth tests imposed as tensile load. With the help of the rest lines, a more precise comparison was possible, because the stepwise loading of the experimental crack propagation steps (given by a rest line) could be simulated by crack propagation in the BE-model. Yet in the calculations only the initial crack front was taken from the rest lines, while all other crack fronts resulted from numerical propagation due to the loading from the tests. Figure 7 shall clarify how the crack growth was simulated by means of rest lines. For each crack propagation step, a K-factor and the crack increase Δa was calculated. The crack growth rate da/dN was determined with Paris-law, using the fracture mechanical constants C and m from small scale tests. The calculated K-values were compared with reference values of the threshold value ΔK_{th} and with measured fracture toughness values K_{Ic}. All K-values were above ΔK_{th} and below K_{Ic}, which legitimated the application of Paris-law, assuming stable fatigue crack growth.

The stress intensity factors turned out to vary in the direction of the plate thickness; therefore the crack fronts were evaluated at the plate surface and in the middle of the plate. In Fig. 8 the results of the experimental crack growth and of the numerical crack growth are presented for test specimen No. 6. The conformity was very high for all geometrical details investigated [7]. Hence, both the crack growth rate and the crack front development could be estimated realistically by the BE-program. These accurate results imply a high accuracy of the numerical models for determining the K-factors which govern the crack growth calculations.

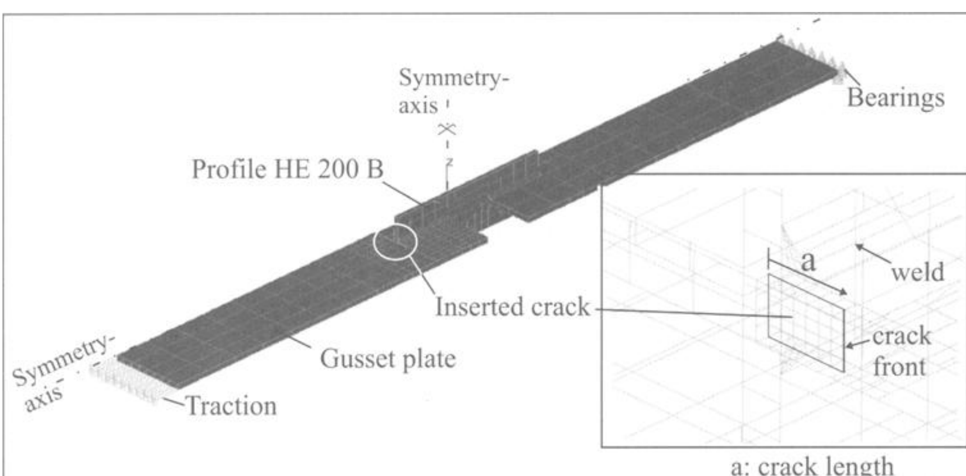

FIG. 6—*BE-model of specimen No. 6 with generated through-thickness crack.*

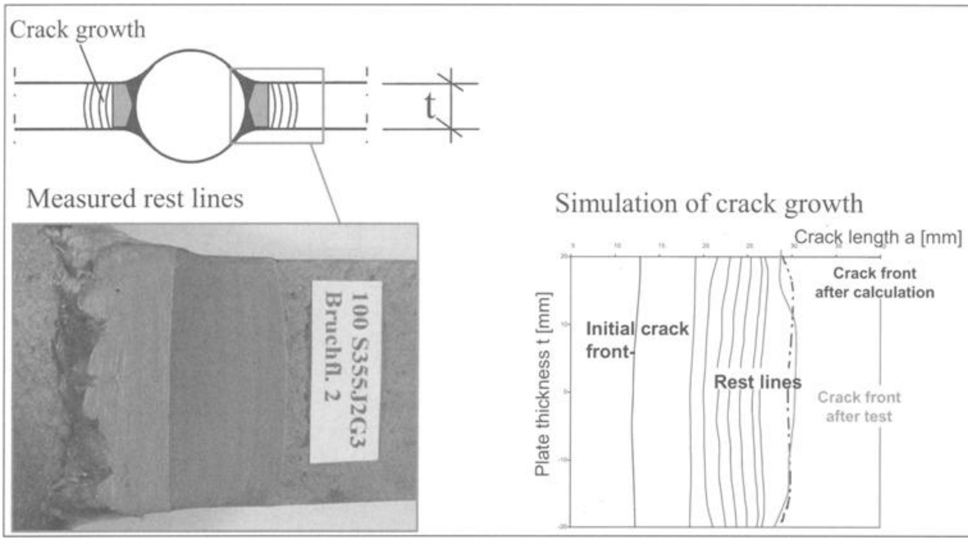

FIG. 7—*Cracked specimen with experimental rest lines due to fatigue loading (left) and numerical simulation of crack growth with rest lines (right).*

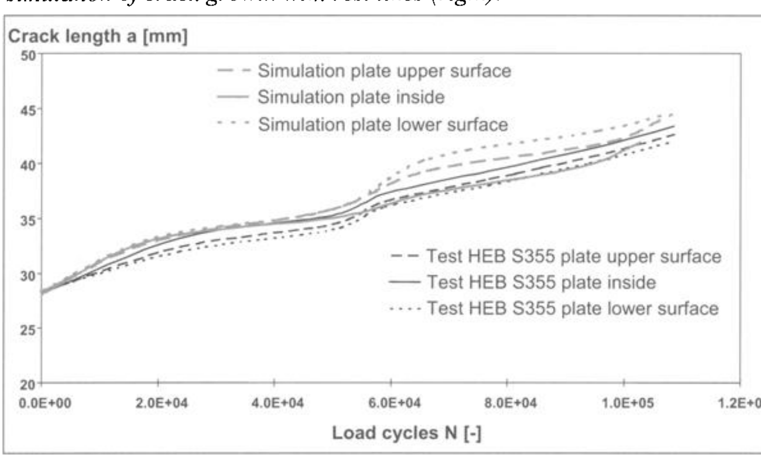

FIG. 8—*Simulation of crack growth test for test specimen No.6, HEB 200 S355.*

Parametric Studies to Develop a Formula for K_{appl}—In order to reduce the amount of parametric studies it was tried to find a solution relating to existing formulae and models for K-values. A general formulation of a function of K is the following:

$$K = \sigma\sqrt{\pi \cdot a} \cdot Y \cdot M_k \tag{4}$$

where σ = stress applied to structural component, a = crack size, Y = function considering shape and geometry of a crack and the dimensions of the cracked structure, and M_k = function including geometrical stress concentration at non-cracked model due to stiffeners, holes, notches etc.

Firstly, existing solutions for the functions Y and M_k (Fig. 9) were checked in how far they could be adjusted to the detail considered.

Calculations showed that for small cracks with crack tips close to the geometrical gap, the function using the factor M_k provides appropriate results. For a remote crack tip, the stress concentration due to the gap loses its influence on the K-values; for that case a continuous central crack can be applied. Figure 9 presents the limit crack sizes and the approaches that were used further on.

Secondly, a possibility to simplify the model configuration was looked for. Substituting the inserted component by simplified cross-sections and comparing the results for M_k -values showed that the actual cross-section of the component had no influence on the results, if the stress distribution in the plate was kept constant (Fig. 10). This means that only one formula had to be developed, that is suitable for I-profiles as well as solid bars or hollow sections.

Figure 11 shows the parameters that were varied during the study. The parameters' gusset plate width w*, weld length L, and component height H turned out to be the significant parameters for the fracture mechanical function. As the plate width w* was the most relevant geometrical parameter, all parameters were based on w*. By means of regression analysis, the calculated results were graphically plotted and fitted into appropriate standard functions to obtain formulations for K, depending on Y and M_k, where the plate width w* is the reference parameter.

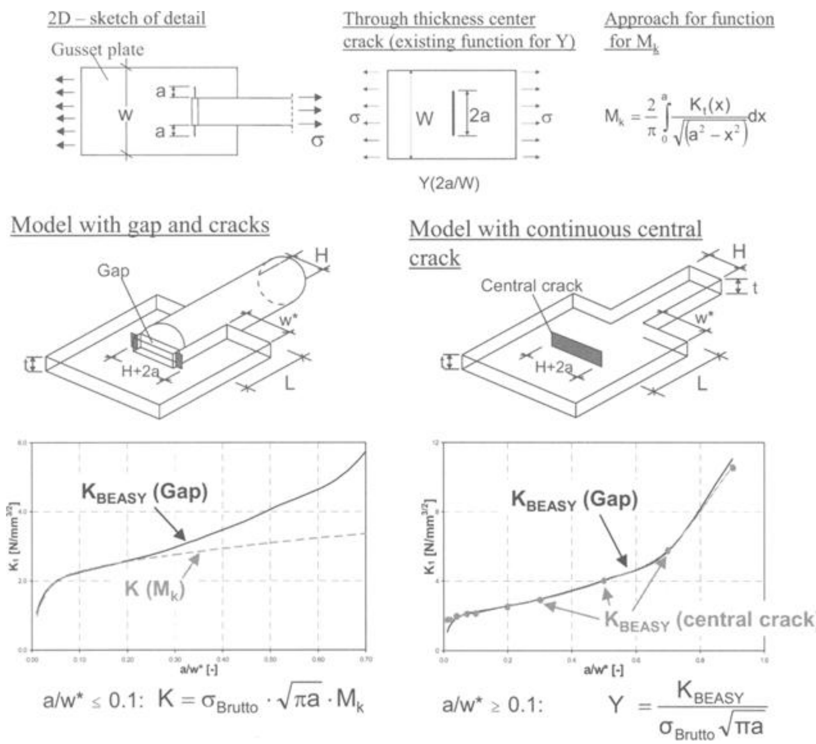

FIG. 9—*Adjustment of existing solutions for Y [10] and M_k [11] and application for models for K-values.*

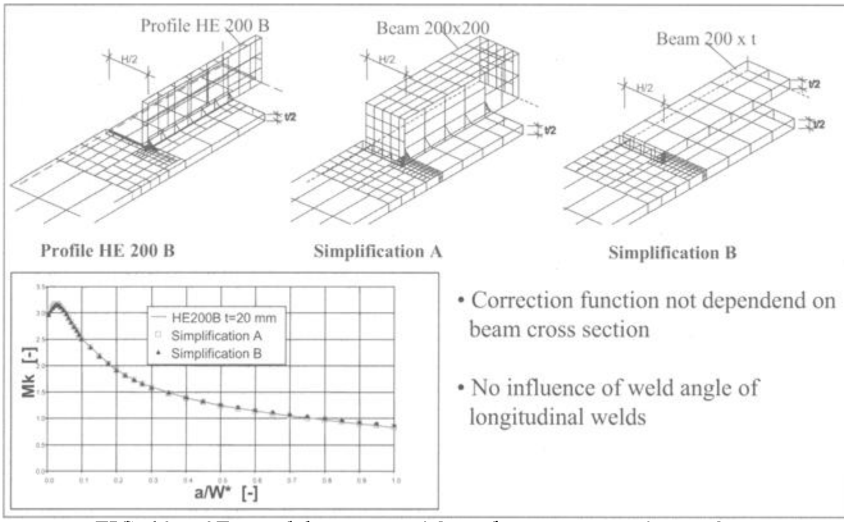

FIG. 10—*BE-simplification models and comparison of M_k-values.*

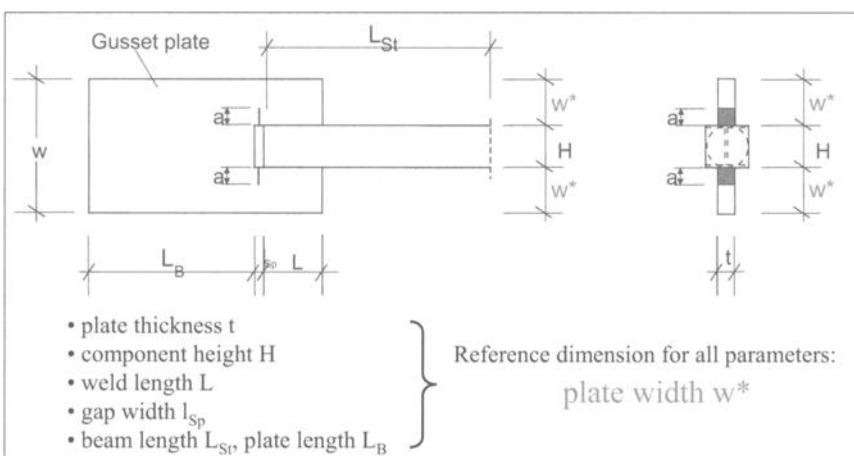

FIG. 11—*Variation of parameters.*

Derivation of Standard Requirement Curves for Details with Through-Cracks

Relevant Geometrical Parameter

The concept for the choice of material in EN 1993-1-10 gives maximum permissible plate thicknesses, because a greater plate thickness provides more severe conditions by three axial stress conditions and a greater likelihood of inhomogeneity of material. The reference design detail for EN 1993-1-10 is a plate under tension with longitudinal stiffener with a semi-elliptical surface crack (see Fig. 12 left). For this detail, the greatest stress intensity factor $K_{appl,d}$ occurs at the deepest point of the crack and causes mainly crack growth in the direction of plate thickness, resulting also in the thickness being main parameter. For details with through-thickness-cracks, the plate thickness t has almost no influence on the stress intensity factor $K_{appl,d}$. Due to the slotted gusset plate with a gap, the relevant crack configuration with a through-thickness crack that grows only in the direction of the plate width (Fig. 12 right).

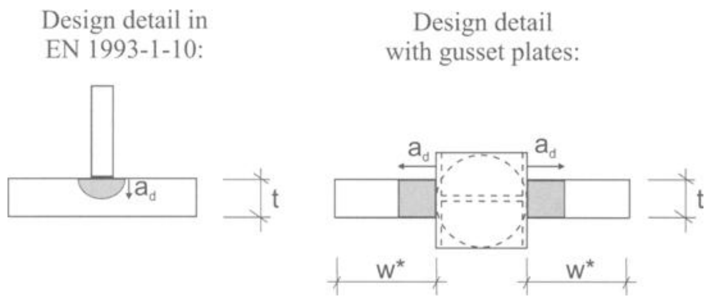

FIG. 12—*Crack configuration of detail with surface crack in EN 1993-1-10 and of a gusset plate detail with through-thickness-cracks.*

For the definition of toughness requirements, the following conclusions were drawn:

- The standard requirement curves for $K_{appl,d}$ were developed as a function of w*.
- The crack size for the relevant design situation influencing the function $K_{appl,d}$ also needed to be a function of w*.
- The tables with permissible dimensions had also to include the parameter w*.

Design Crack Size

For an appropriate design value of crack size, the following aspects needed to be taken into account: the crack could form during fabrication or erection of the member, and it could be overlooked in a weld inspection using non-destructive testing methods. For building structures, normally predominantly static loads are applied, and load variations, e.g., due to gusts of wind, would only produce minor fatigue effects. For safety reasons of structures these minor fatigue effects must be considered in the safety assessment. To cover these fatigue effects, the crack size was only subjected to 20.000 fatigue load cycles with a magnitude $\Delta\sigma$ corresponding to the classification of the detail. In [7] a function for the crack size a(w*) is suggested for this case.

Standard Requirement Curves $K_{appl}(w^*)$

For each geometric parameter combination a standard curve $K_{appl}(w^*)$ could be evaluated. The "worst case" combination [1) in Fig. 13] is a combination with a short weld length L and a great height of component H. It provides the highest toughness requirements for the connection. The parameter combinations 2) and 3) in Fig. 13 represent a more common form.

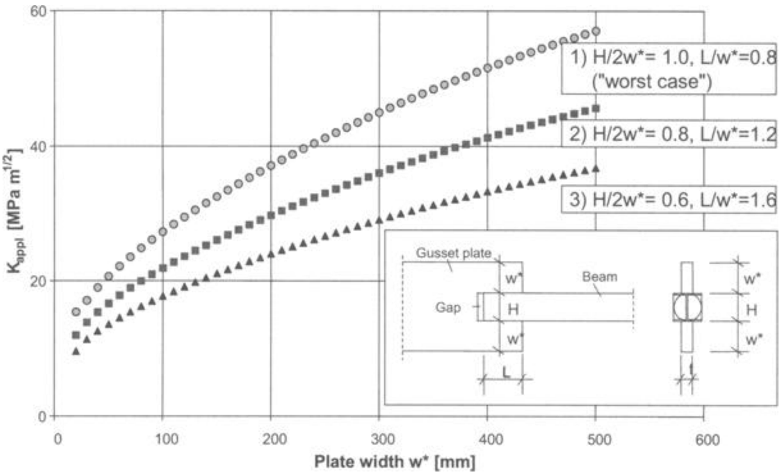

FIG. 13—*Standard-K_{appl}-curves for different geometric parameter combinations.*

Check of the Concept with Large Scale Fracture Tests

The statistical evaluation of the large scale fracture tests according to EN 1990-Annex D [12] provided a saftey element ΔT_R in terms of a temperature shift to meet the reliability requirements in EN 1990. This allowed the calculation of permissible temperature values to avoid brittle fracture for the test specimens. A comparison of calculated temperatures T_{calc} with experimental temperatures T_{exp} shows the safe sidedness of the concept, if the safety element ΔT_R is included (Fig. 14, right).

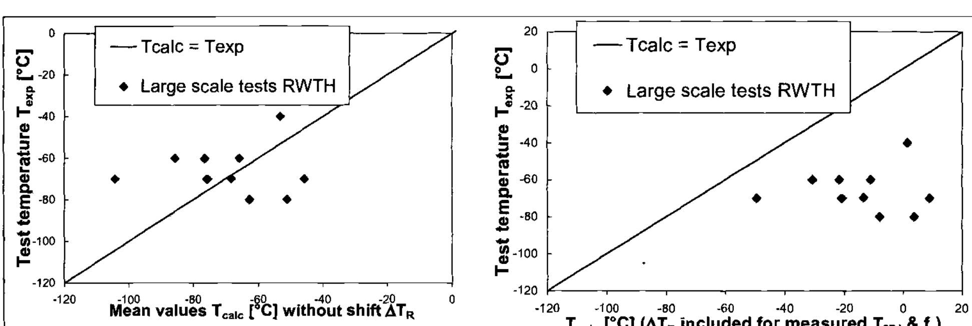

FIG. 14—*Comparison of calculated requirements (T_{calc}) and experimental values (T_{exp}) for mean values (left) and with safety element ΔT_R (right) [7].*

Tables for Permissible Dimensions

For each standard curve, a table with permissible dimensions could be developed, which looks like the table of permissible plate thicknesses in EN 1993-1-10 (Fig. 3). The tables depend on the material toughness properties, the steel grade, the stress level, and the reference temperature of the member. Figure 15 shows as an example a table of permissible plate widths w* that corresponds to the K_{appl}-curve 2) in Fig. 13.

Conclusion and Perspective

A method has been developed for the choice of material for members with particular details to avoid brittle fracture. Following the concept in Eurocode 3 - Part 1.10, tables are provided that are based on standard requirement curves for material toughnesses K. The function of requirement has been established with numerical calculations using BE-methods. The numerical method was compared to experimental results obtained from large scale tests. The comparison proved that the BE-method is a suitable method for calculating stress intensity factors and crack growth.

The verification method for the choice of material applies to the transition area of the toughness-temperature-curve. Linear elastic behavior of the material may be assumed in this area. If steel structures are designed with plastic resistances, elastic plastic material properties are required for an elastic plastic fracture mechanical assessment in the upper shelf region of the toughness-temperature-curve. Further experimental and theoretical studies are necessary to examine the fracture mechanical behavior of members loaded beyond yield strength, which, e.g., may occur in case of seismic actions.

$H/2w^* \leq 0.8$ $L/w^* \geq 1.2$ $t \leq 40mm$
Parameter ranges in [7] need to be considered.

"-": Safety assessment not satisfied, extra investigations are required.

Steel-grade	Sub-grade	Charpy energy CVN		Reference temperature T_{Ed} in °C																	
		at T	J	10	0	-10	-20	-30	-40	10	0	-10	-20	-30	-40	10	0	-10	-20	-30	-40
				$\sigma_{Ed}=0,25*f_y(t)$						$\sigma_{Ed}=0,50*f_y(t)$						$\sigma_{Ed}=0,75*f_y(t)$					
		°C	min.	maximum permissible plate width w* of gusset plate in mm (safety element ΔT_R included)																	
S235	JR	20	27	150	110	80	60	40	30	60	40	30	20	-	-	20	-	-	-	-	-
	J0	0	27	300	210	150	110	80	60	120	90	60	40	30	20	50	30	20	-	-	-
	J2	-20	27	500	420	300	210	150	110	260	180	120	90	60	40	120	80	50	30	20	-
S275	JR	20	27	140	100	70	50	30	20	40	30	20	-	-	-	-	-	-	-	-	-
	J0	0	27	270	190	140	100	70	50	100	70	40	30	20	-	30	20	-	-	-	-
	J2	-20	27	4								100	70	40	30	90	60	30	20	-	-
	M, N	-20	40	5																	
	ML, NL	-50	27	500	500	50															
S355	JR	20	27	110	80	50															
	J0	0	27	210	150	11															
	J2	-20	27	430	300	21															
	K2, M, N	-20	40	500	430	30															
	ML,NL	-50	27	500	500	50															
S420	M, N	-20	40	440	360	26															
	ML, NL	-50	27	500	500	44															
S460	Q	-20	30	330	230	16															
	M, N	-20	40	440	330	23															
	QL	-40	30	500	440	33															
	ML, NL	-50	27	500	500	44															
	QL1	-60	30	500	500	50															
S690	Q	0	40	140	100	60															
	Q	-20	30	200	140	10															
	QL	-20	40	290	200	14															
	QL	-40	30	420	290	20															
	QL1	-40	40	500	420	29															
	QL1	-60	30	500	500	420	290	200	140	250	170	110	70	40	30	80	50	30	-	-	-

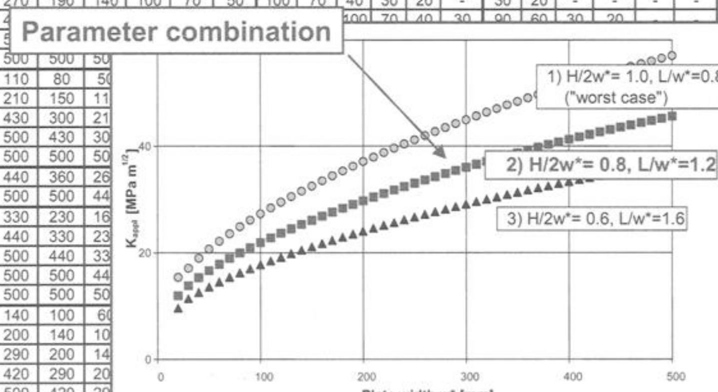

FIG. 15—*Example for toughness requirements for a combination of dimensions.*

References

[1] *prEN 1993-Eurocode 3*: Design of Steel Stuctures, Part 1.10: Selection of Materials for Fracture Toughnes and Through Thickness Properties, Draft 2002.

[2] *prEN 1993-Eurocode 3*: Design of Steel Stuctures, Part 1.9: Fatigue Strength of Steel Structures, Draft 2002.

[3] Milne, I., Ainsworth, R. A., Dowling, R. A., and Stewart, A. T., Assessment of the Integrity of Structures Containing Defects, CEGB Report R/H/R6-Revision, 1986.

[4] Sanz, G. and Marandet, B., "Étude par la mécanique de la rupture de la ténacité d'aciers à resistance moyenne fournis en forte épaisseur, " *Revue de Métallurgie*, 1976, pp.359–383.

[5] Wallin, K., "Methodology for Selecting Charpy Toughness Criteria for Thin High Strength Steels, Part 1, 2, and 3," *Jerkontorets Forskning*, Nr. 4013/89, VTT Manufacturing Technology, VTT Espoo, 1994.

[6] Paris, P. C., Gomez, M. P., and Anderson, W. F., "A Rational Theory in Fatigue," *The Trend in Engineering*, 13, 1961.

[7] Sedlacek, G., Höhler, S., Kühn, B., "Stahlgütewahl nach Betriebsfestigkeitskatalogen," Report No. Se 351/28-2 of German Research Fund (DFG), Institute of Steel Construction, RWTH Aachen, 2003, available for ordering at http://www.tib-hannover.de/.

[8] Dahl, W., Bleck, W., and Buchholz, J., "Stahlgütewahl nach Betriebsfestigkeitskatalo-gen," Report No. Da 85/78-2 of German Research Fund (DFG), Institute of Metallurgy, RWTH Aachen, 2002, available for ordering at http://www.tib-hannover.de/.

[9] BEASY User Guide, Vols. 1 and 2, Computational Mechanics BEASY, Southampton, UK, 1998.

[10] Murakami, Y., Stress Intensity Factor Handbook, Vols. 1 and 2, Pergamon Press, Frankfurt, 1987.

[11] Albrecht, P. and Yamada, K., "Rapid Calculation of Stress Intensity Factors," *Journal of Structural Division*, ASCE, Vol. 103, No. ST2, Proc. Paper 12742, 1977, pp.377–389.

[12] *EN 1990-Eurocode*: Basis of Structural Design, Final Draft, July 2001.

Journal of ASTM International, June 2005, Vol. 2, No. 6
Paper ID JAI12045
Available online at www.astm.org

Volodymyr P. Naumenko[1] *and Grygory S. Volkov*[1]

Assessment of Plane Stress Tearing in Terms of Various Crack Driving Parameters

ABSTRACT: The important role of mechanical parameters characterizing the global fracture behavior of a thin rectangular plate is demonstrated through comparison of various approaches to the investigation of ductile tearing at large amounts of stable crack extension. Tensile tests have been performed on middle-cracked specimens at different in-plane constraint states and on cruciform specimens. The latter geometry is treated as a physical counterpart of the basic structural element usually considered in model descriptions of tension- and/or compression-dominant crack geometries. Attention is focused on the simplest practical problem, namely, assessing the critical states of a center through crack under remote uniaxial tension. The case in point is a comprehensive assessment of the structural behavior of a thin-wall component where failure loads, displacements, and subcritical crack extensions must all be predicted from the crack growth data for a laboratory-size specimen of standard geometry.

KEYWORDS: plane stress tearing, boundary constraint, stress biaxiality, instability, energy dissipation rate, crack-tip opening angle, crack-mouth opening angle, crack volume ratio, ductile aluminum alloy

Nomenclature

CTOA	Crack Tip Opening Angle
CTOD	Crack Tip Opening Displacement
CTOA-ψ_c	Critical value of the CTOA
CTOD-δ_5	CTOD defined for a gauge length of 5 mm
UM	Unified Methodology
TL	Transferring Law
SST	Steady State Tearing
PD	Problem Domain
BSE	Basic Structural Element
ADZ	Active Damage Zone
LG	Loading Gadget
M(T)	Middle-Cracked Tension Specimen
MM(T)	Modified M(T) Specimen
MM(T-TC)	Modified Middle-Cracked Cruciform Specimen
CMOS	Crack Mouth Opening Spacing
LM(T)	Low-Constrained M(T) Specimen
HM(T)	Highly-Constrained M(T) Specimen
CMOA	Crack Mouth Opening Angle
CVR	Crack Volume Ratio

Manuscript received 6 November 2003; accepted for publication 15 September 2004; published June 2005.
Presented at ASTM Symposium on Fatigue and Fracture Mechanics: 34th Volume on 19–21 November 2003 in Tampa, FL; S.R. Daniewicz, J.C. Newman, Jr., and K-H. Schwalbe, Guest Editors.
[1] Leading Scientist and Senior Scientist, respectively, G.S. Pisarenko Institute for Problems of Strength, Department of Fracture Modeling, Kyiv, Ukraine.

Introduction

Thin-wall structures are encountered in many applications in aerospace, mechanical, civil, and ocean engineering. Over the years there has been an urgency to develop valid fracture criteria and standard test methods for unified assessment of fracture behavior of a single mode I crack in the above structural applications. As to thin-wall components made of ductile metallic materials, the majority of up-to-date advancements have been discussed recently by Newman et al. [1] and Schödel and Zerbst [2]. They underline the worldwide interest in the Crack Tip Opening Angle (CTOA) and the Crack Tip Opening Displacement (CTOD) as local fracture parameters for metallic materials. The CTOA-ψ_c and CTOD-δ_5 parameters are treated as the most suited for modeling stable crack growth and instability of the fracture process.

Actually, there is increasing evidence that the known characterizations of plane strain fracture in bend-dominant crack geometries may not be valid for assessing plane stress fracture in tension- and compression-dominant crack geometries. When it comes to the case of nucleation and propagation of an internal tear crack under uniform uniaxial tension, the fracture process is accompanied by the development of low-constrained flow fields. In specimens made from sheet materials, varying the magnitude and sign of an additional load applied parallel to the straight crack can effectively generate different levels of in-plane constraint under biaxial loading. This level is highly reduced when mode I fracture occurs only due to compressive (negative) stress acting along the crack growth line.

The issue of whether or not the well-accepted analyses of elastic-plastic crack tip fields are able to predict the parameters of structural behavior for low-constrained components goes right to the basis of fracture mechanics. Both stress and flow fields associated with low levels of stress triaxiality in thin plates are very different from those for plane strain conditions in bend-dominant geometries. Hutchinson's paper [3] and recent work of Dadkhah and Kobayashi [4] have shown that the displacement fields surrounding a growing crack differ widely from those given by the plane strain HRR distribution [5,6], from the *J-Q* field [7,8], and the *J-T* field [9]. In fact, they did not observe either the *J-Q* or the *J-T* crack-tip fields in thin aluminum plates fractured under uniaxial and biaxial tension. These works taken together with a large body of related literature data support a common knowledge that the concept of *J*-controlled crack growth is invalid. Besides, in thin-sheet materials within a current thickness of the crack tip, the conditions are neither plane stress nor plane strain due to shear lips, slant fracture, or crack tunneling. Thus, the plane-strain model descriptions of elastic-plastic fracture are not valid when used for assessing ductile tearing under plane stress conditions.

The same statement might hold true in respect to the characterization of crack-tip fields by using the stress intensity factor *K*. Until now, there has been no sound explanation of the pronounced size-scale effects described in the literature for the simplest case, namely, brittle fracture under remote uniaxial tension. A very conclusive and troublesome example is the *K*-based characterization of the resistance to fracture initiation in proportionally scaled thin plates of unusually brittle metallic and non-metallic materials, which were tested by Sinclair et al. [10]. It is pertinent to mention here that there is a well-known lack of consensus with respect to the magnitude or direction of the differences in biaxial fracture behavior as compared to uniaxial tension. According to Eftis et al. [11] "...the theories of Griffith and Irwin are incapable of proper treatment of biaxial effect." What is more, they are also conceptually incapable to describe the mode I crack growth under uniform uniaxial compression, i.e., under an extremely low level of in-plane constraint.

The Problem and Approach

Since Griffith's pioneering work [12], the development of a general concept of mode I fracture under tensile and/or compressive loading is of great scientific interest. In practical terms, it would be also very desirable to have a general method such that the structural integrity of components made from brittle and ductile metallic or nonmetallic materials could be assessed in a unified manner. These are precisely the main reasons behind the development of our approach called the Unified Methodology (UM) of mode I fracture investigation by Naumenko et al. [13–23]. The UM aims at formulating a Transferring Law (TL), i.e., a common function of experimental data on crack growth in a simple specimen of relatively small size and a large-scale component of complicated geometry. Our short-term goal is to develop a so-called basic TL with the use of a minimum number of parameters which would allow engineering assessment of stable crack growth under proportional biaxial loading in tension and/or compression.

There is, therefore, a need to simplify the subject matter as far as possible. That is why the problem in question is confined here to the Steady State Tearing (SST) stage of crack extension in the two-dimensional Problem Domains (PDs) shown in Figs. 1 and 2*b*. Their in-plane geometry and stress state are symmetric with respect to both *x*- and *y*-axes. The square PD in Fig. 2*b* is called a Basic Structural Element (BSE). At every instant, the length $2c_s$ of an isolated crack growing in the BSE meets the condition $c_s = c_0 + \Delta c_s \leq 0.1\ W_0$, where $H_0 = W_0$. The SST denotes a continuous process occurring in a notionally homogeneous material at a constant level of the net-section stress, wherein the increments in the crack mouth spacing, $2\Delta s_s$, are in direct proportion to the increments in the crack tip spacing, $2\Delta c_s$. During this omnidirectional and proportional enlargement of the crack cavity, the outer BSE boundaries are free to move under a prescribed value of the stress biaxiality ratio $k = q^{\infty}/\sigma^{\infty}$.

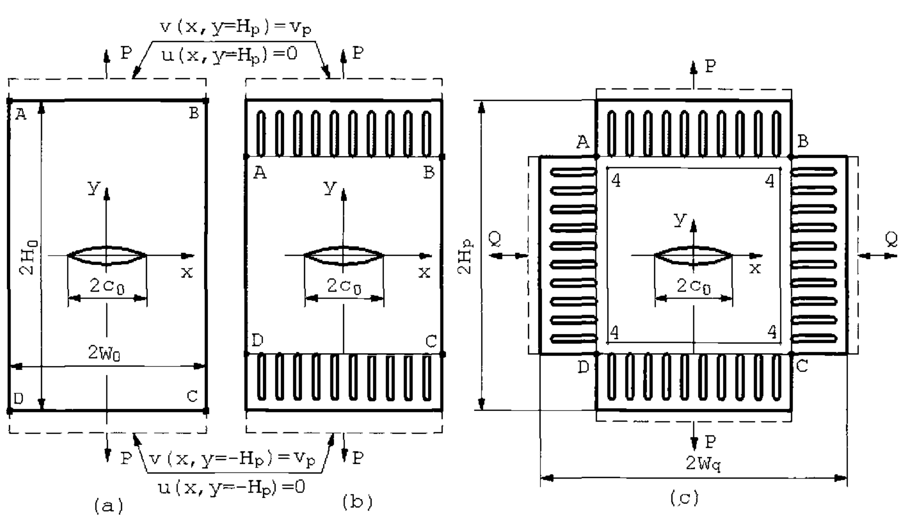

FIG. 1—*The problem domain ABCD attached to different loading gadgets referred to as* (a) – *M(T),* (b) – *MM(T), and* (c) – *MM(T-TC) specimens.*

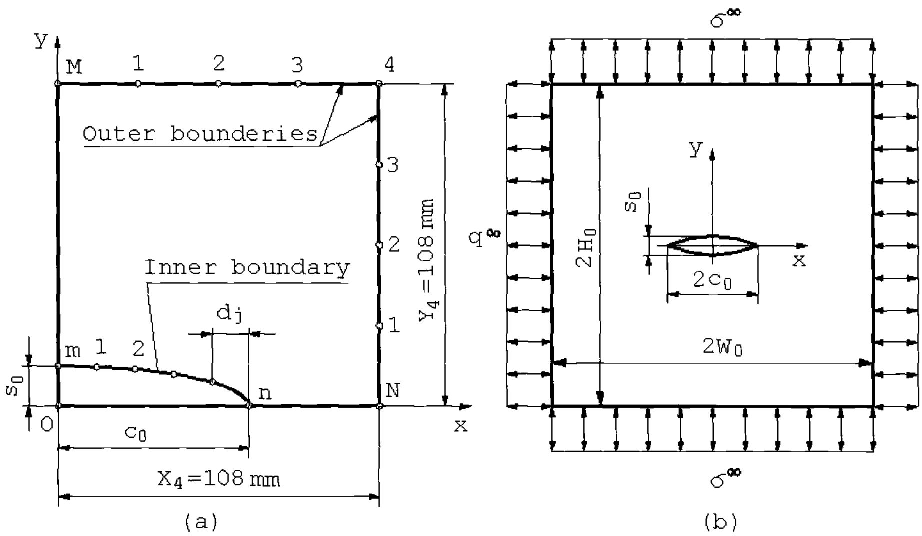

FIG. 2—*One-quarter of a uniformly stressed region in an MM(T-TC) specimen shown schematically* (a) *and the Basic Structural Element* (b).

The input data on the SST are collected on two or more identical specimens with original cracks or starting slots of different length. In this way, the UM attempts to formalize the characterization of the entire crack profile using only the interrelations between loads, displacements, and crack cavity extensions without investigation into the physical damage mechanisms of the fracture process. The emphasis at this point is on studying the effects of the specimen geometry, boundary restraints, and loading conditions on the SST process rather than the effect of the material properties. This purely mechanistic approach is based on the assumption that the material microstructure does not affect some general features of strain localization and plane stress crack growth in a sufficiently large specimen. Consequently, the global fracture behavior expressed in terms of averaged quantities might be assessed immediately from diagrams of loads versus displacements versus distances between extreme points on the specimen surface. The extreme points *m* and *n* on the inner boundaries, i.e., on the crack profile, are shown in Fig. 2*a* together with the corresponding extreme points *M* and *N* on the outer PD boundaries.

As to the effects of particular material properties, special-purpose tensile tests of the UM are performed in parallel on unnotched specimens. They provide baseline data on the mechanical behavior of the material within an Active Damage Zone (ADZ) unaffected by the presence of crack-wake regions ($2c_0 = 0$). We assume that the localized zone of active damage encompasses a certain volume of the severely transformed material in which the tear processes develop a specific damage morphology. At the instant of nucleation of a naturally-forming tear crack, the ADZ is considered to be fully developed. Its parameters taken together with the SST parameters are incorporated in a calculation model describing the BSE static response.

It is instructive to outline the UM approach as applied to analyzing a simple problem of stable crack growth in an extremely brittle engineering material under uniform and proportional loading with the fixed stress biaxiality ratio k [14–16]. The following hypothesis was taken as a starting point: the physical essence of fracture micromechanisms within the ADZ is independent of the values of the k ratio and constraint ratio $L_s = \sigma_{Ns}^{\infty} / \sigma_{ult}$. Here σ_{Ns}^{∞} and σ_{ult} are the tensile stresses averaged over the net-sections of the plate and ADZ, respectively. This suggests that the model descriptions of fracture in tension-dominant and compression-dominant crack geometries might be conceptually identical. The simplest and still physically relevant approach is to treat the SST as a continuous process of omnidirectional extension of an ideal crack in the form of an elliptic hole. This hole in a stress-free BSE has a fixed radius of its tips $\rho_0 = b_0^2 / c_0$, where b_0 and c_0 are the minor and major semi-axes of the hole.

For an isolated elliptical crack in a homogeneous linear elastic material, the potential energy release rate $J_s(k)$ is given by [15,16]

$$J_S(k) = \frac{\pi \cdot \sigma_S^2 \cdot c_S}{E'} \cdot \left[1 + 0.5 \cdot \frac{\rho_0}{c_S} \cdot k^2 + 0.375 \cdot \left(\frac{\rho_0}{c_S} \right)^{1/2} \cdot (1-k)^2 \right], \tag{1}$$

where $E' = E$ for the plane stress state, and $E' = E / (1 - \nu^2)$ for the plane strain, E is the elastic modulus, and ν is the Poisson ratio. In the case of the commonly accepted crack modeling, $\rho = 0$ and, as it follows from Eq 1, $J_s(k) = G_s(0)$, where $G_s(0)$ is Griffith's elastic energy release rate [12]. Our experimental results obtained on specimens from glassy materials of different physical nature demonstrate [13–16] that under conditions of the superimposed compression q^{∞}, the fracture toughness enhances. For example, the ratio of the energy-based characteristics $[J_s(k = -\infty) / J_s(k = 0)]$ for crack growth in silicate-based glass under uniaxial loading in compression and tension attains a value of approximately 64. These and other findings agree with the direction of constraint-dependent variations in the fracture toughness of metallic materials. The case in point is the well-established dependencies of the type $J_c - Q$, where Q is the constraint parameter of O'Dowd and Shih [7,8].

Scope and Limitations

This paper deals with characterization of the SST under uncontained yielding in flat specimens (Fig. 1) made from thin sheets of aluminum alloy. The principal obstacle to the development of the basic TL in the given extremely complicated instance is placed by a need for correlating too many variables governing the plane stress crack growth in ductile materials. These are the parameters of elasticity, including out-of-plane deformation (buckling); plasticity, including residual stress effects; geometrical imperfections and material inhomogeneity; diffuse and localized necking; damage and cracking.

To develop an easy-to-use TL, we accept the following limitations: (i) the specimen and the component are made of the same thin-sheet material, i.e., the initial thickness B_0, its variability, and all other inhomogeneities, including plastic anisotropy, are identical; (ii) during the nucleation and subsequent propagation of a naturally-forming tear crack, the specimen and the component are deformed only in the initial plane; (iii) both crack tips grow slowly and continuously from the instant of fracture initiation until a critical failure event of practical importance occurs, and (iiii) the same critical event is observed in the specimen and the component.

In tensile tests of unnotched thin specimens, necking is an important precursor to nucleation of a tear crack. For a geometrically perfect rate-insensitive sheet metal subjected to tension, Hill [24] developed a theoretical analysis of necking behavior. To predict necking for biaxial stretching, Marciniak and Kuczynski [25] introduced a geometrical imperfection in the form of a band of reduced thickness. In the UM, the initial imperfection is intended to trigger a progressive process of single-site necking followed by single-site cracking in a predefined location and direction. Because of this, we also assume that the unnotched specimens contain a centrally placed geometrical imperfection of sufficiently small size. In practical terms, the sensitivity of test records to this imperfection is thought to be negligibly small.

Despite the above set of highly restrictive limitations, the basic TL can only be an approximation useful for assessing the SST in one structural component or another. The point is that apart from the stress biaxiality ratio, the in-plane constraint depends on the shape and size of an actual component, initial crack length and amount of crack advance, kinematic restraints imposed on its boundaries, far field gradients, including compliant boundary conditions and shear effects, material stress-strain properties, extent of plasticity in metallic or microcracking in nonmetallic materials, prior loading history, and magnitude of applied loads. The effects of the most important (decisive) variables on the SST in a particular component can be assessed numerically, i.e., by the finite element analysis. In assessing its behavior, the BSE should be treated as a square element removed from the component subjected to given operating conditions. The characteristics of the SST and ADZ have to be used in numerical simulations as the basic material properties associated with a prescribed value of the stress biaxiality ratio k.

Specimens and Objectives

A need for a better understanding of the reason for the gap between the results of the model descriptions and measurements dictates the breadth of experimental efforts. Therefore, the fracture tests in question are meant to give the "big picture" of the structural behavior of a middle-cracked plate under different constraint states (Fig. 1). The uniaxial crack extension tests were performed on flat specimens with PDs of various sizes given in Table 1. Each rectangular PD is attached to a specific Loading Gadget (LG).

TABLE 1—*Specimens and specific problems under examination.*

Specimen Code[a]	Principal Dimensions, mm			$2c_0$, mm	Purpose of Investigation
	$2W_0$	$2H_0$	$2H_p$		
M(T)-2.0	240	480	480	96	
M(T)-1.0	240	240	240	96	Elastic response
M(T)-0.5	240	120	120	96	
MM(T)-1.0	240	240	480	96	
MM(T)-0.5	240	120	360	96	
LM(T)-2.0	120	240	240	Variable	Predictive capabilities
HM(T)-0.4	166	66.4	66.4	Variable	
MM(T-TC)[b]	240	240	480	Variable	Structural behavior

[a]The numerical value in a specimen code denotes the shape ratio H_0 / W_0.
[b]$2W_q = 2H_p = 480$ mm (see Fig. 1*c*).

Three types of LGs were used. The first one provides rigid clamping along the horizontal boundaries of a PD (Fig. 1*a*). If the shape requirements $H_0 \geq 2\ W_0$ and $c \leq W_0 / 3$ are fulfilled and buckling is prevented, this geometry is usually referred to as the standard M(T) specimen.

The second LG ensures a nearly uniform distribution of the nominal tensile stress $\sigma^{\infty}(x)$ on the horizontal boundaries of a PD with no initial crack. This specimen geometry (Fig. 1*b*) is referred to as MM(T). Along the lines $y = \pm H_p$, the specimen is rigidly clamped as in the previous case. Finally, the third LG in combination with a square PD represents a cruciform specimen (Fig. 1*c*) designated as MM(T-TC). When $2c_0 = 0$, nearly uniform stresses $\sigma^{\infty}(x)$ and $q^{\infty}(y)$ prevail on the horizontal and vertical boundaries of the given PD, respectively. Along the lines $x = \pm W_q$ and $y = \pm H_p$, the specimen is rigidly clamped.

The problem under consideration is addressed in two parts. We start with comparing the elastic behavior of nominally identical center cracks in rectangular plates of different geometry under different boundary conditions. The intent is to reveal the distinctions between the parameters of an actual and an ideal crack. The latter is commonly specified by the following conditions: $a = c_0 = c_u$ and $s_0 = s_u = 0$ (Fig. 2*a*). Here, $2a$ is the length of an ideal crack, $2c_0$ and $2c_u$ are the lengths of an actual crack in a stress-free and a completely unloaded PD, respectively, and $2s_0$ and $2s_u$ are the Crack-Mouth Opening Spacings (CMOS) of an actual crack in a stress-free and a completely unloaded PD, respectively.

In the second part of this work, three clearly different characterizations of plane stress tearing are contrasted to each other. The objective is to determine whether they can or cannot assess the critical state of a growing crack under uniaxial tension and uncontained yielding. It is reasonable to demonstrate this capability using laboratory-size specimens sufficiently large in comparison with the fully developed ADZ. As such, we take the low-constrained LM(T) and highly-constrained HM(T) specimens (see Table 1). They are used mainly for comparing different characterizations of plane stress tearing. For the LM(T) and HM(T) specimens, the distance $2H_0$ between the clamped boundaries (see Fig. 1*a*) is equal to $2W_0$ and $0.4W_0$, respectively. Here the idea is to extend the range of constraint variation for a relatively small specimen of standard configuration using the same LG.

Experimental Procedure

In collecting test data, a purely mechanistic approach based on the minimum of assumptions was adopted. Elastic displacements as a function of the tensile load P (Fig. 1) were measured concurrently at different points placed near the inner and outer boundaries as shown in Fig. 2*a*. Moreover, we measured the x and y components of the displacement along the x-axis.

Material Properties

The test material is aluminum 1163 AT in as-received condition having the form of 1.05 mm thick sheets. This is a high strength low hardening alloy whose chemical composition and mechanical properties are nearly identical to those of AL 2024-T3. The specimens were all made such that the load P was parallel to the rolling direction of the sheets. The sheet-type specimens were fabricated and tested in accordance with the ASTM Standard Method for Tension Testing of Metallic Materials (E 8M-85). The tensile properties of AL 1163 AT under ambient conditions are as follows: the elastic modulus $E = 73$ GPa, Poisson's ratio $\nu = 0.32$, the 0.2 % offset yield strength $\sigma_y = 334$ MPa, and the ultimate strength $\sigma_u = 446$ MPa.

Original Crack-Like Defects

In the specimen preparation, special care was taken to prevent the introduction of uncontrollable initial damage and residual stresses into the material to be tested. Most of the specimens contain initial fatigue precracks at the tips of a starting slot. However, it is common knowledge that the crack extension resistance of metallic materials may be influenced significantly by the preload history. In particular, a strong influence of the cyclic crack growth history on the fracture toughness of thin-sheet aluminum alloy 2024-T3 was reported in [26] for a specific value of the ratio B_0 / c.

At present, there is no possibility to establish a one-to-one correspondence between the initial fatigue damage near the crack tips in our specimens whose geometry and boundary restraints vary over wide ranges. That is why we perform additional tests pursuing a well-defined goal, namely, concurrent estimation of the response to loading for extremely different crack-like defects. One of them introduces the minimum and the other the maximum levels of initial damage. By convention, a specified starting slot is taken as a damage-free defect. A tearing precrack represents the other extreme of the loading history for which crack-tip blunting, crack tunneling, residual stress-strain fields, local neck, and shear lips are considered to be fully developed.

A centered starting slot of length $2n_t$ was made in each specimen by manual cutting. The depth of cut was kept to the practical minimum for a jeweler's saw. All slots had nominally straight and parallel flanks with the spacing $2s_t$ less than 0.12 mm and the root radii less than 0.06 mm. In low-stress fatigue precracking under constant amplitude cyclic loading by uniaxial tension at the stress ratio $R = 0.4$, the maximum net-section stress σ_N was about 55 MPa. In tear precracking, the σ_N stress level was above the yield strength σ_y of the material. Note that on unloading, a tear crack in the M(T)-2.0 specimens (Table 1) continues to grow by 2–3 mm. The original length $2c_0$ of fatigue and tear precracks extended from both slot ends usually meets the requirement $c_t = n_t + 6B_0$, where $B_0 = 1.05$ mm. The coefficient 6 was used to establish the onset of the pseudo-steady tearing stage from measurements of the near-crack-tip profile (see Fig. 2*a*) in the range $(c_0 - 6B_0) \leq x \leq (c_0 - d_j)$, where $d_j = 0.5$ mm [20].

Specimen Testing

Uniaxial quasi-static tests were conducted in accordance with the main requirements of the ASTM Standard Practice for R-Curve Determination (E 561-92a). All specimens (Table 1) were tested with guide plates lightly clamped against the out-of-plane displacement. Buckling behavior of thin plates is a competitive failure mechanism resulting from the elastic compressive stress acting parallel to the crack. We suggest that various guide plate systems used in our tests do allow decoupling the fracture process from the buckling behavior. However, the stiffness of these plates was different and unknown. It must be noted here that in wide panel tests conducted by Dawicke et al. [27], the load versus crack extension diagram strongly depends on the stiffness of the guide plate system. In practice, buckling is often not restrained, resulting in crack growth at a lower load.

Prior to conducting tests, the elastic compliances of the points located near the crack borders and outer boundaries of a PD (see Fig. 2*a*) were measured along the x- and y-axes. In the course of crosshead-displacement controlled tests, the specimens were loaded incrementally, allowing the time between steps for the crack to stabilize before measuring the load, crack length, and crack profile. To develop R-curves with confidence, we usually assigned more than fifteen steps (data points) for each test condition. Once the crack stabilized within seconds of stopping loading, a close-up photograph of the near-crack-tip profile $[x > (c_t - 6B_0)]$ was taken. In most cases, five diagrams were recorded simultaneously, namely, load P versus $2v(x = 0, y = \pm 1$ mm), load P versus transverse displacement $2v_M$ of the uniform PD region, load P versus load point displacement $2v_p$, load P versus displacement $2u_N$ of the uniform PD region, and load P versus crack-tip displacement u ($x = c_t - 0.5$ mm, $y = \pm B_0$).

Specific Features of the Approach

Our long-term aim is to develop a practical TL for predicting the critical values of loads, displacements, and crack extensions in plates and shells made from brittle and ductile metallic or nonmetallic materials. Conceptually, the critical failure events in question should be observable during stable crack growth in a simple standard specimen and in a structural component of arbitrary geometry and size subjected to arbitrary loading conditions.

Uniformity of the Elastic Stress State

It should be emphasized that providing a sufficiently high degree of the nominal stress field uniformity in tension- and/or compression-dominant PDs is essential for collecting acceptable test data. In the case of tensile loading, this can be achieved through increasing the aspect ratio H_0 / W_0 for the M(T) specimen (Fig. 1*a*). However, when the PD geometry and size are fixed, some special modifications in the LG design must be used. One of them is applying the external load through thin strips placed between the PD and the grips. Such strips in thin-sheet materials are usually made by saw cutting a specimen as shown in Figs. 1*b* and 1*c*.

The larger the number of slots in each side of the LG and the thinner and longer they are, the larger are the sizes $2X_4$ and $2Y_4$ of the stress uniformity region (denoted 4-4-4-4 in Figs. 1*c* and 2*a*). This region was defined for a crack-free PD with the use of the photoelastic and, in parallel, elastic finite element analyses [28]. The accepted number of the specified slots of length equal to 0.85 W_0 in each side of the MM(T-TC) specimen is 15. In this case, the sizes $2X_4$ and $2Y_4$ reach 0.9 of the PD dimensions $2W_0 = 2H_0 = 240$ mm. The deviation of the peak values of the nominal stress distribution from the average values of the elastic stresses $\sigma^\infty(x) = P / 2W_0 B_0$ and $q^\infty(y) = Q / 2H_0 B_0$ does not exceed 2 % within the uniformly stressed region. There are good reasons to suggest that in our specimens the sizes $2X_4$ and $2Y_4$ are larger than those of typical specimens used in biaxial fracture tests. References [11, 29–32] show an example.

Outer Boundary Restraints

Consider unavoidable distinctions between the boundary conditions for the PDs of the specimens (Fig. 1) and the BSE (Fig. 2*b*) under uniaxial tension. The lack of restraints imposed by an actual LG on the deformation of an actual PD is seldom if ever in occurrence. For typical combinations of the specimen and grips, exact stress and displacement conditions along the boundaries between the middle-cracked PD and LGs are usually nonuniform and unknown. Generally, both stress conditions and displacement conditions are present. Under mixed boundary conditions the applied stress is a function not only of position, but also of the crack aspect ratio c/W_0, H_0 / W_0. Mixed boundary conditions are partway toward the general compliant boundary conditions. Such is indeed the case for the elastic-plastic behavior of the specimens shown in Fig. 1.

When the restraints imposed on the outer boundaries are close to the case of displacement-prescribed loading, fracture response strongly depends on the crack length both in quantitative and qualitative sense [33]. Earlier it was shown [34] that the asymptotic values of the energy dissipation rate R for the MM(T) and MM(T-TC) specimens (Fig. 1) made of low-carbon steel are substantially different. On the other hand, the imposition of the "fixed-grip" and "dead-load" constraints on the outer BSE boundaries may have the effect of eliminating the presence of the remote load q^{∞} (Fig. 2*b*) in the energy rate calculations [11].

Failure Events of Practical Importance

Critical fracture events in the current crack assessment procedures usually correspond to the onset of slow-stable crack growth and/or to the onset of unstable crack propagation. The related parameters are indexed by "*i*" and "*c*", respectively. There are a large number of rather arbitrary definitions of these states depending on the material, geometry, and loading of a cracked body. The transition from the stage of stable crack growth to that of unstable one, which separates the desired states of a component from the undesired states, is more a mechanical than a material problem. By applying the displacement-controlled load nearby the crack surfaces close enough to the crack tip, almost any fracture process in any brittle material can be made stable. This statement is supported by the experimental results on stable crack growth in plates and tubes of brittle nonmetallic materials partly presented by Naumenko et al. in [16,35,36].

The principal obstacle to the development of universal definitions of practically important crack states is placed by a need to determine precise values of the Δc_i and Δc_c crack extensions. The problem is in correlating the averaged amounts of crack extension with the occurrence of distinct physical events. Therefore, the states "*i*" and "*c*" are, generally defined in a practical way by using different assumptions and theoretical relationships. Clearly, the available procedures do not allow establishing in a unified manner the critical states of the BSE subjected to biaxial loading with an arbitrary k value. Consider the crack growth under two extremely different stress states. One plate of a brittle material is subjected to uniaxial compression ($k = -\infty$) and another one of a ductile material to uniaxial tension ($k = 0$).

Tensile diagrams for three identical specimens fractured in uncontained yielding are shown in Fig. 3*a* as a typical example. A common tangent to an initial portion of the softening branch of the diagrams represents the SST stage. Here, two "constructed" events "*e*" and "*s*" are introduced through a new macro-interpretation of the test records. These events have the meaning of the lower and upper limits of the critical event "*c*". Attention is concentrated on the softening portion of the test records representing the highest load-carrying capability of the specimen. This is a straight line characterized by a constant level of the net-section stress $\sigma_{\mathrm{N}}^{\infty} = \sigma^{\infty}\,[W_0/(W_0 - c)]$. The use of the fracture initiation point "*i*" as the critical failure event in the plane stress tearing analysis can give unduly conservative predictions of ductile instability conditions.

Earlier it was demonstrated convincingly by way of experimental examples [13,14,35,37,38] that mode I crack extension in plates and tubes of brittle non-metallic materials tested under uniform compression along the crack line is a highly controllable (stable) process up to the instant "*f*" of complete separation. The achievement of this event is not accompanied by the loss of the load-carrying capability as in the previous case of uniaxial tension. The differences between the imaginary stress level q_{Ns}^{∞} and the actual stress levels at the states "*e*", "*p*", "*s*", "*a*", and "*f*" in Fig. 3*b* are intentionally exaggerated to show the distinctions between the listed points. In fact, these distinctions for specimens made of silicate-based glass were negligibly small.

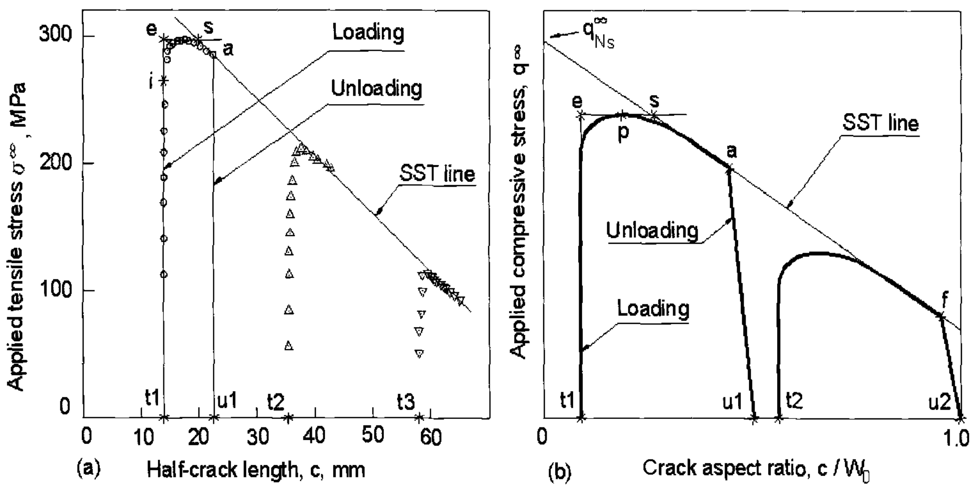

FIG. 3—*Sequences of test records obtained in this work for three aluminum specimens of HM(T)-0.4 geometry with tear precracks of lengths 28, 71, and 116 mm (*a*) and scheme of crack extension in glass specimens as a function of the uniaxially applied compressive stress q^{∞} (*b*).*

The above scheme of establishing the critical states is partly different from the two-point definition of the state "*c*" presented in [20,21]. This is due to the developing nature of the UM. In the previous formulation of the lower limit for the instability event "*c*", the point "*p*," denoting the onset of pseudo-steady tearing, is replaced by the point "*e*" of the pseudo-initiation of tearing (see Fig. 3). This novelty is viewed as a more practical assessment route leading to the development of a sufficiently general TL we search for. Both definitions of the critical state are based on the presentation of test diagrams by linear segments. Such form of treating the test diagrams allows uniform deriving of the failure events "*e*" and "*s*" in specimens of any material directly from raw experimental data.

Fracture Parameters

In the context of this comparison study, the most appropriate characterizations of ductile tearing under large crack extensions are: the CTOA, the Crack Mouth Opening Angle (CMOA), the energy dissipation rate *R*, and a new parameter, the Crack Volume Ratio (CVR). The CTOA is a local variable related to the growing crack tip. Nowadays, it is generally agreed that the constant level ψ_c of the CTOA is a more fundamental fracture criterion value than the J_R or K_R resistance curves [1,2]. Being a parameter of the whole crack border, the CMOA, in comparison with the CTOA, is easy to obtain in an unadulterated form. This advantage of the CMOA comes into particular prominence for testing brittle materials, when the CTOA values are comparatively small. For example, Naumenko and Mitchenko [38] obtained $\psi_1 \cong 0.7°$ and $0.04°$ at the onset of crack growth in PMMA-based and silicate-based glasses, respectively. As regards the energy-based variables, R in comparison with J is a physically more meaningful quantity for describing ductile crack growth. The stationary limit R_∞ of the energy dissipation rate R allows for a physically-based extrapolation beyond the common "validity limits" of J_R-curves [39].

In the characterizations of plane stress tearing based on the measurements of crack-border displacements and energy exchanges, we used the following relationships:

$$\mathrm{CTOA} = \psi = 2 \times \tan^{-1}\left(\delta_g / 2d_g\right), \tag{2}$$

$$\mathrm{CMOA} = \alpha = 2 \times \tan^{-1}\left[\left(s - s^*\right)/c\right], \tag{3}$$

$$R = \frac{1}{2B}\frac{d\left(U - W_{el}\right)}{dc}, \tag{4}$$

where δ_g is the spacing between the upper and the lower crack borders at the fixed distance $d_g = 0.5$ mm behind the moving crack tip, U is the work of the applied force, and W_{el} is the elastic strain energy stored in a PD. The CMOS value $2s^*$ (see Fig. 4) is the main size of a naturally-forming tear crack in a given PD under prescribed boundary conditions.

The CVR is defined as the ratio V_d between the increment ΔM_d in the current volume $M_d = A_d \times B_d$ enclosed by the deformed surfaces of an ideal crack at the instant of interest and the initial volume $M_0 = A_0 \times B_0$ of the same crack at the same instant but for the imaginary state of the PD without structural damage and internal stresses. Here, A_d and A_0 are the in-plane areas of an elliptic hole simulating an actual crack, B_d and B_0 are the crack-tip thickness of the PD. In case of a long initial crack ($2c_0 \geq 10B_0$), the CVR critical values can be determined with the use of simplified equations given by

$$V_e = V_e^{el} + V_e^{pl} = C_e \frac{\left(\sigma_t + \sigma_e\right)}{E} + \frac{2h_{et}}{\pi\sqrt{\rho_0\, c_e}}, \tag{5}$$

$$V_s = V_s^{el} + V_s^{pl} = C_s \frac{\left(\sigma_u + \sigma_s\right)}{E} + \frac{2h_{su}}{\pi\sqrt{\rho_0\, c_s}}. \tag{6}$$

The stress concentration factors C_e and C_s take the form

$$C = F_V\left(\frac{L}{W}\right)\left(1 + 2\sqrt{\frac{c}{\rho_0}} - k\right), \tag{7}$$

where L is the effective size of an equivalent elliptic hole, $L = l + 0.5(1-k)\sqrt{\rho_0 l}$, l is the length of this hole, $l = c + r$, r is the length of an ADZ, F_V is a non-dimensional function of the crack border compliance, σ_t and σ_u are the internal stresses related to the initial state "t" and to the unloaded state "u", respectively (see Fig. 3), and $h_{et} = h_e - h_t$ and $h_{su} = h_s - h_u$ are the increments in the height h of the ADZ due to external loading.

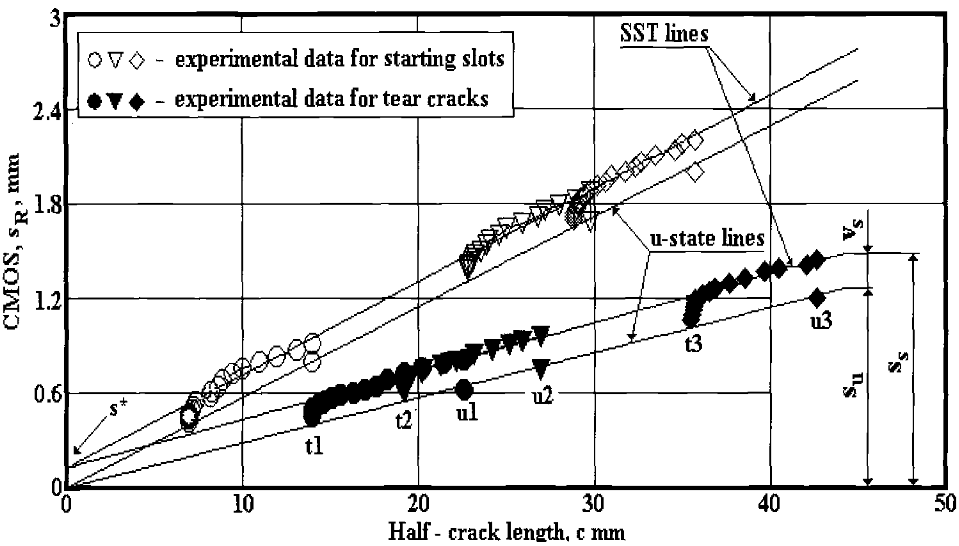

FIG. 4—*Sequences of s_R-curves obtained in this work for three aluminum specimens of HM(T)-0.4 geometry with tear precracks of lengths 28, 71, and 116 mm.*

The radius ρ_0 = 0.262 mm is treated as the characteristic of an actual crack in a given material of a given thickness. The procedures used for estimating the values of ρ_0, h_{et}, and h_{su} are outlined in [15,19–21]. The values σ_t and σ_u for fictitious loading can be defined as uniform tensile stress fields that are internally generated during the accumulation of structural damage expressed in terms of the CMOS values. The corresponding levels of damage are represented in fracture analysis by the global damage ratios $D_t = (s_t / s_f)$ and $D_u = (s_u / s_f)$, where s_t and s_u are the irreversible CMOS components (see Fig. 4). The global fracture parameters V_e and V_s characterizing the variation of the crack-border geometry and the increments h_{et} and h_{su} characterizing the ADZ height variation have the meaning of material constants at a given k ratio for proportional biaxial loading. This suggests that they are unaffected by changes in the PD geometry and size unless there is a change in the outer boundary restraints.

Results and Discussion

First, we consider the correlation between the load and elastic displacements of the fatigue and tear cracks having the length $2c_t$ = 96 mm in a PD of fixed width $2W_t \approx$ 240 mm. The geometry of each PD is characterized by the ratio of the dimensions $H_t \approx H_0$ and $W_t \approx W_0$ (Table 1). This set of test data is compared with the predictions by the appropriate theoretical relationships. The resulting conclusions are helpful for analyzing the experimental data presented in the second part of this work. Here the constraint-dependent critical values of different crack driving parameters are determined and contrasted to each other in an effort to assess the structural behavior of the BSE.

Elastic Displacements of Stationary Crack Borders

Figure 5 shows the displacements $v \approx v_m$ and $u \approx u_n$ measured near the points m and n on the initial crack profiles (see Fig. 2*a*). The reciprocal slopes of the load versus displacement records, v/P and u/P, reveal a significant influence of the PD geometry and boundary restraints on the elastic response of low-stress-level fatigue cracks. As could be expected, the crack-mouth compliance v/P takes the maximum value for the MM(T)-0.5 specimen with nearly free-to-move PD boundaries . However, the value v/P for the M(T)-0.5 specimen having the most constrained PD turns out to be markedly larger than that for the standard M(T) specimen ($H_0/W_0 \geq 2.0$). For the latter, both compliances v/P and u/P are minimal. Referring to Fig. 5*a*, it can be observed that the value v/P has a regular trend toward increasing with a decrease in the H_0/W_0 ratio.

The crack-mouth compliance of all M(T) specimens is higher than the values calculated with the Eftis-Liebowitz equation [40]. This equation was included in the ASTM standard (E 561-92a) in spite of the fact that in the literature empirical determinations of the crack-mouth compliance always give higher values than the above equation. Schijve points out in [41] that the discrepancies vary from a few percent to 11 percent. They may not be due to the approximate character of the Eftis-Liebowitz equation, as exemplified by the finite element analysis presented in [42]. The situation is so unsatisfactory because the above discrepancies could not be explained by the experimental inaccuracies of measurements either.

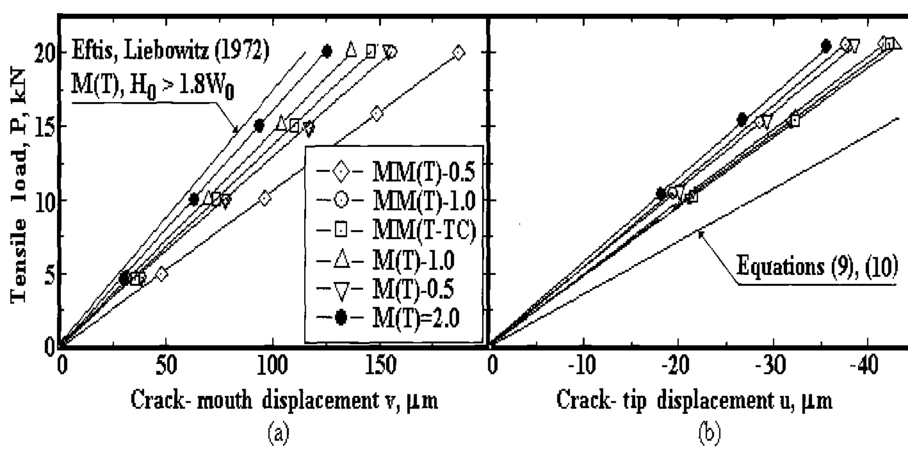

FIG. 5—*Initial portion of test records for fatigue cracks of length $2c_t$ = 96 mm in the PD of the same width $2W_0$ = 240 mm and a varying height.*

To reveal the distinctions between the displacements v and u for an actual crack in an actual PD on one hand and for an ideal crack of the same length in a similar BSE on the other hand, we use the following equations [11]:

$$v = 2\,a\,F_{\mathrm{v}}\left(\frac{a}{W_0}, \frac{H_0}{W_0}\right)\frac{\sigma^{\infty}}{E}, \tag{8}$$

$$u = (k-1)\,a\,F_{\mathrm{u}}\left(\frac{a}{W_0}, \frac{H_0}{W_0}\right)\frac{\sigma^{\infty}}{E}. \tag{9}$$

The normalized values of the crack-mouth F_v and crack-tip F_u compliances are known exactly only for an infinitely large elastic plate subjected to uniform biaxial loading when $F_v = F_u = 1$. The functions F_v and F_u reflect the elastic interaction between the inner and outer boundaries of the finite BSE. As a first approximation, we suggest that in the case of $H_0 \geq W_0$, the appropriate (most simple) functional form is

$$F_v = \left(\sec\frac{\pi a}{2W_0}\right)^{1/2}, \quad F_u \approx F_v. \tag{10}$$

Under this assumption, the v/P value for the BSE is lower, but the u/P value is substantially higher than the respective compliances presented in Fig. 5 for similar specimens. It must be noted here that the stress distributions $\sigma^{\infty}(x)$ and $q^{\infty}(y)$ for the specimens in Figs. 1*b* and 1*c* are noticeably nonuniform even in the case of an isolated crack ($c = 0.1W_0$). This has been established by measurements of elastic displacements in points *M*, *N*, and 1,2,3,4 on the boundaries of the PD (see Fig. 2*a*). Another unexpected result is emerging from comparison of the compliance v/P for a low-stress-level fatigue crack and for a tear crack in the MM(T-TC) specimen. At the top load level $P = 19.6$ kN (see Fig. 5*a*), the measured v values for the tear and fatigue cracks are equal to 108 μm and 140 μm, respectively. At the same time, calculations with the use of Eqs 8 and 10 give $v = 114$ μm. This reverse in "measurements to calculations" interrelation may give additional arguments for discussion on the aforementioned discrepancy between the empirical and theoretical values of the crack-mouth compliance.

Critical Failure States

Hereafter we suggest that the valid criterion of the SST crack growth should be reasonably independent of, at least, the PD geometry, its size, and initial crack length. The local criterion ψ_s depends on the initial crack length $2c_t$ (see Table 2) and boundary restraints (Fig. 6). It is also influenced by changes in the PD size, prior loading history, and load biaxiality [23,43]. The global criterion α_s also depends on all of these variables except for the initial stress raiser length (Fig. 4). In comparison with the surface angle ψ_c, the α_s angle is a more consistent and reproducible quantity, which can be readily measured. It was shown in [44] that a ±10 % scatter in CTOA corresponds to a ±10 % variation in predicted maximum fracture stress.

Transition from the crack-border characterization in terms of the CTOA and CMOA to the energy-based parameter R does not improve the predictive capabilities of fracture analysis. The asymptotic values R_s are sensitive to variations in the PD geometry, initial crack length, and prior loading history (see Table 2). According to the literature data, these values also depend strongly on the type of cracked geometry and specimen size [45,46], boundary restraints, and load biaxiality ratio [34]. It is pertinent to mention that our result for the LM(T)-2.0 specimen ($c_t = 48.3$ mm) nearly coincides with the value $R_s \approx 0.6$ MJ/m^2 presented in [47] for the M(T) specimen made of thin-sheet aluminum 2024 T351.

Going to characterization of the entire crack border, it should be emphasized that there is a strong case for discarding any displacement measurements in favor of the crack-mouth opening displacement $v \approx v_m$ (Fig. 2*a*). When measured during the SST crack extension in conjunction with complete unloading, this quantity allows us to determine the CMOS value $s = s_u + v$ (see Fig. 4). This parameter is used in a three-fold manner: first, as a constituent part of the average

CTOA; second, as a measure of the global damage D accumulated during the SST crack growth in a given PD; and third, as a value needed for the calculation of the UM fracture parameters. The critical values of h and V (Table 2) are determined only for the LM(T)-2.0 specimen due to the lack of the appropriate compliance function F_V for the other specimen geometries.

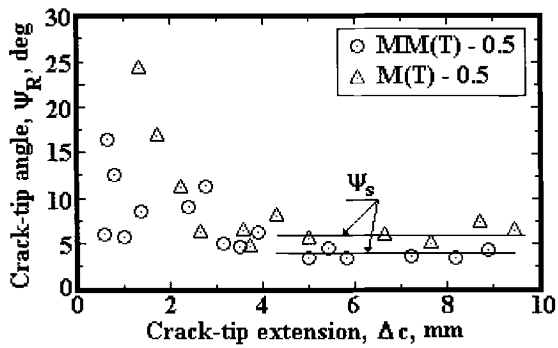

FIG. 6—*Uniaxial ψ_R-curves for fatigue cracks of the same original length $2c_t$ = 96 mm in identical PDs having the same dimensions $2W_0$ = 240 mm and $2H_0$ = 120 mm, which are attached to different LGs shown in Figs. 1*a *and 1*b.

TABLE 2—*Fracture instability parameters for specimens and a square plate: comparison of predictions with measurements.*

Initial stress raiser: type and length, $2c_t$, mm	Normal-sized laboratory specimens					
	Specimen code and size	ψ_s, degree	$\left(\frac{\alpha_s}{\alpha_u}\right)^a$, degree	R_s, MJ/m^2	$\left(\frac{h_{et}}{h_{su}}\right)^b$, mm	$\left(\frac{V_{et}}{V_{su}}\right)^b$
Fatigue precrack 12.4 31.2 48.3	LM(T)-2.0 $2W_0$ = 120 mm $2H_0$ = 240 mm	5.2 ± 1.5 6.3 ± 0.8 8.5 ± 1.5	$\frac{6.57}{5.93}$	1.12 0.88 0.62	$\frac{0.1442}{0.1673}$	$\frac{0.1553}{0.1698}$
Starting slots 14 – 104	HM(T)-0.4 $2W_0$ = 166 mm	...	$\frac{7.52}{7.28}$	1.8 – 0.8	...	...
Tear precracks 28 – 116	$2H_0$ = 66.4 mm	...	$\frac{3.92}{3.63}$	1.1 – 0.7	...	...

Fatigue precrack $2c_t$, mm	Plate of size $2W_0 = 2H_0$ = 240 mm under uniaxial tension					
	Prediction for the BSE			MM(T-TC) tests		
	σ_s, MPa	s_s, mm	Δc_s, mm	σ_s, MPa	s_s, mm	Δc_s, mm
19.35	291.0	0.702	3.2	314.4	0.786	6.1
96.05	153.7	2.805	6.4	194.7	2.510	7.7

[a]The critical CMOA values related to the states "*s*" and "*u*", respectively.
[b]The values above the line refer to the state "*e*" and those below the line to the state "*s*".

Concluding Remarks

In this work, plane stress tearing under general yielding is considered from the viewpoint of a "moving crack tip" embedded into a fully-developed "moving neck." We look at this phenomenon experimentally using in fracture analysis only directly measurable mechanical variables. Eventually, the following conclusions have been made: (i) there is no sufficiently general and practical criterion of the Steady State Tearing (SST) crack growth among the critical values of the Crack Tip Opening Angle (CTOA), ψ_s, Crack Mouth Opening Angle (CMOA), α_u, α_s, energy dissipation rate, R_s, Active Damage Zone (ADZ) dimensions, h_{et}, h_{su}, and r_{su}, and Crack Volume Ratio (CVR), V_{et} and V_{su} determined in this work; (ii) any spacing and any linear or angular displacement measured between any two points on the actual crack border do not govern the SST in a unique manner; (iii) of the above parameters, the quantities α_u, α_s, h_{et}, h_{su}, V_{et}, and V_{su}, when determined in parallel, are preferable, and (iiii) in practical applications, however, these SST characteristics by themselves do not allow us to foresee the effects of the whole variety of Problem Domain (PD) shapes and sizes, boundary restraints, material properties, and service loading conditions.

To get out of this difficulty, the so-called crack distortion d_{cs} and boundary distortion d_{bs} ratios have to be incorporated in the Unified Methodology (UM) of fracture analysis as new in-plane constraint parameters given by:

$$d_{cs} = \frac{u_n}{v_m} \cdot \frac{s_f}{c_f} \text{ and } d_{bs} = \frac{u_N}{v_M} \cdot \frac{H_{Mf}}{W_{Nf}}, \tag{11}$$

where s_f, c_f and H_{Mf}, W_{Nf} designate the characteristic dimensions of the crack cavity and PD, respectively, at the instant of complete fracture. Here, the basic idea is to quantify the interaction between the inner and outer boundaries of a PD in terms of purely geometric variables, which can be readily measured. The fracture parameters α_u, α_s, h_{et}, h_{su}, V_{et}, and V_{su}, on one hand, and the constraint parameters d_{cs} and d_{bs}, on the other hand, should be determined explicitly and related to each other directly.

Our measurements of the displacements u_n, u_N and v_m, v_M (see Fig. 2*a*) demonstrate convincingly that a decrease in the spacing $2H_0$ between the rigidly clamped boundaries of a PD with a fixed dimension $2W_0$ elevates the constraint level. The latter can be expressed in terms of the proximity to the conditions of plane strain necking, when there is no straining of the PD boundaries (AD and BC in Fig. 1) along the crack line. In the case of stable crack growth under general yielding, the smaller was the deviation from the condition $d_{bs} = 0$, the lower were the values of the angle ψ_s [35] and the active component of the CMOA, $\alpha_{st} = \alpha_s - \alpha_{su}$, [48].

It appears that there is a need for too many variables to describe the constraint-dependent crack extension properly. However, a semi-analytic fracture modeling used in the UM may have advantages of an appropriate engineering approximation. The above mechanical parameters all can and have to be readily collected in tests of two or more identical specimens with original cracks of different lengths. In addition, the influence of particular material properties on the fracture process is characterized through performing special-purpose tests of the UM. Preliminary experimental results of Naumenko et al. [49] reveal an intimate relationship between the parameters of the fully-developed ADZ and those of the SST crack growth. This two-step approach keeps the derivation of the basic Transferring Law (TL) from becoming too involved since it accounts for the effects of the plasticity and physical damage mechanisms immediately from test records.

Acknowledgments

We are grateful to the Science and Technology Center in Ukraine and the European Union for providing financial support of this work through the STCU project No 2212. The numerous and valuable critical comments of Prof. J. C. Newman, Jr. are deeply appreciated.

References

[1] Newman, J. C., Jr., James, M. A., and Zebst, U., "A Review of the CTOA/CTOD Fracture Criterion," *Engineering Fracture Mechanics*, Vol. 70, 2003, pp. 371–385.

[2] Schödel, M. and Zebst, U., "Application of the European Flaw Assessment Procedure SINTAP to Thin Wall Structures," *Engineering Fracture Mechanics*, Vol. 71, 2004, pp. 1035–1058.

[3] Hutchinson, J. W., "Plastic Stress and Strain Fields at a Crack Tip," *Journal of Mechanics and Physics of Solids*, Vol. 16, 1968, pp. 337–347.

[4] Dadkhah, M. S. and Kobayashi, A. S., "Two-Parameter Crack-Tip Fields Associated with Stable Crack Growth in a Thin Plate: An Experimental Study," *Fracture Mechanics: Twenty-Fourth Volume, ASTM STP 1207*, J. D. Landes, D. E. Mccabe, and J. A. M. Boulet, Eds., ASTM International, West Conshohocken, PA, 1994, pp.48–61.

[5] Rice, J. R. and Rosengren, G. F., "Plane Strain Deformation Near a Crack-Tip in a Power-Law Hardening Material," *Journal Mechanics Physics of Solids*, Vol. 16, 1968, pp. 1–12.

[6] Hutchinson, J. W., "Singular Behavior at the End of a Tensile Crack in a Hardening Material," *Journal Mechanics and Physics of Solids*, Vol. 16, 1968, pp. 13–31.

[7] O'Dowd, N. P. and Shih, C. F., "Family of Crack-Tip Fields Characterized by a Triaxility Parameter – I. Structure of Fields," *Journal Mechanics and Physics of Solids*, Vol. 39, 1991, pp. 989–1015.

[8] O'Dowd, N. P. and Shih, C. F., "Family of Crack-Tip Fields Characterized by a Triaxility Parameter – II. Fracture Applications," *Journal Mechanics and Physics of Solids*, Vol. 40, 1992, pp. 939–963.

[9] Betegon, C. and Hancock, J. W., "Two-Parameter Characterization of Elastic-Plastic Crack Tip Fields," *Journal of Applied Mechanics*, Vol. 58, 1991, pp. 104–113.

[10] Sinclair, G. B., Kondo, M., and Pieri, R. V., "The Size Dependence of Fracture Toughness for Two Embrittled Materials," *International Journal of Fracture*, Vol. 72, 1995, pp. 3–10.

[11] Eftis, J., Jones, D. L., and Liebowitz, H., "Load Biaxiality and Fracture Synthesis and Summary," *Engineering Fracture Mechanics*, Vol. 36, No. 4, 1990, pp. 537–574.

[12] Griffith, A. A., "The Phenomenon of Rupture and Flow in Solids," *Phil. Trans. Roy. Society*, Ser. A, Vol. 221, 1920, pp. 163–198.

[13] Naumenko, V. P. and Mitchenko, O. V., "Brittle Fracture of a Plate with a Hole in Compression," *Strength of Materials*, Vol. 17, No. 7, 1985, pp. 890–900.

[14] Pisarenko, G. S., Naumenko, V. P., and Stepkov, V. M., "Brittle Fracture under Uniaxial and Biaxial Loading," (in Russian), *Strength of Materials and Structural Components under a Complex Stress State*, Kiev, Naukova Dumka, 1986, pp. 196–201.

[15] Naumenko, V. P., "Brittle Fracture and Strength of Materials under Compression and Tension," (in Russian), *Preprint of the Institute for Problems of Strength of the Ac. Sci. of Ukr.SSR*, Kiev, 1987, 38 pp.

[16] Naumenko, V. P., "Modeling of Brittle Fracture in Tension and Compression," *Fracture Processes in Concrete, Rock and Ceramics (RILEM/ESIS)*, J. G. M. van Mier, J. G. Rots, and A. Bakker, Eds., London, Vol. 8, 1991, pp. 183–192.

[17] Pisarenko, G. S., Naumenko, V. P., and Onishchenko, E. E., "Elasto-Plastic Mode I Fracture of Thin-Sheet Steel under Biaxial Loading," (in Russian), *Preprint of the Institute for Problems of Strength of the Ac. Sci. of Ukr.SSR*, Kiev, 1983, 64 pp.

[18] Naumenko, V. P., and Rakovsky, V. A., "Crack Growth Onset in Biaxially Loaded Elasto-Plastic Plates," *Defect Assessment in Components – Fundamentals and Applications (ESIS/ECF9)*, J. C. Blouel and K.-H. Schwalbe, Eds., London, 1991, pp. 363–377.

[19] Naumenko, V. P., "Why and How the Elastic Response of an Ideal Crack Is to Be Harmonized with That of an Actual Crack," *Fracture from Defects (ECF 11)*, Vol. 2, M. M. Brown, E. R. de los Rios, and K .J. Miller, Eds., Sheffield, UK, 1998, pp. 1083–1088.

[20] Naumenko, V. P., "A Transferring Law for Prediction of the Steady-State Crack Growth in Thin-Wall Structures," *Life Assessment and Management for Structural Components*, V. T. Troshchenko, Ed., Logos, Kiev, Ukraine, 2000, pp. 287–298.

[21] Naumenko, V. P., "Single-Parameter Prediction of Stable Crack Growth in Large-Scale Panels," *Fracture Mechanics Beyond 2000, Proceedings of the ECF 14*, A. Neimitz, I. V. Rokach, D. Kocanda and K. Golos, Eds, Vol.II, pp. 543–550.

[22] Naumenko, V. P. and Volkov, G. S., "Engineering Assessment of Tear Cracks in Large-Scale Panels from Thin-Sheet Aluminium," *Sixth International Conference on Engineering Structural Integrity Assessment*, Manchester, UK, 2002, 8 pp.

[23] Naumenko, V. P., Volkov, G. S., and Atkins, A. G., "Initiation and Propagation of Ductile Tearing: A Search for Biaxial Fracture Criterion," *Proceedings of the Sixth International Conference on Biaxial/Multiaxial Fatigue and Fracture*, M. M. de Freitas, Ed., Lisboa, Vol. 11, 2001, pp. 975–982.

[24] Hill, R., "On Discontinuous Plastic States, with Special Reference to Localized Necking in Thin Sheets" *Journal of Mechanics and Physics of Solids*, Vol. 1, 1952, pp. 19–30.

[25] Marciniak, Z. and Kuszynski, K., "Limit Strain in the Processes of Stretch-Forming Sheet Metal," *International Journal of Mechanical Science*, Vol. 9, 1967, pp. 609–620.

[26] Newman, J. C., Jr., Dawicke, D. S., and Bigelow, C. A., "Finite-Element Analysis and Measurement of CTOA During Stable Tearing in a Thin-Sheet Aluminum Alloy," *Proceedings from the International Workshop on Structural Integrity of Aging Airplanes*, Atlanta, 1992, pp. 167–186.

[27] Dawicke, D. S., Gullerud, A. S., Dodds, R. H., Jr., and Hampton, R. W., "Residual Strength Predictions with Crack Buckling," *The Second Joint NASA/FAA/DoD Conference on Aging Aircraft*, C. E. Harris, Ed., NASA CP-208982, 1999, pp. 565–574.

[28] Pisarenko, G. S., Naumenko, V. P., and Onishchenko, E. E., "A Method for Investigating the Fracture of Sheet Materials in Biaxial Loading," *Strength of Materials*, Vol. 14, No. 3, 1982, pp. 275–282.

[29] Kibler, J. J. and Roberts, R., "The Effect of Biaxial Stresses on Fatigue and Fracture," *Transactions of ASME, Journal of Engineering and Industry*, Vol. 92, 1970, pp. 727–734.

[30] Abou-Sayed, I. S., Broek, D., Forte, T. P., and Stonesifer, R. B., "Plane Stress Fracture under Biaxial Loading," *Advances in Fracture Research (ICF5)*, D. Francois, Ed., Pergamon Press, Vol. 4, 1981, pp. 1707–1713.

[31] Garwood, S. I., Davey, T. G., and Cresswell, S. I., "Behavior of A533B under Biaxial

Loading at +70°C," *International Journal of Pressure Vessels and Piping*, Vol. 36, 1989, pp.199–224.

[32] Dalle Done, C. and Döker, H., "Biaxial Load Effects on Plane Stress J-Δa and $\delta_5 - \Delta a$ – Curves," *Structural Integrity: Experiments, Models and Applications (ECF 10)*, Berlin, 1994, pp. 891–900.

[33] Boiko, A. V., Karpenko, L. N., Lebedev, A. A., Muzika, N. R., and Zagornyak, O. V., "Calculation-Experimental Method for Determining Crack Resistance of Material under Biaxial Loading," *Engineering Fracture Mechanics*, Vol. 64, 1999, pp. 203–215.

[34] Naumenko, V. P. and Kolednik, O., "Load Biaxiality Effects on the Fracture Resistance of Thin Steel Plates," *Structural Integrity: Experiments, Models and Applications (ECF 10)*, Berlin, 1994, pp. 911–917.

[35] Pisarenko, G. S. and Naumenko, V. P., "Experimental Methods of the Materials Fracture Mechanics," *Soviet Material Science*, Vol. 18, No. 2, 1982, pp. 110–120.

[36] Naumenko, V. P. and Sopenko, S. I., "The Test Method for Crack Growth Resistance and Elasticity Characteristics Evaluation for Brittle Nonmetallic Materials," *Fracture Processes in Concrete, Rock and Ceramics (RILEM/ESIS)*, J. G. M. van Mier, J. G. Rots, and A. Bakker, Eds., London, Vol. 8, 1991, pp. 183–192.

[37] Pisarenko, G. S., Naumenko, V. P., and Stepkov V. M., "The Method and Results of an Experimental Investigation of Fracture Kinetics and Crack Resistance of Brittle Materials," *Strength of Materials*, Vol. 16, No. 12, 1984, pp. 1694–1702.

[38] Naumenko, V. P. and Mitchenko, O. V., "Deformation Parameters of Mode I Fracture in Tension and Compression," *Strength of Materials*, Vol. 24, No. 8, pp. 1072–1080.

[39] Anuschewski, P., Brocks, W., and Hellman, D., "Characterization of Ductile Tearing Resistance by the Energy Dissipation Rate: Effects of Material, Specimen Type and Size," *Report GKSS 2002/13*, GKSS Research Centre, Geesthacht, 2002.

[40] Eftis, J. and Liebowitz, H., "On the Modified Westergaard Equations for Certain Plane Crack Problems," *International Journal of Fracture Mechanics*, Vol. 8, No. 4, pp. 383-392.

[41] Schijve, J., "Some Considerations on the Eftis-Liebowitz Equation for the COD Compliance of a Center Cracked Sheet Specimen," *Engineering Fracture Mechanics*, Vol. 55, No. 3, 1996, pp. 341–346.

[42] Lei, Y. and Neale, B. K., "The Fracture Behavior of a Center Cracked Tensile Specimen," *Fatigue and Fracture of Engineering Materials and Structures*, Vol. 20, No. 2, 1997, pp. 201–216.

[43] Naumenko, V. P., Volkov, G. S., and Atkins, A. G., "Comparison Studies of R-Curves for Fatigue and Tear Cracks in a Thin Aluminum Plate," *Fracture Mechanics: Applications and Challenges (ECF 13)*, San Sebastian, Spain, 2000, reference 1A.34, 8 pp.

[44] Dawicke, D. S., Piascik, R. S., and Newman, J. C., Jr., "Prediction of Stable Tearing and Fracture of a 2000-Series Aluminum Alloy Plate Using a CTOA Criterion," *Fatigue and Fracture Mechanics: 27th Volume, ASTM STP 1296*, R. S. Piascik, J. C. Newman, and N. E. Dowling, Eds., ASTM International, West Conshohocken, PA, 1997, pp. 90–104.

[45] Brocks, W., Eberle, A., Fricke, S., and Veith, H., "Large Stable Crack Growth in Fracture-Mechanics Specimens," *Nuclear Engineering and Design*, Vol. 151, 1994, pp. 387–400.

[46] Kolednik, O., Shan, G., and Fischer, D. F., "The Energy Dissipation Rate - A New Tool

to Interpret Geometry and Size Effects," *Fatigue and Fracture Mechanics: 27th Vol., ASTM STP 1296*, R. S. Piascik, J. C. Newman, Jr., and N. E. Dowling, Eds.,ASTM International, West Conshohocken, PA, 1997, pp. 126–151.

[47] Brocks, W., "Energy Dissipation Rate and Crack Propagation Energy in Ductile Tearing," *Proceedings of Euromech* 291, St. Petersburg, 1992, pp. 1–15.

[48] Naumenko, V. P. and Skrypnyk, Yu. D., "Steady State Tearing in Thin Aluminum Sheets under Uniaxial Tension," *To be published in the Proceedings of the ECF15, Advanced Fracture Mechanics for Life and Safety Assessment*, Stockholm, 2004, 8 ppp.

[49] Naumenko, V. P., Volkov, G. S., and Skrypnyk, Yu. D., "Assessment of the Life Cycle for Metal Sheets under Monotonically Increased Loading," *To be published in the Proceedings of the ESIA7, Structural Integrity Assessment for Life Cycle Management*, Manchester, UK, 2004, 8 pp.

Journal of ASTM International, June 2005, Vol. 2, No. 6
Paper ID JAI12847
Available online at www.astm.org

S. C. Forth,[1] *J. C. Newman, Jr.,*[2] *and R. G. Forman*[3]

Evaluation of Fatigue Crack Thresholds Using Various Experimental Methods

ABSTRACT: The accurate representation of fatigue crack threshold, the region defining crack growth as either very slow or nonexistent, is extremely important. If the experimentally measured threshold is unconservatively high, a structural component designed with this data may fail long before the fatigue analysis predicts. The fatigue crack growth threshold is experimentally defined using ASTM standard E 647, which has been shown to exhibit anomalies. Alternate test methods have been proposed, such as the constant K_{max} test procedure, to define the threshold regime without ambiguity. However, only the current test method defined by ASTM is designed to produce the range of fatigue crack thresholds (e.g., low and high *R*) needed to characterize an aerospace loading environment. It is the scope of this paper to determine the fatigue crack growth threshold of a well characterized aerospace alloy, 7075-T7351 aluminum, using different methods, to compare the results, and to draw conclusions.

KEYWORDS: fatigue, threshold, crack growth, test methods, plasticity induced crack closure

Introduction

Fatigue crack growth in a material is typically quantified by the size of the crack, *a*, and the rate at which it propagates, *da/dN*. The crack growth rate through a given material is expressed as a function of the linear-elastic fracture mechanics term, ΔK, the stress intensity factor range. This relationship was originally shown to be linear over a large range of fatigue crack growth rates on a log-log scale [1]. However, the relation between crack growth rate and stress intensity is nonlinear when the cracked body is approaching fracture [2] and when the crack growth rate is very slow [3]. Therefore, the three idealized regions of crack growth are defined as the threshold region (slow growth), the linear region (stable growth), and the fracture region (rapid growth) illustrated in Fig. 1.

Ideally, the fatigue crack growth threshold is the asymptotic value of ΔK at which *da/dN* approaches zero [4]. Currently, the threshold is used as a limit for damage tolerant design [5], e.g., if the stress intensity factor for a given crack is below the threshold value, the crack is assumed to be nonpropagating [6]. However, it has been shown that small cracks propagate at ΔK below the threshold value [7] defined using the ASTM standard test procedure. This small crack work studied the growth of microstructural defects [8] inherent to the material [9] that propagate to failure before the design life is reached. Therefore, if the fatigue crack growth threshold is to be established as a lifing criterion, then the most accurate representation of the fatigue characteristics of a material need to be defined.

Manuscript received 26 April 2004; accepted for publication 24 August 2004; published June 2005. Presented at ASTM Symposium on Fatigue and Fracture Mechanics: 34th Volume on 19–21 November 2003 in Tampa, FL; S.R. Daniewicz, J.C. Newman, Jr., and K-H. Schwalbe, Guest Editors.
[1] Research Engineer, NASA Langley Research Center, 2 West Reid Street, Mail Stop 188E, Hampton, VA 23681.
[2] Professor, Department of Aerospace Engineering, 330 Walker Engineering Lab., Hardy Street, Mississippi State University, Mississippi State, MS 39762.
[3] Senior Scientist, NASA Johnson Space Center, 2101 NASA Road 1, Mail Code EM2, Houston, TX 77058.

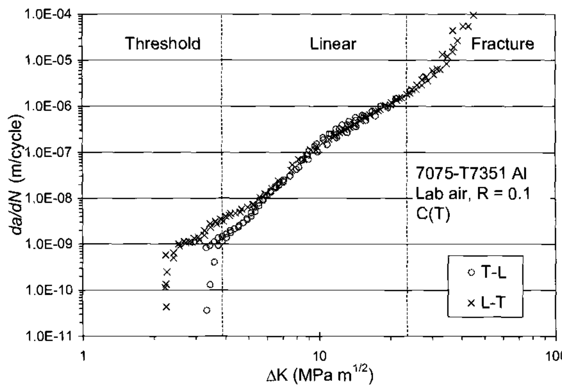

FIG. 1—*Definition of crack growth regions for T-L and L-T data at $R = 0.1$.*

The ASTM Standard E 647 defines an experimental procedure to operationally determine fatigue crack growth threshold. This standard recommends that the threshold stress intensity factor range correspond to a crack growth rate of 10^{-10} m/cycle, which is also used for this study. The specifications for achieving this rate are outlined in the standard using either constant R or constant K_{max} load reduction methods, graphically depicted in Fig. 2. The constant R load reduction method reduces the maximum and minimum load applied to a cracked specimen such that the load ratio, R ($R = K_{min}/K_{max} = P_{min}/P_{max}$) remains constant. The constant K_{max} test procedure imposes a constant K_{max} [10,11] while increasing K_{min} [12,13]. However, for tensile loading, the constant K_{max} test procedure is constrained to producing high R data at threshold. This has been an artifact of the specimen configuration; pin loaded C(T) specimens (similar to the GC(T) specimen in Fig. 3) cannot be subjected to high compressive stresses due to the geometric instability of pin loaded specimens. Hence, to achieve a constant K_{max} threshold for low and negative R values, the middle-crack tension, M(T), specimen (Fig. 4) was employed, which can be tested at high compressive loads [14].

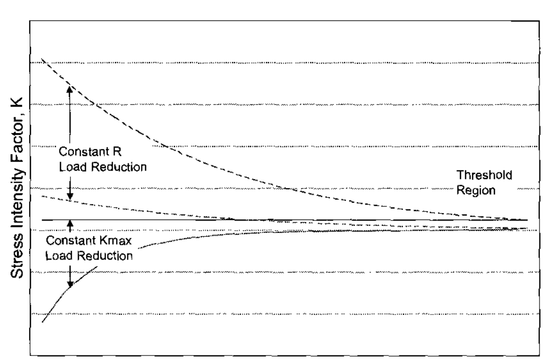

FIG. 2—*Schematic of load reduction methods (Constant R and Constant K_{max}).*

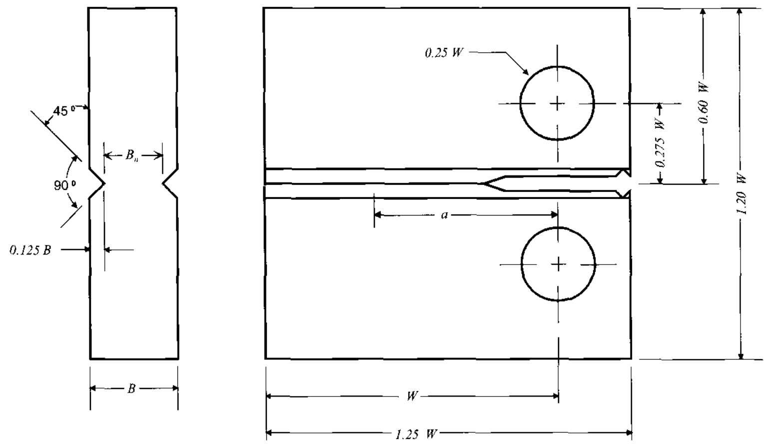

FIG. 3—*Schematic of side-grooved compact tension specimen, GC(T) (W = 76.2 mm, B = 12.7 mm, B_N = 9.53 mm, initial notch length (a) of 19.1 mm).*

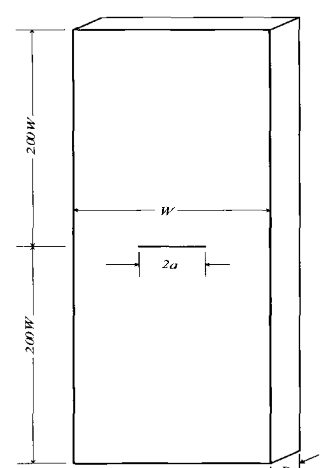

FIG. 4—*Schematic of middle through crack specimen, M(T) (W = 76.2 mm, B = 12.7 mm, initial notch width (2a) of 12.7 mm).*

Experimental results suggest that the constant *R* load reduction test procedure develops remote plasticity-induced crack closure [15,16] that can lead to elevated threshold data. The amount of crack-wake plastic deformation produced during a test is directly related to the magnitude of previously applied crack tip loads, i.e., higher K, more plasticity [17]. The constant *R* load reduction test starts at a high load and sheds load until threshold is reached. Therefore, the initial K will produce larger plastic deformations than subsequent conditions. This plastic wake, or history, can affect the crack driving mechanisms, i.e., during the unloading process the crack will close first at some point along the wake, reducing the effective load at the crack tip [18,19]. This remote closure concept is graphically depicted in Fig. 5. Additionally, the compact tension specimen traditionally used to generate fatigue crack growth data utilizes a notch to initiate crack growth. A crack emanating from a notch often exhibits plane stress behavior near the notch root [20] (Fig. 6) and transitions to a combination of plane strain/stress as the notch effect diminishes. Plane strain plasticity is approximately one-third the size of plane stress [21], further enhancing any plasticity effects at the notch root. Cracks propagating in a material exhibit plane strain behavior in the interior and plane stress behavior at the surface [22], as depicted in Fig. 7, leading to a higher probability of the surface closing prior to the interior. Therefore, if fatigue crack growth data are to be generated with minimal plasticity history effects, so as not to affect test data, then a modification of the specimen geometry and/or test procedure should be made.

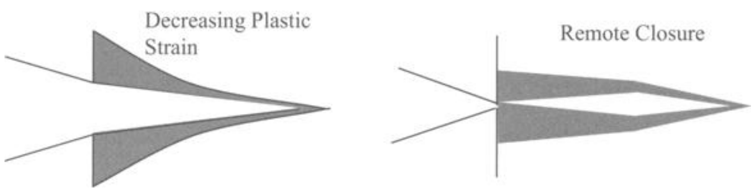

FIG. 5—*Graphical depiction of remote closure.*

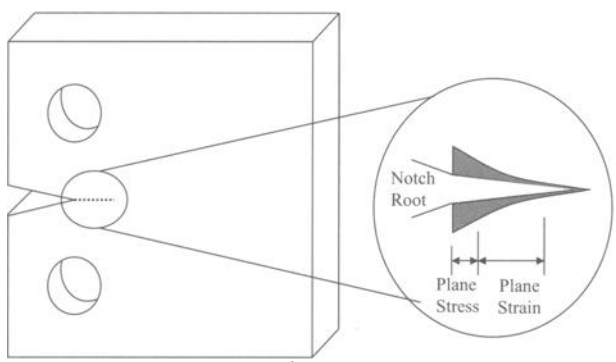

FIG. 6—*Plane stress plastic zone at the notch root.*

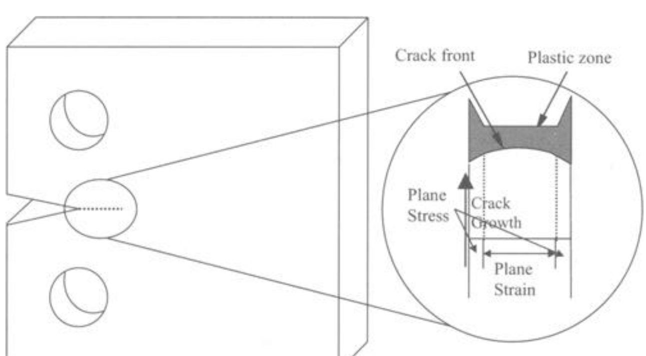

FIG. 7—*Plastic zone in front of the crack.*

Modification of the C(T) specimen geometry to include side-grooves, GC(T), was implemented to force the crack to maintain plane strain behavior by achieving a nearly constant tri-axial stress state along the crack front [23]. The plane strain conditions are realized by removing the material exhibiting plane-stress behavior at the surface, approximately 25 % of the specimen thickness, by introducing 45° grooves along the edges (Fig. 3). As a result, the plastic strains generated along the specimen surface will be as low as one-third that of a full thickness specimen [24].

One way to reduce the effect of remote crack closure is to produce a crack with a larger plastic zone size at the crack tip than along any point in the wake. This can be accomplished by plastically compressing the crack wake [25]. Hence, if compressive loads are used for precracking, the plane stress plastic wake at the notch will be minimal and will not influence the subsequent test results [26]. Another solution to remote closure is to produce fatigue crack growth data by constantly increasing the K under constant amplitude loading conditions [27,28]. The test will impart a constantly increasing plastic zone such that the plastic wake will never close prior to the crack tip closing. Ideally, an increasing K methodology will produce results with little plastic history as steady-state is achieved; there are few plastic wake effects to instigate remote closure, and a "history-free" crack growth curve can be generated using one specimen. In this paper, the authors present fatigue crack growth threshold test data using constant *R* and constant K_{max} load reduction and K increasing test procedures, employing both standard and side-grooved compact tension specimens, as well as constant K_{max} tests with compression-compression precracking.

Experimental Methods

The constant *R* load reduction method, prescribed by ASTM E 647, generates quasi-steady-state fatigue crack growth rates into the threshold region. The generation of near-threshold data is accomplished by reducing the applied load on the specimen in a controlled manner such that the load ratio, *R*, is kept constant, e.g., the maximum and minimum load are continuously reduced throughout the test. The constant K_{max} load reduction method also reduces both the maximum and minimum load to generate threshold data, however the value of K_{max} is constant, while *R* is varying. Controlling the test via stress intensity factors is achieved through monitoring of the crack length during testing and adjusting loads. For the constant K_{max} load reduction test procedure, the applied loads are varied to maintain a constant K_{max} value, while increasing (the absolute value of) K_{min} until the rate of crack growth reaches a predefined amount, in this case the ASTM specified 10^{-10} m/cycle. The rate of load shedding for both procedures is defined by the equation

$$C = \left(\frac{1}{K}\right)\left(\frac{\Delta K}{da}\right) \tag{1}$$

where *C* is the normalized *K* gradient and for the case of a compact tension, C(T), specimen, the stress intensity factors are defined as

$$\Delta K = \frac{\Delta P}{\beta\sqrt{W}}\frac{(2+\alpha)}{(1-\alpha)^{3/2}}\left(0.886+4.64\alpha-13.32\alpha^2+14.72\alpha^3-5.6\alpha^4\right) \tag{2}$$

where

$$\beta = \begin{cases} \mathrm{B} & \text{C(T) specimens} \\ \sqrt{\mathrm{B} \cdot \mathrm{B_N}} & \text{GC(T) specimens} \end{cases}$$ [29], $\alpha = a/W$ for $a/W \geq 0.2$ [30],

ΔP is the applied load range, W is the width of the specimen, B is the thickness of the specimen, B_N is the thickness of the specimen between the side-grooves, and a is the crack length. For this study, the dimensions of the C(T) and GC(T) specimens are defined in Fig. 3, where W = 76.2 mm, B = 12.7 mm, B_N = 9.53 mm (GC(T) only) and an initial notch length of 19.1 mm. The stress intensity solution for an M(T) specimen is given as

$$\Delta K = \frac{\Delta P}{B}\sqrt{\frac{\pi\alpha}{2W}\sec\frac{\pi\alpha}{2}} \tag{3}$$

where $\alpha = 2a/W$ for $2a/W < 0.95$ [31], B is the specimen thickness, and W is the width. For this study, M(T) dimensions are defined in Fig. 4, where W = 76.2 mm, B = 12.7 mm, and the initial notch is 12.7 mm.

The normalized K gradient, C, is algebraically limited to a value greater than $-80\ \mathrm{m}^{-1}$ [32,33], which ensures the rate of load shedding to be gradual enough to: "1) preclude anomalous data resulting from reductions in the stress-intensity factor and concomitant transient growth rates, and 2) allow the establishment of about five *da/dN*, ΔK data points of approximately equal spacing per decade of crack growth rate," as per Section 8.6.2 of the ASTM E 647. Figure 2 graphically depicts the constant R and constant K_{max} load reduction methods.

The compact tension, C(T), and grooved compact tension specimens, GC(T), were precracked with a constant ΔK that is equivalent to the first data point in the load reduction test, unless otherwise noted. These loads were applied until the crack length was an *a/W* of 0.3, as per the ASTM standard. The M(T) tests were precracked using a high compression scheme based on the closure-free test procedures proposed by Au, et al. [34]. The precracking loads, both maximum and minimum loads in compression, were applied until the crack growth rate, *da/dN*, was less than 10^{-10} m/cycle. This compressive scheme was used to produce an initial flaw that had little plastic history [35], so as not to affect the subsequent test [36].

The K increasing test procedure was developed to produce fatigue crack growth data with minimal plastic history effects [27,28]. This was accomplished by first producing a crack from a notch using compressive precracking loads. Then the crack was propagated using a small tensile load, such that the stress intensity factor range was approximately 0.5 MPa $\mathrm{m}^{1/2}$, to grow out of the residual tensile stress field developed by the compressive loading [36]. Then, constant amplitude loading was applied at a specific R value to generate a fatigue crack growth rate curve, i.e., as the crack propagates, K increases as does *da/dN*. The applied load was computed based on prior knowledge of the threshold stress intensity factor and the measured crack length. If the crack growth rate was less than 10^{-10} m/cycle, the applied load was increased by 10 %, and this was continued until the measured crack growth rate exceeded 10^{-10} m/cycle. The remaining data would then be generated at this load level.

Fatigue Crack Growth Rate Data

The constant R and constant K_{max} load reduction tests were conducted using a software-control system on a servo-hydraulic machine with a clip gage to measure compliance and determine crack length, in lab air at a mean temperature of 21°C. The compliance crack length measurements were calibrated visually with a floating microscope. The K_{max} tests conducted using the M(T) specimens were produced under constant load amplitude conditions, and the crack lengths were measured visually on both front and back surfaces using floating microscopes. These tests were also conducted in lab air at a mean temperature of 21°C.

The majority of the constant *R* load reduction tests were performed in the T-L grain orientation as the primary loading direction. On the other hand, the M(T) and GC(T) specimens were orientated such that the L-T grain direction was the primary loading direction. There is evidence in the literature that the grain orientation can have an effect on the fatigue crack growth properties of this aluminum alloy [37]. Therefore, a series of constant *R* load reduction tests was performed in the L-T direction to compare the effect of grain orientation on the fatigue crack growth rate. As shown in Fig. 1, the difference between the two orientations is most pronounced at threshold. Therefore, all plots that contain L-T and T-L data will be marked accordingly. The constant *R* load reduction tests were precracked at a constant ΔK that is equivalent to the first data point in the load reduction test, unless otherwise noted.

The M(T) K_{max} tests were conducted using a high compression scheme for precracking, such that the maximum applied load was –6.79 MPa, and the minimum was –207 MPa at a notch width of 12.7 mm. The first test was run at a constant K_{max} of 1.65 MPa $m^{1/2}$ to achieve a threshold of 1.86 MPa $m^{1/2}$ at $R = -0.13$. The second test was run at a constant K_{max} of 2.20 MPa $m^{1/2}$ to produce a threshold of 0.95 MPa $m^{1/2}$ at an R of 0.57. The third K_{max} test was run at a K_{max} value of 1.65 MPa $m^{1/2}$ producing a threshold of 1.65 MPa $m^{1/2}$ at an R of 0.00. Note that the first and third tests were conducted at the same K_{max} level and load reduction rate, yet they produced different threshold values at different R. The data produced from the constant K_{max} load reduction tests are shown in Fig. 8. Once the threshold rate was achieved (10^{-10} m/cycle), a K increasing test was run corresponding to the R value at threshold. These results are plotted in Fig. 9.

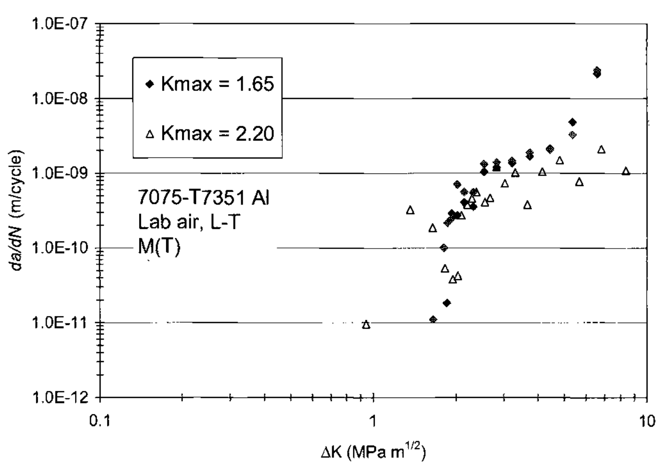

FIG. 8—*Constant K_{max} load reduction data.*

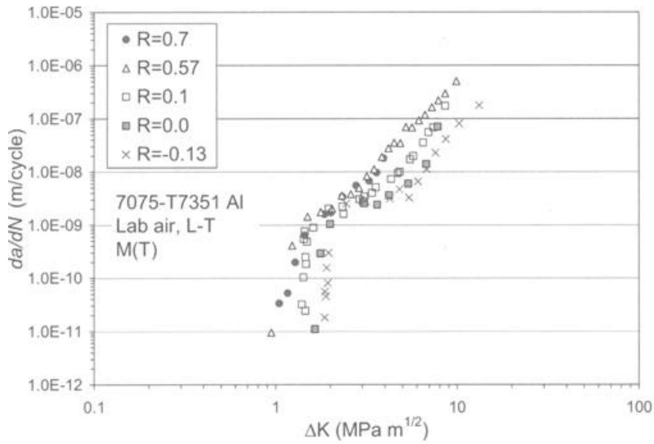

FIG. 9—*K increasing data.*

Data were generated for the R = 0.1 condition because closure was expected at this stress ratio. The data shown in Fig. 10 were generated using constant R load reduction, with standard tensile precracking loads on both standard C(T) and GC(T). The constant R load reduction tests using standard precracking methods on a C(T) yielded a threshold of 2.30 MPa $m^{1/2}$. Using the same load reduction technique on a GC(T) specimen yielded a threshold of 1.37 MPa $m^{1/2}$. The crack growth curves generated using the GC(T) specimens experience a "bounce" at $\Delta K \sim 1.9$ MPa $m^{1/2}$ (i.e., the crack growth rate decreased with decreasing ΔK, then increased with decreasing ΔK, then decreased with decreasing ΔK). This phenomenon is discussed in further detail in the following section. The compression-compression precracking, K increasing scheme used with a GC(T) produced a threshold of 1.46 MPa $m^{1/2}$ without exhibiting this bounce effect. M(T) and C(T) specimens were also run with compression-compression precracking and a K increasing scheme at constant R, and exhibited a threshold value of 1.45 MPa $m^{1/2}$ (M(T)) and 1.49 MPa $m^{1/2}$ (C(T)), respectively. These data are shown in Fig. 11 for the L-T grain orientation, omitting the GC(T) tensile precracking data. A comparison of the K increasing and K decreasing data for the C(T) specimen is shown in Fig. 12. The threshold values are summarized in Table 1.

Data were also generated for the R = 0.7 condition to examine a stress level where closure was not expected. The data shown in Fig. 13 were generated using constant R load reduction, with tensile precracking loads on both C(T)s and GC(T)s. M(T) specimens were run with compression-compression precracking and a K increasing scheme at constant amplitude. The constant R = 0.7 load reduction tests using standard precracking methods on a C(T) yielded a threshold of 1.23 MPa $m^{1/2}$. Using the same load reduction technique on a GC(T) specimen yielded a threshold of 1.12 MPa $m^{1/2}$. The M(T) test, an increasing K test under constant amplitude loading, exhibited a threshold value of 1.05 MPa $m^{1/2}$. The threshold values are summarized in Table 1.

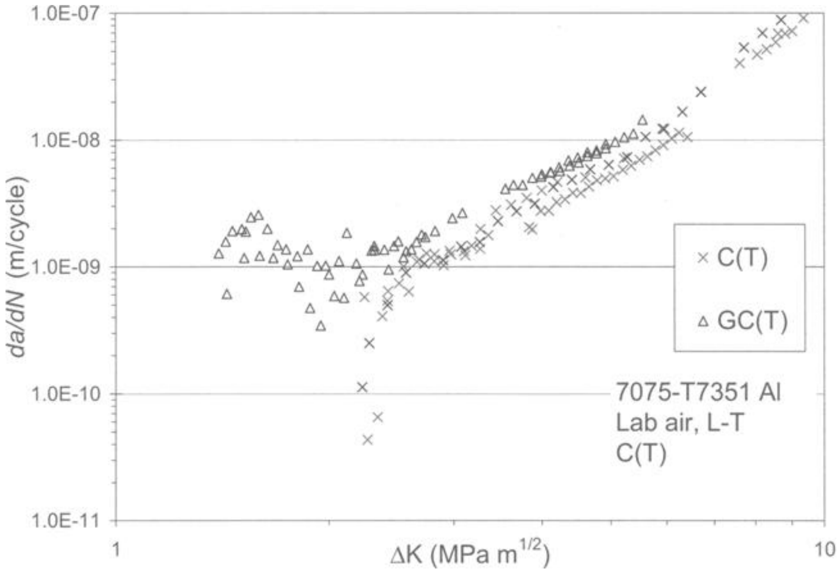

FIG. 10—*R = 0.1 da/dN versus ΔK data.*

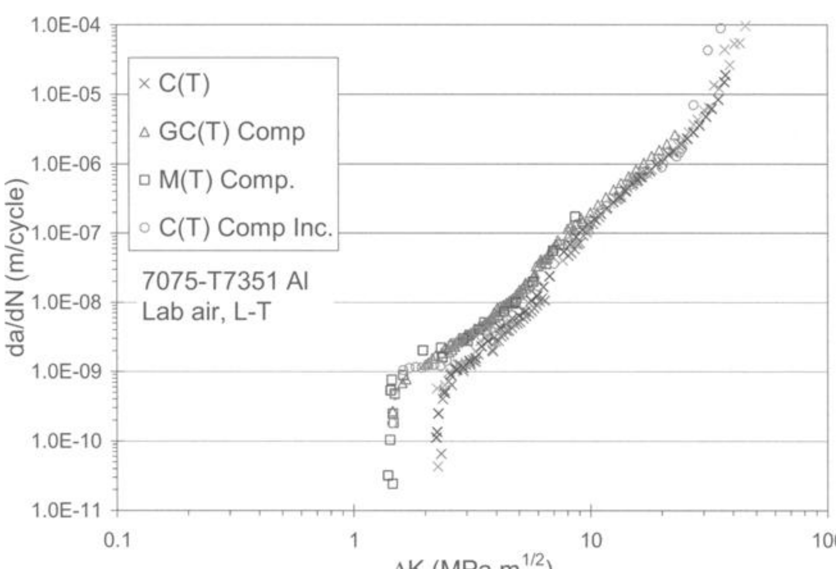

FIG. 11—*R = 0.1 da/dN versus ΔK data.*

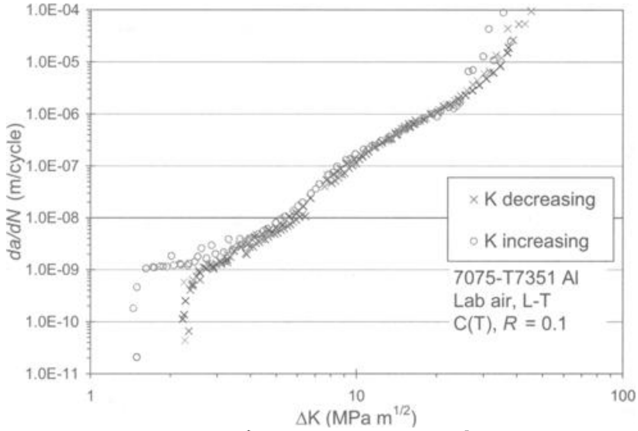

FIG. 12—*Comparison of K increasing and K decreasing test data.*

TABLE 1—*Threshold values using different precracking levels and test methods.*

R = 0.1

Specimen	Tension – K decreasing	Compression – K decreasing	Compression – K increasing
C(T)	2.30	N/A	1.49
GC(T)	1.37	1.46	N/A
M(T)	N/A	N/A	1.45

R = 0.7

Specimen	Tension – K decreasing	Compression – K decreasing	Compression – K increasing
C(T)	1.23	N/A	N/A
GC(T)	1.12	N/A	N/A
M(T)	N/A	N/A	1.05

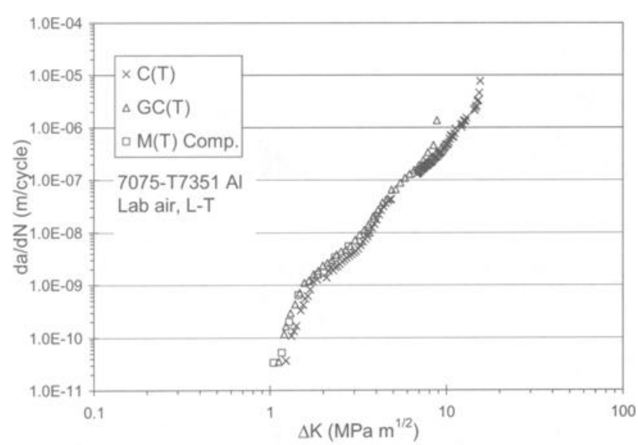

FIG. 13—*R = 0.7 da/dN versus ΔK data.*

Fatigue crack growth threshold data generated in the T-L grain orientation are plotted in Fig. 14. All of the tests were conducted using the constant *R* load reduction procedure on C(T) specimens, with a precracking load equal to the initial data point. Threshold data were generated for *R* of 0.1, 0.4, 0.7, 0.8, and 0.9 with values of 3.34, 2.09, 1.27, 1.27, and 1.05 MPa $m^{1/2}$, respectively. These curves are plotted separately due to the lack of comparative data (i.e., same T-L orientation) using other test procedures. However, these data are valuable baseline data for comparison of future testing.

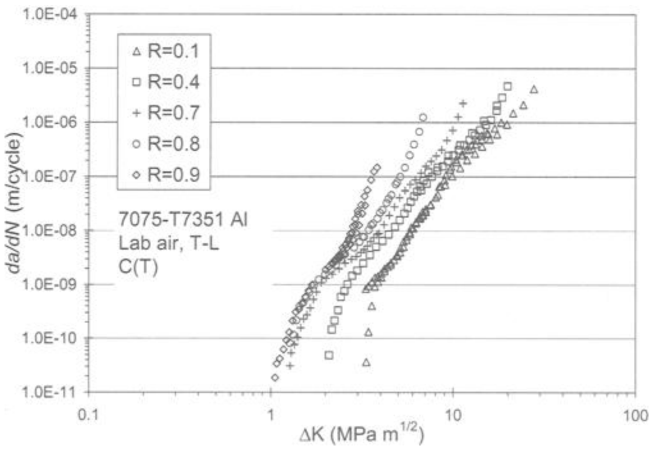

FIG. 14—*Constant R load reduction data.*

Observations

It is apparent that the constant *R* load reduction procedure is producing ambiguous results in 7075-T7351 aluminum alloy for 12.7 mm thick specimens. First, the precracking level of the GC(T) data is studied to identify any effects of remote plasticity-induced crack closure. An odd "bounce" seen in the data at a ΔK of approximately 1.9 MPa $m^{1/2}$ (i.e., the crack growth rate decreased with decreasing ΔK, then increased with decreasing ΔK, then decreased with decreasing ΔK) could be a likely indicator of remote closure. The initial decrease in the crack growth rate (Fig. 10) may be attributable to remote plasticity-induced crack closure, which would cause crack retardation. As the specimen is continued to be cycled, the smashing of the crack faces at the point of remote closure will eventually reduce the influence of the remote closure on the crack tip. As the influence of remote closure diminishes, the crack will accelerate, shown as the rise in the data presented in Fig. 10. Finally, the crack growth rate once again decreases with decreasing ΔK to a threshold value. Examining the data presented in Fig. 10, the specimen with the higher precracking load exhibited a greater shift in crack growth rate, i.e., a bigger bounce. These data support the hypothesis that remote plasticity-induced closure is causing the bounce in the data because the greater the precracking level, the more likely remote plasticity-induced closure exists [19]. Finally, the compression precrack GC(T) data do not exhibit a "bounce," because it is a K increasing test. Remote plasticity-induced closure is not feasible in a compression precrack, K increasing test. Therefore, the constant R load reduction tests must be experiencing remote plasticity-induced crack closure.

Comparison of the C(T) to the GC(T) specimen data (Figs. 10 and 11) illustrates the crack closure effect due to plane-stress zone at the specimen surface. The oxide buildup typically found in a C(T) specimen along the crack front (Fig. 15) was not evident in the GC(T) configuration (Fig. 16). It appears that since the plane-stress plastic zones along the crack surface close prior to the interior plane-strain zone, due to larger plastic deformation at the same K level (Fig. 7), oxide is being trapped in the crack wake in the full thickness specimen causing closure. The GC(T) specimen has a nearly constant tri-axial stress state along the crack front [23], unlike a C(T) specimen, and therefore has less chance of trapping oxide debris in the specimen. Furthermore, there is little evidence of oxide-buildup along the crack face of the M(T) specimen (Fig. 17), which is also nearly plane-strain. These observations suggest that the plane stress zones along the specimen surface do not directly effect the test results, but are the enabling mechanism for the oxide to build up at the crack front, enabling oxide-induced crack closure.

The GC(T) specimen is nearly plane-strain along the entire crack front, unlike the C(T), which is a mixture of plane stress/strain. Therefore, the GC(T) has a slightly higher crack growth rate along the entire range of ΔK compared to the C(T), as shown in Fig. 10. M(T) specimens are also nearly plane-strain, and the crack growth rate data presented in Fig. 11 show good agreement between the GC(T) and M(T) data. However, near threshold, the compression precrack, constant ΔK data appears to be independent of specimen configuration. This would imply that as the plastic zone gets smaller, and there are no remote closure issues, there is no specimen configuration effect.

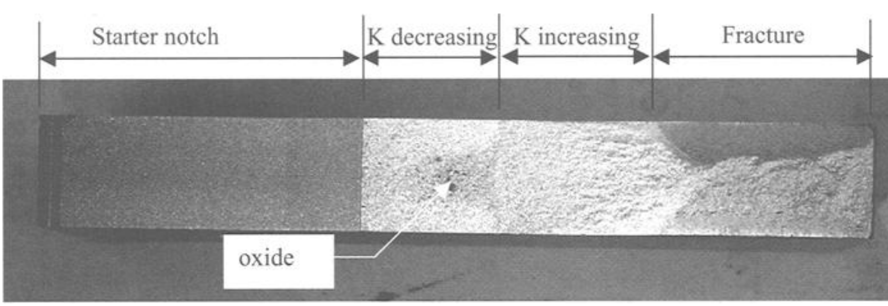

FIG. 15—*C(T) specimen fracture surface.*

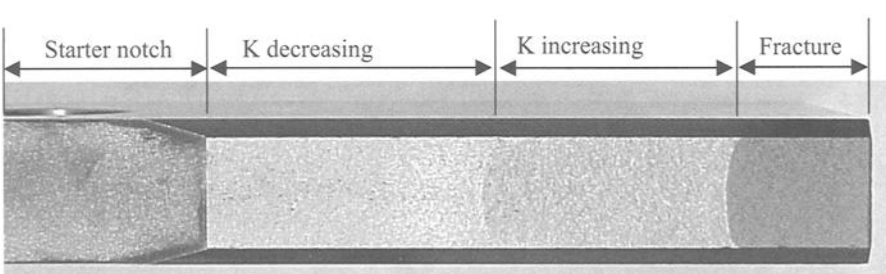

FIG. 16—*GC(T) specimen fracture surface.*

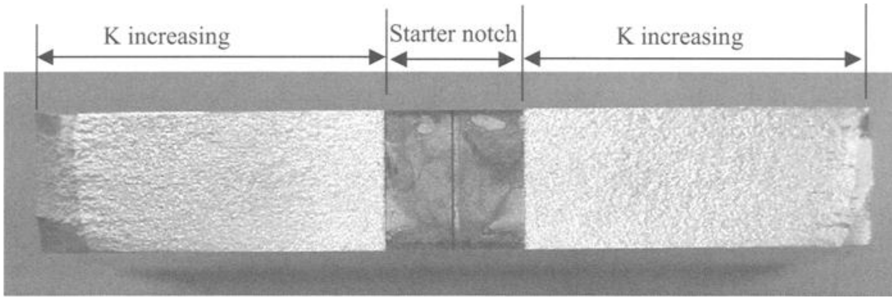

FIG. 17—*M(T) specimen fracture surface.*

Concluding Remarks

ASTM Standard E 647, for producing fatigue crack growth thresholds, produces artificially high values due to crack closure induced by the test procedure in 7075-T7351 aluminum alloy. The foundation for this argument is based upon plasticity theory and mechanics. It is important to note that these findings are based solely on testing in this material (7075 Al) and that continued research into the test methodologies and other materials will be required to make general conclusions. Constantly decreasing ΔK throughout a test will produce remote crack closure if the minimum loads are below the opening load. By implementing a compressive precracking scheme, the effect of the residual plasticity at the notch is virtually eliminated. However, the constant *R* load reduction method still induces remote closure simply by initiating the test at a higher load than at the test conclusion. Conversely, the constant K_{max} load reduction method minimizes this effect by maintaining high *R* load levels that keep the entire crack open. Utilizing middle through crack, M(T), and compact tension, C(T), specimens to produce K increasing data has illustrated that the fatigue crack growth threshold generated using the constant *R* load reduction method can be nonconservative by more than a factor of two (Fig. 11).

The constant *R* load reduction method also enables oxide-induced crack closure in 7075-T7351 aluminum alloy, due to plane stress plasticity at the specimen surface trapping oxide debris in the crack. Oxide-induced closure is not evident in K increasing tests because the crack-tip displacements are increasing throughout the test, precluding the development of oxide-induced closure.

The generation of fatigue crack growth thresholds for 7075-T7351 aluminum alloy has provided the foundation for further research. These new threshold test methods should be further developed and applied to other materials to generate new data sets with accurate threshold values. Future results may indicate that some materials exhibit little plastic deformation, and therefore the current data set remains valid. However, it could be unconservative to assume that any data set is valid without a modicum of tests utilizing the new methods for verification.

It is the authors' goal to develop a fatigue crack growth threshold test method without load history effects due to remote plasticity-induced closure that can be conducted at a specified *R*. At this time, no current ASTM specified method can accomplish this. However, using compression-compression precracking and a K increasing test procedure will generate a fatigue crack growth curve from threshold to fracture at a specific *R* value without load history effects.

[1] Paris, P.C. and Erdogan, F., "A Critical Analysis of Crack Propagation Laws," *Transactions of the ASME, Journal of Basic Engineering*, Series D, 85, 3, 1963.
[2] Barsom, J.M., "Fatigue-Crack Propagation in Steels of Various Yield Strengths," *Transactions of the ASME, Journal of Engineering for Industry*, Series B, *93*, 4, November 1971.
[3] Frost, N.E., "The Growth of Fatigue Cracks," *Proceedings of the First International Conference on Fracture*, Sendai, Japan, 1966, p. 1433.
[4] Bucci, R.J., "Development of a Proposed ASTM Standard Test Method for Near-Threshold Fatigue Crack Growth Rate Measurement" *Fatigue Crack Growth Measurement and Data Analysis, ASTM STP 738*, ASTM International, West Conshohocken, PA, 1981, pp. 5–28.
[5] "Damage Tolerance and Fatigue Evaluation of Structure", *Federal Aviation Regulations*, Title 14 Code of Federal Regulations, Part 25, Section 571.
[6] Engine Structural Integrity Program (ENSIP), MIL-STD-1783 (United States Air Force), 30, November 1984.
[7] Pearson, S., "Initiation of Fatigue Cracks in Commercial Aluminum Alloys and the Subsequent Propagation of Very Short Cracks," *Engineering Fracture Mechanics*, *7*, 2, 1975, pp. 235–247.
[8] Taylor, D. and Knott, J.F., "Fatigue Crack Propagation Behavior of Short Cracks – The Effects of Microstructure," *Fatigue of Engineering Materials and Structures*, *4*, 2, 1981, pp. 147–155.
[9] Taylor, D. and Knott, J.F., "Growth of Fatigue Cracks from Casting Defects in Nickel Aluminum Bronze," *Proceedings of the Metal Society Conference on Defects and Crack Initiation in Environment Sensitive Fracture*, University of Newcastle-on-Tyne, 1981.
[10] Smith, S.W. and Piascik, R.S., "An Indirect Technique for Determining Closure-Free Fatigue Crack Growth Behavior," *Fatigue Crack Growth Thresholds, Endurance Limits, and Design, ASTM STP 1372*, ASTM International, West Conshohocken, PA, 2000, pp. 109–122.
[11] Herman, W.A., Hertzberg, R.W. and Jaccard, R., "A Simplified Laboratory Approach for the Prediction of Short Crack Behavior in Engineering Structures," *Fatigue and Fracture of Engineering Materials and Structures*, *11*, 4, 1988, pp. 303–320.
[12] Hertzberg, R.W., Herman, W.A. and Ritchie, R.O., "Use of a Constant K_{max} Test Procedure to Predict Small Crack Growth Behavior in 2090-T8E41 Aluminum-Lithium Alloy," *Scripta Metallurgica*, *21*, 1987, pp. 1541–1546.
[13] Marci, G., "Fatigue Crack Propagation Threshold: What is it and How is it Measured?" *Journal of Testing and Evaluation*, JTEVA, *26*, 3, 1998, pp. 220–233.
[14] Haddad, M.H., Topper, T.H. and Smith, K.N., "Prediction of Non Propagating Cracks," *Engineering Fracture Mechanics*, *11*, 3, 1979, pp. 573–584.
[15] Newman, Jr., J.C. and Piascik, R.S. (Eds.), *Fatigue Crack Growth Thresholds, Endurance Limits, and Design, ASTM STP 1372*, ASTM International, West Conshohocken, PA, 2000.
[16] Wu, X.J., Wallace, W. and Koul, A.K., "A New Approach to Fatigue Threshold", *Fatigue & Fracture of Engineering Materials & Structures*, *18*, 7/8, 1995, pp. 833–845.
[17] Elber, W., "The Significance of Fatigue Crack Closure," *Damage Tolerance in Aircraft Structures, ASTM STP 486*, ASTM International, West Conshohocken, PA, 1971, pp. 230–242.
[18] Chen, D.L., Weiss, B. and Stickler, R., "Effect of Stress Ratio and Loading Condition on the

Fatigue Threshold," *International Journal of Fatigue*, 14, 1992, pp. 325–329.
[19] Newman, Jr., J.C. and Elber, W. (Eds.), *Mechanics of Fatigue Crack Closure, ASTM STP 982*, ASTM International, West Conshohocken, PA, 1988.
[20] Forman, R.G., "Study of Fatigue-Crack Initiation from Flaws Using Fracture Mechanics Theory," *Air Force Flight Dynamics Laboratory Technical Report AFFDL-TR-68-100*, Wright-Patterson Air Force Base, Dayton, Ohio, Sept. 1968.
[21] Irwin, G.R., "Linear Fracture Mechanics, Fracture Transition, and Fracture Control," *Engineering Fracture Mechanics*, 1, 2, Aug. 1968.
[22] McClintock, F.A. and Hult, J., "Elastic-Plastic Stress and Strain Distribution Around Sharp Notches in Repeated Shear," *Ninth International Congress on Applied Mechanics*, New York, 1956.
[23] Andrews, W.R. and Shih, C.F., "Thickness and side-groove effects on *J*- and δ-resistance curves for A533-B steel at 93°C," *Elastic-Plastic Fracture, ASTM STP 668*, ASTM International, West Conshohocken, PA, 1979, pp. 426–450.
[24] Shih, C.F., deLorenzi, H.G. and Andrews, W.R., *International Journal of Fracture, 13*, 1977, pp. 544–548. [CrossRef
[25] Topper, T.H. and Au, P., "Cyclic strain approach to fatigue in metals," *AGARD lecture series 118, Fatigue Test Methodology*, The Technical University of Denmark, Denmark, Oct. 19-20, 1981.
[26] Conle, A. and Topper, T.H., "Evaluation of small cycle omission criteria for shortening of fatigue service histories," *International Journal of Fatigue*, Jan. 1979.
[27] Pippan, R., Plochl, L., Klanner, F. and Stuwe, H.P., "The Use of Fatigue Specimens Precracked in Compression for Measuring Threshold Value and Crack Growth," *Journal of Testing and Evaluation*, JTEVA, Vol. 22, No. 2, 1994, pp. 98–103.
[28] Forth, S.C., Newman, J.C., Jr., and Forman, R.G., "On Generating Fatigue Crack Growth Thresholds," *International Journal of Fatigue*, Vol. 25, 2003, pp. 9–15.
[29] Shivakumar, K.N. and Newman, Jr., J.C., "Verification of Effective Thicknesses for Side-Grooved Compact Specimens," *Engineering Fracture Mechanics*, *43*, 2, 1992, pp. 269–275.
[30] Newman, Jr., J.C., "Stress Analysis of the Compact Specimen Including the Effects of Pin Loading," *Fracture Analysis, ASTM STP 560*, ASTM International, West Conshohocken, PA, 1974, pp. 105–121.
[31] Feddersen, C.E., "Discussion of Plane-Strain Crack Toughness Testing of Metallic Materials," *Current Status of Plane Strain Crack Toughness Testing of High-Strength Metallic Materials, ASTM STP 410*, ASTM International, West Conshohocken, PA, 1967, pp. 77–79.
[32] Hudak, Jr., S.J., Saxena, S.J., Bucci, A. and Malcolm, R.C., "Development of Standard Methods of Testing and Analyzing Fatigue Crack Growth Rate Data – Final Report," *AFML TR 78-40*, Air Force Materials Laboratory, Wright Patterson Air Force Base, OH, 1978.
[33] Saxena, A., Hudak, Jr., S.J., Donald, J.K. and Schmidt, D.W., "Computer-Controlled Decreasing Stress Intensity Technique for Low Rate Fatigue Crack Growth Testing," *Journal of Testing and Evaluation*, *8*, 1, 1980, pp. 19–24.
[34] Au, P., Topper, T.H. and El Haddad, M.L., "The Effects of Compressive Overloads on the Threshold Stress Intensity for Short Cracks," *Behavior of Short Cracks in Airframe*

Components, *AGARD Conference Proceedings No. 328*, pp. 11-1 to 11-7.

[35] Newman, Jr., J.C., "An Evaluation of the Plasticity-Induced Crack Closure Concept and Measurement Methods," *ASTM STP-1343*, ASTM International, West Conshohocken, PA, 1999, pp. 128–144.

[36] James, M. A., Forth, S. C., and Newman, J. A., "Load History Effects Resulting from Compression Precracking," *Fatigue and Fracture Mechanics: 34th Volume, ASTM 1461*, S. R. Daniewicz, J. C. Newman, Jr., and K.-H. Schwalbe, Eds., ASTM International, West Conshohocken, PA, 2004.

[37] NASGRO Material Database, www.nasgro.swri.org, 2004.

SESSION 4A: SMALL CRACKS I

Journal of ASTM International, January 2005, Vol. 2, No. 1
Paper ID JAI12050
Available online at www.astm.org

J. A. Schneider[1] *and Ed Kenik*[2]

Microstructural Influences on the Development and Growth of Small Fatigue Cracks in the Near Threshold Regime

ABSTRACT: Orientation imaging microscopy (OIM) is being used to investigate the microstructural influence on small crack growth at the crack tip. Although grain and grain boundary orientations have been reported to influence small crack growth, the effect has been difficult to quantify. OIM uses electron backscattered diffraction (EBSD) patterns in a scanning electron microscope (SEM) to form a spatially resolved map of crystal orientation, providing information on intra- and inter-grain orientation relationships.

Mini-extended compact tension (ECT) specimens were machined from an 1100 aluminum cold rolled sheet with a 45° angle, machined notch tip. The specimens were sized to fit into a Philips XL30/FEG SEM equipped with an EDAX/TSL EBSD/OIM system. Initial images were recorded prior to cycling of the mini-ECT specimen. Fatigue testing was conducted at constant amplitude loading in the near-threshold regime where small cracks are considered to be on the order of the corresponding grain size. The constant amplitude load testing was periodically interrupted to obtain EBSD images. The ability to map an area 800 × 1300 μm in front of the machined notch tip was demonstrated. This study determined that the plastic deformation, which occurs in a zone in front of the crack tip, did not degrade the EBSD image quality. Use of this technique provides the capability to characterize local crystal orientation during deformation processes such as fatigue crack growth.

KEYWORDS: fatigue cracks, microstructural influence, OIM

Introduction

Fatigue failure is reported to occur by crack nucleation and propagation. Observed differences in long crack versus short crack growth rates have been discussed in terms of microstructural influences and effects of the prior load history [1]. Crack growth behavior in metals is modeled based on the 3-dimensional stress-strain relationship at the crack tip assuming plane strain conditions. The stress intensity factor at the crack tip is calculated assuming a homogenous material and excludes the influence of microstructural length parameters. Based on the stress intensity factor, a crack growth rate can be calculated based on the material thickness and an initial crack length. The initial plastic zone size is established during the maximum load during the first loading cycle. Under continued cyclic loading, cyclic plastic deformation takes place at the crack tip. Constant amplitude cycling eventually results in a saturation flow stress in which a steady state fatigue crack growth rate can be obtained. The saturation stage of fatigue is reported to be 10 000 cycles in AA 1100 [2]. At this time the dislocation shuttling leads to local

Manuscript received 22 December 2003; accepted for publication 19 April 2004; published January 2005. Presented at ASTM Symposium on Fatigue and Fracture Mechanics: 34th Volume on 19–21 November 2003 in Tampa, FL; S.R. Daniewicz, J.C. Newman, Jr., and K-H. Schwalbe, Guest Editors.
[1] Assistant Professor, Mississippi State University, Department of Mechanical Engineering, Mississippi State, MS 39762.
[2] Staff Scientist, Metals and Ceramics Division, Bldg 4515, MS 6064, Oak Ridge National Laboratory, Oak Ridge, TN 37831.

instabilities and finally to microcracks, reported to be observable after about 25 % of the fatigue life has been expended [2].

In-homogeneity of the material due to grain size, grain orientation, grain boundary geometry, precipitates, and other second phase particles is reported to strongly affect the steady state crack growth rate of small cracks [3]. In pure metals, the most significant features to influence the fatigue crack behavior are the grain orientation and grain boundary geometry [4–7]. The incubation stage of fatigue crack nucleation prior to growth into longer cracks can be greatly affected by the non-homogeneity of the material. In addition to non-homogeneity of a polycrystalline material at the macro-level, non-homogeneous deformation is also observed at the micro-level within a single grain. Permanent deformation occurs as the material deforms along bands of material that slip along specific slip planes and in specific directions. Activation of a particular slip band is controlled by the resolved shear stress on the slip plane in the slip direction. Decohesion results in fatigue cracks manifesting themselves discontinuously in regions between slip bands. In uniaxial loading, alternating slip planes become activated as the part is strained in accordance with the Schmidt criteria. Neumann [7] formulated the mechanism of discontinuous slip processes occurring at a crack tip in push-pull testing of copper single crystals. Macroscopic plane fatigue was found on the {001} orientations in the <011> directions [7]. In addition to Neumann's model [7], two additional microscopically based models have been reported [8,9].

The crack growth mechanisms in polycrystalline materials are theorized to change as the stress intensity and ratio increases. Conditions driving the decohesion between planes change as the controlling stress changes from the resolved shear stress to activate a slip system in an individual grain to the maximum shear stress to activate shear bands across numerous grains [8].

The other bridging feature between single and polycrystalline materials is the influence of grain boundaries. In low amplitude testing at threshold, the growth of small cracks has been reported to be influenced by grain boundaries [10]. The growth rate of cracks as they approach the grain boundary has been reported to both accelerate and decelerate in engineering materials [10]. Research by Li et al. [5,6] has systemically studied the crack transfer across various interfaces in aluminum bicrystals. In these studies, the variations in the crack growth rate were correlated with the grain boundary Σ value. Higher Σ values were found to reduce the crack growth rate more than lower Σ values, although the lower values were found to produce a wider effect [5].

The mode of crack nucleation and the associated deformation phenomena are therefore dependent on the stress amplitude and the slip character of the material being tested. However, experiments to quantify the effects at the microscopic scale are difficult to execute and interpret. Recently, the use of electron backscattered diffraction (EBSD) techniques to obtain orientation image maps (OIM) has been reported in studies of the fatigue cracks, in addition to quantifying the localized stresses at the surface [11–15]. The objective of this study was to determine if EBSD was a feasible tool for investigation of grain orientation in the proximity of a growing crack tip in the threshold regime.

Experimental Procedure

A commercially pure, polycrystalline aluminum alloy, AA1100-H14 (99 % aluminum) was used in this study. Samples of the AA1100-H14 were etched using 0.5 % HF to reveal the grain morphology. The grains were measured using a linear intersect method and compared with results from the OIM imaging. The initial properties of the AA1100-H14 are summarized in Table 1 per the vendor's acceptance standards.

TABLE 1—*Mechanical properties of the material.*

	Specification	Nominal
Elastic modulus		10 000 ksi
Tensile strength	16–21 ksi	18.1 ksi
Yield strength	14 ksi, min	16.7 ksi
Failure elongation	6 %, min	9 %
Brinnell hardness		23

A non-standard specimen was designed for this study to fit within the SEM chamber on an EBSD title stage. Dimensions for the mini-CT specimen are shown in Fig. 1. The crack plane orientation is L-T with a machined notch width of 0.04 in. and a notch tip angle of 45°. One side of the specimen was polished to prepare the specimen for the EBSD imaging. The surface was first mechanically polished using a decreasing series of SiC grit abrasive paper. Final polishing of the surface was made using a 0.5 μm colloidal silica first followed by a 40 nm colloidal silica or Syton polishing.

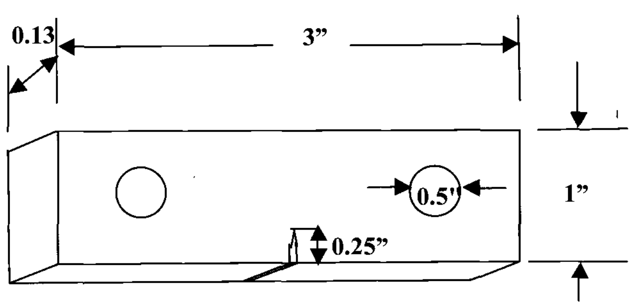

FIG. 1—*Mini-extended CT specimen sized to fit into scanning electron microscope (SEM) chamber.*

The fatigue testing was carried out in an Instron Model 8862 (5.6 kip) servo-hydraulic machine in load control under constant amplitude testing. The specimen was cycled in compression-compression mode for 2.5 M cycles at 10 hz at: R = 0.1, Pmax = –10 lb and Pmin = –200 lb. The large pre-cracking compressive loads were selected to homogenize a tensile plastic zone ahead of the crack tip. An estimate of the tensile plastic zone size is 3644 μm. After precracking, the specimen was tested in tension-tension with planned test interruptions on a 2.5 M cycle interval to image the crack. The tensile loading is estimated to produce a compressive plastic radius of 230 μm. These conditions were selected to ensure fatigue testing in the saturation stage for cold worked AA1100 [2].

Optical images were taken of the specimens prior to imaging in the SEM. The EBSD investigations were carried out in a Philips XL 30 field emission, scanning electron microscope (FE-SEM) equipped with an EBSD detector from TSL, Inc. The geometric principle of EBSD imaging is illustrated in Fig. 2. Some important parameters for imaging of the EBSD patterns include: specimen tilting angle of 70° toward the detector in the SEM chamber; accelerating voltage of 15 kV; beam current of 10 nA; a working distance of 22.3 mm; distance between electron beam and phosphorous screen of 74 mm. Note that the imaging nomenclature in Fig. 2 refers to the orientation of the specimen, not the orientation of the crystallographic planes.

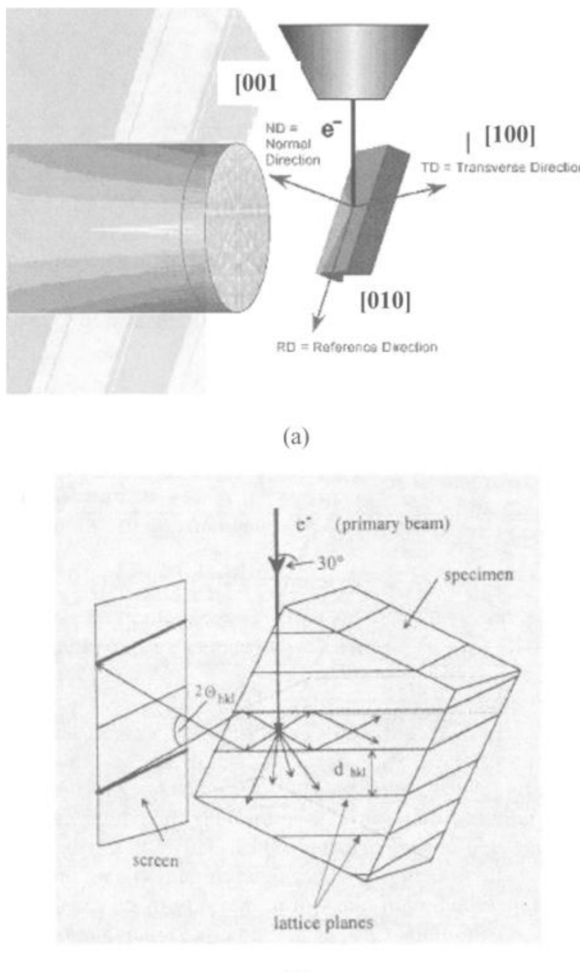

FIG. 2—*Orientation image maps obtained using an electron backscattered detector in a scanning electron microscope. Orientation of specimen and detector (a). Crystalline lattice information is generated as illustrated in (b).*

Results

OIM images were obtained of the rolled sheet material to verify polishing procedures prior to fatigue testing. The grain morphology is shown in Fig. 3, and the distribution of grain boundary misorientation angles is shown in Fig. 4. The color key relates to a section of a stereographic projection for a cubic crystallographic structure. The grain morphology of the initial microstructure is that of elongated grains approximately 200 × 80 mm. Some evidence of recrystallization can be seen in the cold rolled microstructure. Based on the coloration of the grains, in conjunction with the key the texture of the cold rolled sheet is considered to be primarily {100} <001> cubic. A dark line around the grains in Fig. 3 denotes those grains which have greater than 10° misorientation angle.

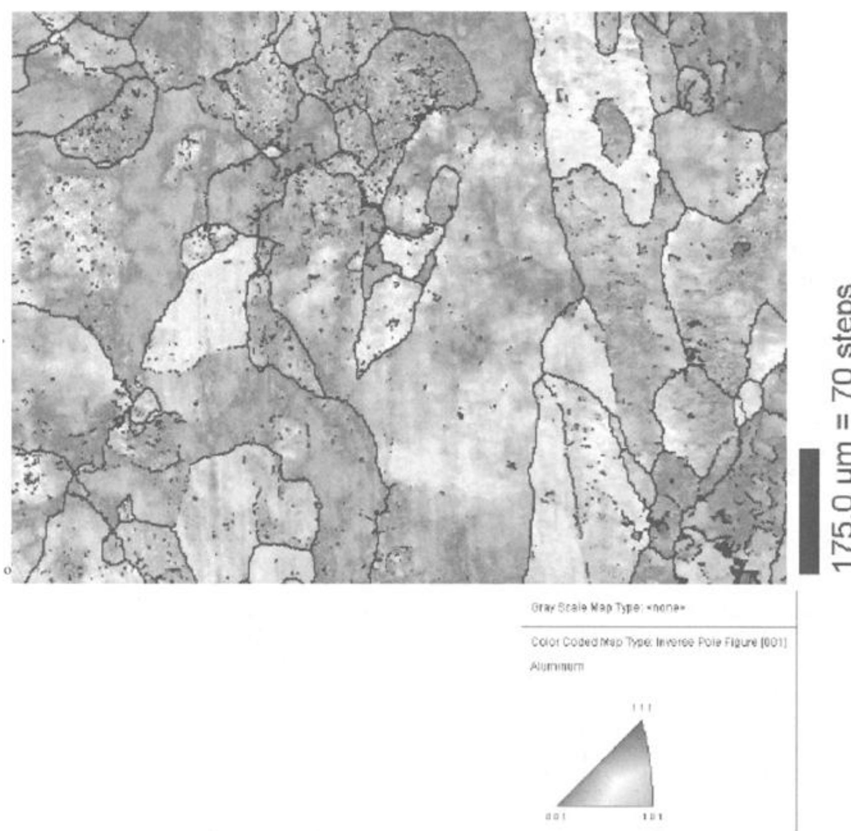

FIG. 3—*Initial cold rolled microstructure indicating primarily a cube texture. Dark lines indicate grain boundaries with misorientations greater than 10°. Color key is common to subsequent EBSD/OIM figures.*

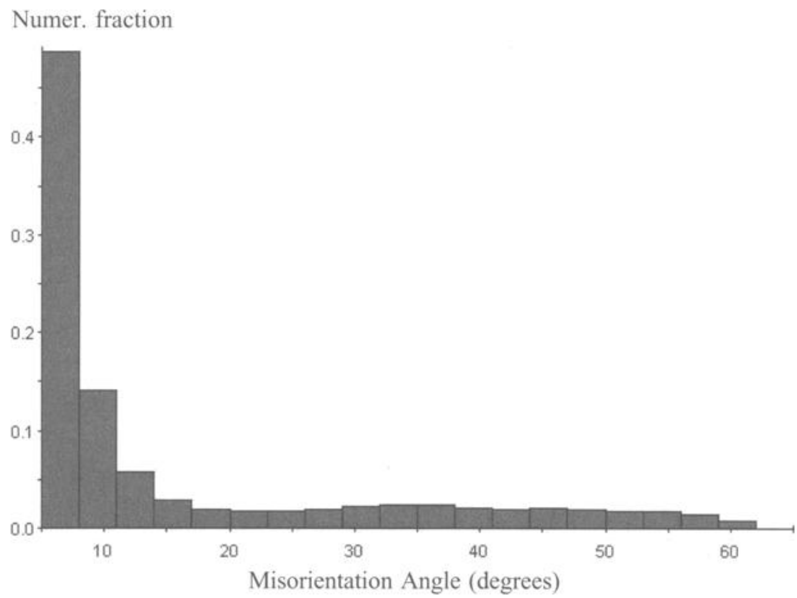

FIG. 4—*Grain boundary misorientation histogram shows a high degree of grain boundary misorientation between grains in initial microstructure.*

The observable slip markings after cyclic deformation are apparent in the light microscopy image of Fig. 5 for the specimen after 2.5 M cycles in compression-compression and an additional 2.5 M cycles in tension-tension testing. The plastic radius size due to monotonic loading is calculated to be 3644 μm and appears to be in agreement with the deformed region noted in Fig. 5. Figure 6 shows the same region shown in Fig. 5, but at a lower magnification after a total of 5 M cycles in tension-tension cycling. Comparison of these two images indicates the size of the initial monotonic induced plastic radius is virtually unchanged, although more surface deformation is noted around the notch tip. A white circle is superimposed on Figs. 5 and 6 to mark the region investigated with EBSD OIM analysis.

Figure 7 shows two different crack morphologies that have developed at the surface of the specimen around the notch tip. One crack follows a zigzag pattern for 0.02 in. emitting from the tip of the crack. The other crack of similar length is straight. To understand the zigzag crack, the crack path was superimposed on the initial OIM image. Due to the damage incurred on the specimen at the notch tip, this information could not be obtained directly. The crack path is noted to alternate between an inter- and trans-granular path.

A magnified image of the straight crack morphology is shown in Fig. 8. This region lies outside of the damaged area, and details of the microstructure deformation can be observed in the SEM secondary electron (SE) image. White lines denote regions of slip band activity. The variation in orientations of these macro-bands corresponds to variations in the grain orientation shown in Figs. 9 and 10.

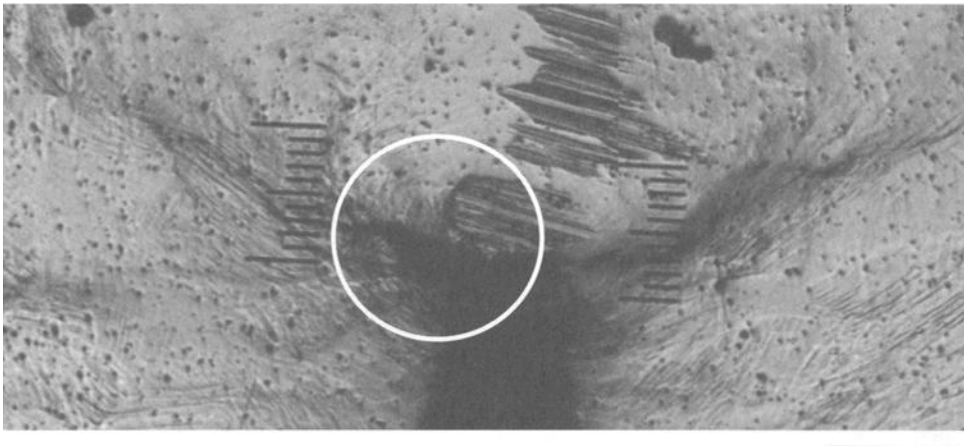

650 μm

FIG. 5—*Al 1100 mini-ECT specimen notch tip after testing for 2.5 M cycles in compression-compression and 2.5 M cycles in tension-tension under constant amplitude load control. White circle denotes region examined in OIM images.*

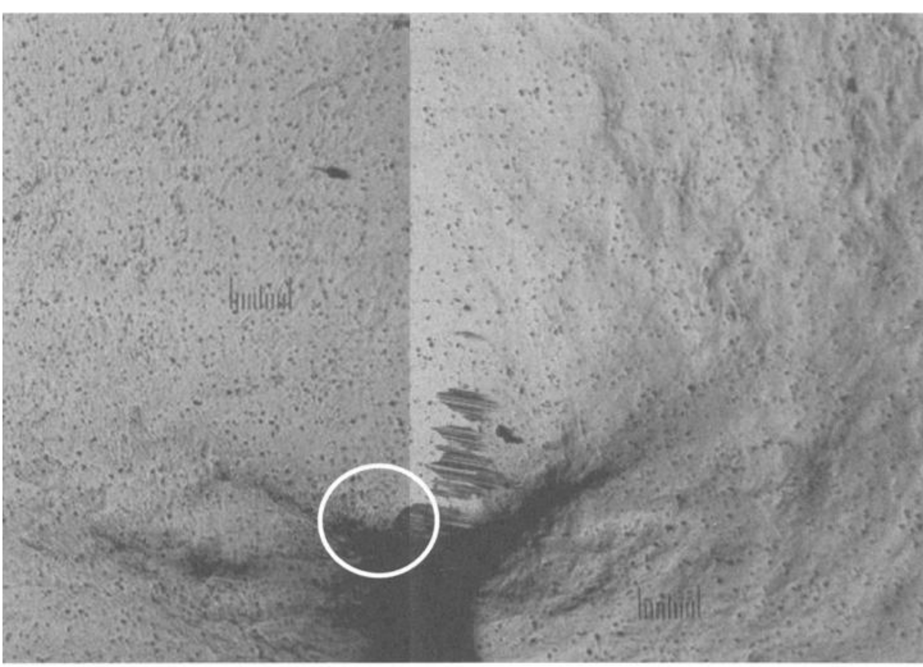

200 μm

FIG. 6—*Al 1100 mini-ECT specimen notch tip after constant amplitude load control for 5 M cycles in tension-tension testing under load control. White circle denotes region examined in OIM images.*

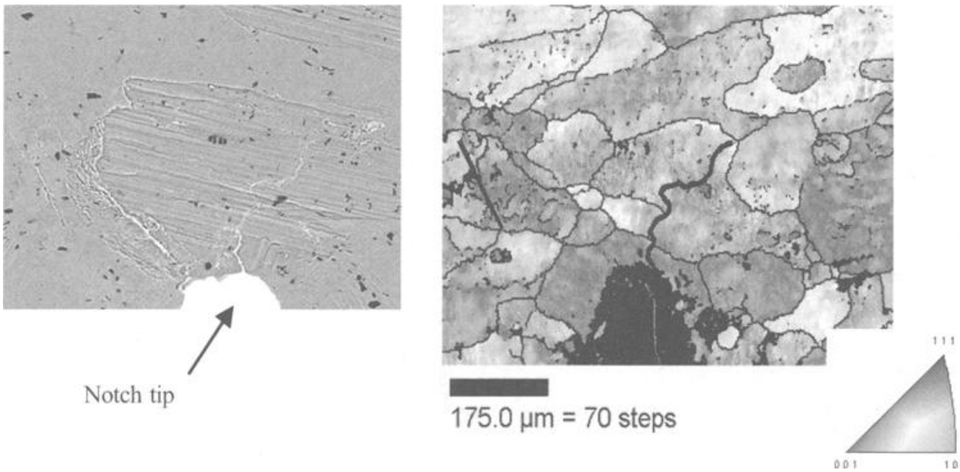

FIG. 7—*Two different crack morphologies are noted in front of the notch tip: optical microscopy image (a) and corresponding SEM/OIM image of same region (b).*

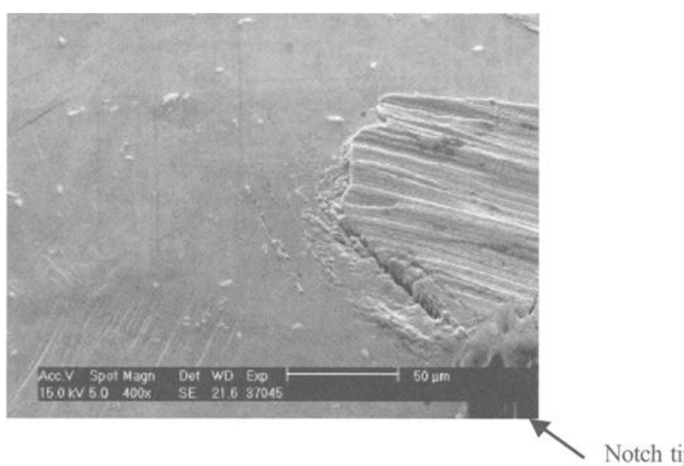

FIG. 8—*Plastically deformed material away from the crack tip displays slip bands and cracks that are parallel to projections of {111} planes.*

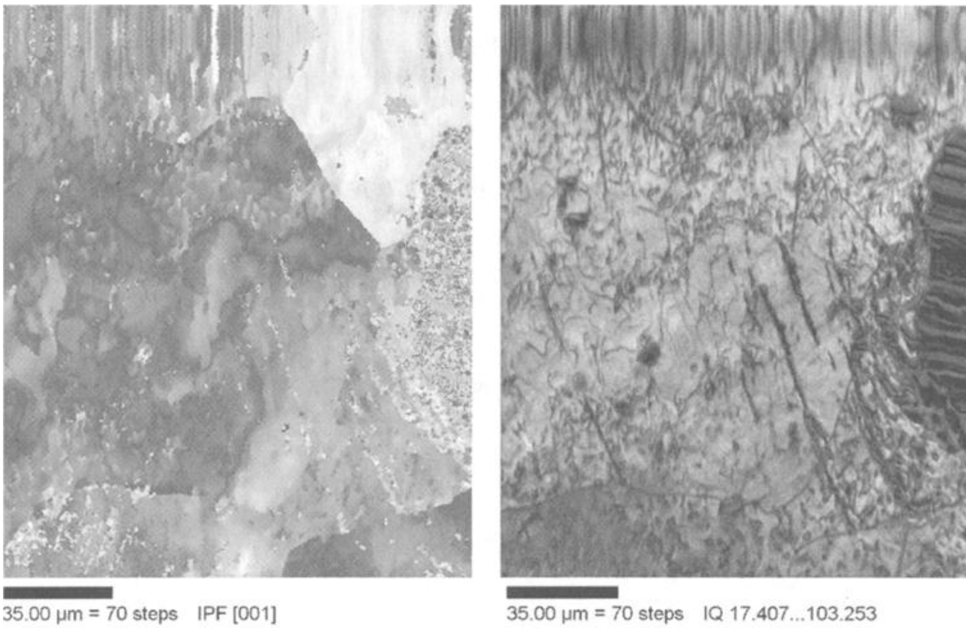

FIG. 9—*Image quality (IQ) maps help to delineate features such as grain boundaries, slip planes, and fatigue cracks. (Note: elongation of the images is due to beam drift during data collection).*

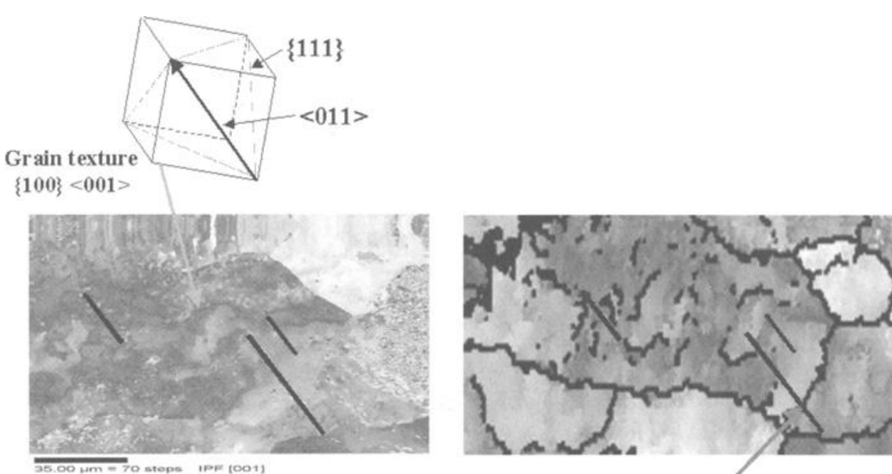

FIG. 10—*Fracture fronts tend to be parallel to <011> directions that lie along projections of the {111} planes.*

The grains containing the region of the straight morphology cracks are shown in the OIM image of Fig. 9*a* and as an image quality (IQ) map of Fig. 9*b*. The data shown in the figures are elongated due to beam drift during the scanning process to collect the EBSD data. Measuring the quality, or degree of contrast and sharpness of the band edges, of the EBSD patterns produces the IQ maps. A grayscale is assigned to this information with white representing the highest measurable pattern quality and black the lowest. The pattern quality can be used to reveal aspects of the microstructure that might otherwise go undetected, such as the grain boundaries that appear as dark lines in the IQ map. Areas of high strain appear darker in the IQ map due to the decrease in pattern quality when the crystal lattice is deformed. Regions of highly localized crystalline slip bands are also readily noted on the IQ map. From stereographic projections, these cracks fall parallel to the $\{111\}$ planes. They extend through the grain boundary in regions where the neighboring grains share directional similarity. This agrees with crack propagation patterns reported in bicrystal testing [5].

The elongation observed in Fig. 9*a* has been compensated in Fig. 10, which offers a comparison of this region in Fig. 10*a* after 5 M cycles and in Fig. 10*b* for the untested grain orientation. Other than the formation of the slip bands, no discernible difference in the grain texture is shown.

Conclusions

Although the specimen suffered damage to the surface, the testing was continued to evaluate the capability of the technique to provide crystallographic imaging of deformed grains. Cracks were noted to have formed at the surface near the outer circumference of the plastic radius in addition to crack growth at the crack tip after 5 M cycles. The cracks at the outer circumference of the plastic zone are noted to form along the strongly localized slip bands or microbands in the affected grains. The ability to image using the EBSD technique in regions where extensive deformation has occurred along displaced shear bands was demonstrated.

Superpositioning of secondary images from the SEM show the crack path from the notch tip alternates between transgranular and intergranular. The ability to show the influences of localized stress on the crack path along the surface crack grain front has not been demonstrated due to specimen damage in this region. However, based on EBSD imaging of grains outside the damaged region, it is believed that this can be accomplished.

Acknowledgments

Research at the Oak Ridge National Laboratory SHaRE Collaborative Research Center was sponsored by the Division of Materials Sciences and Engineering, U.S. Department of Energy, under contract DE-AC05-00OR22725 with UT-Battelle, LLC.

References

[1] Chan, K. S., Lankford, J., and Davidson, D. L., "A Comparison of Crack-Tip Field Parameters for Large and Small Fatigue Cracks," *J. Eng. Mater.*, I, 108, 1986, pp. 206–213.

[2] *Atlas of Fatigue Curves*, H. E. Boyer, Ed., ASM.

[3] Suresh, S., *Fatigue of Materials*, Cambridge University Press, Cambridge, 1991.

[4] Kim, W. H. and Laird, C. "Crack Nucleation and Stage I Propagation in High Strain Fatigue – I. Microscopic and Interferometric Observations," *Acta. Metal.*, 26, 1978, pp. 777–787.
[5] Li, C., Zhang, P., and Zhang, T. "On Crystallographic Crack Transfer Across Interfaces in Four Types of Aluminum Bicrystal," *Mat. Sci. and Engr.*, A183, 1994, pp. 23–30.
[6] Li, C. "Crystallographic Fatigue Crack Growth in Incompatible Aluminum Bicrystals: Its Dependence on Secondary Slip," *Met. Trans. A*, 23, 1992, pp. 3293–3301.
[7] Neumann, P. "New Experiments Concerning the Slip Processes at Propagating Fatigue Cracks – I," *Act. Met.*, 22, 1974, pp. 1155–1165.
[8] Liu, H. W., "A Review of Fatigue Crack Growth Analyses," *Theoretical and Applied Fracture Mechanics*, 16, 1991, pp. 91–108.
[9] Laird, C., *ASTM STP 415, Fatigue Crack Propagation*, ASTM International, West Conshohocken, PA, 1967, p. 131.
[10] Zurek, A. K., James, M. R., and Morris, W. L., "The Effect of Grain Size on Fatigue Growth of Short Cracks," *Metal. Trans. A*, 14, 1983, pp. 1697–1705.
[11] Blochwitz, C., Brechbuehl, J., and Tirschler, W., "Analysis of Activated Slip Systems in Fatigued Nickel Polycrystals Using the EBSD-Technique in the Scanning Electron Microscope," *Mat. Sci. and Engr.*, A210, 1996, pp. 42–47.
[12] Villechaise, P., Sabatier, L., and Girard, J. C. "On Slip Band Features and Crack Initiation in Fatigued 316L Austenitic Stainless Steel: Part 1: Analysis by Electron Backscattered Diffraction and Atomic Force Microscopy," *Mat. Sci. and Engr.*, A323, 2002, pp. 377–385.
[13] Hu, Y. M., Floer, W., Krupp, U., and Christ, H-J, "Microstructurally Short Fatigue Crack Initiation and Growth in Ti-6.8Mo-4.5Fe-1.5Al," *Mat. Sci. and Engr.*, 278, 2000, pp. 170–180.
[14] Blochwitz, C., Richter, R., Tirschler, W., and Obrtlik, K., "The Effect of Local Textures on Microcrack Propagation in Fatigued f.c.c. Metals," *Mat. Sci. and Engr.*, 234/236, 1997, pp. 563–566.
[15] Tatschl, A., Scherer, S., Werth, P., and Kolednik, O., "Automatic Local Deformation Measurements by Means of a Digital Image Analysis System," *Advances in Mechanical Behavior, Plasticity and Damage*, Vol. 2, D. Miannay, P. Costa, D. Francois, and A. Pineau, Eds., Elsevier, 2000, pp. 899–904.

Journal of ASTM International, June 2005, Vol. 2, No. 6
Paper ID JAI11987
Available online at www.astm.org

Eli Altus[1]

Size Effect of Microdamage Growth and Its Relation to Macro Fatigue Life

ABSTRACT: In its initial evolution stage, fatigue damage consists of many microdamage sites, having random sizes and locations. The way in which these sites grow and coalesce has a crucial effect on the macro fatigue life. A statistical micromechanic fatigue model has been developed, in which the material is composed of microelements of random strength with a certain probabilistic dispersion parameter (β). In addition, the model takes into account local interactions between damaged microelements and their first neighbors by considering a failure sensitivity factor (c), which is the probability that the neighbor will survive the local (micro) stress concentration. It was shown analytically in previous studies that β is proportional to the S-N power intensity, and ln(1-c) is proportional to the macro endurance limit. In this study, the analysis is generalized to the case where the growth of each micro-damage is size dependent, i.e., each damage site grows at a rate which depends on its current size. The strength of this rate-size relation controls the order of the governing differential equation. It was found that certain "microdamage growth laws" still preserve the macro power law, so that the power on the S-N diagram can be directly related to the local microdamage evolution. While the analytical micro-macro relation is still under current study, a numerical simulation of fatigue damage evolution has been obtained and revealed that the macro S-N power law prevails in spite of the noticable complexity.

KEYWORDS: micromechanics, damage, fatigue, fractals, endurance, statistics, power laws

Introduction

Implementation of microstructure parameters into macro constitutive equations has been under extensive investigation in recent years [1–6]. However, quantitative relations are still in demand. For example, it is striking that Basquin's and Paris "laws," which constitute two of the very well known relations in fatigue behavior, are purely experimental and still have no theoretical, physically sound basis:

$$\sigma = C \cdot N^{-b}; \qquad \frac{da}{dN} = C \cdot \Delta K^{n}. \tag{1.1a,b}$$

The simplicitly of these laws is especially interesting, and one is tempted to try to unify the two by looking for some relation between the two powers, n and b. Experimental data, taken from different sources in the literature for different types of metals (Fig.1), reveals no such correlaton. Since smooth specimens spend a large portion of their fatigue life without any "visible" crack, the mechanisms underlined in (1.1a) and (1.1b) seem to be different. The difference can also be explained by the fact that microcrack growth rate is controlled not only by its own "state" (crack size, stress, etc.) but also by neighbor defects. Thus, the damage growth is a non-local process. In this paper, we will focus on (1.1a).

Manuscript received 3 November 2003; accepted for publication 14 October 2004; published June 2005. Presented at ASTM Symposium on Fatigue and Fracture Mechanics: 34th Volume on 19–21 November 2003 in Tampa, FL; S.R. Daniewicz, J.C. Newman, Jr., and K-H. Schwalbe, Guest Editors.
[1] Professor, Faculty of Mechanical Engineering, Technion, Haifa 32000, Israel, email: altus@tx.technion.ac.il

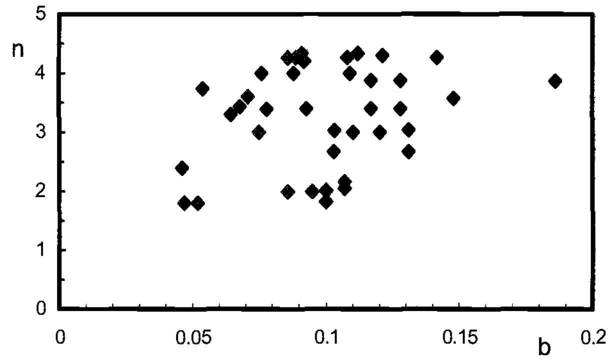

FIG. 1—*Relation between Basquin's and Paris exponents for different metals.*

Eq 1.1a, combined with Fig.1, show that many materials, which are different in their microstructural details, exhibit similar macro failure appearance. This may motivate one to use a simple model which ignores microstructural details and to focus only on absolutely necessary mechanisms, which lead to cyclic failure. Such a model has been developed [7–9] and will be briefly described by way of introduction.

Consider an ensemble of 1D, linear elastic (until breakage) elements on a 2D plane, with uniform direction perpendicular to the plane. The ensemble is organized as uniform cells (square, hexagonal, etc.) or as randomly distributed (Gaussian, etc.) on the plane. Elements are loaded such that all have the same longitudinal strain (ε) and belong to the same set, having a constant stiffness E and a statistical strength distribution function $F(\varepsilon)$, where

$$F(\varepsilon) = \int_0^{\varepsilon} f(\varepsilon')d\varepsilon' \tag{1.2}$$

and $f(\varepsilon)$ is the failure probability density function. This simplified model can be visualized as an idealized group of polymer chains/bundles or a unidirectional fiber composite, where the elements represent fibers, or even metals, where grains are the basic material constituents. Models which are based on similar "simplifications" have been studied extensively [11–13], but rarely for fatigue analysis.

Consider a constant (macro) stress fatigue (cyclic) loading ($\sigma_{max}=\sigma_0$, $\sigma_{min}=0$). During the first cycle, weak elements break, and the others sustain the total load. From equilibrium:

$$\sigma_0 = E_0\varepsilon_1(1 - F(\varepsilon_1)), \tag{1.3}$$

where E_0 and ε_1 are the element stiffness and the maximum strain at the first cycle, respectively. E_0 is also the initial macro modulus of the undamaged ensemble. $F(\varepsilon_1)$ is the failure probability of the elements up to a strain ε_1 and is also the relative number of elements which are broken up to the first loading peak. The local stress concentration may also lead to additional breaks at the same loading cycle, but this possibility is neglected here. However, the effect of broken elements on their unbroken neighbors is still taken into account. It is evident that during the consequent loading cycle the local microstructure in the vicinity of each broken element undergoes many types of relative movements due to irreversible motions: friction, dynamic effects, local heating, bifurcation states, etc. Without entering to a detailed analysis, the end result is divided into two categories: local neighbor strain is higher than for a non-neighbor element (strain concentration higher than 1) or lower. It is the first type which creates a cyclic damage progression effect. Each neighbor has a different local stress concentration factor, according to the specific local geometry. However, from a statistical point of view, only two parameters are needed for further analysis: the relative number of neighbors of the first basic type and the average local stress (strain) concentration factor (k). Moreover, one can simplify the analysis even further, by assuming a very high k value, which practically means that interacted neighbors will definitely fail in the next cycle. It is also assumed that the reason for broken-neighbor interaction depends on the initial local geometry only, i.e., a non-interacting neighbor will not re-interact during subsequent cycles. However, this type of neighbor can still fail as a non-neighbor element. For convenience, the nearest unbroken neighbor of a broken element is termed "neighbor."

The Micromechano-Statistical Fatigue Mechanism

Equilibrium of the first cycle (static) yields:

$$\sigma = E_0(1-d_1)\varepsilon_1 \quad ; \quad d_1 = F(\varepsilon_1) \tag{2.1a,b}$$

where E_0 is the macro modulus of the undamaged state. $F(\varepsilon_1)$ is the failure probability of a strained (up to ε_1) element, and d_1 is the relative damage during the first loading. Normalizing by E_0 we have:

$$E_1 = 1-d_1 = 1-F(\varepsilon_1) \quad ; \quad E_1 = \frac{1}{E_0}\frac{\sigma}{\varepsilon_1} \tag{2.2a,b}$$

where E_1 is the normalized modulus and σ is the macro stress.

Suppose that the damage d_1 is evenly distributed between many small sites, each with a relative area of a_1. The number of microdamage sites created in the first cycle is then

$$m_1 = \frac{d_1}{a_1} \tag{2.3}$$

Now assume that during the second cycle, each of these sites grows from a relative area a_1 to a_2. Then, the total damage area, which initiated in cycle 1, grows in cycle 2 by an increment of

$$d_2^{(a)} = m_1(a_2-a_1) = d_1 \cdot \frac{a_2-a_1}{a_1} = F(\varepsilon_1)\cdot\frac{a_2-a_1}{a_1} \tag{2.4}$$

where (2.1b) has been used. In addition, we have new sites of damage, emerging from the fact that due to the new damage in (2.4), the microstress is now higher for the same macro stress. As a result, the maximum strain of the second cycle is higher, so that new damage sites are "born." The additional damage of this part is:

$$d_2^{(b)} = \frac{F(\varepsilon_2)-F(\varepsilon_1)}{1-F(\varepsilon_1)}\left(1-d_1-d_2^{(a)}\right) \tag{2.5}$$

Again, it is assumed that $d_2^{(b)}$ is composed from many sites, each of a size a_1, which is the size of a "newly born" damage site of a cyclic "age" 1. The number of microdamage sites created in the second cycle is then:

$$m_2 = \frac{d_2^{(b)}}{a_1} \tag{2.6}$$

For convenience, we write from here and throughout: $F_1 \equiv F(\varepsilon_1)$, $F_2 \equiv F(\varepsilon_2)$ etc. Summing (2.4) and (2.5), we have the total damage during the second cycle:

$$d_2 = d_2^{(a)} + d_2^{(b)} \tag{2.7}$$

Applying equilibrium for the second cycle yields:

$$\sigma = E_0(1 - d_1 - d_2)\varepsilon_2 \quad \rightarrow \quad E_2 = \frac{\sigma}{E_0 \varepsilon_2} = E_1 - d_2 \tag{2.8}$$

where (2.2) has been used, and E_2 (as all E_is in the following) is also a normalized modulus. Inserting (2.8) into (2.5) and using (2.7), we obtain:

$$d_2^{(b)} = \frac{F_2 - F_1}{1 - F_1}\left(1 - d_2 + d_2^{(b)}\right) = \frac{F_2 - F_1}{1 - F_1}\left(E_2 + d_2^{(b)}\right) \tag{2.9}$$

Therefore,

$$d_2^{(b)} = \left(\frac{1 - F_1}{1 - F_2} - 1\right)E_2 \tag{2.10}$$

Inserting (2.7) in (2.8) and using (2.1), we obtain also,

$$E_2 = E_1 - d_2^{(a)} - d_2^{(b)} = E_1 - (1 - E_1)\frac{a_2 - a_1}{a_1} - \left(\frac{1 - F_1}{1 - F_2} - 1\right)E_2 \tag{2.11}$$

Rearranging yields:

$$\frac{1 - F_1}{1 - F_2}E_2 = E_1 - (1 - E_1)\frac{a_2 - a_1}{a_1} \tag{2.12}$$

Inserting (2.12) in (2.10), we obtain:

$$d_2^{(b)} = E_1 - (1 - E_1)\frac{a_2 - a_1}{a_1} - E_2 \tag{2.13}$$

By a similar procedure, in the third cycle we have:

$$d_3^{(a)} = m_1(a_3 - a_2) + m_2(a_2 - a_1) = d_1^{(b)}\frac{a_3 - a_2}{a_1} + d_2^{(b)}\frac{a_2 - a_1}{a_1} \tag{2.14}$$

Note that the damage in the first term of (2.14) is of a cyclic "age" of 2. Following (2.9):

$$d_3^{(b)} = \frac{F_3 - F_2}{1 - F_2}\left(1 - d_1 - d_2 - d_3^{(a)}\right) = \frac{F_3 - F_2}{1 - F_2}\left(E_2 - d_3^{(a)}\right) = \frac{F_3 - F_2}{1 - F_2}\left(E_3 + d_3^{(b)}\right) \tag{2.15}$$

from which we have:

$$d_3^{(b)} = \left(\frac{1 - F_2}{1 - F_3} - 1\right)E_3 \tag{2.16}$$

Similar to (2.8), equilibrium at the maximum stress of the third cycle yields:

$$E_3 = E_2 - d_3 = E_2 - d_3^{(a)} - \left(\frac{1 - F_2}{1 - F_3} - 1\right)E_3 \tag{2.17}$$

where (2.16) has been used. After using (2.14) and rearranging:

$$\frac{1 - F_2}{1 - F_3}E_3 = E_2 - d_1^{(b)}\frac{a_3 - a_2}{a_1} - d_2^{(b)}\frac{a_2 - a_1}{a_1} \tag{2.18}$$

so that

$$d_3^{(b)} = E_2 - d_1^{(b)}\frac{a_3 - a_2}{a_1} - d_2^{(b)}\frac{a_2 - a_1}{a_1} - E_3 \tag{2.19}$$

Now, defining the microdamage rate of a single site at "age" j as:

$$a_{,j} = \frac{a_{j+1} - a_j}{a_1} \tag{2.20}$$

we can summarize the above and notice the following systematic relations:

$$d_1^{(b)} = 1 - E_1 \tag{2.21}$$

$$d_2^{(b)} = (E_1 - E_2) - d_1^{(b)} a_{,1} \tag{2.22}$$

$$d_3^{(b)} = (E_2 - E_3) - d_1^{(b)} a_{,2} - d_2^{(b)} a_{,1} \tag{2.23}$$

$$d_4^{(b)} = (E_3 - E_4) - d_1^{(b)} a_{,3} - d_2^{(b)} a_{,2} - d_3^{(b)} a_{,1} \tag{2.24}$$

The unit in (2.21) is the normalized zero (undamaged) modulus. For the n-th cycle we obtain:

$$d_n^{(b)} = \left(\frac{1 - F_{n-1}}{1 - F_n} - 1 \right) E_n \quad ; \quad F_n = F(\varepsilon_n) = F(\frac{\sigma}{E_n}) \tag{2.25a,b}$$

and

$$(E_{n-1} - E_n) = d_1^{(b)} a_{,n-1} + d_2^{(b)} a_{,n-2} + \ldots\ldots + d_{n-1}^{(b)} a_{,1} + d_n^{(b)} \tag{2.26}$$

Equations 2.25 and 2.26 constitute the governing equations for the fatigue damage evolution. It is seen that the solution (essentially E_n) for the n-th cycle depends on the damage history of all previous cycles. Since fatigue life usually involves many cycles, it is obvious that the solution of the above is very cumbersome (in fact, impossible). The source of the difficulty comes from $a_{,n}$, which is the fatigue microdamage growth rate. Motivated by the simple macro behavior seen from experiments, we will examine here specific microdamage growth laws, in which the necessary "history" span is limited. Note that the macrodamage rate is just d_n.

Before further progress is possible, a specific failure probability function $F(\varepsilon)$ for the basic microelement in the ensemble should be chosen. This will be of the common Weibull type:

$$F(\varepsilon_n) \equiv F_n = 1 - \exp\left[-\frac{1}{\beta} \left(\frac{\varepsilon_n}{\varepsilon_s} \right)^{\beta} \right] \tag{2.27}$$

The above form is convenient since ε_s has a physical meaning which is the static (monotonic) failure strain. It can be easily shown that

$$\sigma_s = \varepsilon_s \exp\left(-\beta^{-1}\right) \tag{2.28}$$

where σ_s is the (normalized by E_0) corresponding static failure stress of the ensemble. Using the relation

$$\sigma = E_n \varepsilon_n \tag{2.29}$$

and (2.28), we write (2.27) in a more convenient form as:

$$F_n = 1 - \exp\left[-\frac{\alpha}{\beta} E_n^{-\beta} \right] \quad ; \quad \alpha = \frac{1}{e} \left(\frac{\sigma}{\sigma_s} \right)^{\beta} \tag{2.30}$$

where α is independent of n. Returning to (2.25) and using (2.30):

$$\frac{1 - F_{n-1}}{1 - F_n} - 1 = \exp\left[\frac{\alpha}{\beta} \left(E_n^{-\beta} - E_{n-1}^{-\beta} \right) \right] - 1 \tag{2.31}$$

Furthermore, for high cycle fatigue, it is expected that the damage during each cycle will be very small, i.e.,

$$\frac{E_{n-1}-E_n}{E_n}=\frac{-E_{,n}}{E_n}=\frac{d_{,n}}{d_n}<<1 \quad\rightarrow\quad E_{n-1}^{-\beta}\cong E_n^{-\beta}+\beta E_n^{-\beta-1}E_{,n} \tag{2.32a,b}$$

where

$$E_{,n}\doteq E_{n-1}-E_n \tag{2.32c}$$

is the modulus "cyclic derivative," similar to the notation in (2.20). Therefore,

$$\exp\left[\frac{\alpha}{\beta}\left(E_n^{-\beta}-E_{n-1}^{-\beta}\right)\right]-1\cong-\alpha E_n^{-\beta-1}E_{,n} \tag{2.33}$$

The physical interpretation of (2.33) is that the lower end "tail" region of the Weibull distribution, which is the "usable" part in high cycle fatigue, can be accurately approximated by a power law. Using (2.25), (2.31), and (2.33) we obtain:

$$d_n^{(b)}=-\alpha E_n^{-\beta}E_{,n} \tag{2.34}$$

Now notice that RHS(2.34) can be directly integrated and yields:

$$\int_0^n d_i^{(b)}di=\int_0^n -\alpha E_i^{-\beta}E_{,i}di=-\frac{\alpha}{1-\beta}E_n^{1-\beta}=m(n)\cdot a_1 \tag{2.35}$$

where m(n) is the density of microdamage sites.

The possibility of using (2.32) instead of (2.30) generalizes the analysis to almost any failure probability function, since most of them can be approximated by a power law for the small strain region. Therefore, the following analysis is not restricted merely to the Weibull distribution type but includes all pdfs, which can be approximated to a power relation for small strains.

Simple Microdamage Growth Laws

To proceed further, we need a microdamage evolution equation. A general form includes both the microdamage size and stress:

$$a_{,n}=a_{,n}\left(\sigma^{(m)},a_n\right)=a_{,n}\left(\frac{E_0}{E_n}\sigma,a_n\right) \tag{3.1}$$

Note that $\sigma^{(m)}$ is the "true" macrostress, i.e., the uniform field far from the microdamage tip, which is "cyclic dependent," whereas σ is the constant "engineering" macrostress.

For convenience, examine first the simplest microdamage growth law, i.e.,

$$a_{,1}=a_{,2}=.......=a_{,n}=c \tag{3.2}$$

for which the microdamage rate is independent of its size and is uniform. Now write (2.26) for the n+1 cycle:

$$\left(E_n-E_{n+1}\right)=d_1^{(b)}a_{,n}+d_2^{(b)}a_{,n-1}+.......+d_{n-1}^{(b)}a_{,2}+d_n^{(b)}a_{,1}+d_{n+1}^{(b)} \tag{3.3}$$

and subtract (2.26) from (3.3) to obtain:

$$\left(E_{n-1}-2E_n+E_{n+1}\right)+\left(d_n^{(b)}(c-1)+d_{n+1}^{(b)}\right)=0 \tag{3.4}$$

Inserting (2.34) in (3.4), a nonlinear second order difference equation for the macro-stiffness (or damage) is obtained.

Before proceeding with the solution, notice that (3.4) is a summation of two parts, which must be of the same order. In our case, the number of cycles to failure is large (N_f>1000), so that

$$\frac{d_{n+1}^{(b)} - d_n^{(b)}}{d_n^{(b)}} = O\left[\frac{1}{N_f}\right] <<< 1 \tag{3.5}$$

Then, (2.29) can be modified to yield

$$\left(E_{n-1} - 2E_n + E_{n+1}\right) + c d_n^{(b)} \cong 0 \tag{3.6}$$

For a private case when c = 1, (3.6) is simplified further to:

$$\left(E_{n-1} - 2E_n + E_{n+1}\right) + \left(\frac{1 - F_{n-1}}{1 - F_n} - 1\right) E_n = 0 \tag{3.7}$$

The above is identical to the result of a previous, less general analysis [10], although in a slightly different form. For this private case, it was shown that (3.7) can be transformed to the following differential equation (details are not given here):

$$E_{,kk} - \alpha\beta N_f E^{-\beta} E_{,k} = 0 \quad ; \quad \alpha = \left(\frac{\sigma}{\varepsilon_f}\right)^{\beta} \tag{3.8}$$

N_f is the number of cycles to failure and k is the normalized (by N_f) macro-fatigue "age." By noticing that

$$E^{-\beta} E_{,k} \equiv \frac{1}{1-\beta}\left(E^{1-\beta}\right)_{,k} \tag{3.9}$$

(3.8) is further simplified to

$$E_{,k} - \frac{\alpha N_f}{1-\beta} E^{1-\beta} = C \tag{3.10}$$

C is an integration constant, determined from the last cycle data, i.e., at k = 1 ($N = N_f$), the stiffness vanishes (E = 0). Thus, the uniform microdamage law (3.2) leads to a second order, nonlinear differential equation, for the stiffness (or damage) evolution. Fortunately, a simple power solution is analytically found:

$$\frac{\sigma}{\sigma_s} = \left[e\left(1 - \frac{1}{\beta}\right)\right]^{1/\beta} N_f^{-1/\beta} \tag{3.11}$$

which is consistent with Basquin's law (1.1a).

Consider now a second case, for which the microdamage growth rate is characterized by a uniform gradient, i.e.,

$$a_{,n} - a_{,n-1} = B \tag{3.12}$$

Following (2.26) and (3.3), the (n+2), equation is:

$$\left(E_{n+1} - E_{n+2}\right) = d_1^{(b)} a_{,n+1} + d_2^{(b)} a_{,n} + \dots\dots + d_n^{(b)} a_{,2} + d_{n+1}^{(b)} a_{,1} + d_{n+2}^{(b)} \tag{3.13}$$

Subtracting (3.13) from (3.3) and (3.3) from (2.26), and then again one result from the other, we obtain:

$$\left(E_{n-1} - E_n\right) - 2\left(E_n - E_{n+1}\right) + \left(E_{n+1} - E_{n+2}\right) = d_n^{(b)}\left(a_{,2} - 2a_{,1} + 1\right) + d_{n+1}^{(b)}\left(a_{,1} - 1\right) + d_{n+2} \tag{3.14}$$

Using (3.12) and (3.5), the RHS (3.14) is written as:

$$\begin{aligned} & d_n^{(b)}\left(a_{,2}-2a_{,1}+1\right)+d_{n+1}^{(b)}\left(a_{,1}-1\right)+d_{n+2}= \\ & =\left(d_n^{(b)}-d_{n+1}^{(b)}\right)\left(1-a_{,1}\right)+\left(d_{n+2}^{(b)}-d_n^{(b)}\right)+d_n^{(b)}(B+1)\cong d_n^{(b)}B \end{aligned} \tag{3.15}$$

Thus, by the same procedure as above, a third order differential equation is obtained:

$$E_{,kkk}-B\alpha\beta N_f E^{-\beta}E_{,k}=0 \tag{3.16}$$

Continuing in this manner, it is straightforward to show that for the q-th power correlation

$$a_{,n}=Bn^{q-2} \quad ; \quad q\geq 2 \tag{3.17}$$

a differential equation of order q is obtained.

$$E_{,k^q}-B'\alpha\beta N_f E^{-\beta}E_{,k}=0 \quad ; \quad i\geq 0 \tag{3.18}$$

Thus, (3.18) leads to a stress-life power law relation (1.1a) of the form:

$$\sigma=C\cdot N^{-b} \quad ; \quad b=\frac{q}{\beta} \tag{3.19}$$

We see that the present model proposes a direct relation between macro material behavior and micro statistical parameters. Interestingly, q connects three different aspects of the problem: the macro S-N slope, the order of the governing differential equation, and the microdamage growth law (3.17). Moreover, it is possible for q in (3.17) to be non integer, which leads to a fractional differential equation! This intriguing possibility is under current study.

Morphological Aspects of Damage Evolution

An important aspect of microdamage evolution is the random nature of damage growth. So far, the growth rates (3.17) have been considered in a non-random (although statistical), average manner. However, on the micro-level, a considerable material variability is expected. To examine this effect, a numerical simulation of the governing difference equation (3.26) on a 2-D plane was conducted for different values of the parameter $c<1$, i.e., every unbroken neighbor of each broken element had a c probability of failure in each consecutive cycle. Results of two typical simulations are shown in Fig. 2.

The two lower pictures show a single, isolated microdamage growth. The right picture is for $c = 1$, i.e., 100 % probability that the neighbor element will break and the left picture is for ~40 %. The blue region is where the damage initiated, and the different colors indicate the "age" of breakage of every point. It is seen that a fractal shape is obtained, with a fractal dimension directly related to c. The upper two pictures show the damage fractography just prior to failure for the corresponding cases below. Therefore, the parameter c is also connected to the fracture growth morphology, which may be experimentally measured. Such relation, between mechanical properties and fracture surfaces, is one of the most challenging in fatigue and will be studied in the future.

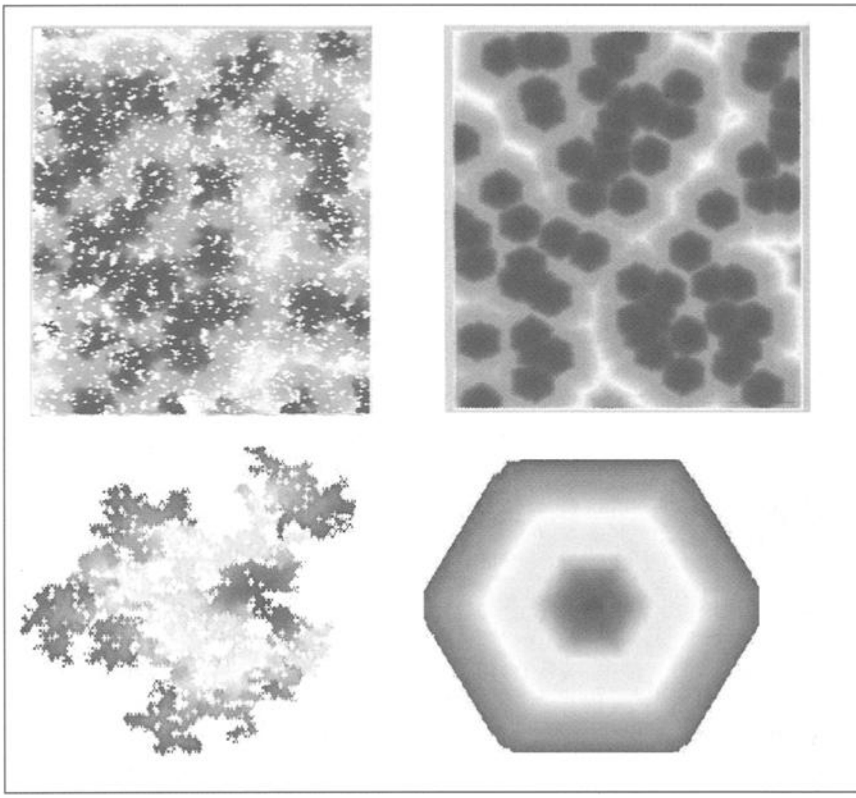

FIG. 2—*Simulation of damage morphology for uniform microdamage rate. Colors reflect the damage "age": blue for damage initiation sites (old) and brown for damage just before total failure. Upper pictures show fractography just before failure, for non-probabilistic local behavior (top right) versus probabilistic one (top left). Lower pictures show morphology progression of a single microdamage on hexagonal net: Non-random (right) versus random (left).*

Conclusions

A statistical micro mechanic model for fatigue damage evolution and failure has been presented. Direct analytical relations between macro (S-N) behavior and micro parameters of damage growth have been found. Specifically, β and q are two parameters which control the S-N power, commonly seen in experiments. B characterizes the probability density function of strength of the microelements, and q controls the rate at which microdamage sites grow in each cycle. In addition, it is shown how geometrical stochastic features of microdamage growth, such as the fractal dimension, and microdamage may be directly related to macro failure.

References

[1] Mahesh, S., Beyerlein, I., Phoenix, S. L., "Size and Heterogeneity Effect on the Strength of Fibrous Composites," *Physica D*, 133, 1999, pp. 371–389.

[2] Delaplace, A., Roux, S., and Pijaudier-Cabot, G., "Damage Cascade in a Softening Interfaces," *Int. J. Solids and Structures*, 36, 1999, pp. 1403–1426.

[3] *Damage and fracture of disordered materials*, Krajcinovich, D. and Van Meir, J., Eds., Inter. Center for Mech. Sciences (CISM), Vol. 410, 2000.

[4] Fedelich B., "A Stochastic Theory for the Problem of Multiple Surface Crack Coalescence," *Int. J. Fracture*, 91, 1998, pp. 23–45.

[5] Fuchs, H. O. and Stephens, R. I., *Metal Fatigue in Engineering*, Wiley, 1980.

[6] Lindley, T. and Pineau, A., "Short Crack Effects in Fracture and Fatigue," Revue de Metallurgie – Science et Genie des Materiaux, February, 1995, pp. 187–201.

[7] Pineau, A., "The Randomness of Fatigue and Fracture Behavior in Metallic Materials and Mechanical Structures," *Mechanics of Random and Multiscale Microstructures*, D. Jeulin and M. Ostoja-Starzewski, Eds., CISM Lecture Notes N 430, Springer Verlag, in press, N-38/01/MM, Paris School of Mines Publication, 2001.

[8] Altus, E., "A Cohesive Micro Mechanic Fatigue Model," *Mech. Mater.*, 11, 1991, pp. 271–280.

[9] Altus, E. and Herszage, A., "A Two-Dimensional Micro Mechanic Fatigue Model," *Mech. Mater.*, 20, 1995, pp. 209–223.

[10] Altus, E., Gerstman, Z., and Golubchick, A., "Two Level Fatigue Loading (H-L) of Mg Alloys: Micromechanic Modeling vs. Experiments," *Metallurgical Science and Technology*, Vol. 20, No. 2, 2002, pp. 3–8.

[11] Altus, E., "Nonlinear Differential Equation for Fatigue Damage Evolution by a Micromechanic Model," *Int. J. Mechanics of Materials*, Vol. 34, No. 5, 2002, pp. 257–266.

[12] McCartney, L. N. and Smith, R. L., "Statistical Theory of the Strength of Fiber Bundles," *J. App. Mech.*, Vol. 50, 1983, pp. 601–608.

[13] Vujosevic, M. and Kracjinovic, D., "Creep Rupture of Polymers - A Statistical Model," *Int. J. Solids and Structures*, Vol. 34, 1997, pp. 1105–1121.

[14] Chakrabarti, B. K. and Benguigui, L. G., *Statistical Physics of Fracture and Breakdown in Disordered Systems*, Oxford Univ. Press, Oxford, 1997.

SESSION 4B: INTEGRITY ASSESSMENT II

Journal of ASTM International, March 2005, Vol. 2, No. 3
Paper ID JAI12038
Available online at www.astm.org

Xin Wang[1] *and Xiao Yu*[1]

On the Constraint-Based Failure Assessment of Surface Cracked Plates under Biaxial Loading

ABSTRACT: Surface cracked plates under biaxial loading represent an excellent model of cracked welded structures experiencing complex loadings. For example, girth and seam welds in pressure vessels are subject to biaxial stress fields. In this paper, the constraint-based failure assessment of surface cracked plates under biaxial tension loading is presented. As a comparison, the assessment of surface cracked plates under uniaxial tension loading is also presented. The elastic T-stress is used as the constraint parameter. The calculation of the stress intensity factors, T-stresses and limit loads for surface cracks under biaxial/uniaxial loadings are discussed. Failure assessments for typical points along the crack front for surface cracks are conducted. The failure assessment results are compared with available experimental observations.

KEYWORDS: surface crack, biaxial loading, failure assessment diagram (FAD), constraint, T-stress, stress intensity factor, limit load

Introduction

The loss of crack tip constraint leads to enhanced resistance to both cleavage and ductile tearing. However, all the conventional failure assessment schemes [1–4] use lower bound toughness obtained from highly constrained test specimens. Over-conservative assessments may occur in situations where the crack in a component is under conditions of low constraint, and may lead to the imposition of prohibitive repair and inspection policies. Constraint effects on fractures have, therefore, received considerable attention recently in efforts to reduce conservatism. Based on the two-parameter fracture mechanics, the frameworks for including the constraint effect in the failure assessment diagram approach were proposed [5]. The recent version of R6 [2] and the newly developed structural integrity assessment procedures for European industry [6] have suggested procedures for failure assessments that include the constraint effect.

The elastic T-stress, or the second term of Williams' series expansion for linear elastic crack tip fields [7], which represents the stress acting parallel to the crack plane, can be used as the parameter to quantify the constraint effect [5]. It has been demonstrated [8–11] that positive T-stress strengthens the level of crack tip stress triaxiality and leads to high crack tip constraint, while negative T-stress reduces the level of crack tip stress triaxiality and leads to the loss of the crack tip constraint. These works have indicated that the T-stress, in addition to the J-integral, provides an effective two-parameter characterization of plane strain elastic-plastic crack tip fields in a variety of crack configurations and loading conditions. In the recent framework for

Manuscript received 4 November 2003; accepted for publication 12 May 2004; published March 2005. Presented at ASTM Symposium on Fatigue and Fracture Mechanics: 34th Volume on 19–21 November 2003 in Tampa, FL; S.R. Daniewicz, J.C. Newman, Jr., and K-H. Schwalbe, Guest Editors.
[1]Associate Professor and Research Assistant, respectively, Department of Mechanical and Aerospace Engineering, Carleton University, Ottawa, Ontario, Canada, K1S 5B6.

constraint-based failure assessment procedures, T-stress has been used as the constraint parameter [5].

Surface cracks are among the most common flaws in the engineering structural components such as pressure vessels, welded joints, and pipes. It has been demonstrated that surface cracks in plates (Fig. 1) under remote tension are under low constraint conditions. Extensive work has been done in the literature for semi-elliptical surface cracks in plates under uniaxial loading (e.g., Fig. 2) [12]. However, many of the surface cracked components are under biaxial loading, for example, girth and seam welds in pressure vessels are subjected to biaxial stress fields. There has been relatively little analytical/experimental research into the effect of biaxiality on the fracture of surface cracked plates, and the existing results have not been particularly conclusive. Results from Brass et al. [13] have indicated a reduction of load carrying capacity under biaxial loading versus uniaxial loading. It has been suggested that the reduction is due to the increase in constraint [13]. However, experimental results from Phaal et al. [14] did not show the same trends.

In this paper, the constraint-based failure assessment of surface cracked plate under biaxial tension loading is presented (Fig. 3). As a comparison, the constraint-based assessment of surface cracked plate under uniaxial tension loading (Fig. 2) is also presented. The elastic T-stress is used as the constraint parameter. The calculations of stress intensity factors, T-stresses and limit load solutions for surface cracked plates under uniaxial/bi-axial tension loading are presented. Failure assessments for typical points along the crack front for surface cracks were conducted. The failure assessment results are compared with available experimental observations.

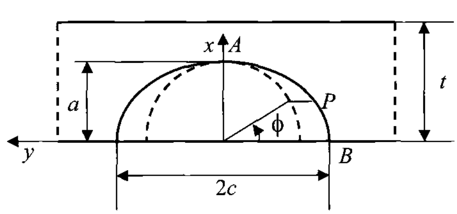

FIG. 1—*Semi-elliptical surface crack.*

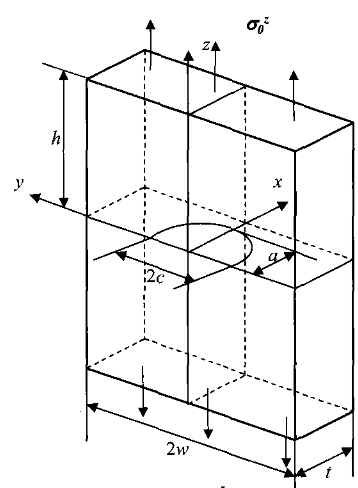

FIG. 2—*Surface cracked plate under uniaxial tension.*

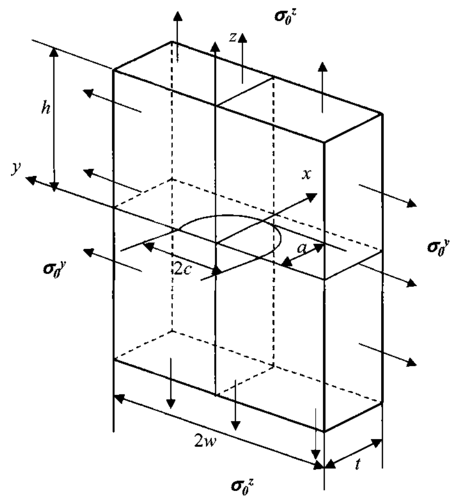

FIG. 3—*Surface cracked plate under biaxial loading.*

Constraint-Based Failure Assessment Diagrams

Allowance for constraint effects in the failure assessment diagram approach was first introduced into the R6 procedure [2] and recently included in SINTAP procedures [6]. Following R6 recommendations [2], the procedure is outlined here.

The conventional failure assessment diagram methods embedded in R6 [1] and PD 6493 [3] are essentially single parameter procedures, in that fracture is assumed to be governed by a single value of toughness or crack opening displacement. The assessment of the potential of failure is determined by the two calculated parameters, (K_r, L_r) determined from

$$K_r = \frac{K_I}{K_{IC}} \tag{1}$$

and

$$L_r = \frac{\sigma}{\sigma_L} \tag{2}$$

Here K_r is the stress intensity ratio with K_I being the stress intensity factor for the cracked component and K_{IC} the toughness of the material. The parameter L_r is the stress ratio, which is the ratio of the applied stress to the limit stress solution of the cracked component calculated based on the yield stress. Failure is avoided if this point (K_r, L_r) lies within a failure assessment diagram, represented by a curve, $K_r = f(L_r)$, and at the same time L_r is less than a cut-off value $L_r^{\max}$.

Based on two parameter fracture mechanics, R6 [2] (Appendix 14) recognizes that a fracture resistance K_{mat}^C relevant to conditions of low constraint may exceed the conventional fracture resistance K_{IC} measured under conditions of high constraint. To include this effect, it suggests that the failure assessment diagram be modified to:

$$K_r = f(L_r)(\frac{K_{mat}^C}{K_{IC}}) \tag{3}$$

Following detailed theoretical and experimental analysis [5,8,9], this increase in fracture toughness can be represented by the following relationship for low constraint conditions:

$$K_{mat}^C = K_{IC}\left[1+\alpha(-\beta L_r)^m\right] \quad \text{for } \beta < 0 \tag{4}$$

where α, and m are material dependent constants, which define the dependence of fracture toughness on constraint; and β is a normalized constraint parameter. Substituting Eq 4 into Eq 3, we have

$$K_r = f(L_r)\left[1+\alpha(-\beta L_r)^m\right] \quad \text{for } \beta < 0 \tag{5}$$

Equation 5 is the constraint-based failure assessment diagram. Failure is avoided if the assessment point (K_r, L_r) (calculated from Eqs 1 and 2) lies within Eq 5, and L_r is less than a cut-off value $L_r^{\max}$. Note that Eq 5 is only applicable for low constraint conditions ($\beta < 0$); for $\beta \geq 0$, corresponding to high constraint conditions, the failure assessment diagram is simply $K_r = f(L_r)$.

The normalized constraint parameter β can be defined from the elastic T-stress:

$$\beta = \frac{T}{\sigma_Y L_r} \tag{6}$$

where σ_Y is the yield stress of the material. Note that here the following estimation of Q stress in terms of T-stress is used [5]:

$$Q = \frac{T}{\sigma_Y} \tag{7}$$

To conduct constraint-based assessment for a cracked body, in addition to the knowledge of the stress intensity factor and the limit load for cracked components, the T-stress is required.

Fracture Parameter/Limit Load Solutions for Surface Cracked Plates

Since we are dealing with a 3D problem, the stress intensity factor and T-stress vary along the crack front. In an isotropic linear elastic body containing a three-dimensional crack subject to symmetric (mode I) loading, the leading terms in a series expansion of the stress field very near the crack front are [7]:

$$\sigma_{11} = \frac{K}{\sqrt{2\pi r}}\cos\frac{\theta}{2}(1 - \sin\frac{\theta}{2}\sin\frac{3\theta}{2}) + T \tag{8a}$$

$$\sigma_{22} = \frac{K}{\sqrt{2\pi r}}\cos\frac{\theta}{2}(1 + \sin\frac{\theta}{2}\sin\frac{3\theta}{2}) \tag{8b}$$

$$\sigma_{33} = \frac{K}{\sqrt{2\pi r}}2\nu\cos\frac{\theta}{2} + E\varepsilon_{33} + \nu T \tag{8c}$$

$$\sigma_{12} = \frac{K}{\sqrt{2\pi r}}\sin\frac{\theta}{2}\cos\frac{\theta}{2}\cos\frac{3\theta}{2} \tag{8d}$$

$$\sigma_{13} = \sigma_{23} = 0 \tag{8e}$$

where the subscripts 1, 2, and 3 suggest a local Cartesian coordinate system formed by the plane normal to the crack front, and the plane tangential to the crack front point s, r; and θ are the local polar coordinates; K is the mode I local stress intensity factor; E is the Young's modulus; and ν

is the Poisson's ratio. The T in Eq 8 is the elastic T-stress, representing a tensile/compressive stress acting parallel to the cracked plane.

In this section, the calculation of fracture parameters: stress intensity factor, elastic T-stress, and the limit load for surface cracked plates under uniaixal and biaxial tension loading are presented. Figures 2 and 3 demonstrated the uniaxial and biaxial cases considered. Note that σ_0^z is the nominal tensile stress in the direction normal to the crack face, and σ_0^y is the nominal tensile stress in the direction parallel to the crack face. The biaxial ratio is defined as follows:

$$\lambda = \frac{\sigma_0^y}{\sigma_0^z} \tag{9}$$

For uniaxial tension, the biaxial ratio $\lambda = 0$.

Stress Intensity Factor Solution

For surface cracked plate under uniaxial load (Fig. 2), the stress intensity factor correlations for semi-elliptical surface cracks were obtained using finite element methods [15,16]. For the current analysis, the stress intensity factors were taken from [16], which presents the stress intensity factors along the crack front for semi-elliptical surface cracks within the range of $0 \le a/c \le 1$ and for a plate geometry within $0 \le a/t \le 0.8$ under general linear and nonlinear loads. The stress intensity factor is presented as follows:

$$K(\phi) = F(\phi) \cdot \sigma_0^z \cdot \sqrt{\pi a / Q_e} \tag{10}$$

where F is the so-called boundary correction factor, $\sigma_0{}^z$ is the nominal tensile stress, and Q_e is the shape factor of an ellipse. The shape factor depends on the crack aspect ratio a/c, and is given by the following equation:

$$Q_e = 1.0 + 1.464(\frac{a}{c})^{1.65} \tag{11}$$

The correlations for the boundary factor $F(\phi)$ for different crack a/c and plate a/t ratios can be found in [16].

Under biaxial tension loading ($\lambda \neq 0$), the stress intensity factor solutions are the same as the corresponding uniaxial loading case ($\lambda = 0$). It is because the stress $\sigma_0{}^y$ is parallel to the crack face, which does not have any contribution to the stress intensity factors. Therefore, Eq 10 can be also used to calculate stress intensity factors for biaxial tension of any biaxial ratio λ.

Elastic T-Stress Solution

Elastic T-stress solutions for the plate with semi-elliptical surface crack under uniaxial tension and bending loads were obtained in [17] using the finite element method. In [17], empirical equations of the T-stress solution are presented for a crack aspect ratio between $0 \le a/c \le 1$ and a relative plate thickness between $0 \le a/t \le 0.8$. The T-stress, for uniaxial tension, $\lambda = 0$, is written as:

$$T^{\lambda=0}(\phi) = V(\phi) \cdot \sigma_0^z \tag{12}$$

where $V(\phi)$ is the normalized T-stress, and σ_0^z is the nominal tensile stress. Equations of V at typical points, along the crack front can be found in [17].

The T-stress solutions for surface cracked plate under biaxial loading can be obtained using superposition method, demonstrated as follows. First, consider a cracked two-dimensional specimen loaded by mode I load system Q, as demonstrated in Fig. 4*a*. The stress field of this problem can be divided into two parts: the regular field which appears under the same loading conditions in the uncracked specimen (Fig. 4*b*), and a corrective field due to the presence of the crack (Fig. 4*c*). Note that the corrective field (Fig. 4*c*) is generated by the crack face pressure, $\sigma_z(x)$, induced by the load system Q in the uncracked body. Therefore, the elastic T-stress for the problem (Fig. 4*a*) can be calculated from the summation of the T-stresses for these two problems:

$$T = T_{uncrack} + T_{crack\ pressure} \tag{13}$$

where $T_{uncrack}$ is the T-stress generated in the regular field, and $T_{crack\ pressure}$ is the T-stress generated by crack pressure. Since the regular stress field (problem Fig. 4*b*) has no singularity at the crack tip, the corresponding stress intensity factor, K, is therefore zero. However, the same cannot be said for the elastic T-stress. Applying the crack tip stress field, Eq 8 and the relationship between local and global coordinates, we can find the corresponding T-stress for the regular field:

$$T_{uncrack} = \lim_{r \to o+} (\sigma_{11}\big|_{\theta=0} - \sigma_{22}\big|_{\theta=0}) = (\sigma_x - \sigma_z)\big|_{x=a,z=0} \tag{14}$$

Here σ_x and σ_z are the stress components from the uncracked body under applied load system Q, and the location is at the crack tip ($x = a$, $z = 0$). Now, substitute Eq 14 into Eq 13, and the T-stress for the problem we are considering, Fig. 4*a*, is then:

$$T = (\sigma_x - \sigma_z)\big|_{x=a,z=0} + T_{crack\ \ pressure} \tag{15}$$

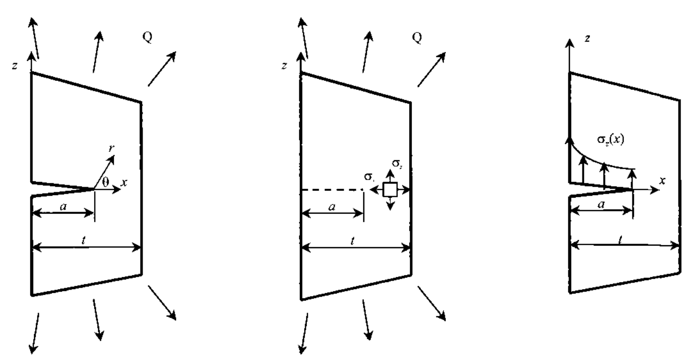

FIG. 4—*Superposition principle for T-stress calculation (*a–c*).*

It is important to note that the current superposition method for T-stress calculation, Eqs 13 and 15 is the extension of the well-known superposition method for the stress intensity factor calculations. From Bueckner [18], stress intensity factor K for the problem in Fig. 4*a*, is the same as the K for the problem shown in Fig. 4*c*, i.e., $K = K_{crack\ pressure}$. However, since the K from the regular uncracked specimen (Fig. 4*b*) is zero, but the T-stress is nonzero (given by Eq 14), the same is not true for the elastic T-stress. Instead, for T-stress calculations, Eq 15 should be used.

Now, let us consider the 3D surface cracked plate. For a cracked problem as shown in Fig. 1, the T-stress is changing along the crack front. The counterpart of Eq 13 is

$$T(P) = T_{uncrack}(P) + T_{crack\ pressure}(P) \tag{16}$$

where P is the general point along the crack front. The uncracked T-stress, the counterpart of Eq 14, is (see Fig. 5)

$$T_{uncrack}(P) = \left\{ \lim_{r \to o+} (\sigma_{11}\big|_{\theta=0} - \sigma_{22}\big|_{\theta=0}) \right\}\Bigg|_P = (\sigma_r - \sigma_z)\big|_P \tag{17}$$

where σ_r and σ_z are the radial direction and normal direction stresses (σ_{11} and σ_{22}) at the location P, respectively. The T-stress for the problem under consideration then becomes:

$$T(P) = (\sigma_r - \sigma_z)\big|_P + T_{crack\ pressure}(P) \tag{18}$$

Here, Eq 18 is used to calculate the T-stress under biaxial loading. For surface cracked plate under uniaxial tension loading, $\lambda = 0$, shown in Fig. 2, and since both $\sigma_x(P)$ and $\sigma_y(P)$ are zeros, $\sigma_r(P)$ is zero. The uncracked T-stress is then:

$$T_{uncrack}^{\lambda=0}(P) = (\sigma_r - \sigma_z)\big|_P = -\sigma_z\big|_P \tag{19}$$

where the coordinates of point a general point along the crack front P are: $x = a\sin\phi$, $y = c\cos\phi$, and $z = 0$.

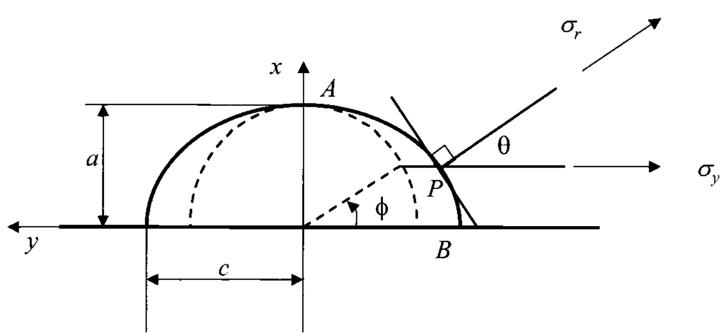

FIG. 5—*Determination of orientation θ.*

For the case of biaxial loading, as shown in Fig. 3, $\sigma_r(P)$ is no longer zero, since $\sigma_y(P)$ is not zero. From the geometry relation as shown in Fig. 5, the angle representing the direction of normal to the crack front, θ, is found to be:

$$\theta = \tan^{-1}\left(-\frac{a}{c\tan\phi}\right) + \frac{\pi}{2} \tag{20}$$

therefore, $\sigma_r(P) = \sigma_y\cos^2\theta$, and the uncracked T-stress for biaxial loading can be written as

$$T_{uncrack}^{\lambda}(P) = (\sigma_r - \sigma_z)\big|_P = (\sigma_y\cos^2\theta - \sigma_z)\big|_P = \sigma_z(\lambda\cos^2\theta - 1)\big|_P \tag{21}$$

where θ is given in Eq 20. Note that the another portion of T-stress, $T_{crack\ pressure}(P)$, is the same for both the uniaxial loading and biaxial loading. Combing Eqs 19, 21 and 18, the following relation between T-stress solutions for uniaxial and biaxial tensions are established:

$$T^{\lambda}(P) = T^{\lambda=0}(P) + \sigma_z \lambda \cos^2 \theta\Big|_P \tag{22}$$

Substituting the T-stress solution for uniaxial tension, obtained earlier, Eq 12, the T-stress solution for any biaxial tension ratio, λ, is found to be:

$$T^{\lambda}(\phi) = \sigma_0^z \cdot V(\phi) + \sigma_0^z \cdot \lambda \cos^2\left(\tan^{-1}\left(-\frac{a}{c\tan\phi}\right) + \frac{\pi}{2}\right) \tag{23}$$

Equation 23 is used in the current analysis to calculate T-stress for surface cracked plates under biaxial tension. This method has been verified in [19]. Three-dimensional finite element analyses were conducted to calculate the T-stress for surface cracked plates under biaxial tension [19]. Excellent agreements were obtained for biaxial tension between the finite element results and predictions from Eq 23.

From Eq 23, it can be seen that the T-stress at the deepest point under biaxial tension is the same as the corresponding T-stress under uniaxial loading. However, for all other points along the crack front, moving away from the deepest point, the T-stress is gradually larger for biaxial cases than the unixial case. Therefore, the constraint level is generally higher along the crack front for the biaxial case. Figure 6 shows results for T-stress along the crack front for a/c = 0.2, a/t = 0.2 for different biaxial ratios. It can be observed that the constraint level is higher for higher biaxial ratio λ.

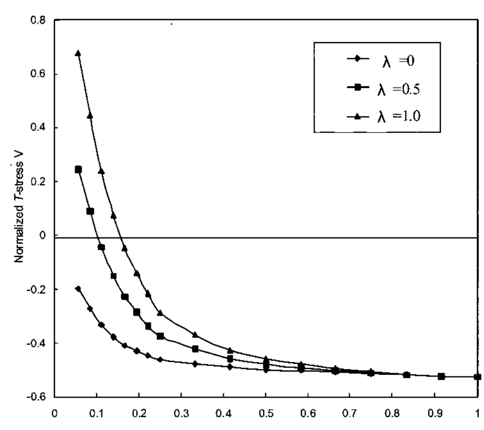

FIG. 6—*Normalized T-stress, $V=T/\sigma_0^z$, along the crack front a/c=0.2, a/t=0.2, λ = 0, 0.5 and 1.*

Limit Load Solution

Different limit load solutions for surface cracked plate under uniaxial tensile loads are presented by different authors. For example, Mattheck et al. [20] proposed an expression for ligament yielding based on Dugdale model calculations. Miller [21] proposed the limit load based on the effective load carrying area. Most recently, Kim et al. [22] suggested expressions based on detailed finite element analysis. In the current work, Kim's expressions are used:

For uniaxial tension:

$$P_L = 2wt\sigma_Y \eta (\frac{\xi}{\zeta + \sqrt{\zeta^2 + \xi}}) \tag{24}$$

where:

$$\xi = (1-\zeta)^2 + 2\zeta(\psi - \zeta)$$
$$\psi = \frac{a}{t}, \qquad \zeta = \frac{ac}{wt} \tag{25}$$

and η is the correction factor for the plate width effect:

$$\eta = \begin{cases} 1 & for \quad w/c \le 4 \\ -0.01(w/c) + 1.04 & for \quad 4 \le w/c \le 9 \\ 0.95 & for \quad w/c \ge 9 \end{cases} \tag{26}$$

Here a, c, t, and w are geometry parameters from Fig. 2, and σ_Y is the yield stress.

For biaxial loads, there are no generally accepted limit load solutions for semi-elliptical surface cracks in flat plates. In the present research, the limit load solutions of Miller [21] for 2D edge cracks under biaxial tension are extended to a semi-elliptical surface crack under remote biaxial tension. The limit load is proposed to be:

$$P_L = 2wt\sigma_Y \eta (\frac{\xi}{\zeta + \sqrt{\zeta^2 + \xi}}) / \sqrt{(1 - \lambda + \lambda^2)} \tag{27}$$

where λ is the biaxial ratio given in Eq 9.

Failure Assessment of Surface Cracked Plate

Based on the stress intensity factor, T-stress, and limit load solutions presented in the last section, failure assessments are now conducted. First, the constraint-based assessment of a surface cracked plate under uniaxial and biaxial loading conditions is demonstrated. Then comparisons of the current assessments with experimental data from Phaal [14] are presented.

Constraint-Based Failure Assessments

First, a surface cracked plate under uniaxial load is assessed. Then the assessment is repeated for a plate under biaxial load. The biaxiality ratios $\lambda = 0.5$ and 1.0 will be used. For each loading, the surface cracked plates were first assessed using the conventional FAD procedure, then reassessed using the constraint-based procedure.

In the current analysis, the material used is A533B (typical nuclear pressure vessel low alloy steel, ASME [23]). The material properties are taken from [23]. At 70°C, the tensile yield stress is 471 MPa, and the ultimate strength is 591 MPa. The Young's modulus of the material is 196.5 $\times 10^3$ MPa. The initiation toughness of the material J_{IC} is assumed to be 0.38 MJ/m^2 based on a conservative estimation. The fracture toughness K_{IC} is then obtained by converting the J_{IC} value. The constraint related material constants α and m, which define the dependence of the fracture toughness on constraint, are assumed to be 1.5 and 1, respectively, which were obtained from experimental results [5]. The thickness of the plate is assumed to be 95.25 mm (3 in.).

The conventional failure assessment diagram equation used in all the analyses in the present work comes from Level 3 of PD 6493 [3]. The lower bound FAD curve in [3] is independent of the geometry and the material:

$$K_r = (1 - 0.14L_r^2)\left[0.3 + 0.7\exp(-0.65L_r^6)\right] \tag{28}$$

Since the load ratio is defined in terms of the yield strength, L_r can be greater than 1. The typical cut-off is 1.2 for C-Mn Steel and 1.8 for austentic stainless steel [3]. Since the flow stress is known for the material of the plate in the current analysis, the ratio of flow stress to the yield stress, σ_f/σ_Y=1.12, is used as the cut-off.

The constraint-based assessments use the failure assessment curve given by Eq 5, from which we have:

$$K_r = (1 - 0.14L_r^2)\left[0.3 + 0.7\exp(-0.65L_r^6)\right]\left[1 + 1.5(-\beta L_r)\right] \quad \text{for } \beta < 0 \tag{29}$$

For any $\beta \geq 0$, corresponding to the high constraint conditions, the conventional FAD of Eq 28 is used.

For a given a/c ratio, a series of cracks with different a/t ratios are assumed. The corresponding FADs are then generated. Since we are dealing with 3D crack problems, any point along the crack front can be assessed for given crack geometry. Typical results of failure assessment diagrams for a/c = 0.2, a/t = 0.2 – 0.8, at deepest point, ϕ = 90° and near the surface point, ϕ = 5° are presented in Figs. 7*a*–7*c*. Three loading conditions were considered, uniaxial case (λ = 0), and two biaxial cases (λ = 0.5 and 1).

At the deepest point, the constraint-based FADs do not change when the biaxiality ratio λ changes from 0 to 1 (Fig. 7*a*), because the constraint parameter (*T*-stress) remains unchanged. However, at ϕ = 5°, the constraint-based FADs converge back to conventional FADs as λ increases from 0 to 1 (Figs. 7*b*–7*c*), because at the surface point, the constraint parameter (*T*-stress) increases from negative to positive as λ increases from 0 to 1.

From the failure assessment diagrams, the maximum load carrying capacity for surface cracks under uniaxial and biaxial loading conditions can be calculated. Note that for this 3D problem, failure assessment can be conducted for any point along the crack front. However, detailed analyses for a typical low aspect ratio crack of a/c = 0.2 have shown that the failures are controlled by the failure at the deepest point.

Based on the failure assessment diagrams at the deepest points, the maximum load carrying capacity for surface cracks under uniaxial and biaxial loading conditions are calculated. The resulting maximum axial stress is normalized as follows:

$$P_n = \frac{\sigma}{\sigma_f} \tag{30}$$

where σ_f, the flow stress of the material, equals $0.5(\sigma_Y + \sigma_u)$, with σ_Y and σ_u ad the yield and ultimate strengths, respectively. The resulting maximum normalized axial stress P_n for a/c=0.2 with different a/t ratios is presented in Figs. 8*a*–8*b*. From the figures, it can be seen that the maximum load carrying capacity is increased using the constraint-based failure assessment diagram comparing to the results from conventional FADs. In the current analysis, it is found that the load carrying capacity is the same for the cases of uniaxial tension and the case of biaxial ratio of 1 (Fig. 8*a*). Due to the difference at the limit load solutions, (see Eq 27), for the case of λ = 0.5, the load carrying capacity is about 15 % higher for than that of λ = 0 or 1 (Fig. 8*b*).

From the above calculations, the low constraint has a significant effect on the allowable tensile stresses, and it can be observed that it is overly conservative to exclude the low constraint effect. By accounting for the effect of low constraint, the increase in the allowable tensile stress can be as much as 16–38 % in the case of uniaxial and biaxial tension cases.

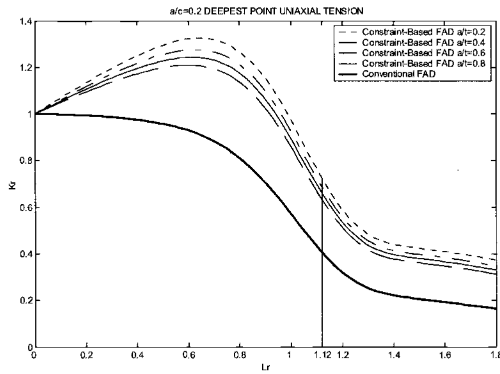

(a)

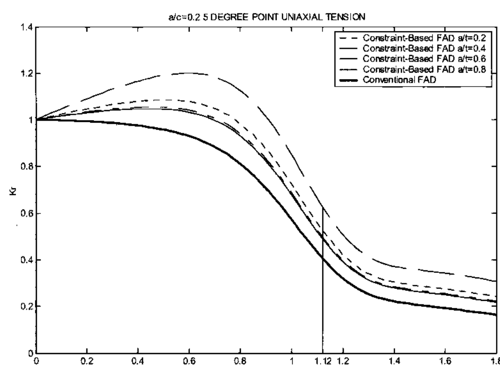

(b)

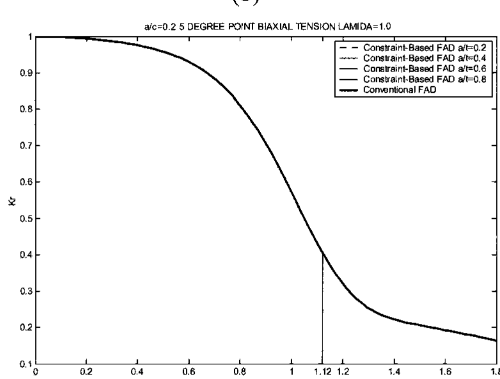

(c)

FIG. 7—*FADs: (a) deepest point, $\lambda = 0, 0.5$, and 1; (b) $\phi = 5°$, $\lambda = 0$; and (c) $\phi = 5°$, $\lambda = 1$.*

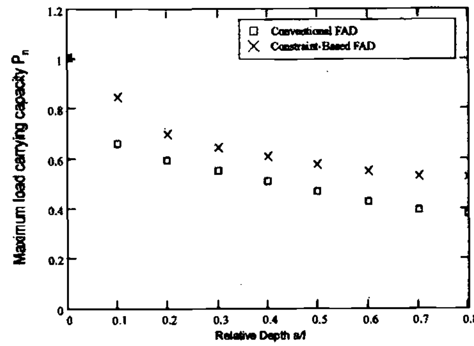

(a)

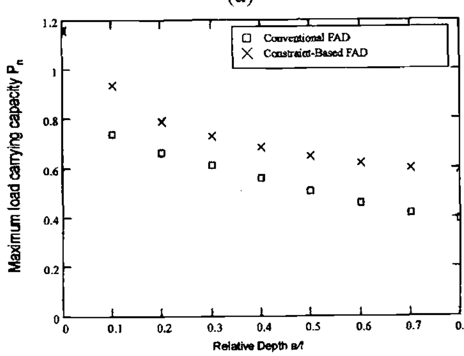

(b)

FIG. 8—*Comparison of conventional and constraint-based FADs, a/c = 0.2: (a)* $\lambda = 0, 1.0$; *(b)* $\lambda = 0.5$.

Comparison with the Experimental Results

Phaal et al. [14] conducted a comprehensive test program investigating the effects of biaxial loading on the fracture behavior of A533B pressure vessel steel. All of their tests have been assessed to the conventional R6/PD6493 procedures, showing that the conventional R6/PD6493 procedures are safe and conservative for assessing A533B under the action of a biaxial stress fields. Results for biaxial tension with biaxial ratio $\lambda = 0$ (uniaxial), $\lambda = 0.5$, and $\lambda = 1$ were presented in [14]. It was observed that the deepest point is the location of crack initiation in all of the testing specimens [14]. The dimensions of the test specimens, crack geometries, and the resulting maximum load carrying stress σ_{max} are summarized in Table 1.

In the present research, both conventional and constraint-based failure assessments are conducted based on the deepest point for the 12 testing specimens. The T-stress solutions for different a/c and a/t crack geometries under different λ ratios are obtained using Eq 23. The resulting FADs are shown in Figs. 9*a*–9*c*, together with the assessment points for each specimen. The assessment points of the testing results are directly obtained from [14]. From all the cases, it can be seen that the constraint-based failure assessment presented is safe, and the conservatism at the conventional failure assessments can be reduced.

TABLE 1—*Summary of testing results from [14].*

Specimen No.	λ	t (mm)	W (mm)	a (mm)	2c (mm)	σ_{max} (MPa)
M01-01	0	51.5	496	24.9	145.8	476
M01-10	0	51.0	500	25.9	135.0	279
M01-11	1	25.0	500	17.0	135.0	460
M01-12	0	25.0	500	14.6	135.0	447
M01-13	0.5	25.0	500	13.4	148.5	618
M01-20(1)	1	51.0	500	24.2	134.5	287
M01-20(2)	0	25.0	500	10.4	135.3	501
M01-21	1	25.0	500	11.3	143.0	491
M01-22	0.5	25.0	500	11.0	145.0	625
M01-23	0.5	26.3	500	10.6	221.1	547
M01-24	1	27.0	500	11.5	145.0	462
M01-25	1	50.5	500	34.3	135.9	294

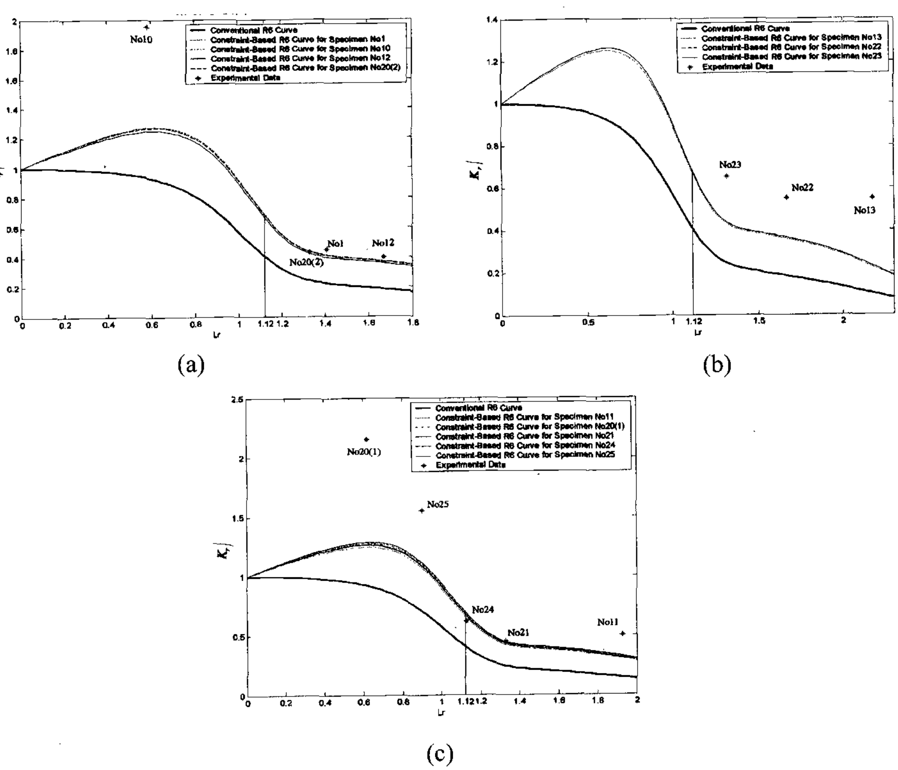

FIG. 9—*Comparison of experimental data [14] and current FADs: (*a*) uniaxial tension, (*b*) biaxial tension, $\lambda = 0.5$, and (*c*) biaxial tension, $\lambda = 1$.*

It is also worth noting that the σ_{max} obtained from the testing for similar geometries is in the same level for $\lambda = 0$ (uniaxial) and $\lambda = 1$; and the σ_{max} is about 20–25 % higher for $\lambda = 0.5$. For example, specimen M01-20(2) ($\lambda = 0$, uniaxial) and M01-21 ($\lambda = 1$), the final stress σ_{max} is around 500 MPa, while M01-22 ($\lambda = 0.5$), the σ_{max} is around 620 MPa. This agrees with the predictions obtained in last section, that is for a given surface crack geometry, the maximum load carrying capacity is the same for the cases of uniaxial and biaxial tension of $\lambda = 1$, but it will be 15 % higher for biaxial tension of $\lambda = 0.5$.

Conclusions

The constraint-based failure assessment of a surface cracked plate under biaxial tension loading was presented. As a comparison, the constraint-based assessment of a surface cracked plate under uniaxial tension loading was also presented. The elastic *T*-stress was used as the constraint parameter. The calculations of stress intensity factors, *T*-stresses, and limit load solutions for surface cracked plates under uniaxial/bi-axial tension loading were demonstrated. For a surface cracked plate under uniaxial tension, the constraint level is low around the whole crack front (*T*-stress below zero). Under biaxial tension, the constraint level remains low around the deepest point, but it increases to high constraint conditions (*T*-stress higher than zero).

Failure assessments for typical points along the crack front for surface cracks were conducted. It is found that the deepest point is still the critical point for fracture for low aspect ratio cracks ($a/c = 0.2$). It has been demonstrated that constraint-based failure assessments give more realistic predictions for fracture, and the conservatism in the conventional failure assessment procedures can be reduced significantly. The FADs for testing specimens obtained from the current analysis agree with the testing data from [14].

From the current analyses, for the same cracked geometry, the maximum load carrying capacity is found to be in the same level for uniaxial tension ($\lambda = 0$) and biaxial tension case of $\lambda = 1$. It is also found for the case of biaxial tension of $\lambda = 0.5$, the maximum load carrying capacity is actually higher than the uniaxial case and the biaxial case of $\lambda = 1$. These results are found to be consistent with the testing results from [14].

Acknowledgments

The authors gratefully acknowledge the financial support from the Natural Sciences and Engineering Research Council (NSERC) of Canada and Materials and Manufacturing Ontario (MMO).

References

[1] Harrison, R. P., Loosemore, K., and Milne, I., "Assessment of the Integrity of Structures Containing Defects," CEGB Report R/H/R6, Berkeley, U. K., 1976.

[2] R6, "Assessment of the Integrity of Structures Containing Defects, Procedure R6, Revision 3," Nuclear Electric Ltd., Gloucester, U.K., 1997.

[3] PD 6493, "Guidance on Some Methods for the Derivation of Acceptance Levels for Defects on Fusion Welded Joints," British Standards Institution, 1991.

[4] ASME Boiler and Pressure Vessel Code, "Assessment of Reactor Vessels with Low Upper Shelf Charpy Impact Energy Levels," Section XI, Division 1, Case N-512, American Society of Mechanical Engineers, New York, NY, 1993.

[5] Ainsworth, R. A. and O'Dowd, N. P., "Constraint in the Failure Assessment Diagram Approach for Fracture Assessment," *ASME Journal of Pressure Vessel Technology*, Vol. 117, 1995, pp. 260–267.

[6] Ainsworth, R. A., Sattari-Far, I., Sherry, A. H., Hooton, D. G., and Hadley, I., "Methods for Including Constraint Effects Within SINTAP Procedures," *Engineering Fracture Mechanics*, Vol. 67, 2000, pp. 563–571.

[7] Williams, M. L., "On the Stress Distribution at the Base of a Stationary Crack," *ASME Journal of Applied Mechanics*, Vol. 24, 1957, pp. 109–114.

[8] Betegon, C. and Hancock, J. W., "Two-Parameter Characterization of Elastic-Plastic Crack Tip Fields," *ASME Journal of Applied Mechanics*, Vol. 58, 1991, pp. 104–110.

[9] Du, Z .Z. and Hancock, J. W., "The Effect of Non-Singular Stresses on Crack Tip Constraint," *Journal of Mechanics and Physics of Solids*, Vol. 39, 1991, pp. 555–567.

[10] O'Dowd, N. P. and Shih, C. F., "Family of Crack Tip Fields Characterized by Triaxiality Parameter—I. Structure of Fields," *Journal of Mechanics and Physics of Solids*, Vol. 39, 1991, pp. 989–1015.

[11] Wang, Y.Y., "On the Two-Parameter Characterization of Elastic-Plastic Crack Front Fields in Surface Cracked Plates," *Constraint Effects in Fracture, ASTM STP 1171*, E. M. Hackett, K. H. Schwalbe, R. H. Dodds, Eds, ASTM International, West Conshohocken, PA, 1993, pp. 120–138.

[12] Wang, X. and Reinhardt, W., "On the Constraint-Based Failure Assessment for Surface Cracked Welded Plates," *Proceedings of the ASME International Conference on Pressure Vessels and Piping*, Cleveland, OH, July 2003.

[13] Bass, B. R., Shum, D. K., and Keeney-Walker, J., "Constraint Effects on Fracture Toughness for Circumferentially Oriented Cracks in Reactor Pressure Vessels," Oak Ridge National Laboratory, NUREG/CR-6608, ORNL/TM-12131, August 1992.

[14] Phaal, R., Andrews R. M., and Gardwood, S. J., "TWI Biaxial Test Program: 1984–1994," *International Journal of Pressure Vessel and Piping*, Vol. 64, 1995, pp. 177–199.

[15] Newman, J. C. and Raju, I. S., "An Empirical Stress Intensity Factor Equation for the Surface Crack," *Engineering Fracture Mechanics*, Vol. 15, 1981, pp. 185–192.

[16] Wang, X. and Lambert, S. B., "Local Weight Functions for Semi-Elliptical Surface Cracks in Finite Thickness Plates," *Theoretical and Applied Fracture Mechanics*, Vol. 23, 1995, pp. 199–208.

[17] Wang, X., "Elastic *T*-Stress for Cracks in Test Specimens Subjected to Non-Uniform Stress Distributions," *Engineering Fracture Mechanics*, Vol. 69, 2002, pp. 1339–1352.

[18] Bueckner, H.F., "A Novel Principle for the Computation of Stress Intensity Factors," *Z Agew Math Mech*, Vol. 50, 1970, pp. 129–146.

[19] Yu, X., "Constraint-Based Fracture Mechanics Analysis for Surface Cracked Plates," Master's Thesis, Carleton University, 2003.

[20] Mattheck, C., Morawietz, P., Munz D., and Wolf, B., "Ligament Yielding of a Plate with Semi-Elliptical Surface Cracks under Uniform Tension," *International Journal of Pressure Vessel and Piping*, Vol. 16, 1984, pp. 131–143.

[21] Miller, A. G., "Review of Limit Loads of Structures Containing Defects," *International Journal of Pressure Vessel and Piping*, Vol. 32, 1988, pp. 197–327.

[22] Kim, Y. J., Shim, D. J., Choi, J. B., and Kim, Y. J., "Elastic Plastic Analyses for Surface Cracked Plates under Combined Bending and Tension," *Journal of Strain Analysis*, Vol. 37, 2002, pp. 33–45.

[23] ASME Boiler and Pressure Vessel Code, Section II, Materials, 2001 ed.

Yil Kim[1], Yuh J. Chao[1,2], Shu Liu,[1] and Seok-Ki Jang[3]

An Experimental Study on Surface Crack Growth under Mode-I Load

Reference: Yil Kim, Yuh J. Chao, Shu Liu, and Seok-ki Jang, **"An Experimental Study on Surface Crack Growth under Mode-I Load,"** *Fatigue and Fracture Mechanics: 34th Volume, ASTM STP 1461*, S. R. Daniewicz, J. C. Newman and K.-H. Schwalbe, Eds., ASTM International, West Conshohocken, PA, 2004.

ABSTRACT: Surface crack growth in plates made of aluminum 7050 alloy is studied by the Rubber Impression Method (RIM). RIM is an experimental technique used to estimate the three-dimensional crack profiles by inserting and taking out gel-state rubber from the crack opening during the test. Far-field tensile loading was applied to the surface-cracked thin plates with various crack geometries. Three stages of fracture are found; (1) flat stable tearing close or up to through thickness (2) unstable lateral tearing with flat tunneling transitioning to slant fracture and (3) unstable fully slant fracture. Crack profiles measured by the RIM were compared with the crack extension marked by fatigue loads. Generally, reasonable agreement is obtained except the region adjacent to the free surface. The Crack Tip Opening Displacement (CTOD) at the center of the crack was obtained by examining the crack opening profiles at different load levels. The results indicate that the shallow cracked specimen has relatively high value of CTOD at the initiation of stable crack growth. Due to complex geometry of the three-dimensional crack the RIM showed its limits in precise measurement of the crack tip details. Nevertheless the RIM could be an effective way to study the overall behavior of ductile crack growth.

KEYWORDS: crack growth, Rubber Impression Method (RIM), surface-cracked thin plate, 7050 aluminum alloy, crack tip opening displacement

Introduction

Since the introduction of CTOD/CTOA by Wells [1] as the fracture parameter for growing cracks in elastic-plastic materials, a great number of experimental studies have been reported to prove its validity as a ductile fracture criterion [2-6]. As a result, standardized procedures have been established for CTOD fracture toughness measurements [7, 8]. However, except for the determination of residual strength of the tension specimen outlined by ASTM E 740-95, test standards use straight and through thickness crack in the test specimen geometry. On the contrary, common cracks detected from real structures often have more complex geometries than straight cracks. Consequently, in order to transfer the fracture toughness data obtained from standard test specimens to real structures, knowledge on the fracture behavior of non-straight, part-through cracks is needed.

For part-through surface cracks, the location of crack initiation site depends on the type of loading, specimen geometry and crack aspect ratio as well as the crack-tip constraint. Assuming

[1] Research Associate, Professor, and Research Associate, respectively, Department of Mechanical Engineering, University of South Carolina, Columbia, SC 29208.
[2] Author for correspondence: Chao@sc.edu; Telephone (803)-777-5869
[3] Professor, Department of Marine Engineering, Mokpo National Maritime University, Mokpo, Chon-nam 530729, Republic of Korea

plane-strain dominance at the deepest region of a part-through crack, there is a high probability that the fracture initiates at the interior of the crack rather than at the free surface. This behavior makes it difficult to validate with generic experimental techniques that depend on measurement at the specimen surface. Furthermore, it is almost impossible to predict what is really happening inside the surface crack during successive crack growth.

In this study, the experimental technique called Rubber Impression Method (RIM) was applied to three-dimensional measurement of growing surface cracks. Unlike the indirect methods such as acoustic emission and ultrasonic method, this method makes it possible to directly measure the three-dimensional crack profiles by inserting the gel-state silicon rubber into the crack, and then taking out the solid-state rubber (or rubber replica) after it solidifies. This technique was previously applied for the study of ductile crack growth in compact tension (CT) specimens by the third author [9]. To verify the applicability of this method for measurement of growing surface crack profiles, in-plane crack growth profiles were also obtained by fatigue markings during the tests and compared with those obtained by RIM. In addition, CTOD was approximated from the crack opening profiles and the characteristics of stable crack growth were examined.

Specimen Geometry and Loading Condition

Aluminum 7050 alloy with yield stress 376 MPa and Young's Modulus E= 66.9 GPa was selected as the test material. Five thin plates were machined as shown in Figure 1(a). At the mid-plane of the plate, a surface crack was introduced by the electric discharge machining (EDM) followed by fatigue pre-cracking. The overall dimensions of the test specimens are listed in Table 1. All the specimens have the same height (H), width (W), and thickness (t). Two kinds of surface crack were considered; one is semi-circular ($a/2c$ = 0.46, for Specimens A and E), and the other is elliptical ($a/2c$ = 0.16, for Specimens B, C and D). Two crack depths (a/t = 0.40 and 0.58) were prepared for semi-circular crack and three different crack depths (a/t = 0.17, 0.34, and 0.53) for semi-elliptical crack. Figure 1(b) shows one half of the surface-crack geometry for Specimens A, B, C, D and E. Due to the small amount of fatigue pre-crack, only the initial crack profiles machined by the EDM are shown in Figure 1(b). It should be noted that the crack shapes fabricated by the EDM are not exactly semi-circular or semi-elliptical as shown in Figure 1(b). The choice of these geometries came from easy reproduction of the specimens with different crack depths but with the same aspect ratio as seen in Table 1.

In this study, as shown in Figure 1(a), a coordinate system is employed such that x-z plane coincides with the crack plane, the x-axis lies along the direction of specimen thickness, the z-axis lies along the direction of specimen width, and the y-axis is orthogonal to the crack plane. Far field tensile loading along the y-direction is applied by a hydraulic loading frame.

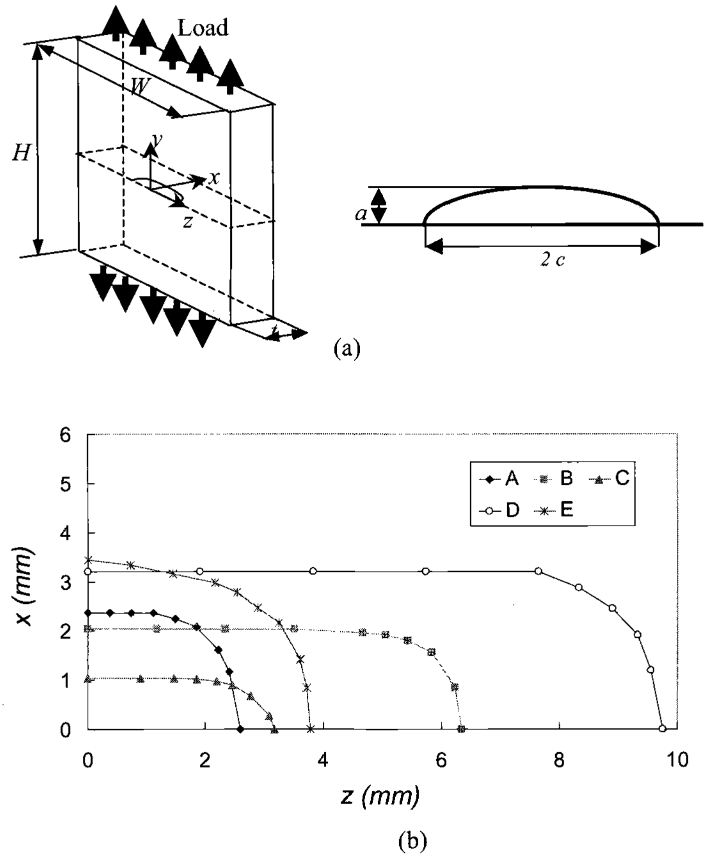

FIG.1- *Specimen; (a) loading condition, and (b) the half crack geometry of specimens A, B, C, D, and E*

TABLE 1 - *Dimensions of specimens*

Specimen	*a, mm*	*c, m*	*a/*	*t, m*	*a*	*W, mm*	*H, mm*
A	2.37	2.5	0.4	6	0.4	50	180
B	2.03	6.3	0.1	6	0.3	50	180
C	1.03	3.1	0.1	6	0.1	50	180
D	3.20	9.7	0.1	6	0.5	50	180
E	3.45	3.7	0.4	6	0.5	50	180

Experimental Procedure

Rubber Impression Method (RIM)

Polysulfidic rubber (normally called silicon rubber) consists of gel-state base material and catalyst sealed in separate containers at room temperature before using. Once they are mixed together with a volume ratio of 50:50 and cast into a mold, the mixture changes to an elastic material as time elapses. On account of this characteristic, silicon rubber has long been used by dentists to mold the teeth set of patients. In this study, similar procedure as used by dentists was applied to fracture testing and named Rubber Impression Method. Mixed compound was injected into the mouth of the surface crack with pressure. In order to minimize the increasing viscosity with time, injection was finished within 30 seconds after mixing. At room temperature, the mixture turned into an elastic material in 5 minutes. Silicon rubber was then pulled out after increasing the load level to open the crack mouth slightly. This rubber replica bears the shape or "impression" of the crack shape or profile. Load or displacement was then increased again for the next crack growth and the new mixture was inserted. This insertion and pullout procedure was repeated until the specimen broke. By measuring the dimensions of the rubber replicas with optical microscope, three-dimensional geometries of the surface cracks at various load levels were obtained. More details about the RIM and fracture test results on CT specimens can be found in [9].

Fracture Test Procedures

Tension tests were performed on five specimens. The cracks were first made by the EDM and then fatigue pre-cracked. Specimens were loaded monotonically under displacement control at room temperature. A Material Test System (MTS) machine was used for the tension test with a crosshead speed of 0.05 *mm/min*. Figure 2 shows the typical loading sequence versus non-dimensional time. The test procedure is as follows.

(a) The gel-state silicon rubber is inserted into the mouth of the crack under a small load.
(b) Wait about 10 minutes for the silicon rubber to solidify, reload to the next level, stop, and pull out the rubber replica.
(c) Apply fatigue loading. The purpose of fatigue loading is to generate the fatigue markings which can be examined later from the broken specimen to retrieve the intermediate crack front profile. Fatigue loading is schematically denoted as two reduced loading points from the overall loading curve, shown in Figure 2. The fatigue load range is 70% ~ 90% of the current loading level and 10,000 cycles were used.
(d) Inject new gel-state silicon rubber into the crack mouth.
(e) Procedures (b) to (d) are repeated until the specimen is broken.

In Figure 2, the load levels when silicon rubbers are inserted into the specimen are marked with circled numbers. The open pairs of symbols for each reduced load denote the beginning and end of fatigue cycling. Applied load levels for each specimen are tabulated in Table 2.

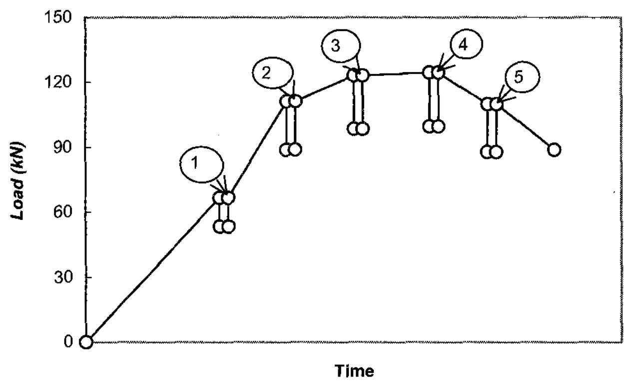

FIG.2 - *Typical loading sequence (from Specimen A)*

TABLE 2 – *Applied load levels*

Specimen	1^{st}, *kN*	2^{nd}, *kN*	3^{rd}, *kN*	4^{th}, *kN*	5^{th}, *kN*
A	66.7	111.2	123.2	124.5	110.0
B	53.4	83.6	93.9	93.9	-----*
C	66.7	105.4	127.5	128.4	126.5
D	44.5	66.7	80.1	-----*	
E	66.7	89.0	97.9	105.7	-----*

* Fracture occurred before reaching the next intended load level

Experimental Results

Fracture mode

Figure 3(a) shows the typical fractured surface where the initial crack is in dark gray and the final crack profile under stable crack growth is marked with solid line. Three distinct fracture modes are observed from the broken samples. The first one is the flat fracture zone that is located at the center part of plate (line A-A in Figure 3(a)). In this zone, crack grew stable initially and when the amount of stable crack growth reached certain size, fast fracture leads to the through-wall crack with nearly flat fracture plane (plane A-A in Figure 3(b)). The second one is the combined zone of flat fracture and slant fracture - the latter is usually referred to as shear-lips (line B-B in Figure 3(a) and plane B-B in Figure 3(b)). In Figure 3(b), plane B-B shows that the shear-lips started to develop at the free surface from both front and the back side of the plate while flat fracture was still dominant at the mid-part of the plate. This behavior is similar to the tunneling effect during crack growth of through-wall cracks. The final one is the fully slant fracture zone with an inclination of approximately 45° to the free surface (line C-C in

Figure 3(a) and plane C-C in Figure 3(b)). In this zone, which corresponds to the late stage of the crack growth, a through-wall crack was already formed and showed unstable crack growth leading to the ultimate catastrophic failure of the plate. All the specimens show remarkable formation of shear-lips before last stage fast fracture. As a good comparative example, similar experimental findings on fast fracture and shear-lips were reported from the study of thin plate with a through-wall crack by Narasimhan *et al.* [10].

In-plane crack growth profiles

To verify the reliability of the RIM on the measurement of the in-plane crack profile, i.e. complete penetration of the molding material to the crack tip, the crack front profiles obtained from the fatigue markings and from the rubber replicas are compared.

Figure 4 shows the fracture surfaces of broken specimens taken by optical microscope. The crack grew from an initial shape that is colored in dark gray. After the crack grew successively, through-wall crack is introduced by fast fracture under the tensile load or the fatigue load. The intermediate crack fronts during the crack growth are better illustrated in Figure 5 from specimen A. In Figure 5(a), dashed lines are drawn along the crack front clearly distinguished by the fatigue markings. The complete set of in-plane crack growth profiles from specimen A is shown in Figure 5(b).

Figure 6 is a magnified view of a typical rubber replica that was pulled out from Specimen A. The contours of initial notch and crack extension are clearly seen. By measuring the outer boundaries of rubber replicas carefully with the help of optical microscope, the crack growth profiles can be obtained. Optical microscope of 14X magnifications equipped with an automatic measurement device (known as Dynascope or LYNX) was used for determining the dimensions of the rubber replicas. The crack profiles were regenerated from the x- and y- coordinates measured by a microprocessor measurement system.

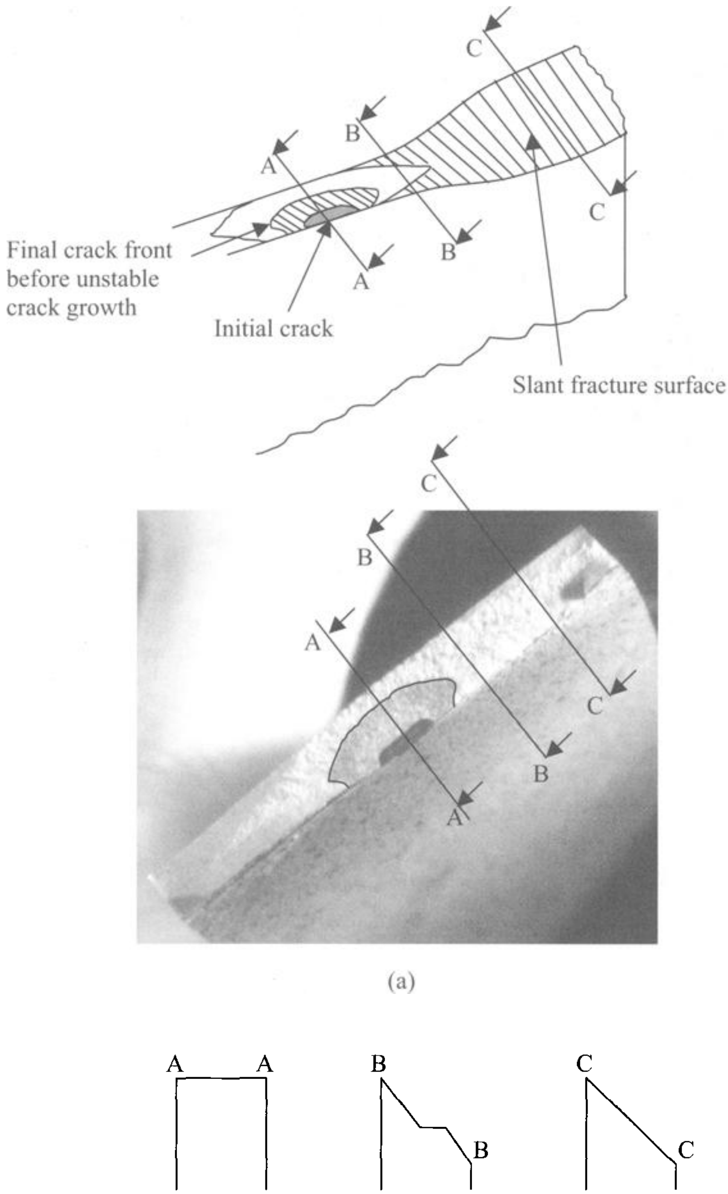

FIG.3 - *(a) Photograph of the fracture surface; and (b)the topography at sections AA, BB and CC*

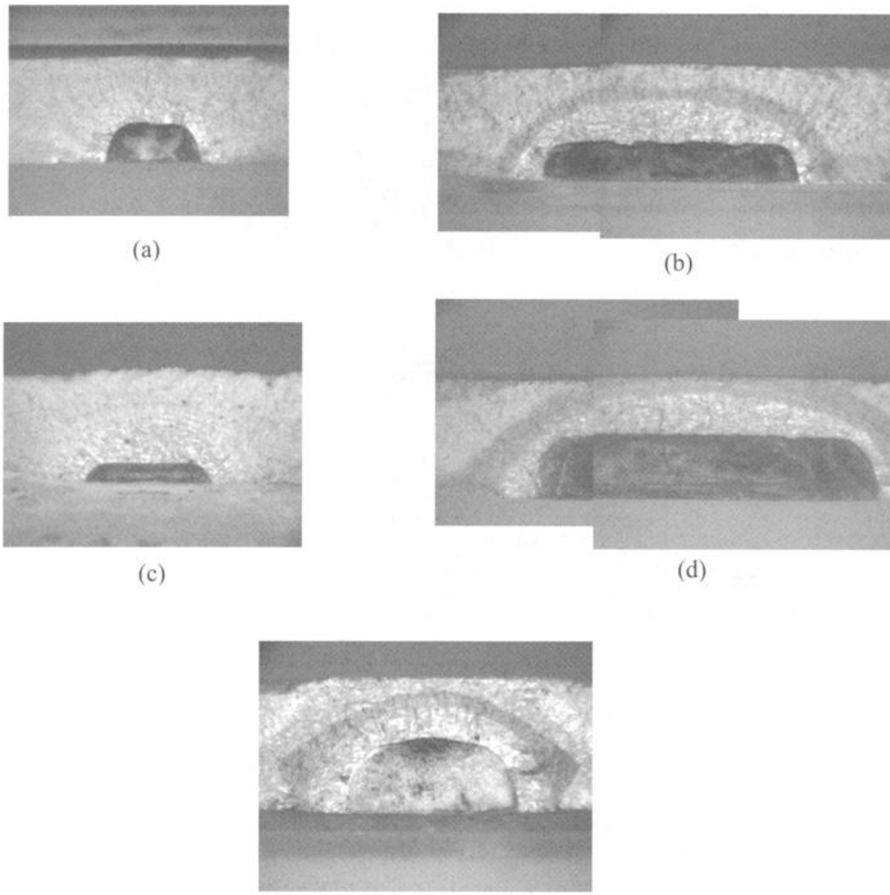

(a) (b) (c) (d) (e)

FIG.4 - *Fracture surfaces with crack growth profiles; (a) ~ (e) for Specimens A ~ E, respectively*

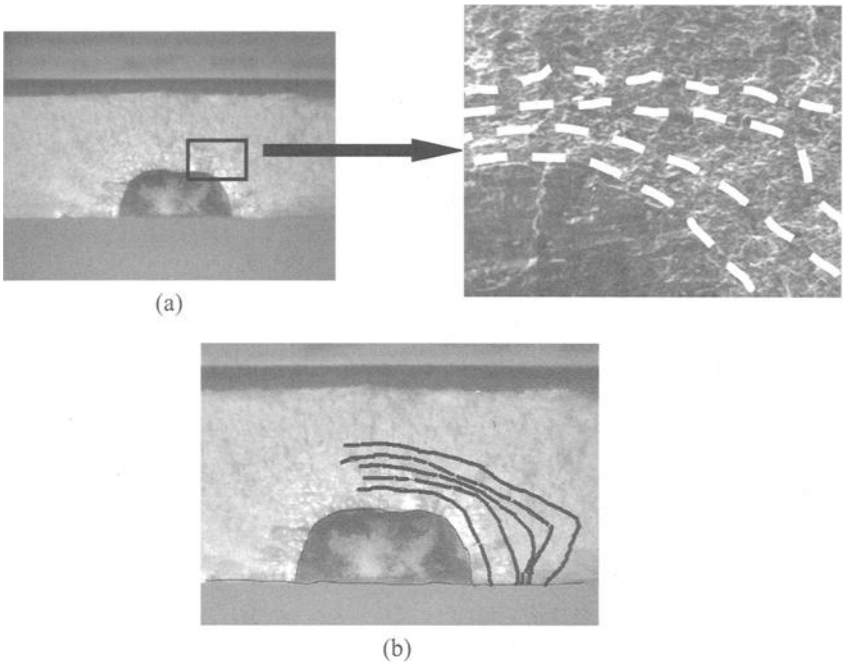

FIG.5 - *Microscopic view of fracture surface of Specimen A; (a) fatigue marks, and (b) successive crack growth profiles*

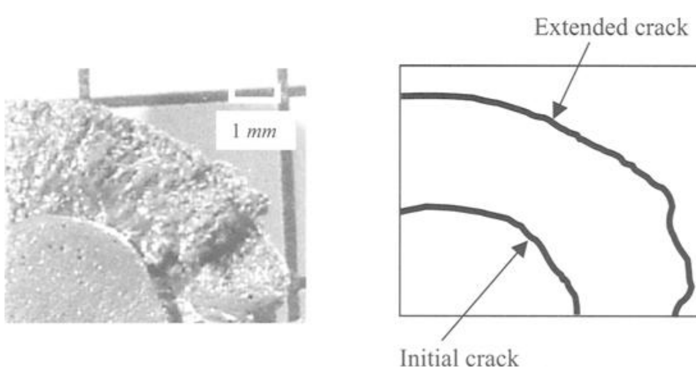

FIG.6 - *The shape of crack growth by silicon rubber for Specimen A (half of the crack is shown.)*

Figure 7 shows the crack profiles from both the RIM (the solid lines) and fatigue markings (the dotted lines). Generally the crack growth contours measured from the RIM compare reasonably well with those from the fatigue markings though there are some mismatches particularly near the free surface region. This mismatch appears to be from the lack of full penetration of the silicon rubber to the crack tip due to the viscosity of silicon rubber and no space for the entrapped air to escape.

It is interesting to note the evolution of crack geometry during the crack extension for the current tests involving monotonic tensile loads. Aside from the butterfly shape of crack growth for all specimens, Figure 8 shows the variation of the aspect ratio (c/a, half of crack length to crack depth) versus the crack extension at the deepest point. The aspect ratio $c/a = 1.0$ is for semi-circular crack and $c/a = 3$ is for semi-elliptical crack considered in this study. As shown in Figure 8, the growth of semi-circular cracks was accompanied by only a slight increase in the aspect ratio (specimen A and E). On the contrary, the growth of semi-elliptical cracks shows significant decrease in the aspect ratio, i.e. changes towards semi-circular crack (specimen B, C and D). Once the semi-elliptical crack reaches the shape of semi-circular crack, it follows the trend of the semi-circular crack (specimen C). Figure 9 is the schematics for this change of crack shape as the crack grows, i.e. semi-circular cracks tend to keep its own aspect ratio and maintain its semi-circular shape during the crack growth. But semi-elliptical cracks tend to grow into the semi-circular shape. Consequently, crack growth of a semi-circular crack is easily noticeable from the crack extension at the free surface. But semi-elliptical cracks grow far more inside the specimen than that at the free surface. This trend explains why, during the current tests, it was not easy to detect the crack growth from the specimen surface until shear-lips were formed.

Crack opening profiles and crack tip opening displacement (CTOD)

In order to obtain the crack opening profile, the center part of the rubber replica was sliced out and its dimensions were measured. Figures 10(a) ~ 10(e) show the crack opening profiles corresponding to the deepest point of the crack (or the center plane of each specimen). These profiles were measured from the same rubber replicas as used for determining the in-plane crack growth profiles in Figure 7. For a clear demonstration of crack opening profiles, the x- and y-axes in Figure 10 are not on the same scale. The profiles are drawn from the initial to the final stage of the crack extension according to the increase of crack extension (Δa). It is found that, at the early stage of crack extension, the material seems to advance just at the crack tip and the whole crack then progressed further. This failure mode is maintained during the entire successive crack growth.

Using the profiles shown in Figure 10, crack-tip opening displacement (CTOD) is estimated. In general, there are two definitions of CTOD that are widely used; the opening displacement at the initial crack tip and the 90° interception [11]. In this study the former definition is used for the calculation of CTOD with the modification that CTOD is measured at the previous crack tip during each crack growth. Figure 11 displays the definition of CTOD (denoted as δ) and crack extension (Δa). The location of the current crack tip is measured from the fracture surface and the CTOD corresponding to this crack tip is measured from the sliced rubber replica.

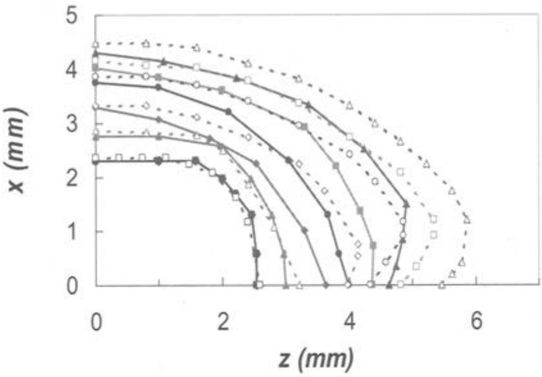

(a)

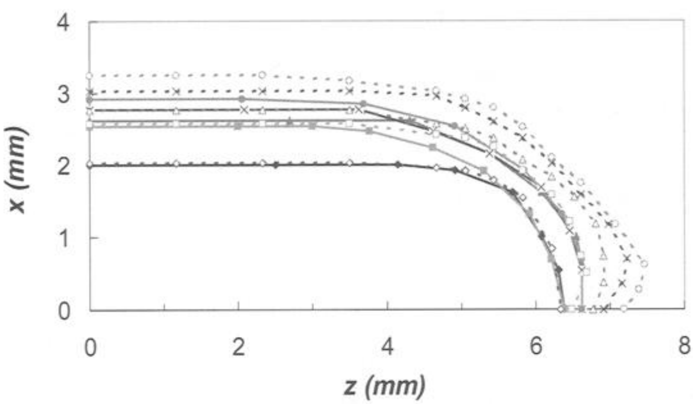

(b)

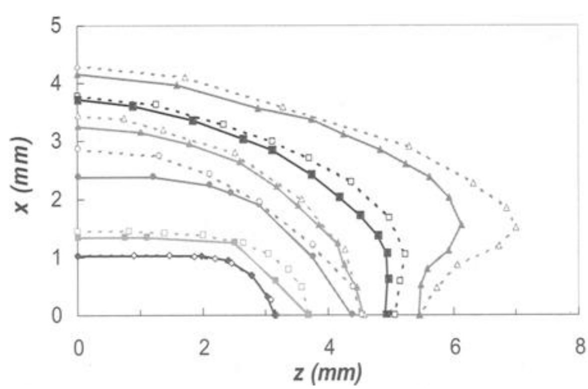

(c)

FIG.7 - *Comparison of the in-plane crack growth profiles (solid line by Rubber Impression Method and dotted line from fracture surface); (a) ~ (e) for specimens A ~ E, respectively*

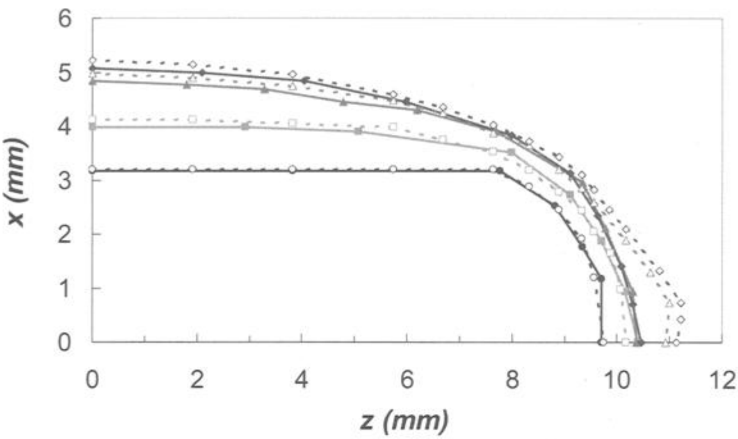

(d)

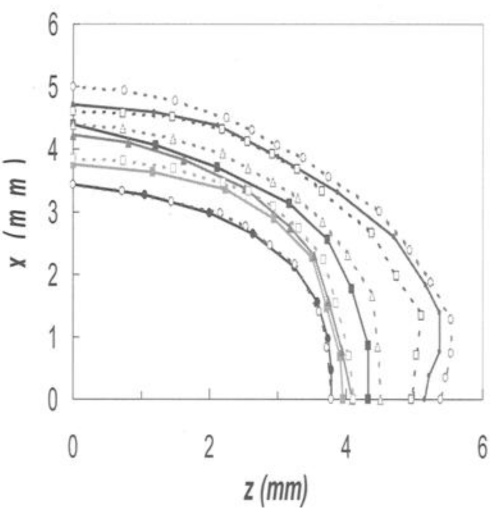

(e)

FIG.7 (Continued)

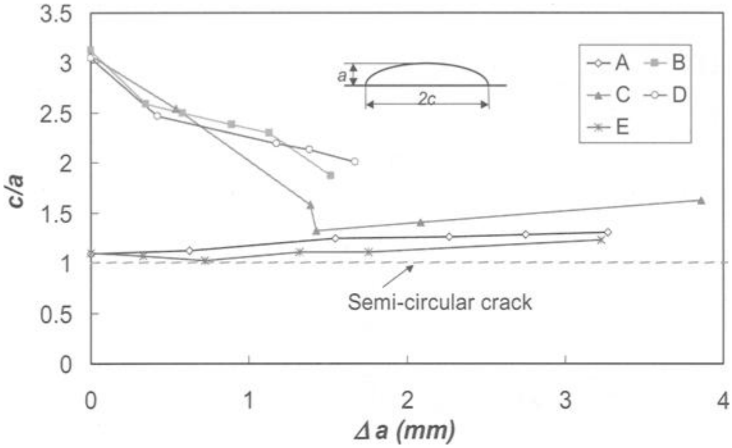

FIG.8 - *Change of crack geometries with crack extension*

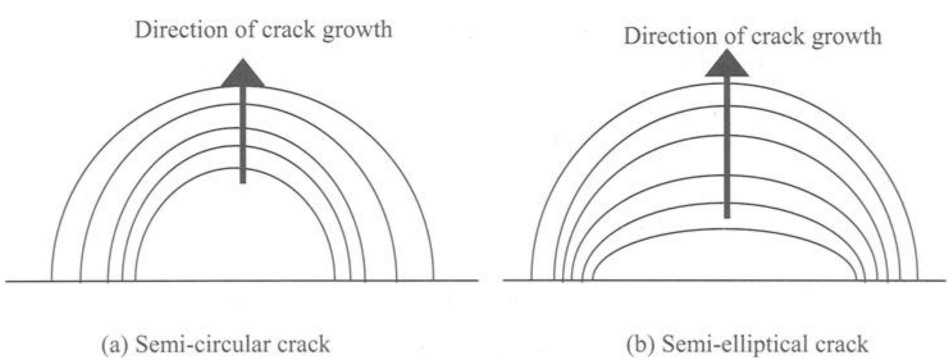

FIG.9 - *Schematics of crack shape as the crack grows*

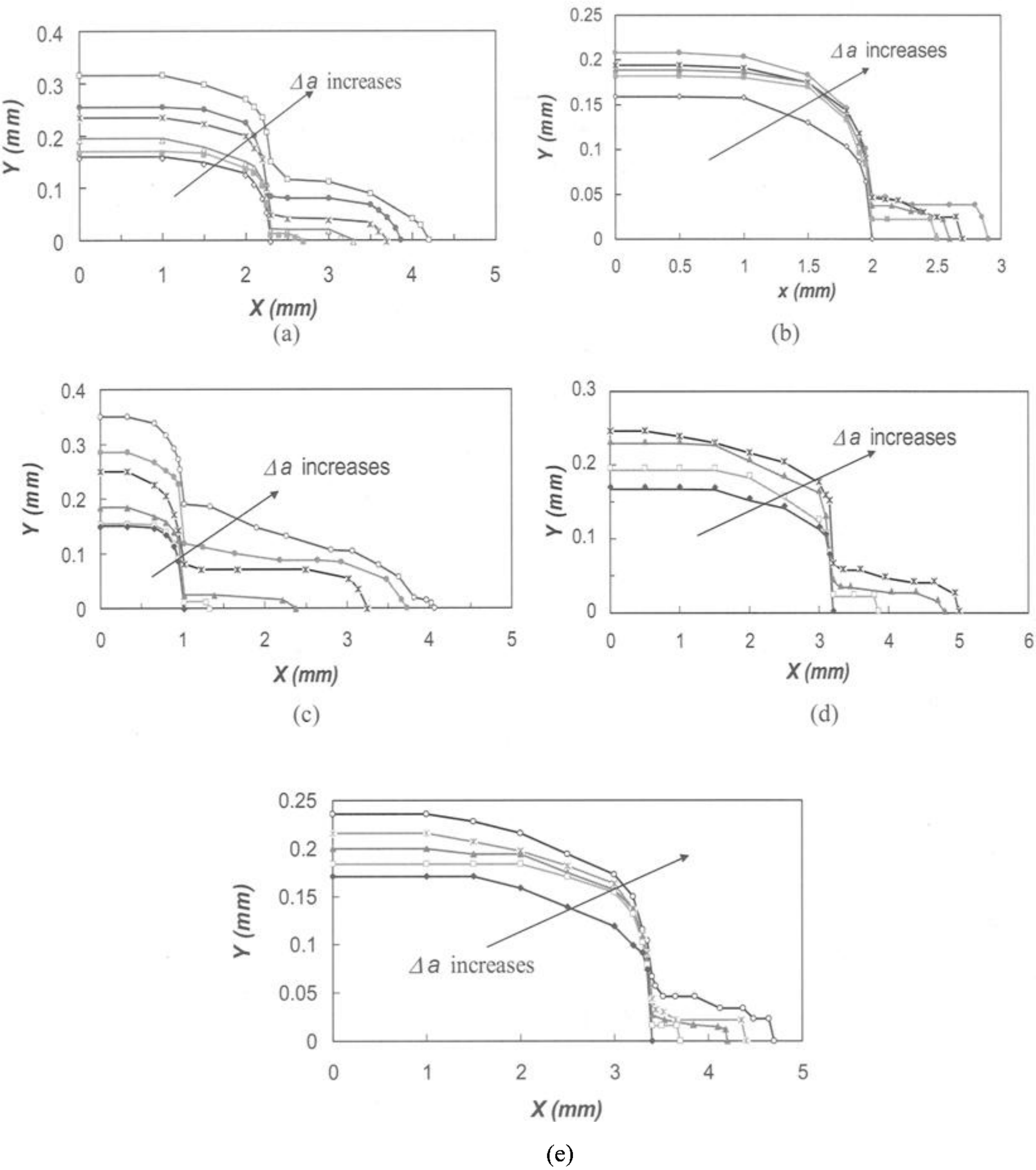

FIG.10 - *Crack opening profiles; (a) ~ (e) for Specimens A ~ E, respectively*

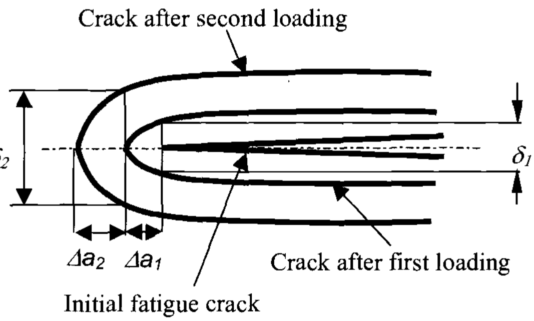

FIG.11 - *Definition of crack-tip opening displacement δ and crack extension Δa adopted in this study*

Variations of CTOD versus crack extension are shown in Figure 12. To calculate CTOD, it is necessary to accurately measure the crack tip dimensions of the rubber replica. But some rubber replicas were too damaged at the center part. As such, only two or three data points are obtained for each specimen. To estimate the critical CTOD at the initiation of stable crack growth, the critical CTOD at $\Delta a = 0$ is obtained by extrapolating the linear fit of the available data to $\Delta a = 0$ (i.e. δ_c in Figure 12(a)). Figure 13 summarizes the critical CTOD (δ_c) versus the ratio of the crack depth to specimen thickness. Due to limited number of data, the precise value of δ_c in each specimen may not be reliable. However, the trend of the critical CTOD's can be reasonably represented by the data. It is clear in Figure 13 that the shallowest cracked specimen C has a relatively high value of δ_c while the others show much lower values. Though the numerical analysis is not performed in this current study to access constraint, the high value of δ_c for the shallowest crack seems to be attributed to the low crack-tip constraint [12, 13].

Conclusions

1. Ductile crack growth behavior of aluminum 7050 alloy was investigated using thin plates containing surface cracks under Mode-I tensile loading. Three distinct stages of fracture are found; (1) flat stable tearing close or up to through thickness (2) lateral tearing with flat tunneling transitioning to slant fracture, and (3) unstable fully slant fracture. Through-wall crack with a flat plane always preceded the global failure where shear-lips were developed with 45° inclination to the free surface.

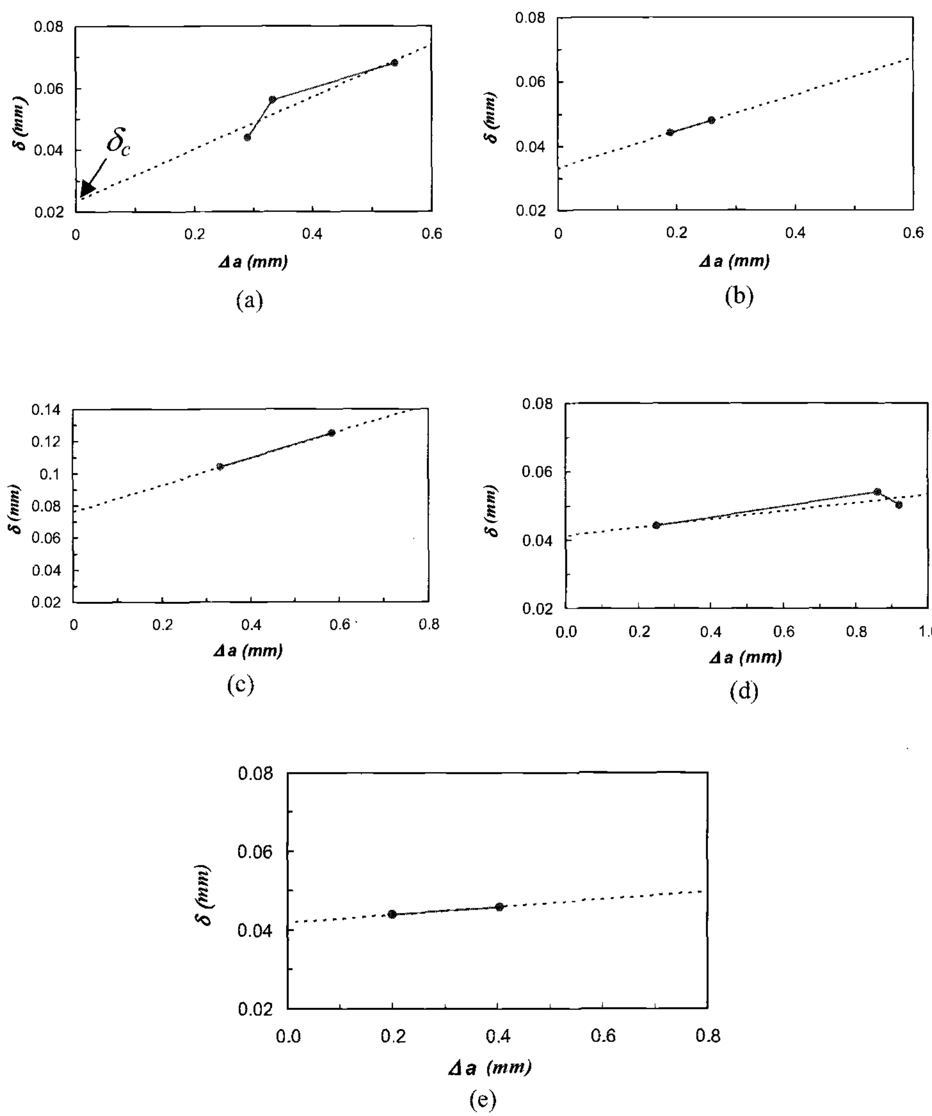

FIG.12 - *Variation of crack-tip opening displacement δ versus crack extension; (a) ~ (e) for specimens A ~ E, respectively*

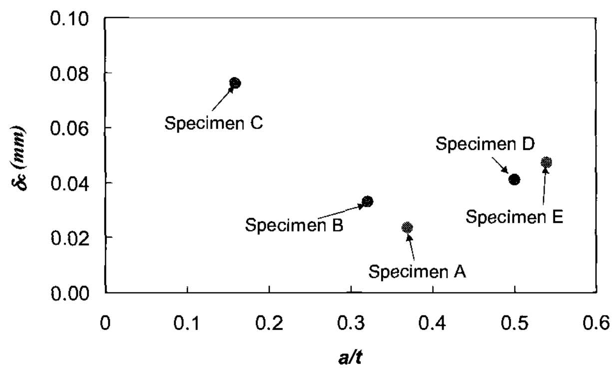

FIG.13 - *Plot of CTOD near the initiation of stable crack growth δ_c, versus a/t*

2. Rubber Impression Method was applied to the three-dimensional measurement of crack profiles in growing surface cracks. Measured in-plane crack front profiles from rubber replicas agree reasonably well with the crack extensions marked on the fracture surface. But due to geometric complexity of the surface crack, inaccurate profiles were obtained at the region adjacent to the free surface.

3. CTOD for the initiation of stable crack growth (δ_c) was estimated from the crack opening profiles. The shallowest crack shows relatively high value of δ_c than the other cracks. Though the numerical analysis is not performed in this current study to access constraint, the high value of δ_c seems to attribute to the low crack-tip constraint

4. Tendency on the evolution of crack shape during crack growth is consistent with previous report, e.g. [13]. As the crack grows, semi-circular cracks tend to remain semi-circular in shape. On the contrary, semi-elliptical cracks tend to develop into semi-circular shape.

5. The lack of full penetration of the silicon rubber to the crack tip appears to be due to the viscosity of silicon rubber and no space for the entrapped air to escape. Future work may benefit from adopting a different molding material (lower viscosity) and/or a different method (i.e. higher pressure) for injecting the un-cured compound.

Acknowledgements

The authors are indebted to Dr. D. S. Dawicke of NASA Langley and Dr. M. A. Sutton of the University of South Carolina in supplying the test specimens. Support for the third author, Dr. S. K. Jang, from his home institution as sabbatical is greatly acknowledged.

References

[1] Wells, A.A., "Unstable crack propagation in metals: cleavage and fast fracture", *Proceedings of the Crack Propagation Symposium*, Vol.1, Cranfield, UK, 1961, Paper 84

[2] Dawes, M.G., "Elastic-plastic fracture toughness testing based on the COD and J-contour integral concepts", *ASTM STP 668, American Society for Testing and Materials*, 1979, pp. 306-333.

[3] Anderson, T.L., McHenry, H.I., and Dawes, M.G., "Elastic-plastic fracture toughness testing with single edge notched bend specimens", *ASTM STP 856, American Society for Testing and Materials*, 1985, pp. 210-229.

[4] Shih, C.F., "Relationship between the J-integral and the crack opening displacement for stationary and extending cracks", *Journal of the Mechanics and Physics of Solids*, Vol.29, 1981, pp. 305-326.

[5] Brocks, W. and Yuan, H., "Numerical studies on stable crack growth", In: *Defect Assessment in Components: Fundamentals and Applications* 9, ESIS Publications, 1991, pp. 19-33.

[6] Newman, J.C., James, M.A., and Zerbst, U., "A review of the CTOA/CTOD fracture criterion", *Engineering Fracture Mechanics*, Vol.70, 2003, pp. 371-385.

[7] ASTM E 1820-99a, Standard test method for measurement of fracture toughness.

[8] BS 5762: 1979, Methods for crack opening displacement (COD) testing, British Standards Institution, London

[9] Dissertation, Jang, S.K., "A study of the ductile crack growth of a SUS 304stainless steel – Polysulfide rubber impression method", Chonnam National University, Kwangju, Korea, 1988

[10] Narasimhan, R., Rosakis, A.J. and Moran, B., "A three-dimensional numerical investigation of fracture initiation by ductile failure mechanisms in a 4340 steel", *International Journal of Fracture*, Vol.56, 1992, pp. 1-24.

[11] Rice, Jr., "A path independent integral and the approximate analysis of strain concentration by notches and cracks", *Journal of Applied Mechanics*, Vol.35, 1968, pp. 379-386.

[12] Wang, Y.Y., On the two-parameter characterization of elastic-plastic crack-front fields in surface-cracked plates, *Constraint Effects in Fracture, ASTM STP1171, American Society for Testing and Materials*, 1993, pp. 120-138.

[13] Newman, C.R., Jr., Reuter, W.G., and Aveline, C.R., Jr., "Stress and fracture analyses of semi-elliptical surface cracks", *Fatigue and Fracture Mechanics: 30th Volume, ASTM STP1360, American Society for Testing and Materials*, 2000, pp. 403-423.

SESSION 5A: FATIGUE I

Journal of ASTM International, March 2005, Vol. 2, No. 3
Paper ID JAI12036
Available online at www.astm.org

Nenad Gubeljak,[1] *Jozef Predan,*[1] *Reinhard Pippan,*[2] *Maks Oblak*[1]

Effect of Residual Stresses on the Fatigue Crack Propagation in Welded Joints

ABSTRACT: The effect of residual stress on the fatigue crack growth was investigated for cyclic tension. Three-point bend specimens were used with through thickness notches at the center line of the welded joint. The experiments were performed for different load amplitudes and load ratios under conditions of small-scale yielding. The influence of the residual stresses on fatigue crack growth was estimated by experimentally observed fatigue crack growth rate and measurement of residual stresses at the surface of specimen. This paper describes an approach taken in two models to estimate the residual stress effect on fatigue crack propagation and to predict remaining service life of a welded structure.

KEYWORDS: fatigue crack propagation, residual stresses, X-ray, fatigue crack growth rate

Nomenclature

$a_{av,j}$	average crack length after number of cycles N_j
$a_{avt,ij}$	length along the crack front in specimen without residual stresses after number of cycles N_j
a_{ij}	real crack front, as results from the presence of a residual stress field
B	thickness of specimen
BM	base metal
C	parameter in power law function (Paris-Erdogan's relation for fatigue crack growth rate) for material free from residual stresses
C_{RS}	parameter in power law function (Paris-Erdogan's relation for fatigue crack growth rate) in the case of the presence of a residual stress field
da/dN	fatigue crack growth rate
F_{max}	maximum fatigue load
F_{min}	minimum fatigue load
H	width of weld gap
$K_{RS,j}$	value of stress intensity factor caused by residual stresses
M	mis-match factor (ratio between the yield stress of the weld metal to the yield stress of the base metal)
m	parameter in power law function (Paris-Erdogan's relation for fatigue crack growth rate) for material free from residual stresses

Manuscript received 21 January 2004; accepted for publication 4 May 2004; published March 2005. Presented at ASTM Symposium on Fatigue and Fracture Mechanics: 34th Volume on 19–21 November 2003 in Tampa, FL; S.R. Daniewicz, J.C. Newman, Jr., and K-H. Schwalbe, Guest Editors.
[1] University of Maribor, Faculty of Mechanical Engineering, Smetanova 17, SI-2000 Maribor, Slovenia, email: nenad.gubeljak@uni-mb.si.
[2] Erich Schmid Institute of Materials Science, Austrian Academy of Sciences, Jahnstr. 12, A-8700 Leoben, Austria.

m_{RS}	parameter in power law function (Paris-Erdogan's relation for fatigue crack growth rate) in the case of the presence of a residual stress field
N	number of cycles
OM	Overmatch weld metal
R	fatigue loading ratio (F_{min}/F_{max})
$R_{p0.2}$	yield stress (index WM denoted weld metal and BM denoted base metal, e.g., $R_{p0.2,WM}$ and $R_{p0.2,BM}$)
R_m	ultimate tensile strength
S	span distance between support
UM	under-match weld metal
W	width of specimen
WM	weld metal
ΔF_j	effective load amplitude
Δa	crack extension
$\Delta K_{eff,j}$	effective stress intensity range
ΔK_j	applied stress intensity range
ΔN_j	interval of number of cycles
$\sigma_{RS,j}$	additional stress caused by residual stresses

Introduction

The effect of residual stresses at the welded joint can have a significant influence on service life and safe use of welded structures [1–3]. In some cases the residual stresses can be higher than service stresses, which can lead to unpredictable failure of structures [4]. Prediction of residual fatigue life in the presence of residual stresses is difficult, because their actual values and distribution are usually uncertain. Since fatigue life of welded structures is significantly affected by residual stresses, considerable research works were performed on these problems in the last decade. Through literature review, it is possible to recognize that theoretical and experimental studies were involved in some works. These studies were either based on the weight function method [5] or summation of the stress intensity factors [6].

Initial residual stresses are usually produced as result of manufacturing process. During the service of components, the residual stresses can also be caused by local plastic deformation. Furthermore, the residual stresses are changed by the presence of the crack, and they are redistributed by the plastic deformation in front of the crack. In ductile materials the residual stresses influence the fatigue crack propagation mainly by a change of the crack closure load. Determining each component of the residual stress and the crack closure on the fatigue crack growth rate is difficult [7,8].

Furthermore, it is important to ensure that the normalization of the crack shape and the redistribution of the residual stresses does not allow a simple summation or subtracting of stress intensity factor over the entire crack path propagation [6]. Nevertheless, even when residual stresses are known, the procedure for determining residual service life requires appropriate modeling and computation [3,9].

Usually it is possible to determine crack length and even in some cases the shape of fatigue crack front (e.g., NDT inspection like neutron scattering technique), but the measurement of residual stresses is difficult or impossible. In spite of this fact, it is possible to estimate the effect of residual stresses to structure integrity by using the recommended residual stress profile, e.g., as according to the SINTAP [10] procedure. In this case, the deviation between estimated and presented residual stresses can lead to either non-conservative prediction or overestimation. The aim of this research is to determine the relation of fatigue crack propagation caused by the residual stresses, then to estimate from this variation the residual stresses and compare them with the real measured residual stresses.

In this paper, the calculated values of residual stresses are compared with measured residual stresses at the surface.

Materials and Welding

A high-strength, low alloy-HSLA (steel ASTM grade HT 50), in a quenched and tempered condition, was used as base metal (BM). Figure 1 shows the arrangement for the welding of the plates. A Flux Cord Arc Welding (FCAW) procedure was applied, and two different tubular wires were selected for the welding in order to produce welded joints in over- and under-matched (OM and UM) configurations. The chemical compositions and mechanical properties of the BM and the OM and UM weld metals are given in Tables 1 and 2. The strength mismatch factors M, i.e., the ratio between the yield stress of the weld metal to the yield stress of the BM, are 0.86 for the under- and 1.19 for the over-matched welded joint.

In Table 2, $R_{p0.2}$ is the engineering yield strength (offset at 0.2 % of strain), and R_m is the engineering ultimate tensile strength-UTS.

Welding with filler wire for over-match configuration was made with preheating at temperature of 55°C and the under-match configuration was made without preheating. Welding was performed using MAG procedure (82 % Ar and 18 % CO_2). The heat input was in the range of 16–20 kJ/cm, and the suit cooling time was between 800 and 500°C was $\Delta t_{8/5} = 9 - 12\,s$. The interpass temperature was 150°C.

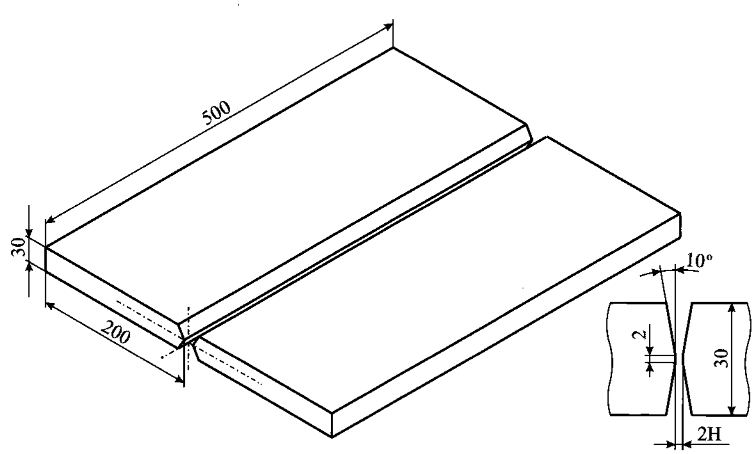

FIG. 1—*Welding arrangement (2H = 6, all units in mm).*

TABLE 1—*Chemical composition of base metal and consumables in weight percentages.*

Material	C	Si	Mn	P	S	Cr	Mo	Ni
Over-match	0.040	0.16	0.95	0.011	0.021	0.49	0.42	2.06
Base metal	0.123	0.33	0.56	0.003	0.002	0.57	0.34	0.13
Under-match	0.096	0.58	1.24	0.013	0.160	0.07	0.02	0.03

TABLE 2—*Mechanical properties of base metal and consumable.*

Material	E $[GPa]$	$R_{p0.2}$ $[MPa]$	R_m $[MPa]$	M $R_{p0.2,WM}/R_{p0.2,BM}$	Charpy Cv $[J/80\,mm^2]$
Over-match	184	648	744	1.19	>40 J at –60 °C
Base metal	203	545	648	...	>60 J at –60 °C
Under-match	208	469	590	0.86	>80 J at –60 °C

Experimental Procedure

Standard specimens with mechanical notch through thickness were cut out of the welded plate as shown in Fig. 2. Specimens were used with through thickness notch at the center line of welded joint. The thickness B and width W are the same, B = W = 25 mm. The mechanical notch was 4 mm in depth, and the specimens are pre-fatigued according to ASTM E 647-99 [11].

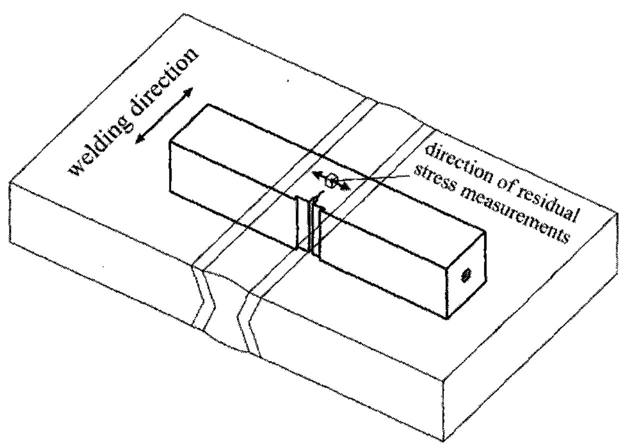

FIG. 2—*Positon of 3-point bend specimen and notch orientation in the welding plate.*

Two series of specimens were tested with over- and under-match weld metal denoted by V and N, respectively. Typical recorded data (crack extension versus cycle numbers) for two loading (R = 0.25 and 0.41) regimes are given in Fig. 3. The maximum load at the change of the stress ratio remains constant. The variation of the R-ratio had been performed in order to mark the shape of the crack front in the interior of specimen.

Based on experimental measured values *Δa-N* (Fig. 3), the differential quotient was calculated with derivations of approximation (polynomial) function. Note that a reasonable high correlation factor is achieved in polynomial function (e.g., 0.9874 and 0.9975).

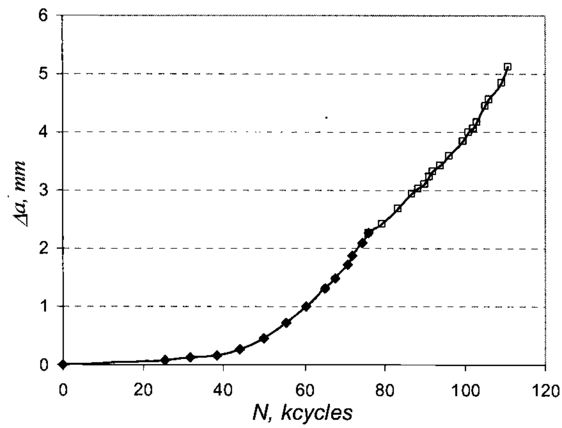

FIG. 3—*Recorded data Δa-N obtained by measuring the crack length at the surface of specimen.*

Measurement of the Residual Stresses

The goal of this research is to compare estimated residual stresses with measured values in crack growth specimens to determine the effects of residual stresses on crack growth. Therefore, to determine the change of residual stresses in dependence of fatigue crack length. Note that the residual stresses at the measured surface can be changed by mechanical treatment for example by grinding of specimen surface. Therefore, after machining (cutting, grinding), the measuring area had electro polishing about 10 microns in depth.

Residual stresses are measured in the transverse direction perpendicular to welding direction, as is shown in Fig. 2 by standard X-ray technique ($\sin^2\theta$ method). The measured direction is defined with change of the arc 2θ or ψ using the X-ray method. In our case we measured the intensity of the reflected X-ray for two different arcs, $\psi = 0^\circ$ and $\psi = 45^\circ$, and the arc 2θ was varied from 152–160°. SIMENS diffraction device was used for the $\sin^2\theta$ method. On the specimen the residual stresses are measured in a region which was 2.5 mm ahead of the fatigue crack tip. In this manner a direct effect of the plastic zone was avoided. Further measurements were performed at the distance of 4 mm in crack growth direction, as is shown in Fig. 4. After each performed measurement set, the specimen was again subjected to fatigue loading until a crack extension of 4 mm was achieved at the surface of the specimen. The residual stress measurement was performed again on the same regions, but it was one point less each time due to the fatigue crack propagation.

The residual stresses are calculated for each of the measured points. Figures 5 and 6 show the distribution of the residual stresses versus the x-axes (in fatigue crack growth direction) at the surface of the specimen. The first (longest solid) line gives the residual stress distribution on the surface of the specimen without crack (only machine notch a_n = 6 mm). Each next line corresponds to measuring of residual stresses at certain fatigue crack lengths (e.g., a_f = 10mm). After residual stresses, measuring the specimen was again subjected to fatigue. After certain fatigue crack increment (approximately 4 mm), the residual stress measurement is performed again. The start of this line is marked again with new crack length a_f = 14 mm. Each measured set is connected by solid line and corresponds to one crack length as shown in Figs. 5 and 6 for the over- and under-match weld metals, respectively.

The dashed line connects measured values and presents the change of the residual stress magnitude near the crack tip during fatigue crack propagation. The results show that in the overmatch weld metal, higher compress residual stress appears than in the under-match weld metal. This is expected, since the welding process (heat input energy, number, and subsequence of welded passes) was the same, and only yield stresses were different. However, the residual stress field in the specimen depends on the location of the specimen in the welded plate, which is varying for each specimen (in middle or at the end of welded plate).

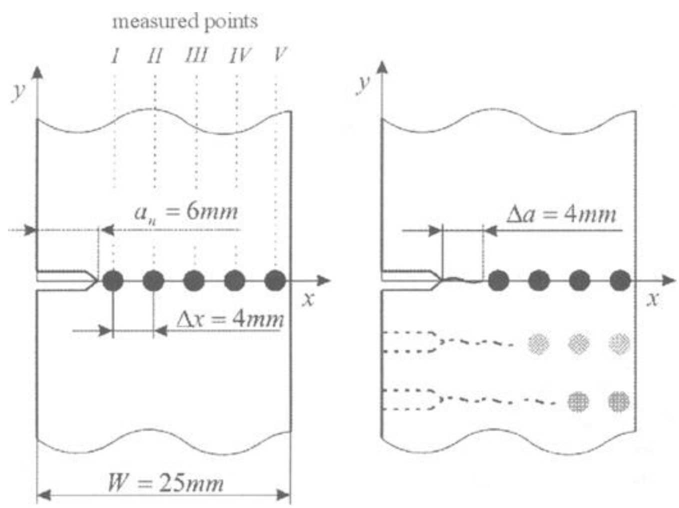

FIG. 4—*Shematic view to distribution of measured points at the surface of the specimen.*

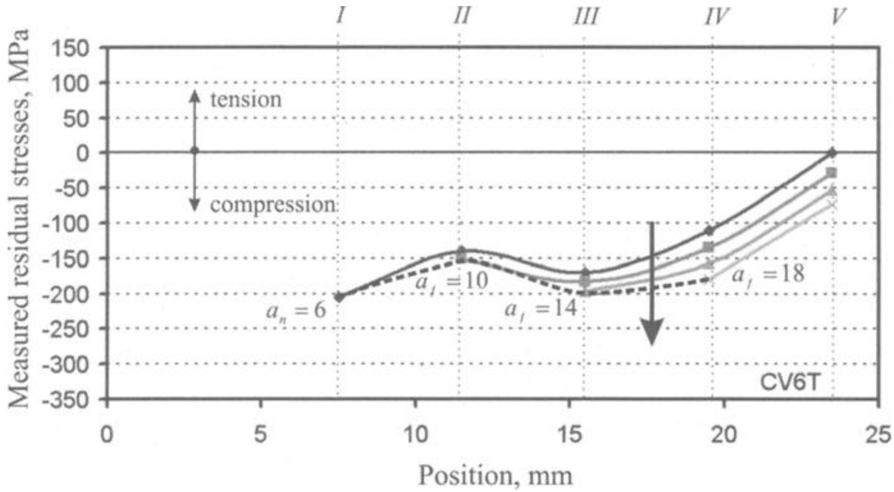

FIG. 5—*The distribution of residual stress on the specimen surface for overmatch weld metal.*

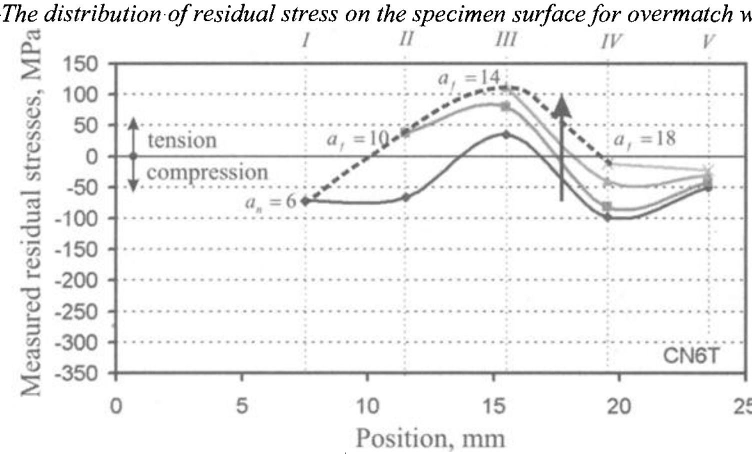

FIG. 6—*The distribution of residual stress on the specimen surface for under-match weld metal.*

Model to Estimate the Residual Stresses from the Fatigue Crack Growth Rate

In Fig. 7 the crack fronts are denoted with index j, and the lines parallel to the surface with the index i. Figure 8 shows that for each average crack length $a_{av,j}$ we have the crack front $a_{avt,ij}$, which will appear if the residual stresses are not present. In reality, the crack front a_{ij} appeared, as a result from the presence of a residual stress field. All mentioned parameters of crack lengths should be taken by observing the crack propagation front-through thickness. The results are analyzed by observing from point-to-point the change of fatigue crack front shape and the knowledge of fatigue crack growth properties of the base material, free from residual stresses. The same approach was applied in [5]. The shape of the crack front was obtained by the crack length measurement after each fatigue regime j. Each fatigue interval j is running at the constant parameters of F_{min} and F_{max}. The shape of the crack front was characterized on the relative deviation of the crack length $d_{av,ij}$ along the crack front for each point i with the follow equation:

$$d_{av,ij} = \frac{a_{ij} - a_{avt,ij}}{a_{av,j}} \tag{1}$$

where a_{ij} is the measured crack length, $a_{avt,ij}$ is the crack length for ideal crack front shape, and $a_{av,j}$ is the average crack length. The index i is the mean line in the crack growth direction (parallel to the surface), and index j is the crack front corresponding to constant number of loading cycles as shown in Figs. 7 and 8. Intermediate relative deviation between two crack length (shape) measurements (e.g., j-1 and j) is possible to estimate by using Eq 1 and the principle shown in Fig. 9. For instance, if average crack length $a_{av,j}$ is chosen, then for certain crack depth i, it is possible to assess deviation of crack length $d_{av,ij}$. Since $a_{avt,ij}$ is also known, it is possible to assume crack length a_{ij}. With this approach, it is possible to determine the fatigue crack front shape through thickness of specimen for chosen number of cycles N, as is shown in Fig. 10.

The reference curve was obtained by observing the surface of specimen and by recording the fatigue crack growth increment Δa versus the number of cycles N. The crack growth rate on the surface of specimen was determined as the ratio of the differential coefficients by the equation:

$$\frac{\Delta a_{ij}}{\Delta N_j} = \frac{a_{ij} - a_{i-1j}}{\Delta N_j} \tag{2}$$

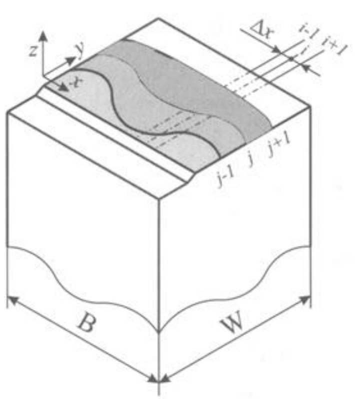

FIG. 7—*Schematic view of fatigue crack front and the used coordinal system.*

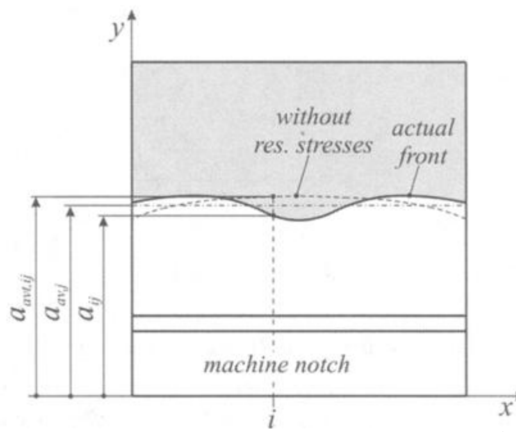

FIG. 8—*Fatigue crack fronts and definition of different types of crack lengths.*

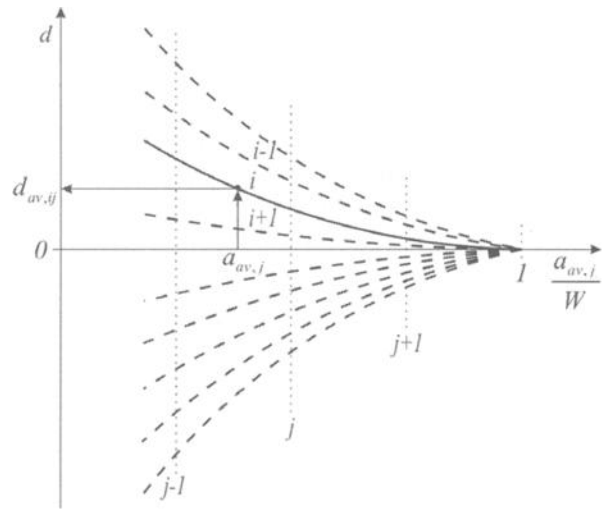

FIG. 9—*Determination of crack front deviation* $d_{av,ij}$ *by interpolation for average crack lengths.*

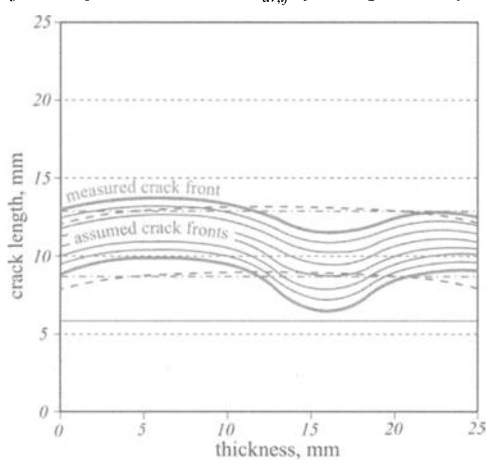

FIG. 10—*The measured and assumed crack front within the analyzed interval.*

Models

A procedure for an estimation of the residual stress effect on the fatigue crack growth is presented. The approximation is based on the following idealizations:

- Stress intensity function-SIF through thickness of the component depends only on average crack lengths.
- Obtained value of SIF is a constant through thickness of component.
- Crack propagation rate is locally driven by the effective stress intensity range ΔK_{eff}.

- The crack is closed over a certain part of the load amplitude along the whole crack front.
- The local crack closure stress intensity factor is not affected by local residual stresses.
- The residual stresses change only K_{min} and K_{max}.

In this case, the variations of the residual stresses are directly reflected in a variation of the effective stress intensity range. The residual stresses are recalculated from the variation of the effective stress intensity range, which can be determined from the local crack propagation rate.

Model 1: Determination of the Residual Stresses Based on the Effective Load Amplitude ΔF_j

The effective range of SIF $\Delta K_{eff,j}$ for a propagation from a_{j-1} to a_j for the known number of cycles ΔN_j can be calculated from

$$\int_{N_{j-1}}^{N_j} dN = \frac{1}{C}\int_{a_{j-1}}^{a_j} \frac{da}{\Delta K_{eff,j}^m} \tag{3}$$

where the $\Delta K_{eff,j}$ and $f(a_j/W)$ for three-point bend specimens are given by the terms:

$$\Delta K_{eff,j} = \frac{\Delta F_{eff,j} \cdot S}{BW^{1.5}} f\left(\frac{a_j}{W}\right) \tag{4}$$

$$f\left(\frac{a_j}{W}\right) = \frac{3\left(\frac{a_j}{W}\right)^{0.5}\left[1.99 - \frac{a_j}{W}\left(1-\frac{a_j}{W}\right)\left[2.15 - 3.93\frac{a_j}{W} + 2.7\left(\frac{a_j}{W}\right)^2\right]\right]}{2\left(1+2\frac{a_j}{W}\right)\left(1-\frac{a_j}{W}\right)^{1.5}} \tag{5}$$

where B is the thickness of specimen, W is the width of specimen, and S is the span distance (usually S = 4W). In Fig. 11, a flow chart is given to show how the experimental data can be used within the crack increment interval for the determination of local effective stress intensity factor $\Delta K_{eff,j}$. A Monte Carlo type simulation is used for determination of $\Delta K_{eff,j}$, with the effective load amplitude ΔF_j as variable in Eq 4.

The additional stress intensity factor $K_{RS,j}$ is calculated by the superposition principle as the difference between an effective SIF $\Delta K_{eff,j}$ and applied SIF ΔK_j. Applied SIF ΔK_j is calculated by using Eq 4.

$$\Delta K_j = \frac{(F_{\max,j} - F_{\min,j})S}{BW^{1.5}} f\left(\frac{a_j}{W}\right) \tag{6}$$

Since the effective range of SIF $\Delta K_{eff,j}$ and the amplitude of the external force (consequently applied SIF ΔK_j) are known within interval j, it is possible to calculate the additional stress intensity factor $K_{RS,j}$.

$$K_{RS,j} = \Delta K_{eff,j} - \Delta K_j \tag{7}$$

The values of the additional stresses $\sigma_{RS,j}$ are calculated from SIF $K_{RS,j}$ by using the term:

$$\sigma_{RS,j} = \frac{K_{RS,j}}{\sqrt{\pi a_j} \cdot f(a_j/W)} \tag{8}$$

Note that SIF $K_{RS,j}$ is obtained for mean crack length and a certain position along the crack front.

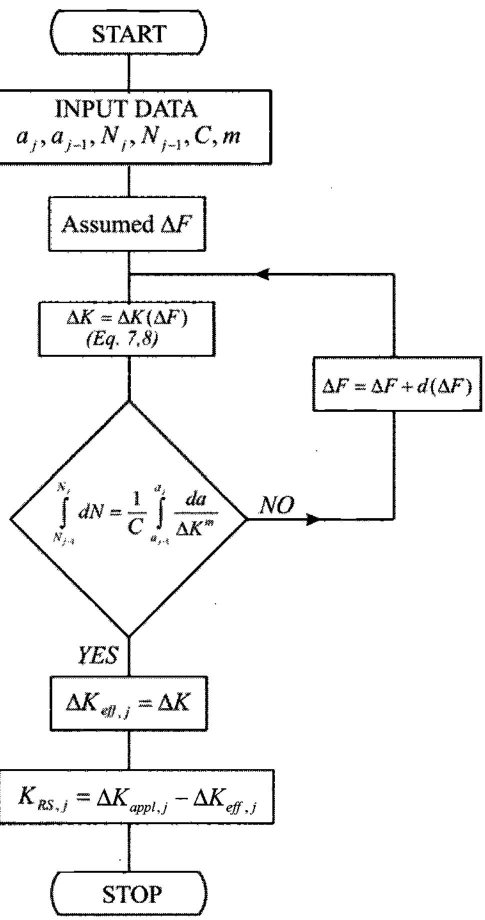

FIG. 11—*Flow chart for determination of local effective stress intensity factor* $\Delta K_{eff,j}$.

Model 2: Determination of the Additional Stress at the Crack Tip from the Fatigue Crack Growth Rate Parameters

By using the above-mentioned assumptions, the Paris-Erdogan relation can be written as:

$$\frac{da}{dN} = C_{RS} \cdot \Delta K^{m_{RS}} = C \cdot (\Delta K + K_{RS})^m \tag{9}$$

where parameters C_{RS} and m_{RS} describe the fatigue crack growth rate, if only the range of stress intensity factor ΔK caused by external load (F_{max}, F_{min}) is known. From the above equation, it is possible to calculate the value of the additional stress intensity factor $K_{RS,j}$:

$$K_{RS,j} = \sqrt[m]{\frac{C_{RS,j} \cdot \Delta K_j^{m_{RS}}}{C}} - \Delta K_j \tag{10}$$

If the parameter $m = m_{RS,j}$ are similar, then $K_{RS,j}$ can be obtained by the term

$$K_{RS,j} = \left(\sqrt[m]{\frac{C_{RS,j}}{C}} - 1 \right) \Delta K_j \tag{11}$$

The values of the additional stresses $\sigma_{RS,j}$ can also be calculated from SIF $K_{RS,j}$ by using Eq 8.

Application in Model

The proposed model is applied to the described fatigue experiment. It was mentioned that the specimens were subjected to different fatigue loading regimes in a load-control mode. After the fatigue tests and residual stress measurements, the specimens were broken at the fracture surface, in order to follow the different fatigue regimes. Figures 12 and 13 show the fractured surface for specimen CV6T of the overmatch and CN6T specimen of the under-match weld metal, respectively. The crack fronts at the end of one fatigue loading regime and the beginning of the second loading regime are visible on the fracture surface. Fatigue crack front is actually denoted by changing the fatigue load ratio. At the beginning, the specimens were fatigued at $R = 0.2$, when the crack is about 4 mm at the surface, the loading ratio was changed to $R = 0.4$, and after approximately 4 mm, the load ratio was again reduced to $R = 0.2$.

Crack length was measured at 26 equidistant lines along crack growth. The crack length was measured for all three cracks fronts.

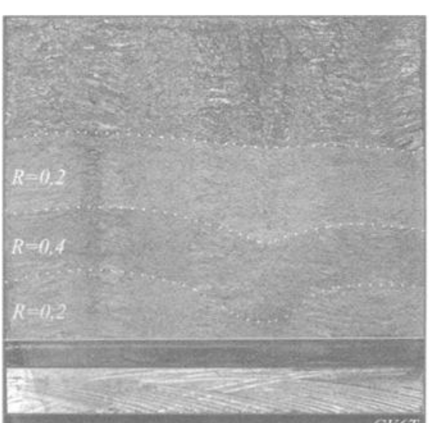

FIG. 12—*The fatigue cracks fronts of the over-match weld sample.*

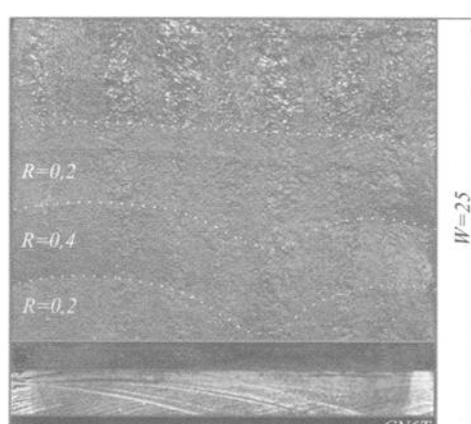

FIG. 13—*The fatigue cracks fronts of the under-match weld sample.*

The deviation d_{ij} was determined by using Eq 1. The values for deviation between the measured points were approximated by a square function. Figures 14 and 15 show the crack front's deviations for CV6T and CN6T specimens, respectively. Note that the deviation $d_{ij}=0$ corresponds to crack front without residual stress and $a_{avt,ij}=a_{ij}$.

On the base of these measurements and the obtained deviations, it is possible to estimate any intermediate increment of fatigue crack front corresponding to the same number of loading cycles and average crack lengths. Figures 16 and 17 show reconstructed fatigue crack fronts (dashed lines) within increments of 1 mm and the measured crack length presented by points. The gray lines in Figs. 16 and 17 present the crack fronts of material free from residual stress. Since the dependence of crack length at the fracture surface vs. number of cycles is measured, the fatigue crack front for a certain number of cycles is also approximately known.

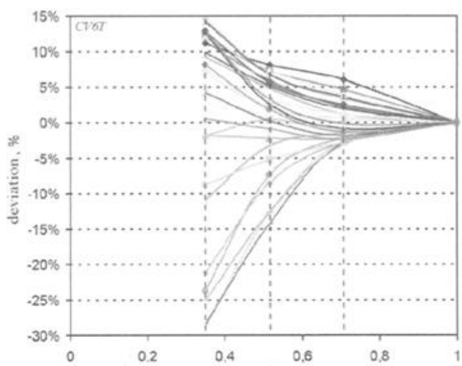

FIG. 14—*The deviation* $d_{av,ij}$ *(in %) of crack length in the overmatch weld.*

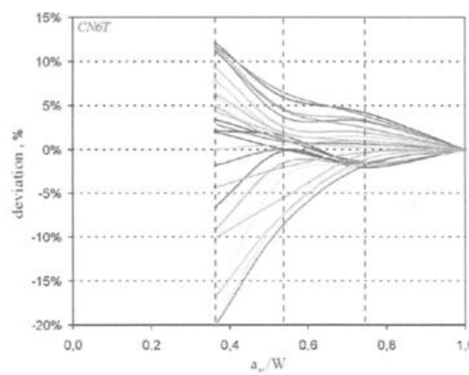

FIG. 15—*The deviation* $d_{av,ij}$ *(in %) of crack length in the undermatch weld.*

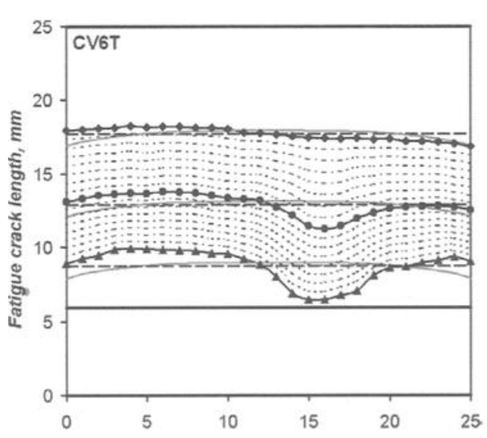

FIG. 16—*The measured and assumed fatigue crack fronts profiles in the overmatch weld.*

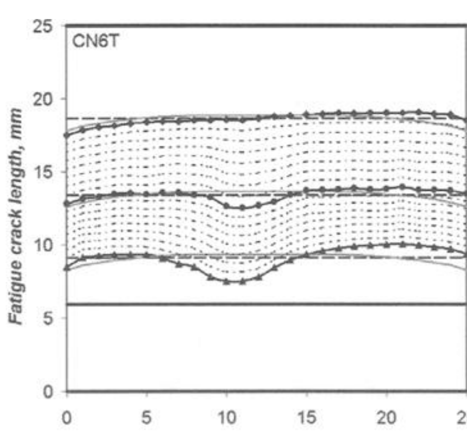

FIG. 17—*The measured and assumed fatigue crack fronts profiles in the undermatch weld.*

Therefore, within each interval, it is possible to determine the shape of the crack front for any crack length at the surface. Hence, it is possible to plot a-N curves for average and the surface crack lengths, as shown in Figs. 18 and 19. The plots show that the average crack propagation plot mainly lies between both surfaces' (back and front) plots. Indirectly, it confirms the assumption that an average SIF value can be roughly used for the description of crack growth on the surface of the specimens. The corresponding stress intensity factor range ΔK, for average crack lengths is determined by using Eq 6. The fatigue crack growth rate is expressed with Paris-Erdogan's relation in double logarithmic plot. Figures 20*a* and 20*b* show the plots of the fatigue crack growth rate for loading regimes R = 0.4 and R = 0.2, respectively, applied to the overmatch weld. Figures 21*a* and 21*b* show the plots of the fatigue crack growth rate for loading regimes R = 0.4 and R = 0.2, respectively, applied in the under-match weld. In all cases the dashed lines correspond to the crack growth rate for the material free from residual stresses (e.g., base material).

For each fatigue loading regime (different R-ratio and ΔF_{app}) one set of fatigue crack growth parameters for front and back side of specimens was obtained. Actually, the parameters C are varied during the fatigue crack propagation due to residual stresses. Hence, it is possible to estimate their maximum and minimum value within the same fatigue loading regime. The assumed values for parameters C are listed in Table 3. Reasonably, the parameter C is constant only for average crack growth rate. Parameters of Paris-Erdogan's relation for material free from residual stresses are C = 8.0 E-12 [mm/cycle] and m = 3.287. On the base of proposed procedures it is possible to estimate the effect of residual stresses on the fatigue crack extension. Figures 22 and 23 show the calculated values $\sigma_{RS,ij}$.

Both proposed models give similar results of the additional stress $\sigma_{RS,ij}$ for fatigue crack propagation caused by residual stresses. This is not surprising, because they are based on the same principles. Figures 22 and 23 show that a significant change of residual stresses is connected by changing the fatigue loading regimes (mainly R-ratio from 0.4 to 0.2), and consequently that of the residual stress is changed. In this transition region the fatigue crack growth was retarded. It leads to lower (compressed) residual stresses. After transitional fatigue crack growth, the change of residual stresses becomes smooth, and the differences between calculated residual stresses values becomes smaller. Figures 22 and 23 also show that the difference between residual stresses from one to the other side (front and back) can be significantly different. A comparison between measured and estimated residual stresses on the surface as a function of crack extension show that actual residual stresses can be higher in compression (Fig. 22) and tension (Fig. 23) than the calculated residual stresses from fatigue crack growth. Therefore, the effect of residual stresses on fatigue crack propagation is underestimated by the proposed model. The main reason for the discrepancy is most likely that the ΔK-variation along the crack front is not taken in account.

However, the performed analysis confirms the results of another researcher [5], that the effect of residual stresses is changing, and this effect is greater at the beginning of fatigue crack propagation (at lower ΔK). The model approximately predicts the changing of residual stresses during the fatigue crack propagation.

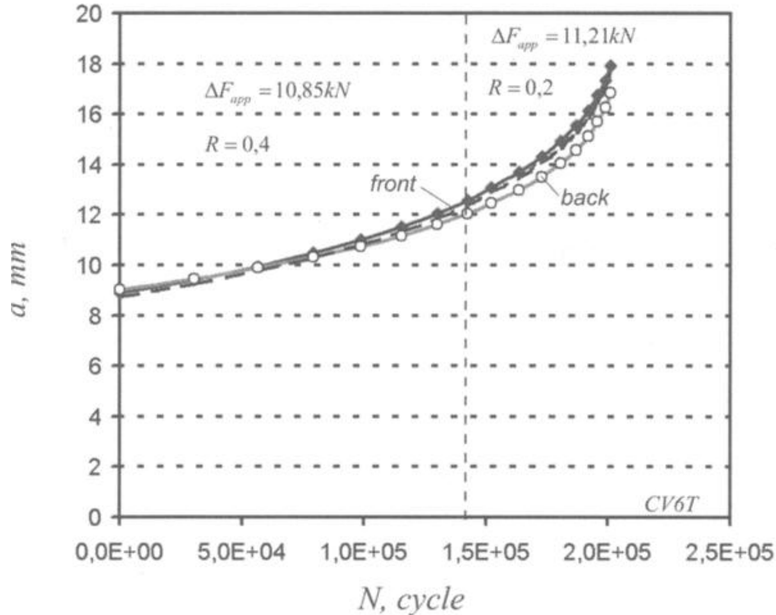

FIG. 18—*Both surface and average (dashed) crack lengths versus number of cycles in the over-match weld.*

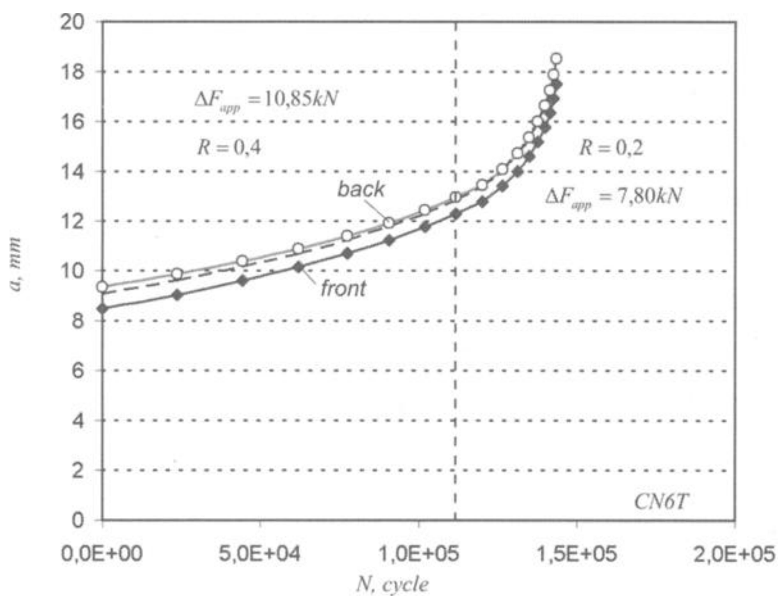

FIG. 19—*Both surface and average (dashed) crack lengths versus number of cycles in the under-match weld.*

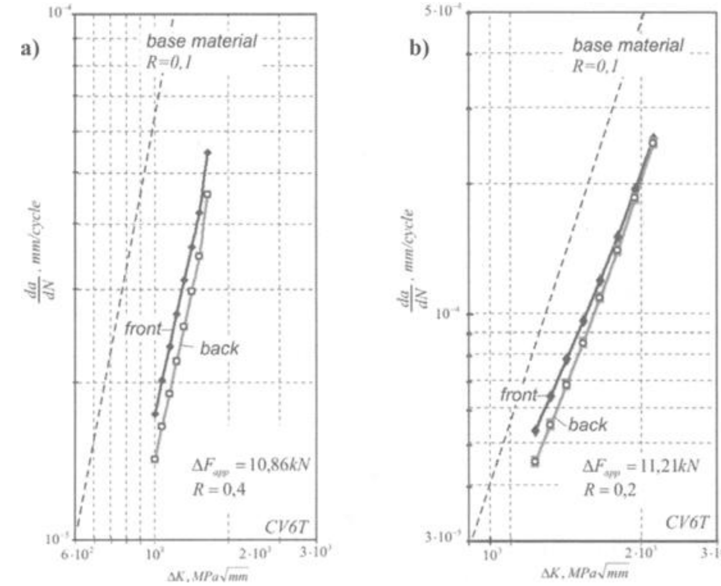

FIG. 20—*Plots da/dN versus ΔK for both surface and average crack growth lines for both fatigue regimes applied in the over-match weld.*

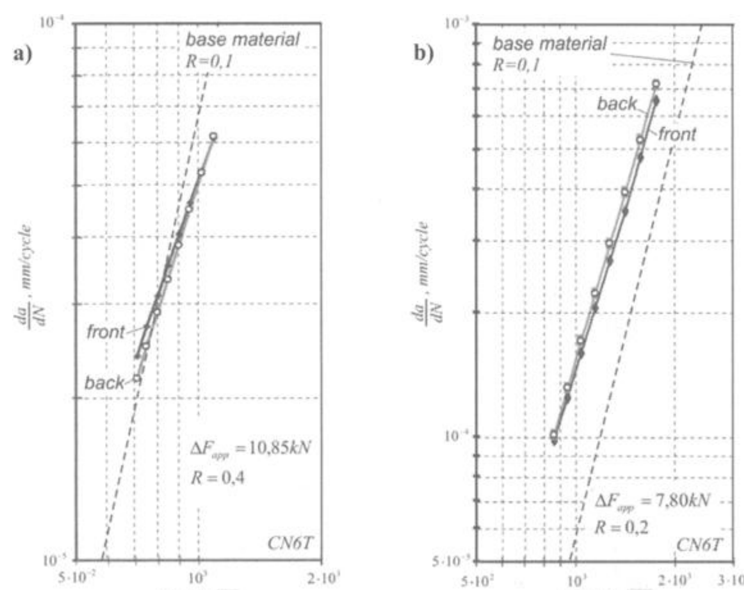

FIG. 21—*Plots da/dN versus ΔK for both surface and average crack growth lines for both fatigue regimes in the under-match weld.*

TABLE 3—*Obtained values of crack growth rate parameters (Paris-Erdogan relation).*

Appl. Ratio	Over-match Weld [mm/cycle]		Under-match Weld [mm/cycle]		Note
R	$C_{RS,min}$	$C_{RS,max}$	$C_{RS,min}$	$C_{RS,max}$	
	2.00E-13	6.22E-12	2.61E-13	2.53E-12	Surface front
0.2	2.76E-14	1,25E-12	4.86E-13	1.19E-12	Surface back
	8.3E-13		3.0E-12		Average
	4.26E-18	5.30E-13	8.43E-12	4.64E-11	Surface front
0.4	1.05E-18	2,92E-13	2.64E-12	8.18E-12	Surface back
	5.5E-13		2.8E-11		Average

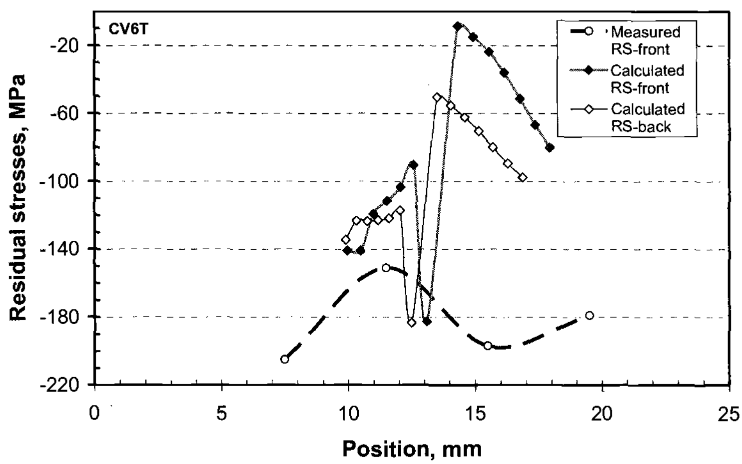

FIG. 22—*Comparisons of residual stresses on the specimen surface as a function of crack extension in the overmatched weld.*

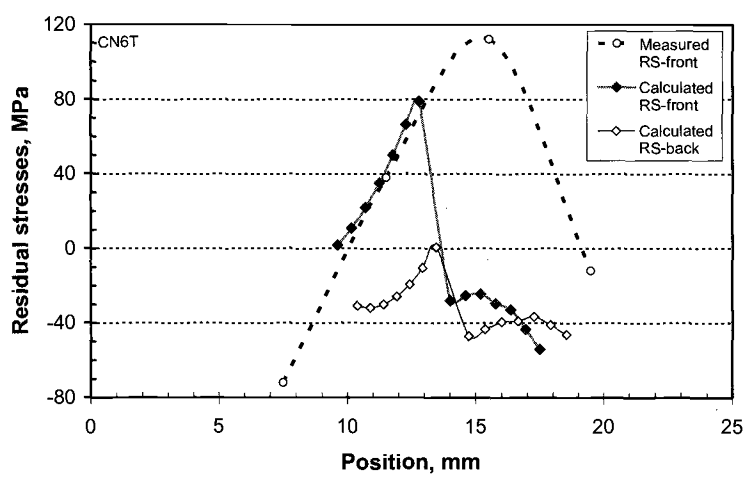

FIG. 23—*Comparisons of residual stresses on the specimen surface as a function of crack extension in the undermatched weld.*

Conclusion

The effect of residual stresses on fatigue crack propagation in welded samples is estimated by means of the difference between the average stress intensity factor (given by applied load) and local effective stress intensity factor necessary to cause the measured local crack growth rate.

The proposed model is applied on two specimens cut out of weld joints of different strength. Comparisons between measured and assumed residual stresses on the surface as a function of crack extension show that the actual measured residual stresses can be higher than the calculated residual stresses from the fatigue crack growth behavior.

The proposed procedure gives the residual stress magnitude $\sigma_{RS,ij}$ at the surface of the specimen and along the crack front. The proposed model helps to estimate the effect of residual stresses without an often impossible and costly residual stress measurements.

References

[1] Shi, Y. W., Chen, B. Y., and Zhang, J. X. "Effects of Welding Residual Stresses on Fatigue Crack Growth Behaviour in Butt Welds of a Pipeline Steel," *Engineering Fracture Mechanics*, Vol. 36, No. 6, 1990, pp. 893–902.

[2] Ninh, N. T. and Wahab, M. A., "The Effect of Residual Stress and Weld Geometry on the Improvement of Fatigue Life," *J. of Materials Processing Technology*, Vol. 48, 1995, pp. 581–588.

[3] Dong P., "Residual Stresses in Aluminium-Lithium Welds and Effects on Structural Fabricability and Integrity," *Mathematical Modelling of Weld Phenomena 5*, H. Cerjak, Ed., 2001, pp. 507–528.

[4] Parker, A. P., "Stress Intensity Factors, Crack Profiles and Fatigue Crack Growth Rates in Residual Stress Fields," *Residual Stress Effects in Fatigue, ASTM STP 776*, ASTM International, West Conshohocken, PA, 1982, pp. 224–234.

[5] Behini, M., Bertini, L., and Vitale, E., "Fatigue Crack Growth in Residual Stress Fields: Experimental Results and Modelling," *Fatigue Fract. Eng. Mater. Struc.*, Vol. 17, No. 12, 1994, pp. 1433–1444

[6] Wang, J., Schneider, G., and Vestergaard, V., "Fatigue Crack Growth in Residual Stress Fields," *Annual Forum Proceedings of the American Helicopter Society*, 57th Annual Forum, Vol. 57, 2001, pp. 429–434

[7] Pippan, R., Reimelmoser, F. O., Bichler, C., "Measurability of Crack Closure," *Advances in Fatigue Crack Closure Measurement and Analysis: 2nd, ASTM STP 1343*, R. C. McClung and J. C. Newman, Jr., Eds., ASTM International, West Conshohocken, PA, 1999, pp. 41–56.

[8] Josefson, B. L., Svensson, T., Ringsberg, J. W., Gustafsson, T., and de Mare, J., "Fatigue Life and Crack Closure in Specimens Subjected to Variable Amplitude Loads under Plane Strain Conditions," *Engineering Fracture Mechanics*, Vol. 66, 2000, pp. 587–600.

[9] Mochizuki M. and Toyoda M., "Numerical Analysis of Residual Stress in Welded Structures Using Inherent Strain," *Mathematical Modelling of Weld Phenomena 5*, H. Cerjak, Ed., 2001, pp. 549–580.

[10] SINTAP: Structural Integrity Assessment Procedure. Final Report. EU-Project BE 95-1462. Brite Euram Program, Brussels, 1999.

[11] ASTM Standard E 647-99: "Standard Test Method for Measurement of Fatigue Crack Growth Rates," ASTM International, West Conshohocken, PA, 1999.

Journal of ASTM International, May 2005, Vol. 2, No. 5
Paper ID JAI12024
Available online at www.astm.org

Ryan J. Morrissey,[1] *Ph.D. and Patrick J. Golden,*[1] *Ph.D.*

Ultrasonic Fatigue Testing of Ti-6Al-4V

ABSTRACT: The objective of this research was to investigate the high cycle fatigue behavior of a titanium alloy using an ultrasonic fatigue system. Fatigue testing up to one billion cycles under fully reversed loading conditions was performed to determine the ultra-high cycle fatigue behavior of Ti-6Al-4V. Endurance limit results were compared to similar data generated on conventional servohydraulic test systems and electromagnetic shaker systems to determine if there are any frequency effects. In addition, specimens were tested with and without cooling air to determine the effects of temperature on the fatigue behavior. Results indicate that the fatigue strength determined from ultrasonic testing was consistent with conventional testing. However, preliminary results indicate that cooling air may increase the fatigue limit stress at very long lives.

KEYWORDS: high cycle fatigue, ultrasonic, Ti-6Al-4V, endurance limit

Introduction

Recent work [1–3] using ultrasonic test systems has shown that many materials, including some steels and titanium alloys, exhibit a sharp decrease in fatigue strength between fatigue lives of 10^6 and 10^9 cycles. This is in contrast to the classical fatigue limit, which assumes a constant minimum fatigue strength below which a material is assumed to have an infinite life (normally assumed to be equal to the fatigue strength at 10^6 or 10^7 cycles).

A large decrease in fatigue strength in the ultra-high cycles fatigue regime could have a major impact on turbine engine design. Recent changes to the Engine Structural Integrity (ENSIP) handbook [4], the Air Force manual used to provide guidance to the engine manufacturers, require that engine components subjected to high cycle fatigue be designed to meet lifetime requirements of 10^9 cycles (as opposed to the previous guideline of 10^7 cycles). Specifically, ENSIP states, "All engine parts should have a minimum HCF life of 10^9 cycles. This number is based on the observation that an endurance limit does not exist for most materials." Due to cost and time constraints, it is impractical to assume that conventional testing methods can be used to gather the experimental data necessary to understand the material behavior in this regime. Ultrasonic fatigue testing offers an alternative testing method for generating the data necessary at very long fatigue lives.

Ultrasonic fatigue testing is not new, but it has not been widely used for fatigue and fracture mechanics applications until fairly recently. This may be due in part to the difficulty in accurately determining the test conditions. Although ultrasonic testing provides a means for generating data at long lifetimes very quickly, it is not an easy test method to control. However, advances in the speed and accuracy of electronic measurement devices have made the determination of displacements and loads during testing easier to ascertain and control. A

Manuscript received 19 February 2004; accepted for publication 2 July 2004; published May 2005. Presented at ASTM Symposium on Fatigue and Fracture Mechanics: 34th Volume on 19–21 November 2003 in Tampa, FL; S.R. Daniewicz, J.C. Newman, Jr., and K-H. Schwalbe, Guest Editors.

[1] Materials Research Engineer, Air Force Research Laboratory (AFRL/MLLMN), Wright-Patterson AFB, OH, 45433.

thorough review of the ultrasonic testing technique for fatigue and fracture applications can be found in [5,6].

The main advantage of ultrasonic fatigue testing is saving time. Experiments using the ultrasonic method can be completed 20–1000 times faster than conventional servo-hydraulic systems or electromagnetic shakers. For endurance limit testing at 10^9 cycles, this means that individual tests can be completed in less than one day versus weeks for conventional systems. This extreme savings in time, and therefore money, means that tests that may otherwise be impractical can now be accomplished. In general, this also allows for a much larger test matrix to be performed within any given time period, which allows for the generation of statistically significant data sets and can be very important depending on the degree of variability in the material properties being considered.

The main disadvantages of ultrasonic test systems are directly related to the speed at which the tests are performed. In order to test in the kHz range, resonance loading conditions are necessary. This restricts the size and shape on specimens that can be tested and means that full component testing would be unlikely. However, for basic material testing, this does not present a problem. A second issue involves the internal heat generation that is produced by the high cycling speeds and which may affect the material behavior leading to incorrect results if not taken into account. This issue will be discussed further in the results section. Another potential issue with ultrasonic testing involves the strain rate sensitivity of the material being tested. Many materials are frequency dependent, and this must therefore be accounted for when reporting data, as well as when using such data for design in applications that may be at much lower operating frequencies.

Experimental Procedure

Material

The test material was a titanium alloy, Ti-6Al-4V, which has been used in many investigations as part of the National Turbine Engine High Cycle Fatigue Program [7] and is shown in Fig. 1. It was produced in accordance with AMS 4928 and forged into flat plates approximately 406 mm × 150 mm × 20 mm. These forged plates were solution heat treated at 932°C for 1 h, vacuum annealed at 705°C for 2 h, and argon fan cooled. More complete details of the material processing are in [8,9]. This resulted in a duplex microstructure, 60 % (volume) of which was the primary-α (h.c.p.) phase, while the remaining was the transformed-β (b.c.c.) phase. This material form is commonly referred to as solution treated and overaged (STOA). The average grain size was approximately 15–20 μm. The room temperature longitudinal tensile properties (along the loading axis) were determined to be E = 116 GPa, σ_y = 930 MPa, and σ_{UTS} = 968 MPa.

Ultrasonic Test System

In order to test the fatigue limit of materials beyond 10^7 cycles, an ultrasonic fatigue system was designed. The main component of the ultrasonic system is a piezoelectric transducer, which converts an electronic signal at a frequency of 20 kHz (± 500 Hz) into a mechanical displacement at the same frequency. The electronic signal is supplied by a power supply that automatically tunes to the natural resonant frequency of the system. If the frequency falls outside the 19.5–20.5 kHz range, the system shuts off automatically. The power supply and transducer are commercial products manufactured by Branson Ultrasonics. They were developed and are traditionally used for ultrasonic welding applications.

Attached to the transducer are a titanium booster and a horn, which served to amplify the mechanical displacement. A specimen designed to run in resonance with the system is then attached to the horn. The specimens used in this study were cylindrical dogbones with a gage section diameter of 4 mm. They were machined using a low stress grind technique to minimize residual stresses. The specimens were designed so that the maximum strain is located in the gage section. The specimen dimensions are shown in Fig. 2. A dynamic analysis of the system is discussed in the following section.

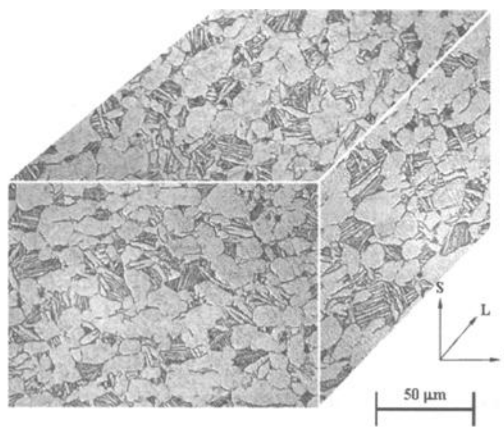

FIG. 1—*Ti-6Al-4V plate microstructure.*

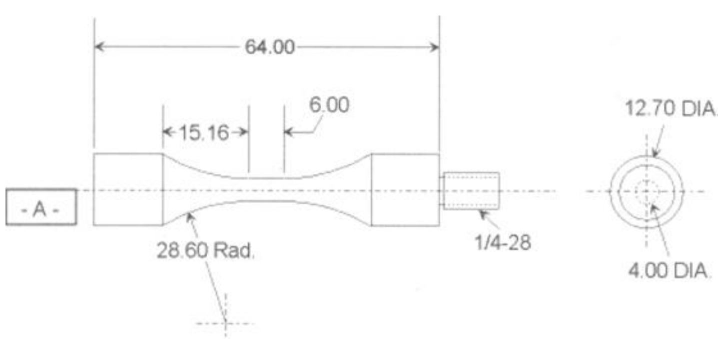

FIG. 2—*Ultrasonic fatigue specimen (all dimensions shown in mm).*

In this study, all testing was performed at a stress ratio, R, of −1.0. For fully reversed loading conditions, the end of the specimen opposite the horn is a free surface. One of the greatest challenges of ultrasonic testing is measuring the applied stress in the material. To that end, an eddy current sensor is used to measure displacement at the free end of the specimen. This displacement is calibrated at the beginning of each test using a resistance strain gage bonded to the gage section. The displacement, with the calibration factor, is then used in a feedback loop during testing to actively control the strain, and therefore stress, in the gage section. The test control software continuously records displacement and controls the output of the power supply and, therefore, indirectly controls the magnitude of the strain in the specimen. Strain gages cannot be used throughout the test because they quickly fall off of the specimen during testing.

Dynamic Analysis

The ultrasonic test setup was modeled using the finite element software STADYN, which was written for the static and dynamic analysis of structures. The problem was modeled dynamically using 1-D rod elements. As described previously, the structure for the fully reversed test was made up of a booster, a horn, and the specimen. Figure 3 has a plot of the profile of the geometry used in the model. Each rod element in the model had an area property that is equal to the average value over the length of the structure that the element represents. The mesh was therefore more refined near locations of changing area and also in the gage section of the specimen. Forty-one total rod elements were used with 15 of these elements in the specimen gage section. This was found to result in a converged solution. The entire structure was made of titanium, and therefore each element used the material properties of Young's modulus $E = 116$ GPa and density $\rho = 2800$ kg/m^3. The boundary conditions of the model were fixed-free. The structure was fixed at the center point of the booster ($X = 0$), which was a displacement node in the system. This was also the location where the booster was physically clamped to the test frame. The end of the specimen ($X = 264$ mm) was modeled as free.

The results of the vibration analysis for the fixed-free system are plotted in Fig. 3. The solid line represents the geometry of the booster, horn, and specimen (from left to right). The mode shape, $u(x)$, results shown are from the third mode, which has a resonant frequency of 20 700 Hz according to the model. The actual experimentally measured resonant frequency for this geometry was 20 250 Hz, a difference of about 2 %. The mode shape shows displacement nodes at the fixed end, at a point within the horn, and at the center of the specimen gage section. The axial strain, $\varepsilon_x = du/dx$, is also plotted in Fig. 3. Two interesting observations can be made from these curves. First, the ends of the specimens are strain (stress) nodes. One end of the specimen is free so it must be stress free, and the end of the specimen that joins the booster also has a very low stress, which is advantageous when testing brittle materials. Second, the gage section of the specimen not only has the peak strain, but it has nearly constant strain over the entire gage length with only a 0.2 % variation according to the analysis results. The strain decreases rapidly outside the gage section.

Staircase Method

The staircase method involves testing specimens at a constant amplitude loading condition approaching the fatigue limit. A stress level is chosen for each specimen based on the results of the test that has just been completed. If the previous test did not fail in some pre-determined number of cycles (such as 10^8), the next test is run at a higher maximum stress. If the previous specimen fails before runout, the next test is run at a lower maximum stress. The stress ratio as well as the stress increment from one test to another (both increasing and decreasing) is kept constant. At the conclusion of this type of testing there are data containing both failures and runouts at stress levels immediately surrounding the fatigue limit stress. Statistical methods can then be used to determine the mean of the distribution to determine the fatigue limit stress.

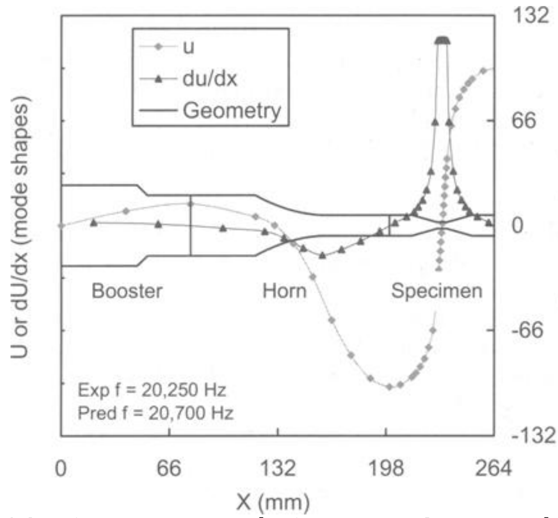

FIG. 3—*Plot of the ultrasonic test rig displacement and strain mode shapes as well as the profile of the test rig geometry for the fully reversed (no mean stress) test configuration.*

Figure 4 shows an example of staircase testing performed as part of the National Turbine Engine HCF Program on the same Ti-6Al-4V plate material used in this study. For that testing, completed at a stress ratio of R = 0.1, the fatigue limit was determined to be 540 MPa with a standard deviation of 60 MPa. It can be seen in Fig. 4 that all of the stress values used are in the near vicinity of the fatigue limit. For this reason, a very accurate value of the mean fatigue limit stress can be determined. However, this type of testing results in a very poor approximation of the standard deviation. In order to obtain a better idea of the true statistical distribution, testing would need to be performed at stress values approaching the tails of the population.

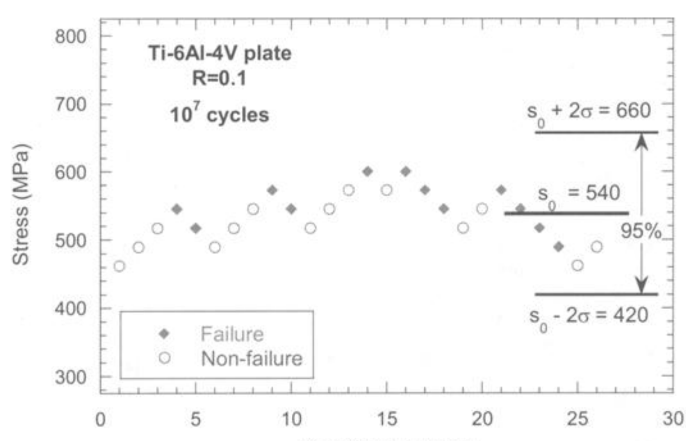

FIG. 4—*Plot of 10^7 cycle endurance limit staircase testing using servohydraulic test frames [7].*

Results

Table 1 shows a summary of the experiments run in this study. In addition, Fig. 5 shows the results of the staircase testing graphically. A stress of 400 MPa was chosen for the initial tests based on 10^7 cycle fatigue limit results from the National Turbine Engine HCF Program. These prior tests had been performed on the same Ti-6Al-4V material on conventional servohydraulic as well as electromagnetic shaker systems at frequencies ranging from 60–400 Hz. When a specimen in the ultrasonic rig failed at less than 10^8 cycles, the maximum stress was decreased by 10 MPa for the following test according to the staircase methodology. A specimen was considered failed when a crack had grown large enough to decrease the natural frequency of the system below the standard operating range (19.5–20.5 kHz). When this occurred, the system would shut down automatically. Typical crack sizes at this point were at least 2 mm, or half the gage section diameter. Due to the relatively long crack sizes at failure, the difference in total life calculations between the ultrasonic fatigue method and those tested using conventional methods (when failure was defined by the specimen breaking into two pieces) was considered minimal. If the specimen did not fail in 10^8 cycles, the maximum stress was increased by 10 MPa for the subsequent test.

The results of these initial experiments seem to indicate that the 10^8 cycle endurance limit of the Ti-6Al-4V material is approximately 390 MPa. However, since only nine experiments were performed, a statistically valid endurance limit stress cannot be determined. The results of the ultrasonic test system can be compared with the previous results from the more conventional testing. These results are plotted together in Fig. 6, which clearly shows that the two sets of data are consistent with each other.

The last four experiments listed in Table 1 show the results of additional ultrasonic testing incorporating cooling air. These tests were performed to see if the specimen heating caused by the dynamic loading was affecting the fatigue lives. Two cooling air jets blowing cold air at approximately 0°C at the gage section of the specimen are used to cool the surface of the material during testing. These tests were also begun at 400 MPa, but unlike the previous tests, the specimens did not fail (see Fig. 5). However, as with the previous results, not enough tests were performed to state conclusively that the cooling air had a significant impact on the fatigue strength of the material.

TABLE 1—*Staircase testing results ($R = -1$).*

Specimen	σ (MPa)	Cooled (Y or N)	Cycles
1	400	N	2.9×10^6
2	400	N	1.8×10^5
3	390	N	7.7×10^5
4	370	N	10^8
5	380	N	10^8
6	390	N	10^8
7	400	N	6.0×10^6
8	390	N	10^8
9	400	N	10^8
10	400	Y	10^9
11	410	Y	10^9
12	420	Y	10^9
13	430	Y	10^9

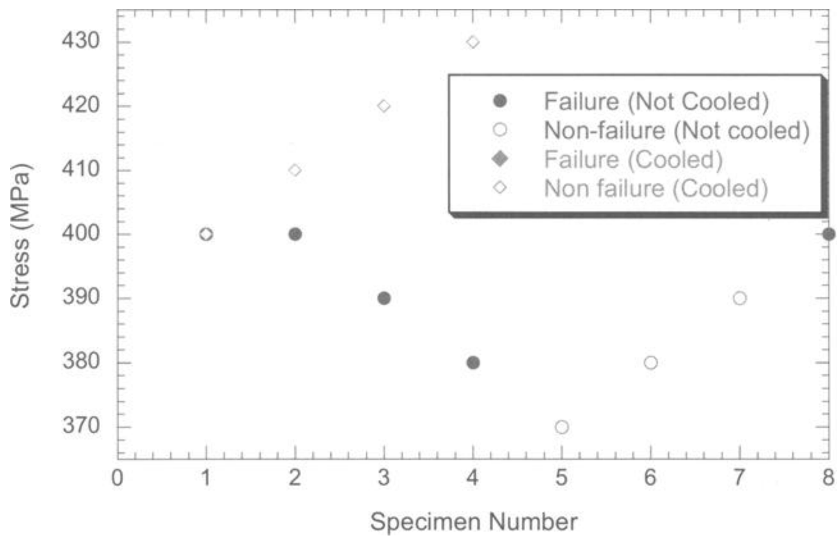

FIG. 5—*Plot of staircase testing results generated at 20 kHz in this study.*

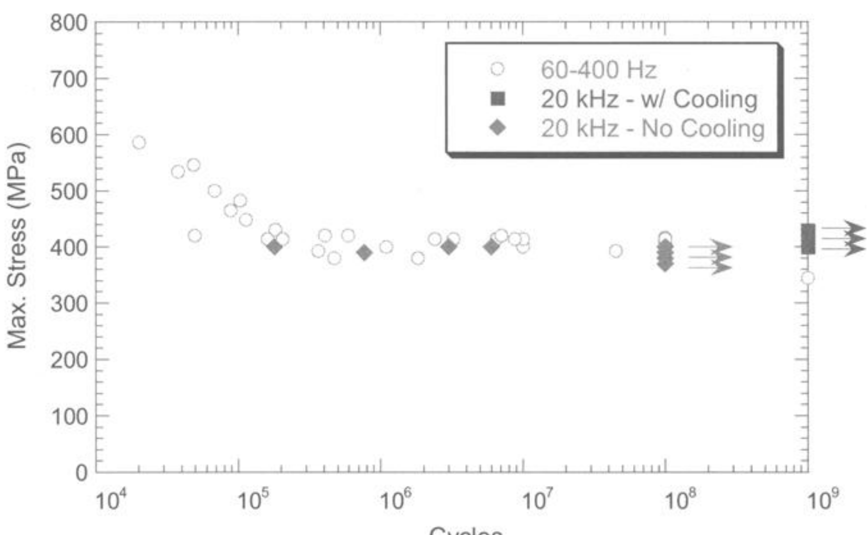

FIG. 6—*Comparison of results from ultrasonic and conventional test systems ($R = -1.0$).*

Failure Analysis

Previous studies using the ultrasonic fatigue method have shown an increase in internal initiation sites as the life to failure increases [10,11]. This has been observed in many materials, including Ti-6Al-4V [10]. The exact reason for this is unknown, but one possible explanation involves a change in failure mechanism. As the stress level decreases at longer lives, the effect of surface defects decreases to the point where internal defects such as inclusions and voids become the initiation points [11]. This results in a bi-modal distribution of failures, shown graphically in Fig. 7. At higher stresses and shorter lives, surface defects dominate, thereby obscuring the intrinsic material S-N curve. However, at longer lives and smaller stresses, this intrinsic material strength becomes the life-limiting factor. This change in failure mechanism is generally accompanied by a sharp decrease in the fatigue limit.

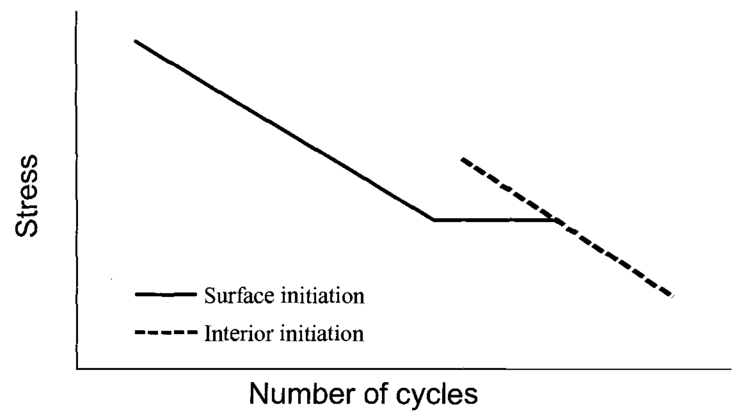

FIG. 7—*Graphical description of bi-modal failure distribution.*

Failure analysis of the specimens in this study showed no indication of internal initiations. All four specimens failed from a surface flaw similar to the one shown in Fig. 8. Figure 8*a* shows the size of the surface crack that had grown before the test machine automatically shut down due to the drop in natural frequency. Also visible in that picture are the areas around the crack tip, which appear to undergo a re-melt process. This is due to the extremely high temperatures generated at the crack tip at these very high strain rates. Figure 8*b* shows the fracture surface of the specimen. The initiation site is located at the top of the specimen in the figure. In order to break the specimen apart, the power supply was turned on manually. This produced a very short stress pulse before it would shut itself down again. This was repeated until failure. There appear to be distinct markings along the crack path due to these pulses.

The lack of internal initiations may indicate that this material does not exhibit the bi-modal failure mechanism seen in other materials, or it may simply mean that the bi-modal mechanism will not appear until longer lives are tested. The processing of the Ti-6Al-4V plate material used as part of the National Turbine Engine HCF Program produced very few internal defects such as voids. Therefore, the intrinsic material strength may be stronger than if a different processing procedure had been used. This would give a possible explanation of why previous work has shown internal initiations at the number of cycles tested in this study. If that is the case, then it might be expected that interior initiations might still occur, but not until even longer lives.

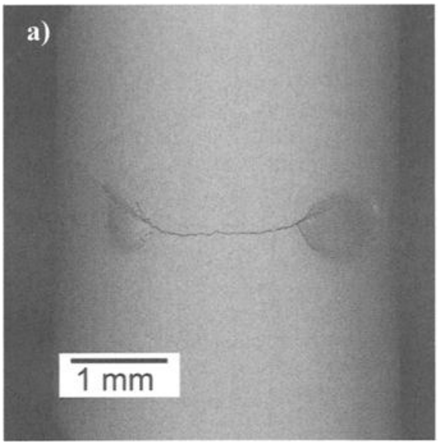

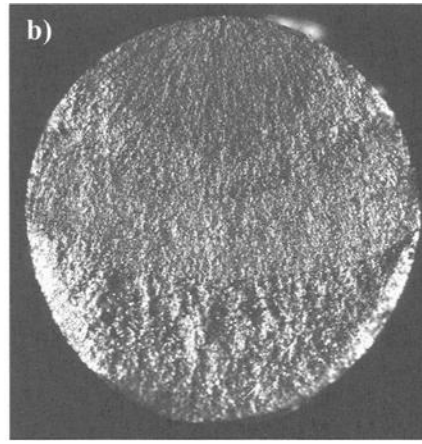

FIG. 8—*SEM photographs of typical failure surfaces after ultrasonic testing:* a) *surface flaw in gage section and* b) *fracture surface.*

Conclusions

The ultrasonic fatigue system provides an efficient way of determining material behavior of Ti-6Al-4V at very high cycles. It allows test matrices to be completed that were previously impractical and provides a potential means for engine manufacturers to meet the new Air Force ENSIP guidelines.

Contrary to what has been reported for many materials, including Ti-6Al-4V, there was no noticeable decrease in fatigue limit of the Ti-6Al-4V plate material after 10^8 cycles at R = –1.0. Instead, the fatigue limit stress agrees with limited data from previous testing on the same alloy using conventional test techniques. In addition, there does not seem to be any significant frequency or temperature effects in this alloy. The fatigue limit at 10^7 and 10^8 cycles is consistent with the previous data at lower frequencies. Based on data from the literature, it may be implied that these results are alloy dependent and may change due to processing and heat treatment. Preliminary data suggest that external cooling may slightly increase the fatigue limit, but additional testing needs to be performed before any statistically valid statements can be made.

References

[1] Marines, I., Dominguez, G., Baudry, G., Vittori, J.-F., Rathery, S., Doucet, J.-P., et al., "Ultrasonic Fatigue Tests on Bearing Steel AISI-SAE 52100 at Frequency of 20 and 30 kHz," *International Journal of Fatigue*, Vol. 25, 2003, pp. 1037–1046.

[2] Papakyriacou, M., Mayer, H., Pypen, C., Plenk, H., and Stanzl-Tschegg, S., "Influence of Loading Frequency on High Cycle Fatigue Properties of B.C.C. and H.C.P. Metals," *Materials Science and Engineering A*, Vol. 308, 2001, 143–152.

[3] Stanzl-Tschegg, S. E. and Mayer, H., "Fatigue and Fatigue Crack Growth of Aluminum Alloys at Very High Numbers of Cycles," *International Journal of Fatigue*, Vol. 23, 2001, pp. S231–S237.

[4] ENSIP, Engine Structural Integrity Program Handbook,

http://engineering.wpafb.af.mil/corpusa/handbook/mh1783/mh1783.pdf, rev. 2002.

[5] Meyer, H., "Fatigue Crack Growth and Threshold Measurements at Very High Frequencies," *International Materials Reviews*, Vol. 44, No. 1, 1999.

[6] Stanzl-Tschegg, S. E., "Ultrasonic Fatigue," *Fatigue 96*, 1996, pp. 1887–1898.

[7] Gallagher, J. P., et al., "Improved High Cycle Fatigue Life Prediction," Report # AFRL-ML-WP-TR-2001-4159, University of Dayton Research Institute, Dayton, OH, January 2001 (on CD-ROM).

[8] Moshier, M. A., Nicholas, T., and Hillberry, B. M., "High Cycle Fatigue Threshold in the Presence of Naturally Initiated Small Surface Cracks," *Fatigue and Fracture Mechanics: 33rd Volume, ASTM STP 1417*, W. G. Reuter and R. S. Piascik, Eds., ASTM International, West Conshohocken, PA, 2002, pp. 129–146.

[9] Mall, S., Nicholas, T., and Park, T.-W., "Effect of Pre-Damage from Low Cycle Fatigue on High Cycle Fatigue Strength of Ti-6Al-4V," *International Journal of Fatigue*, Vol. 25, 2003, pp. 1109–1116.

[10] Atrens, A., Hoffelner, W., Duerig, T. W., and Allison, J. E., "Subsurface Crack Initiation in High Cycle Fatigue in Ti-6Al-4V and in a Typical Martensitic Stainless Steel," *Scripta Metallurgica*, Vol. 17, No. 5, 1983, pp. 601–606.

[11] Wang, Q. Y., Bathias, C., Kawagoishi, N., and Chen, Q., "Effect of Inclusion on Subsurface Crack Initiation and Gigacycle Fatigue Strength," *International Journal of Fatigue*, Vol. 24, 2002, pp. 1269–1274.

Byung-Joo Kim[1] *and Daniel Kujawski*[2]

Fatigue Endurance Diagram for Materials with Defects

REFERENCE: Kim, B.J. and Kujawski, D., **"Fatigue Endurance Diagram for Materials with Defects,"** *Fatigue and Fracture Mechanics: 34th Volume, ASTM STP 1461*, S. R. Daniewicz, J. C. Newman and K.-H. Schwalbe, Eds., ASTM International, West Conshohocken, PA, 2004.

ABSTRACT: Engine and turbine components that experience high cycle fatigue should operate under the fatigue threshold stress level to ensure their safe service life. In general, designers have to consider two types of thresholds, i.e. fatigue stress threshold for crack initiation and fatigue stress intensity factor threshold for crack propagation. These two thresholds overlap for short cracks or materials with defects. A new approach, which is called the fatigue endurance diagram (FED) for the prediction of fatigue threshold of materials with defects, is presented. This approach indicates that the fatigue strength of materials with cracks or defects is determined simultaneously by two parameters, the normalized stress intensity factor range and the normalized stress range. The FED indicates that the fatigue threshold condition is governed mainly by the threshold stress intensity factor and by the fatigue limit for the long and short cracks, respectively.

KEYWORDS: fatigue threshold, fatigue limit, small defect, crack, fatigue endurance diagram (FED), load ratio, adjusting parameter

Introduction

Many structural components experience very high cycle fatigue loading, e.g. the fatigue life of a car engine ranges around 10^8 cycles and the big diesel engines for ships or high-speed trains operate up to 10^9 cycles. Moreover, the fatigue life of a turbine engine is about 10^{10} cycles. To guarantee reliable operation of engine and turbine components under very high cycle fatigue loading, the components should be designed according to the fatigue threshold stress, $\Delta\sigma_{th}$.

There are two types of thresholds currently used in fatigue analyses. One is the fatigue limit of smooth specimen, $\Delta\sigma_{fl}$, that defines a loading criterion under which a fatal crack will not form. The other is the fatigue crack growth threshold, ΔK_{th}, that defines a loading criterion under which an existing crack will not grow significantly. The former threshold is associated with the infinite life approach; it emphasizes initiation rather than crack propagation. The latter threshold presumes the existence of a crack and is used in damage tolerant design.

The fatigue limit is related to the ability of the material to resist strain localization and ultimately its resistance to plasticity. Fatigue cracks are initiated at heterogeneous nucleation sites within the material whether they are preexisting (associated with defects) or are generated during the cyclic straining process itself. A threshold stress intensity factor range, ΔK_{th}, defines a service-operating loading below which a long fatigue crack does not detectably propagate.

Modern defect tolerant design philosophy is based on the premise that all engineering structures are inherently flawed. It is generally accepted that the fatigue strength of materials

[1] Senior Researcher, Structure Research Department, Hyundai Heavy Industries, Co. Ltd., Ulsan 682-792, Republic of Korea.
[2] Professor, Department of Mechanical and Aeronautical Engineering, Western Michigan University, Kalamazoo, MI 49008-5065, USA.

containing defects or flaws is lower than that of a defect free material. Figure 1 illustrates how the threshold stress range, $\Delta\sigma_{th}$, may vary with the crack (or defect) size, *a*. A number of empirical or fracture mechanics based approaches have been proposed for fatigue strength prediction of materials with small defects. These approaches are briefly discussed in the following section on Existing Methods for Small Defects.

This paper presents a new approach based on Fatigue Endurance Diagram (FED) for fatigue strength predictions of materials with defects. The proposed approach gives an effective tool to correlate the observed dependence between the $\Delta\sigma_{th}$ and ΔK_{th} as a function of the existing defect size.

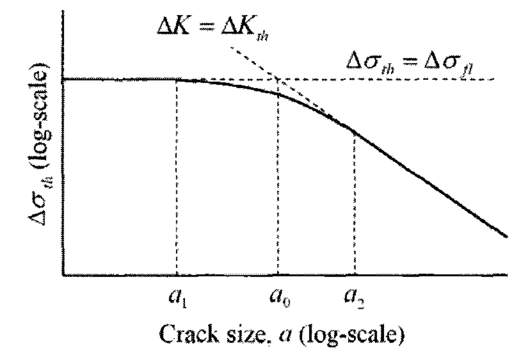

FIG. 1— A Kitagawa-Takahashi type of diagram showing various $\Delta\sigma_{th}$ regimes

Defects in Materials for Marine Engine Components

A defect may be regarded as any lack of perfection: striated metallographic structure, stringers or laminated inclusions, local heating, and other similar effects. In developing a design philosophy, it is proper to assume that all engineering materials contain "defects". A wide variety of defects can be found in a given engineering component. These defects or flaws may result from such sources as material imperfections, defects generated during service, and defects introduced as a result of faulty design practice [1].

For example, typical defects found in the components of marine diesel engines include porosity, cracks, and notches. Cracks are the most harmful defects in terms of fatigue strength deterioration. Porosity is the biggest defect overall in terms of physical size. Cracks are present in both cast and forged components. Common cracks found in cast components are the hot tear, the quench crack from heat treatment, the cold and hot cracks by repair welds, etc. Other defects present in forged components are hydrogen cracks, cracks by rapid heating, quench cracks, etc.

Many of the imperfections found in forgings, as well as problems that occur in forgings during service, can be traced to conditions that existed in the original ingot product. Typical material defects found on ingot are chemical segregation, shrinkage cavity (pipe), hydrogen flakes, and nonmetallic inclusions. Porosities can be as large as 5mm. On the other hand very small defects such as a segregation defect called a "ghost" (typically 0.05~0.2 mm), can be found only when they are grouped together. Parts are inspected for defects or cracks by means of non-destructive techniques. Usually, surface defects are detected by magnetic particle inspection (MPI). Internal defects are detected by ultrasonic testing (UT) methods. In this case, the issue is not the smallest defect that can be detected with a sensor, but the largest defect that can be missed during an inspection schedule that can cause a fatal damage.

Fatigue Strength According to Defect Size

Assuming that small-scale yielding prevails, linear elastic fracture mechanics (LEFM) provides a threshold stress intensity factor range, ΔK_{th}. This ΔK_{th} acts as a characteristic limit value that separates the condition for the propagation/non-propagation of existing flaws. Therefore, fatigue cracks should not grow significantly at stress intensity ranges smaller than the value of ΔK_{th} and would grow at ranges above ΔK_{th}. However, this is only applicable for long cracks. Many works show that the similitude concept of fracture mechanics, i.e. that cracks with the same crack tip condition (characterized by ΔK) will propagate at the same rate, does not hold true for small cracks [2].

The allowable fatigue stress regime is bounded by two limits shown in Fig. 1 (i.e. two thresholds); the upper limit is defined by the fatigue limit of a material without defects, $\Delta\sigma_{fl}$, and the lower limit that is determined by the long crack regime,

$$\Delta\sigma_{th} = \Delta K_{th} / F\sqrt{\pi a} \tag{1}$$

where F is a correction factor for ΔK calculation. The fatigue limit, $\Delta\sigma_{fl}$, is often related to an infinite life of a "defect-free" material.

Figure 1 shows a plot of the threshold stress range, $\Delta\sigma_{th}$ as a function of crack size a using logarithmic scales, which is widely known as the Kitagawa-Takahashi diagram. If ΔK_{th} is a material constant, the line marked as "ΔK=ΔK_{th}", with a slope of -0.5, should apply. This would predict an ever-increasing value of $\Delta\sigma_{th}$ with decreasing crack size. However, it is well known that if the crack size is zero, as for a defect-free specimen, the threshold stress for fatigue is not infinity but is equal to the fatigue limit $\Delta\sigma_{fl}$. Therefore, a horizontal line at the stress value of $\Delta\sigma_{fl}$ can be drawn in Fig. 1. This implies that for short cracks, the threshold stress range will be smaller than $\Delta\sigma_{fl}$ or predicted from the ΔK_{th} value; such cracks will be observed to grow at applied ΔK values less than ΔK_{th}.

Suggested mechanisms in the literature to rationalize short-crack behavior are microstructural effects, crack closure, high applied stress, stress field effects, crack deflection, etc. [3]. All these mechanisms can be expected to exert an influence. Although the relative importance of these different mechanisms is not fully understood, it is postulated that the closure phenomenon is most probably the major reason for the dependence of the short crack threshold on the crack size and on the load ratio R ($=P_{min}/P_{max}$) [4].

Recently, it was suggested by Forth et al. [5] that the short crack propagation at a ΔK below the long crack ΔK_{th} is due to the load history effect generated in standard tests when initiating the test at a high load and shedding load until threshold is reached. They proposed that the short and long crack thresholds are merely an artifact of the constant R load reduction test procedure, which generates artificially high threshold values when compared to steady-state data. Therefore, it is considered that the load history effects introduced into the long crack data has generated a database of artificially high thresholds that do not accurately represent the material response of cracks growing under increasing K.

The fatigue limit of a smooth specimen itself can be understood as a short crack threshold. This fatigue limit is determined by the propagation condition of a microstructurally small crack. Therefore, the fatigue strength is determined by the threshold condition whether the crack will propagate or not regardless of its size.

Existing Methods for Small Defects

Existing approaches for fatigue strength of materials with defects may be classified into the following three groups [6]: Frost's empirical model and other similar models, methods based on fatigue notch factor, and fracture mechanics approaches. The most accepted approaches are briefly discussed in this section. Two methods, namely the El-Haddad et al. [8], and the Murakami et al. [11] are widely used to predict $\Delta\sigma_{th}$ for materials with defects or small cracks. The predictions of these models versus experimental data were found to be load ratio dependent.

Kitagawa and Takahashi [7] first characterized the fatigue threshold for the short cracks quantitatively, namely that ΔK_{th} decreases with decreasing crack size (Fig. 1). Their study contributed much towards the development of many subsequent studies on small cracks and small defects.

El Haddad et al. [8] introduced fictitious or intrinsic crack length, a_0, (see Fig. 1) defined as;

$$a_0 = \frac{1}{\pi}\left(\frac{\Delta K_{th}}{F \cdot \Delta\sigma_{fl}}\right)^2 \tag{2}$$

Although a_0 was considered to be a material constant, the value of a_0 itself does not correspond to any physical dimension within the material and depends on the load ratio, R, and the crack geometry. Equation (3) predicts smoothly varying threshold stress in short crack regime while approaching $\Delta\sigma_{fl}$ and ΔK_{th} as the crack length becomes zero and long enough, respectively.

$$\Delta\sigma_{th} = \frac{\Delta K_{th}}{F\sqrt{\pi(a+a_0)}} \tag{3}$$

Usami and Shida [9,10] assumed that at the fatigue threshold condition the size of the cyclic plastic zone, at a crack tip, is equal to a material constant. Fatigue crack growth and threshold values for short cracks in steels were experimentally obtained and analyzed using non-linear fracture mechanics procedures. The fatigue threshold conditions were expressed in terms of a two parameter diagram for stress amplitude and threshold stress intensity.

Murakami et al. [11] proposed a new geometrical parameter, $\sqrt{area}$, which is defined as the square root of the area obtained by projecting a defect or a crack onto the plane perpendicular to the maximum tensile stress. This approach is based on both microscopic observations on cracking from small surface defects and on three-dimensional numerical stress analyses of cracks with various shapes. Equation (4) enables one to predict σ_{th} without a fatigue test. The concept of the $\sqrt{area}$ parameter suggests that there should be no difference in the σ_{th} due to inclusion shape if the values of $\sqrt{area}$ of two inclusions are identical.

$$\sigma_{th} = \frac{C(H_V + 120)}{\sqrt{area}^{1/6}} \cdot \left[\frac{1-R}{2}\right]^{\alpha} \tag{4}$$

where: C=1.43 for surface defects and 1.56 for internal defects,
$\alpha = 0.226 + H_V \times 10^{-4}$,
H_V : Vickers hardness.

Fatigue Endurance Diagram (FED)

A new approach depicted in Fig. 2, which is called the fatigue endurance diagram (FED) is proposed for the prediction of the fatigue threshold of materials with defects. This approach is an extension of that from Ref. 12 and is applicable for different materials, different load ratios and arbitrary crack or defect geometries. The FED is determined by the following relationship:

$$\left(\frac{\Delta K}{\Delta K_{th}}\right)^m + \left(\frac{\Delta \sigma}{\Delta \sigma_{fl}}\right)^n = 1 \tag{5}$$

where: ΔK and $\Delta\sigma$ are the applied values of the stress intensity and stress range, and
m, n are adjusting parameters

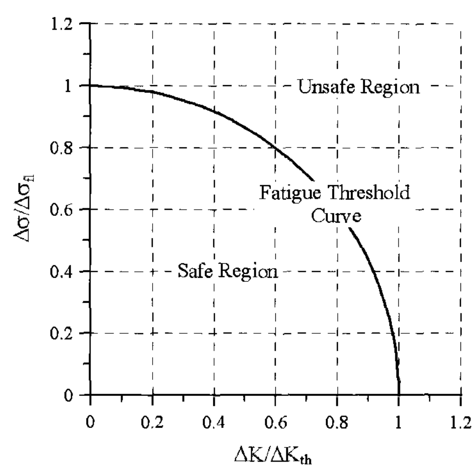

FIG. 2— Fatigue endurance diagram

The two adjusting parameters m and n characterize the apparent behavior of different materials. Equation (5) represents the fatigue threshold condition curve for materials with defects. The FED is plotted using normalized axes of $\Delta K/\Delta K_{th}$ and $\Delta\sigma/\Delta\sigma_{fl}$. The FED indicates that the threshold stress is bounded by the threshold stress intensity factor if the crack is long (when the applied stress is low) and by the fatigue limit if the crack is short (when the applied stress is high). When the crack size is between those two extreme cases, the threshold condition is influenced by both parameters. This means that the fatigue strength of materials with cracks or defects is determined simultaneously by two parameters, the fatigue crack growth threshold and the fatigue limit of smooth specimens, are dependent on the crack length and stress level.

The FED is similar to the two-parameter fatigue threshold expression utilizing σ_w/σ_{yc} and $\Delta K_{th}/\Delta K_{th,R=-1}$ by Usami [10], and the failure assessment diagram for monotonic tensile fractures utilizing σ/σ_c and K_I/K_{Ic} [13] (σ_w : stress amplitude at fatigue limit, σ_{yc} : cyclic yield stress, $\Delta K_{th,R=-1}$: fatigue threshold for R= -1, σ_c : collapse stress, K_{Ic} : fracture toughness).

The proposed diagram is not influenced by the R-ratio or geometrical correction factor, F, in the stress intensity factor equation and different material strengths because all the parameters are normalized. Two exponents in Eq. (5), m and n, can be used to adjust the actual dependencies on the two material strength parameters for different materials. As a particular case, this method is equivalent to the El Haddad approach [8] and the Smith model [14] when m = n = 2 and m = n = ∞, respectively. If m and n are different values, the curve loses its symmetric property with respect to the y = x line. In general, lower values of exponents (e.g. m = n = 1.5) result in conservative predictions.

To properly use this diagram, the fatigue strength of a material, i.e. ΔK_{th} and σ_{fl}, have to be known, estimated, or obtained by fatigue testing. The applied values of $\Delta\sigma$ and ΔK have to be determined for a given geometry, R-ratio, and defect size. Once these values are determined, the data points can be normalized and plotted on the diagram.

For design purposes, a curve considering safety factor can also be drawn (Fig. 3). A safety factor can be introduced by the constant C in Eq. (6). Equation (5) is a particular case of Eq. (6) when SF = 1.

$$\left(\frac{\Delta K}{\Delta K_{th}}\right)^m + \left(\frac{\Delta\sigma}{\Delta\sigma_{fl}}\right)^n = C \tag{6}$$

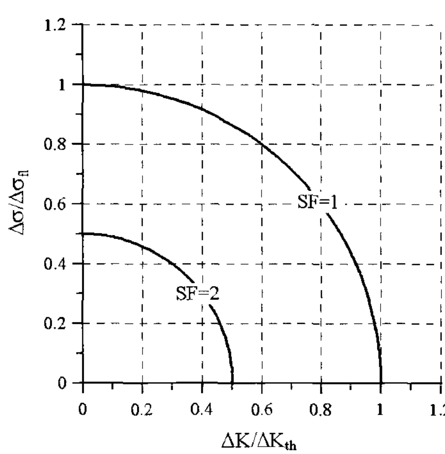

FIG. 3— Fatigue endurance diagram considering design safety factor

To add the information about crack length in the diagram, some reference lines can be drawn corresponding to the actual crack size relative to intrinsic crack size. For example, a line when the crack length is the same as the intrinsic crack length, a_0, this occurs when y = x i.e. $\Delta\sigma/\Delta\sigma_{fl} = \Delta K/\Delta K_{th}$ in Fig. 4. Other lines corresponding to $a = 10a_0$ and $a = a_0/10$, are shown in Fig. 4. Two coordinate axes, $x = \Delta K/\Delta K_{th}$ and $y = \Delta\sigma/\Delta\sigma_{fl}$, correspond to the extreme cases when the crack length becomes infinity and zero, respectively.

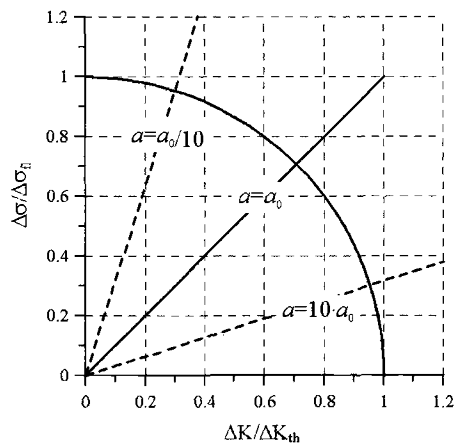

FIG. 4— Lines showing crack length relative to intrinsic crack length

Test Data on Fatigue Endurance Diagram

Fatigue test data from literature [4,8,15–18] were used to validate the FED approach. A total of eight fatigue test data sets for the materials with defects were used. The defects in test specimen range from microstructurally short to long cracks. Test data and adjusting parameters for each case when m = n are shown in Figs. 5-10. Adjusting parameters were calculated by the least square method.

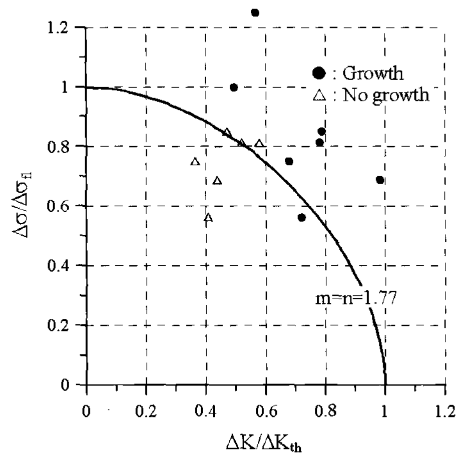

FIG. 5— FOD-induced small cracks in bimodal Ti-6Al-4V [15]

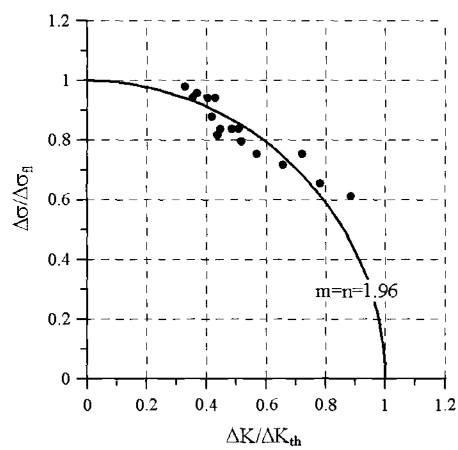

FIG. 6— Fatigue limit of annealed S45C steel with small holes [16]

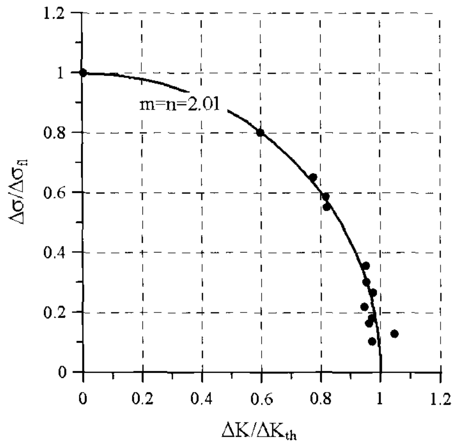

FIG. 7— Threshold stress for fatigue crack growth in G40.11 steel [8]

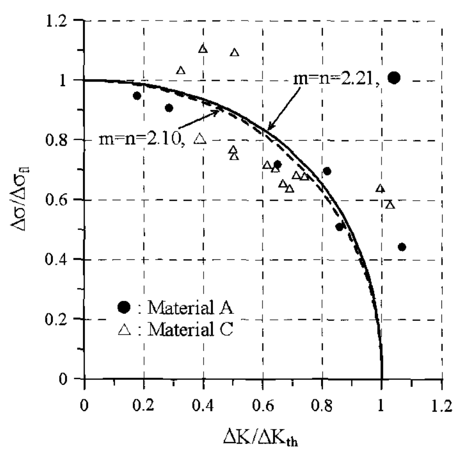

FIG. 8— Effects of grain size and crack length on threshold condition for mild steel [17]

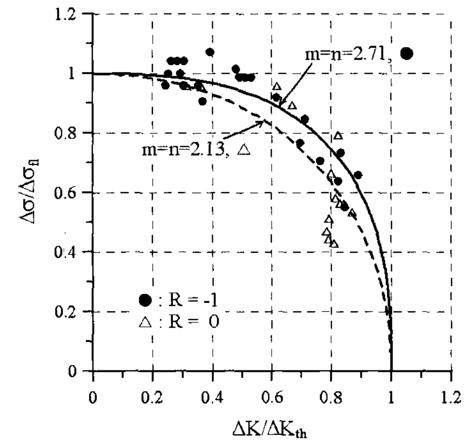

FIG. 9— 2.25Cr-1Mo pressure vessel steel with natural surface cracks [4]

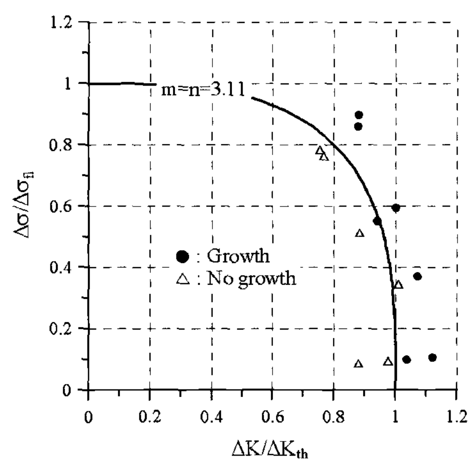

FIG. 10— SM41 steel with edge cracks in flat plate [18]

Considering that the fatigue endurance diagram and the El Haddad curve are equivalent when the exponents m = n = 2, it can be noted that the FED gives clearer estimation whether the data points are safe or not. This is because the Kitagawa-Takahashi diagram is plotted in log-log axes, therefore, points look closer to each other though the error is not very small.

In many cases, the predicted curves with the exponents m = n = 2 agree well with the tested fatigue threshold condition. Calculated m and n factors are plotted with respect to material ΔK_{th} values. Average value of m = n is 2.25. It can be seen from Fig. 11 that the adjusting parameters are increasing with ΔK_{th}. This means that short fatigue crack experiences relatively more resistance to propagate when ΔK_{th} becomes large. It can be stated from Figs. 5-10 that the safety factor SF = 1.5 or 2.0 is sufficient for the fatigue strength evaluation of the material with defects. However, if we consider that these tests were carried out under highly controlled conditions in laboratory, it can be inferred that the safety factor should be at least 2.0 or greater.

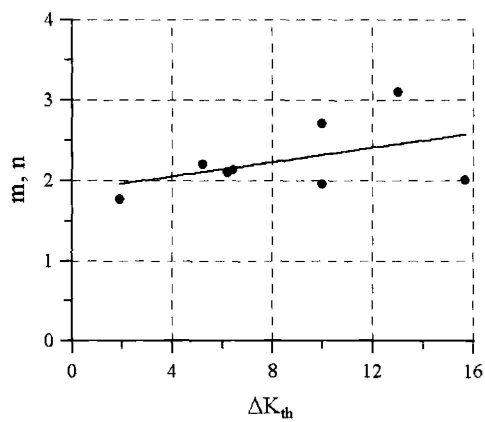

FIG. 11— Effect of ΔK_{th} on adjusting parameters m, n

Conclusions

Fatigue threshold strength, $\Delta\sigma_{th}$, is usually characterized by a fatigue limit, $\Delta\sigma_{fl}$, or by a threshold stress intensity factor range, ΔK_{th}, which are related to infinite fatigue life or non-propagating crack, respectively. A sampling of the literature showed that two approaches, namely the Murakami and the El-Haddad models are widely used to predict $\Delta\sigma_{th}$ for materials with defects or small cracks. Experimental data available in the literature indicate, that predictions by these models are found to be substantially load ratio dependent.

In order to improve predictions, a new approach based on Fatigue Endurance Diagram (FED) was proposed. This new approach gives an effective tool for correlating the observed dependence between $\Delta\sigma$ and ΔK as a function of initial defect size. Fatigue data from literature were used to validate the FED approach. A fairly good correlation of experimental data with normalized $\Delta\sigma/\Delta\sigma_{fl}$ and $\Delta K/\Delta K_{th}$ values was demonstrated for the published fatigue test data. Adjusting parameters were calculated for different test data sets. It was shown that the adjusting parameters are slightly increasing with ΔK_{th}.

Acknowledgments

This research has been supported by Hyundai Heavy Industries and performed at Western Michigan University during B-J Kim's research visit from February 2002 to January 2003.

References

[1] Hertzberg, R.W., *Deformation and Fracture Mechanics of Engineering Materials*, John Wiley and Sons, 1996.

[2] Tabernig, B., Powell, P., and Pippan, R., "Resistance Curves for the Threshold of Fatigue Crack Propagation in Particle Reinforced Aluminum Alloys", *Fatigue Crack Growth Thresholds, Endurance Limits, and Design, ASTM STP 1372,* 2000, pp.96–108.

[3] Taylor, D., *Fatigue Thresholds*, Butterworths, 1989.

[4] Lukas, P. and Kunz, L., "Effect of Mean Stress on Short Crack Threshold", *Short Fatigue Cracks*, Mechanical Engineering Publications, 1992, pp. 265–275.

[5] Forth, S.C., Newman, J.C. Jr and Forman, R.G., "On Generating Fatigue Crack Growth Thresholds", *International Journal of Fatigue*, Vol. 25, 2003, pp.9–15.

[6] Murakami, Y. and Endo, M., "Effects of Defects, Inclusions and Inhomogeneities on Fatigue Strength", *International Journal of Fatigue*, Vol. 16, 1994, pp.163–182.

[7] Kitagawa, H. and Takahashi, S., "Applicability of Fracture Mechanics to Very Small Cracks or the Cracks in the Early Stage", *Second International Conference on Mechanical Behavior of Materials*, ASM, Ohio, 1976, pp. 627–631.

[8] El Haddad, M.H., Topper, T.H., and Smith, K.N., "Prediction of Non Propagating Cracks", *Engineering Fracture Mechanics*, Vol. 11, 1979, pp. 573–584.

[9] Usami, A. and Shida, S., "Elastic-Plastic Analysis of the Fatigue Limit for a Material with Small Flaws", *Fatigue of Engineering Materials and Structures*, Vol.1, 1979, pp.471–481.

[10] Usami, S., "Short Crack Fatigue Properties and Component Life Estimation", *Current Research on Fatigue Cracks*, Elsevier Applied Science, 1987, pp. 119–147.

[11] Murakami, Y. et al, "Effect of Mean Stress on the Fatigue Strength of High-Strength Steels Containing Small Defects or Nonmetallic Inclusions", *Transactions of Japan Society of Mechanical Engineers*, Vol. 56, 1990, pp. 1074–1081.

[12] Kujawski, D., Ellyin, F.,"A Correlation of Threshold Stress and Stress Intensity Conditions for Fatigue Cracks", *Proc. 7th International Conference on the Strength of Metals and Alloys (ICSMA7),* Pergamon Press, 1985, pp. 1367-1372.

[13] Anderson, T.L., *Fracture Mechanics: Fundamentals and Applications*, CRC Press, 1995.

[14] Smith, R.A.,"On the Sort Crack Limitations of Fracture Mechanics", *International Journal of Fracture*, Vol. 13, 1977, pp. 657-665.

[15] Peters, J.O. et al, "On the application of the Kitagawa-Takahashi Diagram to Foreign-Object Damage and High-cycle Fatigue", *Engineering Fracture Mechanics*, Vol. 69, 2002, pp. 1425–1446.

[16] Murakami, Y., *Metal Fatigue: Effects of Small Defects and Nonmetallic Inclusions*, Yokendo, 1993.

[17] Tanaka, K., Nakai, Y., and Yamashita, M., "Fatigue Growth Threshold of Small Cracks", *International Journal of Fracture*, Vol. 17, 1981, pp.519–533.

[18] Ohuchida, H., Usami, S., and Nishioka, A., *Transactions of Japan Society of Mechanical Engineers*, Vol. 41, 1975, pp. 703–712.

SESSION 5B: EXPERIMENTAL METHODS I

Journal of ASTM International, March 2005, Vol. 2, No. 3
Paper ID JAI12041
Available online at www.astm.org

J. R. Donoso,[1] *J. Zahr,*[1] *and J. D. Landes*[2]

Construction of J-R Curves Using the Common and Concise Formats

ABSTRACT: A new method for constructing *J-R* curves is presented, which directly generates the J-Δa relation in a closed, analytical form. This new method makes use of the Concise Format and the Common Format, both developed by Donoso and Landes. These formats relate load, *P*, to ligament length, *b*, and displacement — in the elastic and in the plastic deformation ranges, respectively — and have proved useful in calculations in fracture mechanics. Key to the method is the postulate of a "*crack growth law*" —a power-law relation between crack extension, Δa, and plastic displacement — used to express J_{pl} in terms of material properties, size parameters, and crack extension, giving rise to a J_{pl}-Δa analytical expression, similar to the power law $J = C_1(\Delta a)^{C_2}$ suggested in ASTM Standard Test Method for Measurement of Fracture Toughness (E 1820). A few examples are included to show the use of the method, and comparisons are made with J-Δa curves calculated as per ASTM E 1820.

KEYWORDS: J-R curves, test evaluation, ductile fracture methodology, common format, concise format, fracture toughness

Nomenclature

a; a_j	Crack length; j-th value of crack length
a_o	Initial crack length
a_{Final}	Final measured value of crack length
B	Specimen thickness of a fracture toughness test specimen
b	Ligament size
b_o	Initial ligament size
b_f	Final ligament size
C	Coefficient of geometry function for plasticity
C^*	Coefficient of geometry function for elasticity
C_{el}	Elastic compliance
D	Parameter equal to $\Omega^* \cdot \sigma^*$
E; E'	Young's modulus in plane stress and plane strain, respectively
G	Geometry function
H	Hardening function
J	Total value of the J-integral
J_{el}	Elastic component of J
J_{pl}	Plastic component of J

Manuscript received 31 October 2003; accepted for publication 23 March 2004; published March 2005. Presented at ASTM Symposium on Fatigue and Fracture Mechanics: 34th Volume on 19–21 November 2003 in Tampa, FL; S.R. Daniewicz, J.C. Newman, Jr., and K-H. Schwalbe, Guest Editors.
[1] Materials Science Department and Mechanical Engineering Department, Universidad Técnica Federico Santa María, Valparaíso, Chile.
[2] MABE Department, The University of Tennessee, Knoxville, TN, USA.

K	Stress intensity factor
l_o ; l_1	Coefficient and exponent of Crack Growth Law for plastic displacement
L_o ; L_1	Coefficient and exponent of Crack Growth Law for elastic displacement
m	Exponent of geometry function in plasticity
n	Exponent of hardening function
P	Load
P_N	Normalized load
v_{el}	Elastic displacement
v_N	Normalized plastic displacement, equal to v_{pl}/W
v_{pl}	Plastic displacement
$v_{pl\,Final}$	Final measured value of plastic displacement
v_t	Total displacement (elastic + plastic)
W	Width of a fracture toughness test specimen
Δa	Crack extension
$\Delta a_{\mathrm{Final}}$	Final measured value of Crack Extension
Ω^*	Constraint factor
η	Coefficient used in the calculation of total J
η_{el}	Coefficient used in the calculation of elastic J
η_{pl}	Coefficient used in the calculation of plastic J
μ	Exponent of geometry function in elasticity
ν	Poisson's ratio
σ^*	Coefficient of the plasticity hardening function
σ_o	Yield stress

Introduction

The construction of a material *J-R* curve from a single specimen test is described in ASTM Standard Test Method for Measurement of Fracture Toughness (E 1820). The procedure involves measuring load and displacement during the test, and simultaneously evaluating crack extension by using the elastic compliance technique or other alternative techniques.

Landes et al. [1] developed a method to construct a *J-R* curve, which is extremely convenient when the standard crack length measurement techniques become difficult to apply. When using this method — called normalization — one or more calibration points are needed to evaluate the functional form that relates all three variables.

Working along the same line, Donoso and Landes developed the Common Format [2], and the Concise Format [3]. These formats relate load, P, to ligament length, b, and displacement — in the plastic and in the elastic deformation ranges, respectively — and have proved useful in calculations in fracture mechanics [4]. Based upon these two formats, an improved method for constructing *J-R* curves is presented here, which directly generates the J_{pl}-Δa relation in a closed form, similar to the power law $J = C_1(\Delta a)^{C_2}$ suggested in E 1820.

The method is based upon the analytical integration of P-v_{pl} curves at constant b — or constant crack length, a — by using the Common Format, therefore expressing J_{pl} in terms of v_{pl} and b. Next, a "*crack growth law*" — a power-law relation between crack extension, Δa, and plastic displacement — is used to express J_{pl} in terms of material properties, size parameters, and crack extension, giving rise to a J_{pl}-Δa analytical expression. Only one calibration point is required: that for final load, P_f; total displacement, v_f, and the associated crack length, a_f, at the end of the test. The elastic component is obtained by means of the Concise Format, and it is subtracted from the total displacement. Thus, the coefficient of the crack growth law is obtained from the calibration data ($v_{f,pl}$; a_f), without the need for compliance measurements. The crack growth law exponent, on the other hand, is obtained as the quantity that gives the best fit when reconstructing the actual P-v curve, by using both the Concise and the Common Formats. These formats will be shown next. Although these formats have an extended use for any specimen geometry, all the examples shown correspond to C(T) specimens.

The Common Format Equation, CFE

The Common Format Equation, henceforth CFE, proposed by Donoso and Landes [2] relates the applied load P with two *state* variables representing the deformation of a cracked component: v_{pl}/W, the plastic component of the load-line displacement, normalized by the width W, and b/W, the normalized ligament size. The CFE also includes a term that denotes the constraint, Ω^*, and it is written as:

$$P = \Omega^* \cdot G(b/W) \cdot H(v_{pl}/W) \tag{1}$$

In Eq 1, $G(b/W)$ is a function that depends on the geometry of the specimen, and $H(v_{pl}/W)$ is a hardening function and a material property. Both the geometry and the hardening functions are written as power law expressions of normalized ligament and plastic displacement:

$$G(b/W) = B \cdot C \cdot W \cdot (b/W)^m \tag{2}$$

$$H(v_{pl}/W) = \sigma^* (v_{pl}/W)^{1/n} \tag{3}$$

where B is the specimen thickness, C and m are the G function parameters, and σ^* and n are material properties obtained from a material stress-strain curve [2].

The values of the constraint factor, Ω^*, go from 0.2678 for plane stress to 0.3638 for plane strain. In between, Ω^* may be evaluated by a limit load analysis from a P-v_{pl} plot, based on the following equations:

$$P_{N0} = \frac{P_0}{G(b/W)} \tag{4}$$

$$\Omega^* = \frac{P_{N0}}{\sigma_0} \tag{5}$$

where σ_o is the material yield stress, P_o is the yield load evaluated at $v_{pl}/W = 0.002$, and P_{No} is the yield load normalized by the geometry function, using the initial ligament.

Should the stress-strain data not be available to get the values of σ^* and n, the specimen load-displacement curve may be conveniently used to couple the terms σ^* and Ω^* in one parameter, D:

$$D = \Omega^* \cdot \sigma^* \tag{6}$$

The parameters D and n may be determined by adjusting normalized load and normalized displacement data to a power law relation, in which the coefficient is D and the exponent is $1/n$. Such a relation is obtained by combining Eqs 1 and 3:

$$\frac{P}{G(b/W)} = \Omega^* \cdot H(v_{pl}/W) = \Omega^* \sigma^* (v_{pl}/W)^{1/n} \tag{7}$$

The fit must be performed in a restricted displacement range, from the initial data point through a few percent of normalized plastic displacement. In the model to be described later, it is equally valid to introduce as inputs D and n, or Ω^*, σ^*, and n.

The CFE, through Eqs 1–3 or Eq 7, was originally conceived to yield a mathematical relation to describe the load-displacement behavior for a blunt-notch specimen, or a specimen with a stationary crack (constant b). However, as will be shown in this paper, it may also describe the load-displacement behavior of a specimen with a growing crack, provided an adequate relation between v_{pl} and b is established.

Modification of the CFE by a Crack Growth Law

Because the load in the CFE depends on both the normalized displacement and the normalized ligament size, the inclusion of crack growth requires a relationship between these two variables. This information is usually not known in advance and only gets into play after the crack length is measured concurrently with a test. One example is crack extension measurements by using the elastic compliance technique [5], or other alternative, similar techniques [6,7].

It is always possible to assume a crack growth behavior that matches experimental evidence. Several authors have either proposed [8] or hinted at [9] crack growth laws.

Based upon these ideas, a two-parameter power law type of crack growth that relates the change in crack length, Δa, with normalized plastic displacement, v_{pl}/W, is proposed here, i.e.,

$$\frac{\Delta a}{W} = l_0 \left(\frac{v_{pl}}{W} \right)^{l_1} \tag{8}$$

Since the ligament decreases with increasing crack length, then the normalized ligament size becomes:

$$\frac{b}{W} = \frac{b_0}{W} - \frac{\Delta a}{W} = \frac{b_0}{W} - l_0 \left(\frac{v_{pl}}{W} \right)^{l_1} \tag{9}$$

where b_o/W is the initial normalized ligament size, and l_o and l_1 are the adjustable parameters of the crack growth law. From Eq 9 it may be clearly seen that the term b/W, for an experiment in which there is crack growth, depends on the parameters l_o and l_1, and so will the function G. If both of these parameters are known, then P in the CFE, Eq 7, will change due to changes in b/W and in v_{pl}/W. Most likely, however, these adjustable parameters are not known in advance.

Evaluation of the crack growth law parameters l_o and l_1 of Eqs 8 or 9 requires experimental data. In a fracture toughness experiment, both the initial and the final crack length are obtained from a direct measurement on the fracture surface once the specimen is broken in two. The final crack length, a_f, corresponds with the final total displacement in the test, v_f. Therefore, the experimental datum, $(v_{pl}/W)_{\text{final}} \leftrightarrow (\Delta a/W)_{\text{final}}$, is known, after subtracting the elastic portion of the displacement with the knowledge of the final crack length and the corresponding elastic compliance. Thus, one of the two parameters of Eq 8 becomes fixed in terms of the other, there being actually only one parameter to determine. If we choose to leave l_o in terms of l_1, then:

$$l_0 = \left(\frac{\Delta a_{Final}}{W}\right)\left(\frac{v_{pl\_Final}}{W}\right)^{-l_1} \tag{10}$$

On introducing Eq 9 for the normalized ligament in the geometry function, Eq 2, and bearing in mind Eq 10, the CFE will become a function for the load P in terms only of v_{pl}/W as the independent variable, having thus l_1 as the only adjustable parameter:

$$P = DBCW\left(\frac{b_o}{W} - l_o\left(\frac{v_{pl}}{W}\right)^{l_1}\right)^m \left(\frac{v_{pl}}{W}\right)^{1/n} \tag{11}$$

From Eqs 10 and 11 stems the following modified CFE:

$$P = DBCW\left(\frac{b_o}{W} - \frac{\Delta a_{Final}}{W}\left(\frac{v_{pl}}{v_{pl\_Final}}\right)^{l_1}\right)^m \left(\frac{v_{pl}}{W}\right)^{1/n} \tag{12}$$

Equations 11 or 12 are alternative ways of mathematically describing the load-plastic displacement behavior under a crack growth situation. The value of the exponent l_1 of the crack growth law may be looked at as that which allows the best fit for both the P-v and a-v experimental curves. This fit may be done by using the unloading compliance data to generate the a- $v_{plastic}$ curve as given by Eq 8. The elastic component of the displacement is obtained with the following relations:

$$v_{el} = C_{el} \cdot P \tag{13}$$

and (Concise Format)

$$C_{el} = \left(\frac{A}{BE'}\right)\left(\frac{b}{W}\right)^{-\mu} \tag{14}$$

The Concise Format parameters for C(T) are A = 7.6055; μ = 2.283 [3], and for plane strain Young's modulus is $E' = E/(1-\upsilon^2)$.

If there are no unloading compliance data available — or other type of crack advance measurement — then the theoretical P-v_{total} curve may be obtained by using both formats concurrently: the Concise Format (elastic displacement) and the Common Format (plastic displacement). Then l_1 will be obtained by a fit to the experimental P-v_{total} curve. This second option, used throughout this work, does not require crack advance measurements, since the compliance is calculated with Eq 14, being thus intrinsically included in the total displacement value:

$$v_{total} = v_{el} + v_{pl} \tag{15}$$

This would clearly become an advantage, helping to simplify the experimental procedures, especially those related to the unloading compliance. Equations 12–15 not only provide with a representation in the P-v_{total} plane, but also pave the way to the total J, with the aid of the crack growth law, Eq 8.

As for the l_l parameter, it has not yet been related to material properties, nor to the specimen geometry. Although it is still premature to give a safe value, our results place it between 1.75 and 2.25, with an average of 2.0.

Examples of P-v Fit with Crack Growth

Figure 1 shows an example of a fit to *P-v* data under a crack growth situation, in which crack advance was evaluated by the unloading compliance method [5]. The experimental data belong to an A533 steel specimen, the dimensions of which are shown in Table 1.

Also shown in Table 1 are the parameters of the fit, l_l and n of Eq 12. The model curve obtained with the two formats (C&C) is shown for comparison. The two curves are strikingly similar; the maximum experimentally measured load is overestimated by the C&C curve by only 1.2 %.

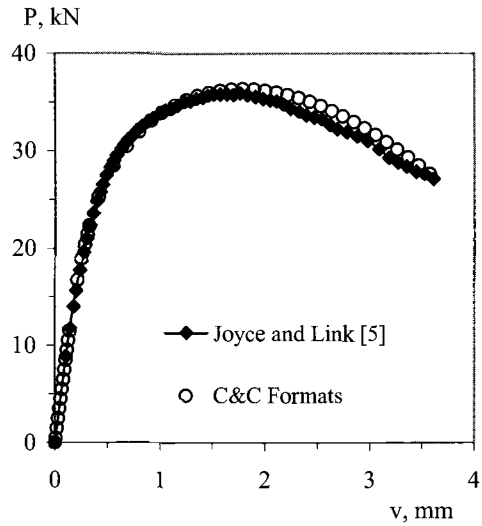

FIG. 1—*Experimental and format model fit (C&C) P-v data for A533 [5].*

TABLE 1—*C(T) specimen dimensions and parameters of the CFE with crack growth.*

Parameter	A533 (Joyce and Link, [5])	A508 (Landes, [10])	A533 (Landes, [10])
W, mm	50	50.8	203
B, mm	25	25.4	2.54
B_N, mm	20	20.32	2.54
a_o, mm	30.3	26.19	101.6
a_f, mm	34.25	33.12	130.5
n	5.65	5.75	8.9
l_l	2.0	1,75	1.75
Data available	P-v; a-v; J-Δa	P-v; a-v; J-Δa	P-v; a-v

Figure 2 shows the a-v data obtained by Joyce and Link [5], together with the C&C fit. The a-v_{pl} behavior has an exponent $l_l = 2.0$. The match between the two sets of data is amazing. In this case the a-v fit was produced *after* doing the fit to the P-v experimental data. This is an important point to make, since the method should be really helpful when there are no a-v data available from the fracture test, only initial and final crack lengths.

The second example is an A508 1T C(T) specimen. Like Joyce and Link's specimen, it has side-grooves. Figure 3 shows the P-v curves, and Figure 4 shows the Δa-v behavior. The CFE parameters are summarized in [10].

The third example is that of a A533 steel C(T) specimen. The planar dimensions are those of a 4T specimen with a thickness B of 2.54 mm (Figs. 5 and 6). Given the ratio of the specimen thickness to its planar dimensions, the situation will be close to plane stress [10]. Once again, the match between the experimental and the C&C data is good.

J Formulations

The J integral, originally proponed by Rice [11], has come a long way as a fracture parameter. Several interpretations and uses have been done of J; the most often employed relations are:

$$J = \frac{\eta}{bB}\left[Area \;\; under \;\; P - v \;\; curve \right] \tag{16}$$

$$J = \frac{\eta_{el}}{bB}\int P dv_{el} + \frac{\eta_{pl}}{bB}\int P dv_{pl} \tag{17}$$

$$J = J_{el} + J_{pl} \tag{18}$$

$$J = \frac{K^2}{E'} + J_{pl} \tag{19}$$

J is the energy introduced into the specimen, divided by the remaining ligament area. When this energy is split into its elastic and plastic components, so is the parameter J into its components, Eq 18. The Unifying Principle [3] allows one to obtain J as one single term, Eq 16, by showing that both η factors — elastic and plastic — are very similar, and in practical terms, equal. In what follows, the relations for J will be obtained separately, since both formats used here have different ways of relating the displacement components — elastic and plastic — to the load. Therefore, even though the total value of J may be obtained with the Unifying Principle relations [3]; J for a crack growth situation will be worked out from its separate components, J_{el} and J_{pl}, and added up again to produce the J-Δa curve. Alternatively, the elastic J may be obtained as K^2/E', this being the first term of Eq 19. Using the latter form for J_{el} does not affect the approach developed for the calculation of J, since the changes in crack length are nonetheless "absorbed" by K through the elastic compliance.

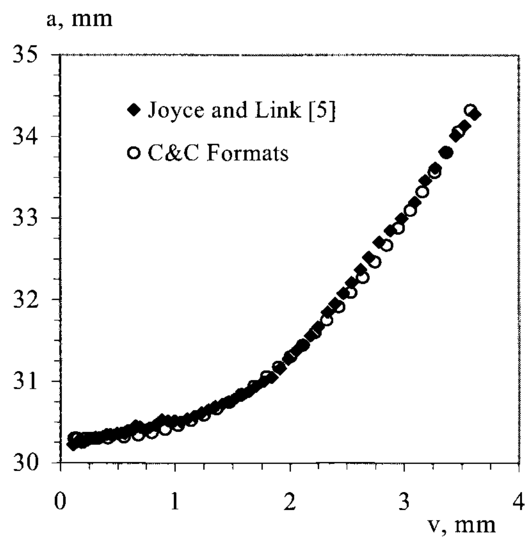

FIG. 2—*Experimental and format model fit (C&C) a-v data for A533 [5].*

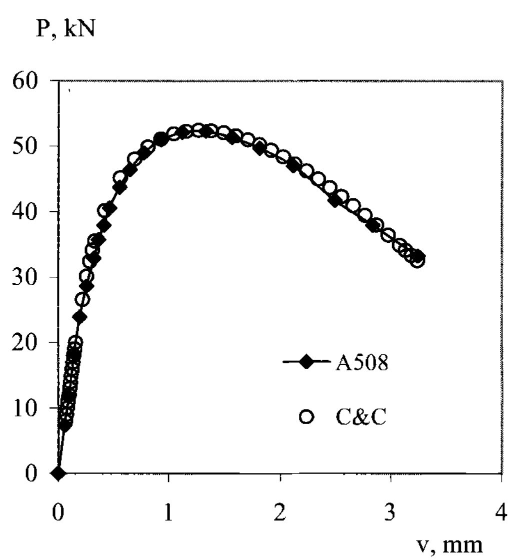

FIG. 3—*Experimental and format model fit (C&C) P-v data for A508 [10].*

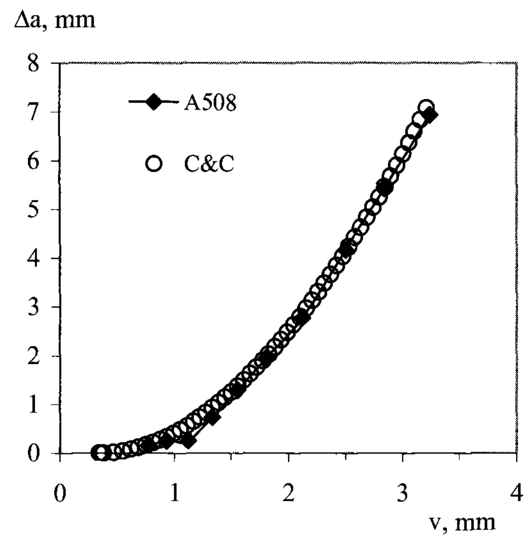

FIG. 4—*Experimental and format model fit (C&C) a-v data for A508 [10].*

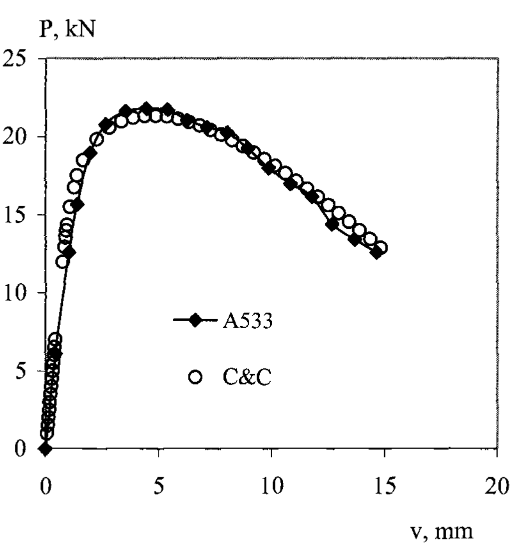

FIG. 5—*Experimental and format model fit (C&C) P-v data for A533 [10].*

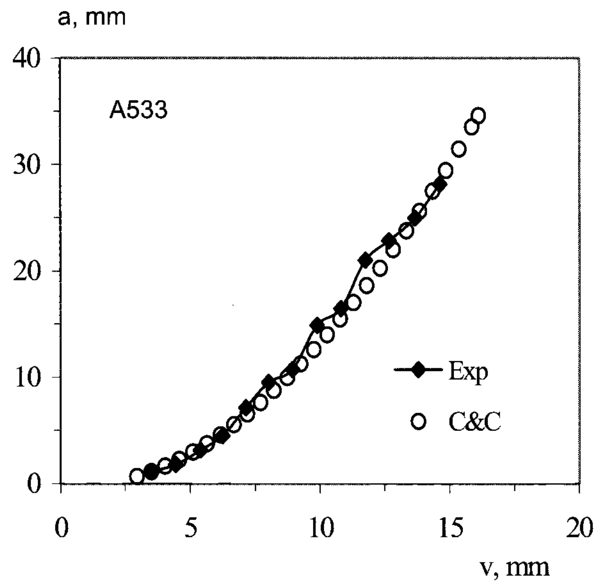

FIG. 6—*Experimental and format model fit (C&C) a-v data for A533 [10].*

An Analytical Model for J Plastic

Equations 16 and 17 are based upon the evaluation of area under a load-displacement curve, not including crack growth during the test. If this is the case, the CFE provides an adequate description of the P-$v_{plastic}$ behavior, summarized in Eq 20:

$$P = \Omega^* \sigma^* BCW\left(\frac{b}{W}\right)^m \left(\frac{v_{pl}}{W}\right)^{1/n} \tag{20}$$

If one considers a generic state (i) at any instant of a load-displacement test, then the value of the plastic component of J may be expressed as:

$$J_{pl(i)} = \frac{\eta_i}{Bb_i} \int_0^{v_{pl(i)}} P\, d(v_{pl}) \tag{21}$$

Substituting P of Eq 20 into Eq 21, the integration may be carried out, considering that: $\eta_{pl} = m$ and $b/W = b_{(i)}/W$ = constant. As shown earlier by Ernst, Paris, and Landes, the integration must be carried out at constant ligament [12].

Upon integrating and collecting terms, one gets:

$$J_{pl(i)} = m\Omega^* \sigma^* CW\left(\frac{b_{(i)}}{W}\right)^{m-1} \frac{n}{n+1}\left(\frac{v_{pl(i)}}{W}\right)^{\left(\frac{1}{n}+1\right)} \tag{22}$$

From Eq 22 one may directly obtain CTOD, as proposed earlier by Wilson and Landes [13]. The power-law-type of crack growth law is now considered, Eq 8, written in terms of Δa:

$$\frac{v_{pl(i)}}{W}=\left(\frac{1}{l_0}\frac{\Delta a_{(i)}}{W}\right)^{1/l_1} \tag{23}$$

and

$$\frac{b_{(i)}}{W}=\frac{b_0}{W}-\frac{\Delta a_{(i)}}{W} \tag{24}$$

Substituting Eqs 23 and 24 into Eq 22 gives $J_{pl(i)}$ directly in terms of crack advance, Δa, and various coefficients. The sub-index (i) may be dropped now, to yield:

$$J_{pl}=m\Omega^*\sigma^*CW\frac{n}{n+1}\left(\frac{b_0}{W}\right)^{m-1}\left(1-\frac{\Delta a}{b_0}\right)^{m-1}\left(\frac{1}{l_0}\frac{\Delta a}{W}\right)^{\left(\frac{1}{nl_1}+\frac{1}{l_1}\right)} \tag{25}$$

The Concise Format

According to the Concise Format [3], it is possible to represent the relation between P and v_{el} in a similar way to the CFE for P-v_{pl}, by the following expression:

$$P=BC^*W\left(\frac{b}{W}\right)^{\mu}E'\left(\frac{v_{el}}{W}\right) \tag{26}$$

An Analytical Model for J Elastic

Following a methodology similar to that employed for J_{pl}, the corresponding relation for J_{el} will be derived from Eq 26:

$$J_{el}=\frac{K^2}{E'} \tag{27}$$

Further, from the Unifying Principle [3], J_{el} may be expressed as:

$$\frac{K^2}{E'}=\frac{1}{2}\mu\frac{P\,v_{el}}{Bb} \tag{28}$$

Substituting Eq 26 into Eq 28, keeping in mind that $E'=E/(1-\nu^2)$, and collecting terms, we obtain:

$$J_{el}=\frac{1}{2}\mu\frac{E}{\left(1-\nu^2\right)}C^*W\left(\frac{b}{W}\right)^{(\mu-1)}\left(\frac{v_{el}}{W}\right)^2 \tag{29}$$

Much like the case of J_{pl}, a power-law-type of crack growth law may be considered, only expressed in terms of the elastic component of the displacement:

$$\frac{\Delta a}{W}=L_0\left(\frac{v_{el}}{W}\right)^{L_1} \tag{30}$$

In terms of crack growth:

$$\frac{v_{el}}{W}=\left(\frac{1}{L_0}\frac{\Delta a}{W}\right)^{(1/L_1)} \tag{31}$$

Making the appropriate substitutions, one gets, finally:

$$J_{el} = \frac{1}{2}\mu \frac{1}{1-\nu^2} EC^* W\left(\frac{b_0}{W}\right)^{(\mu-1)}\left(1-\frac{\Delta a}{b_0}\right)^{(\mu-1)}\left(\frac{1}{L_0}\frac{\Delta a}{W}\right)^{2/L_1} \tag{32}$$

The structure of Eq 32 is the same as that for J_{pl}, if one looks at the following analogies:
$\Omega^* \sim 1/(1-\nu^2)$; $\sigma^* \sim E$; $n/(n+1) \sim 1/2$ (for elastic behavior, $n = 1$)

Summary of Relations for J

$$J_{total} = J_{el} + J_{pl} \tag{33}$$

$$J_{el} = \frac{1}{2}\mu \frac{1}{1-\nu^2} EC^* W\left(\frac{b_0}{W}\right)^{(\mu-1)}\left(1-\frac{\Delta a}{b_0}\right)^{(\mu-1)}\left(\frac{1}{L_0}\frac{\Delta a}{W}\right)^{2/L_1} \tag{34}$$

$$J_{pl} = m\Omega^*\sigma^* C W\left(\frac{n}{n+1}\right)\left(\frac{b_0}{W}\right)^{(m-1)}\left(1-\frac{\Delta a}{b_0}\right)^{(m-1)}\left(\frac{1}{l_0}\frac{\Delta a}{W}\right)^{\frac{1}{l_1}\left(1+\frac{1}{n}\right)} \tag{35}$$

If the assumption $\eta_{el} = \eta_{pl} = m = \mu$ is made [3], then:

$$J_{total} = mW\left(\frac{b_0}{W}\right)^{(m-1)}\left(1-\frac{\Delta a}{b_0}\right)^{(m-1)}\left\{\frac{1}{2}E'C^*\left(\frac{1}{L_0}\frac{\Delta a}{W}\right)^{2/L_1} + \Omega^*\sigma^* C\left(\frac{n}{n+1}\right)\left(\frac{1}{l_0}\frac{\Delta a}{W}\right)^{\frac{1}{l_1}\left(1+\frac{1}{n}\right)}\right\} \tag{36}$$

This form will be termed "C&C Formats," to denote that it was obtained by using both the Common and the Concise Formats. However, since the important issue here is the modeling of the plastic component — as well as the sake of simplicity — all calculations were carried out by using the following, equivalent expression:

$$J_{total} = \frac{K^2}{E'} + m\Omega^*\sigma^* CW\left(\frac{n}{n+1}\right)\left(\frac{b_0}{W}\right)^{(m-1)}\left(1-\frac{\Delta a}{b_0}\right)^{(m-1)}\left(\frac{1}{l_0}\frac{\Delta a}{W}\right)^{\frac{1}{l_1}\left(1+\frac{1}{n}\right)} \tag{37}$$

J-R Curve Results

The two *J-R* curves that follow were constructed using Eq 37. They are compared with available *J-R* curves obtained by using the corresponding ASTM Standard at the time the data were published. In the following two figures, the values of J_{total} obtained with Eq 37 have also been termed "C&C Formats." Figure 7 shows the comparison between Joyce and Link's *J-R* curve for A533 [5] and that given by Eq 37. There is a very good correspondence between the two curves, although the experimental set of data displays a "tale" upwards: in this case the C&C Formats curve underestimates the experimental one by about 7 % at the final Δa point.

Figure 8 compares the results for the A508 specimen *J-R* curve with that given by the C&C Formats. A very good match between the two curves may be seen up to the maximum Δa value. Although the A508 curve has fewer experimental points than the C&C Formats model curve — compared with the large quantity of experimental points of Joyce's A533 specimen shown in Fig. 7 — the C&C Formats points agree with all of the experimental points but two.

There is no experimental *J-R* curve available for the Landes A533 specimen. However, since both the C&C model *P-v* and *Δa-v* curves shown previously (Figs. 5 and 6) agree well with the specimen experimental curves, there is a strong feeling that this new C&C approach ought to produce a *J-R* curve which is representative of both the material fracture toughness and the specimen constraint.

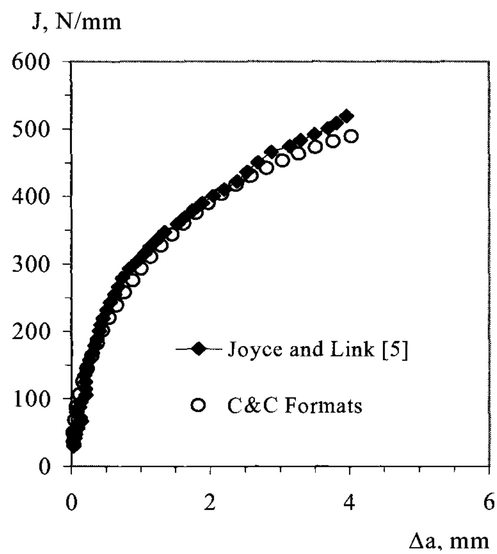

FIG. 7—*Experimental and format model fit (C&C) J-Δa data for A533 [5].*

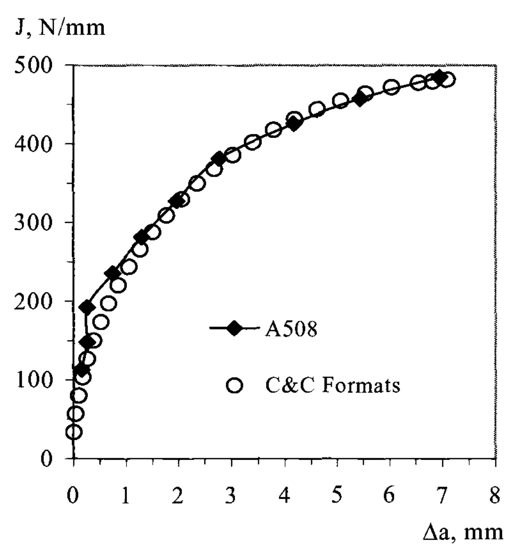

FIG. 8—*Experimental and format model fit (C&C) J-Δa data for A508 [10].*

Summary and Concluding Remarks

A new way to get the *J-R* curve directly from *P-v* data has been presented that takes away the need for a full crack advance measurement concurrent with the test. In this novel method, all that is needed are the initial and final crack length values. Only one calibration point is required: that for the load, P_f, the total displacement, v_f, and the final crack length, a_f, at the end of the test. The method uses the Common Format and the Concise Format to analyze the data. The Appendix at the end of the paper describes, in a step-by-step manner, the methodology used to obtain the J-Δa curve according to this new proposal.

The method rests upon the introduction of a "crack growth law," i.e., a relationship between crack advance, Δa, and the plastic component of the displacement, v_{pl}. The first step of the method is to reproduce the actual *P-v* curve with crack growth. To this effect, the Common Format, the crack growth law, and the Concise Format give rise to the so-called "C&C" *P-v* curve. This analytical expression has only one variable parameter: l_l, the exponent of the crack growth law, which varies between 1.75 and 2.25. The chosen, final value of l_l is that which gives the best C&C *P-v* fit to the actual *P-v* data.

The "C&C" *P-v* curve is the analytical description of the load versus total displacement behavior when there is crack growth in a fracture toughness test. It is important to stress the relevant issue behind the C&C analysis: from now on, there is a way to model the instability behavior of the specimen, i.e., the fact that, when there is crack advance, the load rises to a maximum, then falls because the specimen ligament has decreased. The Common Format allows one to obtain the P-v_{pl} expression, whereas the elastic component of the displacement, v_{el}, and its dependence on the load P, is obtained with the use of the Concise Format. The total displacement, v, will be then the sum of both components, v_{el} and v_{pl}.

The expression for J_{pl} is obtained by the analytical integration of P-v_{pl} curves at constant ligament size, b, by using the Common Format. The crack growth law is then inserted into the said relationship for J_{pl}, giving rise to a straightforward analytical expression for J_{pl} in terms of crack advance, Δa, and various material, geometry, and constraint parameters. The elastic component of J, J_{el}, is obtained by means of the Concise Format; thus the total J is obtained as the sum of the elastic and plastic contributions, and has been termed here "C&C Formats."

The examples presented in this paper show that the method works quite well in reproducing the *P-v*, *a-v*, and J-Δa curves, and may be compared with existing methods as to reproducibility, accuracy, and speed of calculation. This new methodology should be of great help in evaluating the *J-R* curve under circumstances in which the only inputs are the *P-v* curve plus the initial and final values of crack length. This could very well be the case when either the concurrent measurement of crack advance is technically unfeasible, or when it becomes prohibited by cost.

Acknowledgments

This work is partially based on Jorge Zahr's Engineering Thesis at Universidad Santa Maria, and was financed by projects Fondecyt-CHILE 1010151 and UTFSM-DGIP 210321. Fondecyt Travel Grant 7010151 for Professor J.D. Landes is also gratefully acknowledged.

References

[1] Landes, J. D., Zhou, Z., Lee, K., and Herrera, R., "Normalization Method for Developing J–R Curves with the LMN Function," *Journal of Testing and Evaluation*, Vol. 19, No. 4, July 1991, ASTM International, West Conshohocken, PA, pp. 305–311.

[2] Donoso, J. R. and Landes, J. D., "Common Format for Developing Calibration Curves in Elastic–Plastic Fracture Mechanics," *Engineering Fracture Mechanics*, Vol. 47, No. 5, 1994, pp. 619–628.

[3] Donoso, J. R. and Landes, J. D., "A Unifying Principle for Evaluating Fracture Toughness in the Elastic and Plastic Regimes with Two–Dimensional Fracture Specimens," *Fatigue and Fracture Mechanics, 30th Volume, ASTM STP 1360*, P. C. Paris and K. L. Jerina, Eds., ASTM International, West Conshohocken, PA, 2000, pp. 34–50.

[4] Donoso, J. R. and Landes, J. D., "Advantages of the Concise K and Compliance Formats in Fracture Mechanics Calculations," *Fatigue and Fracture Mechanics*, 32nd Volume, ASTM STP 1406, R. Chona, Ed., ASTM International, West Conshohocken, PA, 2001, pp. 261–278.

[5] Joyce, J. A., and Link, R. E., "Effects of Tensile Loading on Upper Shelf Fracture Toughness," Report NUREG/CR–6051, March 1994.

[6] Chen, X., Albrecht, P., Wright, W., and Joyce, J. A., "Improved Load Ratio Method for Predicting Crack Length," *Special Applications and Advanced Techniques for Crack Size Determinations, ASTM STP 1251*, J. J. Ruschau and J. K. Donald, Eds., ASTM International, West Conshohocken, PA, 1995, pp. 83–103.

[7] Joyce, J. A., Albrecht, P., Tjiang, H. C., and Wright, W. J., "Compliance Ratio Method of Estimating Crack Length in Dynamic Fracture Toughness Tests," *Fatigue and Fracture Mechanics, 32nd Volume, ASTM STP 1406*, R. Chona, Ed., ASTM International, West Conshohocken, PA, 2001, pp. 139–157.

[8] Gioelli, P. C. and Landes, J. D., "Normalization Procedures for Enhancing the Calculation of J–R Curves," *Presented at the 32nd National Symposium on Fatigue and Fracture Mechanics*, West Conshohocken, PA, June 14–16, 2000.

[9] Yan, W–Y., Shan, G. X., Kolednik, O., and Fischer, F. D., "A Numerical Simulation of the Crack Growth in a Smooth CT Specimen," Key Engineering Materials, 145–149, 1998, pp. 179–184.

[10] Donoso, J. R. and Landes, J. D., "The Role of Constraint on the Calibration Functions for the Prediction of Ductile Fracture Behavior in Structural Components," *International Journal of Fracture*, Vol. 63, 1993, pp. 275–285.

[11] Rice, J. R., "A Path Independent Integral and the Approximate Analysis of Strain Concentrations by Notches and Cracks," *Journal of Applied Mechanics*, Vol. 35, 1968, pp. 379–386.

[12] Ernst, H. A, Paris, P. C., and Landes, J. D., "Estimations on J–Integral and Tearing Modulus *T* from a Single Specimen Test Record," *Fracture Mechanics, 13th Conference, ASTM STP 743*, Richard Roberts, Ed., ASTM International, West Conshohocken, PA, 1981, pp. 476–502.

[13] Wilson, C. D and Landes, J. D., "Inconsistencies Between CTOD and J Calculations," *Journal of Testing and Evaluation*, Vol. 22, No. 6, November 1994, ASTM International, West Conshohocken, PA, pp. 509–515.

Appendix: Procedure for the Construction of the P-v Curve with Crack Growth and the J-R Curve Based on the C&C Formats

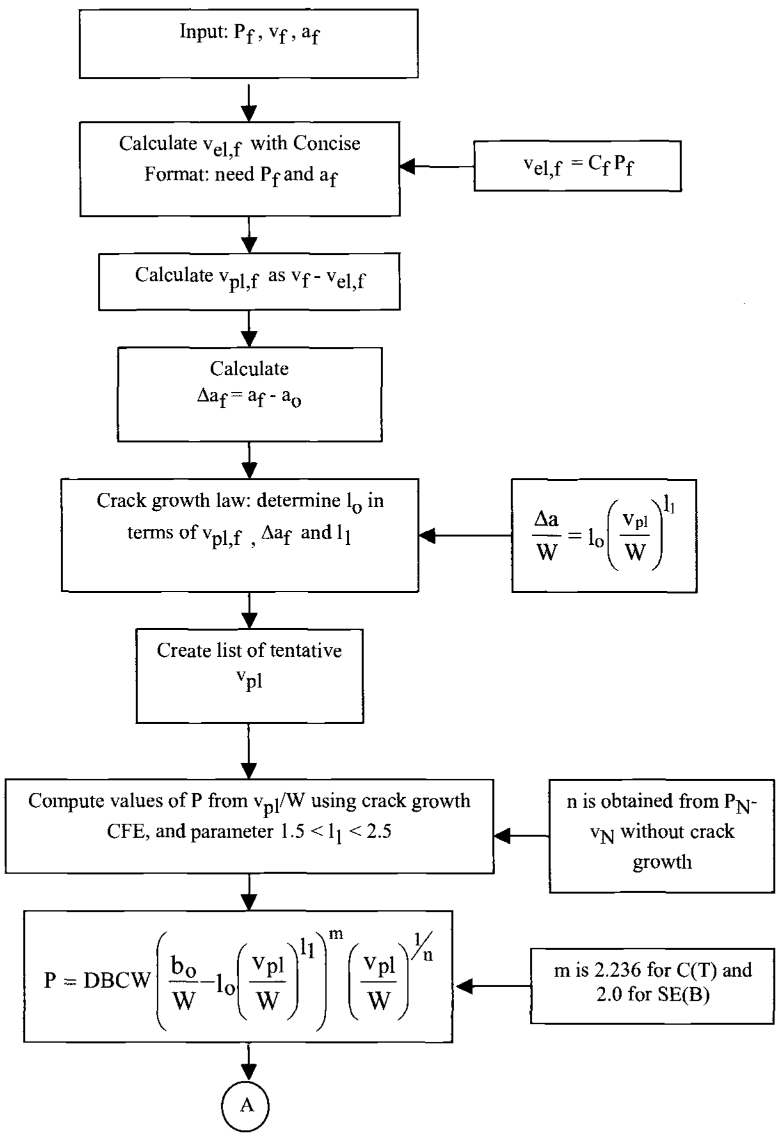

A

Best value of l_1 is that which gives best match between experimental curve and model P-v curve with crack growth

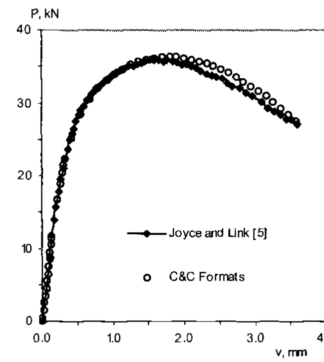

Crack growth law may now be written in the form $a = a(v_{pl})$

The elastic displacement = f(a) is computed from the Concise Format or elastic compliance

Crack growth may be stated as $a = a(v_t)$ and behavior compared to unloading compliance (or other) measurements

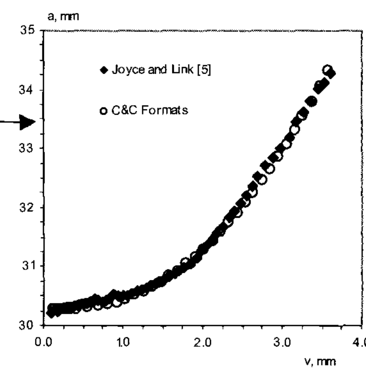

J_{pl} may be calculated with formula as a function of Δa. On the other hand, J_{el} may be calculated as K^2/E'

$$J_{pl} = m\Omega^* \sigma^* C W \left(\frac{n}{n+1}\right)\left(\frac{b_0}{W}\right)^{(m-1)}\left(1-\frac{\Delta a}{b_0}\right)^{(m-1)}\left(\frac{1}{l_0}\frac{\Delta a}{W}\right)^{\frac{1}{l_1}\left(1+\frac{1}{n}\right)}$$

Ready to generate J-R curve from C&C Formats, and compare with experimental, ASTM curve

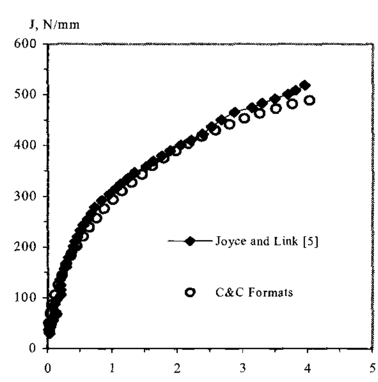

Journal of ASTM International, April 2005, Vol. 2, No. 4
Paper ID JAI12005
Available online at www.astm.org

Douglas M. Bahr[1] *and W. Steven Johnson*[1]

Temperature Dependent Fracture Toughness of a Single Crystal Nickel Superalloy

ABSTRACT: An important application of nickel base superalloys is in the industrial gas turbine (IGT) industry, where the high temperature capabilities of these alloys are exploited. Extensive testing has focused on the tensile and fatigue properties of single crystal versions of these alloys. The single crystals are utilized in the hottest parts of the turbine, where a detailed knowledge of material behavior is critical to design and life assessment. However, studies on the effects of temperature on fracture toughness have largely been absent in both past and present literature. Therefore, the goal of this research is to characterize the fracture toughness properties of a second-generation single crystal nickel superalloy at elevated temperatures. The experimental methods follow ASTM guidelines, as does the analysis for the elastic (K) and plastic (J integral) deformation. The toughness values were invalid for plain strain fracture toughness, but this should be expected from a structural material. In spite of this fact, both the K- and J-based analyses reveal consistent trends. Increased plasticity at elevated temperatures results in an overall increase in toughness as temperature increases. Unusual cases with inclined pre-cracks and microstructural defects did not technically yield valid results, although they were consistent with the nominal cases. Overall, the results indicate that the toughness of single crystal nickel alloys is actually quite high. Thus, the lack of work in this subject is understandable. However, it would seem that any design and lifing work would benefit from an understanding of such a fundamental property.

KEYWORDS: plasticity, elevated temperature, angled pre-crack

When examining current literature for studies on fracture toughness of single crystal superalloys, one theme is prevalent: the lack of any extensive research on the subject. Noted by Walston [1] in 1991 and again by Yue [2] in 1997, there seems to be little attention paid to either experimental toughness studies or predicting such failures. The cause of this trend is tied directly to the applications of single crystal superalloys. Viswanathan [3] points out that turbine blades are primarily subject to high cycle fatigue, thus the dominant concern for stress intensity is the threshold value for crack growth in cyclic loading. The rapid fractures associated with toughness failures are less of a concern, due to the loading conditions and the relatively high values of toughness for nickel base superalloys [4] (at least those that have been reported).

A study by Anton [5] examined Charpy impact results in a single crystal alloy at temperatures up to 1090°C (1994°F). The increase of fracture energy with increased temperature corresponded to the ductile rupture that occurs under these conditions. Conversely, the fracture loads decrease as temperature increases. The "zig-zag" lines observed in some tensile failures were also evident in this study as slip occurred on multiple (111) planes.

An effort by Yue to model fracture behavior based on strain energy density [2] represents one of the few efforts at modeling based on the results of toughness tests. This study recorded the maximum loads and crack mouth displacements for a series of toughness tests on the single

Manuscript received 28 January 2004; accepted for publication 16 June 2004; published April 2005. Presented at ASTM Symposium on Fatigue and Fracture Mechanics: 34th Volume on 19–21 November 2003 in Tampa, FL; S.R. Daniewicz, J.C. Newman, Jr., and K-H. Schwalbe, Guest Editors.
[1] Georgia Institute of Technology, School of Materials Science and Engineering, 771 Ferst Drive NW, Atlanta, GA 30332.

crystal alloy DD3. Comparing the displacements and normal stresses obtained experimentally and via 3-D finite element analysis, the results indicated good agreement for both values. While one of the few efforts of its kind, its use of the strain energy density provided accurate results and perhaps an impetus for future research.

Calculations of actual K_{IC} and J_{IC} toughness values for a nickel base superalloy tend to be primarily related to environmental concerns, including hydrogen embrittlement and neutron irradiation. Walston [1] and Moody [6] both noted a significant drop in toughness results upon exposure to hydrogen for conventional nickel base superalloys and single crystals. Specimens exposed to varying levels of hydrogen could expect drops in toughness of up to 50 % from the unexposed values of 90–123 MPa$\sqrt{m}$ (82–112 ksi$\sqrt{in}$). While the results of such studies typically report K_q values (the brittle nature of superalloys rarely allowing valid K_{IC} results), the use of short rod toughness tests indicates that these results are close to the true toughnesses [7]. The importance of hydrogen embrittlement is of concern to the aerospace industry, specifically in hydrogen fueled engines such as the Space Shuttle Main Engine. Another environmental concern for nickel base superalloys is neutron irradiation, which occurs in nuclear applications. It has been documented that exposure to radiation can greatly enhance the sensitivity of superalloys to flaws [4]. Reported critical values of J (J_C) range from 368–854 kPa·m (2100–4800 psi·in.) at room temperature, with conflicting results on the effects of temperature. However, in all cases, radiation exposure decreased toughness.

In both of the above cases of environmental degradation (at least in the conventional alloys), the decreased toughness seemed to be tied to changes in the mode of slip. The unexposed specimens exhibited homogeneous slip, marked by microcoalescence of voids. However, after exposure (to either hydrogen or radiation), the slip became heterogeneous in nature with channel fracture and slip band failure evident.

Another facet of the limited current literature is tied to the study of single crystal intermetallics, including nickel-base [8] and titanium-base [9]. While these alloys are of great interest to the aerospace industry, where their low densities are valuable to the thrust to weight ratio, it is their limited toughness that has restricted their use in such applications. Thus, there has been considerably more effort made to examine the properties of these alloys than those of the superalloys.

Material

The alloy chosen for this research was Rene N5, a second-generation single crystal superalloy. This single crystal alloys has increased percentages of rhenium (3 % and 6 %, respectively), which increases both the stability and overall volume fraction of the gamma prime.

Two slabs of material were cast in dimensions 254 × 197 × 32 mm (10 × 7.75 × 1.25 in.), such that the [001] crystallographic orientation was controlled along the length of the slab and the [100] orientation along the width.

A standard heat treatment was applied to each slab, consisting of three steps:

1) A solution heat treatment is performed to ensure a proper microstructure in the form of a fine γ' precipitate. This treatment typically takes place at a temperature in excess of 1205°C (2200°F) and requires a cooling rate of at least 55°C (100°F) per minute to ensure the fine γ' size. This step dissolves the coarse γ' and the γ /γ' eutectic, both of which can contribute to the degradation of mechanical properties.

2) A coating heat treatment follows, which is typically used to bond the coating to the base metal. The temperatures during this step range from 980–1120°C (1800–2050°F) for a time of up to 8 h. The combination of heating times and temperatures can result in the growth of γ' particles and influence the material properties.
3) Finally, an aging heat treatment precipitates the final γ' particles. At lower temperatures of 700–900°C (1300–1650°F) and times of up to 32 h, this step precipitates very fine γ' particles. Overall, heat treatments vary slightly in terms of specific temperatures, heating times, and cooling rates. Generally speaking, the specific details are often proprietary information of the individual turbine manufacturers.

Experimental Methods

The testing for fracture toughness was conducted according to ASTM E 1820-01 [10]. The specimen geometry chosen for this batch of testing was compact tension, with a thickness of 12.7 mm (0.5 in.). With W = 50.8 mm (2 in.), the rest of the dimensions meet the requirements stated in the appendix of ASTM E 1820. The testing conditions chosen for the toughness tests included duplicate tests at 22°C, 650°C, 760°C, and 870°C (72°F, 1200°F, 1400°F, and 1600°F) in the [001] crystallographic orientation (where the crystallographic orientation is perpendicular to the plane of the crack).

The CT specimens were first polished in order to facilitate visual measurement of cracks during pre-cracking. A corded drill with an attachment for affixing sandpaper was utilized, rather than sanding by hand. Starting with 320-grit sandpaper and progressing to 400, 600, and 800, both sides of the specimen were polished. Finally, a six-micron diamond paste was used to provide the final finish for observation under a microscope. After both sides had been polished, the notched region was cleaned and flushed with acetone to ensure that no debris would disrupt the crack front.

After polishing, each specimen was pre-cracked on an MTS hydraulic test machine. The 2270 kg (5000 lb) machine, controlled by an analog MTS 457 controller, was capable of applying the sinusoidal loads needed to initiate fatigue cracks. Each pre-crack was grown approximately 2.5 mm (0.1 in.) beyond the machined 23.7 mm (0.9 in.) notch. During pre-cracking, an optical microscope with a rotating dial gauge was used to measure crack extension from the notch. In addition, the use of indirect lighting provided the necessary contrast to view the crack front. A typical pre-cracking procedure would take approximately 150 000 cycles (at 10 cycles/s), with three to four load sheds during the course of testing. To ensure uniform loading, the specimen was flipped every 5000 to 10 000 cycles. In addition, the optical scope could only be placed in one location during testing, and only one crack front could be measured at a time. This restriction further necessitated the flipping procedure.

A specimen with a sufficient pre-crack then had to be machined further, creating a side-groove that reduced the thickness by 20 % (down to 10.2 mm or 0.4). Once the side-grooves had been machined, the pre-cracks were no longer visible, and subsequent cracks measurements were made based on visual inspection of the fracture surfaces after testing.

In the toughness tests, an LVDT (linear variable differential transformer) was used to measure load line displacement. As the notch opens along the load line, the clip gauge depicted in Fig. 1 also opens. With the upper clip attached to a rod that travels inside the cylindrical tube attached to the lower clip, this rod extends down to the LVDT below. The spring loaded mechanism shown in Fig. 2 keeps the clip edges pressed against the inside surfaces of the notch throughout the test, allowing for a continuous and accurate measurement of the load line displacement.

Also shown in Fig. 1 is the attachment of the thermocouples for the high temperature testing. The leads were attached using a Unitek 250 spot welder. Both thermocouples could be read via an Omega temperature monitor.

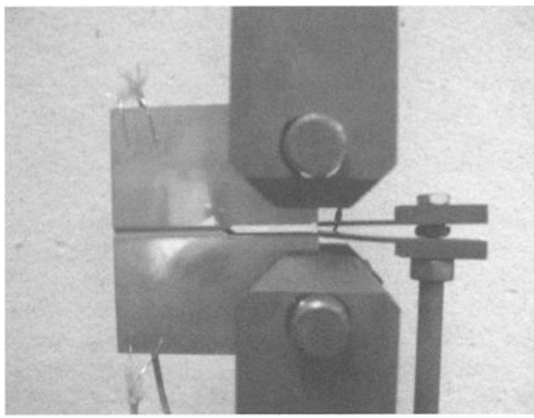

FIG. 1—*Clip gauge for CT specimens.*

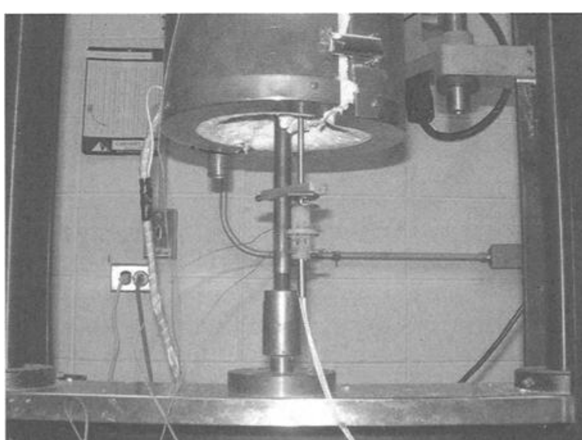

FIG. 2—*View of LVDT in toughness set up.*

Since both the top and bottom pull rods must be fixed while heating the CT specimen, the load must be adjusted continuously during the heating process. As the metals expand, the crosshead must be moved down to maintain a constant load on the specimen, which for most of these tests was around 45 kg (100 lb).

An Applied Testing Systems Furnace and Omega temperature controller were used for the testing at elevated temperatures. Even at a stable, uniform temperature, there is still a small thermal gradient from the top to the bottom thermocouple. This difference was kept to ± 5–10°C (9–18°F), which was the best that could be maintained reasonably. As the heat flowed from the bottom to top, attempting to escape via an effect similar to a chimney, this thermal gradient is created. Efficient and tight packing of the insulation over all parts of the furnace is therefore especially important to minimize such effects.

The pull rods, joints, clevises, and pins were all made of Inconel® 713C (or a comparable alloy), and lubrication was again required at elevated temperatures. Special care was required when packing the bottom part of the furnace not to bump the load line attachment out of alignment, or out of the crack notch altogether.

Once a uniform temperature was attained and held, and the LVDT was in place and tuned to zero displacement, the testing procedure could begin. As stated earlier, a target preload of 45 kg (100 lb) was used for each specimen. This preload would not be reflected in the resulting data files, so it must be recorded by hand and adjusted later. Using the MTI software, the displacement rate is set to 0.042 mm/s (0.0017 in./s) for all tests, with the results file set to record both load and the output from the LVDT. Since the tests were conducted in displacement control, the crack never fully propagated through the remaining ligament during the course of these tests. Generally, a small portion of the ligament remained which could be cyclically loaded to failure after cooling to measure the final crack length. In general, it was deemed sufficient to identify the point where the original pre-crack had reached some critical load at which the unstable crack growth occurred [8]. The calculations for determining a toughness value required this maximum load, the length of pre-crack (as measured along the fracture surface) and interpreting the load versus displacement chart for the purposes of including plasticity effects. Also, several tests produced results where an out of plane pre-crack was observed, necessitating further investigation into a stress intensity solution. The calculations for all of these cases will be discussed and examined in more detail in the results section.

Results and Discussion

The analysis of the toughness data will first follow an elastic interpretation of the test results. Next, the plastic deformation will be included in the analysis via the J integral. Finally, several unusual cases that did not adhere to ASTM standards for valid results will be analyzed and discussed.

The primary result for each toughness test is the curve of load (P) versus load line displacement (v). Each of these values is recorded directly during testing, with P coming from the load cell and v coming from the LVDT monitoring load line displacement. The recorded load (P_m) must be increased by whatever preload (p_l) was applied prior to testing. Also, the initial reading of v (v_o) shall be treated as the zero reference for subsequent measured values (v_{im}), due to the difficulty in tuning the LVDT to exactly zero. This allows one to obtain the actual load line displacement, v_{ia}.

$$P_a = P_m + p_l \tag{1}$$

$$v_{ia} = v_{im} - v_o \tag{2}$$

In addition to the two measured values, the pre-crack length (a_o) must be measured for calculating the stress intensity factors. After the specimen has fractured and the two sides are separated, visual inspection and measurement with calipers is necessary to find a_o. Following

ASTM E 1820, nine measurements are taken of the crack length across the width of the specimen, and an average value is taken. The pre-crack region, with a smooth fracture surface due to the cyclic loading, stands in contrast to the rough surface created by the unstable crack growth during the toughness tests. Figure 3 demonstrates this contrast in an elevated temperature specimen. The oxidation at high temperatures on the smooth pre-crack (right) and fracture surfaces (center region) also makes final length of unstable crack growth easy to identify. When the unstable crack growth fractures the specimen, the remaining ligament (left) is not fractured until after the specimen has cooled, leaving its fracture surface free of oxidation. This phenomenon is also visible in Fig. 3.

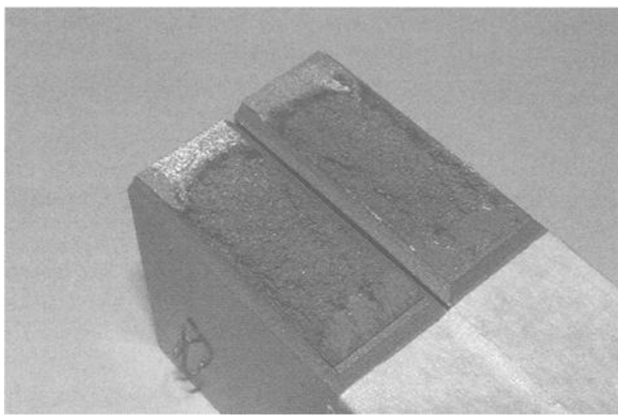

FIG. 3—*Distinctive fracture surfaces in toughness specimen.*

Elastic Analysis

Thus, all the necessary results (P_a, v_{ia} and a_o) have been obtained for each test. The procedure for determining toughness values will follow ASTM E 1820. It is first necessary to use a secant offset to determine a K_q for the test. If the P_q value (either where the two lines intersect, or the value of the maximum load before that point) is at least 90 % of P_{max}, then a K_q can be calculated using the value of a_o. The formula for K_q is simply the stress intensity for a CT specimen at P_q and a_o:

$$K_q = \left(\frac{P_q}{(B \cdot B_n \cdot W)^{1/2}} \right) \cdot f\left(\frac{a_o}{W} \right) \tag{3}$$

where B is the thickness, B_n is the thickness after side-grooving, W is 50.8 mm (2 in.), and $f(a_o/W)$ is defined as:

$$f\left(\frac{a_o}{W}\right) = \frac{\left[\left(2 + \frac{a_o}{W}\right)\left(0.886 + 4.64\left(\frac{a_o}{W}\right) - 13.32\left(\frac{a_o}{W}\right)^2 + 14.72\left(\frac{a_o}{W}\right)^3 - 5.6\left(\frac{a_o}{W}\right)^4\right)\right]}{\left(1 - \frac{a_o}{W}\right)^{3/2}} \tag{4}$$

Once K_q is calculated, it is necessary to determine if this will be a valid K_{IC} test, or if further manipulation will be necessary. If the specimen dimensions a_o, $W-a_o$, and B are more than the following quantity (dim_{max}), then the test results are valid for a K_{IC} test.

$$dim_{max} = 2.5 \cdot \left(\frac{K_q}{\sigma_y} \right)^2 \tag{5}$$

where σ_y is the 0.2 % yield strength.

For structural materials, this is generally not the case in a specimen with small dimensions. In fact, for a typical test performed here, the necessary dimensions would have needed to exceed 45 mm (1.8 in.). Both a_o and $W- a_o$ are approximately 25.4 mm (1 in.), and B is 12.7 mm (0.5 in.). Therefore, it is generally not feasible to expect valid K_{IC} results from materials such as those being studied here (and such was definitely the case with this testing).

However, if one chooses the critical load as the load at which unstable crack growth begins (P_c), then a critical toughness can be defined (K_c). While not the same as K_{IC}, the value does provide a measure of the toughness of the material that is quite accurate relative to the actual toughness [7]. Since the P_c is generally the maximum load during testing (after which a jump is typically seen in displacement as the crack grows), it is easy to identify on the load history plots.

Thus, K_c follows the same formula as K_q, which was the definition of stress intensity in an elastic material:

$$K_c = \left(\frac{P_c}{(B \cdot B_n \cdot W)^{1/2}} \right) \cdot f\left(\frac{a_o}{W} \right) \tag{6}$$

The $f(a_o/W)$ function here is same as in Eq 4 and uses the same pre-crack length that is measured visually. Both toughness measurements assume that the critical crack length is the initial length of the pre-crack, a_o. Figure 4 shows the trends of K_c with temperature obtained from the tests.

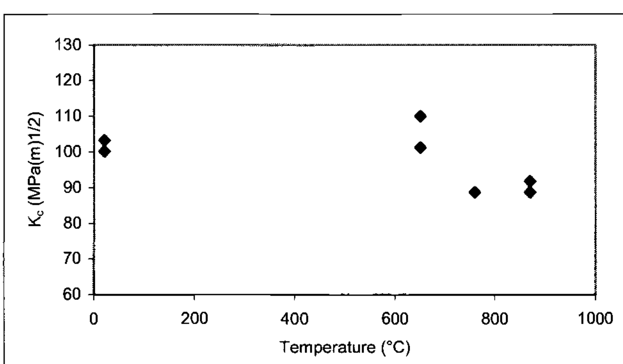

FIG. 4—*K_c results as a function of temperature.*

Effects of Plasticity

To this point, the deformation in the material has been assumed to be elastic. However, the load histories generally indicate that the behavior is not necessarily linear. In order to account for the effects of plasticity, it is necessary to utilize the J integral as defined by ASTM E 1820. The total J consists of both elastic and plastic components.

$$J = J_{el} + J_{pl} \tag{7}$$

$$J_{el} = K_c^{\ 2} \cdot \frac{1-\nu^2}{E} \tag{8}$$

$$J_{pl} = \frac{\eta \cdot A_{pl}}{B_n \cdot b_o} \tag{9}$$

In the preceding equations, ν is the Poisson ratio, E is elastic modulus, η is a constant defined by ASTM (2 + 0.522*b_o/W), A_{pl} is the area under the plastic portion of the P-v, and b_o is the uncracked ligament (W-a_o).

Once a value for J_{pl} has been determined, it can be combined with J_{el} to give a total J. Figure 5 shows how elastic, plastic and total J integral trends evolve with temperature.

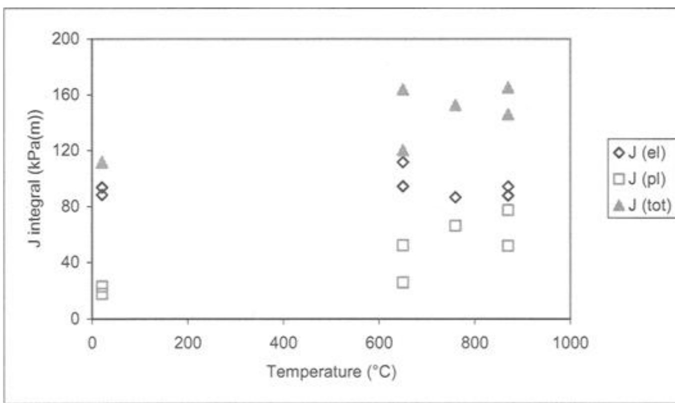

FIG. 5—*Results from J integral calculations.*

Finally, a toughness value based on these J integral estimates is defined as K_{jc}.

$$K_{jc} = \left(\frac{J \cdot E}{1-\nu^2}\right)^{1/2} \tag{10}$$

The K_{jc} results are thus intended to more fully encompass both the elastic and plastic deformation seen during testing. The trends in K_{jc} (in Fig. 6) do not exactly follow the trend already seen by the elastic fracture evaluation, but their appearance can be understood by examining the trends in the J integral calculations in Fig. 5. These trends include the dip in toughness at 760°C (1400°F) observed in the elastic calculations, followed by an apparent increase at 870°C (1600°F). However, once the effects of plasticity are factored into the discussion, it seems the total toughness remains stable, even showing an overall, steady increase. This seems to be in agreement with the results obtained by Anton [5], who noted the increased likelihood of ductile rupture (and therefore enhanced plasticity) at elevated temperatures. The increase in the plastic component of J at elevated temperatures matches what one would expect with increased ductility.

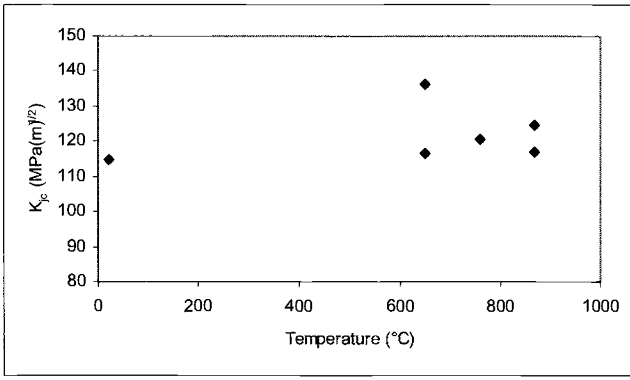

FIG. 6—*Results of K_{jc} calculations.*

As a final note on the K_{jc} results, there appears to be more scatter in the K_{jc} trends than in the J trends. This is due to the variation in modulus between the temperatures. Since the K-J calculations involve a square of the modulus, calculations at different temperatures will be affected differently. This scatter is evident first in the J results, and then appears to be greatly increased in the K_{jc} results as a result of the modulus differences.

Angled Pre-Cracks

In the course of the toughness testing, it was discovered that several pre-cracks had grown at angles in excess of 45°. During the pre-cracking, many of the cracks appeared to grow at extreme angles. However, this was primarily due to plane stress effects on the surface [8,3], and after side-grooving, the remaining crack would be straight. Indeed, once the specimens were tested, the majority of pre-cracks turned out to be straight. However, in several specimens, as mentioned above, this was not the case. For such instances, an alternate solution was developed to try to overcome this obstacle.

Using the solution for an inclined crack in Anderson [11], and in conjunction with work by Chan [12], it is possible to determine the effective stress intensity.

$$K_I' = K_I^0 \cdot \cos(\beta) \tag{11}$$

$$K_{II}' = K_{II}^0 \cdot \cos(\beta) \cdot \sin(\beta) \tag{12}$$

These are the equations provided by Anderson for the stress intensities in Modes I and II for an inclined crack. In each equation, K° is the stress intensity for a specimen with a straight crack, β is the angle of inclination in the specimen, and K' is the resulting equivalent stress intensity. Chan proposes an effective stress intensity (K_{eff}) that combines Mode I and Mode II solutions (along with several constants) obtained via Boundary-Integral-Equation (BIE) techniques. Chan also uses a Mode III term, but only Modes I and II were applicable here. Chan computed the constants (C_1 and C_2) for similar single crystal CT specimens, and the averaged values were used for the results presented here.

$$K_{eff} = \left(K_I^{\,2} + \left(\frac{C_2}{C_1} \right) \cdot K_{II}^{\,2} \right)^{1/2} \tag{13}$$

The results of these calculations for the specimens with angled pre-cracks are presented in Fig. 7, along with the previous results for K_c. For each test, the values for both 50° and 55° angles of inclination are presented. Since these results are outside of ASTM standards, they are simply an attempt to provide approximate solutions. Thus, the range of K values presented indicates approximate results for a crack that falls between these two angles.

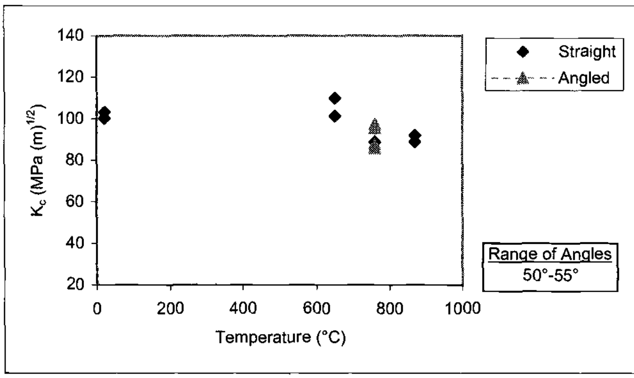

FIG. 7—*Approximate, K_{eff}(inclined), and actual, K_c(straight), solutions.*

From Fig. 7, it is evident that the range of calculated, inclined results at least approximately follows the pattern of the straight results. Indeed, at 760°C (1400°F), the valid result fits inside the range of the inclined results. Thus, while the inclined K solutions are not ASTM standard, they do follow the same trends seen in the valid results.

Microstructural Anomalies

Another interesting result from the toughness testing was the unusual behavior of several specimens during unstable crack growth. The straight pre-crack reached a critical load, at which point the specimen began to rupture perpendicular to the loading axis. However, it then appears that the crack stopped and actually went out of the side-groove to eventually break nearly parallel to the loading axis.

Initially, it may appear as though the fracture could have been related to placement of the thermocouples on the surface. In fact, the fracture runs right along where the leads were welded to the specimen. However, further examination indicates a different cause. Figure 8 shows a microstructural defect, perhaps a low angle grain boundary, within the fractured material.

It is also evident in Fig. 8 that there was some initial fracture in the horizontal direction before the defect was encountered. The load history of these specimens reflects their unusual fracture behavior, with multiple gaps indicating unstable growth.

The jump in load line displacement after the critical load is reached corresponds to the initial fracture. The subsequent loads represent the reloading prior to vertical failure. Since the initial toughness value was for a valid pre-crack and fracture occurred perpendicular to the loading, this value could be used. This anomaly was observed several other times, but for each instance where a valid pre-crack was present, an initial toughness value could be obtained (calculated from the maximum load prior to initial fracture). A second toughness value could be obtained from the point where the final failure began. In the above specimen such a value would be invalid since fracture occurs vertically.

A similar defect was observed, both physically and in the load history, in another specimen. However, in this case, the secondary fracture continued along the horizontal plane, and a second toughness value could be extracted. Using the P-v curve for this specimen, this second rupture point produces a K_c of 91.7 MPa$\sqrt{m}$ (83.7 ksi$\sqrt{in.}$). This value is consistent with the valid results (86.7–94.2 MPa$\sqrt{m}$) at this testing condition. Thus, while such a result is not necessarily valid by ASTM standards, it is interesting to note. Also, it indicates the sensitivity of the single crystal casting process to defects and how these defects can affect mechanical properties. See Table 1 for a summary of toughness results.

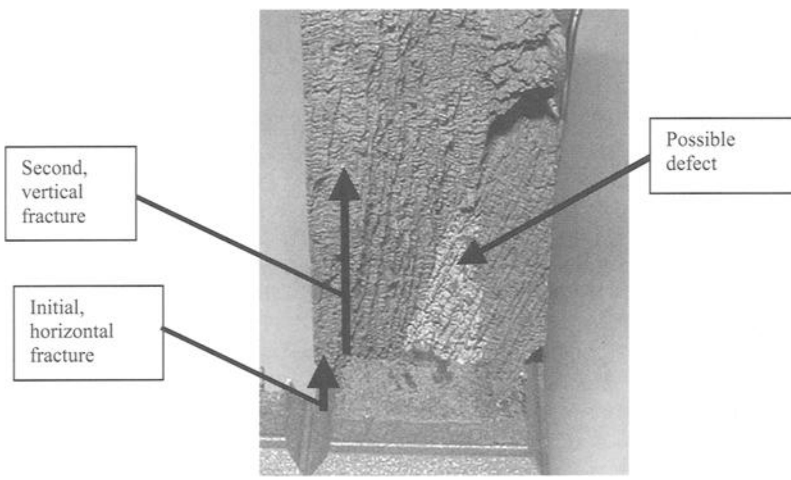

FIG. 8—*Straight-on view of the defect in toughness specimen 1-2.*

TABLE 1—*Summary of toughness results.*

Specimen	Temperature (°C)	K_c (MPa m$^{1/2}$)	J_{el} (kPa m)	J_{pl} (kPa m)	J_{tot} (kPa m)	K_{jc} (MPa m$^{1/2}$)
1-1	21	103.2	93.8	17.9	111.8	115
1-1a	21	100.2	88.3	23.1	111.4	114.8
1-4	650	100.2	94.4	25.9	120.3	116.8
1-4a	650	110	111.6	52.2	163.8	136.2
1-3-high	760	97.4	...	...	...	...
1-3-low	760	87.6	...	...	...	...
1-3a-high	760	95.6	...	...	...	...
1-3a-low	760	85.9	...	...	...	...
1-6	760	88.7	86.5	66.1	152.6	120.5
1-2	870	94.2	94.2	51.9	146.1	117.1
1-2a	870	86.7	87.8	77.4	165.2	124.6
1-2a (#2)	870	91.7	...	...	...	...

Notes: *(a)* 1-3 and 1-3a have inclined cracks and the reported values are for angles between 50 (high) and 55 degrees (low). *(b)* 1-2a(#2) is the secondary fracture point for this specimen.

Conclusions

The results of the fracture toughness testing provided a measure of critical stress intensities prior to unstable crack growth. Initially, only an elastic analysis was performed. This analysis revealed steady (if slightly increasing) toughness up to 650°C (1200°F), with a drop occurring at the peak test temperature of 760°C (1400°F). However, when the effects of plastic deformation were accounted for, all the toughness values showed a small (but steady) increase with temperature. While previous research on toughness is limited, the results here are supported by previous conclusions. The increased likelihood of ductile rupture at higher temperatures is evident when examining the plastic component of the J integral. While the elastic properties do show a decrease at elevated temperatures, it is the increase in the plastic J integral at higher temperatures that results in an overall increase in toughness. Recalling that the presence of γ' can enhance ductility of an alloy, this trend should not be unexpected.

The difficulties presented by testing single crystals are also evident during the toughness tests. Inclined cracks and microstructural defects are unfortunate (for the researcher attempting to obtain valid results) but necessary side effects of testing with such an advanced material. While inclined, crystallographic cracks are inherent to all single crystals at room temperature; the appearance of a defect during testing highlights the difficulties in manufacturing these alloys. Controlling these conditions is not always possible, so developing alternate solutions can be greatly beneficial. For this research, results were obtained after encountering both of these unique conditions. Those specimens with inclined pre-cracks and a specimen with a defect that impeded fracture were both analyzed using elastic techniques. When compared with the valid results, these initially invalid tests provided useful data that matched the trends seen in the rest of the data.

The primary reason for the lack of data on the toughness of these alloys, as stated earlier, is that rapid fracture is generally not a concern. With elastic toughness values in the range of 87–110 MPa$\sqrt{m}$ (79–100 ksi$\sqrt{in}$) and overall results (including the effects of plasticity) of 115–136 MPa$\sqrt{m}$ (105–124 ksi$\sqrt{in}$), this alloy certainly is resistant to rapid, unstable crack growth. Such values are comparable to those of advanced aluminum and titanium aircraft alloys [9] of similar dimensions. Also, for the loading conditions in which these alloys are utilized, it is not the high end of the stress intensity regime that is of great concern. The growth of smaller, non-critical cracks over time (due to both fatigue and creep) is the likely route to failure. While it is therefore important to concentrate on crack growth, it would seem imprudent to simply ignore the fundamental fracture properties obtained via toughness tests.

Recommendations

In terms of toughness testing, it has already been noted that critical toughness values are not utilized to a great extent. However, should modeling demands dictate that toughness values become more of a significant factor, the effects of plane strain and plane stress should certainly be discussed. As the thickness of test specimens vary, so too does the toughness (as a result of changing boundary conditions). If deemed important to life assessments, the critical toughness results should then be related to those conditions and geometries where they are actually used.

Acknowledgments

This work was supported by GE Power Systems. The technical monitor was Dr. Massoud Mirdamadi.

References

[1] Walston, W. S. et al., "Comparisons of K_{JIC} and K_{IC} Values from Tests on a Single Crystal Nickel Base Superalloy," *Scripta Metall et Mater*, Vol. 25, 1991, pp. 1333–1337.
[2] Yue, Z. F., "Fracture Behavior of a Nickel Base Single Crystal Superalloy as Predicted by the Strain Energy Density Criterion," *Theoretical and Applied Fracture Mechanics*, Vol. 26, 1997, pp. 89–104.
[3] Viswanathan, R., "Damage Mechanisms and Life Assessment of High Temperature Components," ASM International, Metals Park, OH, 1989, pp. 473–475.
[4] Mills, W. J., *Eng Frac Mech*, Vol. 26, 1987, pp. 223–238. [CrossRef]
[5] Anton, D. L., "Fracture of Nickel Base Superalloy Single Crystals," *Mat Sci and Eng*, Vol. 57, 1983, pp. 97–105.
[6] Moody, N. R., et al., *Metall Tran*, Vol. 18A, 1987, pp. 1469–1482.
[7] Walston, W. S., Ph.D. Thesis, Carnegie Mellon University, 1990.
[8] Flores, K. M. and Dauskardt, R. H., "Fracture and Fatigue Crack Growth Behavior of Single Crystal NiAl," *Scripta Mater*, Vol. 36, No. 12, 1997, pp. 1377–1382.
[9] Dogan, B. and Schwalbe, K. H., "Fracture Toughness Testing of TiAl Base Intermetallic Alloys," *Eng Frac Mech*, Vol. 56, No. 2, 1997, pp. 155–165.
[10] ASTM Standard E 1820–01, "Standard Test Method for Measurement of Fracture Toughness," ASTM International, West Conshohocken, PA.
[11] Anderson, T. L., *Fracture Mechanics*, 2nd ed., CRC Press, 1995, pp. 91–95.
[12] Chan, K. S. and Cruse, T. A., "Stress Intensity Factors for Anisotropic Compact Tension Specimens with Inclined Cracks," *Eng Frac Mech*, Vol. 23, No. 5, 1986, pp. 863–874.

SESSION 6A: FATIGUE CRACKS GROWTH IN THE RAILROAD INDUSTRY

Journal of ASTM International, September 2005, Vol. 2, No. 8
Paper ID JAI12013
Available online at www.astm.org

Wei Zhao[1] *and Michael A. Sutton*[1]

Structural Reliability Analysis of Railroad Tank Cars Subjected to Fatigue and Corrosion

ABSTRACT: Reliability analysis of tank car structures undergoing fatigue crack growth and general corrosion (tank wall thinning) is illustrated to support informed decision-making and planning for reliability-centered maintenance. Two specific mechanisms that contribute to tank car deterioration are considered: (1) corrosion with negligible fatigue crack growth; and (2) corrosion-accelerated fatigue crack growth. Reliability analysis of corrosion-accelerated fatigue crack growth is performed with a time-dependent tank wall thickness reduction and a fatigue crack growth model that incorporates a three-degrees-of-freedom surface crack obeying Walker crack growth law under tank car spectrum loading. System reliability problems involving multiple corrosion sites are considered to illustrate important features of failure probability for a series system in relation to failure probability of individual corrosion sites.

KEYWORDS: structural reliability, failure probability, series system, system reliability, general corrosion, fatigue crack growth, railroad tank car, surface crack

Introduction

Safe transport of hazardous materials is of vital importance to tank car builders, users, federal regulatory agencies, and the general public. Reliability-centered maintenance can be used to provide an acceptable level of integrity for tank car systems in guarding against lading (tank car cargo) loss due to equipment failures. Adequate and cost-efficient maintenance decisions depend on the ability to (a) understand a tank car's characteristics and its response under various service conditions and (b) predict tank car's performance and resistance deterioration as a function of usage.

The usefulness of the reliability methods in quantifying the effects of uncertainty in structural analysis has long been realized. Examples of development and applications involving fatigue and/or corrosion can be found in the literature [1–13], where the focus has been on aircraft and aerospace structures. In recent years, reliability analysis methodologies have also been developed and applied to deteriorating railroad tank car structures due to fatigue crack growth [14,15].

To support informed decision-making and planning for a reliability-centered maintenance process through quantitative risk analysis and prediction, the objective of this work is to illustrate how to perform reliability analysis of tank car structures subjected to fatigue and corrosion, two of the commonly-encountered deterioration mechanisms for the railroad tank car structures. The form of tank car corrosion damage is manifold. In this study, general corrosion (tank wall thinning) is considered. Three conditions are distinguished: (i) fatigue crack growth with negligible corrosion, (ii) corrosion with negligible fatigue crack growth, and (iii) corrosion-

Manuscript received 26 November 2003; accepted for publication 7 March 2005; published September 2005.
Presented at ASTM Symposium on Fatigue and Fracture Mechanics: 34th Volume on 19–21 November 2003 in Tampa, FL; S.R. Daniewicz, J.C. Newman, Jr., and K-H. Schwalbe, Guest Editors.
[1] Research Professor and Carolina Distinguished Professor, respectively, University of South Carolina, Mechanical Engineering Department, Columbia, SC 29208.

accelerated fatigue crack growth. Since (i) has been studied previously [15], the focus in this work is on (ii) and (iii). Here, the effect of corrosion on fatigue crack growth is modeled as a reduction in tank wall thickness. This corresponds to a scenario in which fatigue crack growth occurs on one (outer or inner) surface of the tank, while corrosion damage occurs on the opposite surface of the tank, i.e., no coupling in the mechanisms between crack growth and corrosion.

For corrosion reliability analysis, a simple, phenomenon-based, tank car general corrosion model is proposed. Using the methodology developed and demonstrated recently by the authors [15], reliability analysis of corrosion-accelerated fatigue crack growth is performed with a time-dependent tank wall thickness reduction due to corrosion and a fatigue crack growth model that incorporates a three-degrees-of-freedom (3-dof) surface crack obeying Walker crack growth law under tank car spectrum loading.

System reliability problems involving multiple corrosion sites are considered to illustrate important features of failure probability for a series system in relation to failure probability of individual corrosion sites.

Reliability Analysis of Tank Car General Corrosion

A phenomenon-based general corrosion model is proposed and used for reliability analysis of corrosion without fatigue crack growth. Five cases with different corrosion rate/corrosion initiation time are considered individually to illustrate the effects of major parameters.

A Phenomenon-Based General Corrosion Model

As is well documented in the literature [16], corrosion behavior is sensitive to both material characteristics and environmental variables. Different corrosion behaviors occur for different combinations of material/environment systems, as dictated by thermodynamic conditions and kinetic laws for specific operating situations. Without attempting to analyze a specific corrosion mechanism, the current work for corrosion reliability analysis is based on a phenomenon that is common to tank car general corrosion process. This common phenomenon is the material loss (tank wall thinning) as a function of time.

Figure 1 shows a schematic of tank wall cross-section, where B_0 is the original tank wall thickness; the area designated "corroded" is the material loss (tank wall thinning) at time t; $B(t)$ is remaining thickness at a corrosion site at time t; B_c is a critical tank wall thickness below which leakage or rupture may occur. The length unit used in this work is in inches. The time is in years.

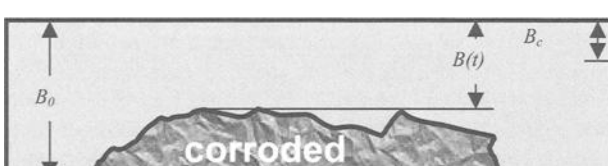

FIG. 1—*A schematic of tank wall cross-section with corrosion damage.*

Tank thickness at time t is equal to initial thickness minus thickness loss, i.e.:

$$B(t) = B_0 - C_r(t - t_i)^d \quad for\ t > t_i \tag{1a}$$

$$B(t) = B_0 \quad for\ t \le t_i \tag{1b}$$

where C_r is a corrosion rate in inch/year; t_i is corrosion initiation time, representing the effect of tank car with a lining or a coating for corrosion protection; and d is an empirical parameter to account for potential nonlinear behavior in time ($d=1$ is assumed in this work). Equation 1 is the proposed phenomenon-based general corrosion model for tank cars. Although it is phenomenon-based, specific corrosion mechanisms and the corresponding material and electrochemical variables can readily enter into the model through kinetic laws dictating the corrosion rate and the corrosion initiation time. Thus, the phenomenon-based model retains generality to accommodate specific corrosion mechanisms and the corresponding parameters.

Performance Function and Basic Random Variables for Corrosion

Since leakage or rupture will occur when the tank thickness, $B(t)$, reduces to the critical thickness, B_c, the failure criterion is simply

$$B(t) \le B_c \tag{2}$$

Using Eqs 1 and 2, a performance function for reliability against corrosion, g_{co}, can be expressed as:

$$g_{co} = B(t) - B_c = [B_0 - C_r(t - t_i)] - B_c \tag{3}$$

The probability of failure due to corrosion, P_f, is therefore,

$$P_f = P(g_{co} \le 0) = P\{[B_0 - C_r(t - t_i)] - B_c \le 0\} \tag{4}$$

In a general situation, B_0, B_c, C_r, and t_i are all random variables; B_0 varies within tolerances of the rolling process that produced the steel plate; B_c will change due to variations in the tank radius, loading density, tank pressure, material properties, as well as uncertainties involved in the measurement; the corrosion rate, C_r, is influenced by variability in numerous factors related to materials and operating conditions. B_0 also has variability due to tank car manufacturing operations, such as rolling and grinding. In addition, if the initial condition is not "as-manufactured," then variability will occur due to prior history, such as a case where B_0 represents a measured thickness after a certain period of service, instead of starting from a pristine condition.

Five different combinations of (C_{rj}, t_{ij}) with $j=1{\sim}5$ are considered for a given tank wall thickness, B_0, and a critical thickness, B_c. Table 1 lists the assumed probability density distributions for B_0, B_c, C_r, and t_i.

In Table 1, N(μ, σ) stands for normal distribution with a mean value of μ and a standard deviation of σ; also, LN(μ, σ) stands for lognormal distribution with a mean value of μ and a standard deviation of σ. The tank thickness of 0.4375 in. is representative of non-pressure tank cars. It is noted that the values listed in Table 1 are for illustration purposes and do not represent any specific tank car design or usage data.

TABLE 1—*Probabilistic distributions for the basic random variables in corrosion.*

Name	Symbol	Probabilistic Density Function
Initial tank thickness	B_0	N(0.4375 in., 0.021875 in.)
Critical tank thickness	B_c	N(0.2 in., 0.01 in.)
Corrosion rate at site 1	C_{r1}	LN(0.010 in./year, 0.010 in./year)
Corrosion rate at site 2	C_{r2}	LN(0.008 in./year, 0.004 in./year)
Corrosion rate at site 3	C_{r3}	LN(0.010 in./year, 0.010 in./year)
Corrosion rate at site 4	C_{r4}	LN(0.006 in./year, 0.003 in./year)
Corrosion rate at site 5	C_{r5}	LN(0.012 in./year, 0.012 in./year)
Corrosion initiation time at site 1	t_{i1}	LN(5 years, 1.5 years)
Corrosion initiation time at site 2	t_{i2}	LN(3 years, 0.9 years)
Corrosion initiation time at site 3	t_{i3}	LN(7 years, 2.1 years)
Corrosion initiation time at site 4	t_{i4}	LN(1 years, 0.3 years)
Corrosion initiation time at site 5	t_{i5}	LN(7 years, 2.1 years)

Results and Discussion for Corrosion Reliability Analysis

Using commercial software for structural reliability analysis, STRUREL [17] and a second order reliability method (SORM) [18] to account for nonlinearities in the performance function, component reliability analysis is performed to determine P_f expressed in Eq 4 for the cases listed in Table 1. The SORM solution is further improved and verified using an importance sampling technique [18].

Figure 2 shows the results of failure probability, P_f, versus service time, t, where the vertical axis is in log scale to discern variations for small P_f. As expected, three common trends are observed. First, P_f increases with time. Second, for the same distribution of the corrosion initiation time, t_i, P_f increases with corrosion rate (compare sites 3 and 5). Third, for the same distribution of C_r, P_f increases as t_i decreases (compare sites 1 and 3). It is also noted that the curves of P_f versus t may cross each other at a certain time in service when a higher corrosion rate occurs at a site with a longer corrosion initiation time (compare sites 2 and 4 or 1 and 5).

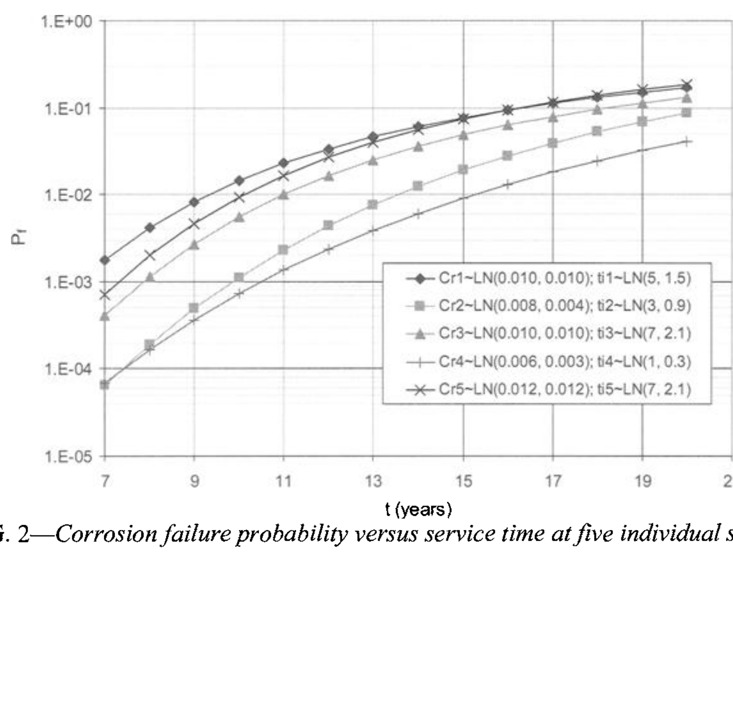

FIG. 2—*Corrosion failure probability versus service time at five individual sites.*

The above component reliability analysis is for individual sites. When a tank car has corrosion at multiple locations, the failure probability for the tank car depends upon the failure probabilities at individual locations and is strongly influenced by the degree of correlation between individual failure events. This will be illustrated in the section on system reliability.

Reliability Analysis of Corrosion-Accelerated Fatigue Crack Growth

The recently developed reliability analysis methodology for tank car fatigue crack growth [15] is used for reliability analysis of corrosion-accelerated fatigue crack growth by introducing a time-dependent tank wall thickness. The acceleration of fatigue crack growth is due to a thickness reduction caused by the corrosion, corresponding to a scenario in which fatigue crack growth occurs on one (outer or inner) surface of the tank, while corrosion damage occurs on the opposite surface of the tank, i.e., no coupling in mechanisms between crack growth and corrosion. The corrosion-accelerated fatigue crack growth model is described, followed by example results and discussion.

Corrosion-Accelerated Fatigue Crack Growth Model

Figure 3 shows a schematic for the corrosion-accelerated fatigue crack growth scenario, where the time-varying thickness, $B(t)$, is expressed in Eq 1. The fatigue crack growth model for a three-degrees-of-freedom (3-dof) surface crack is described in Ref. [15] and is capable of considering an asymmetric stress field present at a fatigue critical location in tank car structures. The 3-dof surface crack also allows unsymmetrical geometry, i.e., $e \neq 0$.

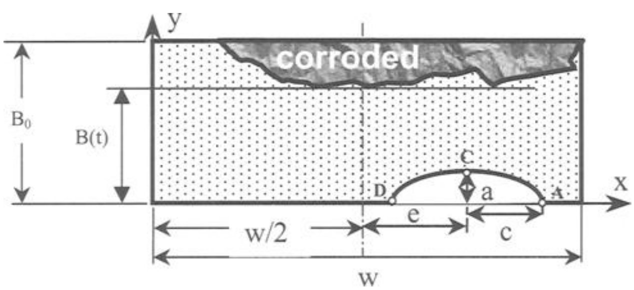

FIG. 3—*A schematic for the corrosion-accelerated fatigue crack growth scenario.*

To introduce the thickness reduction caused by corrosion into fatigue crack growth process, it is necessary to relate corrosion time with the fatigue load spectrum. Tank car usage can vary greatly, for example, from a few thousand miles a year to about 20 000 miles a year. For illustration purposes, a consensus tank car usage of 14 000 miles per year is adopted in this work. Therefore, one year of corrosion time corresponds to a fatigue load spectrum representing 14 000 miles of travel distance. More information about the tank car load spectrum can be found in [15].

The life prediction algorithm for the 3-dof surface crack has been given in [15], and is extended in the following to include the time-dependent thickness. The Walker fatigue crack growth law [19] is adopted, which can be expressed as follows:

$$\frac{da}{dN} = C_W(R)[\Delta K]^m \tag{5a}$$

$$C_W(R) = \frac{C}{(1-R)^q} \quad \text{for } R < R_{co} \tag{5b}$$

$$C_W(R) = \frac{C}{(1-R_{co})^q} \quad \text{for } R \geq R_{co} \tag{5c}$$

where R_{co} is the cutoff value of the R-ratio (load ratio) above which the R-ratio effect diminishes in the Paris regime. The estimated mean values for the parameters in Eq 5 for A516-70 steel are as follows: $C=1.36 \times 10^{-10}$ $in/(ksi\sqrt{in})^m$, $q=2.09$, $m=3.15$ and $R_{co}=0.5$, with crack growth rate, da/dN, expressed in *in./cycle*.

The stress intensity factor for the 3-dof surface crack is determined with an enhanced 3D weight function method based on [20,21] utilizing a 2D weight function for eccentric cracks developed by Chen and Albrecht [22]. The functional form of the stress intensity factor range accounting for corrosion-thinning is as follows:

$$\Delta K_j = \Delta S_j \alpha_{j-1} f_j \left[a_{j-1}, c_{j-1}, e_{j-1}, w, B(t_{j-1}), \varphi, S(x,y)\right] \tag{6}$$

where ΔS_j is the stress range corresponding to load step j in the tank car spectrum; α_{j-1} is a stress magnification factor due to tank wall thinning and defined as $B_0/B(t_{j-1})$; $S(x, y)$ is the stress distribution due to a unit load; φ is a parametric angle of the crack varying from 0–$180°$ with $\varphi=0°$ at point A in Fig. 3, $\varphi=90°$ at point C, and $\varphi=180°$ at point D; and f_j is stress intensity factor due to the unit load. The crack growth and corrosion time increments are calculated as follows:

$$\Delta a_j = C_w(R_j)\left[\Delta K(90°)_j\right]^m \Delta N_j \tag{7a}$$

$$\Delta c_{Aj} = C_w(R_j)\left[\Delta K(0°)_j\right]^m \Delta N_j \tag{7b}$$

$$\Delta c_{Dj} = C_w(R_j)\left[\Delta K(180°)_j\right]^m \Delta N_j \tag{7c}$$

$$\Delta e_j = \Delta c_{Aj} - \Delta c_{Dj} \tag{7d}$$

$$\Delta t_j = \Delta N_j / N_{py} \tag{7e}$$

where R_j is the stress ratio for load step j, ΔN_j is the number of cycles for the load step, and N_{py} is the total number of load cycles corresponding to one year of tank car usage. Sub-incrementation of ΔN_j will be performed if a large crack growth increment may occur during ΔN_j load cycles. Then, the crack size, eccentricity, and the corrosion time are updated as follows:

$$a_j = a_{j-1} + \Delta a_j \tag{8a}$$

$$c_{Aj} = c_{Aj-1} + \Delta c_{Aj} \tag{8b}$$

$$c_{Dj} = c_{Dj-1} + \Delta c_{Dj} \tag{8c}$$

$$e_j = e_{j-1} + \Delta e_j \tag{8d}$$

$$t_j = t_{j-1} + \Delta t_j \tag{8e}$$

The accumulated corrosion time, t_j, is used to determine the current thickness, $B(t_j)$, using Eq 1. The stress magnification factor, α_j, is then determined as $B_0/B(t_j)$.

The analysis procedure starts from an initial crack size and tank wall thickness and continues until the crack propagates through the tank wall. Fracture, as a potential failure mode, is not active for the cases considered because leakage occurs before break, as preliminary analyses showed.

Performance Function and the Basic Random Variables

Defining failure as leakage due to corrosion-accelerated fatigue crack growth, a performance function is expressed as follows:

$$g_{cf} = Ln(N_P) - Ln(N_D) \tag{9}$$

where N_P is the predicted fatigue life, and N_D is the demanded (expected) fatigue life during which a tank car is required to perform without leakage due to corrosion accelerated fatigue crack growth. As described in [15], the logarithm is taken to reduce the non-linearity of the performance function in the independent, standard normal space. The failure probability is, therefore,

$$P_f = P(g_{cf} < 0) = P([Ln(N_P) - Ln(N_D)] < 0) \tag{10}$$

which is determined using STRUREL [17] with the importance sampling technique [18] after locating the β-point (the most probable point on the failure surface) with the first order reliability method (FORM) [23].

The basic random variables involved in Eq 9 are summarized in Table 2, in which *U*, *LN*, and *N* stand for uniform (rectangular), lognormal, and normal distributions, respectively. The parameters for these distributions are distribution intervals for the uniform distribution and are the mean and standard deviation for the lognormal and normal distributions. The dimensions for *C* correspond to crack growth rate expressed in *in./cycle*. The stress uncertainty factor, S_{uf}, represents the combined influence of uncertainty in amplitudes for the load spectrum and the stress analysis. For the corrosion rate, C_r, three different sets of values of $LN(\mu_{cr}, \sigma_{cr})$ are considered. They are as follows: $\mu_{cr1}=0.0005$ *in./year*, $\sigma_{cr1}=0.0001$ *in./year*; $\mu_{cr2}=0.001$ *in./year*, $\sigma_{cr2}=0.0002$ *in./year*; and $\mu_{cr3}=0.0015$ *in./year*, $\sigma_{cr3}=0.0003$ *in./year*. For the case of corrosion-accelerated fatigue crack growth, the corrosion rate is such that the corrosion alone will not cause failure during the fatigue crack growth period analyzed.

In addition, the following parameters are treated deterministically: fracture toughness, K_c=250 $ksi\sqrt{in}$; initial tank wall thickness, B_0=0.4375 in.; welding residual stresses, S_r=6.5 *ksi* (45 *MPa*), which is achieved by adding a mean load of 7.6 *kip* in the load spectrum. The parameters *m* and *q* in the Walker equation are constants as given in Eq 5.

TABLE 2—*Probabilistic distributions for the basic random variables in corrosion-accelerated fatigue crack growth.*

Name	Symbol	Probabilistic Density Function
Initial crack depth	a_0	U(0.0125 in., 0.2 in.)
Initial crack aspect ratio	$(a/c)_0$	U(0.1, 1)
Crack growth coefficient	C	LN(1.36e-10, 0.272e-10)
R ratio cutoff value	R_{co}	N(0.5, 0.03)
Initial crack eccentricity	e_0	U(0 in., 3 in.)
Stress uncertainty factor	S_{uf}	N(1, 0.08)
Corrosion rate	C_r	LN(μ_{cr}, σ_{cr})

Results and Discussion for Corrosion-Accelerated Fatigue Crack Growth

Figure 4 shows failure probability as a function of corrosion initiation time, t_i, for the corrosion-accelerated fatigue crack growth, where t_i is assumed to be a constant. The result is for a required fatigue life, N_D, corresponding to about 28.5 years of service. The trends show that (a) a longer corrosion initiation time means a longer lasting protection of the tank from corrosion, thus a lower failure probability; (b) at a given t_i, a higher corrosion rate corresponds to a higher failure probability, which is most pronounced at t_i=0 and disappears at t_i=28.5, at which the failure probability is equal to that for the case of no corrosion.

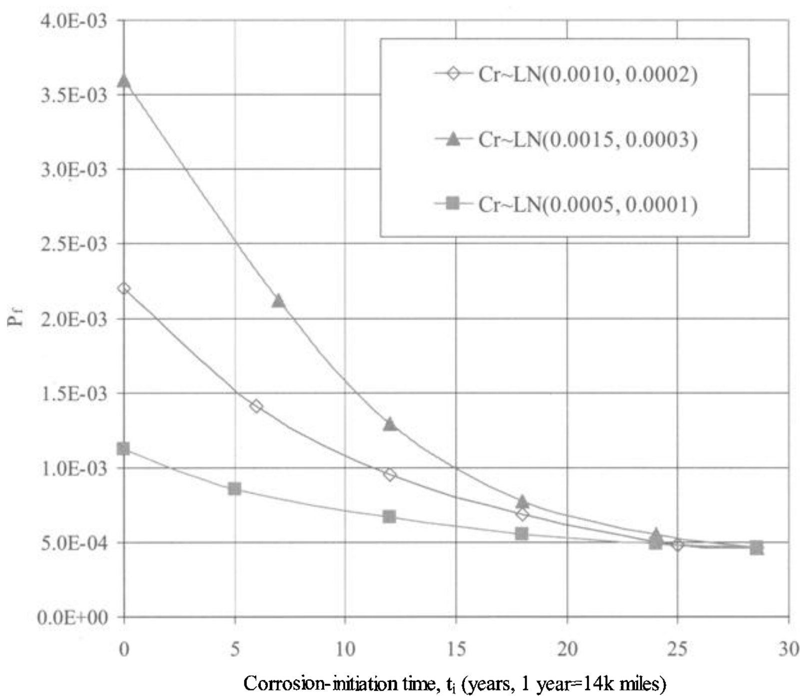

FIG. 4—*Failure probability for corrosion-accelerated fatigue crack growth.*

System Reliability Analysis for Multiple-Site Corrosion

The previous corrosion reliability analyses have been focused on individual sites. When a tank car has corrosion at multiple locations, the failure probability of the tank car depends on failure probabilities at individual locations and is strongly influenced by the degree of correlation between individual failure events. For a tank car having corrosion at multiple locations, failure occurs when leakage is predicted at one or more of the corrosion sites. Therefore, the tank car failure event is a union of the failure events at individual locations, i.e.:

$$F_{sys} = \bigcup_{j=1}^{j_0} F_j \tag{11}$$

where F_{sys} is the system (tank as a whole) failure event, F_j is an individual failure event for location j, with $j=1\sim5$ for this example. The failure probability for the system is, therefore,

$$P_{f\,sys}(F_{sys}) = P(\bigcup_{j=1}^{j_0} F_j) \tag{12}$$

The system reliability problem represented in Eq 12 can be solved using SYSREL, a component for system reliability analysis in the STRUREL software suite [17]. The solution process of a series system is based on Ditlevsen's bounding method [24], which involves determination of: (a) β-point (the most probable point on the failure surface) for the individual failure events; and (b) joint β-point for the pairwise intersections of the individual failure events, by using FORM, or SORM in this case. For this simple series system, an alternative formulation is to consider the complementary event, $\overline{F}_j$, i.e., no failure at location j. Thus, the system failure probability can be represented as an intersection of $\overline{F}_j$ as follows:

$$P_{f\,sys}(F_{sys}) = 1 - P(\bigcap_{j=1}^{j_0} \overline{F}_j) \tag{13}$$

which is solved by the multi-normal integral based on FORM and SORM concepts [25] using SYSREL. In this work, the complementary formulation, Eq 13, is adopted to determine the system failure probability because it has only one cut-set (intersection of failure events), and the result is failure probability itself, instead of failure probability bounds in the case of unions of five cut-sets from Eq 12.

The system failure probability versus service time is shown in Fig. 5. For the same five individual components (locations) shown in Fig. 2, four different cases are considered with different degrees of correlation between the components. For comparison, Fig. 5 also shows the result for the individual component for site 1 (dashed line), which represents approximately the highest failure probability of all five individual locations (Fig. 2). In all the cases, a correlation coefficient in t_i between different corrosion sites is assumed to be *0.50* for the system reliability analysis. Four different values of correlation coefficient in C_r between different corrosion sites are considered. The key *cccr=0.50* in Fig. 5 means that the correlation coefficient between corrosion rate C_{rj} and C_{rk} ($j\neq k$) is equal to *0.50*, similarly for *cccr=0.80*, etc. The higher *cccr* between the basic variables corresponds to a higher correlation between failures at different locations. The correlation coefficient between failure events at site i and site j, ρ_{ij} ($i\neq j$), varies from *0.03–0.08* for *cccr=0*, from *0.55–0.58* for *cccr=0.5*, and from *0.81–0.84* for *cccr=0.8*. It can be seen in Fig. 5 that (1) the system failure probability can be significantly higher than that of the highest individual failure probability; and (2) the higher the correlation between the individual failure modes (locations), the lower the system failure probability. On the other hand, negative correlation between components increases the system failure probability, as can be seen for cccr=-0.10. This is consistent with the reliability theory for series systems. If all the failure locations were perfectly correlated, the system failure probability would reduce to that for the location with the highest failure probability. This example shows the importance of system reliability analysis, since a tank car may have deterioration at more than one location and/or in more than one form.

Again, the numerical values for P_f presented in Figs. 2, 4, and 5 are not specific to any tank cars, as the input parameters used in these analyses are not from specific designs and operating conditions.

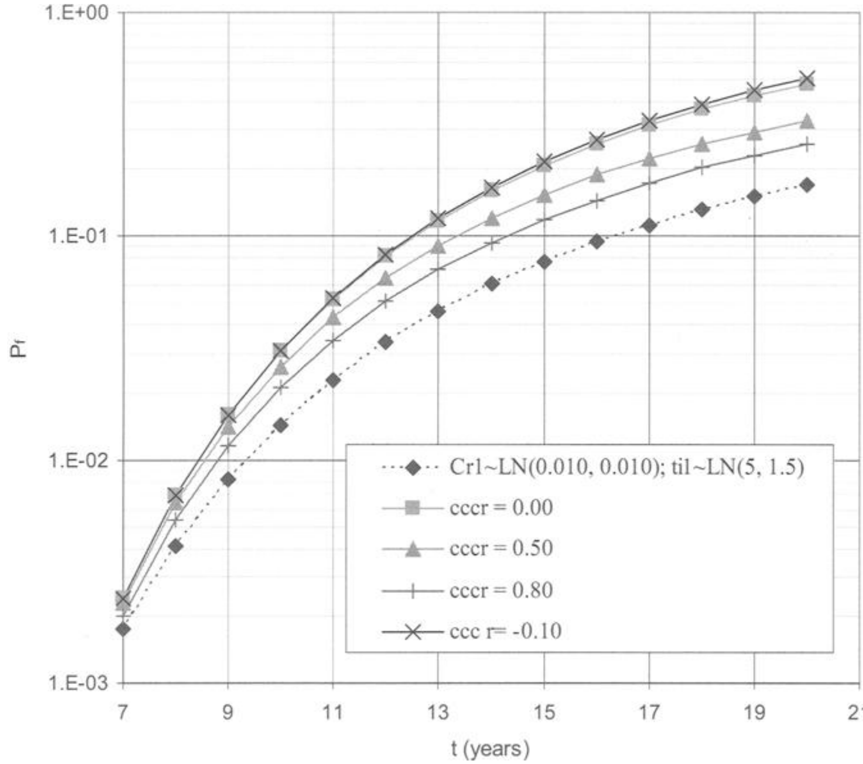

FIG. 5—*System failure probability for corrosion versus service time.*

Sensitivity of the system reliability index, β_{sys} (defined as $\beta_{sys}=-\Phi^{-1}(P_{f\ sys})$; Φ is the cumulative distribution function of a standard normal variable), with respect to the component reliability index, β_i ($\beta_i=-\Phi^{-1}(P_f)$), is a measure of importance for the components and is useful for identifying the relative importance of the components to the system reliability. Equation 14 defines one such a measure [17]:

$$\gamma_i = \left(\frac{\partial \beta_{sys}}{\partial \beta_i}\right) / \left\| \frac{\partial \beta_{sys}}{\partial \beta_i} \right\| \tag{14}$$

Figure 6 shows the relative importance according to Eq 14 for *cccr=0.50* at *t=10* years. It can be seen that in this case none of the components is dominant, with site *1* more important than any of the other sites, and sites *2–5* being about equally important. This information indicates that an improvement in the reliability at site 1 has a more beneficial effect on the system reliability than a similar degree of improvement at one of the other sites.

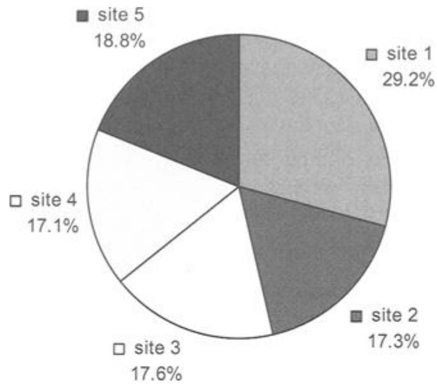

FIG. 6—*Importance of the five components to the system reliability for cccr=0.50 at t=10 years.*

Concluding Remarks

A phenomenon-based tank car general corrosion model is proposed, which includes the effect of coating or lining's protection of the tank metal from corrosion. The model has the versatility to incorporate specific corrosion mechanisms through characterization of corrosion rate and corrosion initiation time using applicable kinetic laws. Corrosion reliability analysis performed has illustrated the usefulness of the reliability method in quantifying and predicting failure probability as a function of usage for given operating conditions.

Expanding a previously developed fatigue reliability analysis methodology for tank cars, reliability analysis of corrosion-accelerated fatigue crack growth is performed with a time-dependent tank wall thickness reduction due to corrosion and a fatigue crack growth model that incorporates a three-degrees-of-freedom surface crack obeying Walker crack growth law under tank car spectrum loading. Illustrative examples are given for quantifying the effects of corrosion rates and corrosion initiation time on probability of failure caused by corrosion-accelerated fatigue crack growth.

System reliability problems involving multiple corrosion sites are considered to illustrate important features of failure probability for a series system in relation to failure probabilities of individual corrosion sites. The results show that the tank car reliability may be lower than that predicted for the most severe site, confirming the importance of system reliability analysis in developing a reliability-centered maintenance program.

Acknowledgments

The authors want to thank Mr. Jose Penã, Technical Representative, Federal Railroad Administration, for his support and helpful technical discussions on tank car issues. Enlightening discussions on system reliability issues from Dr. Stephan Gollwitzer, RCP GmbH, regarding STRUREL, are greatly appreciated. Financial support from the Federal Railroad Administration under Grant No. DTFRDV-00-G-60020 is thankfully acknowledged.

References

[1] Wu, Y.-T. and Wirsching, P.H., "Advanced Reliability Method for Fatigue Analysis," *Journal of Engineering Mechanics*, ASCE, Vol. 110, No. 4, 1984, pp. 536–553.

[2] Ortiz, K. and Kiremidjian, A.S., "Time Series Analysis of Fatigue Crack Growth Rate Data," *Engineering Fracture Mechanics*, Vol. 24, No. 5, 1986, pp. 657–675.

[3] Madsen, H.O., Krenk, S., and Lind, N.C., "*Methods of Structural Safety*," Prentice-Hall, Inc., Englewood Cliffs, New Jersey, 1986.

[4] Sutharshana, S., Creager, M. Ebbeler, D., and Moore, N., "A Probabilistic Fracture Mechanics Approach for Structural Reliability Assessment of Space Flight Systems," *ASTM STP 1122*, M.R. Mitchell and R.W. Landgraf, Eds., ASTM International, West Conshohocken, PA, 1992, pp. 234–246.

[5] Manning, S.D., Yang, J.N., Pretzer, F.L., and Marter J.E., "Reliability Centered Maintenance for Metallic Airframes Based on a Stochastic Crack Growth Approach," *ASTM STP 1122*, M.R. Mitchell and R.W. Landgraf, Eds., ASTM International, West Conshohocken, PA, 1992, pp. 422–434.

[6] Harkness, H.H., Belytschko, T., and Liu, W.K., "Finite Element Reliability Analysis of Fatigue Life," *Nuclear Engineering and Design 133*, 1992, pp. 209–224.

[7] Millwater, H.R., Wu, Y.T., and Cardinal, J.W., "Probabilistic Structural Analysis of Fatigue and Fracture," *AIAA-94-1507-CP*.

[8] Tryon, R.G., Cruse, T.A., and Mahadevan, S., "Development of a Reliability-Based Fatigue Life Model for Gas Turbine Engine Structures," *Engineering Fracture Mechanics 53*, 5, 1996, pp. 807–828.

[9] Berens, A.P., "Applications of Risk Analysis to Aging Military Aircraft," *41st International SAMPE Symposium*, March 24–28, 1996, pp. 99–107.

[10] Harlow, D.G. and Wei, R.P., "A Probability Model for the Growth of Corrosion Pits in Aluminum Alloys Induced by Constituent Particles," *Engineering Fracture Mechanics*, Vol. 59, No. 3, 1998, pp. 305–325.

[11] Akpan, U.O., Koko, T.S., Ayyub, B., and Dunbar, T.E., "Risk Assessment of Aging Ship Hull Structures in the presence of Corrosion and Fatigue," *Marine Structures*, Vol. 15, 2002, pp. 211–231.

[12] Shi, P. and Mahadevan, S., "Corrosion Fatigue and Multiple Site Damage Reliability Analysis," *International Journal of Fatigue*, Vol. 25, 2003, pp. 457–469.

[13] Liao, M. and Komorowski, J.P., "Corrosion Risk Assessment of Aircraft Structures," *Probabilistic Aspects of Life Prediction, ASTM STP 1450*, W. S. Johnson and B. M. Hillberry, Eds., ASTM International, West Conshohocken, PA, 2004, pp. 183–198.

[14] Cardinal, J.W. and Enright, M.P., "Tank Car Stub Sill Damage Tolerance Analysis (DTA) Sensitivity Studies," *43rd Mechanical Working and Steel Processing Conference Proceedings*, The Iron & Steel Society, Charlotte, NC, Oct. 28–31, 2001, pp. 895–906.

[15] Zhao, W., Sutton, M. A., and Penã, J., "A Methodology for Assessing Fatigue Crack Growth Reliability of Railroad Tank Cars," *Probabilistic Aspects of Life Prediction, ASTM STP 1450*, W. S. Johnson and B. M. Hillberry, Eds., ASTM International, West Conshohocken, PA, 2004, pp. 240–254.

[16] "Corrosion," *ASM Handbook*, Vol.13, ASM International, 1996.

[17] STRUREL, "A Structural Reliability Analysis Program System", URL: http://www.strurel.de, Reliability Consulting Programs, RCP GmbH, 2000.

[18] Hohenbichler, M. and Rackwitz, R., "Improvement of Second-Order Reliability Estimates by Importance Sampling," *Journal of Engineering Mechanics*, ASCE, 114, 12, 1988, pp. 2195–2199.

[19] Walker, E.K., "Effects of Environments and Complex Load History on Fatigue Life," *ASTM STP 462*, ASTM International, West Conshohocken, PA, 1970, pp. 1–14.

[20] Zhao, W., Newman, J.C., Jr., and Sutton, M.A. "A Three-Dimensional Weight Function Method - Evaluation and Applications," *ASTM STP 1296*, ASTM International, West Conshohocken, PA, 1997, pp. 563–579.

[21] Zhao, W., Sutton, M.A., and Newman, J.C., Jr., "K3D - A Program for Determining Stress Intensity Factors of Surface and Corner Cracks from a Hole," *ASTM STP 1321*, ASTM International, West Conshohocken, PA, 1997, pp. 656–670.

[22] Chen, X.G. and Albrecht, P., "Weight Functions for Eccentric Cracks," *ASTM STP 1207*, ASTM International, West Conshohocken, PA, 1994, pp. 581–614.

[23] Rackwitz, R. and Fiessler, B., "Structural Reliability under Combined Random Load Sequences," *Computers and Structures 9*, No. 5, 1978, pp. 489–494.

[24] Ditlevsen, O., "Narrow Reliability Bounds for Structural Systems," *Journal of Structural Mechanics 7*, No. 4, 1979, pp. 453–472.

[25] Gollwitzer, S. and Rackwitz, R., "An Efficient Numerical Solution to the Multinormal Intergral," *Probabilistic Engineering Mechanics*, 3, 2, 1988, pp. 98–101.

Journal of ASTM International, May 2005, Vol. 2, No. 5
Paper ID JAI12040
Available online at www.astm.org

S. Beretta[1] *and M. Carboni*[1]

Simulation of Fatigue Crack Propagation in Railway Axles

ABSTRACT: The need for optimizing inspection intervals of wheelsets has led to increasing attention to those of railway axles. This paper addresses this issue by comparing predictions obtained by an EPFM model and two widely used fatigue crack growth softwares (namely AFGROW and NASGRO) with a set of propagation data derived from small and full-scale specimens made of 30NiCrMoV12, a high strength steel used for railway axles. Comparisons, made under constant amplitude and block loading, support the application of the considered fatigue crack growth algorithms to the estimation of inspection intervals.

KEYWORDS: axles, fatigue crack growth, AFGROW, NASGRO, strip-yield, block loading

Nomenclature

a	Crack length
a_i	Initial crack length
a_o	El-Haddad's parameter
da/dN	Crack growth rate
d	Specimen diameter
D	Mechanical threshold
EPFM	Elastic-Plastic Fracture Mechanics
f	Newman's closure function
FCG	Fatigue Crack Growth
R	Stress ratio
SIF	Stress Intensity Factor
S_{op}	Crack opening stress
ΔK	Stress Intensity Factor range
ΔK_{eff}	Effective SIF range
$\Delta K_{th,LC}$	Threshold SIF range for long cracks
ΔS (S)	Applied stress range (amplitude)
$\Delta\sigma_{wo}$ (σ_{wo})	Fatigue limit stress range (amplitude) for smooth specimens
$\Delta\sigma_w$ (σ_w)	Fatigue limit stress range (amplitude) in presence of a crack or defect
$\sqrt{area}$	Murakami's parameter for calculating SIF
$\sqrt{area_o}$	El-Haddad's parameter in terms of Murakami's parameter
$\sqrt{area_{th}}$	Threshold crack size at a given ΔS in terms of Murakami's parameter

Manuscript received 1 March 2004; accepted for publication 15 June 2004; published May 2005. Presented at ASTM Symposium on Fatigue and Fracture Mechanics: 34th Volume on 19–21 November 2003 in Tampa, FL; S.R. Daniewicz, J.C. Newman, Jr., and K-H. Schwalbe, Guest Editors.
[1] Professor, and Researcher, respectively, Politecnico di Milano, Dipartimento di Meccanica, Via La Masa 34, 20158 Milano, Italy.

Introduction

Failure of railway axles is the technical problem that prompted the early fatigue studies of metallic materials [1]. The design of these components is based on technical recommendations [2] which essentially consider mild steels and the definition of maximum allowable fatigue stresses in a given combination of loads acting on the axle. However, applications to high speed trains (like Pendolino, TGV, and ICE) involve hollow axles and high strength steels. Therefore, besides the "classical" approach that defines the minimum strength requirements for axles, new design criteria are needed [3].

In particular, there is an increasing demand for reliability assessment, especially in terms of a new definition of safety factor, which can be addressed with a defect tolerant approach [4], and inspection intervals, which involve predicting axle failure in terms of crack growth under service loads [5]. This prediction, the topic of the present paper, is based on fracture mechanics and fatigue crack growth (FCG) algorithms. The possible FCG approaches are: i) to fit "theoretical models" [6] to experimental tests carried out in conditions similar to applications (namely $R = -1$ for railway axles), and ii) to use currently applied fatigue crack growth algorithms, which are based on the estimation of crack opening load (S_{op}) either from reference data (e.g., AFGROW [7]) or from Strip-Yield calculations coupled with the effective propagation curve da/dN-ΔK_{eff} (e.g., NASGRO [8]).

The first approach was already addressed in a previous paper [4] where short crack thresholds and growth data under constant amplitude rotating bending were analyzed with an "EPFM" growth model, which was successfully applied to full-scale tests. However, such a procedure cannot be applied to variable amplitude loading, especially in the case of inspection intervals of high speed axles, whose load spectra are characterized by a great scatter [9].

It is therefore necessary, for a reliable estimation of inspection intervals of real components, to use updated algorithms that are able to simulate crack growth under variable amplitude loads. The scope of this paper is to compare the previously obtained EPFM model [4] and two widely used FCG softwares, namely AFGROW and NASGRO, for the prediction of crack growth in 30NiCrMoV12 steel, a high strength steel adopted for the production of railway axles [10]. In particular the main points presented in the paper are: i) the previous set of experiments under constant amplitude rotating bending and their interpolation with EPFM model [4]; ii) the fatigue crack growth experiments carried out for determining growth parameters for FCG software; and iii) the comparison between the EPFM model, AFGROW, and NASGRO in fatigue crack propagation at $R = -1$ under constant amplitude and block loading. Results support the application of FCG models to crack growth prediction in railway axles made of high strength steel.

Experiments under Rotating Bending and EPFM Model

Material

The material under analysis is a high strength quenched and tempered 30NiCrMoV12 steel (according to UNI6787-71 [11]) used in the construction of railway axles produced by Lucchini Sidermeccanica S.p.A. (Italy). Mechanical properties of this material are [10]: tensile strength $R_m = 1050$ MPa, yield strength $R_{p0.2} = 995$ MPa, reduction of area $Z = 67$ %, fracture toughness at 20°C $K_{IC} = 120$ MPa$\sqrt{m}$, impact test at room temperature (U notch) KCU = 70 J, cyclic yield strength $R_{p0.2cyc} = 730$ MPa, and Vickers hardness = 330 HV.

Threshold Tests on Micro-Notched Specimens at R = –1

The "sensitivity" of the examined steel to the presence of defects and micro-cracks was investigated with a series of fatigue tests under rotating bending. In order to reproduce the presence of defects, hourglass shaped specimens with a gauge diameter "d" of 8 mm and 10 mm were micro-notched with four different series of micro-drilled holes, whose geometry, with dimensions in the range of 140–840 μm, is shown in Fig. 1, in terms of the Murakami's parameter $\sqrt{area}$ [12]. Specimen preparation consisted of: i) hand polishing with emery paper up to #1000 grit; ii) buff polishing; iii) electro-polishing in a phosphoric acid solution in order to remove a 30 μm surface layer (the surface residual stresses were reduced to a level of –30/–50 MPa); and iv) hole drilling [4].

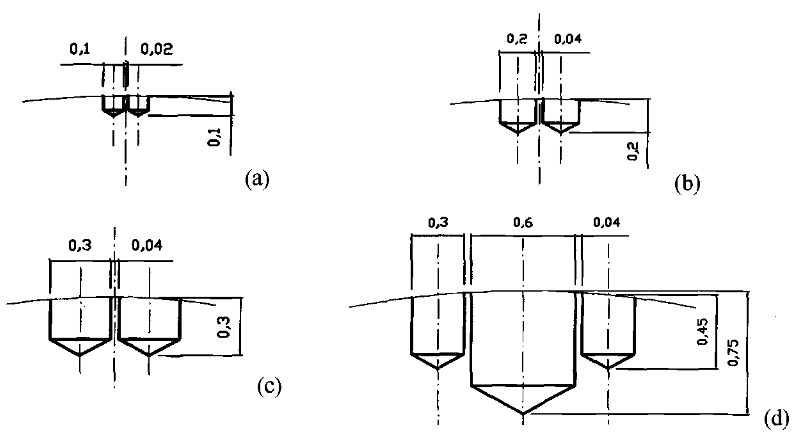

FIG. 1—*Shape and increasing size of micro-notches adopted for fatigue limit tests: a)* $\sqrt{area}$ *= 140 μm; b)* $\sqrt{area}$ *= 260 μm; c)* $\sqrt{area}$ *= 420 μm; d)* $\sqrt{area}$ *= 840 μm.*

Stair-case sequences (interruption of tests after 10^7 cycles) were carried out in order to determine the fatigue limit corresponding to the different micro-notches by means of a 35 Nm rotating bending facility. Similar tests were also carried out on smooth specimens of the same steel batch: the fatigue limit was $\sigma_{wo} = 525$ MPa (R = –1).

Run-out micro-notched specimens always showed non-propagating cracks at the tip of the micro-holes (Fig. 2). It can be said, according to Murakami's concepts [13], that the fatigue limit of the micro-notched specimens is controlled by the threshold condition of the non-propagating cracks and that micro-notches should be treated as small cracks.

Considering this fact, data were modelled by an El-Haddad threshold model [14], whose original equation had been slightly modified for application to 3-D defects [15]:

$$\sigma_w = \sigma_{wo} \cdot \sqrt{\frac{\sqrt{area_o}}{\sqrt{area} + \sqrt{area_o}}} \qquad (1)$$

This model was then fitted to the experimental results by the least square method, and the value of $\sqrt{area_o}$ was found to be equal to 130 μm. It can be seen from Fig. 3 that this modified El-Haddad model is able to describe accurately the data with maximum error of about 3 %.

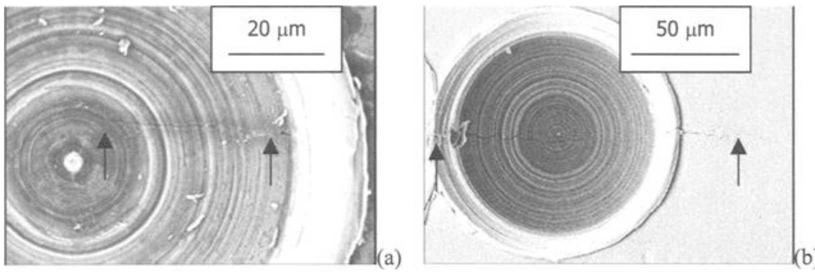

FIG. 2—*Non-propagating cracks on run-out specimens: a) a crack at the tip of a micro-hole; b) a small surface crack from a micro-notch [4].*

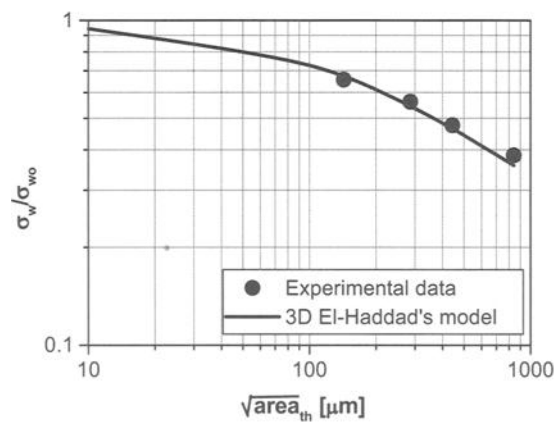

FIG. 3—*Relationship between fatigue limit and defect size: experimental data and comparison with 3D El-Haddad's model.*

Fatigue Crack Propagation and EPFM Model

The run-out micro-notched specimens were then subjected to a series of experiments for determining the short crack growth rate. In particular: i) crack growth rates were calculated from measurements of crack surface length obtained by means of plastic replicas; ii) the crack shape was determined interrupting the tests (Fig. 4*a*); and iii) the Stress Intensity Factor (SIF) was defined by Carpinteri's solutions [16]. Experimental results are summarized in Fig. 4*b*.

The data show a slight "short crack effect" (i.e., the data for the same stress ratio but at different stress levels do not fall onto the same curve), and they could be interpolated with an EPFM model [4] of the type:

$$da/dN = C \cdot \left(\Delta K^m - D^m\right) \tag{2}$$

where D represents the "mechanical threshold" (according to Miller's definition [6]), which has been determined by threshold experiments [4]. Particularly, since the experimental tests were carried out in the region of the Kitagawa diagram between the fatigue limit of smooth specimens and the LEFM region ($S < 0.3 \cdot \sigma_{wo}$ [6]), the threshold value $\sqrt{area_{th}}$ is a function of the applied stress range ΔS [4]:

$$\sqrt{\text{area}}_{th} = \sqrt{\text{area}}_{o}\left[\left(\frac{\Delta\sigma_{wo}}{\Delta S}\right)^{2} - 1\right] \tag{3}$$

and the mechanical threshold can then be computed by means of the well known Murakami's formulation for the SIF of surface defects [13]:

$$D(\Delta S) = 0.65 \cdot \Delta S \cdot \sqrt{\pi \cdot \sqrt{\text{area}}_{th}} \tag{4}$$

The D parameter in Eq 2 shows the observed short crack growth effect in the EPFM model. Furthermore, it is important to add that the D parameter increases with the defect size, and it tends to $\Delta K_{th,LC}$ for long cracks (Fig. 5).

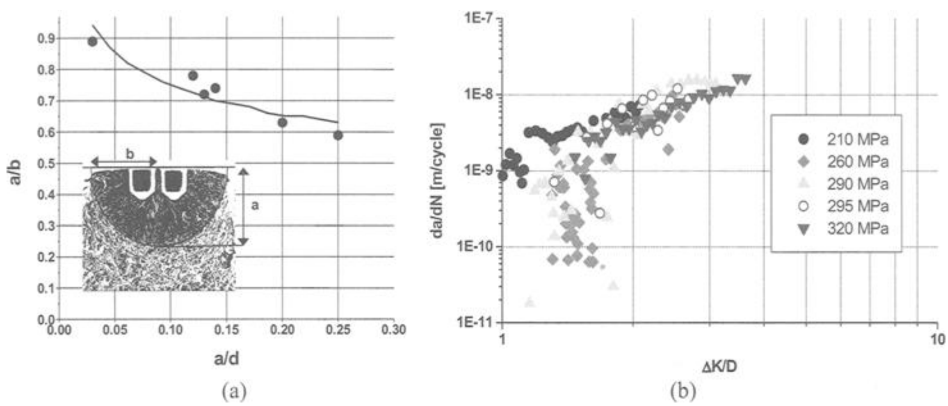

FIG. 4—*Summary of crack growth experiments on small cracks:* a) *shape of propagating cracks;* b) *crack growth data.*

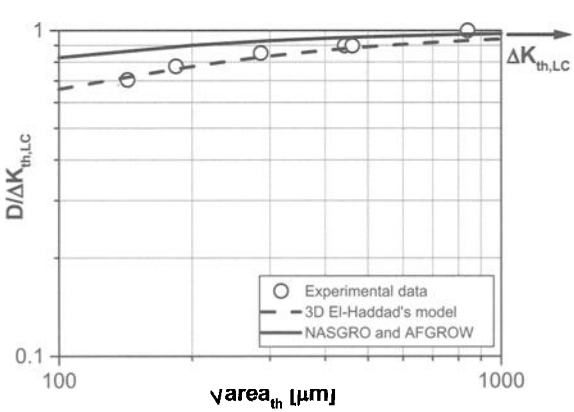

FIG. 5—*Significance of the mechanical threshold D.*

EPFM Model Validation by Full-Scale Tests

Other tests were carried out on full scale specimens, with minimum diameter of 140 mm, by means of a test rig with a capacity of 250 kNm. Tests were carried out at a nominal alternating stress of 210 MPa. Crack growth was tracked by measuring surface crack length via a microscope equipped with an image analyzer [4] (Fig. 6).

The EPFM crack growth model obtained on small scale specimen data, which incorporates the short crack effect, was successfully compared with experimental results obtained in the case of a small specimen subjected to high applied stress (Fig. 7*a*, where results were normalized with respect to $\Delta K_{th,LC}$ at $R = -1$). Furthermore, a good correlation can also be seen (Fig. 7*b*) between the model, a small specimen subjected to low applied stress and full-scale specimens: this means that there was no other scale effects in crack propagation experiments (in particular under the conditions: $a/d > 0.1$ and $S < 0.6\ \sigma_{wo}$) [4].

Fatigue Crack Propagation Algorithms

Different fatigue crack propagation algorithms for predicting life of cracked components are available in literature. In the present work, AFGROW v.4.0008.12.11 [7] and NASGRO v.3.0.21 [8] (derived from Newman's FASTRAN II [17]) will be considered together with the empirical EPFM model. AFGROW and NASGRO have been chosen because they are the reference algorithms for this type of analysis. Particularly, both of the considered FCG algorithms take into account the different effects on crack propagation rate in metallic materials (i.e., stress ratio and load interaction effects) by means of "plasticity-induced crack closure" [18].

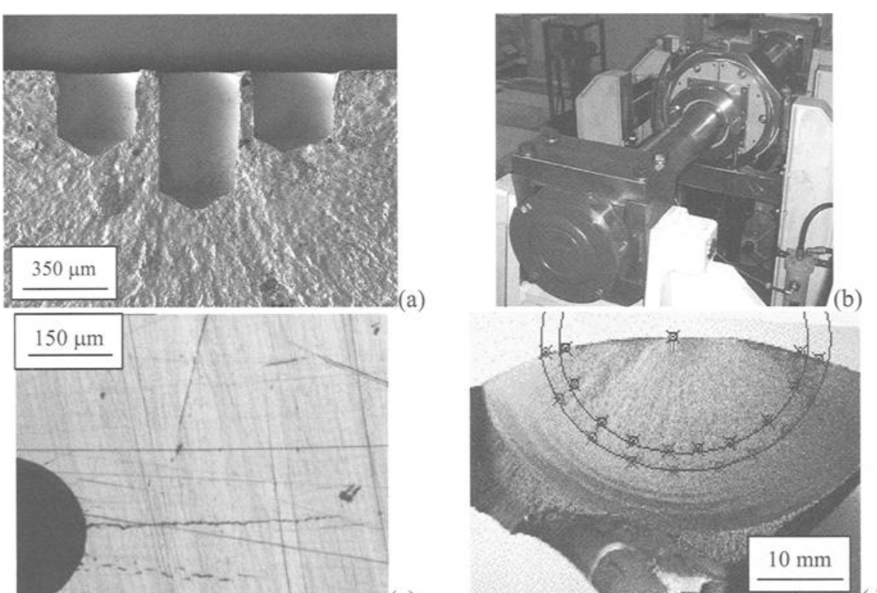

FIG. 6—*Details of full-scale experiments [4]:* a) *micro-holes on full-scale specimen;* b) *test rig;* c) *example of axle surface during a propagation test;* d) *analysis of crack shape evolution.*

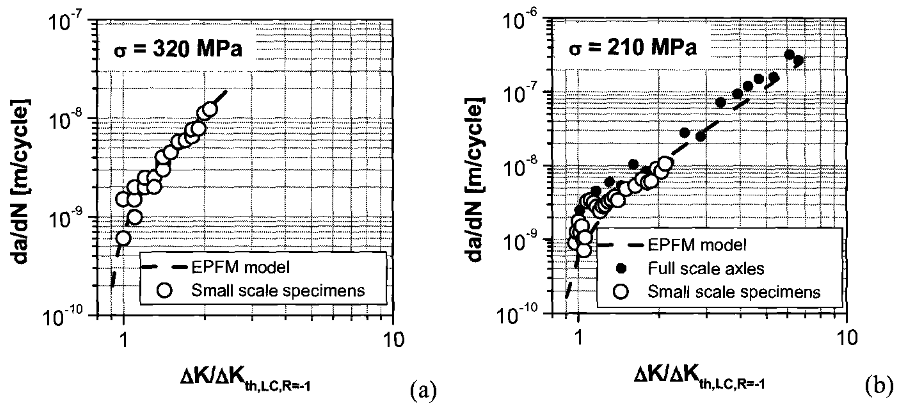

FIG. 7—*Propagation tests at $R = -1$:* a) *comparison between experimental data and EPFM model for high applied stress;* b) *same comparison for low applied stress.*

Paris-Based Algorithms

Both AFGROW and NASGRO let the user choose between different crack propagation law formulations. In this work only the "NASGRO equation" [7,8] will be considered:

$$\frac{da}{dN} = C\left[\left(\frac{1-f}{1-R}\right)\Delta K\right]^{n} \frac{\left(1-\dfrac{\Delta K_{th}}{\Delta K}\right)^{p}}{\left(1-\dfrac{K_{max}}{K_{crit}}\right)^{q}} \tag{5}$$

Equation 5 is a development of the classical Forman's formulation and incorporates all the important regions of propagation curves (from threshold to K_{crit}). The most important parameter is "f" (called "Newman's closure function" [8]), representing the closure effect. This parameter depends on the constraint factor "α," on the ratio between the maximum applied stress and the yield stress, and on the stress ratio.

In order to introduce the dependence of thresholds on the crack size and stress ratio, the ΔK_{th} parameter included in Eq 5 has been described by the expression [7,8]:

$$\Delta K_{th} = \Delta K_{o} \cdot \frac{\sqrt{\dfrac{a}{a+a_{o}}}}{\left[\dfrac{1-f}{(1-A_{o})(1-R)}\right]^{(1+C_{th}R)}} \tag{6}$$

where R is the stress ratio, f is the Newman's closure function, A_o is a constant used in the formulation of f, ΔK_o is the threshold SIF range at $R = 0$, C_{th} is an empirical constant, a is the crack length, and a_o is the El-Haddad's parameter in terms of crack length. The dependence of $\Delta K_{th,LC}$ on stress ratio is controlled by the parameter C_{th}; different values of C_{th} have to be considered for positive and negative R values. For the versions of AFGROW and NASGRO considered here, the El-Haddad's parameter a_o has a fixed value equal to 38.1 μm, while the value corresponding to $\sqrt{area_o}$ = 130 μm is 88 μm (assuming a semicircular crack); the effect of the fixed a_o on ΔK_{th} is shown Fig. 5.

Strip-Yield Models

More advanced models for crack propagation are based on the Strip-Yield model originally proposed by Newman [19]. NASGRO contains a module implementing this kind of model.

The starting point for these models is the determination of the crack surface displacements and of the plastic zone dimension by the Dugdale model. The propagation is then simulated by cyclic loading so that the plastic wake is generated. Eventually, the plastic wake allows the determination of opening load by means of equilibrium and compatibility of all the elements forming the crack and the elastic continuum in which it is inserted. The major feature of Strip-Yield models is the ability to calculate S_{op} under variable amplitude loading.

The drawback of these models is the need to finely tune the constraint factor formulations by means of propagation data. It has been shown that formulations valid for Al alloys are inadequate for predictions on mild steels and stress ratios below zero [20].

Fatigue Crack Propagation Tests on 30NiCrMoV12 Steel

Constant amplitude tests for characterizing propagation behavior of 30NiCrMoV12 steel were carried out on CT, M(T), and SE(B) specimens (Fig. 8*a*) at stress ratios R = –1, R = –0.5, R = 0, R = 0.3, and R = 0.7 following the ASTM E 647-00 "Standard test method for measurement of fatigue crack growth rates." On most of the specimens, the "ΔK-decreasing" technique proposed in ASTM E 647-00 was also applied in order to determine the propagation threshold at different stress ratios. The crack growth rate chosen to define the threshold value was 10^{-10} m/cycle.

In the case of tests at $R \geq 0$, CT and M(T) specimens were loaded by means of a SCHENCK Hydropuls facility, a uni-axial servo-hydraulic machine with a maximum nominal load equal to 250 kN. The tests frequency was 15 Hz. In the case of tests at $R < 0$ on SE(B) specimens, the test system was formed by a crack gage glued onto the specimen (Fig. 8*b*), a RUMUL Fractomat® control unit, and a resonant bending machine with a capacity of 160 Nm. The test frequency was 120 Hz.

The comparison of all of the obtained crack growth curves, normalized with respect to $\Delta K_{th,LC}$ at R = –1, is shown in Fig. 9*a*. The ΔK_{th} versus R relationship was obtained by fitting experimental data by means of Eq 6 (see Fig. 9*b*).

Comparative Application of FCG Algorithms

Application to an M(T) Specimen at R = –1

On the basis of the propagation data obtained on the specimens, it has been possible to apply the different FCG algorithms previously described for estimating the crack growth rate at R = –1. In particular, a first analysis was carried out considering a center cracked panel (W = 200 mm, B = 20 mm), with an initial crack a_i = 0.25 mm subjected to a 210 MPa alternating stress.

Results, normalized with respect to $\Delta K_{th,LC}$ at R = –1, are shown in Fig. 10; it can be clearly seen that all the considered algorithms are very close to experimental data.

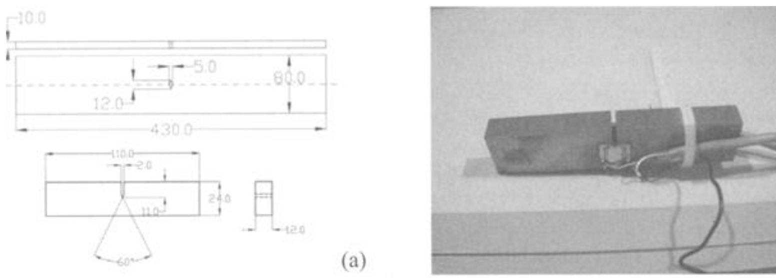

FIG. 8—*Details of fatigue crack growth experiments:* a) *M(T) and SE(B) specimens;* b) *SE(B) specimen equipped with a crack gage.*

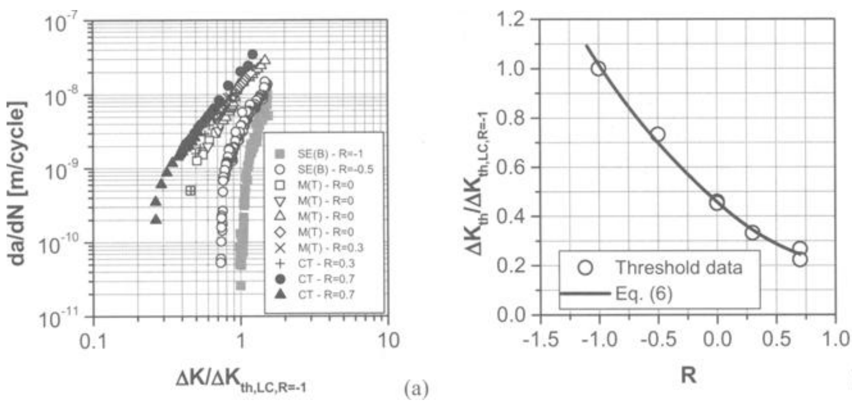

FIG. 9—*Results of fatigue crack growth experiments:* a) *obtained crack growth data;* b) *ΔK_{th} versus stress ratio.*

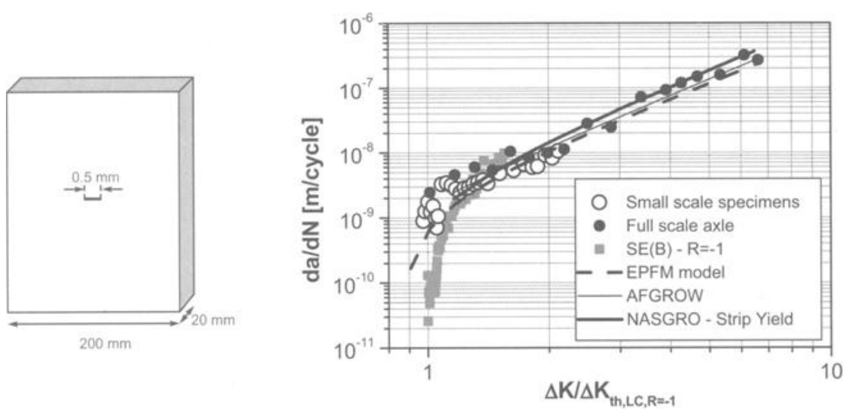

FIG. 10—*Comparisons of different FCG algorithms on a M(T) specimen (W = 200 mm, B = 20 mm, a_i = 0.25 mm) at R = –1.*

Application to an Axle Subjected to Plane Bending

The second analysis was carried out considering a 140 mm solid round bar containing a penny shaped crack of initial depth $a_i = 1$ mm loaded by an alternating plane bending stress of ±210 MPa (both AFGROW and NASGRO do not consider rotating bending).

Results, in terms of crack depth against cycles, are shown in Fig. 11*a*; the estimates are similar for the considered FCG algorithms. In addition, it should be mentioned that the predicted evolution of crack shape (which can be directly output by NASGRO) is not too far from the experimental results at $R = -1$ (Fig. 11*b*), thus suggesting that for smooth bars the crack propagation under rotating bending can be reasonably approximated with plane bending.

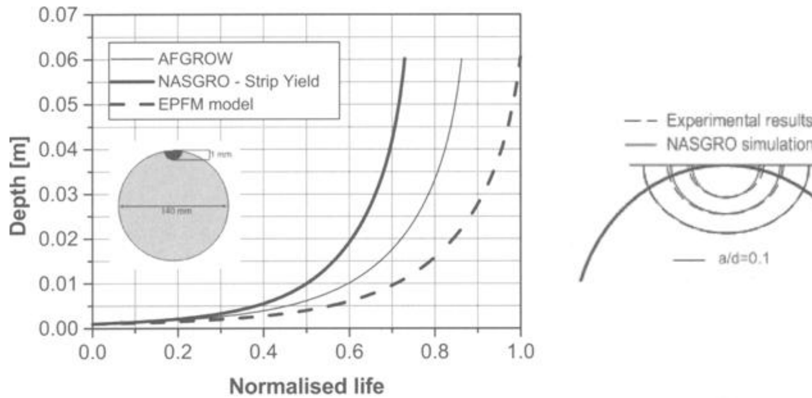

(a) (b)

FIG. 11—*Comparative applications of FCG algorithms to a solid round bar ($d = 140$ mm, $a_i = 1$ mm) subjected to a 210 MPa alternating stress under plane bending:* a) *a-N curves;* b) *crack shapes.*

Application to an Axle Subjected to Spectrum Loading

The application of fatigue crack growth tools to real components should consider the application of random loads. On the basis of a simple load spectrum derived from experimental results on a high speed train [10] (Fig. 12*a*) and normalized to a maximum stress of 210 MPa, a simple block loading consisting of nine blocks was derived (Fig. 12*b*). The so defined block loading is 6 % more damaging than the original spectrum; this entity of error is commonly accepted during the discretization of real load spectra [21].

Results show that there is little difference between the Strip-Yield model adopted by NASGRO and the AFGROW algorithm (Fig. 13), which is otherwise based on the concept of a "perturbation" of S_{op} at different load blocks [7].

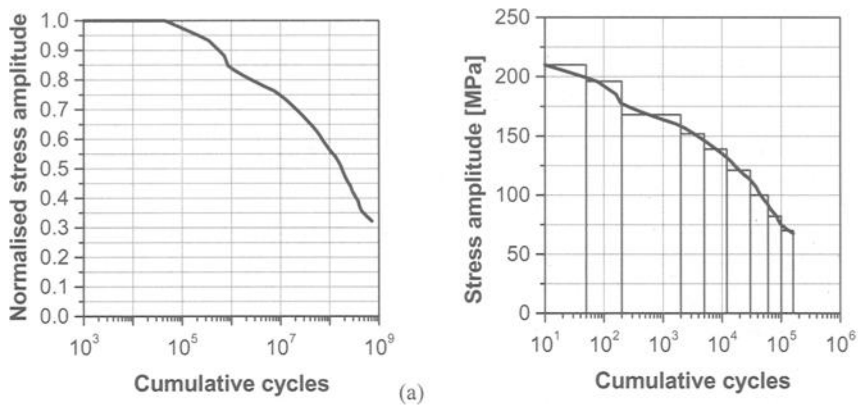

FIG. 12—*Stress spectra:* a) *normalized cumulative stress spectrum corresponding to 10^7 km onto Italian railway lines [10];* b) *truncated and amplified spectrum for 2200 km.*

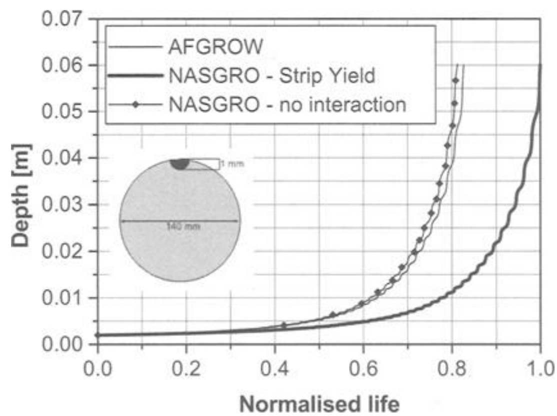

FIG. 13—*Comparative application onto a 140 mm axle subjected to plane bending and block loading (d = 140 mm, a_i = 1 mm).*

Comparison with Variable Amplitude Tests at R = –1

The most remarkable point of Fig. 13 is that predictions without considering load interaction effects seem very close and comparable to those obtained considering this effect. In order to check the correctness of this observation, we made a comparison between FCG predictions and a set of experimental tests [22] carried out on micro-notched specimens survived to previous fatigue limit tests. In the first test, the spectrum shown in Fig. 12*b* had been applied to an hourglass shaped specimen with a gauge diameter d = 10 mm and a starting micro-notch equal to $\sqrt{area}$ = 840 μm. Figure 14 shows the non-propagating crack before and after a number of spectrum blocks corresponding to 10^7 km of service; crack growth is less than 20 μm. It is then possible to conclude that fatigue thresholds are not altered by spectrum loads – both AFGROW and NASGRO predict no growth under the spectrum.

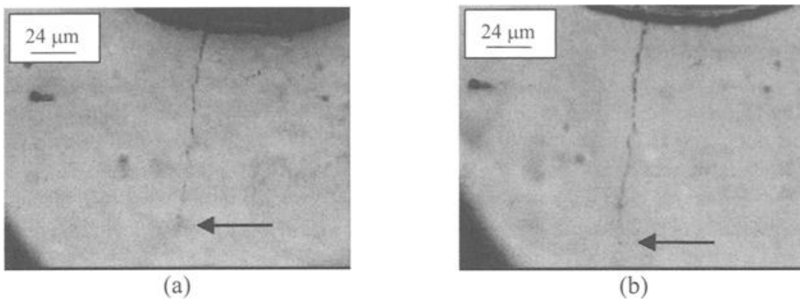

FIG. 14—*Effect of spectrum loads on fatigue thresholds:* a) *initial crack emanating from a micro-hole;* b) *crack length after cycles corresponding to 10^7 km (d = 10 mm, a_i = 750 μm) [22].*

The second series of experiments [22] dealt with a specimen similar to the one shown in Fig. 14, but with a micro-notch corresponding to $\sqrt{\text{area}}$ = 260 μm. Hi-Low blocks characterized by S_H = 320 MPa and S_L = 260 MPa were applied, and crack growth was measured by plastic replicas. The comparison between experimental data, the EPFM model (no interaction), AFGROW, and NASGRO predictions is shown in Fig. 15.

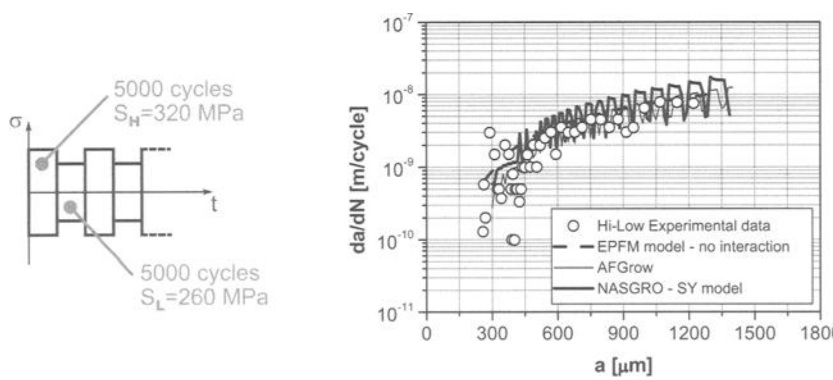

FIG. 15—*Analysis of crack growth experiments under block loading (d = 10 mm, a_i = 300 μm).*

As it can be seen, the prediction carried out by means of the constant amplitude EPFM model is very similar to the experimental fatigue crack growth data obtained under block loading and to AFGROW and NASGRO predictions. This means that the load interaction effects during propagation are negligible for the considered material.

The difference between block loading and constant amplitude growth is, however, expected to increase in a real spectrum with a high variability of applied stresses and fluctuations above and below the thresholds.

Concluding Remarks

This paper compares an EPFM model and two widely used FCG software (namely AFGROW and NASGRO) with a set of propagation data obtained on small and full-scale specimens made of 30NiCrMoV12 steel used for the construction of railway axles. Results can be summarized as follows:

- FCG algorithms could predict experimental results at R = –1 of long and short cracks both for stress levels below $0.3\cdot\sigma_{wo}$ (LEFM region) and for the range $0.3\cdot\sigma_{wo} < S < 0.6\cdot\sigma_{wo}$ (EPFM region).
- Comparative application of FCG algorithms to a block loading shows little load interaction effect and agrees with experimental results.
- Present results support future application of FCG models to crack growth prediction for railway axles made of high strength steel under service spectrum.

Acknowledgments

The authors wish to thank Lucchini Sidermeccanica S.p.A., especially Dr. A. Ghidini, for permission to publish the results presented here and for their useful suggestions.

References

[1] Timoshenko, S. P., *History of Strength of Materials*, Dover Publications Inc., New York.
[2] *European Standard prEN 13104*, C.E.N. European Committee for Standardization, Brussels, 1999.
[3] Smith, R. A., "Fatigue of Railway Axles: A Classic Problem Revisited," In: *Fracture Mechanics: Applications and Challenges*, M. Fuentes, M. Elices, A. Martin-Meizoso, and J. M. Martinez-Esnaola, Eds., Elsevier, 2000, pp. 173–181.
[4] Beretta, S., Ghidini, A., and Lombardo, F., "Fracture Mechanics and Scale-Effects in the Fatigue of Railway Axles," *Engineering Fracture Mechanics*, Vol. 72, 2005, pp. 195–208.
[5] Smith, R. A. and Hillmansen, S., "Monitoring Fatigue in Railway Axles," *Proceedings of the 13th Int. Wheelset Congress*, Rome, Italy, 2001.
[6] Miller, K. J., "Materials Science Perspective of Metal Fatigue Resistance," *Materials Science and Technology*, Vol. 9, 1993, pp. 453–462.
[7] Harter, J. A., "AFGROW Users Guide and Technical Manual," *AFRL-VA-WP-TR-2002-XXXX*, U.S. Air Force Research Laboratory Technical Report, 2002.
[8] Anon., "Fatigue Crack Growth Computer Program 'NASGRO' version 3.0 – Reference Manual," *JSC-22267B*, NASA Technical Report, 2001.
[9] Fischer, G., Grubisic, V., and Widmayer, H., "Fatigue Tests on Wheelset under Simulated Service Stress Spectra," *Proceedings of the 9th Int. Wheelset Congress*, Montreal, 1988, pp. 3.2.1–3.2.13.
[10] Cantini, S. and Ghidini, A., *Technical Report #R15/2003*, Lucchini Sidermeccanica S.p.A., Lovere, Italy, 2003.
[11] *UNI 6787-71*, "Assi fucinati di acciaio speciale legato, bonificati, ad elevate caratteristiche di fatica e di tenacità per sale montate di rotabili ferroviari. Qualità, prescrizioni e prove," Ente Nazionale Italiano di Unificazione, 1971.
[12] Murakami, Y., "Analysis of Stress Intensity Factors of Mode I, II and III for Inclined Surface Cracks of Arbitrary Shape," *Engineering Fracture Mechanics*, Vol. 22, 1985, pp. 101–104.
[13] Murakami, Y. and Endo, M., "Effects of Hardness and Crack Geometries on ΔK_{th} of Small

Cracks Emanating from Small Defects," In: *The Behaviour of Short Fatigue Cracks*, K. J. Miller and E. R. De Los Rios, Eds., MEP, London, 1986.

[14] El-Haddad, M. H., Smith, K. N., and Topper, T. H., " Fatigue Crack Propagation of Short Crack," *J. Eng. Mater. Tech., ASME Trans.*, Vol. 101, 1979, pp. 42–46.

[15] Beretta, S., "Propagation of Short Cracks in a High Strength Steel for Railway Axles," *Proceedings of the 14th European Conference on Fracture*, Krakow, Poland, 2002.

[16] Carpinteri, A. and Brighenti, R., "Part-Through Cracks in Round Bars under Cyclic Combined Axial and Bending Loading," *International Journal of Fatigue*, Vol. 18, 1996, pp. 33–39.

[17] Newman, Jr., J. C., "FASTRAN II: A Fatigue Crack Growth Structural Analysis Program," *NASA Technical Memorandum 104159*, Langley Research Center, Hampton, VA, 1992.

[18] Elber, W., "The Significance of Fatigue Crack Closure," In: *Damage Tolerance in Aircraft Structure*, ASTM STP 486, ASTM International, West Conshohocken, PA, 1971, pp. 230–242.

[19] Newman, Jr., J. C., "A Crack Closure Model for Predicting Fatigue Crack Growth under Aircraft Spectrum Loading," In: *Methods and Models for Predicting Fatigue Crack Growth under Random Loading, ASTM STP 784*, ASTM International, West Conshohocken, PA, 1981, pp. 53–84.

[20] Beretta, S., Carboni, M., Machniewicz, T., and Skorupa, M., "Correlation Between Experiments and Strip Yield Model Results on Fatigue Crack Growth in Structural Steel," *Proceedings of the 14th European Conference on Fracture*, Krakow, Poland, 2002.

[21] Grubišic, V., "Criteria and Methodology for Lightweight Design of Vehicle Components," *Technical Report #TB-176*, Fraunhofer Institut für Betriebsfestigkeit (LBF), Darmstadt, Germany, 1986.

[22] Beretta, S., "Propagation of Short Cracks in Railway Axles under Spectrum Loading," *Research Contract #18/00 Final Report*, Politecnico di Milano, Dipartimento di Meccanica, Milan, Italy, 2000.

SESSION 6B: EXPERIMENTAL METHODS II

Journal of ASTM International, January 2005, Vol. 2, No. 1
Paper ID JAI12022
Available online at www.astm.org

J. A. Joyce,[1] *R. E. Link,*[2] *and J. Gaies*[3]

Evaluation of the Effect of Biaxial Loading on the T_0 Reference Temperature Using a Cruciform Specimen Geometry

ABSTRACT: A series of 12 cruciform geometry fracture toughness specimens has recently been tested using A533B base plate obtained from the decommissioned Shoreham plant pressure vessel. Specimens were tested at −100°C, placing them in the lower ductile to brittle transition of this ferritic structural steel. The overall objective of this work is to compare the results of these biaxial cruciform tests to the results of standard and shallow crack fracture toughness tests to assess the effect of biaxial loading on the measured master curve and the T_0 reference temperature as defined by ASTM E 1921. Previous work done at Oak Ridge National Laboratory (ORNL) appeared to demonstrate an increase in the T_0 reference temperature due to the presence of the biaxial stress field established in the cruciform test geometry. Because of the cost of the ORNL tests, only a few specimens could be run, and full statistical support of the "biaxial effect" could not be demonstrated. A second goal is to demonstrate that smaller size specimens, and hence lower cost tests, can be used to evaluate the magnitude of the biaxial effect in nuclear reactor pressure vessel materials. This report presents a brief overview of the test procedure, presents the test results, and compares the results to the database available on standard and shallow crack fracture toughness results available for the Shoreham plate material.

KEYWORDS: J-integral, elastic-plastic fracture, bi-axial loading, ductile to brittle transition, Master Curve, T_0 reference temperature

Introduction

The Master Curve introduced by Wallin and co-workers [1–3] has become accepted for characterizing the fracture toughness transition of ferritic steels. ASTM has recently passed a new standard, E 1921, that prescribes a methodology to measure the Master Curve index temperature T_0 based on as few as six replicate fracture tests [4]. This procedure has the potential for characterizing the entire ductile to brittle transition from tests on surveillance capsule Charpy size specimens, and for this reason it has become very important to the commercial nuclear power industry. The small size of these specimens has caused concern as to whether the resulting T_0 is accurate for applications involving large cross-sections, shallow crack geometries, and biaxial loading.

A series of large (102 × 102 mm or 153 × 153 mm cross-section by 0.91 m square span) cruciform specimens has been tested by Oak Ridge National Laboratory (ORNL) [5,6], which seems to demonstrate an effect of the biaxial loading on the Master Curve reference temperature, T_0. Specifically, the T_0 of shallow crack specimens increased in the presence of biaxial loading, and the scatter in the toughness was reduced. The biaxial loading effect offset the reduction in

Manuscript received 24 November 2003; accepted for publication 12 March 2004; published January 2005.
Presented at ASTM Symposium on Fatigue and Fracture Mechanics: 34th Volume on 19–21 November 2003 in Tampa, FL; S.R. Daniewicz, J.C. Newman, Jr., and K-H. Schwalbe, Guest Editors.
[1] Professor, United States Naval Academy, Annapolis, MD 21402.
[2] Associate Professor, United States Naval Academy, Annapolis, MD 21402.
[3] Research Engineer, Naval Surface Warfare Center, Carderock Division, West Bethesda, MD 20817.

T_o normally attributed to a loss of constraint in shallow cracked specimens. Because of the complexity and the large cost of these tests, too few large cruciform specimens have been tested to give full statistical support to the concept of a "biaxial effect."

In this program, smaller specimens have been utilized to dramatically reduce the cost of specimen preparation and testing so that the reference temperature can be obtained in the spirit of ASTM E 1921. The lower cost and easier test methodology allow more specimens to be tested, resulting in a better statistical characterization of the ductile to brittle transition. Basically 1T plan, 50.8 mm (2 in.) thick cross-sections were used for the cruciform geometry, giving a basic specimen configuration of about 230 mm (9 in.) square. This specimen was then loaded in biaxial bending using a dual 203 mm (8 in.) bend span fixture. The bend fixture was made to accommodate a range of bend spans in each direction, but for the first set of 12 tests, a 203 × 203 mm bend span arrangement was used. Most other features of the ORNL design have been kept, including the stress control grooves and the shallow crack with a/W = 0.12. In the following sections the specimen geometry is described in more detail, the precracking and testing plans are outlined, and a preliminary 3-D finite element analysis is described briefly. In subsequent sections, the results of 12 tests are presented and compared to existing ductile to brittle transition data available for this alloy.

Description of Experiments

The cruciform specimen geometry is shown in the photograph in Fig. 1. Specimens were machined from the center 100 mm of the 150 mm thick Shoreham plate with the crack in the L-S orientation. The full geometry was cut using a wire EDM machine including the stress control slots. The crack starter notch was introduced using a plunge EDM process. The machined notch depth gives a/W = 0.07, and the expected test crack depth after fatigue sharpening is a/W = 0.11–0.12. To test these specimens in biaxial loading, a simple 5-point bend apparatus was constructed, shown in Fig. 2. The rollers were made adjustable at all four supports so that bend spans could be adjusted from 178–229 mm, though in this study 203 mm (8-in.) spans were used for both bend components. With two rollers removed, the fixture can be used for uniaxial loading of the test samples. Prior to specimen precracking, a single reverse four-point bend loading was applied to each specimen to facilitate initiating the fatigue crack that was used to sharpen the shallow notch. The load used is based on standard E 399 LEFM calculations for a 1T SE(B) geometry with a/W = 0.07 and W = B = 50.8 mm. Some insight obtained from the 3-D finite elements described below was also used to develop this load. The objective is to obtain a reverse plastic zone of approximately 0.5 mm. The subsequent fatigue crack growth of 1.2 mm will extend well through the initial reverse plastic zone. This procedure has been found to work well in shallow crack standard SE(B) geometries[7].

Fatigue precracking was done in a 250 kN servohydraulic machine using standard compliance procedures. This loading was done using uniaxial 3-point bending with a "ring gage" inserted in the crack mouth to measure the crack mouth opening displacement. This procedure has been used for several years to develop shallow crack fracture toughness specimens, and the procedure is presently in a draft annex format for possible inclusion in ASTM E 1820. The ring gage is mounted on integral 90° edges machined into the specimen across the crack mouth with an initial gage length of 0.5 mm. This allows the ring gage to measure the crack mouth opening displacement right at the specimen surface with a very small modification of the specimen geometry.

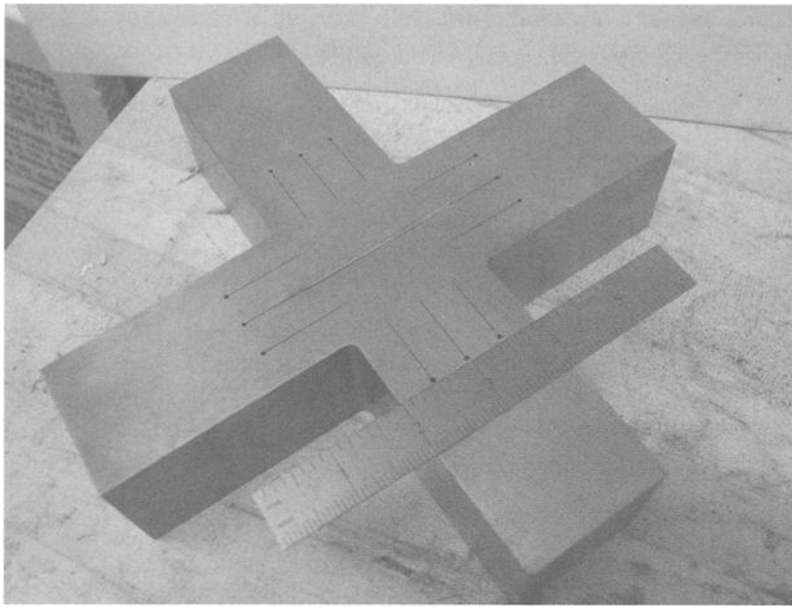

FIG. 1—*Cruciform specimen with size scale (in inches).*

FIG. 2—*Cruciform specimen in test machine with loading ram in place.*

Precracking was done at room temperature. The finite element analysis showed that for cracks with a/W on the order of 0.1, the standard SE(B) compliance equations of E 1820 could be used to estimate the crack depth during elastic loading or cycling. As the crack extended to a/W = 0.125, the standard compliance equations would underestimate the crack length as the side extensions on the cruciform specimen came into play, effectively stiffening the specimen. Target precrack lengths were kept short so that the extra stiffness provided by the specimen side extensions would not result in excessively long initial precracks.

Specimens were tested at –100°C, enclosed in a lab-built environmental chamber cooled by a liquid nitrogen spray system. Ten self-adhesive thermocouples were mounted at various locations on the fixtures and specimen and were used to measure the temperature distribution of the specimen as mounted in the environmental chamber. Thermocouples were adhered on both the upper and lower surfaces and along the edges of the loading arms near the center test region. Temperature uniformity was checked over a range of temperatures at which it is expected that fracture tests will later be conducted, namely at temperatures from –40°C to –110°C. In each case, it was found that the specimen could be maintained at a uniform temperature within ±2°C as required by ASTM E 1921.

Analysis

The cruciform specimens were modeled using finite element analysis to predict the deformation behavior and the crack driving force as a function of applied loading. One quarter-symmetric, three-dimensional models of the specimen were developed for several crack lengths. The general purpose finite element code, ABAQUS, was used to perform all analyses.

The specimens were modeled with a combination of twenty-node bricks and ten-node tetrahedral elements. The crack tip was modeled with a keyhole-style blunt notch with a root radius of 0.025 mm (0.001 in.). Focused elements were used to capture the high stress and strain gradients in the near crack tip region. There were 12 rings of elements distributed along the crack front to account for variations of the crack tip stress and strain fields parallel to the crack front. A typical mesh shown in Fig. 3 had 15 000 elements and 124 000 degrees of freedom. The analysis incorporated elastic-plastic material response, large strain geometric nonlinearity, and modeling of the contact region where the loading tip contacted the specimen.

A piecewise linear, elastic-plastic material model was used for the analyses. The stress-strain curve for the Shoreham A533B steel plate at –100°C shown in Fig. 4 was estimated by interpolating between experimental stress strain curves measured at –80°C and –120°C.

Uniaxial Loading

Uniaxial loading was used to model the fatigue precracking conditions. Models with crack length ratios, a/W = 0.09 and 0.125, were used to determine the specimen compliance and the stress intensity factor. Only the results from the first load step of the analysis, which remained elastic, were used to determine the specimen compliance.

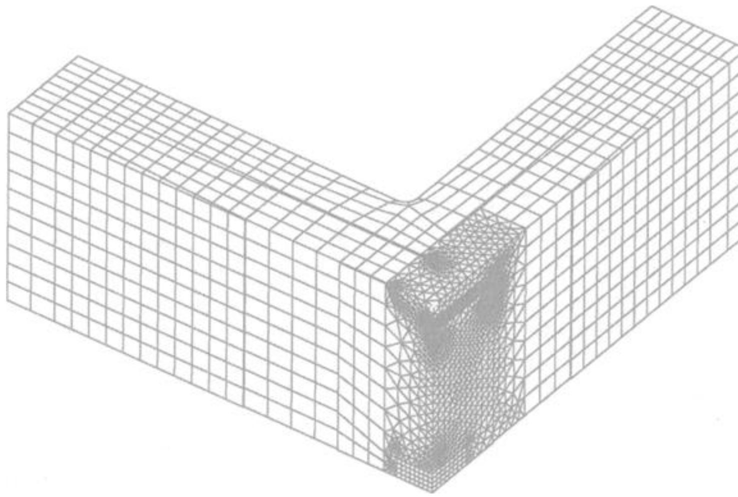

FIG.3—*Quarter-symmetric finite element model of the cruciform specimen geometry.*

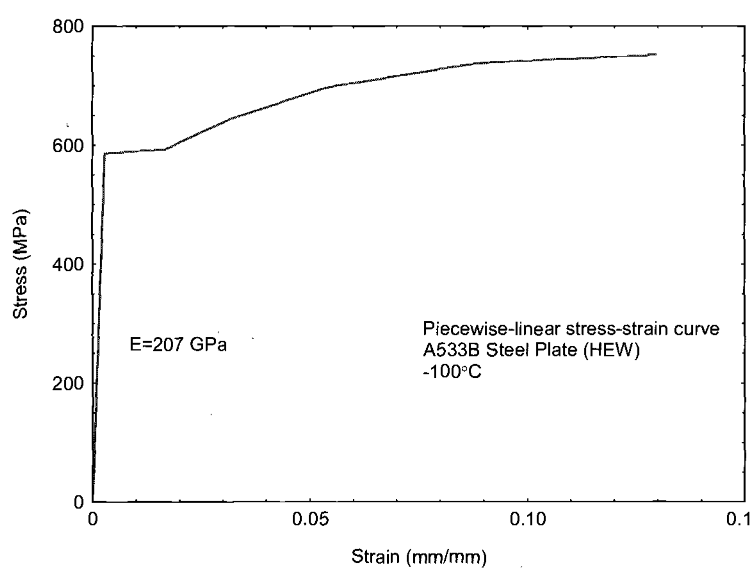

FIG. 4—*Stress-strain curve for A533B steel plate (HEW) at –100°C used in finite element analysis.*

Crack length was related to compliance using the relationships that:

$$\frac{a}{W} = -1.8617\,u + 0.8123 \tag{1}$$

$$u = \frac{1}{\left[\dfrac{BWEC}{S/4}\right]^{1/2} + 1} \tag{2}$$

These equations utilize a linear fit to the numerical crack opening displacement compliance results at a/W = 0.09 and 0.125. A comparison of a/W versus compliance for FE results and standard SE(B) compliance expressions is presented in Table 1. The standard ASTM E 1820 SE(B) compliance expression underestimates the crack length of the cruciform specimen for a given compliance. This is due to the increased stiffness of the cruciform specimen resulting from the transverse loading arms.

Stress intensity factor calculations (at mid-plane) also show that the presence of the cruciform specimen arms results in a lower stress intensity factor at the specimen centerline than that predicted for the standard SE(B) specimen geometry. These results are shown in Table 2.

TABLE 1—*Comparison of compliance results for a standard SE(B) geometry and the uniaxially loaded cruciform specimen.*

a/W	Compliance mm/N	u (see Eq 2)	a/W (FE)	a/W (SE(B))	% diff.
0.090	2.68×10^{-7}	0.3880	0.090	0.076	−15
0.125	3.14×10^{-7}	0.3692	0.125	0.088	−30

TABLE 2—*Comparison of stress intensities at the specimen centerline for the SE(B) and cruciform specimen.*

a/W	f(a/W) FE	f(a/W) SE(B)	% diff.
0.09	0.7085	0.8075	12
0.125	0.7502	0.935	20

Biaxial Analyses

A full elastic-plastic analysis of the biaxial specimen with a/W = 0.112 and contact conditions at the load point was run on the model in Fig. 3 using ABAQUS. The analysis was used to determine the crack driving force, K_J, as a function of crack mouth opening displacement, to determine suitable locations on the specimen for attaching strain gages, and to predict the evolution of plasticity in the specimen.

The predicted load versus crack mouth opening displacement (CMOD) for the biaxial specimen is plotted in Fig. 5. The CMOD is reported at three locations along the crack mouth – at the mid-plane, at the end of the crack, and midway between these points. The CMOD is nearly constant over the center 50 % of the crack front and falls slightly lower toward the end of the crack as expected due to the extra stiffness of the transverse loading arm.

The strains at a position near mid-span of the loading arms are plotted in Fig. 6. The strains are greater on the transverse arm than on the opening arms. The ratio of transverse tensile strains to the opening tensile strain is approximately 1.1:1, and the ratio of compressive strains is about

1.05:1. The support reaction forces and bending moments in the loading arms are another way of characterizing the biaxiality ratio, and the ratio of transverse to opening bending moment was about 1.1:1.

The crack driving force at the mid-plane of the specimen, expressed in terms of J and K_J as a function of the mid-plane CMOD, is presented in Fig. 7. For this analysis, The J-integrals were calculated by the ABAQUS finite element code using the domain integral method and converted to K_J from the relationship:

$$K_J = \sqrt{J \times E/(1-\upsilon^2)} \tag{3}$$

The variation of driving force along the crack front, J(z)/J(z = 0), is plotted in Fig. 8. The crack driving force is very uniform over the center 75 % of the crack front. As the slot is approached, the driving force increases by up to 20 % (in terms of J, or about 10 % in terms of K_J) and then falls off dramatically. This is due in part to shielding of the slot-crack region by the adjacent slots in the transverse arm. There is considerable plasticity at the adjacent slots that may be redistributing the stresses away from the end of the crack and leading to a concentration where the shielding breaks down. The J distribution along the crack front is similar to that noted by Nevalainen and Dodds [8] in an analysis of a side-grooved C(T) specimen, which produced a concentrated peak in the local J as the side-groove root was approached and then fell off. The accuracy of the predicted J distribution in the vicinity of the slot, z> $0.9(B_{net}/2)$ is questionable because of the complex stress state that develops where the crack intersects the slot geometry.

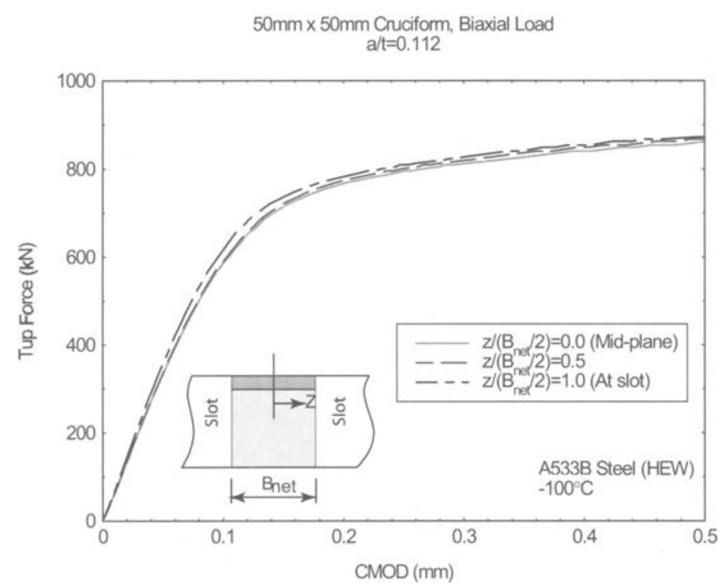

FIG. 5—*The predicted tup force versus crack mouth opening displacement at several locations along the crack mouth for the biaxially-loaded cruciform specimen.*

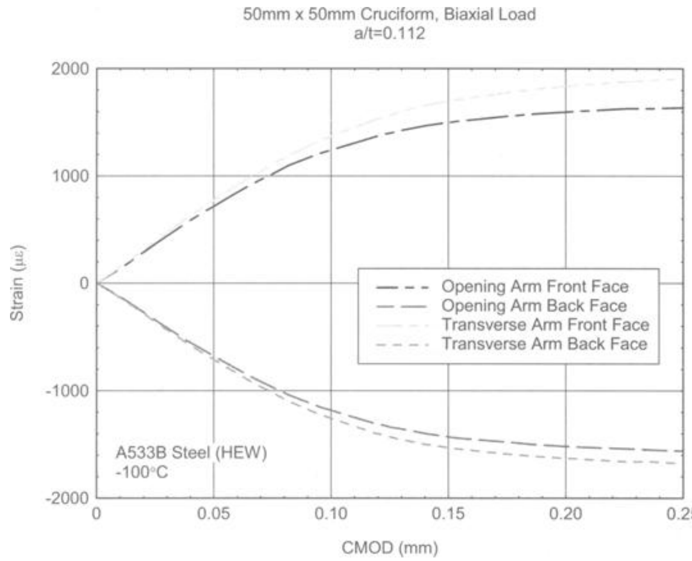

FIG. 6—*Predicted strains approximately mid-span along the cruciform specimen loading arms.*

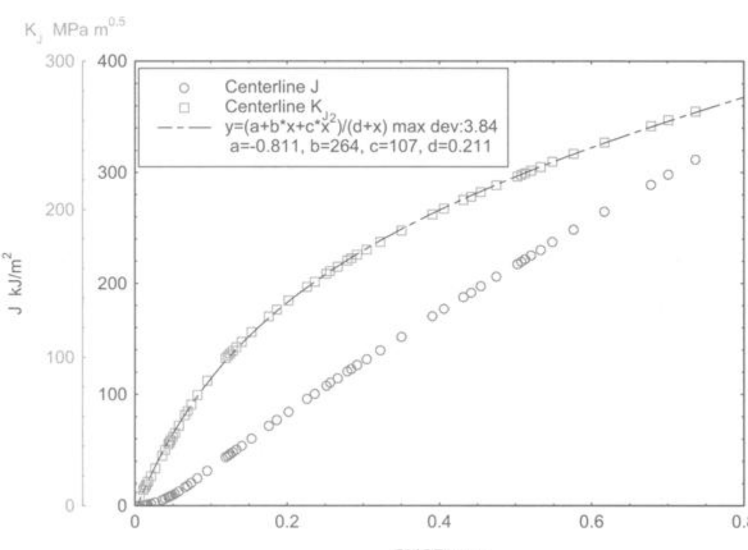

FIG. 7—*J and K_J along the specimen mid-plane as a function of CMOD for the biaxially-loaded cruciform specimen.*

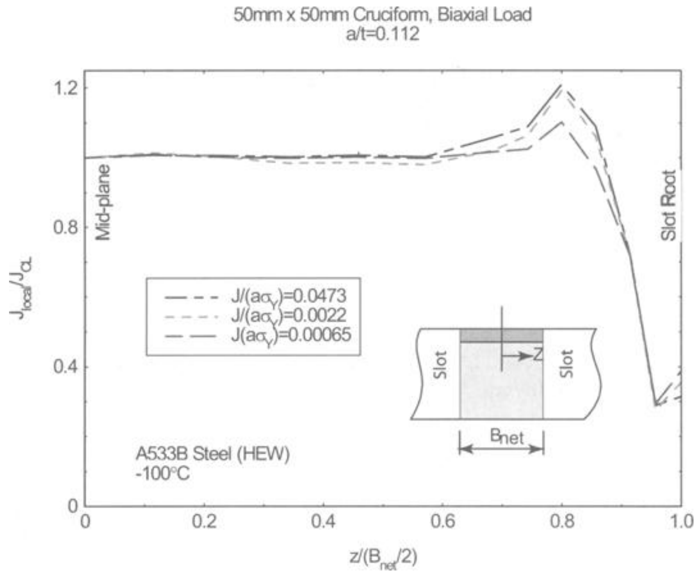

FIG. 8—*Normalized variation of crack driving force along the crack front for the biaxially-loaded cruciform specimen.*

The exact details of the stress distribution near the slot are not expected to be of great significance as long as the cleavage initiates well away from the slot root. Despite the variation in J along the crack front, the fatigue precracks remained remarkably straight, as shown in Fig. 9, with only a slight indication of accelerated crack growth near the root of the stress control slot.

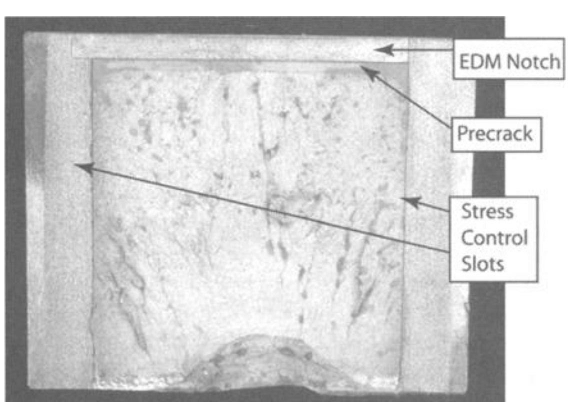

FIG. 9—*Fracture surface showing the fatigue precrack geometry.*

The evolution of plasticity in the vicinity of the crack was monitored to determine when the plastic zones extend from the crack tip to the specimen boundary. The crack-tip plastic zone reaches the plastic zone from the loading tup at a CMOD = 0.15 mm. By the time the CMOD increases to 0.2 mm, the crack-tip plastic zone boundary extends back to the front surface of the specimen, and the test section is fully yielded. Calculations of the crack tip-constraint characterizing parameters such as the T-stress [9] or Q [10] may prove useful in interpreting the experimental results but were not performed as part of this analysis.

Experimental Testing

Selection of the Test Temperature

Considerable ductile to brittle transition data are available on the Shoreham vessel material. Work by Tregoning and Joyce [11–13] has shown that this material has a high upper shelf toughness and has very uniform fracture toughness and tensile properties. The Master Curve reference temperature depends quite dramatically on specimen geometry [12], being approximately –77°C for the C(T) geometry, –92°C for the deep crack SE(B) geometry, and –118°C for the shallow crack SE(B) geometry with a/W = 0.1–0.15. The results for the deep crack SE(B) specimen were verified by the thesis work of Rathbun [14] for a wide range of B, W, and b specimen dimensions. The objective here is to test near the expected T_o temperature, so it was decided to use a test temperature of –100°C for this series of cruciform specimens. These specimens are shallow cracked, with a/W = 0.1–0.112, but they have the additional "constraint" possibly gained from the bi-axial loading. Several sets of deep crack and shallow crack specimens have been tested at similar temperatures, including 1T SE(B), 1/2T SE(B), and 1/2T SE(B) with a square cross-section. The presence of a "bi-axial" effect should be observable in a set of 12 cruciform specimens tested at this temperature.

Experimental Details

The ring gage was installed on the specimen, and the specimen was installed in the test fixture and centered under the loading ram. Four to eight mid arm strain gages were connected to conditioning amplifiers, and all signals, CMOD, load, table stroke, and the strain gage outputs were input to a 16 bit analog to digital module inserted in a standard PC. Data were acquired and calibrated using VisualBASIC software, presented graphically on the monitor and stored on the PC hard drive. An initial loading was taken to a load of approximately 100 kN, and the load arm strain gages were monitored to ensure that the specimen was centered properly in the test fixtures. Adjustments were made as necessary. After the specimen was aligned properly, the chamber was closed, and the cooling process was begun. Cooling generally required between 2–3 h. The specimen was held at the final temperature for ½ h. The specimen was then slowly loaded, and most tests took 15–30 min to fracture.

Load versus CMOD records for several specimens are shown in Fig. 10. Also shown in Fig. 10 is the load versus CMOD prediction obtained from the finite element analysis. The load-CMOD records are repeatable, except for the point of cleavage interruption, and tend to lie somewhat above the finite element model prediction.

Typical strain gage data are shown in Fig. 11 compared with the results of the finite element analysis. The agreement between the experiment and the model is excellent initially, but the experimental strains fall below the predictions after plasticity develops in the loading arms.

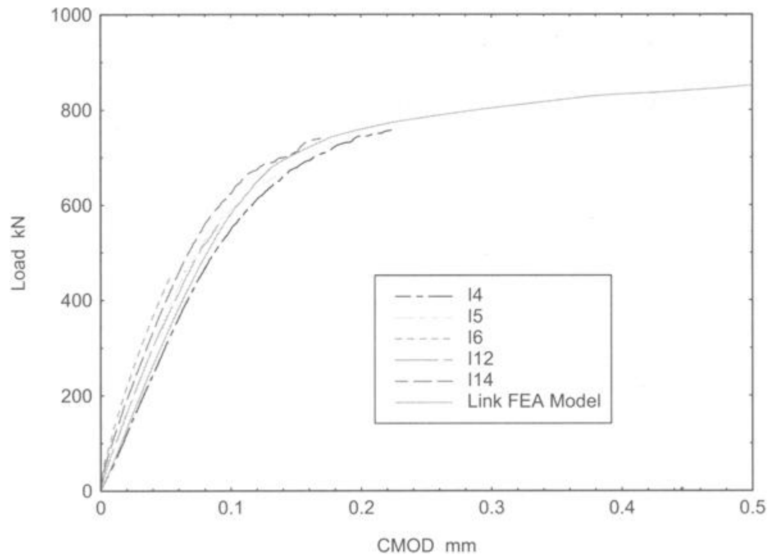

FIG. 10—*Load versus CMOD for several cruciform specimen tests. The predicted relationship from the finite element analysis is shown for comparison.*

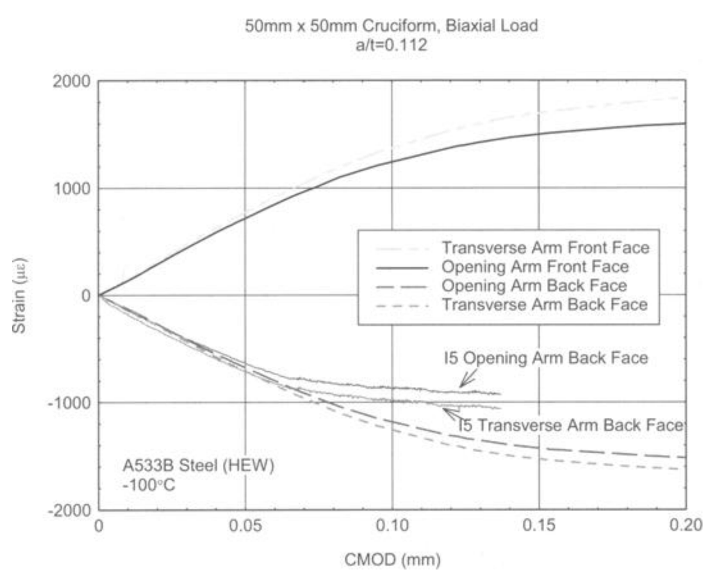

FIG. 11—*Mid-arm strain gages showing comparison between measured strain and model prediction for specimen I5.*

The experimental results were used for specimen alignment and also for showing the ratio of the experimental moments in the two bending directions. Both the experimental results and the computations show that the presence of the crack acts to reduce the moment acting to open the crack by about 10 % in comparison to the moment acting in the transverse direction. Using this as a basis, the biaxiality of the loading can be estimated as 1.1:1, corresponding closely to the 1:1 ratio targeted by the more sophisticated system used at ORNL.

Post-test photographs of cruciform specimens are shown in Figs. 12 and 13. High-energy fractures caused nearly full separation of the specimen, while low energy fractures resulted in no observable cracking, being identified only by a sudden load drop during the test. Most specimens were given a heat tint, then immersed in liquid nitrogen prior to being broken open to expose the crack surface after the test. For specimens like I4 in Fig. 12, the side arms were sawed off to facilitate exposing the crack after immersion in liquid nitrogen. Most tests resulted in crack arrests at the end of the center stress control slot as shown in Fig. 12, while the cracks in other cases propagate out the end of the load arms or turn to the surface beyond the center stress control slot, as shown in Fig. 13. Specimens that demonstrated very low toughness, such as specimen I6, showed no observable crack extension until the specimen had been heat tinted and broken open.

The critical J integral at onset of cleavage was estimated by using the centerline finite element analysis presented in Fig. 7. These computational results were converted from J to K_J using Eq 3 as shown in Fig. 7, then fit with a function of the form:

$$K_J = \frac{a + bCOD + cCOD^2}{d + COD} \tag{4}$$

where a, b, c, and d are fitting coefficients. A spreadsheet was then used to evaluate the critical J_c at onset of unstable fracture for each specimen at the critical CMOD at onset of cleavage. The results for all tests are presented in Table 3; all specimens cleaved at a CMOD $\leq$ 0.26 mm.

Discussion of Results

The results of the 12 cruciform tests are summarized in Table 3 and plotted for comparison with other data sets obtained from the Shoreham plant material in Fig. 14. The Master Curve and confidence bounds plotted on this figure correspond to the deep crack 1T SE(B) data presented with the open circle data points on the figure. While the standard deep crack data sets generally correspond well with these confidence bounds, shallow crack data generally have a larger variability as shown in Fig. 14 and are concentrated above the confidence zone described by the deep cracked SE(B) test results. The cruciform data set demonstrates the same pattern as the shallow crack data sets with a larger scatter and an elevation of the measured toughness in comparison with the deep crack data sets, resulting in a much lower T_o reference temperature.

Tables 4 and 5 summarize 15 deep crack SE(B) data sets and 6 shallow crack data sets and include the results of the biaxial cruciform data sets obtained in this project. The first six tests were conducted at the US Naval Academy (USNA), but the test program was then rudely interrupted when Hurricane Isabel flooded the laboratory spaces with 0.8 m (32 in.) of Chesapeake Bay water. Fixtures and the environmental chamber were transported to Naval Surface Warfare Center, Carderock (NSWC) for the final six tests. The data sets were analyzed separately and then combined, and the results are presented in Table 5.

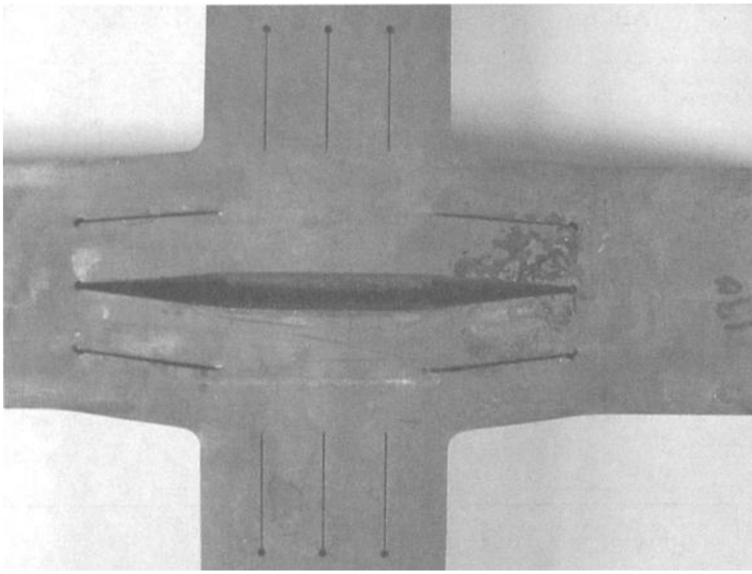

FIG. 12—*Specimen I4 showing arrested crack after testing.*

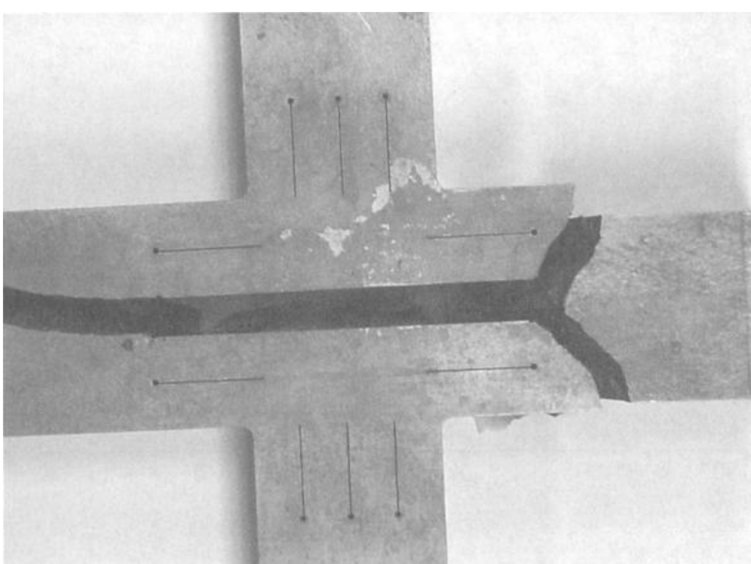

FIG. 13—*Specimen I5 shown after testing.*

TABLE 3—*Summary of cruciform specimen test results.*

Spec. ID	K_{Jc} MPa $m^{0.5}$	K_{Jc1T} MPa $m^{0.5}$	Rank (K_{Jc})	a/W	$CMOD_c$ mm	M (b)	M (a)
I4*	145	168.6	11	0.119	0.22	206	28
I5*	106	122.3	5	0.104	0.14	392	46
I14*	122	141.3	8	0.112	0.17	294	37
I3*	128	148.4	10	0.108	0.18	268	32
I12*	79	90.2	3	0.109	0.090	703	86
I1*	157	182.9	12	0.114	0.26	177	23
I13	113	130.6	7	0.109	0.15	337	48
I11	123	142.5	9	0.103	0.17	285	41
I6	50	55.7	1	0.111	0.053	1723	246
I8	67	75.9	2	0.109	0.074	960	137
I7	94	108.0	4	0.109	0.10	487	70
I2	108	124.6	6	0.115	0.14	369	53

*Tested at USNA before Hurricane Isabel. Other tests conducted at NSWC Carderock using the same fixtures but a different test machine.

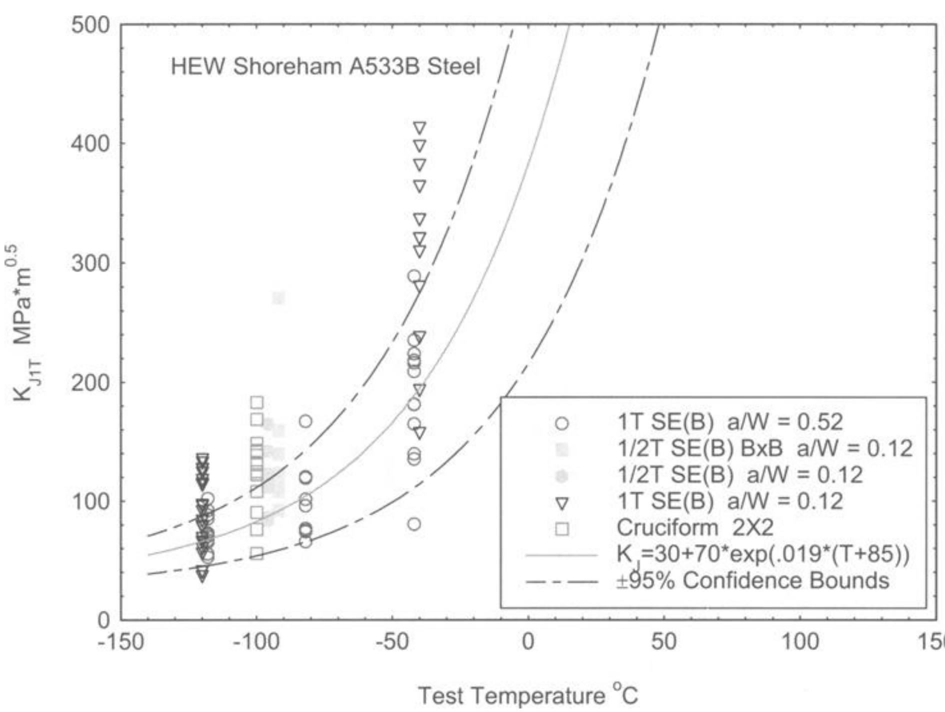

FIG. 14—*Comparison of cruciform data with other deep and shallow crack SE(B) data obtained previously on the Shoreham plate material.*

TABLE 4—*Summary of Shoreham T_o measurements – deep crack.*

Specimen Configuration	Test Temp. °C	T_o °C	N	r	a/W	M_{Avg}
1T	–12	–80.2	7	4	0.53	31
1T	–27	–84.2	7	7	0.53	46
1T	–42	–86.5	12	12	0.53	100
1T	–82	–87.7	9	9	0.51	368
1T	–118	–94.1	12	12	0.50	592
1/2T	–40	–97.5	8	2	0.53	21
1/2T	–50	–94.	6	3	0.53	46
1/2T	–60	–82.2	6	6	0.53	58
1/2T	–116	–87.1	8	8	0.55	303
1/2T	–81	–94.1	8	6	0.74	50
1/2T	–115	–98.5	7	7	0.76	101
1/2T	–79	–101.1	8	7	0.51	116
1/2T BxB	–118	–93.8	8	8	0.51	413
1/2T BxB	–76	–93.6	8	8	0.51	99
1/2T BxB	–50	–90.5	12	9	0.54	56
Average	...	–91.1*	...	...	...	...

*Average taken of data with r > 5 only.

TABLE 5—*Summary of Shoreham T_o measurements – shallow crack.*

Specimen Configuration	Test Temp. °C	T_o °C	N	a/W	M_{Avg} (b)	M_{Avg} (a)
1T	–120	–117.9	23	0.15	1001	179
1T	–40	–112.4	12	0.12	77	10
1/2T	–115	–127.7	15	0.12	323	42
1/2T	–96	–108.5	8	0.12	83	24
1/2T BxB	–120	–109.3	8	0.12	650	92
1/2T BxB	–92	–126.0	8	0.12	165	23
Average	...	–117.0	...	...	...	...
Cruciform/USNA	–100	–124.0	6	0.11	340	148
Cruciform/NSWC	–100	–107.0	6	0.11	545	197
Cruciform Avg.	–100	–118.0	12	0.11	516	192

The cruciform combined data set with a T_o = –118°C corresponds closely to the shallow crack data sets with an average T_o = –117°C in contrast with the deep crack data sets with an average T_o = –91.1°C. The variation in the results between the USNA and NSWC tests is consistent with the variation found in the shallow crack data sets. Load versus CMOD curves were compared between the data sets of the two laboratories, and no systematic difference was found. The T_o obtained from the larger 1T SE(B) specimens demonstrates an even larger difference with an average T_o = –86°C. Only a small biaxial effect of approximately 1°C is measured with the combined data set, with the result of the biaxial tests being essentially identical to the average result of the shallow crack uniaxial specimen data sets.

ASTM E 1921 requires that the critical K_{Jc} obtained for each specimen satisfy:

$$K_{Jc} \leq \left(\frac{Eb\sigma_{ys}}{M} \right)^{1/2} \tag{5}$$

where M = 30. Generally, higher values of M correspond to higher crack tip constraint at the onset of cleavage. The M value for each cruciform specimen calculated from:

$$M = \frac{Eb\sigma_{ys}}{K_{Jc}^{\ 2}} \tag{6}$$

is presented in Table 3. For shallow crack specimens the crack length, a, is often substituted for the remaining ligament b = (W–a) in calculating M since the crack tip is much closer to the crack free surface for this geometry. These values are also presented in Table 3, and the values measured here are generally larger than 30 even when based on the crack length.

One concern with the shallow crack results in Table 5 is the tendency for the smaller data sets to have higher measured T_o results than larger data sets. Since the variability of the critical K_{Jc} is much greater for shallow crack specimens, larger data sets might be required to obtain equivalent accuracies when using sets of shallow crack specimens. Also noteworthy is that the 1T data set at –40°C includes some very high J_c values, and since the specimens are shallow cracked, no censoring has been used in the evaluation of T_o. While the M_{Avg} was 77 for this data set, if the M calculation was based on the crack length rather than on the remaining ligament, M_{Avg} would be approximately 10. Similar calculations are included in Table 5 for the other shallow specimen data sets. Additional work is underway at USNA to obtain more shallow crack SE(B) data to fill out some of the data sets presented in Table 5. Recent on-going work on 3-D constraint correction by Petti and Dodds [15] might help by developing a censoring procedure for shallow crack specimens consistent with what is currently prescribed in E 1921 for the standard SE(B) test geometry.

In the final technical paper reporting on the results of the ORNL cruciform tests [6], the authors cite an unpublished analysis result that demonstrates that a cross-section of 100 mm is required to observe the biaxial effect. The unpublished analysis shows that containment of the plastic strains is a requirement for the biaxial effect to be observed. The M_{Avg} observed for the cruciform specimens in this program is quite high, whether the calculation is based on remaining ligament or on crack length, corresponding to high crack tip constraint, even though the cracks are shallow. As described above, the finite element analysis predicts that the plastic zone expands from the tup region and intersects the crack tip plastic zone at a CMOD of about 0.15 mm, and that the plastic zone then breaks through to the crack surface when the CMOD is approximately 0.2 mm. As shown in Table 3, the critical CMOD at cleavage onset is between 0.053 and 0.26 mm with only two specimens exceeding 0.2 mm. If one sets a full constraint requirement of CMOD less than 0.15 mm, only six of the specimens tested in this data set can be taken as fully constrained, and it is possible that the lack of full constraint still affects the results of this data set.

An analysis for this geometry, like that performed by Dodds and Nevalainen [8], which would establish requirements for crack tip constraint in terms of M based on the remaining ligament or the crack length, would be very useful to the interpretation of this data. Publication by ORNL of the basis of their requirement would also help clarify the situation.

To address this issue further, it is proposed that another set of specimens be tested at a somewhat lower temperature to approach a full containment of the plastic strains during biaxial loading. Additional specimens would also be tested in a uniaxial mode to demonstrate that these specimens give results consistent with the "standard" shallow crack results obtained for this alloy as shown in Table 5. It is also proposed that a set of 50 × 50 mm cruciform specimens be made from the ORNL Plate 14 material and tested using the procedure described in this report so that a direct comparison of the 50 × 50 mm and 102 × 102 mm cross-sections can be made in this embrittled material. This material is now being made available by ORNL.

Conclusions

Cruciform specimens can be machined, precracked, and tested to develop shallow crack, biaxial loading E 1921 T_0 reference temperature data at a reasonable cost, at least if specimens with a 50 × 50 mm cross-section are acceptable. Precracking can be done using a 250 kN servohydraulic machine, while the fracture testing requires a 1 MN test machine. Straight precracks of a repeatable size were readily obtained using a plunge EDM starter notch sharpened using uniaxial three point bending fatigue.

The resulting T_0 reference temperature does not show the presence of a "bi-axial" effect. The measured T_0 is essentially identical to the average result obtained using shallow notch SE(B) tests loaded using uniaxial three point bending. The scatter in cleavage initiation toughness observed from the cruciform data set is also consistent with what is generally observed from shallow notch ductile to brittle transition data sets.

Relatively large scatter in T_0 in the existing database for shallow crack specimens makes the determination of the magnitude of the "biaxial effect" difficult, even with the relatively large data set of twelve cruciform specimen results obtained in this study.

Further study of plastic zone containment within the cruciform ligament and the ORNL assertion that this is a prerequisite for the bi-axial effect to be observed is required. A second series of 50 × 50 mm (2 × 2 in.) cruciform specimens fabricated from the Shoreham material and tested at a lower temperature and a series of ORNL Plate 14 50 × 50 mm (2 × 2 in.) cruciform specimens could also help establish if the 100 mm cross-sectional requirement is valid.

Acknowledgments

The authors would like to acknowledge the support of the U.S. Naval Academy Technical Support Department, specifically Derek Baker, who machined the test fixtures, and to Greg Denevan, who built the environmental chamber. We also acknowledge the support of Shah Malik and Rob Tregoning of the U.S. Nuclear Regulatory Commission, who supported this work financially. This work was supported in part by a grant of computer time from the DOD High Performance Computing Modernization Program at the Engineering Research and Development Center (ERDC), Vicksburg, MS.

References

[1] Wallin, K., Saario, T., and Torronen, K., "Statistical Model for Carbide Induced Brittle Fracture in Steel," *Metal Science*, Vol. 18, 1984, pp. 13–16.

[2] Wallin, K., "The Scatter in K_{Ic} Results," *Engineering Fracture Mechanics*, Vol. 19, 1984, pp. 1085–1093.

[3] Wallin, K., "Optimized Estimation of the Weibull Distribution Parameters," Research Report 604, Technical Research Center of Finland, Espoo, Finland, 1989.

[4] Merkle, J. G., Wallin, K., McCabe, D. E., "Technical Basis for an ASTM Standard for Determining the Reference Temperature, T_o, for Ferritic Steels in the Transition Range," NUREG/CR-5504, U.S. Nuclear Regulatory Commission, 1998.

[5] Bass, B. R., Bryson, J. W., Theiss, T. J., and Rao, M. C., "Biaxial Loading and Shallow-Flaw Effects on Crack-Tip Constraint and Fracture Toughness," USNRC Report, ORNL, NUREG/CR-6132, (ORNL/TM-12498), 1994.

[6] Bass, B. R., McAfee, W. J., Williams, P. T., and Pennell, W. E., "Fracture Assessment of Shallow-Flaw Cruciform Beams Tested under Uniaxial and Biaxial Loading Conditions," *Nuclear Engineering and Design*, Vol. 188, No. 3, 1999, pp. 259–288.

[7] Link, R. E. and Joyce, J. A., "Experimental Investigation of Fracture Toughness Scaling Models," *Constraint Effects in Fracture Theory and Applications, ASTM STP 1244*, Mark Kirk and Ad Bakker, Eds., 1995, pp. 286–315.

[8] Nevalainen, M. and Dodds, R. H., Jr., "Numerical Investigation of 3-D Constraint Effects on Brittle Fracture in SE(B) and C(T) Specimens," *International Journal of Fracture*, Vol. 74, 1995, pp. 131–161.

[9] Betegon, C. and Hancock, J. W., "Two Parameter Characterization of Elastic-Plastic Crack Tip Fields," *Journal of Applied Mechanics*, Vol. 58, 1991, pp. 104–110.

[10] Shih, C. F., O'Dowd, N. P., and Kirk, M. T., "A Framework for Quantifying Crack Tip Constraint," *Constraint Effects in Fracture, ASTM STP 1171*, E. M. Hackett, K.-H. Schwalbe, and R. H. Dodds, Jr., Eds., 1993, pp. 2–20.

[11] Tregoning, R. L. and Joyce, J. A., "T_o Evaluation in Common Specimen Geometries," *Proceedings of the PVP Conference, ASME, PVP-412*, Seattle Washington, 2000, pp. 143–152.

[12] Joyce, J. A. and Tregoning, R. L., "Quantification of Specimen Geometry Effects on the Master Curve and T_o Reference Temperature," *ECF13*, San Sebastian, Spain, 2000.

[13] Tregoning, R. L. and Joyce, J. A., "Application of a T-Stress Based Constraint Correction to A533B Steel Fracture Toughness Data," *Fatigue and Fracture Mechanics: 33rd Vol., ASTM STP 1417*, W. G. Reuter and R. S. Piascik, Eds., ASTM International, West Conshohocken, PA, 2002.

[14] Rathbun, H. J., "On the Size Scaling of Cleavage Toughness in the Transition: A Single Variable Experiment and Model Based Analysis," Ph.D. Thesis, Department of Mechanical and Environmental Engineering, University of California, Santa Barbara, 2003.

[15] Petti, J. and Dodds, R. H., Jr., "Constraint Differences Between C(T) and SE(B) Specimens: 3-D Analysis," Presented at the ASTM E 08.06 Task Group Meeting, Kansas City, MO, 6 May 2003.

SESSION 7A: SMALL CRACKS II

Journal of ASTM International, June 2005, Vol. 2, No. 6
Paper ID JAI11988
Available online at www.astm.org

S. R. Daniewicz[1]

The Effect of Load Reduction Scheme on Crack Closure in the Near-Threshold Regime

ABSTRACT: Three-dimensional elastic-plastic finite element analyses were conducted to model fatigue crack growth in an M(T) specimen. Variable amplitude loading with a continual load reduction was used to simulate the load history associated with fatigue crack growth threshold measurement. Load reductions with both constant load ratio R and constant maximum stress intensity K_{max} were used.

Results indicated that load reduction with constant R generated a plastic wake such that remote crack opening occurred during loading, with the crack front opening prior to a region remote to the crack front. The last region to open was located at the point at which the load reduction originally began, and at the free surface. In contrast, for load reduction with constant K_{max}, the crack front was the last to open. The results also indicated the crack opening process is three-dimensional in nature, with regions in the interior opening prior to regions near the free surface.

KEYWORDS: fatigue, crack propagation, threshold, crack closure

Introduction

Experimental measurement of the fatigue crack growth threshold ΔK_{th} requires that a gradual reduction in the stress intensity factor range be applied during a fatigue crack growth test. The ASTM standard test method E 647 recommends that the load ratio R be held fixed during the required load reduction. ASTM E 647 also allows load reduction under a fixed mean or maximum stress intensity factor, if either of these are more representative of service conditions. Load reduction under a fixed maximum stress intensity factor K_{max} has attracted interest because it enables crack closure to be avoided as the threshold is approached [1–4]. This type of load reduction results in a continually increasing R such that threshold measurement is made in the absence of crack closure. The resulting effective threshold stress intensity $(\Delta K_{eff})_{th}$ is often referred to as an intrinsic measurement of fatigue crack growth resistance [1–4]. In contrast, Donald and Paris [5] and Vasudevan et al. [6] have suggested a K_{max} effect such that both ΔK_{th} and K_{max} are needed to define resistance to fatigue crack growth in the near threshold regime.

Krenn and Morris [7] have argued that a $(\Delta K)_{th}$ and K_{max} driving force model is mathematically compatible with a $(\Delta K_{eff})_{th}$ based model, because the opening stress associated with plasticity-induced crack closure and required to convert $(\Delta K)_{th}$ to $(\Delta K_{eff})_{th}$ is a function of K_{max}. A threshold measurement methodology which employs constant amplitude loading has also been recently investigated by Forth et al. [8].

Manuscript received 17 November 2003; accepted for publication 27 August 2004; published June 2005. Presented at ASTM Symposium on Fatigue and Fracture Mechanics: 34th Volume on 19–21 November 2003 in Tampa, FL; S.R. Daniewicz, J.C. Newman, Jr., and K-H. Schwalbe, Guest Editors.

[1] Professor, Department of Mechanical Engineering, Mississippi State University, Mississippi State, MS 39762.

When a load reduction using a fixed R is used, plasticity-induced closure will occur, and the presence of the plastic wake will influence the resulting measured threshold. The effective and applied stress intensity factor ranges ΔK_{eff} and ΔK are related as follows:

$$\frac{\Delta K_{eff}}{\Delta K} = \frac{S_{max} - S_o}{S_{max} - S_{min}} = \frac{1 - S_o/S_{max}}{1 - R} \tag{1}$$

where S_{max} and S_o are the maximum and opening stresses, respectively. From Eq 1, the relationship between ΔK_{th} and $(\Delta K_{eff})_{th}$ may be written as:

$$\Delta K_{th} = \frac{1 - R}{1 - S_o/S_{max}} \left(\Delta K_{eff}\right)_{th} \tag{2}$$

If one considers $(\Delta K_{eff})_{th}$ to be a material constant, then changes in the crack opening stress S_o will result in changes in the measured threshold ΔK_{th}. The measured threshold is now a function of plasticity-induced closure and no longer an intrinsic measurement of fatigue crack growth resistance. Under a fixed K_{max} load reduction, there is no closure in the threshold regime with $S_o/S_{max} \rightarrow R$ and $\Delta K_{th} = (\Delta K_{eff})_{th}$.

Donald and Paris [5] conducted fatigue crack growth experiments using AA6061-T6 and AA2024-T3 M(T) specimens and measured opening loads using compliance measurements. In the threshold regime, they conducted load shedding at fixed load ratios of $R = 0.1$ and 0.7. The data generated at $R = 0.7$ was a closure-free baseline data set with $\Delta K = \Delta K_{eff}$. Donald and Paris demonstrated that above the threshold regime, the closure-free data and the data generated at $R = 0.1$ and corrected for closure correlated well. In the threshold regime, however, the measured opening stresses became excessively large such that the subsequently computed $(\Delta K_{eff})_{th}$ were too small when compared with the baseline data. A K_{max} effect was used to explain this anomaly. Their observations could also be explained with the aid of Eq 2.

Two-dimensional fatigue crack growth simulations conducted by Newman [9] also resulted in large opening stresses in the threshold regime. Using a modified strip-yield model and a load reduction with a fixed load ratio R, remote crack closure away from the crack tip was observed. This remote crack closure resulted in the crack tip opening prior to regions remote to the crack tip during loading, and a subsequent rapid rise in the magnitude of the opening stress S_o required to fully open the crack. For a M(T) specimen with $R = 0$ and a pre-cracking stress level of $S_{max}/\sigma_o = 0.277$, where σ_o is the flow stress, Newman observed closure within the region where the constant amplitude pre-cracking was terminated and the load shedding procedure was initiated. It should be noted that Newman did not observe remote closure and elevated crack opening stresses when pre-cracking at a stress level of $S_{max}/\sigma_o = 0.108$. Analyses conducted using a load reduction with a fixed K_{max} resulted in closure-free crack surfaces as the threshold was approached, with the opening load below the minimum load.

Two-dimensional plane stress simulations were also conducted by McClung [10,11], using both the finite element method [10,11] and a modified strip-yield model [11]. The type of load reduction considered was restricted to fixed R. McClung observed elevated crack opening stresses from the finite element analyses during the load reduction, although these elevated crack opening stresses were not associated with remote crack closure except for simulations employing large initial stress intensity factor ranges ΔK_o.

The objective of this paper is to elucidate the differences between a fixed R and fixed K_{max} load reduction from a mechanics perspective. A comparative study was performed simulating fatigue crack growth in an M(T) specimen under a gradually reducing stress intensity factor range using both a fixed R and fixed K_{max} load reduction. Three-dimensional elastic-plastic finite element analyses were used to simulate the plasticity-induced crack closure developed, and the subsequent crack opening behavior as the stress intensity factor range was reduced.

The two-dimensional modified strip-yield model analyses conducted by Newman averaged three-dimensional constraint effects through the thickness using an empirical constraint factor. The analyses conducted by McClung considered only plane stress. The three-dimensional analyses conducted in this study allowed a more realistic three-dimensional perspective of the crack opening behavior. However, while Newman and McClung utilized many analyses to investigate the effects of numerous variables, the current study was limited to two finite element analyses.

Finite Element Modeling Methodologies and Difficulties

The use of three-dimensional elastic-plastic finite element analysis to model plasticity-induced closure in cracked bodies undergoing cyclic loading has been limited as discussed by McClung [12]. Chermahini et al. [13,14] used three-dimensional elastic-plastic analyses to investigate the crack opening behavior of M(T) specimens under constant amplitude loading. Chermahini et al. [15], Zhang et al. [16], and Skinner et al. [17] performed similar analyses focused on the more complex semi-elliptical surface crack under constant amplitude loading. More recently, Roychowdhury and Dodds simulated crack growth under small-scale yielding conditions [18].

Fatigue crack growth was modeled by repeatedly loading, advancing the crack, and then unloading. The model was incrementally loaded to the maximum load, at which time the crack front nodes were released, allowing the crack to advance uniformly one elemental length per load cycle. The applied load was then incrementally lowered until the minimum load was attained. Each load cycle then corresponds to two monotonic analyses. For constant amplitude loading, perhaps five load cycles are required to achieve an approximate steady state condition in which the crack opening loads remain relatively constant.

Utilizing three-dimensional finite element analyses to model plasticity-induced closure is in general a computationally intensive effort because the finite element models required must be analyzed multiple times in succession. A large number of elements in the crack tip region is necessary to ensure adequate mesh refinement so that perhaps 5–10 elements exist within the plastic zone at any point on the crack front under the maximum loading. Alternately, mesh refinement requirements may be defined using the crack-tip reversed plastic zone generated upon unloading [12]. The computationally intensive nature of three-dimensional plasticity-induced closure simulation is further aggravated when a variable amplitude load reduction such as that used for threshold measurement is considered. Large amounts of crack growth are required to generate meaningful results in which the stress intensity factor range undergoes a significant reduction. To simulate large amounts of crack growth under the cyclic loading, a large number of load cycles is required, which will generally exceed the number needed for a constant amplitude simulation. In addition, the decreasing maximum stress intensity associated with fixed R load shedding results in a decreasing plastic zone size along the crack front. This necessitates a more refined mesh to ensure an adequate number of elements in the plastic zone as the maximum stress intensity factor diminishes. Under a fixed K_{max} load reduction, the decreasing stress intensity factor range results in a decreasing reversed plastic zone size and similar mesh refinement concerns.

Finite Element Analyses

The M(T) specimen exhibits three planes of symmetry, and consequently only one eighth of the geometry was modeled using eight-noded hexahedral elements as illustrated in Fig. 1. The model consisted of 13 430 nodes and 12 906 elements. Both model generation and solution were performed using the commercial finite element analysis program ANSYS. A thickness $B = 4.78$ mm, width $W = 80$ mm, and crack length $2a = 34$ mm were used. The material was assumed to be an elastic-perfectly plastic aluminum alloy with modulus $E = 70$ GPa and flow stress $\sigma_o = 400$ MPa. The von Mises yield criterion and the associated flow rule were used. Small deformation theory was employed. A total of 25 load cycles was used for the load reduction with fixed R, while a total of 19 load cycles was used for the load reduction with fixed K_{max}. The crack front was advanced uniformly one element length during each cycle with $da = 0.125$ mm.

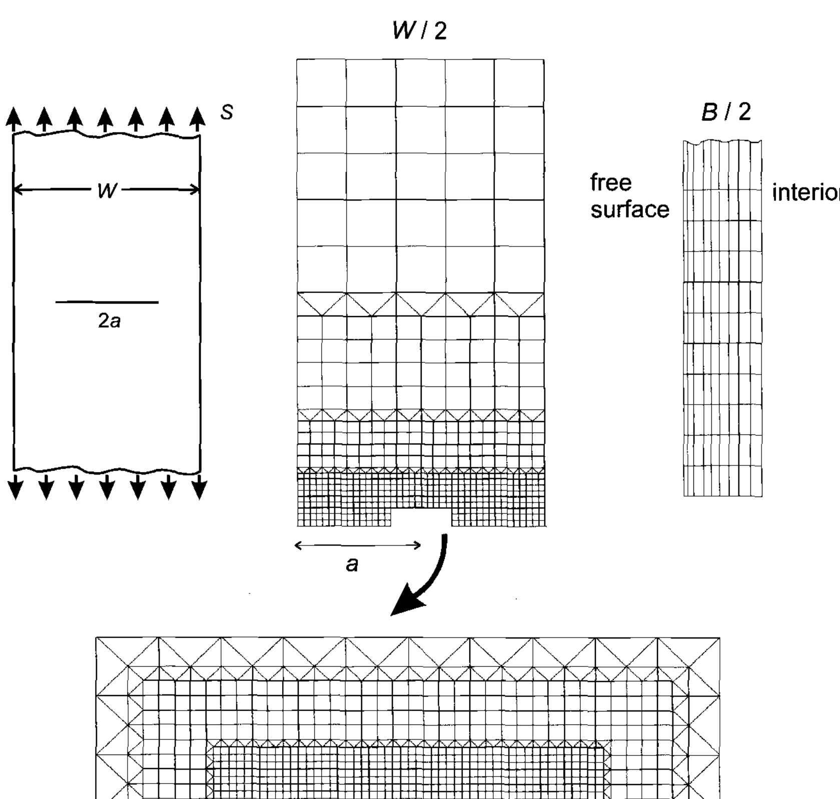

FIG. 1—*M(T) finite element model.*

To advance the crack, node release at the maximum applied load was performed in an incremental manner to avoid convergence difficulties [19]. This was accomplished using bundles of truss elements to initially connect all nodes which were later to be released as part of the analysis. These truss elements were then released individually such that total node release took place in an incremental manner. Contact elements were placed along the crack surface, allowing the contact stress along the crack surface to be computed. This enabled determination of the opening load as that load which first produced zero contact stress along the entire crack surface during loading. The contact elements also allowed a determination of which region of the crack surface was the last to open under an increasing load. For additional details regarding the use of finite element analysis to simulate fatigue crack growth, the reader is referred to Solanki et al. [20].

Two finite element analyses were conducted. The first modeled a load reduction conducted under fixed R conditions, while the second considered load reduction with a constant K_{max}. The load shedding used was defined using the following relationship

$$\Delta K = \Delta K_0 e^{C\Delta a} \tag{3}$$

where Δa is the amount of crack growth following pre-cracking, ΔK_o is the initial stress intensity factor range at the start of load reduction, and C is a constant.

In the current study, $\Delta K_o = 30$ MPa$\sqrt{\text{m}}$ was used. For the loading with fixed R, a value of $R = 0$ was used. For the loading with fixed K_{max}, a value of $K_{max} = 30$ MPa$\sqrt{\text{m}}$ was used. Of the total load cycles employed, five were used to simulate constant amplitude pre-cracking with $\Delta K = \Delta K_o$ and $R = 0$. The remaining load cycles were used to simulate load shedding such that $\Delta a = 2.5$ mm for the fixed R load reduction, and $\Delta a = 1.75$ mm for the load reduction with fixed K_{max}.

While ASTM E 647 recommends a maximum value for C of -0.08/mm, a value of -0.25/mm was employed in this study. This large value was chosen because small values of C result in the need for large amounts of crack growth before appreciable reductions in the stress intensity factor range are produced. Large amounts of crack growth in turn require an excessive number of sequential finite element analyses. The magnitude of C has been shown to exhibit negligible influence on the opening stresses predicted from finite element analyses when increasing C an order of magnitude above the ASTM value [11].

With the Δa as given above and $C = -0.25$/mm, the final ΔK employed during the load shedding was 16.1 MPa$\sqrt{\text{m}}$ for the fixed R load reduction and 19.4 MPa$\sqrt{\text{m}}$ for the load reduction with fixed K_{max} as computed using Eq 3. It should be noted that these values are well above the threshold value for aluminum alloys. Consequently, while the simulations performed addressed the load shedding process used for threshold measurement, they did not consider the threshold regime directly.

To validate the adequacy of the mesh refinement used, a monotonic analysis was performed using an applied stress intensity of $K = 30$ MPa$\sqrt{\text{m}}$. In the crack plane ahead of the crack front, the plastic zone size varied and was found to encompass between 9 and 13 elements. This level of refinement was considered adequate. Assuming the crack tip plastic zone is proportional to K^2, for $K = 16$ MPa$\sqrt{\text{m}}$ the plastic zone would encompass between 3 and 4 elements. At this level of stress intensity, which would exist at the termination of the fixed R load reduction, the level of refinement is suspect.

The total amount of crack growth modeled considering both the pre-cracking and the load shedding was $\delta a = 3.125$ mm (fixed R) and 2.375 mm (fixed K_{max}). The newly formed crack surface created by the crack growth is illustrated in Fig. 2 for the fixed R load reduction.

Following the simulation of crack growth, the contact stress on the rectangular region shown was monitored using contact elements to determine which region was the last to open under an increasing applied stress.

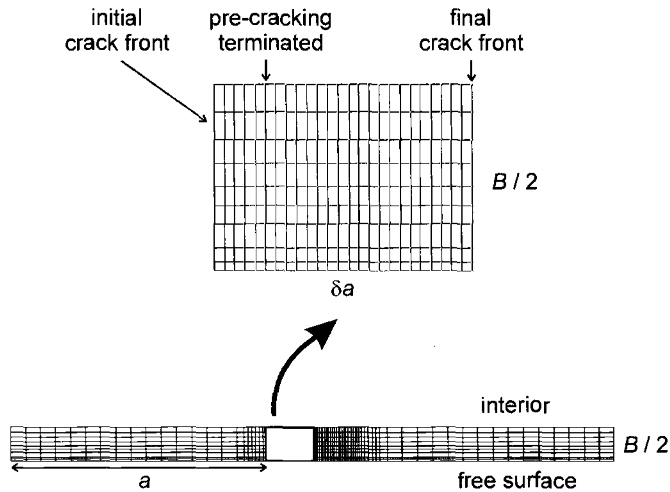

FIG. 2—*Crack surface formed by cyclic loading (fixed R load reduction).*

Results for the crack growth simulations with fixed R and fixed K_{max} are shown respectively in Figs. 3 and 4. The rectangular region shown in these figures is the crack growth region illustrated in Fig. 2. The dark areas indicate regions of the crack surface which are closed. From Fig. 3, note that remote closure was observed such that the crack front was not the last region to open. The crack front region was observed to open at an applied stress of $S/S_{max} \approx 0.40$, while the crack became completely open at a value of $S/S_{max} \approx 0.70$. The last region to open was located at the free surface where the pre-cracking was terminated.

The observed normalized opening stress value $S_o/S_{max} \approx 0.70$ is a relatively large value. Constant amplitude three-dimensional finite element analyses conducted by Chermahini et al. [13] at an applied stress level of $S_{max}/\sigma_o = 0.25$ resulted in $S_o/S_{max} \approx 0.60$. No remote closure was observed, with the crack front at the free surface being the last region to open. For the simulations conducted here, the analysis started with $S_{max}/\sigma_o \approx 0.29$ and terminated with $S_{max}/\sigma_o \approx 0.12$. In general, for constant amplitude loading, increases in the applied stress result in lower opening stresses. Thus, it is unclear whether the increased opening stress value determined here from the fixed R load shed was due to remote closure or simply the result of a lower applied stress. It should also be noted that an increase in the amount of simulated crack growth for the fixed R load reduction could result in an increased opening stress, with the normalized opening stress possibly exceeding the value of 0.70 reported here.

From Fig. 4, for a load reduction with a fixed maximum stress intensity factor, the crack front was the last region to open, and remote closure was not observed. Again, the last region to open was located at the free surface. The opening stress for this load reduction was similar to that determined for the fixed R load reduction with $S/S_{max} \approx 0.72$. Thus, while the crack opening behaviors for fixed R and fixed K_{max} were significantly different, the magnitude of the opening stresses were essentially the same. Clearly, the amount of crack growth simulated was not sufficiently large to produce a closure free condition, which is the intent during threshold measurement. The results shown in Fig. 4 suggest that the threshold regime is approached without the occurrence of remote closure.

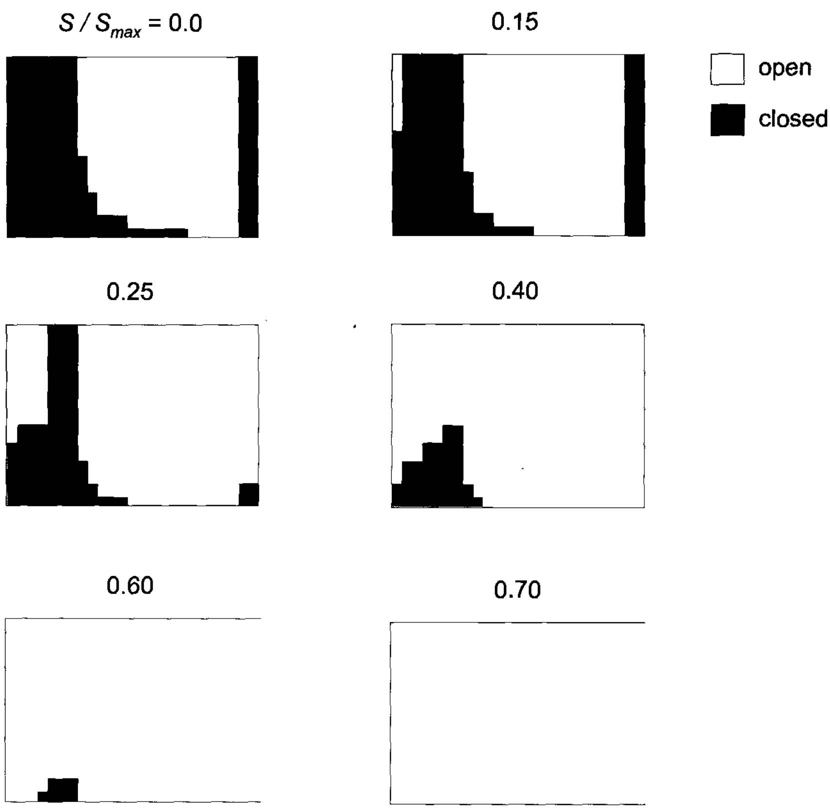

FIG. 3—*Crack opening behavior under fixed load ratio.*

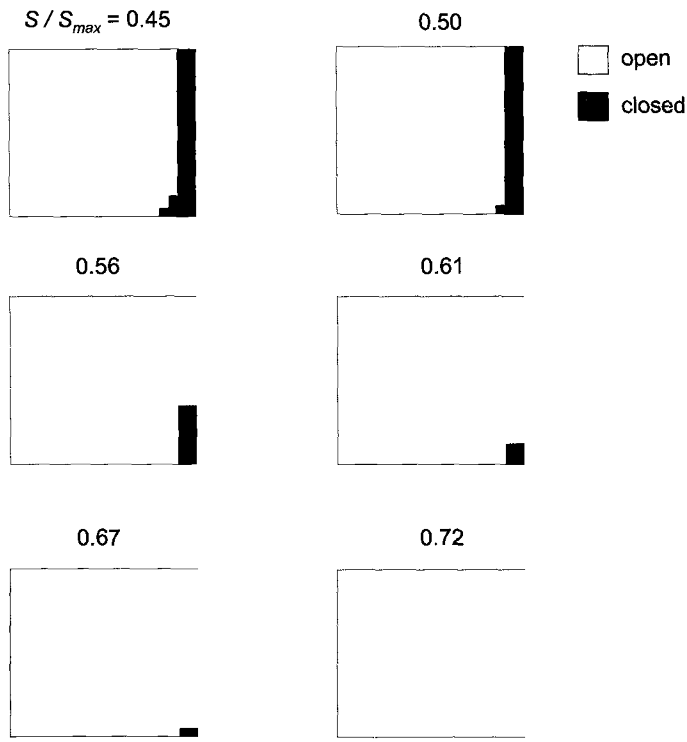

FIG. 4—*Crack opening behavior under fixed maximum stress intensity.*

Summary and Conclusions

Three-dimensional elastic-plastic finite element analyses were conducted to model fatigue crack growth in an M(T) specimen. Variable amplitude loading with a continual load reduction was used to simulate the load history associated with fatigue crack growth threshold measurement. The analyses were conducted to compare the crack opening behavior under a fixed R and fixed K_{max} load reduction.

Results indicated the crack opening process is three-dimensional in nature, with regions in the interior opening prior to regions near the free surface. Load reduction with constant R generated a plastic wake such that remote crack opening occurred during loading. The last region to open was located at the point at which the load reduction originally began and at the free surface. This remote opening resulted in an opening stress S_o with $S_o/S_{max} \approx 0.70$. In contrast, for load reduction with constant K_{max}, the crack front was the last to open with a similar opening stress of $S_o/S_{max} \approx 0.72$. The amount of crack growth simulated for the load reduction with constant K_{max} was not sufficiently large to produce a closure free condition, which is the intent of such a test.

Due to the severe computational requirements of simulating fatigue crack growth and plasticity-induced closure in three-dimensional bodies undergoing large amounts of crack growth, only two analyses were performed. The results given are thus limited in scope, and further research is required to assess the effects of the initial stress intensity factor range ΔK_o, the load ratio R, the load shed rate constant C, and material properties such as flow stress and the degree of strain hardening. The amount of crack growth modeled was also limited, such that the final ΔK values used were not in the threshold regime. Further research is needed using models which simulate more extensive crack growth to explore the crack opening behavior in the threshold regime.

References

[1] Doker, H., Bachmann, V., and Marci, G., "A Comparison of Different Methods of Determination of the Threshold for Fatigue Crack Propagation," *Fatigue Thresholds*, EMAS, 1982, pp. 45–58.

[2] Herman, W. A., Hertzberg, R. W., Newton, C. H., and Jaccard, R., "A Re-Evaluation of Fatigue Threshold Test Methods," *Fatigue '87, Third International Conference on Fatigue and Fatigue Thresholds*, Vol. II, 1987, pp. 819–828.

[3] Marci, G., Castro, D. E., and Bachmann, V., "Fatigue Crack Propagation Threshold," *Journal of Testing and Evaluation*, Vol. 17, No. 1, 1989, pp. 28–39.

[4] Hertzberg, R. W., "On the Calculation of Closure-Free Fatigue Crack Propagation Data in Monolithic Metal Alloys," *Material Science & Engineering*, A190, 1995, pp. 25–32.

[5] Donald, J. K. and Paris, P. C., "An Evaluation of ΔK_{eff} Estimation Procedures on 6061-T6 and 2024-T3 Aluminum Alloys," *International Journal of Fatigue*, Vol. 21, 1999, pp. S47–S57.

[6] Vasudevan, A. K., Sadananda, K., and Louat, N., "A Review of Crack Closure, Fatigue Crack Threshold and Related Phenomena," *Materials Science and Engineering*; Vol. A188, 1994, pp.1–22.

[7] Krenn, C. R. and Morris, J. W., "The Compatibility of Crack Closure and K_{max} Dependent Models of Fatigue Crack Growth," *International Journal of Fatigue*, Vol. 21, 1999, pp. S147–S155.

[8] Forth, S. C., Newman J. C., and Forman R. G., "On Generating Fatigue Crack Growth Thresholds," *International Journal of Fatigue*, Vol. 25, 2003, pp. 9–15.

[9] Newman, J.C., "Analyses of Fatigue Crack Growth and Closure Near Threshold Conditions for Large-Crack Behavior," *Fatigue Crack Growth Thresholds, Endurance Limits, and Design, ASTM STP 1372*, American Society for Testing and Materials, 2000, pp. 227–251.

[10] McClung, R. C., "Finite Element Modeling of Crack Closure During Simulated Fatigue Threshold Testing," *International Journal of Fracture*, Vol. 52, 1991, pp. 145–157.

[11] McClung, R. C., "Analysis of Fatigue Crack Closure During Simulated Threshold Testing," *Fatigue Crack Growth Thresholds, Endurance Limits, and Design, ASTM STP 1372*, ASTM International, West Conshohocken, PA, 2000, pp. 209–226.

[12] McClung, R. C., "Finite Element Analysis of Fatigue Crack Closure: A Historical and Critical Review," *Fatigue '99, Seventh International Fatigue Conference*, 1999.

[13] Chermahini, R. G., Shivakumar, K. N., and Newman, J. C., "Three-Dimensional Finite-Element Simulation of Fatigue Crack Growth and Closure," *Mechanics of Fatigue Crack Closure, ASTM STP 982*, ASTM International, West Conshohocken, PA, 1988, pp. 398–413.

[14] Chermahini, R. G. and Blom A. F., "Variation of Crack-Opening Stresses in Three-Dimensions: Finite Thickness Plate," *Theoretical and Applied Fracture Mechanics*, Vol. 15, 1991, pp. 267–276.
[15] Chermahini, R. G., Palmberg, B., and Blom, A. F, "Fatigue Crack Growth and Closure Behavior of Semicircular and Semi-Elliptical Surface Flaws," *International Journal of Fatigue*, Vol. 15, No. 4, 1993, pp. 259–263.
[16] Zhang, J. Z. and Bowen, P., "On the Finite Element Simulation of Three-Dimensional Semi-Circular Fatigue Crack Growth and Closure," *Engineering Fracture Mechanics*, Vol. 60, 1998, pp. 341–360.
[17] Skinner, J. D. and Daniewicz, S. R., "Simulation of Plasticity-Induced Fatigue Crack Closure in Part-Through Cracked Geometries Using Finite Element Analysis," *Engineering Fracture Mechanics*, Vol. 69, No. 1, 2002, pp. 1–11.
[18] Roychowdhury, S. and Dodds, R. H., "Three-Dimensional Effects on Fatigue Crack Closure in the Small Scale-Yielding Regime," *Fatigue & Fracture of Engineering Materials & Structures*, Vol. 26, 2003, p. 663.
[19] Wu, J. and Ellyin, F., "A Study of Fatigue Crack Closure by Elastic-Plastic Finite Element Analysis for Constant Amplitude Loading," *International Journal of Fracture*, Vol. 82, 1996, pp. 43–65.
[20] Solanki, K., Daniewicz, S. R., and Newman, J. C., "Finite Element Analysis of Plasticity-Induced Fatigue Crack Closure: An Overview," *Engineering Fracture Mechanics*, Vol. 71, 2004, pp.149–171.

Journal of ASTM International, April 2005, Vol. 2, No. 4
Paper ID JAI11990
Available online at www.astm.org

Y. Kondo,[1] *C. Sakae,*[1] *M. Kubota,*[1] *and M. Kashiwagi*[2]

Interpretation of Material Hardness, Stress Ratio, and Crack Size Effects on the ΔK_{th} of Small Cracks Based on Crack Closure Measurement

ABSTRACT: Fatigue tests were performed on materials containing small cracks to investigate the effects of material hardness, mean stress, and crack size on the threshold stress intensity factor of small cracks. The crack closure measurement on a very small crack was done. Although most of those effects could be explained by the characteristic behavior of crack closure in small cracks, it was also shown that $(\Delta K_{eff})_{th}$ was also affected by crack size. The combination of $(\Delta K_{eff})_{th}$ and the crack closure behaviors caused the peculiar characteristics of ΔK_{th} in small cracks. At an extremely high R region, an unusual decrease in ΔK_{th} was found to occur. The large reduction occurred under the conjunction of three factors: extremely high stress ratio higher than 0.8, shallow crack less than a few tenths of a millimeter, and hard material whose HV is higher than 300. The near-threshold fatigue crack propagation rate could be uniquely evaluated even in such a short crack regime using the effective stress intensity factor with the following modification $\{\Delta K_{eff} - (\Delta K_{eff})_{th,a}\}$. This expression could be applicable in the short crack regime. ΔK_{eff} still plays a role as the governing parameter for fatigue crack propagation of short crack as short as 0.04 mm.

KEYWORDS: fatigue, fatigue limit, small crack, fatigue threshold, hardness, stress ratio, crack closure, threshold stress intensity factor

Introduction

The threshold stress intensity factor for fatigue crack propagation (ΔK_{th}) of long cracks is relatively independent of material hardness and crack size. On the contrary, Murakami and Endo [1] found dependencies of ΔK_{th} on material hardness and crack size in the case of small defects. They formulated the ΔK_{th} as a function of material hardness and defect size as shown in Eq 1 for fully reversed loading:

$$\Delta K_{th} \propto (\mathrm{HV}+120)(\sqrt{area})^{1/3} \tag{1}$$

where HV is the Vickers hardness and $\sqrt{area}$ is the square root of defect area projected to the stress direction and $\sqrt{10}\,a$ for two-dimensional defect whose depth is a.

In this study, fatigue tests of materials containing small cracks were performed under a wide range of mean stresses for steels with different hardness. Since the crack closure behavior [2] was assumed to play an important role, experimental effort was made to measure the crack closure of a small crack. The cause of peculiar dependencies on material hardness, mean stress, and crack size in the case of small cracks was examined based on the crack closure behavior.

Manuscript received 28 October 2003; accepted for publication 15 June 2004; published April 2005. Presented at ASTM Symposium on Fatigue and Fracture Mechanics: 34th Volume on 19–21 November 2003 in Tampa, FL; S.R. Daniewicz, J.C. Newman, Jr., and K-H. Schwalbe, Guest Editors.

[1] Professor, Associate Professor, and Research Associate, respectively, Department of Intelligent Machinery and Systems, Kyushu University, Fukuoka, 812-8581, Japan.
[2] Graduate Student, Kyushu University, Japan.

Test Specimen and Test Method

Four JIS (Japanese Industrial Standard) materials were used. S25C is a low carbon steel with normalizing heat treatment. S45C is a medium carbon steel with quench and temper heat treatment. SCM435 and SNCM439 are low alloy steels with quench and temper heat treatment. Chemical compositions and mechanical properties are shown in Table 1.

The configuration of test specimen is shown in Fig. 1*a*. It has a 0.11-mm deep notch through the thickness. Two-dimensional cracks were used as initial cracks. At first, a 0.06 mm deep pre-crack was introduced at the notch root by fatigue, and a 0.17 mm deep pre-cracked specimen including the notch was prepared. After the pre-cracking, an appropriate amount of material was removed from the surface by grinding and polishing to prepare the desired initial crack shallower than 0.17 mm. In the case of initial crack deeper than 0.17 mm, a fatigue pre-crack was introduced so that the sum of notch and fatigue pre-crack was equal to the desired initial crack depth.

TABLE 1—*Chemical compositions and mechanical properties of test materials.*

	Chemical Composition (wt%)									Mechanical Properties (MPa, %)					
Material	C	Si	Mn	P	S	Ni	Cr	Mo	Cu	$\sigma_y, \sigma_{0.2}$	σ_B	δ	φ	HV
S25C	0.26	0.20	0.50	0.008	0.023	0.02	0.02	-	0.01	305	544	34.3	59.3	141
S45C	0.45	0.22	0.78	0.020	0.021	0.01	0.15	-	0.01	585	790	27.1	60.9	261
SCM435	0.35	0.19	0.75	0.022	0.014	0.02	1.09	0.19	0.02	870	989	22.4	65.4	305
SNCM439	0.40	0.19	0.83	0.028	0.008	1.60	0.78	0.15	0.12	1128	1201	17.1	52.2	386

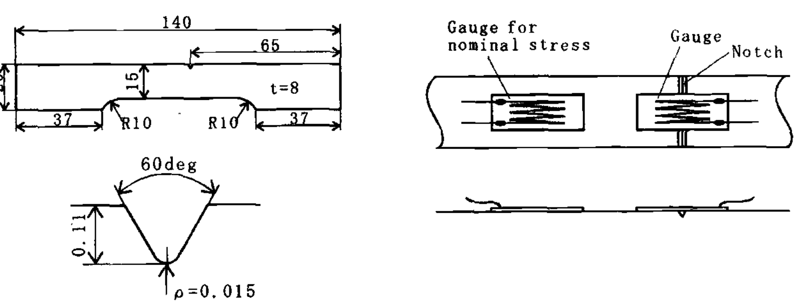

(a) Test specimen (b) Strain gage

FIG. 1—*Test specimen* (a) *and strain gage* (b).

The physical substance of the major disturbance introduced by the pre-cracking is the undesirably raised crack closure stress [3], which might result in obtaining non-conservative results. In this study, compressive pre-cracking was used as the pre-cracking procedure, which prevents the undesirable increase of crack closure without applying additional heat treatment. The crack closure stress is sensitive to the maximum stress. If we apply stress amplitude higher than that in the fatigue test at the same stress ratio in pre-cracking, an excessively raised crack closure might be created. Therefore, the maximum stress in pre-cracking was chosen not to exceed the maximum stress in the fatigue test. In addition to this, the stress amplitude was chosen at a stress slightly higher than the fatigue limit because too excessively compressive stress would introduce an artificial decrease of crack closure stress. The pre-cracking condition was determined as shown in Fig. 2. For fatigue tests whose stress ratios were equal to or higher than $R = -1$, the same pre-cracking condition was used. At first, the fatigue limit diagram of the 0.11 mm deep notch specimen was experimentally determined as shown by the solid line. Secondly, the fatigue threshold at $R = -1$ for the specimen with the designated pre-crack depth was estimated as shown by the open circle in the figure. This estimation can be done using Ref [1] for example. Here, the broken line intersecting the open circle is the line on which the maximum stress is the same as that of open circle. The intersection of the solid and broken lines is the fatigue limit of notched specimen whose maximum stress is the same as that of the open circle. The pre-cracking was performed at a stress slightly higher than the intersection as indicated by the solid circle. The specific stress ratio and maximum stress was dependent on material. As a consequence, the stress ratio in the pre-cracking was about $R = -2$. The maximum stress in tension was within 30 %, and the maximum stress in compression was within 60 % of the yield stress or the 0.2 % proof stress, which is considered not to be too excessive compression loading.

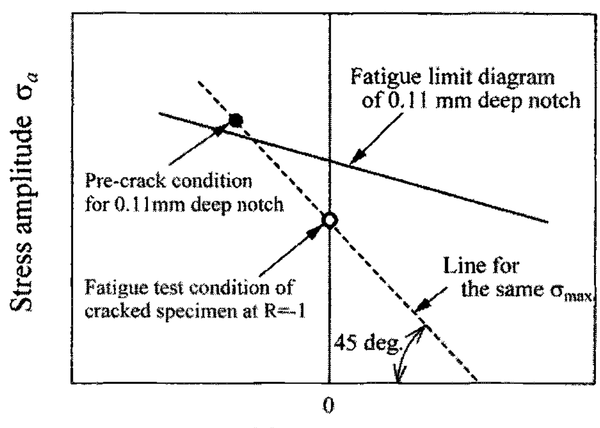

FIG. 2—*Pre-cracking condition for specimens tested at* $R \geq -1$.

Some fatigue tests were done at stress ratios lower than $R = -1$ for S25C. The principle of the pre-cracking procedure was the same as the above-mentioned, except that the maximum stress of pre-cracking was determined for each stress ratio R.

It cannot be completely denied that an artificial influence on the crack closure was introduced by the compressive pre-cracking. However, the pre-crack was introduced at a stress slightly higher than the fatigue limit. Therefore, it is considered that the artificially introduced disturbance on the crack closure by the compressive pre-cracking was not so excessive, and conservative data of ΔK_{th} were obtained.

A strain gage was pasted at a nominal section to measure the applied nominal stress. Another strain gage was pasted directly on the crack to measure the crack closure behavior as shown in

Fig. 1*b*. These two signals were put into a computer. The offset stress-displacement curve was calculated by the unloading elastic compliance method [4] to monitor the crack depth and the crack closure behavior. In-plane bending moment was applied to the specimen. The cyclic stress was applied at a frequency of 28 Hz. Fatigue tests were done in air at an ambient temperature.

The ΔK_{th} was determined in the following way. A number of test specimens were prepared, and fatigue tests were conducted at different stress levels to determine the *S-N* curve for each test condition, i.e., crack depth, stress ratio, and material. The crack growth was monitored by the unloading elastic compliance method, whose resolution of crack depth measurement was 0.01 mm. The stress levels that caused crack growth and those that did not were identified. The fatigue threshold of pre-cracked specimen was defined as no-break at 10^7 cycles. The non-broken specimen was heat tinted after fatigue test. The crack was opened, and the final crack depth was measured on the fracture surface. The stress intensity factor was calculated using the equation for pure bending [5].

Effects of Stress Ratio (*R*) and Material Hardness on ΔK_{th}

Fracture Mechanics Evaluation of Fatigue Threshold of Small Crack

The ΔK_{th} data of long cracks from the literature [6–8] are shown in Fig. 3. It covers low carbon steels and low alloy steels whose tensile strengths were ranging between 400 MPa and 1200 MPa. The ΔK_{th} of long cracks is relatively independent of material hardness. This data band of the long cracks is used as a reference.

Specimens 0.17 mm deep cracked were used to examine the effects of stress ratio and material hardness. The ΔK_{th} for fatigue threshold of small cracks is shown in Fig. 4. The hatched band shows the conventional ΔK_{th} data of long cracks shown in Fig. 3. In spite of the ΔK_{th} of long cracks being relatively insensitive to material hardness, small cracks behaved differently depending on material hardness and stress ratio. At low stress ratio $R = -1$, a strong dependency of the ΔK_{th} on material is seen. That is, softer material had lower ΔK_{th}.

On the other hand, at high stress ratio around $R = 0.5$, no remarkable dependency is seen. The difference between long and short crack was caused by the difference in crack closure behavior.

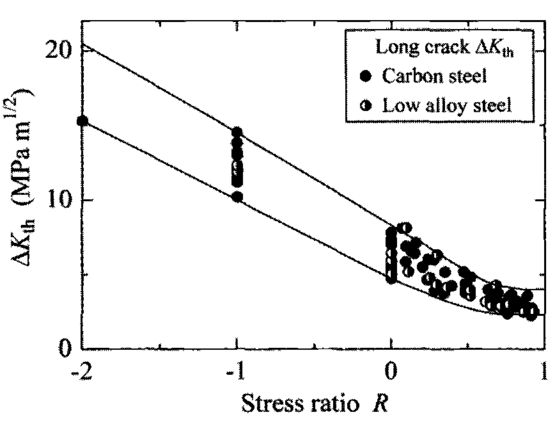

FIG. 3—*Conventional ΔK_{th} of long cracks [6–8].*

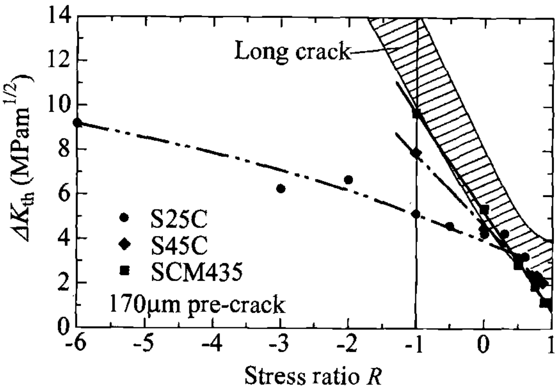

FIG. 4—*Effect of material and stress ratio on ΔK_{th}.*

Measurement of Crack Closure of Small Crack

The offset stress-displacement curves at fatigue thresholds are shown in Fig. 5. A short horizontal bar next to each curve indicates the crack opening stress. No crack closure was observed in the region higher than $R = 0.6$. A clear difference between materials was observed in the low R region. At $R = -1$, the crack opening stress of soft material (S25C) shown in Fig. 5*a* was zero. On the contrary, the crack closure in harder materials (S45C and SCM435) as shown in Figs. 5*b* and *c* was definitely higher. The crack closure was difficult to be formed in the case of short cracks in a soft material.

The effect of stress ratio on $(\Delta K_{eff})_{th}$ is shown in Fig. 6. The $(\Delta K_{eff})_{th}$ of long cracks has been considered to be almost constant irrespective of stress ratio and material as shown by the hatched band. Solid symbols show the $(\Delta K_{eff})_{th}$ obtained for small cracks in this study. Most of them were almost constant. However, a remarkable decrease in $(\Delta K_{eff})_{th}$ was observed in an extremely high R region in the case of SCM435. Such a remarkable decrease has never been experienced by the authors in the case of long cracks. This phenomenon is examined in a later section.

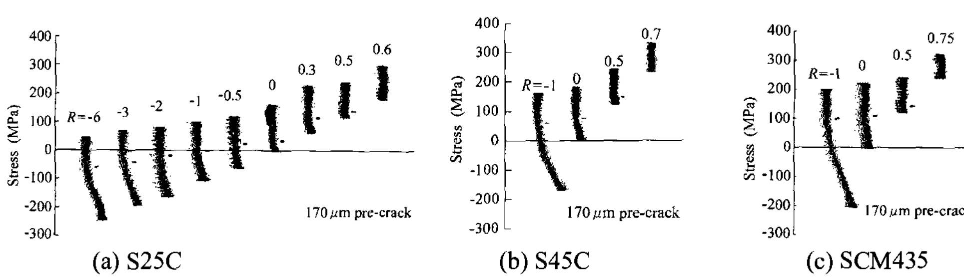

FIG. 5—*Offset stress-displacement curves at fatigue thresholds.*

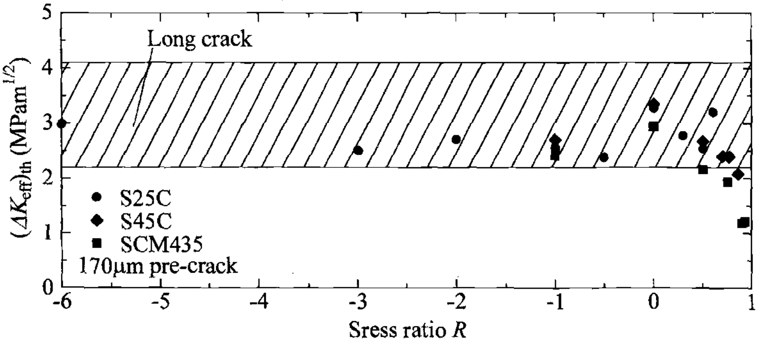

FIG. 6—*Effect of stress ratio R on* $(\Delta K_{eff})_{th}$.

Interpretation of Material Hardness Effect on the ΔK_{th} *of Small Cracks*

The effect of material hardness on crack opening stress intensity factor (K_{op}) is shown in Fig. 7. Figure 7*a* shows the results for $R = -1$. K_{op} shown by solid circles were strongly dependent on material hardness. K_{op} was higher in harder material. Since $(\Delta K_{eff})_{th}$ was almost constant, irrespective of material hardness as shown by the hatched band, the higher crack closure stress increased the capability to withstand higher applied stress, which resulted in higher fatigue threshold of harder material. It is not clear presently why the crack closure stress is affected by material hardness in the case of small cracks. Another study is necessary to investigate the reason of this phenomenon and to specify which kind of crack closure mechanism [2,9] is operating.

On the other hand, K_{op} in high R region were not so much affected by material hardness as shown in Fig. 7*b*. It resulted in almost constant ΔK_{th} irrespective of material hardness.

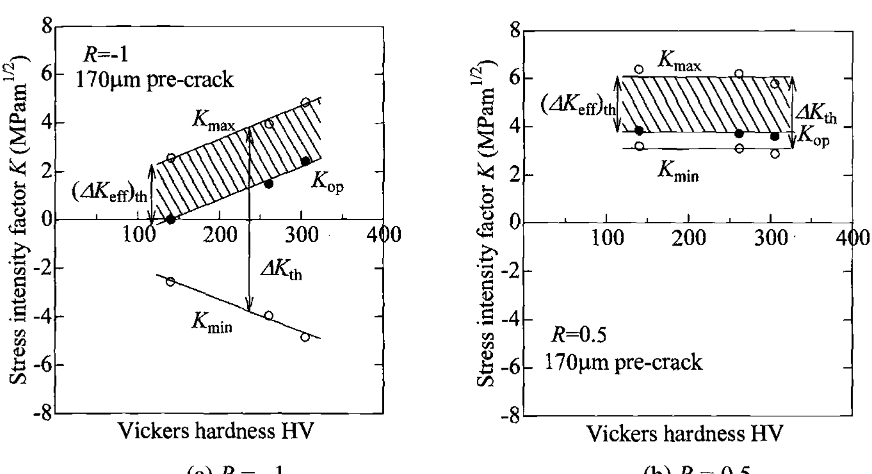

FIG. 7—*Effect of material hardness on the crack opening stress.*

Effect of Crack Size on ΔK_{th}

Fracture Mechanics Evaluation of Fatigue Threshold of Specimen with Small Crack

The effect of crack size was examined using S25C at $R = -1$ and high R. The high R condition was chosen such that the maximum stress was equal to the yield stress. As a consequence, R was higher than 0.47. The effect of crack depth on fatigue threshold is shown in Fig. 8. Circular symbols show the results for $R = -1$. Half solid circles show that they endured 10^7 cycles without any crack growth. When the initial crack was deeper than 0.2 mm, some amount of crack growth occurred, and then it ceased to grow at the point indicated by the solid circle. Square symbols show the results for high stress ratios. Cracks did not start to grow from the initial crack at fatigue threshold in the case of high stress ratio. Here, the slope of each curve was the same for crack shallower than 0.1 mm, and it was about 1/6 as Murakami and Endo reported [1].

Fatigue threshold specimens were heat tinted after fatigue tests. The crack was opened, and the crack depth was measured on the fracture surface. ΔK_{th} for fatigue threshold was calculated using the final crack depth. ΔK_{th} was plotted against crack depth in Fig. 9. The value of the abscissa shows the initial crack depth for no-growth specimen and the final crack depth for crack-arrested specimen. The crack size at which size effect became apparent depended on mean stress condition. In the case of $R = -1$, the size effect was present in relatively wide range up to a few millimeters. On the other hand, at high stress ratio, the size effect was present only for crack shallower than 0.1 mm. This difference can be explained by the crack closure.

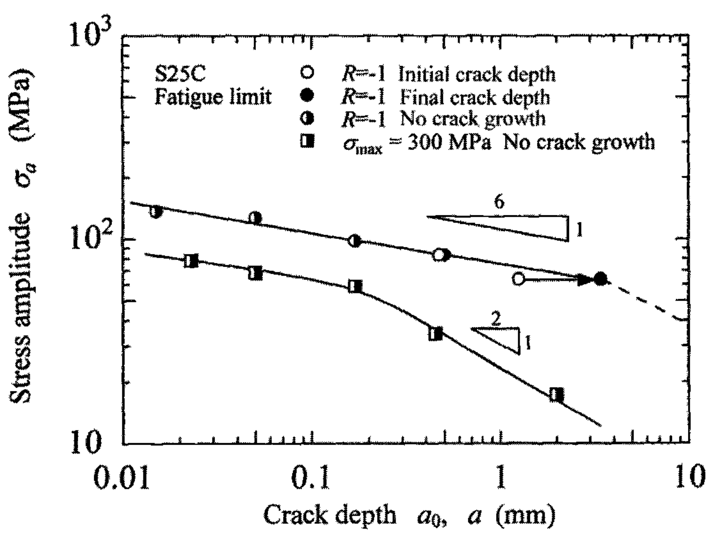

FIG. 8—*Effect of crack depth on fatigue threshold.*

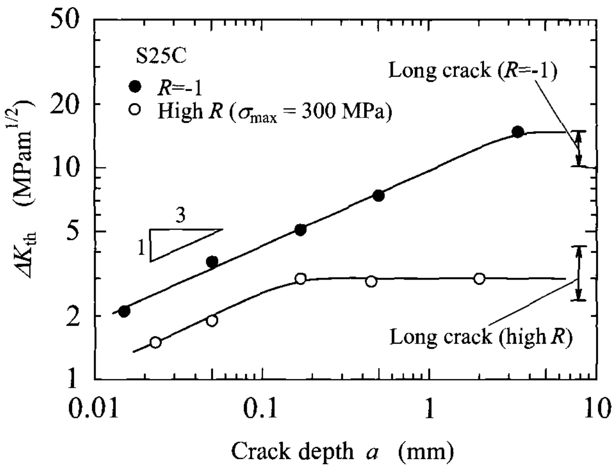

FIG. 9—*Effect of crack depth on ΔK_{th}.*

Effect of Crack Depth on Crack Closure

The offset stress-displacement curves at fatigue thresholds for $R = -1$ are shown for each final crack depth in Fig. 10. The crack opening stress indicated by a short horizontal bar for the crack shallower than 0.1 mm was quite low and slightly negative. In the case of relatively deep initial crack, the crack closure was formed as crack grew and the crack was arrested. For high R conditions, the cracks were fully open for any crack depth.

$(\Delta K_{eff})_{th}$ is shown in Fig. 11. For a crack deeper than 0.1 mm, $(\Delta K_{eff})_{th}$ was independent of crack depth and was the same as that of long cracks. What should be noted here is that $(\Delta K_{eff})_{th}$ was not a constant value but was dependent on crack depth shallower than 0.1mm.

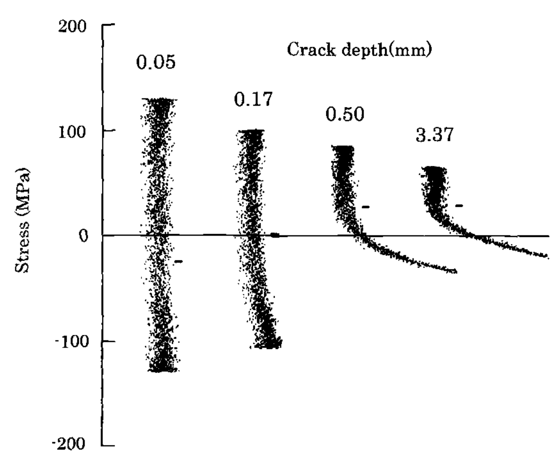

FIG. 10—*Stress-offset displacement curves at fatigue limit (S25C, $R = -1$).*

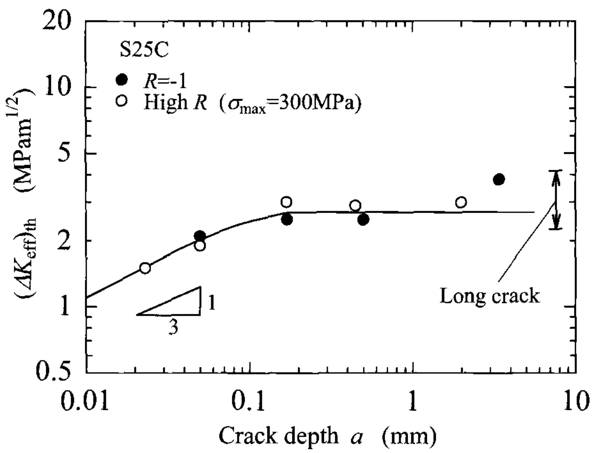

FIG. 11—*Effect of crack depth on $(\Delta K_{eff})_{th}$.*

Interpretation of Crack Size Effect on ΔK_{th} Based on Crack Closure

As shown in Fig. 12, the ΔK_{th} for $R = -1$ was proportional to $a^{1/3}$, which well agrees with the dependency in Eq 1. The cause of this dependency can be interpreted by the crack closure. Open circles show the ΔK_{th}. The crack size effect was caused by the following two reasons: for value larger than 4.6μm$^{1/3}$ in the abscissa, which corresponds to the crack deeper than 0.1mm, K_{op} was higher in deeper crack; and $(\Delta K_{eff})_{th}$ shown by the hatched band was almost constant in this region. As a consequence, the increase of K_{op} caused the increase of ΔK_{th}.

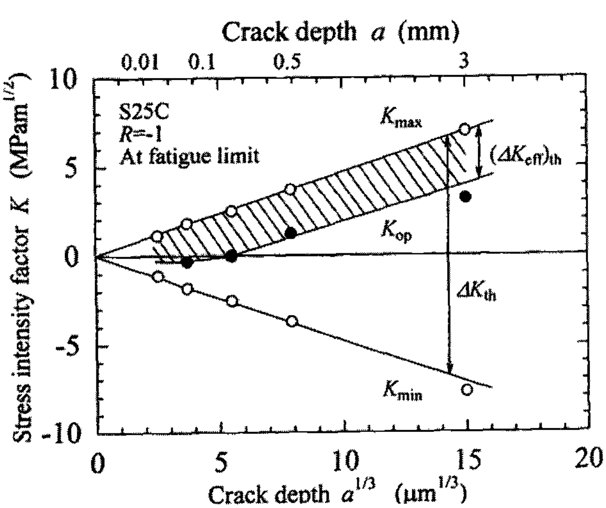

FIG. 12—*Effect of crack depth on ΔK_{th} behavior.*

For value less than 4.6 $\mu m^{1/3}$, where the crack was shallower than 0.1 mm, K_{op} was almost zero, and the $(\Delta K_{eff})_{th}$ tended to decrease as was shown in Fig. 11. Although the $(\Delta K_{eff})_{th}$ for the shortest crack could not be detected in this study, the general trend of $(\Delta K_{eff})_{th}$ in Fig. 11 shows that $(\Delta K_{eff})_{th}$ decreases in shallow crack region.

These combinations of K_{op} and $(\Delta K_{eff})_{th}$ behaviors caused the peculiar behavior of ΔK_{th} in short crack. As a consequence, the 1/3 power law of crack depth holds in relatively wide range.

Large Reduction of $(\Delta K_{eff})_{th}$ at Extremely High Stress Ratio

Effect of Crack Depth on the Reduction of $(\Delta K_{eff})_{th}$

The authors experienced a large reduction of $(\Delta K_{eff})_{th}$ as shown in Fig. 6 at an extremely high stress ratio in hard material. The authors have never experienced such an unusual decrease in $(\Delta K_{eff})_{th}$, even at high R region in the case of long cracks. Since crack depth was supposed to affect this phenomenon, the effect of crack depth was examined. Other conditions were kept as follows: the stress ratio was chosen at extremely high value at R = 0.85–0.95, and SNCM439 was used as an example of hard material. Test results are shown in Fig. 13. Numbers next to symbols show crack depth in millimeter. When the crack was deeper than 1 mm, ΔK_{th} was within the data band of long cracks. ΔK_{th} decreased for cracks shallower than 1 mm. Since no crack closure occurred at high R condition, $(\Delta K_{eff})_{th}$ also decreased as shown in Fig. 14.

The dependency of $(\Delta K_{eff})_{th}$ on crack depth is shown in Fig. 15. In the figure, all of the data obtained by the authors including materials with different hardness and different stress ratios were plotted. The hatched band represents the major trend of small cracks in this study. It covers soft material irrespective of stress ratio and hard material at low stress ratio. The results for hard material at extremely high R behaved differently as shown by the solid line. An extraordinary decrease was found in this case. The dependency of crack depth could be expressed by a 1/3 power law of crack depth also in this case. The mechanism of such a large reduction is not clear yet. Since the maximum stress was less than 40 % of $\sigma_{0.2}$ for SNCM439 and less than 50 % of $\sigma_{0.2}$ for SCM435, the large scale yielding is not considered to be the possible cause of this phenomenon.

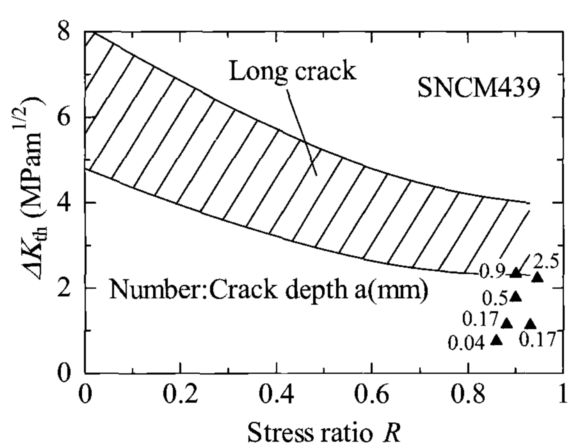

FIG. 13—*Effect of crack depth on the ΔK_{th} of hard material.*

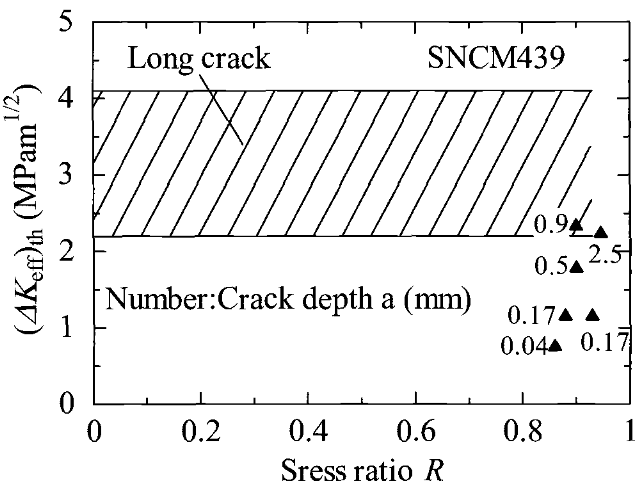

FIG. 14—*Effect of crack depth on the $(\Delta K_{eff})_{th}$ of hard material.*

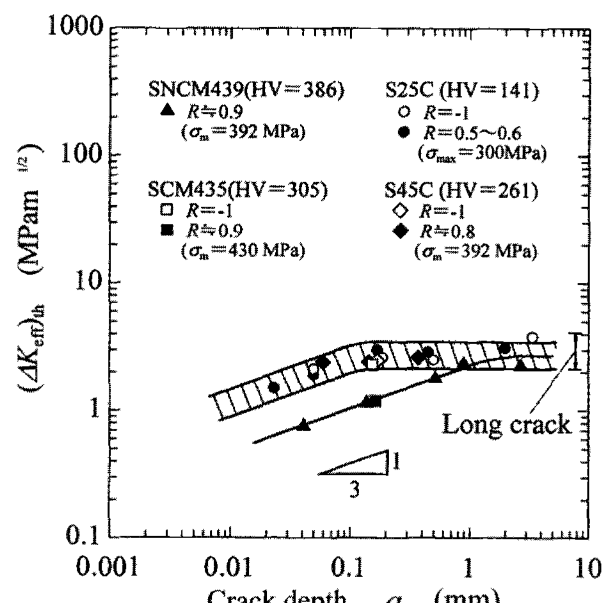

FIG. 15—*Effect of crack depth on $(\Delta K_{eff})_{th}$.*

Near Threshold Crack Growth Behavior of Short Crack at High Stress Ratio

The crack propagation rates are shown in Fig. 16. Square symbols show the reference data of 3.5NiCrMoV low alloy steel (0.24 % C, 0.2 % Si, 0.35 % Mn, 3.5 % Ni, 1.8 % Cr, 0.40 % Mo, 0.12 % V), which has a similar strength to SNCM439. It is the "worst case" data [10] obtained at high stress ratio in crack closure free condition. The other symbols are for short cracks with different initial crack depth. The point with the arrow is for each fatigue threshold specimen and the other data were obtained tested at a stress slightly above each fatigue threshold. It was shown that short crack did propagate below the $(\Delta K_{eff})_{th}$ of long cracks.

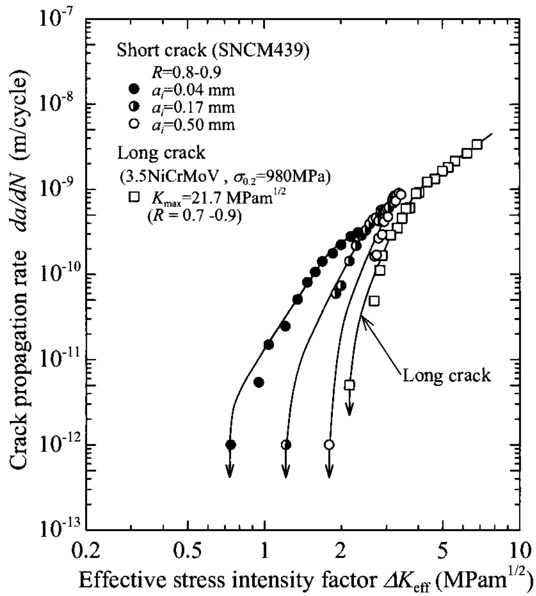

FIG. 16—*Effect of crack length on fatigue crack propagation rate.*

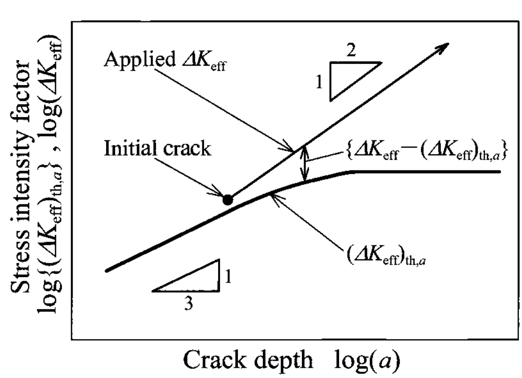

FIG. 17—*Definition of a parameter for fatigue crack propagation.*

Although ΔK_{eff} as it is has failed to uniquely evaluate the crack growth behaviors of short cracks, the authors introduced a modification similar to the proposal by Ishihara and McEvily [11]. They proposed a new model to express the fatigue crack propagation rate. They expressed the crack propagation rate as a power law of $\{\Delta K_{eff} - (\Delta K_{eff})_{th}\}$. However, the $(\Delta K_{eff})_{th}$ varied depending on crack depth as shown in Fig. 17, and the authors defined $(\Delta K_{eff})_{th,a}$ for an instantaneous crack depth a and introduced a new parameter, $\{\Delta K_{eff} - (\Delta K_{eff})_{th,a}\}$. This shows the deviation of applied stress intensity from the resistance of material. The re-evaluated results are shown in Fig. 18. All of the data fell in a narrow band irrespective of crack size including long crack. The result shows that ΔK_{eff} still plays an important role to govern fatigue propagation rate also in the short crack regime as short as 0.04 mm.

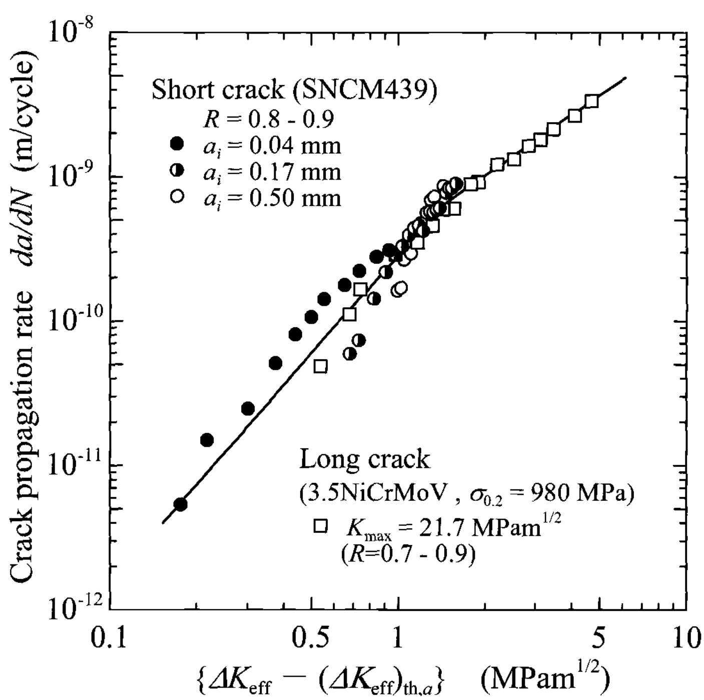

FIG. 18—*Fatigue crack propagation rate of short crack plotted against* $\{\Delta K_{eff} - (\Delta K_{eff})_{th,a}\}$.

Fractographic Examination

Since the large decrease in $(\Delta K_{eff})_{th,a}$ was observed only in hard materials at high stress ratio, an environmental effect was suggested. Fractographic examination was done and is shown in Fig. 19. In the diagram, solid squares show no-breaks, and cross marks show failures. The fracture surface was a usual transgranular morphology, which is characteristic of low fatigue crack propagation rate. Although the effect of atmospheric environment on this behavior cannot be denied, no typical morphology suggesting the existence of environmental cracking was observed, at least on the fracture surface.

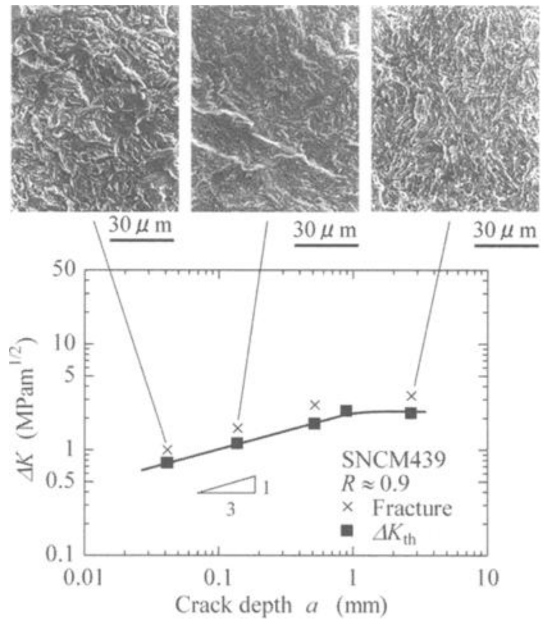

FIG. 19—*Fracture surface of SNCM439.*

Conclusions

Effects of material hardness, mean stress, and crack size on the ΔK_{th} of small cracks were studied using two-dimensionally cracked specimens. The cause of these effects was investigated on the basis of crack closure behavior. The crack closure measurements on very shallow cracks were done. The obtained results are as follows:

1. The ΔK_{th} of small cracks were substantially affected by material hardness in the low stress ratio region. No material hardness effect was seen in the high stress ratio region.
2. The crack closure measurement showed that higher K_{op} resulted in higher ΔK_{th} in harder material in low stress ratio region. It was also found that the crack was closure free in high R region, which resulted in the independency of material hardness in high R region.
3. The crack size effect was caused by two reasons. Higher K_{op} in deeper crack region and smaller $(\Delta K_{eff})_{th}$ in shallower crack region caused a 1/3 power law dependency of ΔK_{th} on crack depth.
4. A substantial decrease of $(\Delta K_{eff})_{th}$ was observed in the case of small crack at extremely high R condition in hard material. The large reduction of $(\Delta K_{eff})_{th}$ was not caused by the environmental cracking. Even in such a case, the crack propagation rate could be uniquely evaluated using a new parameter $\{\Delta K_{eff} - (\Delta K_{eff})_{th,a}\}$ to account for the change of resistance against fatigue crack growth.

References

[1] Murakami, Y. and Endo, M., "Effects of Hardness and Crack Geometries on ΔK_{th} of Small Cracks Emanating from Small Defects," *The Behavior of Short Fatigue Cracks*, K. J. Miller and E. R. de los Rios, Eds., *Mech. Eng. Pub.*, 1986, pp. 275–293.

[2] Elber, W., "The Significance of Fatigue Crack Closure," *Damage Tolerance in Aircraft Structures, ASTM STP 486*, ASTM International, West Conshohocken, PA, 1971, pp. 230–242.

[3] Kondo, Y., Sakae, C., Kubota, M., and Kudou, T., "The Effect of Material Hardness and Mean Stress on the Fatigue Limit of Material Containing Small Defect," *Fatigue and Fracture of Engineering Materials and Structures*, Vol. 26, 2003, pp. 675–682.

[4] Kikukawa, M., Jono, M., Tanaka, K., and Takatani, M., "Measurement of Fatigue Crack Propagation and Crack Closure at Low Stress Intensity Level by Unloading Elastic Compliance Method," *Journal of the Society of Materials Science, Japan*, (in Japanese), 1976, pp. 899–903.

[5] Brown, W. F., Jr. and Srawley, J. E. "Plain Strain Crack Toughness Testing of High Strength Metallic Materials," *ASTM STP 410*, ASTM International, West Conshohocken, PA, 1966, p. 13.

[6] Usami, S., "Applications of Threshold Cyclic-Plastic-Zone-Size Criterion to Some Fatigue Limit Problem," *Fatigue Thresholds*, Eng., Advisory Service, 1982, pp. 205–238.

[7] Nakai, Y., Tanaka, K., and Kawashima, R., "Stress-Ratio Effect on Fatigue Crack Growth Threshold in Steels," *Journal of the Society of Materials Science, Japan*, (in Japanese), 1984, pp. 1045–1051.

[8] Barsom, J. M. and Rolfe, S. T., *Fracture and Fatigue Control in Structures*, 3rd ed., ASTM International, West Conshohocken, PA, 1999, p. 199.

[9] Suresh, S. and Ritchie, R. O., "Near-Threshold Fatigue Crack Propagation: A Perspective on the Role of Crack Closure," *Fatigue Crack Growth Threshold Concepts*, The Metallurgical Society of AIME, 1984, pp. 227–261.

[10] Ritchie, R. O., Davidson, D. L., Boyce, B. L., Campbell, J. P., and Roder, O., "High-Cycle Fatigue of Ti-6Al-4V," *Fatigue and Fracture of Engineering Materials and Structures*, Vol. 22, 1999, pp. 621–632.

[11] Ishihara, S. and McEvily, A. J., "An Analysis of the Rate of Growth of Small Fatigue Cracks," *Proc. of Fatigue 2002*, Vol. 3, 2002, pp. 1981–1988.

SESSION 7B: DUCTILE-TO-BRITTLE TRANSITION

Journal of ASTM International, April 2005, Vol. 2, No. 4
Paper ID JAI12051
Available online at www.astm.org

Kim R. W. Wallin[1]

Critical Assessment of the Standard ASTM E 399

ABSTRACT: The plane-strain fracture toughness, K_{IC}, defined by ASTM E 399, is assumed to represent a size insensitive lower bound value. The interpretation is due to the original work by George Irwin. In this work the consistency of the ASTM K_{IC} plane-strain fracture toughness standard (ASTM E 399) is examined by reassessing the original data used to develop the standard, based on present knowledge about fracture micromechanisms. Originally, the standard was based on continuum mechanics assumptions, which have later been found inadequate to describe the real physical fracture process. The materials used for the development of ASTM E 399 were generally aluminum and titanium alloys or extra high strength steels. The materials had in common that their fracture micro-mechanism was ductile fracture, i.e., the materials showed a rising tearing resistance curve. Therefore, the fracture toughness did not show the expected decreasing trend with increasing specimen size, but generally the opposite trend. The specimen thickness was assumed to be the limiting dimension, even though much of the experimental data indicated that the specimen ligament size, not the thickness, controlled the fracture toughness value.

KEYWORDS: K_{IC}, E 399, size effects, plane-strain, fracture toughness, tearing resistance

Introduction

Integrity assessment of structures containing planar flaws (real or postulated) necessitates the use of fracture mechanics. Fracture mechanics compares in principle two different crack growth parameters: the driving force and the material resistance. The driving force is a combination of the flaw size (geometry) and the loading conditions, whereas the material resistance describes the material's capability to resist a crack from propagating. To date, there exist several different testing standards (and non-standardized procedures) by which it is possible to determine some parameter describing the materials fracture resistance (ASTM E 399, ASTM E 1820, BS 7448, ESIS P2, etc.). Unfortunately, this has lead to a myriad of different parameter definitions, and their proper use in fracture assessment may be unclear.

Historically, fracture mechanics evolved from a continuum mechanics understanding of the fracture problem. It was assumed that there existed a single fracture toughness value controlling the materials fracture. If the driving force were less than this fracture toughness, the crack would not propagate, and if it exceeded the fracture toughness, the crack would propagate. Thus, crack initiation and growth were assumed to occur at a constant driving force value. The only thing assumed to affect this critical value was the constraint of the specimen (or structure). Since at that time there were no means to quantitatively assess the effect of constraint on the fracture toughness, the fracture toughness had to be determined with a specimen showing as high a constraint as possible. This lead to the use of deeply cracked, bend specimens for the fracture toughness determination.

Manuscript received 6 October 2003; accepted for publication 24 May 2004; published April 2005. Presented at ASTM Symposium on Fatigue and Fracture Mechanics: 34th Volume on 19–21 November 2003 in Tampa, FL; S.R. Daniewicz, J.C. Newman, Jr., and K-H. Schwalbe, Guest Editors.
[1] Research Professor, VTT Industrial Systems P.O. Box 1704, FIN-02044 VTT, Finland.

Historically, the micro-mechanisms of fracture were not considered. It was assumed that the stress state assumption of the continuum mechanics analysis was valid for fracture toughness as well, regardless of fracture micro-mechanism. This allegation has later been proven to be wrong. Different fracture micro-mechanisms exhibit different physical features that affect the properness of a specific fracture toughness parameter to describe that fracture micro-mechanism.

The common interpretation of the plane-strain fracture toughness K_{IC}, defined by ASTM E 399, is a specimen size insensitive lower bound fracture toughness corresponding to plane-strain stress state. The interpretation is due to the original work by George Irwin where he postulated the expected effect of specimen thickness on fracture toughness (Fig. 1). George Irwin based his conclusions on maximum load toughness behavior of center cracked tension (CC(T)) specimens and 3-point bend (SE(B)) specimens of two aluminum alloys, combined with the specimens macroscopic fracture surface appearance [1]. Even though the experiments did not really correspond to any proper fracture toughness description, nor fracture event, the postulated thickness effect was soon adopted as representing the physical "truth" of fracture behavior. This constituted also the expectations for the development of the ASTM E 399 testing standard.

The original Irwin data did not, however, reflect the effect of specimen size on fracture toughness. The original data are shown in Fig. 2 [2]. In reality, the data show the difference in maximum load toughness between low constraint specimens with a large slim ligament and high constraint specimens with a short nearly square ligament. The aluminum alloy in question failed by a typical ductile fracture mechanism. Today it is commonly known that the ductile fracture process is connected with a rising tearing resistance curve. The steepness of the curve is related to, besides material, loading geometry and ligament slimness (Fig. 3).

The CC(T) specimens with a slim ligament, or a large W-a, in relation to B, show a steeper tearing resistance curve than the bend specimens. This explains part of the fracture toughness difference observed by Irwin [2]. Additionally, the amount of ductile crack growth that corresponds to maximum load is roughly proportional to the original ligament size. The CC(T) specimens used by Irwin, had a 200 mm long ligament compared to the 25 mm ligament of the bend specimens he used. This means that the crack growth of the CC(T) specimens was nearly 10 times larger than for the bend specimens. This is the main reason for the fracture toughness difference observed by Irwin [2]. Actually, in the original test report [2] it is mentioned that the CC(T) specimens experienced large crack growth before load maximum. The amount of crack growth was even monitored during the test by making ink markings on the specimens. This large crack growth was, however, ignored, as it occurred during the rising load part of the test. This erroneous interpretation was made because the existence of rising tearing resistance curves was not recognized. Even though the experiments in no way reflected the effect of specimen thickness, the thickness effect was still taken as the postulate for the development of ASTM E 399. The assumption was that a valid K_{IC} value must represent a minimum toughness value of the material.

The materials used for the development of ASTM E 399 were generally aluminum and titanium alloys or extra high strength and maraging steels. The materials had in common that their fracture micro-mechanism was ductile fracture, i.e., the materials showed a rising tearing resistance curve. Unfortunately, this was not understood at that time, when the continuum mechanics type fracture behavior was assumed. The standard developers therefore confronted a new problem, when it was observed that the fracture toughness did not generally show the expected decreasing trend with increasing specimen size, but the opposite trend as shown by Fig. 4 [3]. This increasing toughness introduced the additional demand that $P_{max}/P_Q < 1.1$.

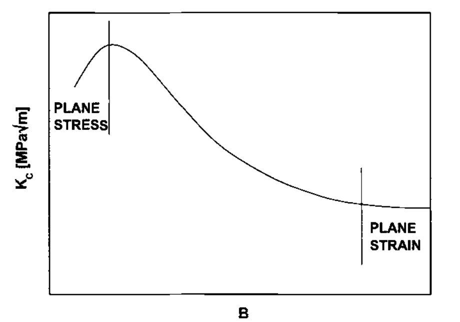

FIG. 1—*Schematic presentation of the assumption of thickness effect on fracture toughness.*

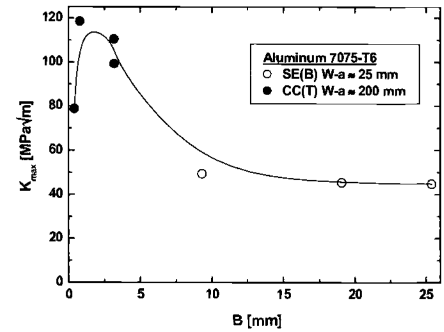

FIG. 2—*Original Irwin data used to postulate classical thickness effect [2].*

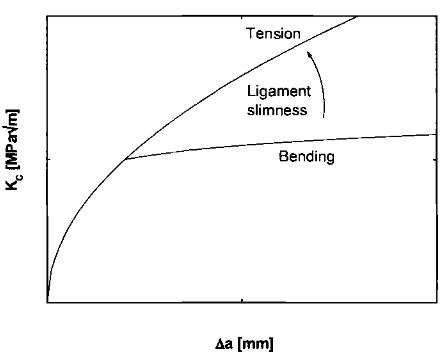

FIG. 3—*Schematic presentation of the geometry effect on tearing resistance.*

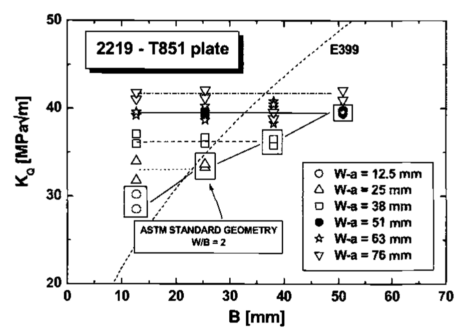

FIG. 4—*Old K_Q data used to develop ASTM E 399 showing increasing toughness with increasing specimen size [3].*

The specimen thickness was still assumed to control the materials fracture toughness, as postulated by Irwin. The assumption prevailed, even though the experimental data indicated that it is the specimen ligament size, not thickness, that controls the fracture toughness value (Fig. 5) [3]. The belief in the plane-strain, plane-stress postulate was so strong that this evidence was disregarded. Also, the plane-strain fracture toughness was assumed to be a lower bound specimen size insensitive material parameter, even though the results indicated the reverse, i.e., that K_{IC} increases with specimen size. Evidently, because it was tried to explain the results solely based on the constraint effect, the real reason for this increase in toughness was never understood correctly. Based on the present physical understanding of ductile fracture, the increase in fracture toughness is easy to explain.

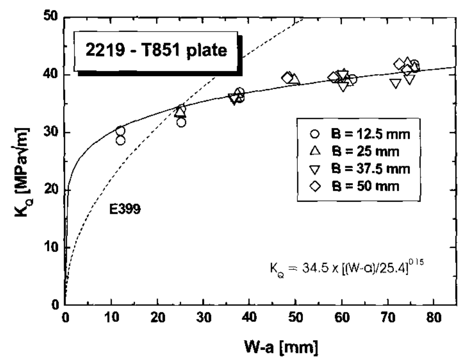

FIG. 5—*Same data as in Fig. 4 showing that ligament size controls the increasing toughness [3].*

Assessment of Experimental Data

At the time of the development of the K_{IC} standard, there were no reliable means of monitoring crack growth during the test, and also crack growth was assumed to occur at a constant value of K_{IC}. This led to using the 95 % secant method for the determining K_Q. If all non-linearity in a load-displacement curve of a K_{IC} test specimen were due to crack growth, a 95 % secant would correspond to approximately a 2 % crack growth with respect to the ligament. With increasing ligament size, the absolute crack growth, defined by the 95 % secant, also increases. Knowing that materials in the case of ductile crack growth exhibit rising tearing resistance curves, the increasing toughness with increasing specimen size is quite understandable.

Much of the original work studying the size effects on fracture toughness was performed with other than bend specimens. Since the present ASTM E 399 covers only bend geometries, this assessment focuses on bend specimens. Next, vintage (and some newer) data for the different material types are examined in the view of the present understanding of ductile fracture.

Aluminum Alloys

Besides the comprehensive data set presented in Figs. 4 and 5, a few other size effect studies on aluminum alloys have been performed. Figure 6 shows results for a high strength aluminum alloy [4]. It is noteworthy that the thinnest and thickest specimens with the same ligament size show essentially the same fracture toughness. The intermediate thickness specimen, having the smallest ligament, produces the lowest fracture toughness. Figure 6*c*, which contains additional data, lacking ligament size information, also fails to show any clear dependence on thickness.

A newer data set for a lower strength aluminum alloy behaves similarly (Fig. 7) [5]. In this case, the smallest thickness specimens also had the smallest ligaments. Thus, both increasing thickness as well as increasing ligament size increase the fracture toughness. The scatter in K_Q is, however, clearly less when plotted in terms of ligament size. Also here, specimens with different thickness but the same ligament size produce the same fracture toughness.

The most recent data set shows again the same trend as can be seen in Fig. 8 [6]. Also here, the fracture toughness is clearly controlled by the ligament size, not the specimen thickness.

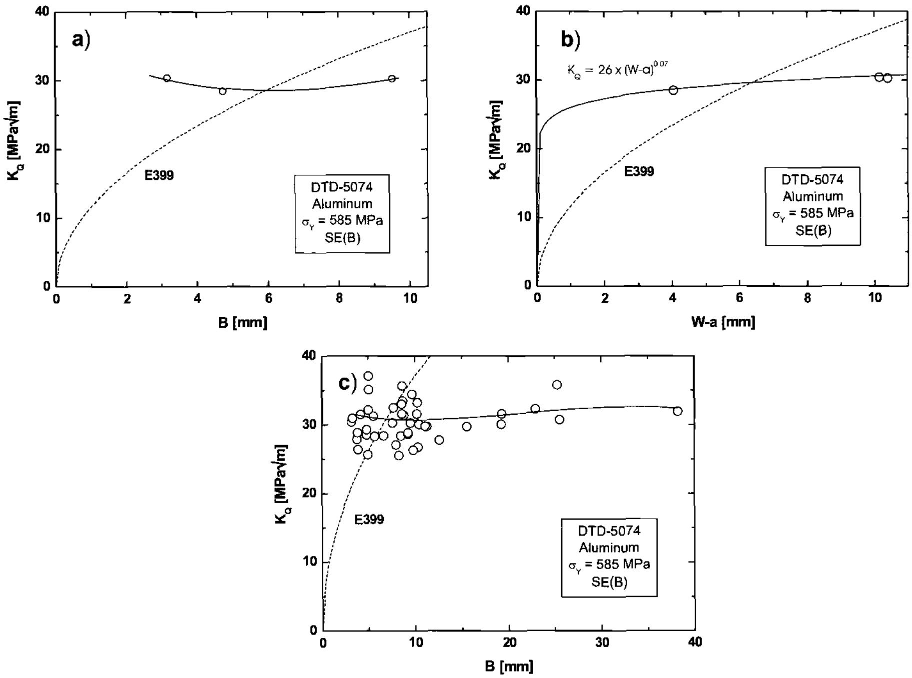

FIG. 6—*Old K_{IC} data used to develop British K_{IC} standard showing no correlation with thickness, but increasing toughness with increasing specimen ligament size [4]; Fig. 6*c *shows additional data, lacking ligament size information.*

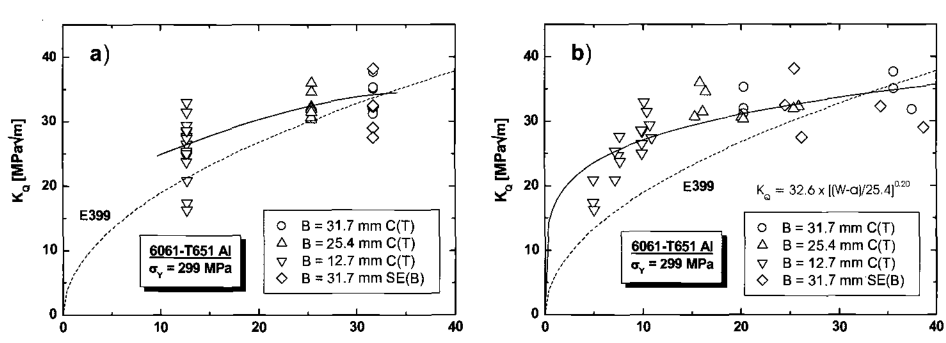

FIG. 7—*Newer K_{IC} data showing increasing toughness with increasing specimen thickness and ligament size [5].*

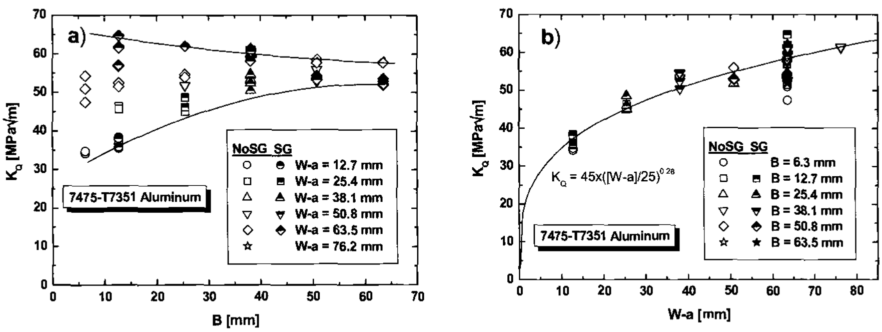

FIG. 8—*Recent K_{IC} data showing no correlation with thickness but increasing toughness with increasing specimen ligament size [6].*

Titanium Alloys

Due to their higher strength, titanium alloys have been investigated a little more widely than aluminum alloys. Figure 9*a* shows a classical data set used to defend the size criteria in ASTM E 399 [7]. The fracture toughness first decreases and then becomes constant with increasing thickness. The data are affected, however, by the fact that the specimen ligament size is constant. This means that the results actually indicate that the tearing resistance curve for this material is unaffected by specimen ligament geometry as long as the ligament is less than five times the specimen thickness (Fig. 9*b*).

When the ligament geometry becomes very slim, the tearing resistance curve will start to become increasingly steeper. Since the ligament size is constant, all specimens experience approximately the same amount of crack growth at K_Q. Very slim ligaments, having steeper resistance curves, will thus provide higher K_Q values. The behavior seen in Fig. 9 is thus not connected to absolute thickness of the specimen, but to the ligament geometry (B/(W-a) < 0.2).

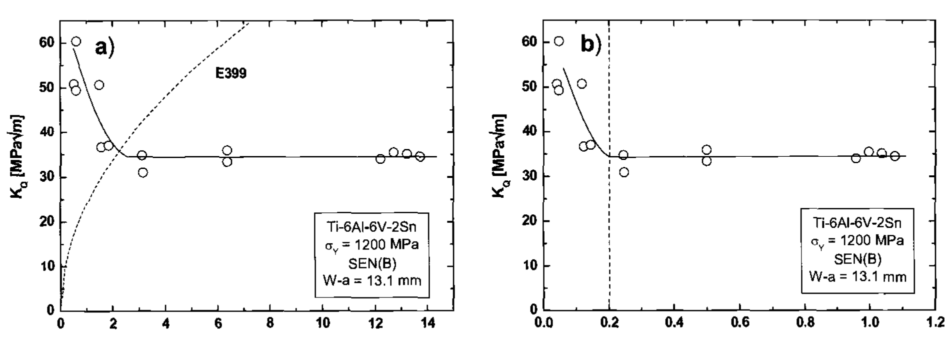

FIG. 9—*Old K_{IC} data used to develop ASTM E 399 showing reducing toughness followed by constant toughness with increasing specimen thickness [7]. The increase in toughness is related to ligament slimness (B/(W-a) < 0.2).*

Another old data set, where also the ligament size is varied, shows again the typical behavior of increasing fracture toughness with increasing ligament size (Fig. 10) [4]. Figure 10*a*, which also contains data lacking ligament size information, fails to show any clear dependence on thickness.

Two slightly newer data sets were generated by Munz [8]. His data for two different heats are presented in Figs. 11 and 12. Both data sets show increasing fracture toughness with increasing ligament size and thickness. The most revealing point of the Munz data is that for one heat, he also determined the material's actual tearing resistance curve (Fig. 11*c*). The tearing resistance curve shows no effect of specimen thickness. The reason is probably that the shortest ligaments were also connected with the thinnest specimens. Thus, the problem with extreme ligament slimness was avoided. Another very significant detail of the results is the similarity between the tearing resistance curve (Fig. 11*c*) and the fracture toughness (K_Q) as a function of ligament size (Fig. 11*b*). If, the assumption of the K_Q value representing a 2 % crack growth is valid, one would actually expect exactly the seen dependence. The Munz data provide very strong proof for the assumption that the K_Q values are simply a function of ligament size, not thickness.

An even more recent data set [5] shows the same as the previous ones (Fig. 13). The fracture toughness is controlled by the ligament size, not the thickness.

Extra High Strength Steels

Extra high strength steels are typically alloyed quenched and tempered steels like AISI 4340. An old data set for AISI 4340 is shown in Fig. 14 [9]. This data set, like the one in Fig. 9, has been used to justify the ASTM E 399 size criteria. However, as in Fig. 9, the specimen ligament size was also held constant here, thus producing a slim ligament for the thinnest specimens (Fig. 14*b*). Because of the slim ligament, the data set cannot be used as evidence of an absolute thickness effect.

Two other old data sets for high strength steels are presented in Fig. 15 [10]. The steels (A517F AM and HY-130 AM) are so tough that valid K_{IC} results are not obtained. However, both materials show increasing toughness with increasing ligament size. Because of this toughness increase with size, it is not possible to obtain a valid K_{IC} for these materials even with extremely large specimens. The tearing resistance curves are too high to fulfill the size criteria at 2 % crack growth.

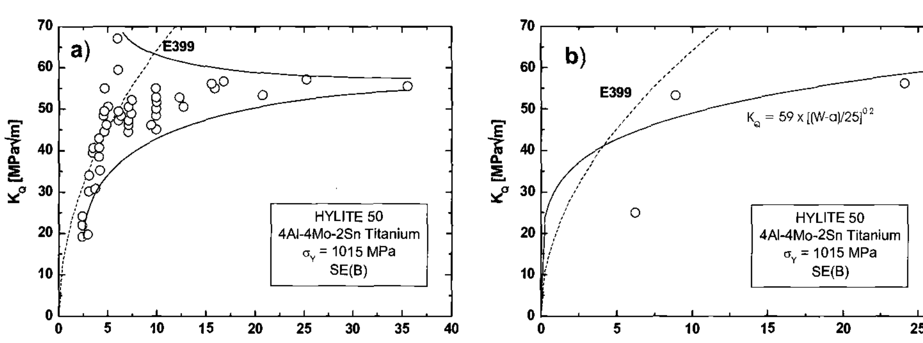

FIG. 10—*Old K_{IC} data used to develop British K_{IC} standard showing increasing toughness with increasing specimen ligament size, but no correlation with thickness [4].*

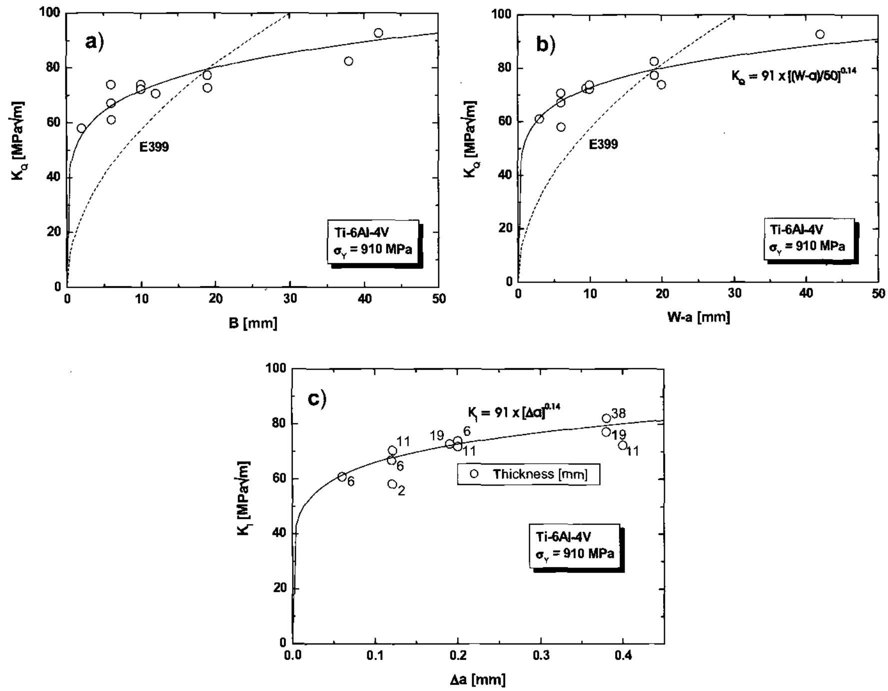

FIG. 11—*Newer K_{IC} data showing increasing fracture toughness with increasing specimen thickness and ligament size [8]; Fig. 11*c *shows the tearing resistance curve.*

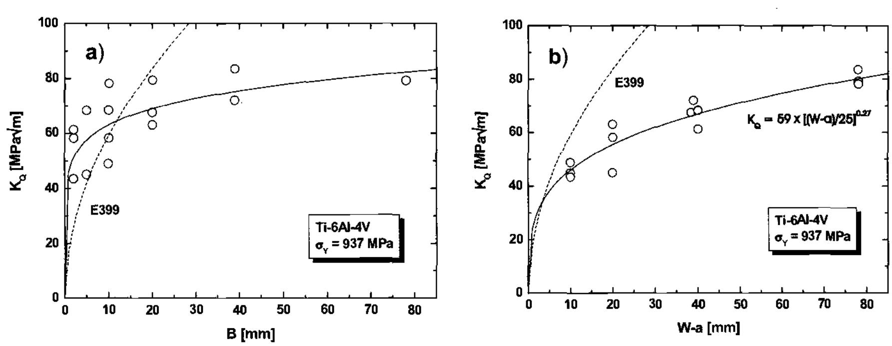

FIG. 12—*More K_{IC} data similar to Fig. 11 [8].*

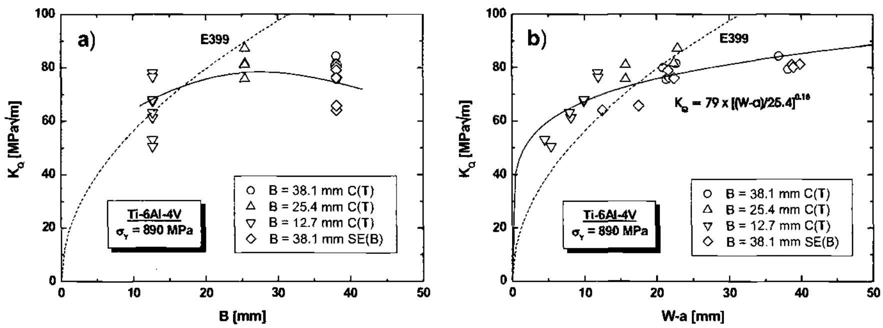

FIG. 13—*Newer K_{IC} data showing increasing fracture toughness with increasing specimen ligament size but not with thickness [5].*

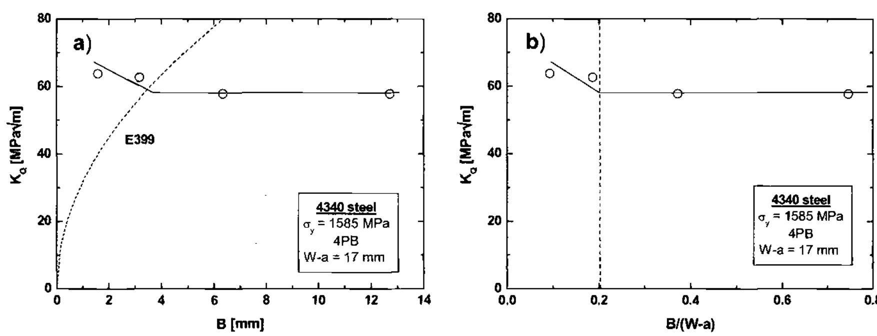

FIG. 14—*Old K_{IC} data used to develop ASTM E 399 showing reducing fracture toughness followed by constant toughness with increasing specimen thickness [9].*

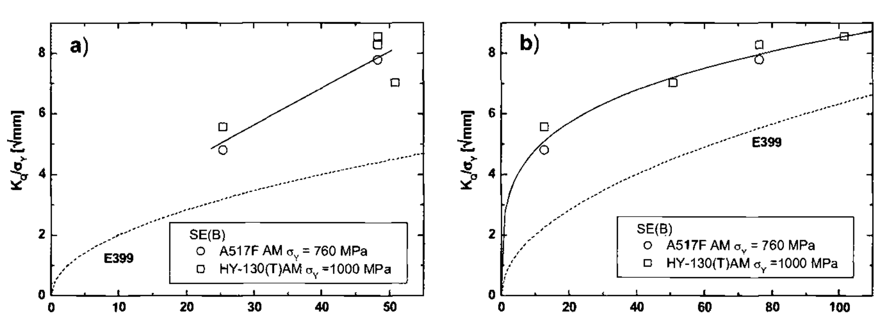

FIG. 15—*Old K_{IC} data showing increasing fracture toughness both with increasing specimen thickness and ligament size [10].*

An exceptional old data set for AISI 4340, where also the tearing resistance curves were estimated is presented in Fig. 16 [7]. The fracture toughness increases again with ligament size, but is essentially unaffected by thickness. The tearing resistance curves (Fig. 16*c*) show well the effect of ligament slimness on the steepness of the curves. The thinnest specimen with a slim ligament has a steeper tearing resistance curve than the thicker specimens. This is not related to the absolute thickness, but to the ligament shape.

A newer data set for AISI 4340 shows the same trend as before (Fig. 17) [5]. The fracture toughness increases both with increasing ligament size and thickness, but the scatter in K_Q when plotted in terms of ligament size is less.

Maraging Steels

Maraging steels were popular materials in the development of ASTM E 399. They are precipitation hardened steels with exceptionally high yield strengths. Because of this, they are ideal for linear elastic fracture tests. The steels seemed to have an additional bonus. They appeared to behave according to the assumption of the thickness-based constraint effect, where increasing thickness decreases fracture toughness until a constant lower bound value is reached. Three such "vintage" data sets are presented in Fig. 18 [9].

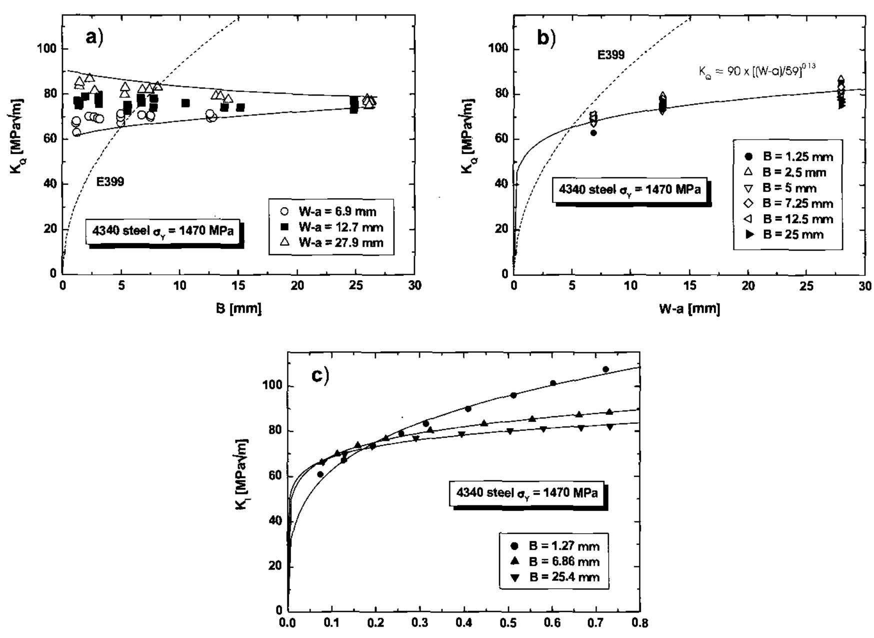

FIG. 16—*Old K_{IC} data showing increasing toughness with increasing specimen ligament size but not with thickness [7]; Fig. 16*c *shows effect of ligament slimness.*

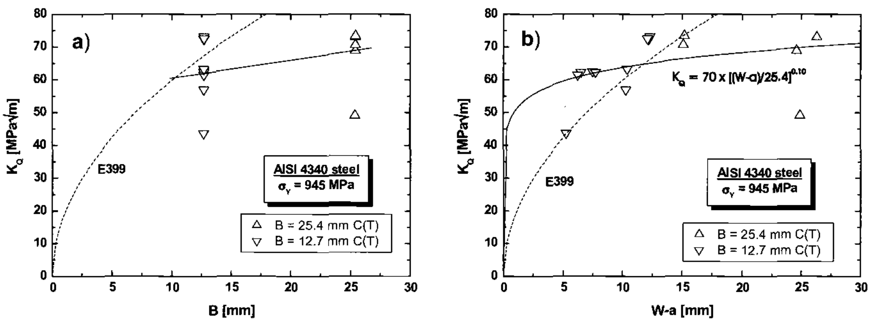

FIG. 17—*Newer K_{IC} data showing increasing toughness with increasing specimen thickness and ligament size [5].*

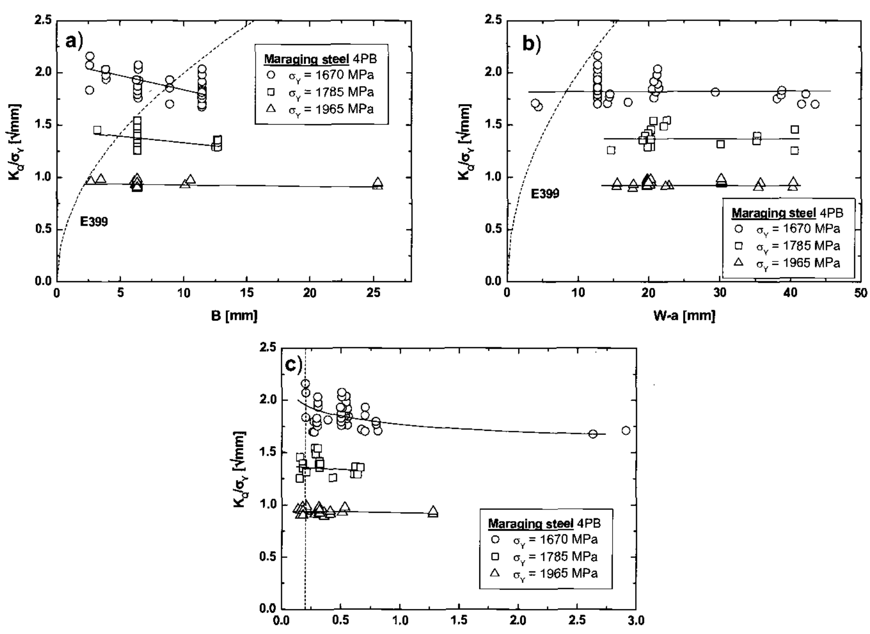

FIG. 18—*Old K_{IC} data used to develop ASTM E 399 showing slightly reducing toughness with increasing specimen thickness, but no effect of ligament size [9]. Increase in toughness is related to ligament slimness.*

All three data sets are strikingly similar. The fracture toughness appears to be practically unaffected by the ligament size, but slightly dependent on specimen thickness. The lack of visible ligament size dependence means that the tearing resistance curves for these maraging steels are flat. However, in all three cases, the fracture toughness increase is connected to slim ligaments (Fig. 18*c*).

A fourth old data set showing the same behavior is shown in Fig. 19 [7]. Also here, the fracture toughness increase is related to the ligament slimness, not absolute specimen thickness.

When data from specimens with less slim ligaments are examined, also the apparent thickness effect changes. Figure 20 shows data used to develop the British equivalent of ASTM E 399 [4]. Here, one large specimen provides a low fracture toughness value, whereas all other specimens yield size insensitive values. The large specimen behavior is likely to be caused by material inhomogeneity, not by the specimen size itself. The smallest specimens show actually a decreasing toughness with decreasing size (Fig. 20*a*). Unfortunately, ligament size information is not given for these specimens [4].

Figure 21 shows old data for two maraging steels with typical moderate fracture toughness [10]. Since these steels have a flat tearing resistance curve, the fracture toughness also appears to be insensitive to both specimen thickness and ligament size. When higher toughness versions of the same steel types were tested, it was difficult to obtain valid K_{IC} results (Fig. 22) [10]. The increased toughness also led to the typical trend of increasing fracture toughness with increasing ligament size.

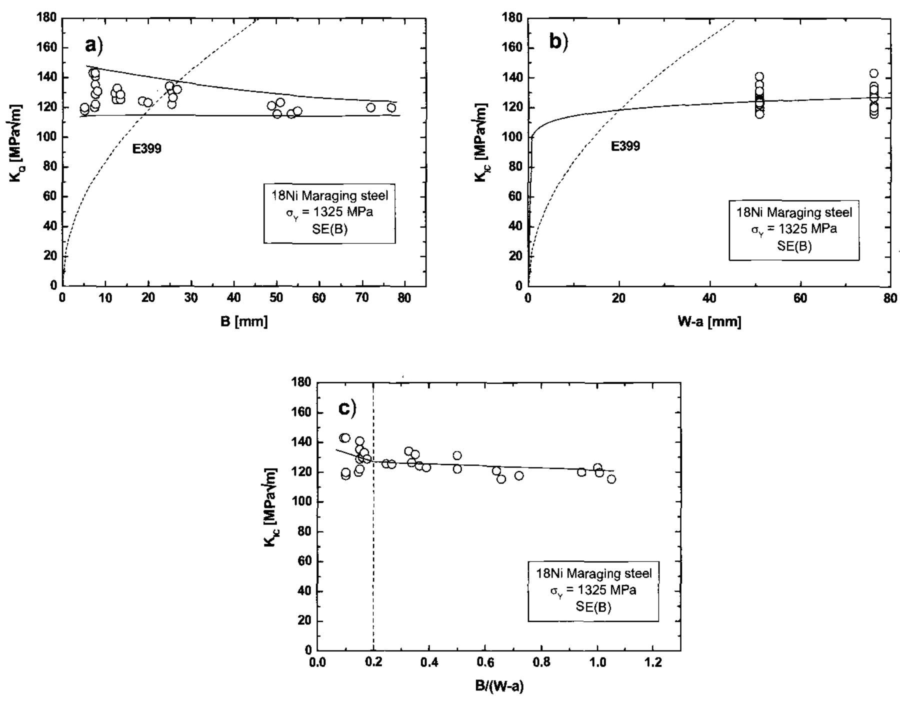

FIG. 19—*Old K_{IC} data used to develop ASTM E 399 showing slightly reducing toughness with increasing specimen thickness, but no effect of ligament size [7]. Increase in toughness is related to ligament slimness.*

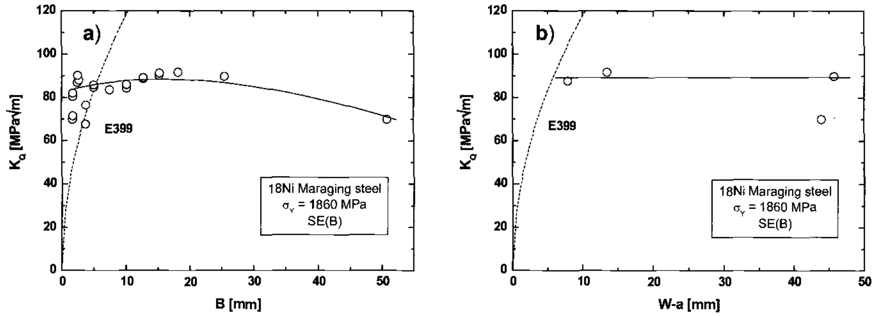

FIG. 20—*Old K_{IC} data used to develop British K_{IC} standard showing no effect of specimen ligament size, but slight decrease with decreasing thickness [4].*

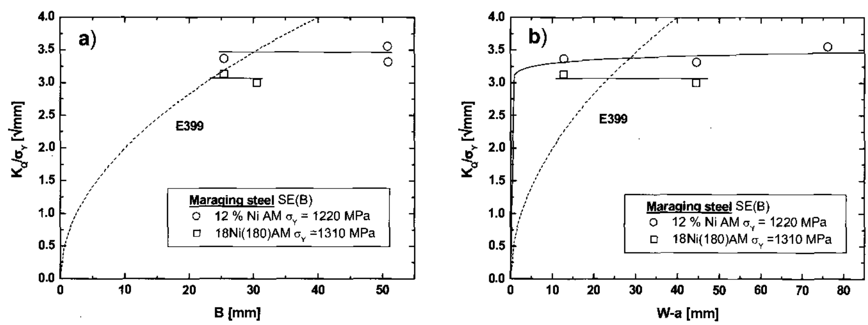

FIG. 21—*Old K_{IC} data showing constant toughness both with increasing specimen ligament size and thickness [10].*

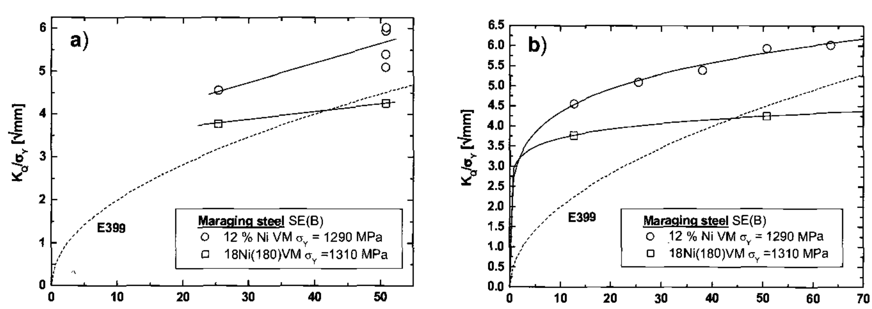

FIG. 22—*Old K_{IC} data showing increasing toughness both with increasing specimen thickness and ligament size [10].*

Discussion

All examined data sets show identifiably consistent trends. The absolute specimen thickness is not relevant for the fracture toughness value determined according to ASTM E 399. If the material has a rising tearing resistance curve, the fracture toughness will be simply a function of the specimen's ligament size. Only if the ligament becomes so slim that the steepness of the tearing resistance curve is affected, thinner specimens begin to show increasing fracture toughness. Since the standard does not allow slim ligaments, even this phenomenon will not affect the results. For standard geometries, only the ligament size affects the fracture toughness. This size dependence is a direct consequence of the 95 % secant procedure used in ASTM E 399 to define K_{IC}. The only way to remove the ligament size dependence would be to determine K_{IC} at some absolute amount of crack growth, like in the case of J_{IC} as defined in ASTM E 1820. The problem was partly recognized in the development of ASTM E 399, but since the rise in fracture toughness was connected to thickness and not ligament size, only a partly functional remedy to the problem was pursued. The solution was thought to be the $P_{max}/P_Q \leq 1.1$ criterion that was introduced as a consequence of the data presented in Fig. 4 [3]. It was assumed that the P_{max}/P_Q ratio was a function of constraint, since the rising tearing resistance curve was thought to be the result of insufficient constraint. In reality, P_{max}/P_Q is mainly connected to the tearing resistance of the material. A simplified analysis of the significance of the criterion is given next.

Significance of the $P_{max}/P_Q \leq 1.1$ Criteria

In a linear-elastic situation, the crack driving force K_I is a function of load and crack length (Eq 1):

$$K_I = P \cdot g(\text{geometry}) \cdot f(a/W) \tag{1}$$

The ductile tearing resistance of the material can usually be approximated by a power law expression (Eq 2).

$$K_I = A \cdot \Delta a^m \tag{2}$$

Combining Eqs 1 and 2 enables the load to be written as a function of crack growth. Maximum load occurs when the derivative of the function equals zero. Thus, the amount of crack growth at maximum load is for linear-elastic loading described by Eq 3.

$$\Delta a_{max} = \frac{m \cdot f}{f'} \tag{3}$$

The amount of crack growth is governed by the power of the tearing resistance curve. It is equally easy to estimate the amount of ductile crack growth at the load P_Q, using the specimen compliance equation. The crack growth at P_{max} and P_Q is presented graphically for C(T) and SE(B) specimens in Fig. 23. P_Q corresponds quite closely to a 2 % crack growth of the ligament, in accordance with the experimental results of Munz (Fig. 11) [8].

The knowledge of crack growth both at P_{max} and P_Q also enables an estimation of the P_{max}/P_Q ratio as a function of crack length and tearing resistance curve steepness. The result is presented in Fig. 24.

Figure 24 reveals some interesting details. Regardless of specimen type, the tearing resistance curve must be quite flat ($m < 0.1$) to fulfill the P_{max}/P_Q criterion. It is slightly easier to fulfill the criteria with C(T) specimens than with SE(B) specimens. The crack length has a negligible effect on the P_{max}/P_Q ratio. The above derivation is of course highly simplified, and it should not be regarded as the absolute truth. Qualitatively, the outcome of the derivation is valid. An example of the predictive capability of the above derivation is presented in Fig. 25. Here, the K_Q data from Fig. 5 were used to predict the maximum load K_{max} values for the same specimens [3]. On average, the prediction is quite good, but the K_{max} values show trends that are not described by the simplified derivation. The prediction overestimates the large specimens and underestimates the smallest specimens. The trend is due to crack tunneling, which is also connected to the specimen slimness effect. For a specific specimen thickness, the ligament slimness increases with increasing ligament size. This causes the tearing resistance curves to become steeper and the K_{max} values to become higher. Ductile crack growth in a plane sided specimen occurs mainly in the center of the specimen. The crack growth at the side surface of the specimen is suppressed, causing the crack to form a tunnel shape. Ligament slimness enhances the tunneling effect, and this is the main reason for the steepening of the tearing resistance curve. At relatively small crack growths, like at K_Q, the tunneling effect is still quite small, and quite slim ligaments are needed to see a significant enhancement of the fracture toughness. At maximum load, the crack growth is significantly larger, and thus the ligament slimness effect is also enhanced. An example of this is seen in Fig. 25, where the different thickness specimens lead to different K_{max} values, contrary to the K_Q results in Fig. 5.

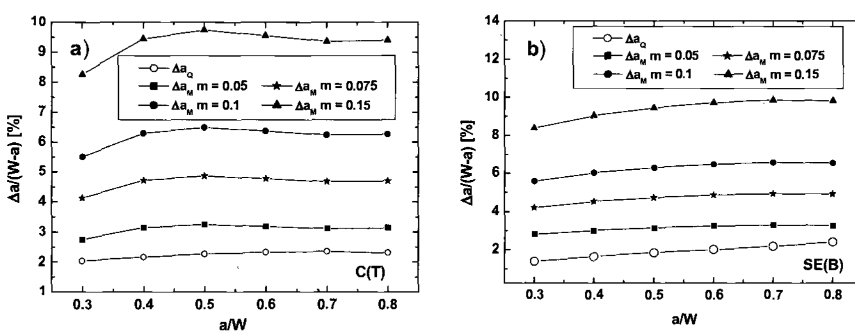

FIG. 23—*Theoretical estimation of crack growth at maximum load in a linear-elastic test:* a) *C(T) specimen,* b) *SE(B) specimen.*

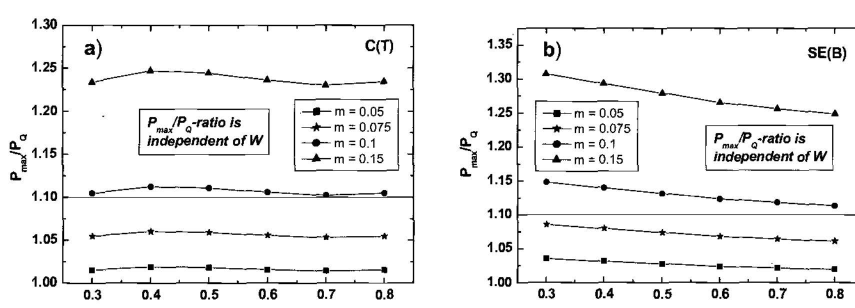

FIG. 24—*Theoretical estimation of the P_{max}/P_Q ratio as a function of crack length and tearing resistance curve steepness;* a) *C(T) specimen,* b) *SE(B) specimen.*

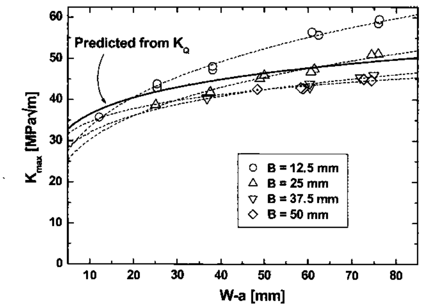

FIG. 25—*Effect of ligament size and thickness on load maximum values [3], compared to simple prediction based on K_Q behavior.*

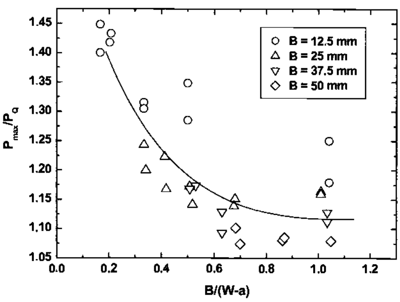

FIG. 26—*P_{max}/P_Q ratio as a function of ligament slimness [3].*

Figure 26 shows the P_{max}/P_Q ratio as a function of ligament slimness. A clear rising trend is visible with increasing slimness. This is a direct result of the crack tunneling. Noteworthy is that the ligament size dependence of K_Q predicts an average P_{max}/P_Q ratio of approximately 1.24, but the actual data indicate a saturated average value of 1.12. This shows something about the qualitative nature of the simplified analysis.

The one thing that is clear, based on the simple analysis, is that the P_{max}/P_Q criteria have no significance whatsoever concerning the matter of plane-strain. First, it describes only events occurring after K_Q has already been reached, and second it only gives information regarding the steepness of the materials' tearing resistance curve. There is no theoretical justification for the criteria to be used as a measure of plane-strain. Use of side-grooved specimens removes the tunneling and thus also the slimness effect. For some materials, side-grooving may lower the tearing resistance curve, thus lowering the P_{max}/P_Q ratio. However, since there is no need for this ratio in the first place, discussions regarding side-grooved specimens are not needed. Side-grooving is not expected to affect the K_Q value, only the K_{max} value. Since K_Q is considered the critical value, there is no reason not to allow the use of side-grooved specimens.

Significance of the Size Criterion

The size criterion in ASTM E 399 is really not needed to ensure plane-strain conditions at the crack tip. Elastic-plastic standards like ASTM E 1820 allow a magnitude of smaller specimens, and even these have a plane-strain condition at the crack tip. Globally, the specimens are closer to plane-stress, but locally at the crack tip, where fracture takes place, the stress state is plane-strain. The real need for a size criterion in the K_{IC} standard comes from the need to be able to describe the fracture toughness based only on load. This requires that the specimen is globally in the linear-elastic regime. If excess plasticity occurs, the fracture toughness estimated based on load only underestimates the true fracture toughness. Since linear-elasticity, not the stress state, is the controlling requirement, the size criterion should be given in terms of the ligament, not thickness.

A simple analysis of the possible error in fracture toughness as a function of loading can be performed, i.e., using the Irwin plasticity correction [11]. This way it is possible to express the ratio between the plasticity corrected K_{ep} and the linear part K_I as a function of the linear loading

K_I. An example of this is presented in Fig. 27. Based on the Irwin plasticity correction, the present size criteria produces at maximum approximately a 4 % underestimate of the true fracture toughness. If a 10 % error could be tolerated, the criteria could be relaxed from 2.5 to 1.1. Since the plasticity correction does not account for strain hardening, it will usually overestimate the true fracture toughness to some extent. An example of a real material is given in Fig. 28. Here data from a cold formed stainless steel are compared with the Irwin plasticity correction. The data, from a 25 mm thick C(T) specimen, are presented in the form of normalized elastic plastic K_J and the linear part of loading from load only. For this real material, it is seen that the error in using a criterion of 1.1 (instead of 2.5) still leads to a negligible error in the fracture toughness estimate.

If the present ASTM E 399 size criterion is compared to the specimens limit loads, one can see that the reserve, with respect to general yielding, is approximately a factor of 2 (Fig. 29). If the criterion would be relaxed to 1.1, the reserve would still be approximately 1.5. In most cases, a criterion of 1.1 would result only in a slight underestimation of the true fracture toughness.

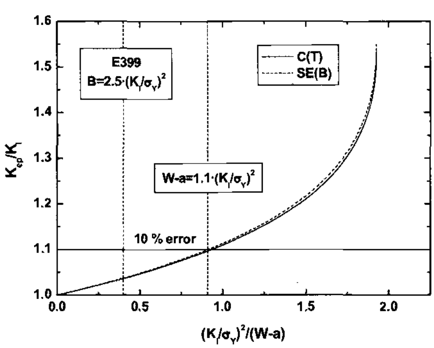

FIG. 27—*Simple estimate of plasticity induced error in K_I, based on the Irwin plasticity correction [11].*

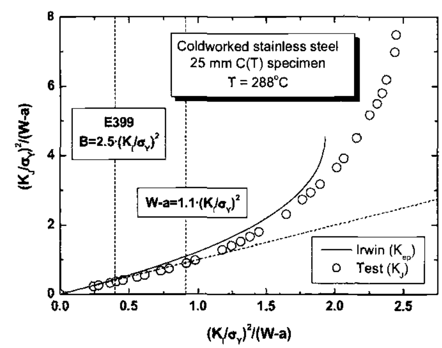

FIG. 28—*Comparison of the Irwin plasticity correction with behavior of real strain hardening material.*

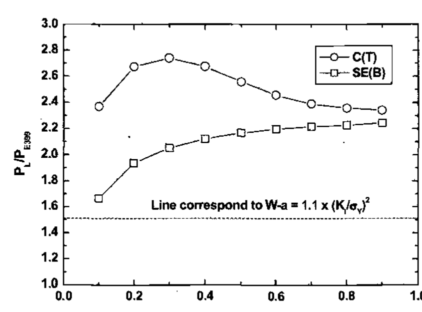

FIG. 29—*Examination of distance between load corresponding to ASTM E 399 size criterion and limit load.*

Recommended Practice Changes

The major drawback of ASTM E 399 is the ligament size dependence that comes from the use of the 95 % secant to define K_Q. The only way of getting specimen size insensitive fracture toughness values is to make the P_Q-secant dependent on ligament size. The problem is to define a target crack growth for P_Q. ASTM E 1820 defines J_{IC} at 0.2 mm crack growth, but excludes blunting. This means that from a compliance change point of view, J_{IC} corresponds to more than 0.2 mm crack growth. On the other hand, a popular specimen size is the 25 mm thick specimen with a 25 mm long ligament. With an approximately 2 % crack growth, this would correspond to 0.5 mm. It seems that a choice of 0.5 mm would make the fracture toughness values quite well in line with the definition of J_{IC} and with most vintage K_{IC} data.

Figure 30 gives a graphical and functional form of a new P_Q-secant definition, which is a function of ligament size. Use of this definition leads to approximately 0.5 mm crack growth, regardless of specimen size. The graph can be used for crack lengths in the range a/W = 0.4–0.6. This means that the present crack length requirements can be somewhat loosened. The size criteria, which should be based on the ligament size, not thickness, can also be somewhat relaxed to $W\text{-}a \geq 1.1 \cdot (K_{IC}/\sigma_Y)^2$. The thickness is not a limiting dimension as long as the ligament is not made too slim. Thus, allowable thickness could be in the range $B = (W\text{-}a)/2 \ldots (W\text{-}a) \cdot 2$. The P_{max}/P_Q ratio is not related to the significance of K_{IC}, and it unduly punishes materials with a good tearing resistance. Therefore, the P_{max}/P_Q criterion should be removed. Also, since side-grooving mainly affects the P_{max}/P_Q ratio and not the K_{IC}, moderate side-grooving should be allowed. With these small changes, the ASTM E 399 standard can well continue to service the materials science for many years, by furnishing linear-elastic plane-strain fracture toughness values.

The proposed changes were checked for the three data sets, shown in Figs. 7, 13, and 17, for which the raw data became available[2]. The data, analyzed with the new P_Q-secant definition, are presented in Fig. 31.

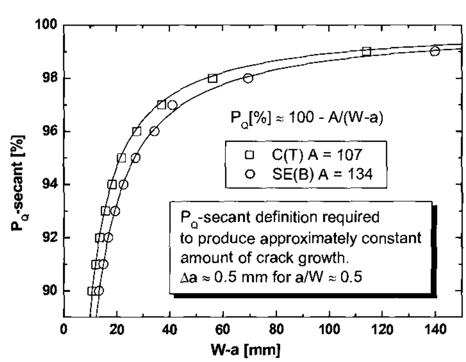

FIG. 30—*New specimen ligament size dependent P_Q-secant definition, providing approximately 0.5 mm crack growth at P_Q.*

[2] J. Joyce, personal communication.

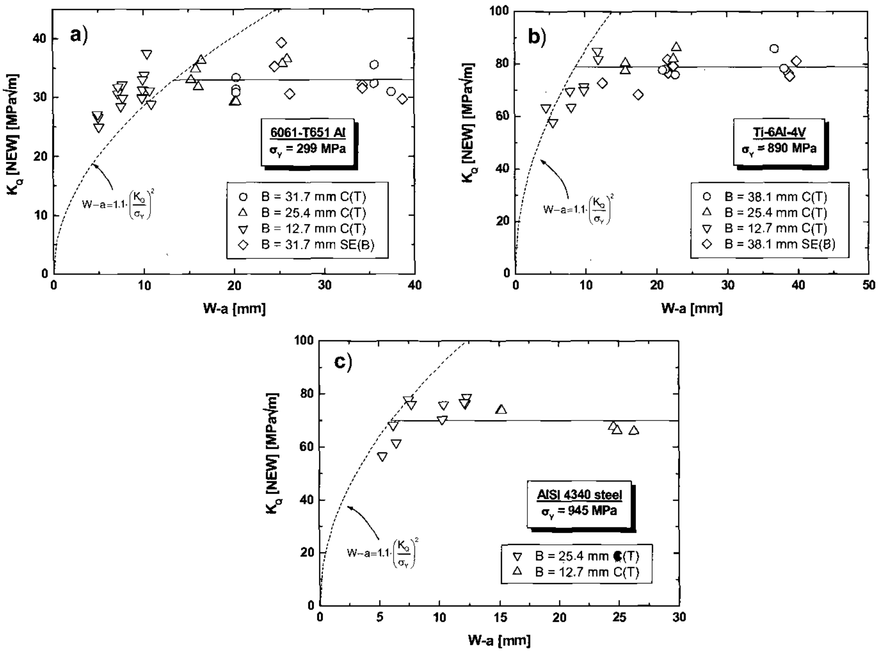

FIG. 31—*Analysis of fracture toughness data from Figs. 7, 13 and 17 using the new P_Q definition.*

The K_{IC} values based on the new P_Q-secant definition are clearly less size dependent than the present definition. Close to the new size criterion, the K_{IC} values start to decrease. This is connected to the beginning of yielding. The decrease is fully in line with the theoretical analysis. If no effect of yielding is accepted on the measured K_{IC}, then the size criteria must be increased to W-a $\geq 1.5\cdot(K_{IC}/\sigma_Y)^2$. However, if up to a 10 % conservative error is acceptable, W-a $\geq 1.1\cdot(K_{IC}/\sigma_Y)^2$ is adequate.

Summary and Conclusions

Many old and some newer data sets containing data revealing the effect of specimen size on the K_{IC} defined by ASTM E 399 have been analyzed based on present knowledge regarding the fracture mechanisms. All examined data sets show consistent trends. The absolute specimen thickness is not relevant for the fracture toughness value determined according to ASTM E 399. If the material has a rising tearing resistance curve, the fracture toughness will be simply a function of the specimen's ligament size. Only if the ligament becomes so slim that the steepness of the tearing resistance curve is affected, thinner specimens will begin to show increasing fracture toughness. Since the standard does not allow slim ligaments, this phenomenon will not affect the results. For standard geometries, only the ligament size affects the fracture toughness. This size dependence is a direct consequence of the 95 % secant procedure used in ASTM E 399 to define K_{IC}. The only way to remove the ligament size dependence is to determine K_{IC} at some constant amount of crack growth. Based on the analysis, the following can be concluded:

- The specimen thickness is not the controlling dimension in a K_{IC} test.
- The controlling dimension is the ligament size, which, due to the 95 % secant definition of P_Q, leads to specimen size dependent fracture toughness values.
- The ligament size dependence can be removed by introducing a ligament size dependent P_Q-secant definition.
- The P_{max}/P_Q criterion should be removed.
- The specimen size criteria can be somewhat relaxed and should be based on ligament size, not thickness.
- Moderate side-grooving should be allowed.

Acknowledgments

This work is a part of the Integrity and Life Time of Reactor Circuits project (INTELI) belonging to the Safety of Nuclear Power Plants - Finnish national research programme 2003–2006 (SAFIR), financed by the Ministry of Trade and Industry, the Technical Research Centre of Finland (VTT), and the Radiation and Nuclear Safety Authority (STUK).

References

[1] Irwin, G. R., "Fracture Mode Transition for a Crack Traversing a Plate," *Journal of Basic Engineering*, 1960, pp. 417–425.

[2] Irwin, G. R., Kies, J. A., and Smith, H. L., "Fracture Strengths Relative to Onset and Arrest of Crack Propagation," *ASTM Proceedings*, Vol. 58, 1958, pp. 640–660.

[3] Kaufman, J. G. and Nelson, F. G., "More on Specimen Size Effects in Fracture Toughness Testing," *Fracture Toughness and Slow-Stable Cracking, ASTM STP 559*, ASTM International, West Conshohocken, PA, 1973, pp. 74–98.

[4] May, M. J., "British Experience with Plane Strain Fracture Toughness (K_{IC}) Testing," *Review of Developments in Plane Strain Fracture Toughness Testing, ASTM STP 463*, ASTM International, West Conshohocken, PA, 1970, pp. 41–62.

[5] Joyce J. A. and Tregoning R., "Development of Consistent Size Criteria for ASTM Combined Fracture Mechanics Standards," *Fatigue and Fracture Mechanics: 30th Volume, ASTM STP 1360*, K. L. Jerina and P. C. Paris, Eds., ASTM International, West Conshohocken, PA, 2000, pp. 357–376.

[6] Bray, G. H., "Effects of Specimen Size and Side-Grooving in Plane Strain Fracture Toughness Testing of Aluminum Alloys," ASTM Technical Committee E08 Meeting, May 7, 2001.

[7] Jones, M. H. and Brown, Jr., W. F., "The Influence of Crack Length and Thickness in Plane Strain Fracture Toughness Tests," *Review of Developments in Plane Strain Fracture Toughness Testing, ASTM STP 463*, ASTM International, West Conshohocken, PA, 1970, pp. 63–101.

[8] Munz, D., Galda, K. H., and Link, F., "Effect of Specimen Size on Fracture Toughness of a Titanium Alloy," *Mechanics of Crack Growth, ASTM STP 590*, ASTM International, West Conshohocken, PA, 1976, pp. 219–234.

[9] Brown, Jr., W. F. and Srawley, J. E., "Plane Strain Fracture Toughness Testing of High Strength Metallic Materials," *ASTM STP 410*, ASTM International, West Conshohocken, PA, 1969, p. 145.

[10] Rolfe, S. T. and Novak, S. R., "Slow-Bend K_{IC} Testing of Medium-Strength High-Toughness Steels," *Review of Developments in Plane Strain Fracture Toughness Testing, ASTM STP 463*, ASTM International, West Conshohocken, PA, 1970, pp. 124–159.

[11] Anderson, T. L., "Fracture Mechanics - Fundamentals and Applications," 2nd ed., CRC Press, Boca Raton, FL, 1995.

SESSION 8A: FATIGUE II

Journal of ASTM International, January 2005, Vol. 2, No. 1
Paper ID JAI12030
Available online at www.astm.org

Kilian Wasmer,[1] *Kamran M. Nikbin,*[1] *and George A. Webster*[1]

Sensitivity of Creep Crack Initiation and Growth in Plates to Material Properties Variations

ABSTRACT: In this paper, creep crack initiation and growth data are reported on type 316L(N) stainless steel at 650°C on compact tension (CT) specimens and on plates containing a semi-elliptical surface defect. The compact tension tests were carried out according to standard ASTM E 1457 procedures, and the results are plotted against experimental determinations of the creep fracture mechanics parameter C^* derived from load-line displacement rate. Generally, satisfactory agreement is found between the CT specimen and plate results, although longer initiation times and slower cracking rates were observed in the plates consistent with the lower constraint anticipated in this specimen geometry. Also, predictions of the cracking behavior of the plates have been made using deterministic and probabilistic methods. In the former case, combinations of upper and lower bound material properties were used, which were based on the ± 2 standard deviation (± 2*SD*) limits obtained from the measured scatter in the data. In the latter, a Monte Carlo simulation was adopted. It is found that the combination of bounds (± 2*SD*) giving the shortest failure time corresponds with a failure probability of about 0.05 % from the probabilistic calculations.

KEYWORDS: creep, fatigue, crack growth, crack initiation, life prediction, 316L(N), probabilistics

Nomenclature

A, A'	Norton power law creep constant in Eqs 5 and 14
$\dot{a}$	Creep crack growth rate
a, a_{ini}, a_{fin}	Depth of surface crack, initial and final depths of the surface crack
Δa	Crack extension
B, B_n	Thickness and net thickness
c, c_{ini}, c_{fin}	Half-length of surface crack, initial and final half-lengths of surface crack
C^*	Steady state creep fracture mechanics parameter
C^*_{ref}	Value of C^* estimated from the reference stress
D, D', D_i, D_i'	Constant in Eqs 1, 12, 7, and 15
E	Error of the Monte Carlo Simulation in Eq 16
e_{ϕ}, e_{ϕ_i}, e_{t_i}	Random uncertainties in ϕ, ϕ_i, and t_i
$e_{\dot{a}}$, e_{t_R}, $e_{\dot{\varepsilon}}$	Random errors in $\dot{a}$, t_R, and $\dot{\varepsilon}$
F	Factor depending on specimen geometry and creep index n
J	Elastic-plastic fracture mechanics parameter
K	Stress intensity factor
L	Length of the plate
N	Number of simulations (or iterations)
n	Norton stress index in power law creep Eq 5

Manuscript received 14 January 2003; accepted for publication 13 May 2004; published January 2005. Presented at ASTM Symposium on Fatigue and Fracture Mechanics: 34th Volume on 19–21 November 2003 in Tampa, FL; S.R. Daniewicz, J.C. Newman, Jr., and K-H. Schwalbe, Guest Editors.

[1] Research Assistant, Principal Research Fellow, and Professor, respectively, Department of Mechanical Engineering, Imperial College, London, SW7 2BX, United Kingdom.

P	Applied load
R	Minimum to maximum load ratio in cyclic tests
t_i, t_R, t_h	Initiation time, rupture time, and hold time
SD, SE	Standard deviation of the errors and standard error
W	Width of CT specimen- Half width of plate
X_{C^*}	Number of C^* data points
$z_{\alpha/2}$	Normalizes the standard deviation SD to a standard normal distribution
ϕ, ϕ_i	Constant in Eqs 1 and 7
ε_f	Uniaxial creep failure strain
$\dot{\varepsilon}$, $\dot{\varepsilon}_s$	Creep strain rate and secondary (or minimum) creep strain rate
$\dot{\varepsilon}_{ref}$, $\dot{\varepsilon}_0$	Creep strain rate at reference stress and constant strain rate
κ_i, κ_s	Scaling factor for creep crack initiation and growth
σ, σ_b, σ_m	Stress, bending stress, membrane stress
σ_{ref}, $\sigma_{ref\,Plate}$	Reference stress and reference stress for plates
$\dot{\Delta}^c$	Creep load-line displacement rate

Subscript

CT	Refers to compact tension specimen
CP	Refers to cracked plate data
i	Refers to initiation

Introduction

For safety reasons and certification for life extension, components that operate at elevated temperatures must be inspected periodically. This has led to the development of life assessment codes that deal with crack initiation and growth in components which operate in the creep regime (e.g., BS 7910 [1], R5 [2], R6 [3], ASME [4], and A16 [5]). These codes are designed to predict the onset of crack initiation and crack growth rate of defects that are found before or during in-service inspections in order to avoid unplanned stoppages and unscheduled replacement of cracked components unnecessarily.

Most defect assessment codes [1–5] propose methods to estimate creep crack initiation and growth in components that are based on a deterministic approach using the creep fracture mechanics parameter C^*. In order to estimate C^* for components, the reference stress (σ_{ref}) method [6,7] is usually used. On the other hand, in measuring creep crack initiation and growth properties from laboratory tests on compact tension (CT) specimens, the parameter C^* is derived directly from the experimental load-line displacement rate, as recommended in the standard test procedure ASTM E 1457-00 [8]. This means that different methods of estimating C^* are used for making predictions of cracking behavior in components than are used for determining material crack initiation and growth properties from CT specimens. The main reason for the use of small laboratory CT specimens as "benchmark" data is that it is very rare that actual component or "feature" component test data are available due to the prohibitive costs of performing the tests. As a result of these shortcomings, a number of recent collaborative projects (see Acknowledgments) have been created to examine large components such as plates.

Like creep deformation and rupture data, there is often a large scatter in creep cracking behavior. In such circumstances over the last few years, there has been a rising need to develop a quantifiable method based on a statistical and probabilistic approach to reduce the over-conservatism arising from the use of a worst-case combination of upper and/or lower bounds of material property data. Such approaches are expected to lead to an increase in confidence in the usage of the Codes of Practice [1–5].

In this paper, crack initiation and growth data are reported on CT specimens of type 316L(N) stainless steel at 650°C under static and slow cycling loading conditions. The results are compared with similar information that was collected on pre-cracked plates that each contained a semi-elliptical surface defect. Deterministic and probabilistic methods are used to interpret the findings.

Steady State Crack Growth Analysis

A steady state analysis considers the behavior of a crack in a creeping solid once a steady state distribution of stress and creep damage has been developed ahead of a crack tip. In such cases, it is usually found that creep crack growth rate $\dot{a}$ can be described by an expression of form (e.g., [8–10]):

$$\dot{a} = D \cdot C^{*\phi} \tag{1}$$

where D and ϕ are material constants which can be determined experimentally or from models of the cracking mechanism. Most often these constants are obtained from tests that are carried out on compact tension (CT) specimens based on the recommendations of the ASTM E 1457-00 [8] procedure. In this procedure, C^* is estimated experimentally from measurements of creep load-line displacement according to:

$$C^* = \frac{P \cdot \dot{\Delta}^c}{B_n \cdot (W - a)} \cdot F \tag{2}$$

where P is the applied load, B_n is the net thickness between side-grooves (if used), W is the width of the specimen, a is the crack length, $\dot{\Delta}^c$ is the creep load-line displacement rate, and F is a factor which depends on geometry and creep stress index, n. For CT specimens, F can be expressed by:

$$F = \frac{n}{n+1} \cdot \left[2 + 0.522 \cdot \left(1 - \frac{a}{W} \right) \right] \tag{3}$$

The data obtained from CT specimens from Eqs 2 and 3 are usually considered as "benchmark" creep crack growth properties of a material in the same way creep strain rate and rupture are for uniaxial creep tests. These data are then employed directly in the crack initiation and growth models [9,10] described in the different codes [1–5] to estimate residual lives in components.

When making calculations for components such as plates, C^* must be determined from finite element analysis or estimated from approximate reference stress methods. In this study, the reference stress procedure is adopted in line with that used in the defect assessment codes [1–5]. With this approach, C^* is expressed approximately as [6,7,10]:

$$C^*_{ref} = \sigma_{ref} \cdot \dot{\varepsilon}_{ref} \cdot \left(\frac{K}{\sigma_{ref}} \right)^2 \tag{4}$$

where $\dot{\varepsilon}_{ref}$ is the creep strain rate at the appropriate σ_{ref} for the component, and K is the stress intensity factor corresponding to the applied loading. When the creep strain rate $\dot{\varepsilon}$ at an applied stress σ can be described in terms of the Norton creep law [11]:

$$\dot{\varepsilon} = A \cdot \sigma^{n} \tag{5}$$

where A and n are material constants at constant temperature, Eq 4 can be rewritten as:

$$C^{*}_{ref} = A \cdot \sigma^{n-1}_{ref} \cdot K^{2} \tag{6}$$

The typical value for n is between 5 and 12 for most metals. These equations will be used in the subsequent analysis to compare the cracking behavior of the plates with the material properties data obtained from the compact tension specimens.

Crack Initiation Analysis

When a structure containing a defect is first loaded, the stress distribution is given by the elastic K-field or the elastic-plastic J-field. Therefore, time is required for the stresses to redistribute to the steady state creep stress distribution controlled by C^*. During this period, transient conditions exist which are not uniquely defined by C^*. In addition, a period of time is needed for creep damage to fully develop around the crack tip [12]. Furthermore, due to the practical limitations of crack detection equipment, the initiation of crack growth is difficult to determine precisely. Typically, this ranges between an extension Δa of between about 0.1 and 0.5 mm depending on component and crack dimensions. For laboratory test pieces such as CT specimens, ASTM E 1457-00 [8] identifies an extension of 0.2 mm to cover the entire transition time to steady state conditions, and this distance also takes into account the resolution of crack monitoring equipment. However, for consistency in crack measurement in the CT and plate specimens, it has been determined in this present work that Δa = 0.5 mm is the best value to choose to compare both sets of data.

From Eq 1 it may be expected that the time, t_i, to initiate a crack extension of Δa can be expressed by:

$$t_i = \frac{D_i}{C^{*\phi_i}} \tag{7}$$

where D_i and ϕ_i are material constants. For steady state conditions D_i may be expected to be given approximately by $\Delta a / D$ with $\phi_i = \phi$ so that Eq 7 can be rewritten as [13]:

$$t_i = \frac{\Delta a}{D \cdot C^{*\phi_i}} \tag{8}$$

Equation 8 assumes that during the entire initiation period a steady state distribution of stress and creep damage has developed ahead of the crack tip. This cannot be expected to be true during at least part of the initiation period t_i. The applicability of Eqs 7 and 8 will be examined for both types of specimen.

Reference Stress Solutions for Plates

Although it has been shown previously [14,15] that the majority of the codes employ Eq 4 to calculate C^*, often different formulae are used to evaluate K and σ_{ref}. It has also been demonstrated in the past [15] that greater sensitivity of C^* to reference stress, rather than to K in

Eq 6 is obtained, since typically $n >> 1$. It has also been demonstrated previously that "global" collapse solutions, which are based on collapse of the entire cross-section at the site of a defect, represent best the cracking behavior in components [16,17]. Although the results are not presented here, the same conclusion has been found for the plate [17]. Consequently, in this present paper, a reference stress based on "global" collapse derived by Goodall and Webster [18], has been chosen which is expressed as follows:

$$\sigma_{ref\,\mathrm{Plate}} = \frac{(\sigma_b + 3\cdot\gamma\cdot\sigma_m) + \left\{(\sigma_b + 3\cdot\gamma\cdot\sigma_m)^2 + 9\cdot\sigma_m^2\cdot\left[(1-\gamma)^2 + 2\cdot\gamma\cdot(\alpha-\gamma)\right]\right\}^{1/2}}{3\cdot[(1-\gamma)^2 + 2\cdot\gamma\cdot(\alpha-\gamma)]} \tag{9}$$

where σ_m and σ_b are the elastic membrane and bending stresses, respectively, $\gamma = (a\cdot c) / (W\cdot B)$, and $\alpha = a/B$. In this equation, a is crack depth, c is half crack length at the surface, B is the thickness of the plate, and W is its half-width.

Predictive Methods for Creep Crack Growth and Initiation

The purpose of most of the codes dealing with cracks is to predict the cracking behavior in components [1–5]. Equations 1 and 7 and are used in conjunction with Eq 4 to carry out predictions of crack initiation and growth. However, in these equations, error and variability exist in the different constants, which must be taken into account. Therefore, it is important that in Eqs 1, 5, and 7 the following are considered: uncertainties in the values of D and ϕ and errors in $\dot{a}$ for creep crack growth; A, n, and $\dot{\varepsilon}$, for strain rate; and D_i, ϕ_i, and t_i, for initiation. Combinations of mean, upper, and lower bound properties or a probabilistic assessment can be adopted to develop a predictive methodology based on a simple deterministic sensitivity approach or a full probabilistic analysis. In the former case, the material constants D, ϕ, A, n, D_i, and ϕ_i, are obtained from regression lines which use least squares methods. Typically a ± 2 standard deviation of the errors in $\dot{a}$, $\dot{\varepsilon}$, and t_i, termed *SD*, is used to set the bounds. To develop a probabilistic model, the scatter in the data as well as the uncertainties in the constants must be employed to determine the probability of failure, and Eqs 1, 5, and 7 must be modified. The methodology is shown graphically in Fig. 1. Hence, Eq 1 becomes:

$$\dot{a} = \left(D\cdot 10^{e_D}\right)\cdot C^{*(\phi+e_\phi)}\cdot 10^{e_{\dot{a}}} \tag{10}$$

where e_D and e_ϕ are the uncertainties in log(D) and in ϕ, and $e_{\dot{a}}$ is the error in log($\dot{a}$) as illustrated in Fig. 1. Consequently, the uncertainty in D and the error in $\dot{a}$ are described by a lognormal distribution and the uncertainty in ϕ by a normal distribution. For the different mean lines obtained due to the uncertainty in ϕ to all pass through the "center of gravity" of a log($\dot{a}$) – log(C^*) data set, the uncertainties in D and ϕ must be related according to:

$$e_D = e_\phi\cdot\left\{\frac{\sum[Log(C^*)]^2}{X_{C^*}}\right\}^{1/2} = e_\phi\cdot\left(\pm\frac{SE_D}{SE_\phi}\right) \tag{11}$$

where X_{C^*} is the number of C^* data points, and SE_D and SE_ϕ are the standard errors in log(D) and ϕ, respectively. Consequently, D can be simplified according to:

$$D' = D\cdot 10^{e_D} = D\cdot 10^{e_\phi\cdot\left(\pm\frac{SE_D}{SE_\phi}\right)} \tag{12}$$

where D' is a modified value of D due to a change in the slope ϕ. Hence, Eq 10 becomes:

$$\dot{a} = D' \cdot C^{*(\phi + e_\phi)} \cdot 10^{e_{\dot{a}}} \tag{13}$$

where e_ϕ and $e_{\dot{a}}$ represent the variation in their respective parameters as shown graphically in Fig. 1. Also by analogy for creep strain rate and for crack initiation, Eqs 5 and 7 become, respectively:

$$\dot{\varepsilon} = A' \cdot \sigma^{(n + e_n)} \cdot 10^{e_{\dot{\varepsilon}}} \tag{14}$$

$$t_i = \frac{D'_i}{C^{*(\phi_i + e_{\phi_i})}} \cdot 10^{e_{t_i}} \tag{15}$$

where A' and D'_i are the modified A and D_i material constants, e_n and e_{ϕ_i} represent the uncertainties in n and ϕ_i, respectively, and $e_{\dot{\varepsilon}}$ and e_{t_i} are the errors in their respective parameters.

In order to apply the probabilistic method, Monte Carlo Simulation (MCS) has been used to choose points randomly from the specific distribution for each variable. It is evident that the accuracy of the outcome will depend strongly on the number of iterations, N, selected. In fact, the accuracy of the Monte Carlo Simulation increases only as the square root of N [19,20]. Therefore, the error of the MCS, E is given by:

$$E = \frac{z_{\alpha/2} \cdot SD}{\sqrt{N}} \tag{16}$$

where $z_{\alpha/2}$ normalizes the standard deviation SD to a standard normal distribution. For a 95 % level of confidence, $z_{\alpha/2}$ equals 1.96.

The only requirement of a Monte Carlo Simulation (MCS) is that the physical (or mathematical) system be described by probability density functions (pdf). However, this does not imply that a simple substitution of a distribution for a constant will produce an accurate MCS. This is due to the fact that the statistical relationships among the constants are often ignored [21]. Here normal and lognormal distributions are used depending on the parameter concerned.

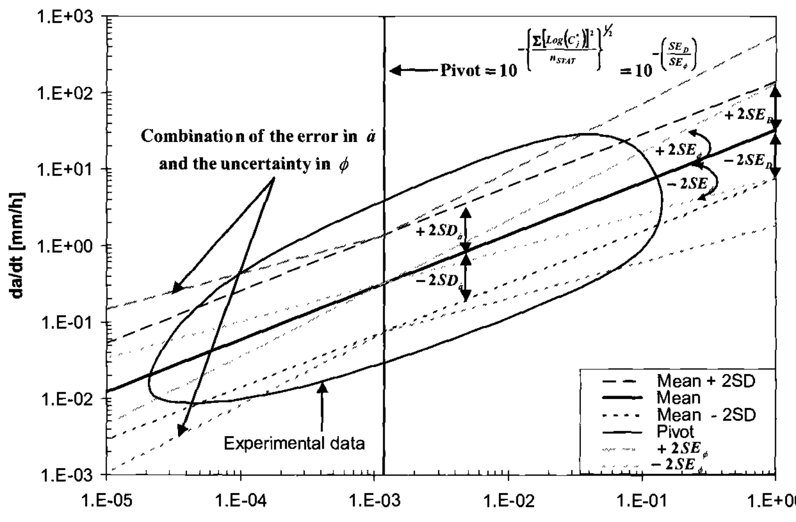

FIG. 1—*Representation of error analysis including ±2* SD *and the uncertainties in the slope,* ϕ*, and intercept,* D.

Experimental Results

Creep Crack Growth Data

The material examined was type 316L(N) stainless steel with the chemical composition shown in Table 1. The "benchmark" crack growth data were generated at 650°C from standard CT specimens of width $W = 50$ mm which contained 20 % deep side-grooves on each side. Some tests were carried out at a constant load; others were subjected to slow load cycling at a frequency of less than 10^{-2} Hz at a load ratio $R = 0.1$. The procedure adopted was that specified in ASTM E 1457-00 [8]. The results are shown in Fig. 2. It is evident that the results can be expressed in the form of Eq 1 with the values of D and ϕ and their respective errors and uncertainties given in Table 2. It is apparent that both the static and cyclic loading results can be accommodated within the same scatter band of plus or minus two standard deviations, indicating little influence of cycle-dependent fatigue at $R = 0.1$ on the cracking process at frequencies of 10^{-2} Hz or less. Also in both cases the fracture surfaces were mainly intergranular, which is indicative of creep type fracture.

TABLE 1—*Chemical composition of 316L(N) steel (in weight %).*

	C	Si	Mn	P	S	Cr	Mo	Ni	Cu	Al	N
316L(N)	0.04	0.31	1.83	0.036	0.020	17.30	2.46	11.90	0.03	—	0.07

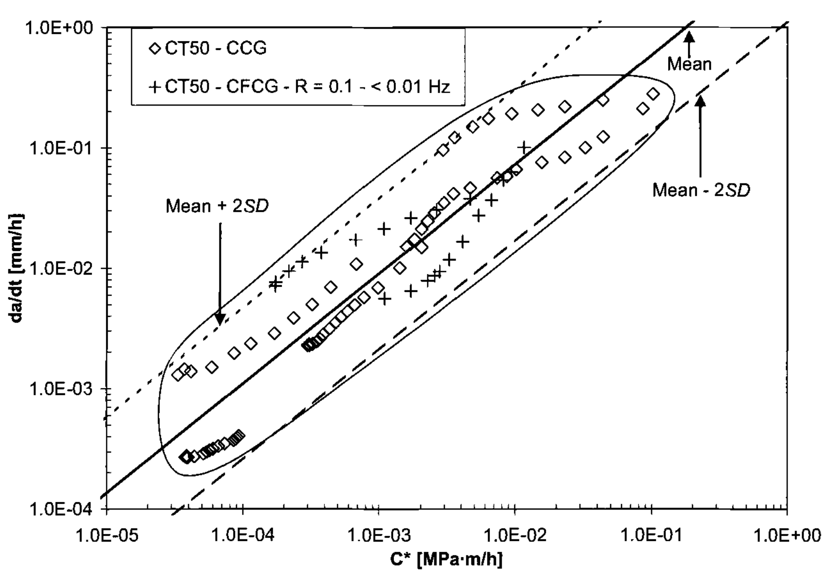

FIG. 2—*Creep crack growth data for 316L(N) stainless steel compact tension (CT) specimens at 650°C.*

TABLE 2—*Mean and standard deviation of log(D) and ϕ for CT laboratory tests.*

Materials	Temperature (°C)	$\log(D_{CT})$	SE $\log(D_{CT})$	ϕ_{CT}	$SE\ \phi_{CT}$	$SD\ \dot{a}_{CT}$
316L(N)	650	0.68	0.12	0.91	0.04	0.31

C^* in MPa·m/h, $\dot{a}$ in mm/h.

The plates examined had a thickness B = 24.5 mm and a width $2W$ = 350 mm. Each was provided with a semi-elliptical surface defect (by electric discharge machining of 2.5 mm deep and total length between 80–85 mm), which was then extended by fatigue pre-cracking to between 7 and 17 mm deep and 87 to 121 mm long at the surface to give an aspect ratio, $a/c \cong 0.25$. Six specimens were tested in total; one at constant load, two at $R = 0.1$, and three at $R = -1.0$. The holding time at the maximum load was either 1 h or 3 h for plates subjected to cycling loads. The results are included in Fig. 3 together with the bounds obtained from the CT specimens. During cracking, the aspect ratio of the defects remained approximately constant, and the cracking rate at the deepest point (corresponding to an angle of 90° from the surface) has been recorded. In making estimates of C^* for the plates, the "global" reference stress taken from Eq 9 has been employed [14–18]. The mean uniaxial creep properties given in Table 3 were used to calculate the reference strain rate from Eq 5.

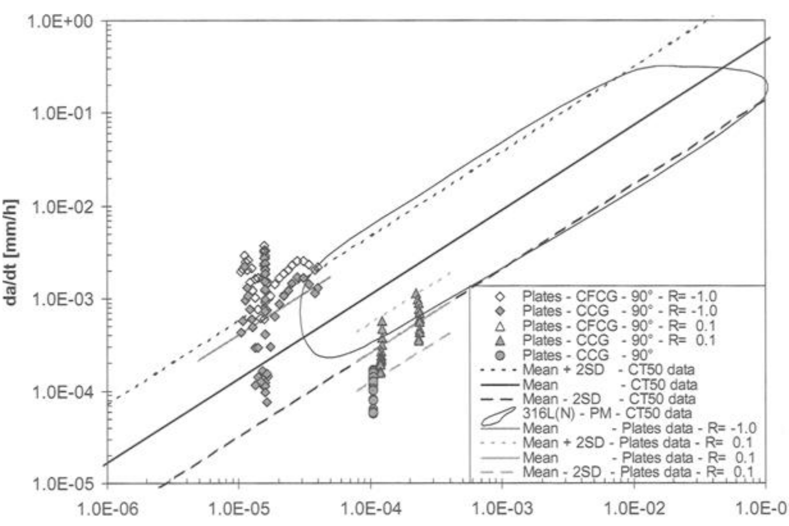

FIG. 3—*Effect of static and cyclic loading on crack propagation for 316L(N) stainless steel at 650°C for both CT and plate specimens.*

TABLE 3—*Mean and standard deviation of log(A) and n.*

Materials	Temperature (°C)	$\dot{\varepsilon}$ (h^{-1})	$\log(A)$ ($Mpa^{-1}\cdot h^{-1}$)	SE $\log(A)$	n	$SE\ n$	$SD\ \dot{\varepsilon}$
316L(N)	650	Secondary	−24.99	1.98	9.41	0.88	0.104

σ in MPa, $\dot{\varepsilon}$ in h^{-1}.

It is evident from Fig. 3 that the plate data scatter around the CT results. In some instances, the crack growth rate in the plates increases at an almost constant C^* value. This is attributed to the build up of creep damage ahead of the machined notches during the early stages of cracking. It can also be seen that crack growth is faster in the $R = -1.0$ tests than in the other tests. Approximately, the constant load and $R = 0.1$ results scatter about the –2 standard deviation (*SD*) CT data and the $R = -1.0$ about the CT + 2*SD* results, indicating a significant fatigue contribution in this later case. Nonetheless, by considering all the results together, it may be argued that it is possible to assume the same slope ϕ for both the CT and plate data. In such circumstances, Eq 1 for the plate can be written as follows:

$$\dot{a}_{cp} = D_{cp} \cdot C_{cp}^{*\ \phi_{CT}} \tag{17}$$

Eq 17 corresponds to Eq 1 where the subscripts *cp* and *CT* stand for component (plate) and CT specimens, respectively. Furthermore, D_{cp} can be related to D_{CT} by:

$$D_{cp} = \kappa_s \cdot D_{CT} \tag{18}$$

where κ_s is a scaling factor which identifies the difference between the cracked plate and the "benchmark" CT results shown in Fig. 3. This factor is related to the intrinsic difference in the methods of estimating C^* in the plate and CT specimens and also to the difference in constraint that exists between the two geometries. Obviously, if $\kappa_s < 1$, prediction of $\dot{a}_{cp}$ using CT data will be conservative. Provided that the methods of estimating C^* for the plates and CT specimens are consistent, it may be expected that a value of $\kappa_s < 1$ is obtained due to the lower constraint anticipated in the plate specimens. The actual mean values of D and ϕ and their uncertainties for each R-value are listed in Table 4 together with the respective κ_s estimates. When creep dominates $\kappa_s = 0.23$, which is less than unity as expected. At $R = -1.0$, $\kappa_s \approx 2.98$, corresponding to an increase in cracking rate by a factor of about 12 due to a fatigue contribution for this R-ratio.

TABLE 4—*Mean and standard deviation of ϕ_{cp} and log (D_{cp}), and κ_s for plates.*

Materials	Temperature (°C)	R	$\log(D_{cp})$	ϕ_{cp}	$SD\ \dot{a}_{cp}$	κ_s
316L(N) –90°	650	–1.0	1.15	0.91	0.49	2.98
316L(N) –90°	650	0.1	0.05	0.91	0.16	0.23

C^* in MPa·m/h, $\dot{a}$ in mm/h.

Creep Crack Initiation

In this investigation, creep crack initiation has been defined as the time to reach a crack extension of $\Delta a = 0.5$ mm. The results for both the CT and plate specimens are presented in Fig. 4. The respective mean values of D_i and ϕ_i are given in Tables 5 and 6. Similar trends are observed for initiation as for crack growth rate. The plates with $R = -1.0$ have lower initiation times than the constant load and $R = 0.1$ tests. Also the same value of ϕ_i can be used for the plate and CT specimens so that Eq 7 can be rewritten for initiation time as:

$$t_{i\,cp} = \frac{D_{i\,cp}}{C_{cp}^{*\ \phi_{i\,CT}}} \tag{19}$$

In Eq 19, like Eq 17, the subscripts *cp* and *CT* refer to the plate and CT specimens, respectively. Consequently, D_{icp} can be correlated with D_{iCT} in the following form:

$$D_{icp} = \kappa_i \cdot D_{iCT} \tag{20}$$

where κ_i allows for the difference in constraint and the method of calculating C^* in the two specimen geometries. In this case a value of $\kappa_i > 1$ results in a conservative prediction of initiation times in the plate from CT data. Table 6 indicates that this is the case for the constant load and $R = 0.1$ tests but that at $R = -1.0$, fatigue significantly shortens initiation times. Examination of κ_s and κ_i in Tables 4 and 6 implies that $\kappa_i \approx 1 / \kappa_s$ for the respective constant load and $R = 0.1$ tests and the $R = -1.0$ tests. This suggests that the method of calculating C^* and the effects of constraint in the two specimen geometries have the same influence on crack growth behavior and initiation times.

The predictions of Eq 8 for the CT data are also shown in Fig. 4. It indicates a reasonably satisfactory correlation with the experimental results, suggesting that a steady state distribution of stress and damage builds up quickly in the tests on the CT specimens.

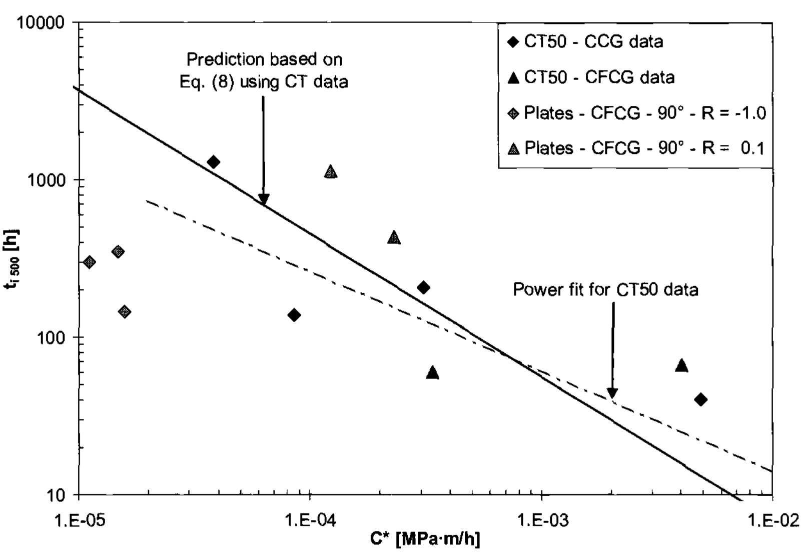

FIG. 4—*Effect of static and cyclic loading on time to crack initiation,* t_i, *based on a crack extension of 0.5 mm for 316L(N) stainless steel at 650° for both CT and plate specimens.*

TABLE 5—*Mean and standard deviation of* $log(D_i)$ *and* ϕ_i *for CT laboratory tests.*

Materials	Temperature (°C)	$\log(D_{iCT})$	$SE\ log(D_{iCT})$	ϕ_{iCT}	$SE\ \phi_{iCT}$	$SD\ t_{iCT}$
316L(N)	650	-0.13	0.80	0.64	0.24	0.48

C^* in MPa·m/h, $\dot{a}$ in mm/h.

TABLE 6—*Mean and standard deviation of ϕ_{icp} and log (D_{icp}), and κ_i for plates.*

Materials	Temperature (°C)	R	$\log(D_{icp})$	ϕ_{icp}	$SD\ t_{icp}$	κ_i
316L(N) – 90°	650	–1.0	–0.70	0.64	0.18	0.27
316L(N) – 90°	650	0.1	0.44	0.64	0.18	3.70

C^* in MPa·m/h, t_i in h.

Sensitivity Analysis of the Number of Simulations

Distribution functions provide a more effective way of characterizing results than just mean and standard deviations. Both cumulative density functions (cdf) and probability density functions (pdf) can be used. They each have their strengths and weaknesses. The advantage of a cdf is that it allows easy extraction of the probability of failure. On the other hand, the type of density function is very difficult to determine. In contrast, a pdf is easy to identify but does not allow easy extraction of the probability of failure. Consequently, Saltelli [19] recommends that both are plotted.

In order to make a sensitivity analysis of the number of simulations, one of the $R = 0.1$ tests, termed PLAQFLU5, has been examined. Details of the test conditions are given in Table 7. A hold time t_h of 3 h was imposed between each cycle, and a crack extension $\Delta a = 1.1$ mm was obtained in 3800 h. Figure 5 and Table 8 show the results of repeat simulations of 1000 MCS and others up to 10^5 runs. In making the calculations for the CT specimen, only steady state conditions were assumed. Because initiation was ignored, all the calculations give average times less than what were measured experimentally. It is evident from Table 8 that it is necessary to undertake 10^5 MCS runs to achieve a safe probability of failure of 0.001 % but that as few as 1000 MCS runs are sufficient to give a satisfactory failure probability of 0.1 % to within a lifetime of about 10 %. From Fig. 5 it is apparent that the biggest difference occurs in the pdf at low probabilities, whereas the cdf values virtually superimpose.

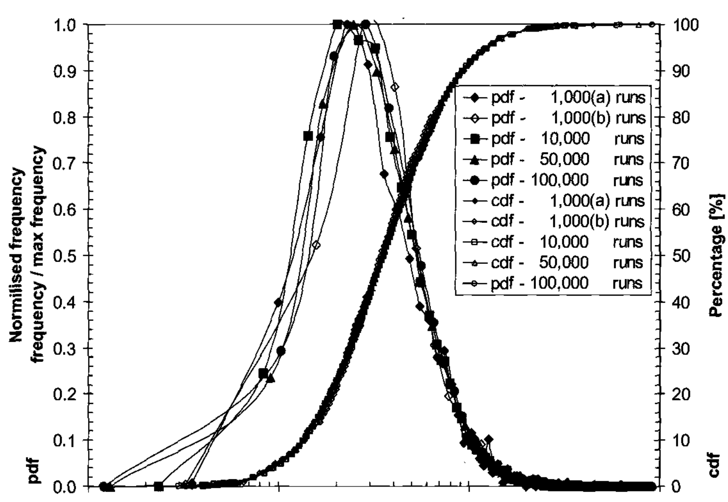

FIG. 5—*Analysis of the number of Monte Carlo simulations to predict a crack extension of 1.1 mm in specimen PLAQFLU5, assuming only steady state conditions.*

TABLE 7—*Loading conditions and geometries for plate test PLAQFLU5 used in calculation.*

Materials	F_{max} (kN)	R	Component geometry (mm)							t_h (h)	t_i (h)	t_R (h)
			$2W$	B	L	a_{ini}	$2c_{ini}$	Δa	Δc			
316L(N)	27.5	0.1	350.0	24.5	250.0	11.6	87.9	1.1	2.4	3.0	1143	3800

TABLE 8—*Results of sensitivity analysis between the number of runs for the plate PLAQFLU5.*

Probability of Failure %	Time 1000a runs	Time 1000b runs	Time 10 000 runs	Time 50 000 runs	Time 100 000 runs
0.001	N/A	N/A	N/A	N/A	120
0.01	N/A	N/A	234	198	195
0.1	352	325	299	323	336
0.2	410	451	357	398	402
0.5	492	496	460	502	501
1.0	630	660	584	602	607
50.0	3527	3410	3513	3526	3530
Mode	2285	2816	2017	2471	2854
$t_{R\,\mathrm{Mean}}$ or Case 1	3525	3525	3525	3525	3525
Additional Information					
SD Log($t_{R\,\mathrm{MCS}}$)	0.33	0.32	0.30	0.33	0.33
Log(E)	2.05×10^{-2}	2.01×10^{-2}	6.46×10^{-3}	2.88×10^{-3}	2.03×10^{-3}

Comparison of Deterministic and Probabilistic Predictions

Deterministic predictions of the cracking behavior have been made for six different combinations of uniaxial creep strain rate, crack growth rate, and initiation time properties as shown in Table 9. The uniaxial creep properties are tabulated in column (i) and were used to estimate the C^* values. Column (ii) contains the creep crack growth material properties, which were employed to predict the steady state crack growth phase. Finally, the creep crack incubation material properties are tabulated in column (iii). Case 1 assumed average material properties throughout, whereas the other cases considered various combinations of mean and ± 2 standard deviations (*SD*) or standard errors (*SE*) in properties. The times to reach a crack extension of 1.1 mm for specimen PLAQFLU5 for each case are given in Fig. 6. All of these cases result in conservative predictions, which are due to an under-prediction of initiation times. The use of average properties throughout (Case 1) gives a life of 2779 h, and assumptions of upper bound uniaxial creep and crack growth rate behavior combined with lower bound initiation times (Case 2) result in a life of 362 h. All other combinations give intermediate predictions.

Also included in Fig. 6 are the predictions obtained by MCS using 50 000 runs assuming a fixed slope of ϕ and variability in ϕ. Little influence of variability in ϕ is apparent. Assumption of average properties (Case 1) corresponds to a failure probability of about 40 % (instead of 50%) due to the under-prediction of initiation times. Choice of worst-case ± 2*SD* in the deterministic calculations (Case 2) corresponds to a failure probability of 0.05 %. Other combinations of properties give intermediate predictions.

TABLE 9—*Material properties used in the deterministic method 316L(N).*

Calculations	(i) (Calculate C^*) Creep Strain Rate (σ in MPa and $\dot{\varepsilon}$ in h^{-1})		(ii) (Steady State) Creep Crack Growth (C^* in MPa·m/h and $\dot{a}$ in mm/h)		(iii) (Initiation) Initiation Time (C^* in MPa·m/h and t_i in h)	
	A	n	D	ϕ	D_i	ϕ_i
Case 1	1.02×10^{-25} Mean	9.41 Mean	1.13 Mean	0.91 Mean	2.76 Mean	-0.64 Mean
Case 2	1.64×10^{-25} + 2SD	9.41 Mean	4.78 + 2SD	0.91 Mean	0.30 - 2SD	–0. 64 Mean
Case 3	1.64×10^{-25} + 2SD	9.41 Mean	1.13 Mean	0. 91 Mean	2.76 Mean	–0. 64 Mean
Case 4	1.02×10^{-25} Mean	9.41 Mean	4.78 + 2SD	0. 91 Mean	0.30 - 2SD	–0. 64 Mean
Case 5	1.02×10^{-25} Mean	9.41 Mean	0.66 Mean	0.84 – 2SD	111.01 Mean	–0.16 + 2SD
Case 6	9.28×10^{-22} Mean	7.65 –2SD	0.66 Mean	0.84 – 2SD	111.01 Mean	–0.16 + 2SD

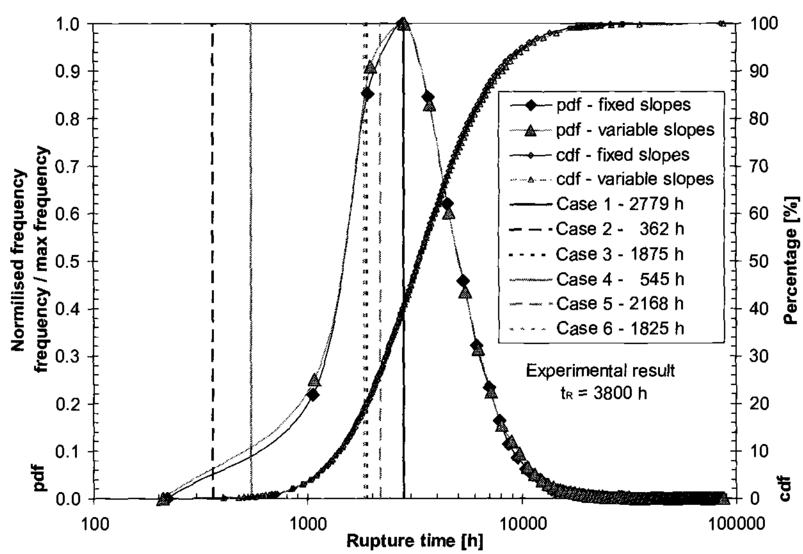

FIG. 6—*Comparison of deterministic and probabilistic times to reach a crack extension of 1.1 mm in specimen PLAQFLU5, assuming combined initiation and steady state crack growth.*

Summary and Conclusions

Creep crack initiation and growth data have been obtained on type 316L(N) stainless steel at 650°C on standard compact tension (CT) specimens and plates containing a semi-elliptical surface defect. The compact tension tests were carried out according to standard ASTM procedures and the results plotted against experimental determinations of the creep fracture mechanics parameter C^*. Some tests were performed at constant load; others were conducted at a minimum to maximum load ratio $R = 0.1$ at frequencies of less than 10^{-2} Hz. No appreciable difference was found in C^* between the constant load and cyclic test results.

The CT data have been compared with the results obtained on the plate tests. These tests were performed at constant load and $R = 0.1$ and -1.0. In the case of the plates, C^* was calculated by reference stress methods. Generally, it has been found that initiation takes longer, and crack growth rate is slower in the plates than in the CT specimens consistent with the lower constraint anticipated in the plates. A significant acceleration due to fatigue was observed in the $R = -1.0$ tests in the plates.

Predictions of the cracking behavior of the plates have been made using deterministic and probabilistic methods. Monte Carlo simulation was used to make the probabilistic calculations using statistical distributions obtained from the measured experimental scatter in the CT specimen data. Combinations of upper and lower bound material properties data were used to make the deterministic predictions. It has been found that choice of worst-case combinations (based on ± 2 standard derivations) corresponds with a failure probability of about 0.05 % from the probabilistic calculations.

Acknowledgments

The authors would like to acknowledge the provision of data from partners in the EU Brite/Euram "HIDA" (1996–2000) project and l'Ecole Nationale Superieure des Mines de Paris and the financial support of British Energy Generation Ltd.

References

[1] BS 7910, "Guide on Methods for Assessing the Acceptability of Flaws in Fusion Welded Structures," London, BSI, 2000.

[2] R5-British Energy, "Defect Assessment Code of Practice for High Temperature Metallic Components," British Energy Generation Ltd., 1999.

[3] R6, Assessment of the Integrity of Structures Containing Defects, Revision 3, British Energy Generation, 2000.

[4] ASME Boiler & Pressure Vessel Code, Section XI, 1998.

[5] Commissariat, à l'Energie Atomique, "A16: Guide pour les Etudes de Fuite avant Rupture et les Analyses de Nocivité de Défaut associées," 4th ed., Saclay: CEA, 2002.

[6] Ainsworth, R. A., "Some Observations on Creep Crack Growth," *International Journal of Fracture*, Vol. 20, 1982, pp. 147–159.

[7] Ainsworth, R. A., "The Assessment of Defects in Structure of Strain Hardening Materials," *Engineering Fracture Mechanics*, Vol. 19, 1984, pp. 633–642.

[8] ASTM E 1457-00: Test Method for Measurement of Creep Crack Growth Rates in Metals, *Annual Book of ASTM Standards*, Vol. 3, 2001, pp. 936–950.

[9] Nikbin, K. M., Smith, D. J., and Webster G. A., "Prediction of Creep Crack Growth from Uniaxial Creep Data," *Proceeding of Royal Society of London*, Vol. 396, 1984, pp. 183–197.

[10] Webster, G. A. and Ainsworth, R. A., *High Temperature Components Life Assessment*,

Chapman & Hall, 1993.
[11] Norton, F. H. "The Creep of Steel at High Temperatures," McGraw and Hill, London, 1929.
[12] Nikbin, K. M., "Transition Effects in Creep-Brittle Materials," *Mechanics of Creep Brittle Materials II*, A. C. F. Cocks, A. R. S. Ponter, Eds., Elsevier Applied Science, 1991, pp. 14–24.
[13] Austin, T. S. P. and Webster, G. A., "Prediction of Creep Crack Growth Incubation Periods," *Fatigue and Fracture of Engineering Materials and Structures*, Vol. 15, 1992, pp. 1081–1090.
[14] Webster, G. A., Nikbin, K. M., Chorlton, M. R., Célard, N. J. C., and Ober, M., "Comparison of High Temperature Defect Assessments Methods," *Material at High Temperature*, Vol. 15, 1998, pp. 337–346.
[15] Wasmer, K., Nikbin, K. M., and Webster, G. A., "A Sensitivity Study of Creep Crack Growth in Pipes," PVP, Vol. 438, New and Emerging Computational Methods: Applications to Fracture, Damage and Reliability, ASME, New York, 2002, pp. 17–24.
[16] Wasmer, K., Nikbin, K. M., and Webster, G. A., "Creep Crack Initiation and Growth in Thick Section Steel Pipes under Internal Pressure," *International Journal of Pressure Vessels and Piping*, Vol. 80, Nos. 7 and 8, 2003, pp. 489–498.
[17] Wasmer, K. "Creep Crack Growth Prediction in a Range of Steels," Ph.D. Thesis, Mechanical Engineering, Imperial College, London, July 2003.
[18] Goodall, I. W. and Webster, G. A., "Theoretical Determination of Reference Stress for Partially Penetrating Flaws in Plates," *International Journal of Pressure Vessels and Piping*, Vol. 78, 2001, pp. 687–695.
[19] Saltelli, A., Chan, K., and Scott, E. M., "Sensitivity Analysis," *Probability and Statistics*, Wiley, 2000.
[20] Montgomery, D. C. and Runger, G. C. "Applied Statistics and Probability for Engineers," John Wiley & Sons, 1994.
[21] Annis, C., "Probabilistic Life Prediction *Isn't* as Easy as it Looks," *ASTM STP 1450: Probabilistic Aspects of Life Prediction*, Johnson and Hillberry, Eds., ASTM International, West Conshohocken, PA 2003, pp. 1–13.

Journal of ASTM International, May 2005, Vol. 2, No. 5
Paper ID JAI12031
Available online at www.astm.org

Hyukjae Lee[1] *and Shankar Mall*[1]

Fretting Fatigue and Stress Relaxation Behaviors of Shot-Peened Ti-6Al-4V

ABSTRACT: Relaxation behavior of residual stress and its effect on fretting fatigue response of shot-peened titanium alloy, Ti-6Al-4V were investigated at room and elevated temperatures under constant amplitude cycling condition using two contact configurations, cylinder on flat and flat on flat. Measurements by X-ray diffraction method before and after tests showed that residual compressive stress relaxed during fretting fatigue. Fretting fatigue life depended on the amount of stress relaxation as well as on the applied stress range. Elevated temperature induced more residual stress relaxation relative to that at room temperature, which, in turn, resulted in a reduction of fretting fatigue life. There was no effect of contact geometry on fretting fatigue life on the basis of the applied cyclic stress on the specimen, which did not account for any effects from contact stresses, even though less residual stress relaxation occurred with flat pad. A critical plane based fatigue crack initiation model, modified shear stress range parameter (MSSR), was computed from finite element analysis for tests incorporating various levels of stress relaxation. It showed that not only crack initiation but also crack propagation should be considered to characterize fretting fatigue behavior of shot-peened specimens.

KEYWORDS: fretting fatigue, residual stress, shot-peening, stress relaxation, crack initiation parameter

Introduction

Shot-peening improves the fatigue strength of metallic parts by inducing the residual compressive stress on the surface of components. The residual compressive stress on the surface can prevent or delay crack initiation and propagation as well as close the pre-existing cracks when they are within the residual compressive stress zone. Therefore, there have been several investigations about the fatigue response and relaxation behavior of residual stress under various loading and environment conditions. However, relaxation of compressive residual stress also occurs under cyclic loading conditions that result in a reduction of its beneficial effects. Further, fretting conditions and/or an elevated temperature environment generally accelerate the stress relaxation process. Relaxation of residual stress at elevated temperature is a thermal recovery process in which elevated temperature accelerates a rapid annihilation of crystalline defects. Fretting involves micro-slip of contacting bodies subjected to cyclic load, which promotes and/or induces the stress relaxation process. Kodama [1] reported that the residual stress relaxation behavior in the shot-peened mild steel showed a linear logarithmic decrease of residual stress with an increasing applied number of fatigue cycles. Holzapfel et al. [2] investigated the residual stress relaxation behavior of AISI 4140 steel under the plain fatigue loading condition at elevated temperatures and found that thermal and mechanical mechanisms for the relaxation of residual stress could be regarded as independent processes. Kato et al. [3,4] studied effects of shot-

Manuscript received 7 November 2003; accepted for publication 24 May 2004; published May 2005. Presented at ASTM Symposium on Fatigue and Fracture Mechanics: 34th Volume on 19–21 November 2003 in Tampa, FL; S.R. Daniewicz, J.C. Newman, Jr., and K-H. Schwalbe, Guest Editors.
[1] Research Scientist and Professor, respectively, Department of Aeronautics and Astronautics, Air Force Institute of Technology, Wright-Patterson AFB, OH 45433-7765.

peening on fatigue strength of Ti-6Al-4V alloy at elevated temperatures. Their investigation showed that plain fatigue strength of a shot-peened specimen decreased with temperature up to 350°C and reached the lower value than that of unpeened specimen at 450°C due to the relaxation of compressive residual stress at elevated temperatures. Also, it has been demonstrated that fretting fatigue lives of shot-peened components increase as compared to unpeened components [5,6].

The blade/disk attachments (dovetail joints) in gas turbine engines generally fail due to fretting fatigue. Titanium alloy, Ti-6Al-4V is a representative material used in these components of gas turbine engines, and its maximum usage temperature is about 275°C. In recent studies [7,8], shot-peened Ti-6Al-4V showed longer fretting fatigue life than unpeened Ti-6Al-4V at room temperature, however this increase in fatigue life was significantly reduced at elevated temperature, and the difference in fatigue life between shot-peened and unpeened Ti-6Al-4V became negligible at 260°C. This was attributed to an increased relaxation of residual stress at elevated temperature. These previous studies were conducted under the cylinder-on-flat contact configuration. As contact configuration in dovetail joints is basically a flat with rounded edge-on-flat, the present study is an extension of these previous studies to include this contact geometry. The present study investigated both residual stress relaxation and fretting fatigue behavior of shot-peened Ti-6Al-4V alloy with flat with rounded edge-on-flat contact configuration at room and elevated temperatures. Finite element analysis was also conducted to evaluate the ability of a critical plane based crack initiation parameter to characterize fretting fatigue crack initiation behavior of the tests.

Experimental Procedure

A forged titanium alloy, Ti-6Al-4V was used in the present study. The material was preheated and solution treated at 935°C for 105 min, cooled in air, vacuum annealed at 705°C for 2 h, and then cooled in argon. The resulting microstructure showed the nucleation of 60 % volume of α (HCP) phase (platelets) in 40 % volume of β (BCC) phase (matrix). The measured grain size was about 10 μm. The material has elastic modulus of 126 GPa and yield strength of 930 MPa at room temperature, and elastic modules of 92 GPa and yield strength of 741 MPa at 260°C. A dog-bone type of specimen was machined by the wire electrical discharge method. Both width and thickness of the reduced gage section of the specimen were 6.4 mm. After machining, specimens were shot-peened as per SAE Aerospace Material Specification (AMS) 2432 standard, using computer controlled equipment with an intensity of 7 Almen. The process was conducted with ASR 110 cast steel shots with 100 % surface coverage. Two types of pads, which were also made of Ti-6Al-4V, were used: a cylindrical pad with a radius of 50.8 mm and a flat pad with rounded edges, which had an edge radius of 2.54 mm and a flat region of 4.45 mm. Figure 1 shows schematic drawings of the specimen and pad used in this study.

A servo-hydraulic uniaxial test machine was equipped with a fretting fatigue fixture to conduct tests at a frequency of 10 Hz. The details of fretting fixture as well as fretting fatigue test are provided in the previous studies [7,8]. Two pads were pressed symmetrically against specimen surface through this fixture. Normal contact load of 1335 N was applied on the specimen through pads. The specimen was fatigued under constant amplitude condition at different maximum stress levels, σ_{max}, ranging from 333–666 MPa with a stress ratio, R of 0.1. To conduct fretting fatigue tests at elevated temperature, two heaters, placed at the front and back of specimen, were used to heat and maintain the temperature at 260°C over a gage section

(10 mm) surrounding the contact region. Heaters were controlled through a feedback controlled system with two separate silicon controlled rectifiers (SCR). During fretting fatigue test, temperature in the gage section of the specimen was maintained within ±3°C of the desired temperature. X-ray diffraction measurements of residual stress were conducted using a two-angle sine-squared-psi technique, in accordance with SAE J784a, employing Cu K-alpha radiation from the (213) planes of the HCP structure of the Ti-6Al-4V. The depth profile of the residual stress (i.e., away from the contact surface) was measured by iterative removal of thin layers of material by electro-polishing method followed by X-ray measurements.

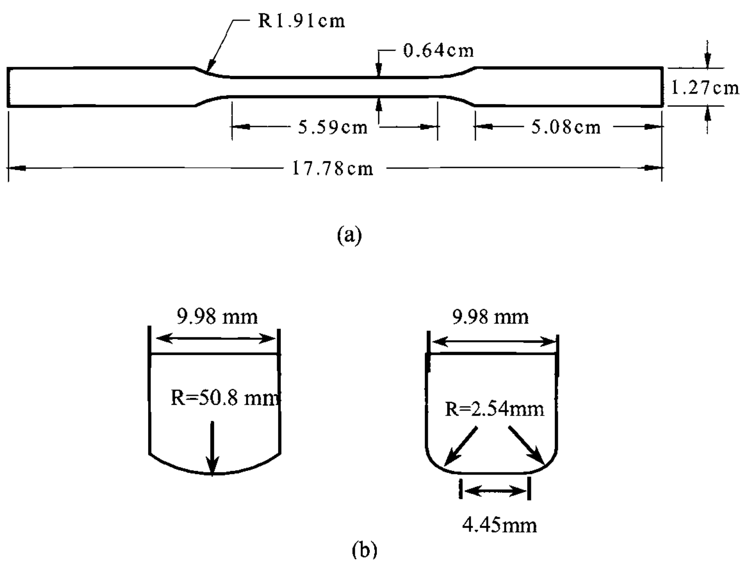

FIG. 1—*Schematic of* a) *specimen and* b) *pad.*

Finite Element Analysis

Finite element analysis (FEA) was conducted using a commercially available code, ABAQUS [9], to determine the stress, strain, and displacement in the contact region between pad and specimen. The 4-node, plane strain elements along with the master-slave contact algorithm on the contact surface between the fretting pad and specimen were used. Figure 2 shows the finite element model along with loads and boundary conditions. The fretting pad was constrained by a rigid body constraint in the longitudinal direction of the specimen. A multi-point constraint (MPC) was applied at the top of the pad to prevent it from rotation due to the applied loads. There was also a multi-point constraint between the border elements where element size changed to prevent free nodes of smaller elements penetrating into the bigger elements. The normal contact load, P, was applied at the top, and the tangential load, Q, was applied on the pad. Axial stress, σ_{axial}, was applied on the specimen. Loads were applied to the finite element model in three steps. Normal load was applied in the first step on the top of pad as a distributed load to establish contact. In the second step, maximum tangential load, Q_{max}, and maximum axial stress, $\sigma_{axial,max}$, obtained from experiments at the maximum cyclic load condition were applied. Then, minimum tangential load, Q_{min}, and minimum axial stress, $\sigma_{axial,min}$, obtained from the experiments at minimum cyclic loading condition, were applied in the third step. Further details of FEA can be found in a previous study [6].

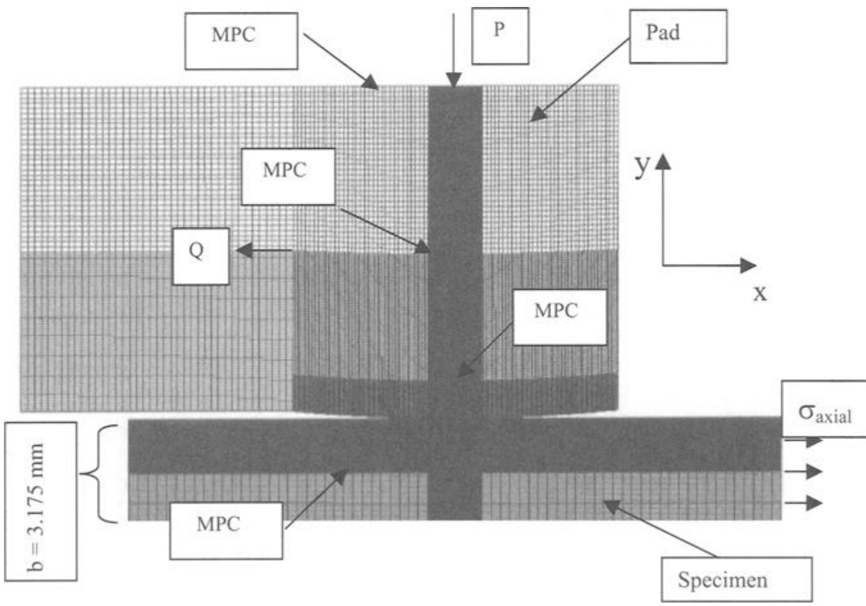

FIG. 2—*Finite element model.*

Results and Discussion

Fretting Fatigue Life

Figure 3 shows the fretting fatigue life, N_f, of shot-peened Ti-6Al-4V as a function of applied stress range ($\Delta\sigma = \sigma_{max} - \sigma_{min}$) for two contact geometries (i.e., cylindrical versus flat with rounded edge) at room and elevated temperatures (RT and 260°C). As mentioned earlier, fatigue tests were conducted at several stress levels with contact load of 1335 N at room temperature (RT) and 260°C, which provided the complete S-N relationships at these two conditions with both contact geometries, and these are shown in this figure by two trend lines. It can be clearly seen that an increase in temperature reduced the fretting fatigue life of shot-peened Ti-6Al-4V relative to that at room temperature at a given stress range level for both contact geometries. Further, contact geometry appears to have no effect on fatigue life, on the basis of applied stress range, as data from these fall within a scatter band at a given test temperature, i.e., data show two distinct trends depending on test temperature but not on contact geometry. Figure 3 also shows the corresponding relationships for the un-peened Ti-6Al-4V for the same two contact geometries (cylinder on flat and flat on flat) for both room and elevated temperatures. There appears again to be no effect of the contact geometry on these S-N relationships from these two geometries when plotted on the basis of applied stress range. This is not always the case, i.e., S-N relationship could depend on the contact geometry [16]. Further, there was no effect of the elevated temperature on the S-N relationship in the case of un-peened material unlike shot-peened material. This was due to the larger relaxation of residual stress at elevated temperature than at room temperature in the shot-peened material as discussed next. Such a phenomenon was not present in the un-peened material. In spite of the relaxation, Fig. 3 clearly shows the beneficial effect of shot-peening, especially in the high cycle fatigue regime.

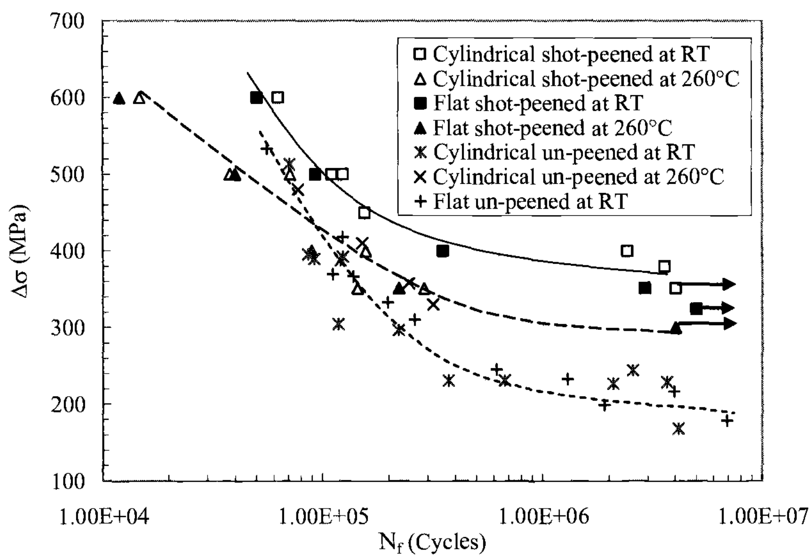

FIG. 3—*Applied stress range versus cycles to failure with two different temperatures (RT and 260°C) and contact geometries (flat and cylindrical pads). Contact load was 1335 N.*

Residual Stress Relaxation

Figure 4 shows three representative residual stress profiles in shot-peened specimens as a function of the depth (i.e., distance) from the contact surface. These three cases are for virgin specimen, i.e., before fretting test, and for specimens after fretting fatigue test until their failure at room and elevated temperatures. For untested shot-peened specimen, compressive stress was 575 MPa at the surface and increased with depth up to 814 MPa at a depth of 25 μm, after which it gradually decreased to zero at a depth of 164 μm. Although it is not shown in Fig. 2, the compensating tensile stress would be present at the depth below where compressive stress becomes zero, to maintain internal forces equilibrium inside the specimen, i.e., the area under both the tensile and compressive stress profiles should be the same [6]. Further, it was assured that shot-peening generates a biaxial state of stress in the plane, $\sigma_{xx} = \sigma_{yy}$, as in a previous study [10], and Fig. 4 shows one of this stress components. The σ_{xx} component (i.e., along the longitudinal direction) of the specimen was measured by the X-ray diffraction method.

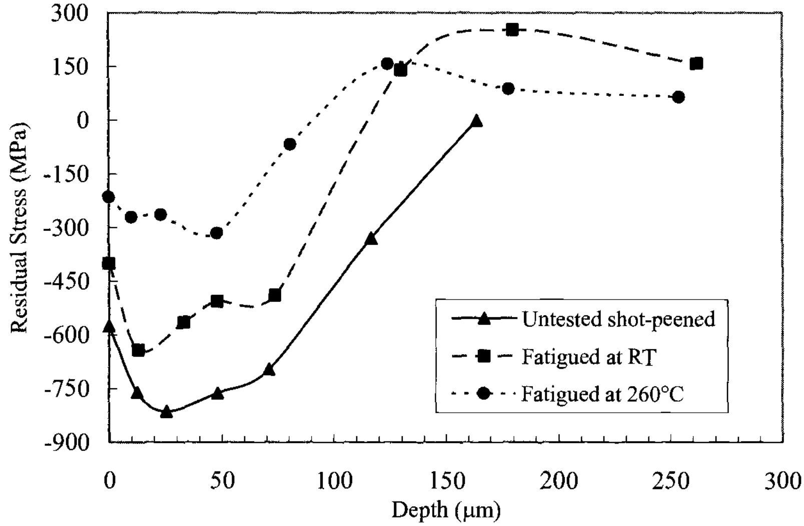

FIG. 4—*Residual stress profiles as function of depth from contact surface. Fatigued specimens were tested with cylindrical pads at the contact load of 1335 N.*

Figure 4 also shows the residual stress profiles in the fretting fatigued specimen, which was subjected to the applied stress range of 400 MPa up to their failure at room temperature and 260°C. The residual stress measurements were taken at the center of the fretting scar (i.e., stick region). Further, the difference in measured residual stress between the stick and slip regions was negligible. For the specimen fatigued at room temperature, the compressive residual stress at the contact surface after the fretting fatigue test was 400 MPa, which was 69 % of that on the untested shot-peened specimen. The specimen tested at 260°C showed greater stress relaxation. The compressive residual stress at the contact surface was 215 MPa, which was 38 % of the surface residual stress on the untested shot-peened specimen. The depth from the contact surface, where the residual compressive stress reached to zero, also decreased after fretting fatigue at elevated temperature, i.e., 110 μm for the specimen tested at room temperature versus 90 μm for the specimen tested at 260°C. Overall, the amount of stress relaxation inside the specimen (i.e., away from the contact surface) showed almost the same trend as that on the contact surface. Thus, it can be assumed that approximately 30 % of residual stress relaxation occurred due to the fretting fatigue and an additional 30 % relaxation occurred due to the exposure to elevated temperature.

Figure 5 shows the relaxation behavior of residual stress at the contact surface under various test conditions, i.e., when specimens were tested at two stress levels (350 and 500 MPa), and at two temperatures (RT and 260°C) for both contact geometries. In Fig. 5, the magnitude of surface residual stress is represented by a percent value of the initial surface residual stress from the untested shot-peened specimen. Stress relaxation behavior at the contact surface was only analyzed since the relaxation behavior inside the specimen was similar to that on the contact surface. Although most of the residual measurements were done at two temperatures (RT and 260°C), one measurement at 100°C was also conducted with cylindrical pad, which is also shown on this figure. Based on this, a linear dependence of stress relaxation on temperature for a given test condition is assumed, so this trend is shown by straight lines in Fig. 5. Further, any discussion on the relaxation behavior in this study is not affected by this assumption. Figure 5 clearly shows that a greater stress relaxation occurred when a specimen was exposed to either higher temperature or applied stress range. Further, specimens with a flat pad showed less stress relaxation compared to those with a cylindrical pad under all test conditions of this study. This might be due to a lower magnitude of stress components at contact surface with flat pad relative to the cylindrical pad, which will be discussed later. The trend lines between the stress relaxation and temperature for both contact geometries show relatively higher slopes at the stress range of 350 MPa than those at the stress range of 500 MPa. This was due to the fact that specimens with both flat and cylindrical pad did not fail at room temperature due to run out limit on fatigue cycles, i.e., they survived 4 million cycles. A previous study showed that there was an additional stress relaxation during the crack initiation/propagation phase, which contributed a good portion toward the total residual stress measured after the specimen failure [2]. Therefore, un-failed specimens tested at the applied stress range of 350 MPa did not have this part in the measured value of residual stresses, and hence they show relatively smaller amount of stress relaxation than if they had failed.

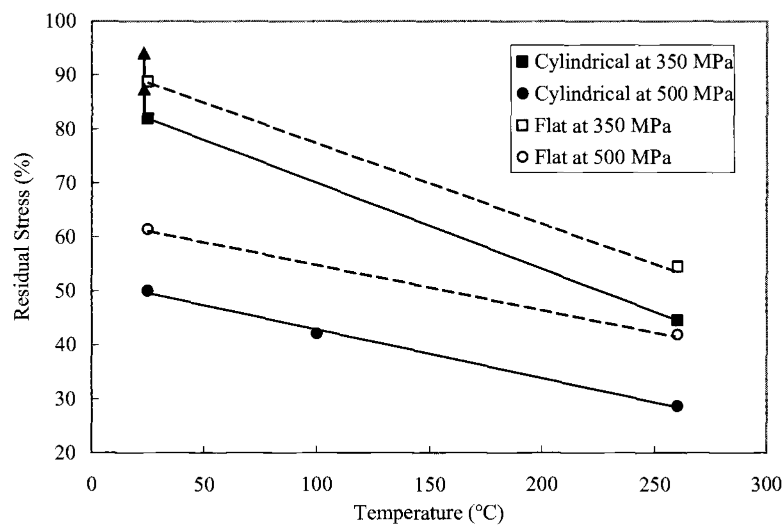

FIG. 5—*Residual stress at contact surface as a function of test temperature for two applied stress ranges and contact geometries. Residual stresses were measured after specimen failure. Applied contact load was 1335 N. Arrows represent un-failed specimens at 4 000 000 cycles.*

Contact Stress State and Crack Initiation Parameter

A previous study investigated the fretting fatigue behavior of the same unpeened material, Ti-6Al-4V at room temperature and 260°C experimentally as well as by finite element analysis [11]. There was no difference in fretting fatigue lives at these two temperatures, which is also shown in Fig. 3. Further, this study showed that there was no difference between FEA at room temperature and 260°C [11]. This was due to the fact that specimens were heated first before applying any load required to conduct fretting fatigue tests and all loads, used in analysis, were measured after specimen achieved the test temperature of 260°C. For this reason, all FEA computations were conducted without applying temperature to the model except for material properties used at 260°C, which were Young's modulus = 92 GPa and Poisson's ratio = 0.3. Figure 6 shows the variation of longitudinal normal stress, σ_{xx}, along the cyclic loading direction of the specimen (x-direction) at the contact surface. Note that the distance x in this figure is normalized by the semi-contact width, a. The contact width, 2a was 0.92 mm and 5.08 mm for the cylindrical and flat pads, respectively. There is a very little effect of temperature on stress magnitude and its variation on the contact surface for a given contact geometry, but the specimen in contact with a flat pad has smaller magnitude of σ_{xx} along the contact surface due to its wider contact width. The maximum value of σ_{xx} is located at the trailing edge for all cases, where all specimens failed in this study, and the absolute value of the maximum σ_{xx} at the trailing edge is much larger for cylinder-on-flat contact configuration.

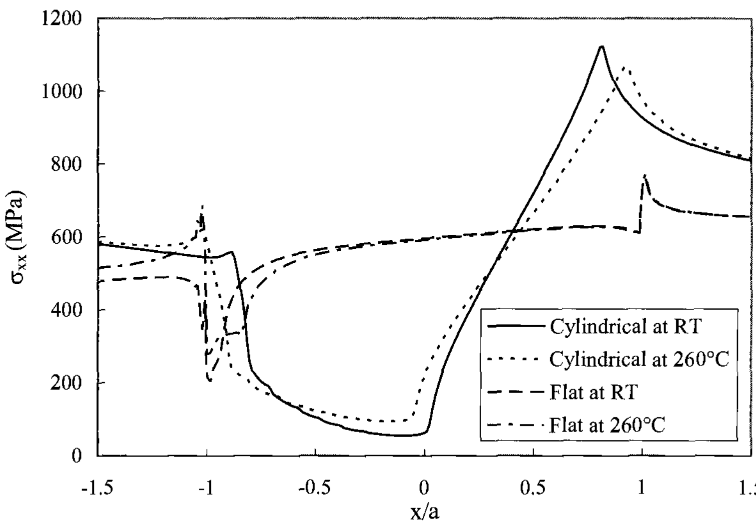

FIG. 6—*Variation of σ_{xx} in x direction at contact surface of fretting specimen. Two different pads (cylindrical pad and flat pad) were used. The x-axis is normalized by contact half width, a.*

Stress state in contact region subjected to fretting fatigue is of multi-axial nature. Hence, it is essential to utilize a fatigue parameter/model/criterion which can account for multi-axial stress for characterizing the fretting fatigue crack initiation process. Several attempts have been made to predict crack initiation life under fretting fatigue condition using critical plane based parameters/models [12–16]. Among them, a modified shear stress range (MSSR) parameter has been shown to be the most effective in terms of predicting fretting fatigue life from plain fatigue data as well as orientation and location of crack initiation [16]. Further, it has been shown that this parameter is also the most effective in terms of correlating fretting fatigue crack initiation lives from different contact geometries. This parameter involves a combination of shear and normal stresses on the critical plane and is elaborated next.

To compute MSSR parameter, shear stress was calculated at all points along all planes ranging from $-90° < \theta < 90°$ from the state of stress (σ_{xx}, σ_{yy}, τ_{xy}) computed from FEA by:

$$\tau = -\frac{\sigma_{xx} - \sigma_{yy}}{2} \sin 2\theta + \tau_{xy} \cos 2\theta \qquad (1)$$

where θ is the orientation from a vertical to the applied axial load direction (x-direction) on the specimen. Then, shear stress range, $\Delta\tau = \tau_{max} - \tau_{min}$, was computed at all planes and at all points. τ_{max} and τ_{min} are shear stresses due to maximum and minimum applied axial loads, respectively. From these, the value of the maximum shear stress range, its location, and the critical plane where it was acting were obtained. Since the mean stress or stress ratio also affects fatigue behavior, this effect on the critical plane was accounted by incorporating a technique proposed by Walker [17]. Then, $\Delta\tau_{crit}$ was calculated from:

$$\Delta\tau_{crit} = \tau_{max}(1-R_\tau)^m \qquad (2)$$

where τ_{max} and R_τ are the maximum shear stress and shear stress ratio on the critical plane, respectively, and m is a fitting parameter, which was determined to be 0.45 from a previous study [15]. Finally, MSSR parameter was calculated by combining $\Delta\tau_{crit}$ with the maximum normal stress on the critical plane of maximum shear stress range as:

$$MSSR = A\Delta\tau^B{}_{crit} + C\sigma^D{}_{max} \qquad (3)$$

where σ_{max} is the maximum normal stress on the critical plane defined by shear stress range. A, B, C, and D are the fitting constants determined by curve fitting, and these were determined empirically in a previous study [16], A = 0.75, B = 0.5, C= 0.75, and D = 0.5.

MSSR parameters were calculated at all locations, and the maximum value of MSSR parameter for each test was chosen as a value of MSSR parameter for the fatigue life diagram as shown in Figs. 7–9. These fatigue life diagrams include the effects of contact stresses unlike the one shown in Fig. 3, which is based on the applied axial stress to the specimen. Figure 7 shows MSSR parameter calculated for all four different test conditions, without incorporating the residual stress from the shot-peening into the computed stresses from finite element analysis, as a function of fretting fatigue life. Unlike Fig. 3, specimens fretted with cylindrical pad show that MSSR parameter versus cycle-to-failure relationships are different than their counterparts from specimens fretted with flat pad. Further, specimens tested at 260°C showed shorter fatigue lives on the basis of MSSR parameter for both pad geometries. The maximum values of MSSR parameter for all cases in Fig. 7 were located at the contact surface, which will be discussed later.

When initial residual stress from shot-peening (i.e., before fretting fatigue test) was added to the computed values of σ_{xx} and σ_{yy} from FEA, values of MSSR parameter decreased significantly as shown in Fig. 8. And the difference in MSSR parameter versus cycles-to-failure relationship between two different contact geometries increased since the decrease in MSSR parameter due to the addition of residual stress for specimens with flat pad was relatively larger than that in the case of cylindrical pad. This larger decrease in MSSR parameter for specimens with flat pad was due to their relatively lower value of initial stresses as shown in Fig. 6, so that the effect of residual stress was more compared to specimens with cylindrical pad. Figure 9 shows the fatigue life relationships when relaxed residual stresses obtained after fretting tests were included in the computation of MSSR parameter. For this, 42 % and 61 % of stress relaxation at room temperature and 260°C, respectively, were used at all locations at and away from the contact surface for both cylindrical and flat pads. Still, four separate scatter bands of data, i.e., MSSR parameter versus cycles-to-failure relationships, can be seen based on temperature and contact geometry, however, the difference among them is now less as compared to that in Fig. 8.

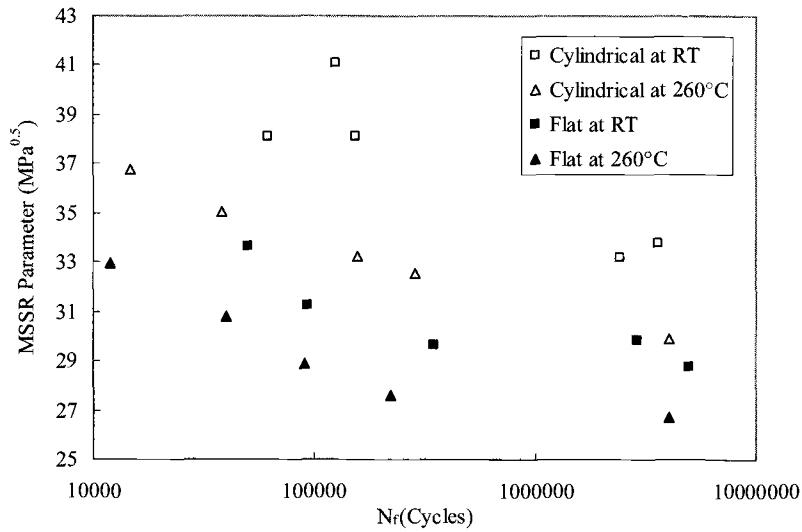

FIG. 7—*MSSR parameters versus number of cycles to failure without residual stresses.*

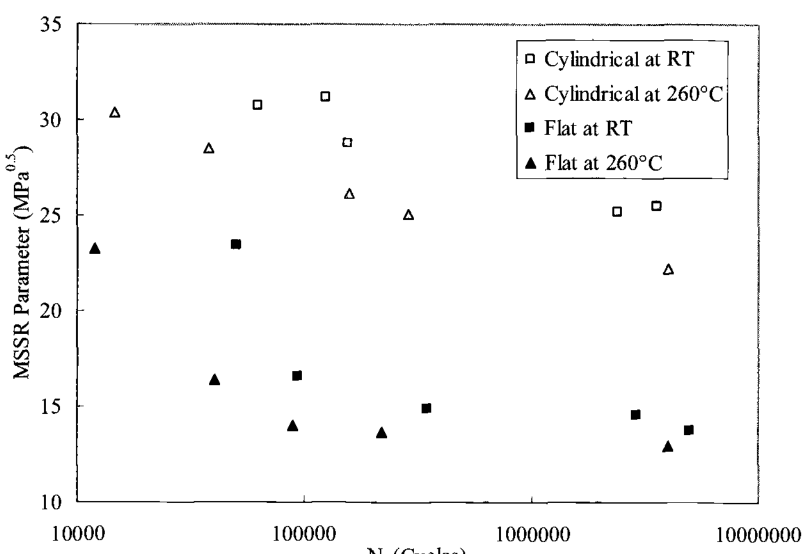

FIG. 8—*MSSR parameters versus number of cycles to failure after including initial residual stresses, i.e., before stress relaxation.*

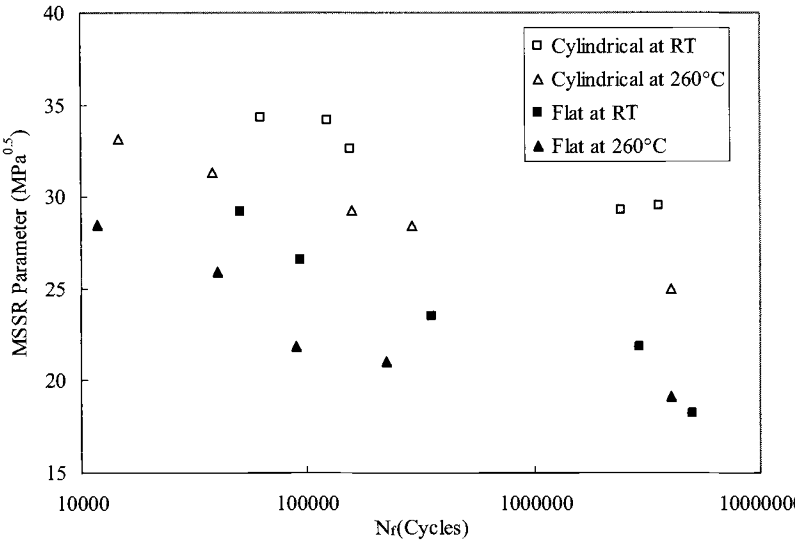

FIG. 9—*MSSR parameters versus number of cycles to failure after including relaxed residual stresses from tested specimen.*

As mentioned earlier, previous studies showed that MSSR parameter versus fatigue life relationships of un-peened specimens under different test conditions, i.e., fretting and plain fatigue, two contact geometries, and room and elevated temperatures, were within a scatter band [11,16]. Considering that residual compressive stress can prevent or delay not only crack initiation but also propagation in the region where this stress is present, it can be expected that shot-peened specimens would show different fatigue life relationships from those for un-peened specimens. Among several fatigue life relationships shown in Figs. 7–9, the most appropriate ones are in Fig. 9, since they include the effects of relaxation of residual stress due to fretting fatigue. However, there are still differences in the MSSR parameter versus cycles-to-failure relationship from various test conditions in Fig. 9. This can be attributed to the differences in relative contribution of crack nucleation/initiation versus propagation phases in the total fatigue life. In previous studies with un-peened specimens, the nucleation and initiation part, which involved formation of a crack of ~ 0.1–0.2 mm length, was about 90–95 % of cycles-to failure, i.e., total life [16]. This may not be the case with shot-peened specimens where it is expected that crack propagation phase would contribute to a good part of the total life. So the differences in the MSSR parameter versus cycles-to-failure relationship from various test conditions in Fig. 9 may be due to the difference in crack propagation behavior between two contact geometries. This probably explains why data from flat pad at both temperatures fall below their counterparts from cylindrical pad. It is to be noted that after accounting the residual stress from shot-peening stress state was more compressive in magnitude, and it spanned over the longer depth away from the contact surface in flat pad than in the cylindrical pad (see Fig. 6). This would retard the crack initiation and/or the crack propagation. Further, the difference in MSSR parameter versus cycles-to-failure relationship between two temperatures for a given contact geometry suggests that crack nucleation/initiation in shot-peened materials may be temperature dependent phenomenon. Thus, further investigation is needed to understand these behaviors.

Next, the variation of MSSR parameter along the depth from contact surface will be looked into to understand its effects on crack nucleation/initiation. These are shown in Figs. 10–13 for four fretting test conditions of this study, which involved two pad geometries and two temperatures. Without including residual stress from shot-peening in the computed stresses, maximum values of the MSSR parameter were always located at the contact surface as shown in Figs. 10–13. When the initial residual stress from shot-peening (i.e., no relaxation) was added, values of the MSSR parameter lowered significantly, and the locations of maximum values of MSSR parameter were not at the contact surface but at a depth of about 170 μm for all cases. However, when residual stress after relaxation was included in the calculation of MSSR parameter, it changed the location of the maximum MSSR parameter. Maximum values of MSSR parameter for specimens tested at room temperature for both contact geometries were still about 170 μm away from the contact surface, but the difference between the values of MSSR parameter at the contact surface and at a depth of 170 μm was significantly reduced as shown in Figs. 10 and 11. This small difference as well as microscopic damage at the contact surface from the fretting action (i.e., fretting scar) probably caused the crack initiation at the contact surface instead of away from it as seen in the experiments.

At 260°C, a greater stress relaxation yielded higher value of MSSR parameter at/near contact surface in comparison to room temperature as shown in Figs. 12 and 13. These again show that the crack could initiate at contact surface or any location from contact surface at 150–200 μm inside the specimen, since variation in the MSSR parameter is not much over this distance when relaxed residual stress is accounted for for its calculation. However, crack initiated at the contact surface in all tests can again be attributed to the combination of maximum value of MSSR and microscopic damage from fretting fatigue at the contact surface, i.e., fretting scar. On the other hand, with no stress relaxation, a crack would have initiated within the specimen away from the contact surface, where maximum value of MSSR parameter occurred as shown in Figs. 10–13. As more and more stress relaxation occurs, the location of crack initiation moves toward the contact surface.

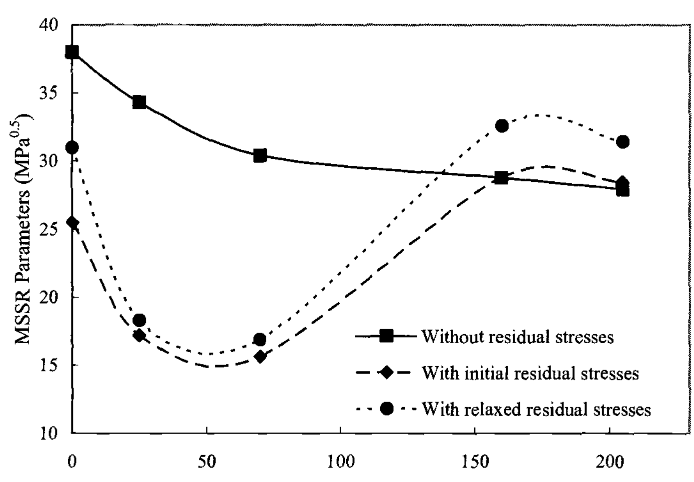

FIG. 10—*MSSR parameters with different states of residual stress as a function of depth. Data from specimen in contact with cylindrical pad and tested at room temperature.* σ_{max} = *500 MPa and* σ_{min} = *50 MPa.*

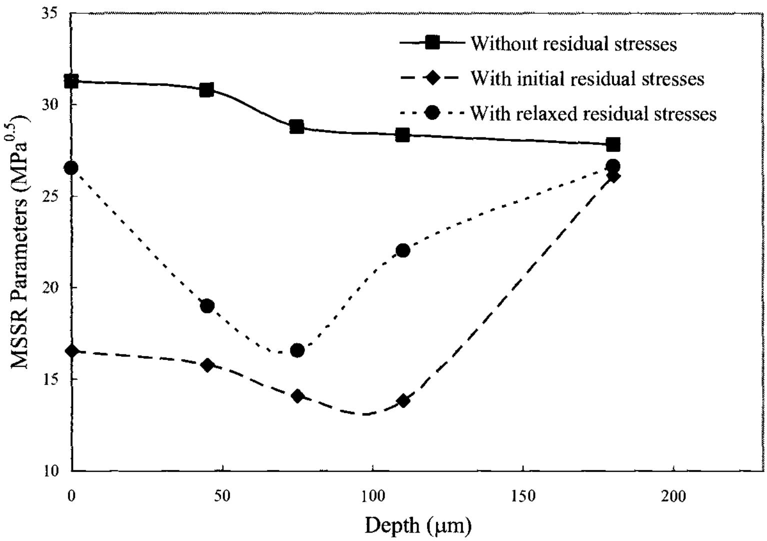

FIG. 11—*MSSR parameters with different states of residual stress as a function of depth. Data from specimen in contact with flat pad and tested at room temperature.* σ_{max} = *555 MPa and* σ_{min} = *55 MPa.*

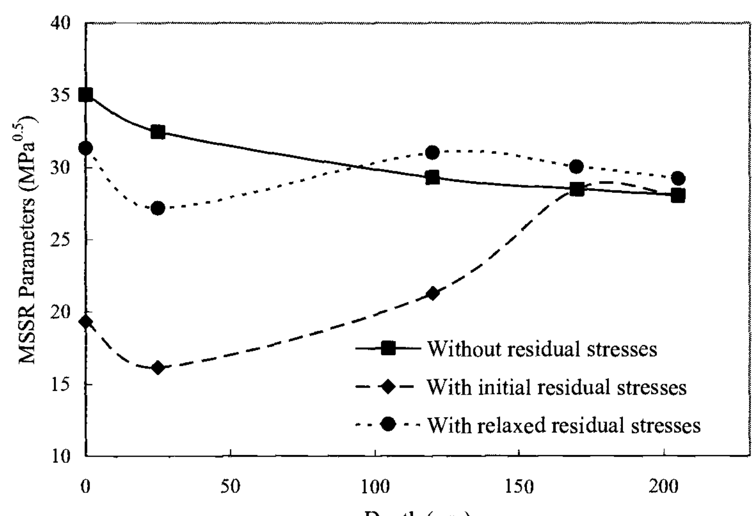

FIG. 12—*MSSR parameters with different states of residual stress as a function of depth. Data from specimen in contact with cylindrical pad and tested at 260°C.* σ_{max} = *555 MPa and* σ_{min} = *55 MPa.*

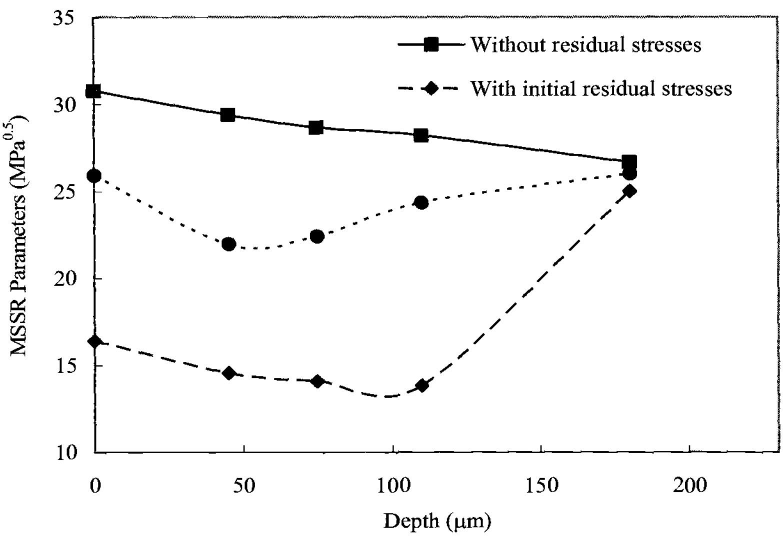

FIG. 13—*MSSR parameters with different states of residual stress as a function of depth. Data from specimen in contact with flat pad and tested at 260°C. σ_{max} = 555 MPa and σ_{min} = 55 MPa.*

Conclusions

Fretting fatigue behavior of shot-peened titanium alloy, Ti-6Al-4V, with two contact conditions (cylinder-on-flat and flat-on-flat) was investigated at room temperature and 260°C. Residual stress measurements before and after the fretting test showed that it relaxed during fretting fatigue, and higher applied cyclic load and elevated temperature fostered more stress relaxation. As more relaxation occurred at elevated temperature, fretting fatigue life of shot-peened specimen at 260°C was reduced. However, no effect of contact geometry on fretting fatigue life was observed on the basis of the applied cyclic stress on the specimen, which did not account for any effect from the contact stress, even though less residual stress relaxation occurred when specimen was fretted with a flat pad. A critical plane based fatigue crack initiation model, modified shear stress range parameter (MSSR), was computed from finite element analysis. It showed that not only a crack initiation but also a crack propagation process should be considered to characterize fretting fatigue behavior of shot-peened specimens. Cracks always initiated at the contact surface in this study, which was correctly predicted by the MSSR parameter.

Acknowledgments

The authors gratefully acknowledge the support of Dr. Jeffrey Calcaterra, High Cycle Fatigue Program at Materials and Manufacturing Directorate, Air Force Research Laboratory. Also the help of Ms. Sonia Martinez in some measurements of residual stress is gratefully appreciated.

References

[1] Kodama, S., "The Behavior of Residual Stress During Fatigue Stress Cycles," *Proceedings of International Conference on Mechanical Behavior of Metals*, Vol. 2, Society of Materials Science, Kyoto, Japan, 1972, pp. 111–118.

[2] Holzapfel, H., Schulze, V., Voehringer, O., and Macherauch, E., "Residual Stress Relaxation in an AISI 4140 Steel Due to Quasistatic and Cyclic Loading at High Temperatures," *Materials Science and Engineering A*, Vol. A248, 1998, pp. 9–18.

[3] Kato, Y., Takafuji, S., and Kiriyama, M., "Effect of Shot Peening on Fatigue Strength of Ti-6Al-4V Alloy at Elevated Temperatures," *Journal of the Society of Materials Science*, Japan, Vol. 45, 1996, pp. 43–47.

[4] Kato, Y. and Takafuji, S., "Fatigue Properties of Shot Peened Ti-6Al-4V Alloy at Elevated Temperatures," *Journal of the Society of Materials Science*, Japan, Vol. 46, 1997, pp. 1136–1142.

[5] Mutoh, Y., Satoh, T., and Tsunoda, E., "Improving Fretting Fatigue Strength at Elevated Temperatures by Shot Peening in Steam Turbine Steel," *Standardization of Fretting Fatigue Test Methods and Equipment, ASTM STP 1159*, M. H. Attia and R. B. Waterhouse, Eds., ASTM International, West Conshohocken, PA, 1992, pp. 199–209.

[6] Namjoshi, S. A., Jain, V. K., and Mall, S., "Effect of Shot-Peening on Fretting-Fatigue Behavior of Ti-6Al-4V," *Journal of Engineering Materials Technology*, Vol. 124, 2002, pp. 222–228.

[7] Lee, H., Jin, O., and Mall, S., "Fretting Fatigue Behavior of Shot-Peened Ti-6Al-4V at Room and Elevated Temperature," *Fatigue and Fracture of Engineering Materials and Structure*, Vol. 26, 2003, pp. 767–778

[8] Lee, H. and Mall, S., "Stress Relaxation Behavior of Shot-Peened Ti-6Al-4V under Fretting Fatigue at Elevated Temperatures," *Materials Science and Engineering A*, Vol. A366, 2004, pp. 412–420

[9] ABAQUS Standard User's Manual, Hibbit, Karlsson and Sorensen Inc., 2000.

[10] Martinez, S. A., Sathish, S., Blodgett, M. P., and Shepard, M. J., "Residual Stress Distribution on Surface-Treated Ti-6Al-4V by X-Ray Diffraction," *Experimental Mechanics*, Vol. 43, 2003, pp. 141–147

[11] Sahan, O., *Fretting Fatigue Behavior of a Titanium Alloy Ti-6Al-4V at Elevated Temperature,* M.S. Thesis, Air Force Institute of Technology, Dayton, OH, 2002.

[12] Szolwinski, M. and Farris, T., "Mechanics of Fretting Fatigue Crack Formation," *Wear*, Vol. 198, 1996, pp. 93–107.

[13] Fatemi, A. and Socie, D. "A Critical Plane Approach to Multiaxial Fatigue Damage Including Out of Phase Loading," *Fatigue and Fracture of Engineering Materials and Structure*, Vol. 11, 1988, pp. 149–165.

[14] Findley, W. N., "Fatigue of Metals under Combination of Stresses," *Transactions of ASME*, Vol. 79, 1975, pp. 1337–1348.

[15] Lykins, C. D., Mall, S., and Jain, V. K., "A Shear Stress Based Parameter for Fretting Fatigue Crack Initiation," *Fatigue and Fracture of Engineering Materials and Structure*, Vol. 24, 2001, pp. 461–473.

[16] Namjoshi, S. A., Mall, S., Jain, V. K., and Jin, O, "Fretting Fatigue Crack Initiation Mechanism in Ti-6Al-4V," *Fatigue and Fracture of Engineering Materials and Structure*, Vol. 25, 2002, pp. 955–964.

7] Walker, K., "The Effective Stress Ratio During Crack Propagation and Fatigue for 2024-T3 and 7075-T6 Aluminum," *Effects on Environment and Complex Load History on Fatigue Life, ASTM STP 462*, ASTM International, West Conshohocken, PA, 1970, pp. 1–14.

SESSION 8B: ADDITIONAL FRACTURE TOPICS

Journal of ASTM International, April 2005, Vol. 2, No. 4
Paper ID JAI11997
Available online at www.astm.org

Jaroslav Pokluda,[1] *Pavel Šandera,*[2] *and Jana Horníková*[3]

Analysis of Roughness-Induced Crack-Tip Shielding in Terms of Size Ratio Effect

ABSTRACT: A new theoretical concept is introduced to describe the roughness-induced shielding effects in metallic materials. It is based on the statistics of the local ratio between the characteristic microstructure distance and the plastic zone size. Both the crack branching and the crack closure phenomena are generally described in the frame of linear elastic fracture mechanics under the assumption of the remote Mode I loading. Using this approach, intrinsic values of fracture toughness and fatigue crack growth threshold can be determined, and the roughness-induced component can be separated from other closure components, such as plasticity or oxide induced closure. In order to estimate the total RIS effect, standard material data as the yield stress, the mean grain size, the surface roughness, and the fracture mode are only necessary. Application examples concerning static fracture and fatigue are presented for UHSLA steels, ARMCO iron, aluminum, and titanium alloys.

KEYWORDS: roughness-induced shielding, crack branching, crack closure, size ratio, statistical approach

Introduction

Two basic types of mechanisms called intrinsic and extrinsic toughening [1] contribute to material resistance against the crack growth. The first mechanism represents the inherent matrix resistance in terms of atomic bond strength or matrix ductility. Appropriate modifications of the chemical composition or of the heat treatment are typical technological ways improving the intrinsic fracture toughness. On the other hand, processes like kinking, splitting, or meandering of the crack front (hereafter called crack branching) induced by microstructural heterogeneities belong typically to the extrinsic toughening mechanisms [2]. They lead to a decrease in the crack driving force due to both the prolonged crack path and the local mixed Mode I + II + III at the crack front even in case of a pure remote Mode I loading. Moreover, rough asperities remaining in the wake of a tortuous crack often cause a premature crack closure under cyclic loading [3]. Both effects, hereafter called roughness-induced shielding (RIS), lead to an apparent increase in the intrinsic resistance to the crack growth caused, in fact, by extrinsic factors.

The technology of artificially induced crack branching was successfully used for enhancing fracture toughness in advanced ceramics. Due to the negligible plasticity of most ceramics, such a type of crack tip shielding is generally very important and can be relatively simply quantified using LEFM [4]. In the case of metallic materials, however, the assessment of the contribution of the RIS appears to be a more complicated problem. Many experiments indicate that this type of shielding plays a significant role only in special materials and under particular loading

Manuscript received 29 October 2003; accepted for publication 16 June 2004; published April 2005. Presented at ASTM Symposium on Fatigue and Fracture Mechanics: 34th Volume on 19–21 November 2003 in Tampa, FL; S.R. Daniewicz, J.C. Newman, Jr., and K-H. Schwalbe, Guest Editors.
[1] Professor, Brno University of Technology, Brno, CZ-61669, Czech Republic.
[2] Associate Professor, Brno University of Technology, Brno, CZ-61669, Czech Republic.
[3] Assistant Professor, Brno University of Technology, Brno, CZ-61669, Czech Republic.

conditions [5–7]. In the last two decades, several two-dimensional models of RIS have been submitted [3,5,8–11]. However, none of them explains the diverse nature and manifestation of RIS in fatigue and fracture of metallic materials in a sufficiently general manner.

This paper attempts to introduce a more general approach to RIS in metallic materials. Its theoretical concept is based on the statistical effect of the local ratio between the characteristic microstructure distance and the plastic zone size. For crack stability and growth assessments, the one-parameter LEFM is considered to be relevant. Therefore, conditions of both small-scale yielding and plane strain are particularly assumed to be fulfilled in all analyzed cases.

Statistical Aspects of the Size Ratio Effect

During the last three decades of fatigue and fracture research, a lot of experimental evidence was collected concerning a special role of the ratio between the characteristic microstructure size d and the plastic zone size r_p – the so-called size ratio $S_R = d / r_p$. The parameter d means, for example, the grain size, the packet size, or the distance between inclusions or large incoherent precipitates. Hitherto, the mean values d_m or S_{Rm} were only taken into consideration. Numerous experiments, e.g., [5,12,13], have shown that the crack path is particularly influenced by microstructure (grain boundaries, interphase boundaries, precipitates, inclusions) when the relation $S_{Rm} \geq 1$ is fulfilled when the plastic zone size is comparable to or lower than the characteristic microstructure size. Intergranular or crystallographic fracture morphology is predominantly observed in these circumstances. On the other hand, the crack path becomes insensitive to the microstructure in case of $S_{Rm} \ll 1$, where the plastic zone size embraces many microstructural elements. Many authors, e.g., [12–14], reported the maximum percentage of intergranular facets in those sites of the fatigue fracture surface, where the cyclic plastic zone size is exactly equal to the mean grain size ($S_{Rm} = 1$). The recently published theory of the yield stress gradient effects in inhomogeneous materials [15] yields a general basis for the explanation of the above-mentioned phenomenon. According to this theory, the interaction between the crack tip and the near inhomogeneous region becomes significant only when $S_R \geq 1$. Following this interaction, the crack will either circumvent a hard-strength heterogeneity or deflect to the low-strength one.

In most engineering materials, a large scatter of the grain size and particle spacing means a variation of the parameter d within more than two orders along the crack front. On the other hand, a sharp decrease of the stress with distance from the crack front causes localization of the plastic deformation within a narrow zone of a nearly constant width. As a consequence, the size ratio S_R varies in a wide range along the crack front. In other words, there are many sites where $S_R \ll 1$ or $S_R \geq 1$ is to be expected.

The basic idea of the statistical approach, first introduced in [11], lies in the assumption that the microstructure elements can be simply divided into two main categories - with a low and a high S_R. It means that the low-S_R part of the probability density function does not influence the shielding phenomenon controlled by the high-S_R part. The boundary value is denoted S_{Rc} and the related structural parameter $d_c = S_{Rc} r_p$. Although one can usually assume $S_{Rc} \approx 1$, the S_{Rc} value is expected to change, e.g., with the impurity concentration at grain boundaries – a higher impurity concentration means a lower S_{Rc} value. Therefore, it is to be considered as a rather free (fitting) parameter in the transient range $S_{Rc} \in (0.3, 3.0)$, where the plastic zone size becomes within an order comparable to that of the characteristic microstructure parameter d.

When denoting $p(S_R)$, the probability density function in terms of S_R, the relative length of the crack front contributing to the shielding effect, can be expressed as

$$\eta = \frac{\int_{S_{Rc}}^{\infty} S_R \cdot p(S_R) \mathrm{d}S_R}{\int_{0}^{\infty} S_R \cdot p(S_R) \mathrm{d}S_R}. \tag{1}$$

In other words, the parameter η means the probability of finding a shielded element of the crack front. This statistical parameter is suggested to be a suitable measure of the RIS efficiency and will be used in the further analysis. For a particular material, value η can be calculated when determining both the yield stress from the tensile test (in order to estimate r_p) and the statistical distribution of d from a metallographical sample. The ratio S_R can be simply estimated as

$$S_R = \frac{d}{r_p} = \varsigma d \left(\frac{\sigma_y}{K} \right)^2, \tag{2}$$

where σ_y is the yield stress, K is either the applied stress intensity factor (SIF) in case of the monotonic loading or its amplitude $K_a = \Delta K/2$ in case of the fatigue loading, $\varsigma = \pi$ for plane stress or $\varsigma = 3\pi$ for plane strain. In all analysed cases, Weibull statistics of S_R are used as

$$p(S_R) = \frac{\xi S_R^{(\xi-1)}}{\mu^{\xi}} \exp\left[-\left(\frac{S_R}{\mu} \right)^{\xi} \right], \quad S_{Rm} = \frac{d_m}{r_p} = \mu \Gamma \left(1 + \frac{1}{\xi} \right), \tag{3}$$

where μ and ξ are Weibull parameters, Γ is the Gamma function, S_{Rm} is the mean size ratio, and d_m is the mean characteristic microstructure parameter. The value $\xi \approx 2.2$ can be considered acceptable for all metallic microstructures [10, 11].

The total effect of both the shielded and the unshielded parts of the crack front can be approximately estimated by means of a proportional rule, as it will be shown later.

Theoretical Concept of Roughness-Induced Shielding

Shielding Ahead of the Crack Front

A local mixed-Mode I+II+III generally exists ahead of a tortuous crack front even in case of a pure remote Mode I loading. In that case, friction forces between fracture surfaces are minimized owing to the large crack tip opening, and the crack propagates perpendicularly to the external stress direction in a microscopically self-similar manner. Hence, the energetic criterion in terms of SIFs

$$K_{eff} = \sqrt{K_I^2 + K_{II}^2 + \frac{1}{1-\nu} K_{III}^2} \tag{4}$$

can be used for the crack stability description [16].

The standardized procedure ASTM E 399-72 for calculation of the K_{Ic} value assumes only a planar crack of a straight front and neglects the extrinsic RIS effect. According to the approach introduced by Faber and Evans [4] and generalized in [17], a simple relation

$$K_{Ic} = \frac{R_S^{1/2}}{k_{eff}} K_{Ici} \tag{5}$$

can be applied, where K_{Ic} is the measured (nominal) fracture toughness, K_{Ici} is the intrinsic toughness of the material, k_{eff} is the local effective SIF normalized by the remote K_I for the straight crack front, and R_S is the surface roughness, defined as the ratio of real and projective areas of the fracture surface. A larger fracture area ($R_S > 1$) is created, and a smaller local SIF ($k_{eff} < 1$) is available at a tortuous crack front in comparison with a straight one and consequently, $K_{Ic} > K_{Ici}$. Since $K_{Ic} = K_{Ici} + K_{Ice}$, one can also write

$$K_{Ice} = \left(1 - \frac{k_{eff}}{R_S^{1/2}}\right) K_{Ic}, \tag{6}$$

where K_{Ice} is the extrinsic component. Unfortunately, increase in K_{Ice} often observed in case of microstructure coarsening is usually accompanied with a decrease in most other mechanical properties [6]. Since Eq 5 holds in the whole applied SIF range, one can define the global effective SIF as

$$K_{eff,g} = \frac{k_{eff}}{R_S^{1/2}} K_I \text{ ,} \tag{7}$$

assuming $K_{eff,g} \equiv K_{Ii}$. A single elementary kink approximation

$$k_{eff} = \left(k_1^2 + k_2^2\right)^{1/2} / K_I = \cos^2 \vartheta/2 \text{ ,} \tag{8}$$

where ϑ is the kink angle, is often used in the simplified 2D crack models [5].

Microscopically tortuous crack fronts typically appear in brittle fracture associated with intergranular or cleavage morphology (see Fig. 1*a*). However, mixed brittle-ductile morphology is observed in most practical cases, and the transgranular ductile part of the crack front can be considered to be straight, i.e., $R_S = 1$ (see Fig. 1*b*). Fine dimples reflect the plasticity (intrinsic) response of the matrix itself, so that the corresponding micro-roughness should be neglected when calculating the extrinsic component. Therefore, in a pure ductile fracture mode, the equality $K_{eff,g} = K_I$ is to be accepted.

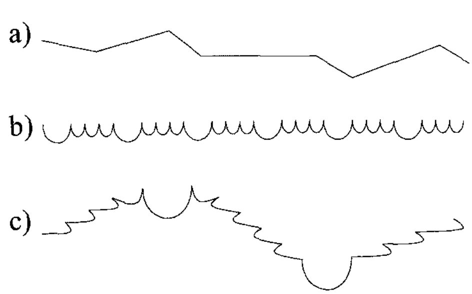

FIG. 1—*Schematic line profiles of fracture surface morphology:* a) *intergranular or cleavage,* b) *straight ductile,* c) *zigzag ductile.*

The portion p_t of the tortuous (brittle) morphology can be theoretically assessed by setting $p_t = \eta$, since the parameter η means a probability of finding a shielded (tortuous) element at the crack front. Assuming the proportional rule, the following expression can be accepted for the mixed brittle-ductile case:

$$K_{eff,m} = \left(1 - \eta + \eta \frac{k_{eff}}{R^{1/2}}\right) K_I \,. \tag{9}$$

Equation 9 reduces to Eq 7 for $\eta = 1$ (pure brittle fracture) and to the identity $K_{eff,m} \equiv K_I$ for $\eta = 0$ (pure ductile fracture). It should be emphasized that the R_S value does not correspond to the averaged surface roughness but to the tortuous (brittle) part of the fracture surface.

A tortuous crack front can be produced also by a special mode of ductile fracture morphology modified by large inclusions or incoherent precipitates (Fig. 1*c*). In that case, the prolonged crack front ($R_S > 1$) has to be taken into account, provided that the plastic zone is smaller than crack deflections. On the other hand, the shielding caused by crack branching can be neglected ($k_{eff} = 1$) in very ductile metals, where the dislocation fracture mechanism is controlled by shear stress instead of the effective stress [18]. Consequently,

$$K_{eff,m} = \left(1 - \eta + \eta R_S^{-1/2}\right) K_I \,. \tag{10}$$

Shielding in the Wake of the Crack Front (Crack Closure)

The roughness-induced crack closure (RICC) represents an additional important component of RIS particularly in case of long fatigue cracks. Its existence is determined by asperities on fracture surfaces in the wake of the tortuous crack front. Suresh and Ritchie [3] offered a simple two-dimensional LEFM model describing the essential mechanism of this phenomenon. Irreversible working of the local Mode II at the front of the tortuous crack causes the mutual horizontal shifting of fracture surfaces and their premature contact. Large-scale crack tip cyclic plasticity in comparison with the characteristic microstructure size allows multiple slip systems to operate. It means an easy overcoming of microstructural barriers as well as an inhibition of large pile-ups. As a result, a very limited and almost reversible Mode II slip is to be expected. On the other hand, $r_{pc} \leq d_m$ means that the crack path is controlled by crystallography or grain boundaries. Long dislocation pile-ups produce a mixed trans-intergranular fracture surface with large facets and a high degree of the Mode II displacement irreversibility [7, 10]. Hence, a high level of RICC is to be expected in microstructure elements where $S_R \geq 1$, whereas the local contribution to RICC can be neglected if $S_R \ll 1$. Similarly to the previously mentioned models, RICC due to Mode III displacements is considered to be equivalent to that of Mode II by neglecting their superposition effects.

The two-dimensional zigzag crack path characterized by an average angle ϑ is assumed to produce the RICC according to the scheme in Fig. 2. During the loading part of the cycle, the crack tip is opened in the mixed-mode reaching the maximum CTOD denoted as δ_{max} at the moment of the peak stress (Fig. 2*a*). This displacement is composed of the reversible normal component δ_I and the irreversible shear component δ_2. During the unloading phase, the shear displacement is not recovered so that the crack surfaces come into the contact before the applied stress becomes zero (Fig. 2*b*).

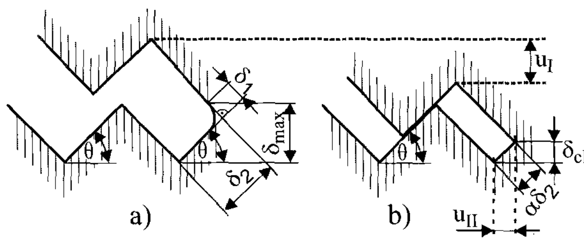

FIG. 2—*Mechanism of roughness-induced crack closure.*

Let us denote α the irreversibility level. For the simplicity reason, $\alpha = 0$ is assumed in grains with $S_R \ll 1$, unlike $\alpha = 1$ in grains with $S_R \geq 1$. In terms of our statistical approach, the mean value $\alpha_m \equiv \eta$ is considered to be the relevant irreversibility parameter. Following the scheme in Fig. 2, one can easily obtain

$$\frac{\delta_{cl}}{\delta_{\max}} = \frac{\eta \delta_2 \sin \vartheta}{\delta_1 \cos \vartheta + \delta_2 \sin \vartheta}. \tag{11}$$

For a periodical zigzag crack path approximation [19], one can accept

$$\frac{\delta_1}{\delta_2} = \left(\frac{k_1}{k_2}\right)^2 = \frac{2}{3}\cot^2\frac{\vartheta}{2}. \tag{12}$$

By substituting Eq 12 into Eq 11, one obtains

$$\frac{\delta_{cl}}{\delta_{\max}} = \frac{\eta}{\frac{2}{3}\cot^2\frac{\vartheta}{2}\cot\vartheta + 1}.$$

Since $R_S = 1/\cos\vartheta$, the final relation for RICC ratio can be written as follows:

$$\frac{\delta_{cl}}{\delta_{\max}} = \frac{K_{Ricl}^2}{K_{\max}^2} = \frac{3\eta\left(R_S - 1\right)^{3/2}}{2\left(R_S + 1\right)^{1/2} + 3\left(R_S - 1\right)^{3/2}}. \tag{13}$$

In case of $\eta = 1$, Eq 13 can be rearranged to the form derived by Suresh and Ritchie [3]:

$$\frac{K_{Ricl}^2}{K_{\max}^2} = \frac{\kappa \tan\vartheta}{1 + \kappa \tan\vartheta},$$

where

$$\kappa = \frac{3}{2}\cdot\frac{R_S - 1}{R_S + 1}.$$

The value $\kappa = 0.5$ for $R_S = 2$ can be considered to be an upper band of the displacement ratio u_{II}/u_I in terms of the statistical model (see Fig. 2). It is in agreement with the highest experimentally obtained data [5]. The profile (linear) roughness R_L is often used instead of R_S, and the simple relation $R_S \approx 1.15 R_L$ can be nearly accepted [20].

For the cyclic loading characterized by the asymmetry ratio R, the "opening" value

$$\Delta K_{op} = K_{\max} - K_{cl} = \left(1 - \frac{K_{cl}}{K_{\max}}\right) K_{\max} = \left(1 - \frac{K_{Ricl}}{K_{\max}} - \frac{K_{pcl}}{K_{\max}}\right)\frac{\Delta K_I}{1 - R}, \tag{14}$$

where $K_{cl} = K_{Ricl} + K_{pcl}$, K_{Ricl} is the roughness-induced SIF component at the moment of the crack closure, and K_{pcl} is the sum of other closure components, in particular the plasticity-induced one (PIC). The notation $K_{pcl}/K_{\max} = C_{pcl}$ and $K_{Ricl}/K_{\max} = C_{rcl}$ will be used further, and, in the range of $R \in \langle -0.1, 0.7 \rangle$, one can write

$$C_{pcl} = C_0\left(1 + 0.2R + 0.8R^2\right), \tag{15}$$

where C_0 is the material constant [5].

Fatigue Threshold Values of Long Tortuous Cracks

Let η be the fraction of elements of $S_R \geq 1$ at the crack front. Then the weighted average of the local SIF range along the crack front can be, similarly to Eq 9 and omitting the index I, expressed as

$$\Delta K_{eff,m} = (1-\eta)\Delta K + \eta \Delta K_{eff,g} = \left(1 - \eta + \eta \frac{k_{eff}}{\sqrt{R_S}}\right)\Delta K. \tag{16}$$

Considering the branching effect, the nominal ΔK_I in Eq 14 has to be replaced by $\Delta K_{eff,m}$ from Eq 16, and both branching and closure effects can be described as follows:

$$\Delta K_i \equiv \Delta K_{eff,op} = \Omega \frac{\Delta K}{1-R}, \tag{17}$$

where

$$\Omega = \Omega_1 \cdot \Omega_2,$$

$$\Omega_1 = 1 - C_{rcl} - C_{pcl} = 1 - \left(\frac{3\eta (R_S - 1)^{\frac{3}{2}}}{2(R_S+1)^{\frac{1}{2}} + 3(R_S - 1)^{\frac{3}{2}}}\right)^{\frac{1}{2}} - C_0\left(1 + 0.2R + 0.8R^2\right),$$

$$\Omega_2 = 1 - \eta + \eta \frac{k_{eff}}{\sqrt{R_S}}.$$

The term Ω_1 reflects the closure effect and Ω_2 the branching shielding. It should be noted that experimental SIF data corrected for the crack closure effect, the so-called ΔK_{eff} values, retain the geometrical shielding contribution ahead of the crack tip. Therefore, they can be obtained from intrinsic (opening) values as follows:

$$\Delta K_{eff} = \Delta K_i / \Omega_2. \tag{18}$$

The shielding factor Ω expresses a total reduction of the nominal SIF range caused by RIS. It means that, in the long crack threshold region, the intrinsic ΔK_{thi} value is lower than the measured ΔK_{th} according to the relation

$$\Delta K_{thi} = \frac{\Omega}{1-R} \Delta K_{th}.$$

The extrinsic component

$$\Delta K_{the} = \frac{1 - R - \Omega}{1-R} \Delta K_{th}$$

increases with decreasing Ω, that is with increasing η and R_S (microstructure coarsening).

Interpretation of Experimental Results

Application of the theoretical concept to experimental data of K_{Ic} or ΔK_{th} enables us to calculate the intrinsic values K_{Ici} or ΔK_{thi} and to determine both the RIS and PIC contributions to the measured K_{Ic} or ΔK_{th} values. One needs only standard materials data as the yield stress, the mean size of characteristic microstructure elements (grains, packets, secondary phase particles), the surface roughness, and the dominant type of the fracture morphology. Setting the boundary value $S_{R_c} = 1$, the only one fitting parameter in the analysis remains to be C_0 in Eq 15.

Increase in K_{Ic} with Increasing Prior Austenite Grain Size in UHSLA Steels

During the 1970s and 80s, many authors reported an increase in fracture toughness of ultra-high strength low alloy (UHSLA) steels with increasing prior austenite grain size (Fig. 3). However, the impact absorbed energy dramatically decreased, although the values of fracture toughness and absorbed energy are usually well correlated [25]. This anomalous behavior was explained in [6] as follows: while the fine-grained samples exhibited a transgranular dimple fracture morphology, those coarse grained fractured by an intergranular decohesion along prior austenite grain boundaries. The latter process is accompanied by a high level of RIS at microscopically tortuous, intergranular crack fronts. The two-dimensional and deterministic model [8] attempting to quantitatively estimate the intergranularly induced shielding level was only partially successful.

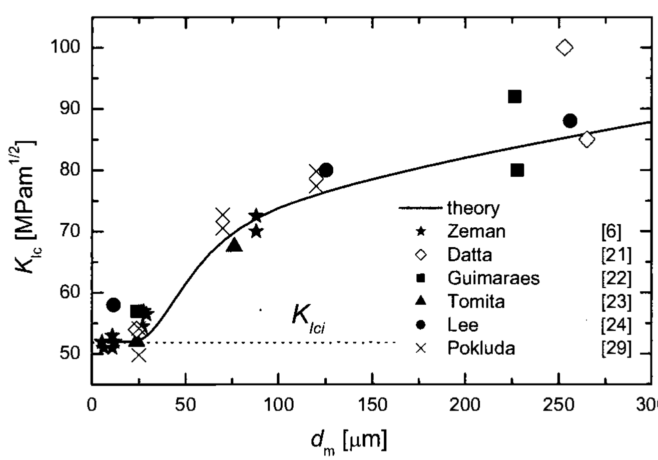

FIG. 3—*Fracture toughness of UHSLA steels in dependence on the mean size of prior austenite grains.*

For the 3D assessment of RIS effect by means of the statistical approach, the following steps were preliminary realized:

1. construction of a realistic 3D model of an intergranular crack
2. calculation of local values k_1, k_2 and k_3 along the crack front
3. determination of the surface roughness R_S

The first step was succeeded by means of the computer procedure generating an intergranular crack within the 3D Voronoi tessellation simulating the grain boundary network [26]. The second problem was solved using the program system FRANC3D [27] based on the boundary element method. The third step demands a quantitative fractography of real and artificial fracture surface [26]. Finally, a simple pyramidal model of the intergranular crack front was proposed as an efficient method for practical reasons [28] (Fig. 4). Each oblique segment of the pyramidal front can be understood to be associated with one grain of an idealized regular grain boundary network related to the real one by the same mean grain size d_m. The maximal angle Θ_m at the end of the oblique segment is related to Φ as

$$d_m \tan\Phi = 2\Delta a \tan\Theta_m, \ \Delta a = r_p/2. \tag{19}$$

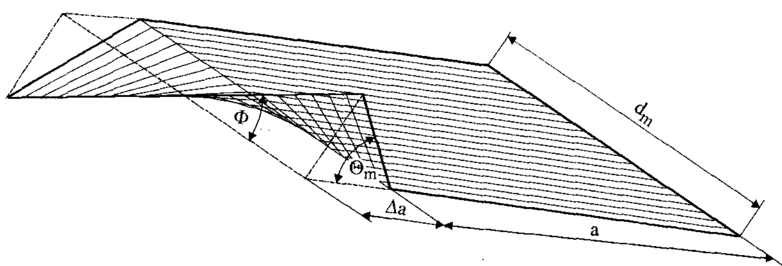

FIG. 4—*Pyramidal model of an intergranular element at the crack front.*

The value $\Phi = \pi/4$ corresponds to the profile (linear) roughness $R_L \approx 1.4$ $(R_S \approx 1.6)$ typical for intergranular crack surfaces in metallic materials independently on the mean grain size [20,26]. To calculate normalized local SIFs at the tortuous crack front, following analytical relations can be used as derived from simple tensor transformations:

$$\begin{aligned} k_1 &= \cos\left(\frac{\Theta}{2}\right).\left[2\nu\sin^2\Phi + \cos^2\left(\frac{\Theta}{2}\right)\cos^2\Phi\right], \\ k_2 &= \sin\left(\frac{\Theta}{2}\right)\cos^2\left(\frac{\Theta}{2}\right), \\ k_3 &= \cos\left(\frac{\Theta}{2}\right).\sin\Phi\cos\Phi\left[2\nu - \cos^2\left(\frac{\Theta}{2}\right)\right]. \end{aligned} \tag{20}$$

Using Eq 7 for a pure intergranular crack, the global normalized effective factor $k_{eff,g}$ for the pyramidal approximation can be computed as

$$k_{eff,g}^2 = \frac{k_{eff}^2}{R_S} = \frac{1}{3.2\Theta_m}\int_0^{\Theta_m}\left(k_1^2 + k_2^2 + \frac{k_3^2}{1-\nu}\right)\mathrm{d}\Theta. \tag{21}$$

Using Eqs 9, 19, 20, and 21, the increase in the extrinsic component K_{Ice} with increasing d_m can be calculated. The yield strength $\sigma_y \approx 1500$ MPa determined by their martensitic matrix was nearly the same for all steels. Values $\xi = 2.2$ and $K_{Ici} \equiv K_{Ic} = 52\ \mathrm{MPa\cdot m^{1/2}}$ for the ultra fine-grained UHSLA steels ($d_m < 10\ \mu$m) were used for the statistical analysis. The parameter η reflects correctly the portion of intergranular morphology of fractured CT specimens [29]. The computed values $K_{Ic} = K_{Ici} + K_{Ice}$ are plotted in Fig. 3 as a solid line. The agreement between experiment and theory is very good in spite of a slight underestimation of the shielding level for steels with coarsest prior austenite grains ($d_m \geq 200\ \mu$m). This seems to be caused by often observed splitting of some intergranular crack front segments that is not taken into account in the pyramidal model.

Dependence of ΔK_{th} on Grain Size and Cyclic Ratio in ARMCO Iron

Recently, the statistical model was applied to a quantitative elucidation of the experimental dependence ΔK_{th} versus d_m obtained in the ARMCO iron [11]. This interpretation can be further modified and generalized by including the ΔK_{th} versus R dependence. Experimental data for different grades of the ARMCO iron [7,30] are summarized in Table 1. The measured intrinsic threshold $\Delta K_{thi} = 2.75\ \text{MPa}\cdot\text{m}^{1/2}$ does not depend on the mean grain size. Also, the parameters $R_S = 1.6$ and $\xi = 2.17$ can be considered to be the same for all investigated grades. The shear mode fracture in the very ductile ARMCO iron means that $k_{eff} \approx 1$. The only one fitting parameter $C_0 = 0.05$ was obtained as a difference between theoretical and experimental data for various d_m.

The calculated ΔK_{thi} values in Fig. 5 lie close to the experimental doted and dashed line. The decisive contribution of RIC ($C_{rcl} \gg C_{pcl}$) explains well the strong dependence $\Delta K_{th}(d_m)$ observed in the experiment. Note that $\Delta K_{th} \approx \Delta K_{thi}$ for $R \geq 0.55$, which means no closure during cycling.

TABLE 1—*Experimental data for ARMCO iron.*

d_m, μm	D_{dm}[4], μm	σ_y, MPa	R	ΔK_{th}, MPam$^{1/2}$
2	1.0	530	0.1	4.50
2	1.0	530	0.7	2.90
20	10	240	0.1	5.30
20	10	240	0.7	2.90
90	44	150	0.1	6.80
90	44	150	0.55	3.65
90	44	150	0.7	2.80
90	44	150	0.8	2.90
410	200	108	0.1	8.70
410	200	108	0.7	3.20
3550	1700	96	0.1	10.30
3550	1700	96	0.7	3.60

[4] D_{dm} is the standard deviation.

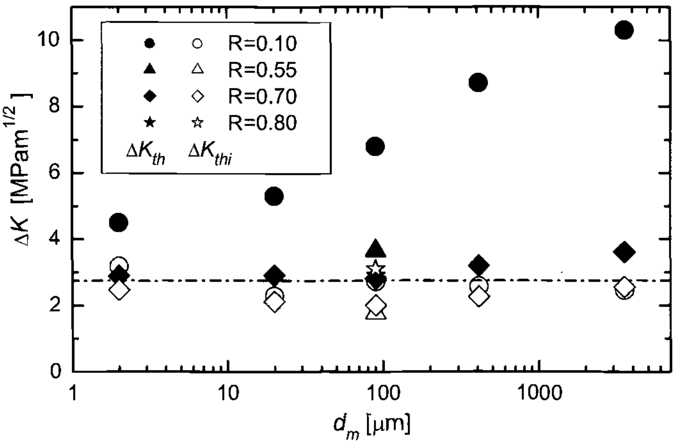

FIG. 5—*Experimental and intrinsic threshold values of the SIF range in dependence on the mean grain size of ARMCO iron.*

Aluminum Alloys at Fatigue Crack Growth Threshold in Air and Vacuum

The crack closure contribution in the threshold region ($da/dN = 10^{-10}$ m/cycle, $R = 0.1$) has been experimentally studied using underage and overage compact tension samples of a 7475 aluminum alloy in air and vacuum [31]. Different thermomechanical treatments have produced microstructures with grain sizes of 18 μm and 80 μm. The experimental and theoretical data are displayed in Table 2. The value $\eta \approx 1$ could be generally applied since $S_{Rm} \gg 1$ for all microstructures.

TABLE 2— *Experimental and theoretical data for 7475 aluminum alloy.*

R_S	d_m μm	σ_y MPa	ΔK MPam$^{1/2}$	C_{pcl}	C_{rcl}	ΔK_{thi} MPam$^{1/2}$	ΔK_{eff} MPam$^{1/2}$
vacuum							
1.30	18	505	4.0	0.01	0.37	2.12	2.74
1.21	18	455	2.9	0.01	0.30	1.85	2.23
1.90	80	451	8.8	0.01	0.65	1.82	3.28
1.25	80	445	4.1	0.01	0.33	2.41	2.99
air							
1.30	18	505	2.6	0.31	0.38	0.69	0.90
1.21	18	455	1.7	0.31	0.30	0.62	0.74
1.36	80	451	2.7	0.31	0.42	0.61	0.82
1.25	80	445	2.2	0.31	0.33	0.71	0.88

The calculated ΔK_{thi} values for the tests in air are practically identical. Values ΔK_{eff} obtained according to Eq 18 lie only slightly below the measured data [31] and perfectly within the range of $\Delta K_{eff} \in \langle 0.75,\ 0.9 \rangle$ reported by Pippan [32] for aluminum alloys. Values $\Delta K_{eff} \in (2.2, 3.3)$ for the vacuum tests are distinctly higher and, again, well comparable with the experiment, except of the extremely high value $\Delta K_{eff} = 7.1\,\mathrm{MPa \cdot m^{1/2}}$ for the underaged 80 μm sample [31]. This discrepancy can be understood in terms of the extremely high value $R_S = 1.9$ corresponding to very irregular and sharp crystallographic facets, while a regular zigzag linear profile is assumed in the RICC model. As expected, the very low values of C_{pcl} in vacuum indicate much more suppressed plasticity in comparison with the air environment.

Titanium Alloys near Fatigue Crack Growth Threshold

Near-threshold crack growth experimental data $(\mathrm{d}a/\mathrm{d}N = 10^{-9}\ \mathrm{m/cycle})$ for various α-titanium grades of different mean grain sizes d_m [33] were analyzed by means of the statistical approach. Values $R_S = 1.45$ (determined from Fig. 11 [33] for Ti 115) and $\xi \approx 2.2$ were considered for all grades. Calculated values $\eta \in \langle 0.9, 1.0 \rangle$ reveal that practically all grains contributed to the RIS effect. The experimental ΔK_{th} and the calculated ΔK_{thi} in dependence on the mean grain size are plotted for Ti115 ($d_m = 35\ \mu$m, $230\ \mu$m), Ti130 (40 μm), and Ti155 (20 μm, 210 μm) in Fig. 6. Intrinsic values lie in a sufficiently close range of $\Delta K_{thi} \in \langle 1.0, 1.9 \rangle\ \mathrm{MPa \cdot m^{1/2}}$ contrary to the large scatter of experimental ΔK_{th} points. The computed range of $\Delta K_{eff} \in (1.4, 2.7)$ is in the best agreement with the averaged measured value of $2\ \mathrm{MPa \cdot m^{1/2}}$ [34]. As expected, the calculated C_{rcl} was higher than C_{pcl} particularly for lower asymmetries ($R = 0.07$).

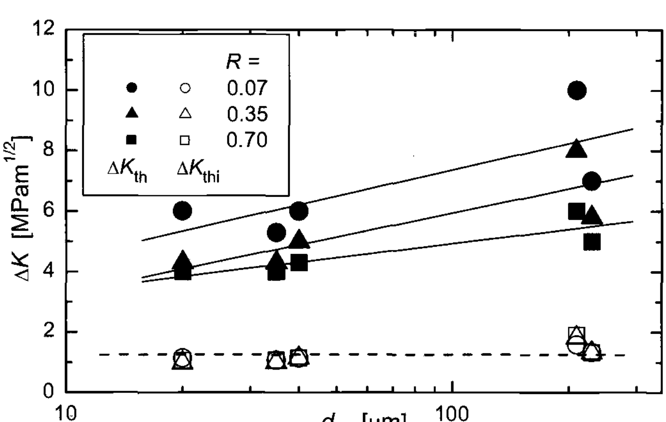

FIG. 6—*Experimental and intrinsic values of the SIF range near the threshold in dependence on the mean grain size of α-titanium alloys.*

Experimental and theoretical threshold data ($da/dN = 10^{-10}$ m/cycle) for two grades of Ti-2.5%Cu are displayed in Table 3 [10]. The microstructures consisted of coarse lamellar colonies of $d_m = 580\,\mu\text{m}$ and a fine basket weave Widmanstätten microstructure of $d_m \approx 10\,\mu\text{m}$, respectively. The value $R_S \approx 1.32$ ($R_L = 1.15$) was used for both microstructures [10]. Again, ΔK_{eff} values correspond well to the measured $\Delta K_{eff} \approx 1.5\,\text{MPa}\cdot\text{m}^{1/2}$. For comparison, the averaged value $\Delta K_{eff} \approx 3.2\,\text{MPa}\cdot\text{m}^{1/2}$ was obtained for Ti-6Al-4V alloys [35]. The calculated C_{rcl} ratio is somewhat smaller than C_{pcl}.

TABLE 3—*Experimental and theoretical data for Ti-2.5%Cu.*

d_m μm	σ_y MPa	ΔK_{th} $\text{MPam}^{1/2}$	R	η	C_{pcl}	C_{rcl}	ΔK_{thi} $\text{MPam}^{1/2}$	ΔK_{eff} $\text{MPam}^{1/2}$
580.0	420.0	9.0	0.1	1.00	0.43	0.39	1.37	1.79
10.0	499.1	7.0	0.1	0.81	0.43	0.35	1.37	1.69

Conclusion

The analysis of roughness induced shielding effects in terms of the size ratio enables us to separate the extrinsic component of fracture toughness or fatigue crack growth resistance from experimental data. In addition, the intrinsic component can be directly related to either the fracture energy of the matrix or the surface energy of grain boundaries in order to assess the materials quality or the degradation level caused by the impurity segregation. Inputting materials data are the yield stress, the mean grain (or packet) size, the surface roughness, and the dominant type of the fracture micromechanism in a particular material. The sum of components other than the roughness-induced closure is, in fact, the only one fitting parameter. The method can be applied successfully to a quantitative interpretation of some interesting or even surprising phenomena observed in fatigue and fracture. Some examples presented in this paper yield the following main results:

1. A change in fracture toughness values of UHSLA steels treated by different austenitizing temperatures was a quantitatively elucidated on the basis of the change in the roughness-induced shielding level.
2. Calculated values of the intrinsic ΔK_{thi} and crack closure ratio revealed a decisive role of roughness-induced closure in coarse-grained ARMCO iron grades.
3. For titanium and aluminum alloys, a good agreement was achieved between the calculated and experimentally determined ΔK_{eff} values near the crack growth threshold.
4. For all investigated materials, the computed intrinsic ΔK_{thi} values do not exhibit an apparent dependence on either microstructure coarseness or cyclic ratio.

Acknowledgments

This work was supported by the Grant Agency of the Czech Republic in the frame of projects No. GA101/02/0683 and No. GA106/02/0253.

References

[1] Ritchie, R. O., "Mechanisms of Fatigue Crack Propagation in Metals, Ceramics and Composites: Role of Crack Tip Shielding," *Materials Science and Engineering*, A103, 1988, pp. 15–28.

[2] Suresh, S., "Crack Deflection: Implications for the Growth of Long and Short Fatigue Cracks," *Metallurgical Transactions*, 14A, 1983, pp. 2375–2385.

[3] Suresh, S. and Ritchie, R. O., "A Geometric Model for Fatigue Crack Closure Induced by Fracture Surface Roughness," *Metallurgical Transactions*, 13A, 1982, pp. 1627–1631.

[4] Faber, K. T. and Evans, A. G., "Crack Deflection Processes – I. Theory," *Acta Metalurgica*, 1983, pp. 565–576.

[5] Suresh, S., *Fatigue of Materials*, Cambridge University Press, Cambridge, UK, 1998.

[6] Zeman, J., Rolc, S., Buchar, J., and Pokluda, J., "Microstructure and Fracture Toughness of Cast and Forged Ultra-High-Strength, Low-Alloy (UHSLA) Steels," *Fracture Mechanics: 21st Symposium, ASTM STP 1074*, J. P. Gudas, J. A. Joyce, and E. M. Hackett, Eds., ASTM International, West Conshohocken, PA, 1990, pp. 396–418.

[7] Pippan, R., "Threshold and Effective Threshold of Fatigue Crack Propagation in ARMCO Iron. I: The Influence of Grain Size and Cold Working," *Materials Science and Engineering*, A138, 1991, pp. 1–13.

[8] Pokluda, J., Šandera, P., and Zeman, J., "Effect of Intergranular Crack Branching on Fracture Toughness Evaluation," *Fracture Mechanics: 22nd Symposium (Vol. I), ASTM STP 1131*, H. A. Ernst, A. Saxena, and D. L. McDowell, Eds., ASTM International, West Conshohocken, PA, 1992, pp. 653–664.

[9] Llorca, J., "Roughness-Induced Fatigue Crack Closure: A Numerical Study," *Fatigue and Fracture of Engineering Materials & Structures*, 15, 1992, pp. 655–669.

[10] Wang, S. H. and Müller, C., "Fracture Surface Roughness and Roughness-Induced Fatigue Crack Closure in Ti-2.5% Cu," *Materials Science and Engineering*, A255, 1998, pp. 7–15.

[11] Pokluda, J., Šandera, P., and Horníková, J., "Statistical Model of Roughness-Induced Crack Closure," *Fracture Mechanics: Applications and Challenges*, ECF 13, M. Fuentes, M. Elices, A. Martin-Meizoso, and J. M. Martinez-Esnaola, Eds., Elsevier, 2000, CD-ROM.

[12] Pokluda, J. and Siegl, J., "Mixed Fatigue Fracture Morphology of Ferritic Ductile Iron," *Fatigue and Fracture of Engineering Materials & Structures*, 13, 1990, pp. 375–385.

[13] Cook, J. R., Irwing, J. R., Booth, G. S., and Beewers, C. J., "The Slow Fatigue Crack Growth and Threshold Behaviour of Medium Carbon Alloy Steel in Air and Vacuum," *Engineering Fracture Mechanics*, 7, 1975, pp. 67–77.

[14] Kunz, L. and Lukáš, P., "Fatigue Crack Growth in 15CH2NFA Steel," VI. National Conference on Fractography, V. Karel and D. T. Zilina, Eds., Czechoslovakia, 1982, pp. 273–293 (in Czech).

[15] Kolednik, O., "The Yield Stress Gradient Effect in Inhomogeneous Materials," *International Journal of Solids and Structures*, 37, 2000, pp. 781–808.

[16] Magill, M. A. and Zwerneman, F. J., "An Analysis of Sustained Mixed Mode Fatigue Crack Growth," *Engineering Fracture Mechanics*, 56, 1997, pp. 9–24.

[17] Pokluda, J., "Tortuous Cracks under Remote Mode I: The Statistical LEFM Approach," *Mechanika*, 67, 2001, pp. 277–296.

[18] Pippan, R., "The Crack Driving Force for Fatigue Crack Propagation," *Engineering Fracture Mechanics*, 44, 1993, pp. 821–829.

[19] Noda, N. and Oda, K., "Zig-Zag Edge Crack in Semi-Infinite Plain under Uniaxial Tension," *Stress Intensity Factors Handbook*, Vol. IV, TSMS, Japan and Elsevier Science Ltd., Y. Murakami, Ed., 2001, pp. 402–403.

[20] Underwood, E. E. and Banerji, K., "Quantitative Fractography," *ASM Handbook, Fractography*, Vol. 12, K. Mills, et al., Eds., 1992, pp. 193–210.

[21] Datta, K. P. and Wood, W. E., "On the Relationship of Toughness, Fracture Initiation Energy, and Specimen Deflection in Sharpy Tests," *Journal of Testing and Evaluation*, Vol. 9, 1981, pp. 111–117.

[22] Guimaraes, R. and Savedra, A., "The Mean Size of Plate Martensite: Influence of Austenite Grain Size Partitioning, and Transformation Heterogeneity," *Metallurgical Transactions*, Vol. 16A, 1985, pp. 329–336.

[23] Tomita, Y., "Effect of Microstructure on Plain-Strain Fracture Toughness of AISI 4340 Steel," *Metallurgical Transactions*, Vol. 19A, 1988, pp. 2313–2321.

[24] Lee, S., Maino, L., and Asaro, R. J., "Correlation of Microstructure and Fracture Toughness in Two 4340 Steels," *Metallurgical Transactions*, Vol. 16A, 1985, pp. 1633–1648.

[25] Server, W. L., "Charpy Impact Testing," *ASM Handbook, Mechanical Testing*, Vol. 8, J. R. Newby, et al., Eds., 1992, pp. 261–268.

[26] Pokluda, J., Saxl, I., Šandera, P., Ponížil, P., Matoušek, M., Podrábský, T., et al., "Real-Like Polycrystal with Intergranular Crack," *Advances in Mechanical Behaviour, Plasticity and Damage - Euromat 2000*, D. Miannay, P. Costa, D. Francois, A. Pineau, Eds., Elsevier, Tours, 2000, p. 449.

[27] Ingrafea, T., et al., "FRANC3D, 3D FRacture ANalysis Code," The Cornell University Fracture Group, Cornell University, Ithaca, NY, 1996.

[28] Šandera, P., Pokluda, J., and Horníková, J, "Pyramidal Model of Intergranular Crack Front," *Materials Structure & Micromechanics of Fracture (MSMF-3)*, P. Sandera, Ed., VUTIUM Brno, 2001, pp. 786–790.

[29] Pokluda, J., Vlach, B., Šandera, P., and Jurášek, L., "Antagonism in Fracture and Notch Toughness of UHSLA Steels," Charpy Centenary Conference 2001, D. Francois and A. Pineau, Eds., SF2M, Les Fontelles, 2001, pp. 465–472.

[30] Pippan, R., Berger, M., and Stüwe, H. P., "The Influence of Crack Length on Fatigue Crack Growth in Deep Sharp Notches," *Metallurgical Transactions*, 18A, 1987, pp. 429–435.

[31] Carter, R. D., Lee, E. W., Starke, Jr., E. A., and Beevers, C. J., "The Effect of Microstructure and Environment on Fatigue Crack Closure of 7475 Aluminium Alloy," *Metallurgical Transactions*, Vol. 15A, 1984, pp. 555–563.

[32] Pippan, R., "The Effective Threshold of Fatigue Crack Propagation in Aluminium Alloys. II. The Influence of Particle Reinforcement," *Philosophical Magazine*, 77A, 1998, pp. 861–873.

[33] Robinson, J. L. and Beevers, C. J., "The Effects of Load Ratio, Interstitial Content, and Grain Size on Low-Stress Fatigue-Crack Propagation in □-Titanium," *Metal Science Journal*, Vol. 7, 1973, pp. 153–159.

[34] Gregory, J. K., "Fatigue Crack Growth of Titanium Alloys," *ASM Handbook, Fatigue and Fracture*, Vol. 19, S. R. Lampman, et al., Eds., 1996, pp. 845–853.

[35] Boyce, B. L. and Ritchie, R. O., "Effect of Load Ratio and Maximum Stress Intensity on the Fatigue Threshold in Ti-6Al-4V," *Engineering Fracture Mechanics*, 68, 2001, pp. 129–147.

Journal of ASTM International, March 2005, Vol. 2, No. 3
Paper ID JAI12053
Available online at www.astm.org

Mark A. James[1] *and James C. Newman, Jr.*[2]

Characterization of Crack Length Measurement Methods for Flat Fracture with Tunneling

ABSTRACT: This paper compares area-average and unloading compliance crack-growth values with experimental crack-front shapes recorded at various stages of crack growth during fracture tests conducted on 2024-T351 aluminum alloy plate. Crack-front shapes were determined by fracturing the specimen up to a predetermined amount of crack growth and fatigue cycling the specimen for about 4000 cycles at a high stress ratio to mark the crack-front location. For each shape, the area-average and unloading compliance crack lengths were determined. Boundary collocation results provide an approximation to the δ_5 unloading compliance crack length. The crack tunneling results show that the area-average technique produces crack-length measurements more representative of the straight-front finite element analyses than optical based surface measurements. The δ_5 technique is significantly more sensitive to tunneling than the CMOD technique and is easier to apply than the area-average technique.

KEYWORDS: CTOA, crack growth, unloading compliance, area-average, tunneling, δ_5, resistance curve, finite-element analysis

Nomenclature

a	crack length, mm
B	specimen thickness, mm
d	distance behind moving crack tip where CTOA is measured, mm
E	Young's modulus, MPa
F	tunneling fraction ($F = t / T$)
P	applied load, kN
P_{max}	maximum applied load, kN
P_{min}	minimum applied load, kN
R	stress ratio (minimum to maximum applied stress)
S	applied remote stress, MPa
t	difference between average crack-growth and surface crack-growth, mm
T	tunneling depth, mm
V_i	crack-opening displacement at location i, mm
V_{LL}	crack-opening displacement at centerline of pin, mm
W	specimen width, mm
Δa	crack growth, mm
Δa_i	interior (centerline) crack growth, mm
Δa_s	surface crack growth, mm

Manuscript received 12 November 2003; accepted for publication 11 March 2004; published March 2005.
Presented at ASTM Symposium on Fatigue and Fracture Mechanics: 34th Volume on 19–21 November 2003 in Tampa, FL; S.R. Daniewicz, J.C. Newman, Jr., and K-H. Schwalbe, Guest Editors.
[1] Staff Scientist, National Institute of Aerospace, 144 Research Dr, Hampton, VA 23666.
[2] Professor, Mississippi State University, Mississippi State, MS 39762.

ν Poisson's ratio
δ_5 crack-tip-opening displacement measured at the original crack-tip location with a 5-mm gauge length, mm
σ_y Yield stress, MPa
Ψ_c crack-tip-opening angle measured at a fixed distance, d, behind moving crack tip, deg

Introduction

During the 1990s, as part of a national aging aircraft program, NASA Langley Research Center (LaRC) conducted intensive research on the fracture behavior of thin sheet aluminum alloys [1]. Some of the products of that research were the constant critical crack-tip-opening-angle fracture criterion (CTOA, Ψ_c), optical/digital imaging means for measuring CTOA, and optical methods for measuring surface crack growth [2]. Two additional means of characterizing crack growth, unloading compliance and area-average, were not used in favor of the optical methods. One consistent observation of fracture prediction results that were performed using the constant CTOA fracture criterion is that the analysis results consistently over-predicted crack growth, even when the analysis is able to predict maximum load very accurately.

The objective of this work is to gain a better understanding of the shortcomings of the comparisons between the experimental crack length measurements and the finite element analysis results. Figure 1 shows a schematic of a typical flat fracture surface for a compact tension, C(T), specimen. Initially, the aluminum alloy material fails by ductile fracture, most likely due to micro-void coalescence. Tunneling occurs in the interior and maintains the tunnel shape until fracture. In some cases, shear bands start on the surface and eventually join to form a single shear dominated fracture surface. Other possibilities exist, such as V-shear fracture, where the shear bands join to form a V-shaped fracture surface. This work is restricted to the case shown in Fig. 1, where the fracture surface remains flat for the duration of the test. This paper presents a comparison of experimental crack-front shapes recorded at various stages of crack growth with crack length values calculated using unloading compliance and area-average techniques. This paper also shows how these various measures compare with surface measured crack length and typical straight crack-front finite element predictions.

Background

Wells originally proposed the use of the crack-tip-opening displacement (CTOD) as a fracture criterion during his experimental work in the 1960s [3]. The crack-tip-opening angle, CTOA (Ψ_c), which is related to CTOD, is applied here as the angle formed by a stable tearing crack measured at a fixed distance, *d*, behind the moving crack tip (typically, *d* is taken as 1 mm). The fracture methodology developed as part of the NASA program assumes that the critical CTOA is constant and independent of loading and in-plane configuration, as long as the crack length and remaining ligament are greater than about four times the plate thickness [4]. The criterion has been applied in both two-dimensional (2D) and three-dimensional (3D) finite-element analyses (FEA). The methodology is applied by finding Ψ_c such that the analysis matches the average maximum load for coupon tests (preferably, compact tension specimen, W = 152 mm). This angle is used in subsequent analyses for predictions of crack growth, failure loads, and R-curves.

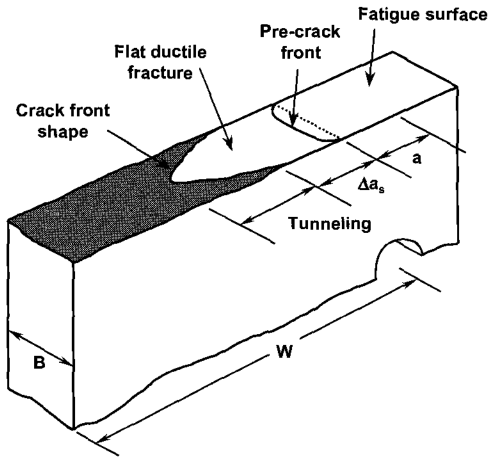

FIG. 1—*Schematic of a flat fracture surface for a C(T) specimen.*

Recently, a wide variety of fracture tests and analyses was performed on 6.35-mm thick 2024-T351 aluminum alloy in the LT orientation [5]. Both C(T) (compact tension) and M(T) (middle-crack tension) specimens were tested. Analyses were run using ZIP3D [6], a small strain FEA computer program, and WARP3D [10,11], a large strain FEA computer program. In both cases, the analyses used the above-described methodology with the constant CTOA fracture criterion. Figure 2 shows load versus surface measured crack growth results on 152-mm wide C(T) specimens, including both test and analysis results. These results were used to find Ψ_c, the critical value of CTOA, by matching the analysis with the average maximum load for the tests. This value of Ψ_c was used to predict the behavior of the other C(T) and M(T) configurations. Two different angles resulted because of the differences in computer program formulation (small strain versus large strain). The dash-dot line in Fig. 2 shows the plane-stress limit load based on the material flow stress, i.e., average between yield and ultimate, using the EPRI solution for a C(T) compiled by Anderson [7].

Figure 3 compares the predicted load-crack growth behavior with test results for a specimen restrained from buckling by anti-buckling guide plates and with test results for buckling specimens without anti-buckling guides. The results of the previous study [5] show that the constant critical CTOA fracture criterion is transferable between C(T) and M(T) specimens and that the analyses were able to accurately predict the maximum load for C(T) specimens ranging in size from 50–152 mm and for M(T) specimens ranging in size from 75–1016 mm, each to within 3 % of their respective test maximum loads.

A consistent observation made of these load-crack growth curves (and similar curves for other thin sheet and plate materials) is that the straight crack-front analysis generally over-predicts crack growth, before and after maximum load. A number of factors could be contributing to the discrepancies in crack growth, including crack-front tunneling, transition from initially flat fracture to slant fracture after maximum load, and the simplification of the assumed constant value of CTOA.

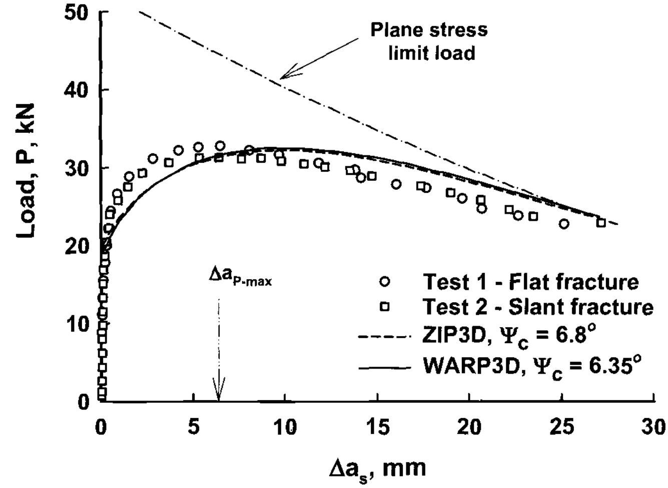

FIG. 2—*Experimental and numerical load versus surface measured crack growth for 152 mm C(T) specimens.*

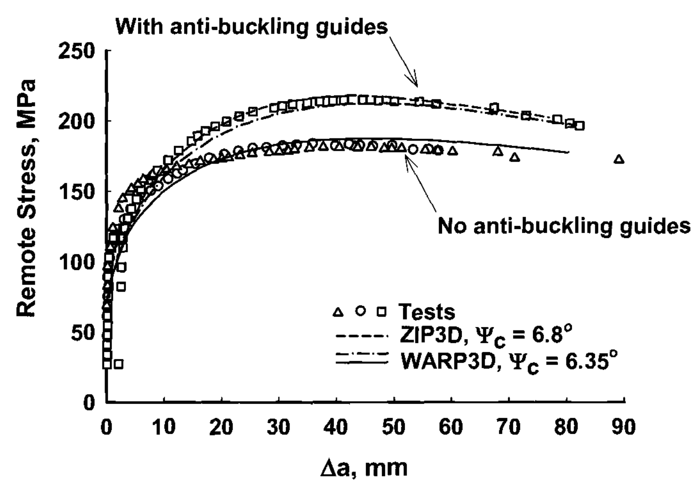

FIG. 3—*Experimental and numerical load versus surface measured crack growth for 1016 mm M(T) specimens (Δa is average of left and right tips).*

CTOA is a local fracture criterion that for this work is always measured a fixed distance from the current crack tip. An alternative fracture criterion is δ_5, which is the displacement measured across the original crack tip location using a 5 mm gauge length. δ_5 is initially a local parameter, but after crack growth behaves more like a remote parameter. δ_5 was measured using either of two non-contacting methods: 1) a high resolution traveling microscope was used to measure the distance between two surface marks at the δ_5 location on the surface of the specimen [2]; 2) a digital image correlation system, where a high contrast surface preparation in the region of interest (i.e., around the crack tip for δ_5 measurements) facilitates high resolution and high accuracy displacement measurements [8,9]. Figures 4 and 5 show load-δ_5 plots for the 152-mm wide C(T) and 1016-mm wide M(T) specimens, respectively, from the previous study [5]. In contrast to the load-crack growth comparisons, shown in Figs. 2 and 3, the analysis matches the δ_5 behavior of the tests very well. The δ_5 results compared very well, both before and after maximum load, corresponding respectively to the local and remote stages of crack growth.

The results in Figs. 4 and 5 strongly suggest that the flat, straight crack-front in the 3D analysis represents the "average" crack length at any given load. Returning to Fig. 2, the amount that the analysis over-predicts crack growth is on the order of the plate thickness. The crack growth was measured on the surface of the specimen during the test using a traveling-stage optical microscope. The surface measured value is the shortest crack length if the specimen is experiencing crack-front tunneling. A more appropriate comparison metric may be to use an average crack length measure, such as unloading compliance or area-average.

Fracture Analyses

Fracture analyses were conducted for this study using two different approaches. Elastic analyses were conducted to investigate the compliance crack length, including baseline straight-crack-front analyses, and tunneling crack-front analyses. The analysis code WARP3D [10,11] was used for these 3D fracture analyses. Material properties used for the 2024-T351 aluminum alloy were the same as in the previous study [5]: E = 71360 MPa, $\nu = 0.3$, and $\sigma_y = 345$ MPa. The finite-element mesh used throughout this study was refined to a 0.5 mm element size at the crack front and used eight elements through the half-thickness. The model used two planes of symmetry: the crack plane and the specimen center plane. The average crack growth was characterized by using four parameters: 1) traditional unloading compliance using CMOD from ASTM E1820-99a "Test Method for Measurement of Fracture Toughness;" 2) a new δ_5 unloading compliance method based on calibrations from 2D FEA analyses; 3) a 2D boundary-collocation analysis approximation to the δ_5 opening displacement; and 4) area-average crack length based on measured crack front shapes from the tunneling tests described in a subsequent section.

CMOD Unloading Compliance Verification

The CMOD calibration for unloading compliance described in E1820-99a is based on plane stress boundary-collocation analysis results [12]. Because the current study is primarily concerned with 3D fracture analyses, it seems appropriate to verify that the 2D analysis results (currently used in compliance measurement methods) accurately represent the unloading behavior of the 3D cracked specimens under investigation. Linear elastic 3D analyses were conducted for the C(T) specimen with a/W= 0.3, 0.5, and 0.7 for the 152-mm wide specimen with B = 6.35 mm, and V_0, V_{LL}, V_1, and V_2 from ASTM E 647 were evaluated. Rotation corrections were not considered because the analyses were linear elastic. The 3D FEA compliance differed from the original 2D boundary-collocation compliance [12] by less than 2 % in all cases.

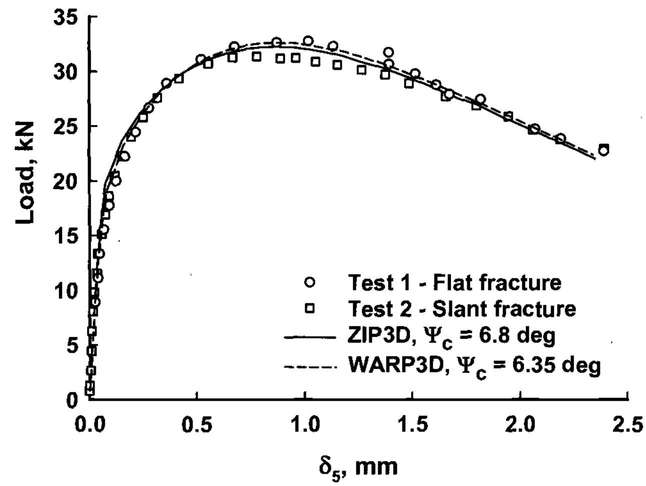

FIG. 4—*Experimental and numerical load-δ_5 for 152 mm C(T) specimens.*

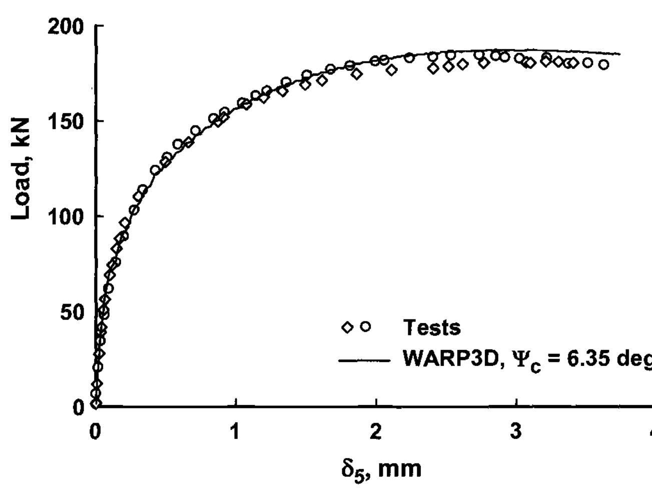

FIG. 5—*Experimental and numerical load-δ_5 for 1016 mm M(T) specimens.*

δ_5 Unloading Compliance Calibration

The δ_5 displacement works very well as an R-curve fracture parameter because it is unique up to a maximum load and remains valid within a tolerance for significant crack growth past maximum load for many configurations [5,13]. δ_5 is essentially a local fracture parameter for small amounts of crack growth and transitions into a more remote parameter as crack growth proceeds because it is measured at a fixed material position, rather than traveling with the crack. For small amounts of crack growth, δ_5 is significantly more sensitive to tunneling than CMOD and has the potential to respond to small changes in crack growth much more effectively than CMOD [14]. One way to express the sensitivity of δ_5 or CMOD to tunneling is to consider the percent change in the parameter as tunneling evolves. Figure 6 shows FEA results where the percent compliance change was calculated for a tunneling crack-front relative to a straight crack-front for δ_5, and CMOD compliance with $a_s/W = 0.4$. δ_5 is about two orders of magnitude more sensitive to the tunneling changes than CMOD.

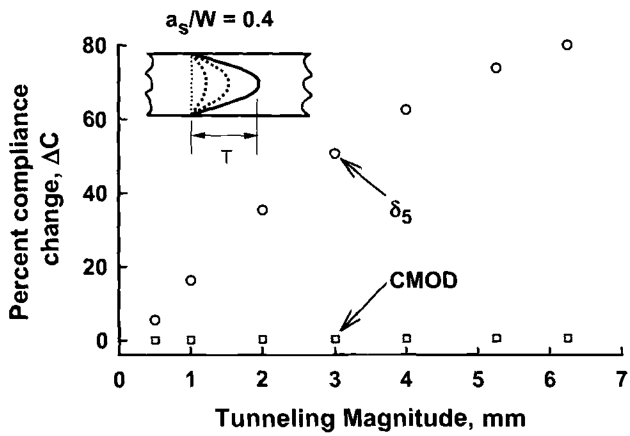

FIG. 6—*δ_5 and CMOD sensitivity to tunneling.*

This increased sensitivity motivated a new approach to unloading compliance based on δ_5 to describe crack growth. Mall and Newman [15] developed equations for the opening displacement behind the crack tip of a C(T) specimen based on previous work [12]. They developed polynomial expressions for compliance as a function of crack length based on a boundary collocation analysis of the specimen. Given compliance, the equations were easily solved for crack length using the Method of False Position [16]. This approach introduces two additional approximations: 1) the δ_5 displacement is approximated by the collocation crack face opening displacement (see inset, Fig. 7); 2) the 3D surface value is approximated by the 2D collocation value (centerline average). Figure 7 compares δ_5 from 2D FEA using the FRANC2DL code [17] with the crack face collocation results using normalized compliance as a function of crack-length-to-width ratio for five crack configurations. The lines show the 2D FEA results of δ_5, and the circles show the collocation approximation. The collocation model gives crack-opening displacements, which approach zero as the crack growth approaches zero. However, for Δa greater than 1 mm and for $0.3 \leq a/W \leq 0.8$, the collocation equations for compliance were within 4 % of the 2D FEA results. A crack length comparison for W = 152 mm, a/W = 0.4, and $1 < \Delta a < 5.4$ mm, shows that the collocation approximation produced less than 1 % error in crack length.

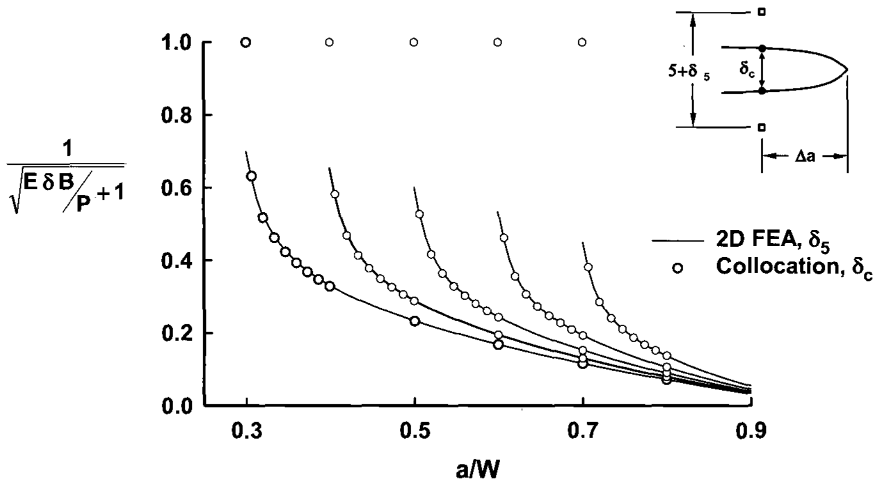

FIG. 7—*δ_5 compliance from 2D FEA and the collocation approximation [15].*

As discussed above, δ_5 is initially a local surface displacement, rather than a far-field centerline displacement. But the collocation model approximates δ_5 using 2D plane stress, which is effectively a centerline model. Table 1 summarizes 3D FEA results that show how δ_5 is affected by the 3D geometry. The results show that the δ_5 compliance is somewhat sensitive to changes in thickness. The 25-mm thick material is 7.4 % less compliant than the 6.35-mm thick material of the current study. The 1-mm thick material is 4.6 % more compliant than the current material. As might be expected, the 1-mm thick material behaves closer to plane stress, and the 25-mm thick material behaves closer to plane strain. The 6.35-mm thick material is of the order of the δ_5 gage length and behaves between the two thicknesses listed in Table 1.

TABLE 1—*Percent Change in Compliance Relative to B = 6.35 mm, 152-mm wide C(T), a/W = 0.4.*

Δa (mm)	B = 25 mm	B = 1 mm
0.0	–7.4 %	4.6 %
0.5	–6.5 %	3.3 %
1.0	–5.8 %	2.2 %
1.5	-5.1 %	1.4 %

Tunneling Tests

Experiments were performed to characterize the crack tunneling for the 6.35-mm thick 2024-T351 aluminum alloy. One approach to characterize crack tunneling is to perform a multiple specimen test to obtain one crack-front per specimen [2]. In an effort to obtain more data per specimen, a combined approach was taken here. Five specimens are single crack-front tests, while two specimens were used as multiple crack-front specimen tests.

The specimens were fatigue pre-cracked at low stress-intensity factor levels (8 $MPa\sqrt{m}$) to an a/W ratio of 0.4. Each specimen was loaded in displacement control just enough to cause a predetermined amount of surface-crack growth. Then the fracture crack-front was marked using fatigue crack growth at a high stress ratio (R = 0.75 or 0.8) and a relatively high maximum load (80 % of the current fracture load). Typically about 4000 cycles were applied to mark the crack front. After the test was concluded, the specimens were broken open, and the crack-front shapes were measured using an optical microscope with X-Y traveling stages.

For each specimen, some or all of the following were collected: load, load-line displacement, crack-mouth-opening displacement using a clip gage, δ_5 using digital image correlation [8,9], surface-crack growth, and surface field displacements in the vicinity of the original crack tip. Loading proceeded in 2.2 kN increments. Unloading compliance measurements were recorded at each increment by unloading 2.2 kN for loading greater than 4.4 kN. The amount of crack growth was based on the desire to characterize the tunneling progression along the crack front for various loading levels. The first specimen was loaded until about 0.25 mm of surface-crack growth was visible. Two subsequent specimens were loaded to lower loads based on the CMOD unloading compliance load-crack growth curve. Other specimens were loaded to higher loads and more crack growth (see [18] for details). The load corresponding to K_{Ic} for this material and crack configuration is about 10.7 kN.

Unloading compliance calculations were performed for the CMOD and δ_5 displacement measurements. Representative data were examined over the unloading range, and no significant nonlinearities were found. Over the monotonic unloading range, the first and last points were excluded, and the remaining points were least-squares fit with a straight line.

Results

The visual surface crack length is in many cases the shortest crack length for a tunneling crack front, and this single value may not be representative of the average behavior of the specimen. Two other crack length measures are unloading compliance and area-average. The CMOD unloading compliance crack length can be calculated using the calibration in ASTM E 1820. The area-average crack length can be calculated from the measured crack face tunneling profile using the nine-point weighted average in ASTM E 1820. For this work, the trapezoidal rule was used because more than nine points were collected and because the points were not evenly spaced.

Figure 8 shows a typical measured fatigue pre-crack shape and the fracture surface crack shape. The fatigue marking process, although at a high load ratio and high maximum load, does in most cases leave a damage zone near the specimen side surface apparently caused by the closure of the ligaments near the surface. The optically measured side-surface crack growth lies within the damage zone, as shown in Fig. 8. The average surface crack-growth was calculated by averaging the fracture surface values from both sides of the specimen. The consistent location of the visual surface measurement in the cyclic damage zone indicates that both the fracture surface tunneling shape and the tunneling magnitude may be affected by the fatigue cycling.

Figure 8 also compares several other crack length measures with the crack profile shape. The measured CMOD unloading compliance crack length is nearly the same as the visual crack length. However, an elastic FEA analysis with this same tunneled crack front shape showed that the elastic analysis CMOD compliance crack length extends into the tunneling region by about

35 % of T, the tunneling magnitude. The experimental tunneling is approximately the same as the material thickness, B, so the discrepancy between the measured and computed crack-growth is about 1.8 mm. One possible explanation for this is that the crack closes in the ligaments near the specimen surface as unloading occurs.

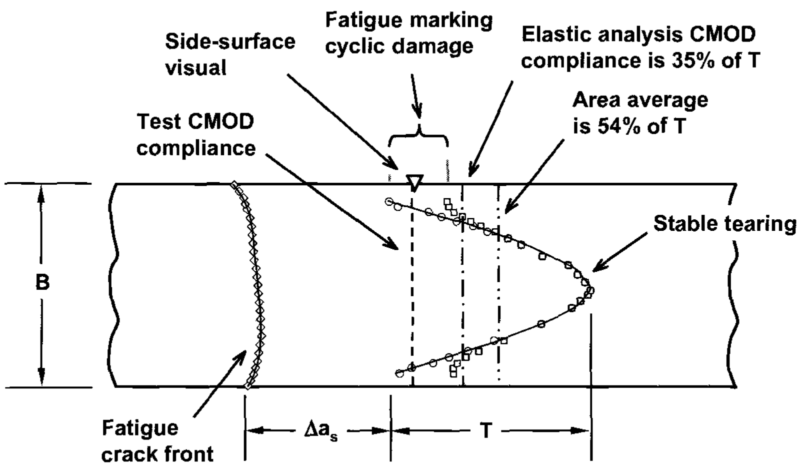

FIG. 8—*Scale drawing of crack length measures compared with a tunneling crack front shape.*

Another measure shown in Fig. 8 is the area-average crack length. The crack front shape nearly matches a half sine-wave form. The mean-value theorem applied to a sine-wave yields a crack growth that is 64 % of T. Experimental area-average values from the trapezoidal rule on the through-thickness data ranged from 46–60 % and were dependent on symmetry of the crack-front shape. The area-average length in Fig. 8 is 54 % of T.

Figure 9 shows measured fatigue and fracture crack fronts from a single specimen test. As in Fig. 8, the side surface visual crack-growth value always falls in the fatigue damage zone. The area-average crack length is always the longest of the calculated crack-growth measures, and the experimentally measured CMOD compliance is always the shortest. The experimentally measured δ_5 compliance value always falls between CMOD compliance and area-average. The ZIP3D straight crack-front results were determined at the respective equivalent load for each of the measured crack-front shapes. These results agree well with the area-average crack-length measurements from the tunneling specimens.

Figure 10 shows the normalized tunneling magnitude versus normalized surface crack growth. The figure shows an estimate of the cyclic damage zone on the tunneling magnitude. The symbols show the measured data, and the lines show the best-fit curve through the data. The open symbols show the tunneling from the fracture surface data. The closed symbols show the tunneling corrected by the amount that the side-surface visual measurement exceeds the respective fracture surface measurement. The first three data points were not corrected because the damage zone was small. The overall difference in the tunneling magnitude between the fracture surface measurements and the side-surface visuals ranges from about 10 % after one of thickness of growth, to about 15 % after three thicknesses of growth.

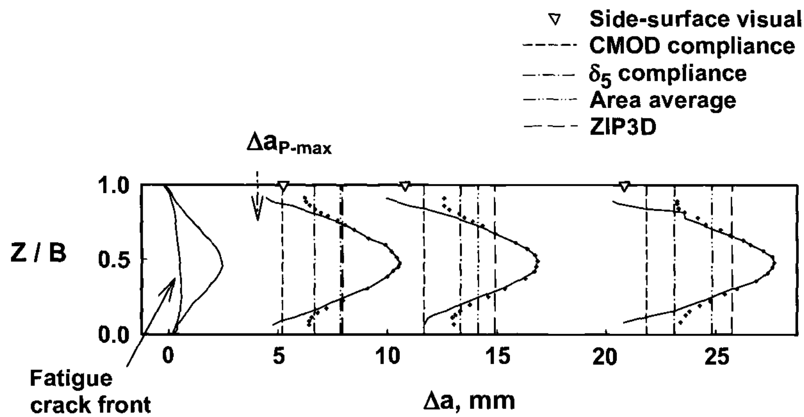

FIG. 9—*Measured crack face tunneling profiles and calculated crack length measures.*

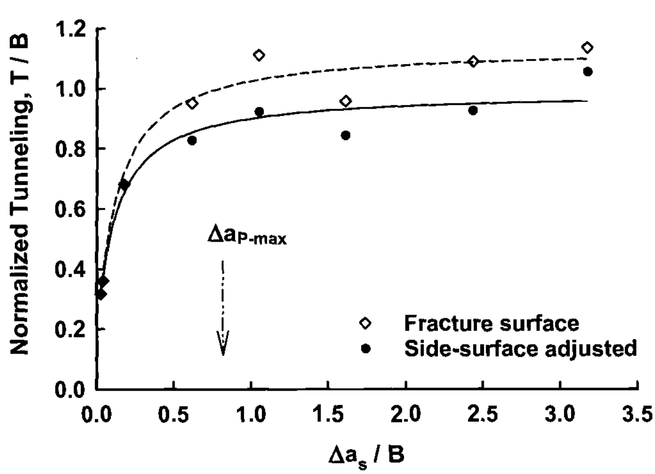

FIG. 10—*Calculated crack tunneling magnitude.*

Figure 11 shows the normalized tunneling fraction as a function of crack growth on the interior of the specimens for all of the flat-fracture specimens. The normalized tunneling fraction is the location of each crack length measure relative to the respective tunneled crack front shape. The area-average crack length is the longest experimental crack-length measure with an overall average value of 54 % of T. The experimentally measured CMOD compliance is the shortest measure at 17 % of T. For each, there is more variability early, but as tunneling stabilizes after about 2B of crack growth, the tunneling fraction is approximately constant for all three measures. Figure 11 also shows the tunneling fraction for ZIP3D analyses obtained by interpolating the ZIP3D load-crack growth curve with the load for each tunneling shape. The overall average value for ZIP3D is 75 % of T.

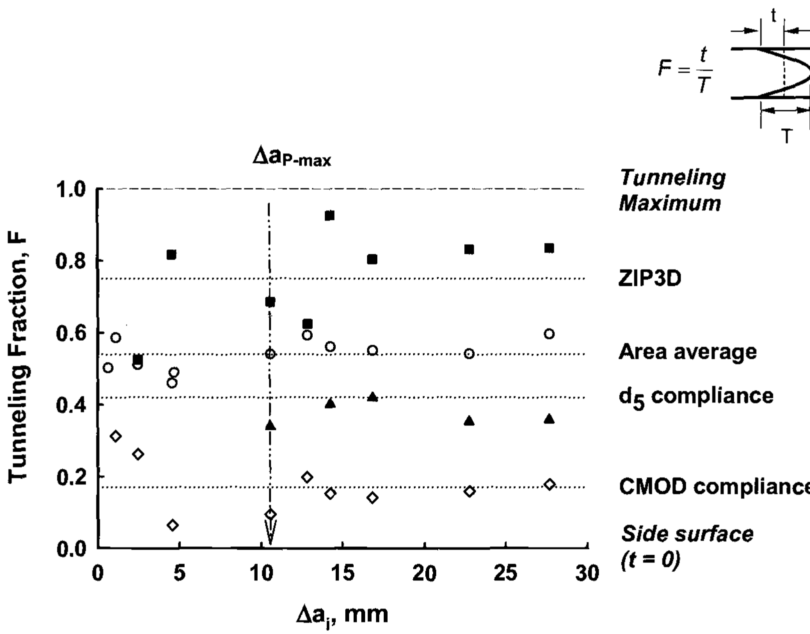

FIG. 11—*Comparison of tunneling fraction for various crack length measures.*

Figure 12 compares tunneling data with surface crack growth and analysis results. The open symbols show the "original" surface measured data from Fig. 2. The closed symbols show the new data from the tunneling test. The circle is the "tunneling surface" value of the tunneling crack growth, the inverted triangle is the "tunneling area-average," and the upward pointing triangle is the "tunneling maximum" value. Before maximum load, the tunneling surface values show shorter crack growth than the original tests, as discussed for Figs. 8 and 9. After maximum load the tunneling surface values follow the original values. The longest crack length measure is the maximum tunneling value, as shown in Fig. 11, and the analysis results fall between the area-average and maximum values. The points up to maximum load are unique first-front markings on each specimen. The points after maximum load, and the fourth point, are from multiple front specimens, where more than one tunneling shape was obtained from a single specimen. Since the surface values do not deviate significantly from the original values, the data are valid within a reasonable tolerance. The variability may lie in the evolution of tunneling for each specimen; however, there does appear to be a trend (see Fig. 10).

Figure 13 compares analysis predicted crack growth with experimental values. These data are generated by evaluating the analysis crack growth at the load for each point of the two experimental curves. The dashed lined indicates perfect agreement between analysis and test. Points above the line indicate over-predicted growth, and points under the line indicate under-predicted growth. Figure 13 shows that the analysis consistently over-predicts the surface measurement crack growth and consistently under-predicts the tunneling maximum.

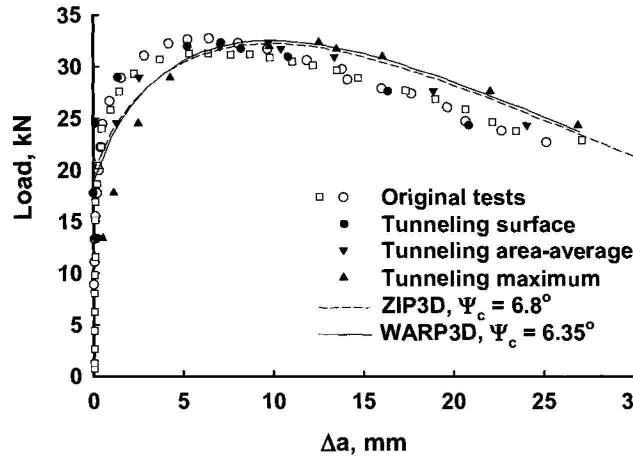

FIG. 12—*Comparison of tunneling results with surface measured crack growth and analysis results.*

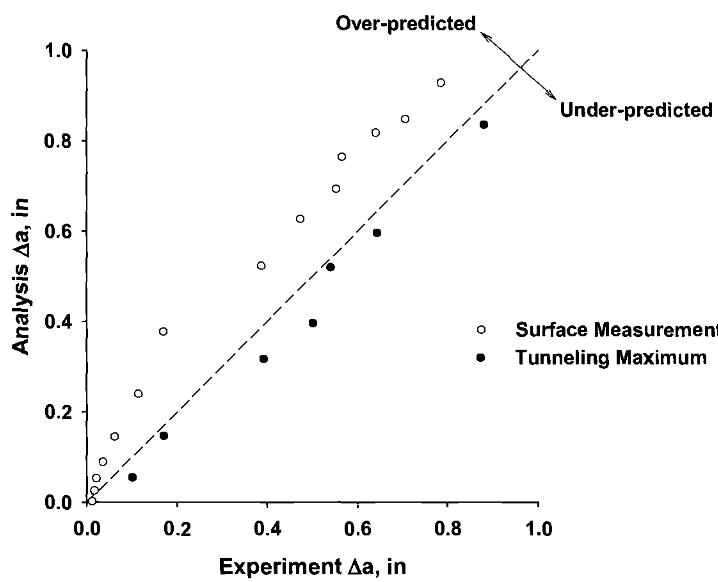

FIG. 13—*Comparison of analysis predicted crack grow with experimental values.*

Discussion

Figures 9 and 10 show that tunneling develops rapidly and is nearly developed after only $\Delta a_s/B = 0.5$, so surface crack measurements are significantly different from the maximum crack length in the interior at maximum load. In Fig. 11 the area-average crack growth is closest to the analysis results, but the analysis still over predicts area-average by about 20 % of the tunneling magnitude. However, the straight crack-front analysis does fall within the tunneling range throughout the full extent of the test data. The experimental CMOD compliance based length is the shortest of the crack length measures, in most cases essentially matching the side-surface length (i.e., t = 0.0).

The δ_5 based crack length is between the area-average and CMOD lengths, but is only about 12 % of the tunneling fraction below the area-average. It is unclear from this study why the δ_5 measurement is closer to the area-average than the CMOD measurement. Figure 6 shows that the δ_5 compliance is significantly more sensitive to tunneling. That sensitivity may outweigh the influence of other factors such as crack closure of faces behind the crack front as unloading occurs. The unloading fraction early in the test process was about 15 % of the current load, while at maximum load it was slightly less than 10 %. This provides more opportunity for closure at the lower loads, but at the higher loads plasticity is more developed, also increasing the possibility of closure. No obvious changes were observed in the unloading curves, which may indicate closure.

Figures 11 and 12 show that although the FEA results do over-predict the surface measurement crack length, the FEA results also always under-predict the tunneling maximum crack length for flat fracture. But one detail from Fig. 2 complicates the matter. Of the two experimental curves, one specimen failed in flat fracture and one specimen failed in slant fracture. The flat-to-slant transition was complete near maximum load, so the curve after maximum load was failing with slant fracture. But the load-crack growth curve is essentially the same as the curve for flat fracture. The slant fracture crack-front has very little tunneling, so the average crack length is nearly the same as the surface measured value. The flat fracture crack-front has significant tunneling by approximately the material thickness, so the average crack length after maximum load is longer (by approximately half the material thickness). The 3D FEA over-predicts the crack length for the slant fracture experimental results.

This evidence is consistent with the previous argument that the straight crack-front analysis is approximating the area-average crack length of the specimens that fail in flat fracture with tunneling. This evidence simply supports the argument that the specimen that fails in slant fracture has a different failure mode than the flat fracture specimens, and that the flat fracture analysis results are not representative of this difference. Note however that for many analyses of specimens that failed in slant fracture, maximum load was predicted accurately, even for very complex structural configurations [19,20,21].

The analysis load-crack growth results of the wide panel in Fig. 3 also over-predict the crack-growth by about the material thickness. These specimens typically failed in a combination of flat and flat-to-slant fracture, and the presented crack growth values are averages of the two crack tips. A careful inspection of the tunneling behavior of these specimens may recover part of the over-prediction, but Dawicke and Sutton [2] found that M(T) specimens tunnel less than C(T) specimens and concluded that the reduced in-plane constraint for the M(T) was likely a significant contributor to the difference in tunneling.

Since tunneling does occur in many cases, it is desirable to account for the tunneling either in the analysis or in the test data. The most desirable approach is to modify the analysis to include crack-front shapes that match the experimental results [22] or use a modeling methodology that allows the tunneling to evolve naturally as part of the analysis [23,24]. This is a topic for future work.

Conclusions

The excellent match between the experimental and analytical results for the load versus local crack-tip displacements (δ_5) curves is compelling and led us to consider the tunneling issue more carefully. The objective set down at the onset of this paper was to gain a better understanding of the shortcomings of the comparisons between the experimental crack length measurements and the finite element analysis results. The load versus crack-growth results show improved correlation between the area-average test data and the analysis results compared to the original load-surface crack growth. Optical measurement methods for crack growth will likely remain the method of choice for the buckling wide panel tests. Unloading compliance measurements are difficult for buckling panels, and direct current potential difference (area-average) is not currently a viable option for tests with large-scale plasticity. However, unloading compliance is relatively straightforward for constrained specimens. The δ_5 compliance approach is the overall best here because it is sensitive to tunneling, approaches the area-average measurements, and is relatively easy to implement using digital imaging systems. The results show that although the FEA results do over-predict the surface measurement crack length, the FEA results also always under-predict the tunneling maximum crack length for flat fracture.

References

[1] Harris, C. E., Newman, J. C., Jr., Piascik, R., and Starnes, J. H., Jr., "Analytical Methodology for Predicting the Onset of Widespread Fatigue Damage in Fuselage Structure," *Journal of Aircraft*, Vol. 35, No. 2, 1998, pp. 307–317.

[2] Dawicke, D. S. and Sutton, M. A., "CTOA and Crack Tunneling Measurements in Thin Sheet 2024-T3 Aluminum Alloy," *Experimental Mechanics*, Vol. 34, No. 4, 1994, p. 357.

[3] Wells, A. A., "Application of Fracture Mechanics at and Beyond General Yielding," *British Welding Journal*, Vol. 11, 1961, pp. 563–570.

[4] Newman, J. C., Jr., Crews, J. H., Jr., and Bigelow, C. A., "Variations of a Global Constraint Factor in Cracked Bodies under Tension and Bending Loads," *ASTM STP 1244*, M. Kirk and Ad Bakker, Eds., ASTM International, West Conshohocken, PA, 1995, pp. 21–42.

[5] James, M. A. and Newman, J. C., Jr., "Three Dimensional Analysis of Crack-Tip-Opening Angles and δ_5-Resistance Curves for 2024-T351 Aluminum Alloy," *Fatigue and Fracture Mechanics: 32nd Volume, ASTM STP 1406*, Ravinder Chona, Ed., ASTM International, West Conshohocken, PA, 2002, pp. 279–297.

[6] Shivakumar, K. N. and Newman, J. C., Jr., "ZIP3D – An Elastic and Elastic-Plastic Finite-Element Analysis Program for Cracked Bodies," NASA TM 102753, NASA Langley Research Center, 1990, Hampton, VA.

[7] Anderson, T. L., *Fracture Mechanics, Fundamentals and Applications*, 2nd ed., CRC Press, Boca Raton, FL, 1995.

[8] Helm, J. D., "Use of Three-Dimensional Digital Image Correlation for the Experimental Characterization of Buckling in Large, Thin, 2024-T3 Aluminum, Middle-Crack Tension Specimens," Ph.D. Thesis, University of South Carolina, Columbia, SC, 1999.

[9] Helm, Jeffery D., VIC-2D Data Analysis User's Guide, Correlated Solutions, Inc., Columbia, SC, 1998.

[10] Koppenhoefer, K. C., Gullerud, A. S., Ruggieri, C., Dodds, R. H., Jr., *WARP3D -- Release 10.8 User's Manual*, Department Of Civil Engineering, University of Illinois at Urbana-Champaign, Urbana, IL, 1998.

[11] Gullerud, A. S., Dodds, R. H., Jr., Hampton, R. W., Dawicke, D. S., "Three-Dimensional Modeling of Ductile Crack Growth in Thin Sheet Metals: Computational Aspects and Validation," *Engineering Fracture Mechanics*, 63, 1999, pp. 347–374.

[12] Newman, J. C., Jr., "Crack-Opening Displacements in Center-Crack, Compact, and Crack-Line Wedge-Loaded Specimens," NASA TN D-8268, NASA Langley Research Center, 1976, Hampton, VA.

[13] Schwalbe, K. H., "The Engineering Flaw Assessment Method (EFAM)," *Fatigue and Fracture of Engineering Materials and Structures*, Vol. 21, 1998, pp. 1203–1213.

[14] Abdel Mageed, A. M. and Pandey, R. K., "Effect of Measurement Location and Fatigue-Loading Parameters on Crack Closure Behavior," *Materials Science and Engineering*, Vol. A150, 1992, pp. 43–50.

[15] Mall, S. and Newman, J. C., Jr., "The Dugdale Model for Compact Specimen," *Fracture Mechanics 16th Symposium, ASTM STP 868*, ASTM International, West Conshohocken, PA, 1985, pp. 113–128.

[16] Stark, Peter A., *Introduction to Numerical Methods*, Macmillan Publishing Co., Inc., 1970.

[17] James, M. A. and Swenson, D. V., "FRANC2D/L: A Crack Propagation Simulator for Plane Layered Structures," Department of Mechanical and Nuclear Engineering, Kansas State University, Manhattan, KS, 1997, http://www.mne.ksu.edu/~franc2d/.

[18] James, M. A. and Newman, J. C., Jr., "Importance of Crack Tunneling During Fracture: Experimental Results And CTOA Analyses," ICF-10, 10th International Congress of Fracture, Honolulu, HI, December 2001.

[19] Seshadri, B. R. and Newman, J. C., Jr., "Residual Strength Analyses of Riveted Lap-Splice Joints," *Fatigue and Fracture Mechanics: 31st Volume, ASTM STP 1389*, G. R. Halford and J. P. Gallagher, Eds., ASTM International, West Conshohocken, PA, 2000, pp. 486–504.

[20] Hampton, R. W. and Nelson, D., "Stable Crack Growth and Instability Prediction in Thin Plates and Cylinders," *Engineering Fracture Mechanics*, 70, 2003, pp. 469–491.

[21] Hsu, C-L, Lo, J., Yu, J., Lee, X-G, Tan, P., "Residual Strength Analysis Using CTOA Criteria for Fuselage Structures Containing Multiple Site Damage," *Engineering Fracture Mechanics*, 70, 2003, pp. 525–545.

[22] Dawicke, D. S., Newman, J. C., Jr., and Bigelow, C. A., "Three-Dimensional CTOA and Constraint Effects During Stable Tearing in Thin Sheet Material," *ASTM STP 1256*, W. G. Reuter, J. H. Underwood, and J. C. Newman, Jr., Eds., ASTM International, West Conshohocken, PA, 1995, pp. 223–242.

[23] Ortiz, M. and Pandolfi, A., "Finite Deformation Irreversible Cohesive Elements for Three-Dimensional Crack-Propagation Analysis," *International Journal for Numerical Methods in Engineering*, n 44, 1999, pp. 1267–1282.

[24] Siegmund, T. and Brocks, W., "Modeling Crack Growth in Thin Sheet Aluminum Alloys," *Fatigue and Fracture Mechanics: 31st Volume, ASTM STP 1389*, G. R. Halford and J. P. Gallagher, Eds., ASTM International, West Conshohocken, PA, 2000, pp. 475–485.

SESSION 9: CRACK CLOSURE

Journal of ASTM International, June 2005, Vol. 2, No. 6
Paper ID JAI12017
Available online at www.astm.org

Daniel Kujawski[1] *and Stoyan Stoychev*[1]

A New Method for Opening Load Determination from Compliance Measurements

ABSTRACT: A brief review of the most popular compliance based methods for determination of the crack opening load is included in the introduction. This review reveals the demand for a noise resistant method that is especially needed in the near-threshold region where a partial crack closure prevails and the existing ASTM method does not calculate the correct opening load. With this in mind, a new technique was developed ('Q' method). It uses integration instead of differentiation of the compliance data. It also accounts for the partial crack closure situations. The derivation of the Q method is discussed together with its relation to the ASTM procedure, and both methods were used to analyze experimental data of 2324-T39 and 7475-T7351 Al alloys tested at 0.1 and 0.9 load ratios. On average, the crack opening load values from the Q method are smaller by the factor of about $2/\pi$ in comparison to those obtained from the ASTM procedure.

KEYWORDS: crack opening load, crack closure, partial crack closure, compliance, load ratio, correlation

Nomenclature

A_{cl}	Closure area
A_Q	Area under a load-displacement curve
CC	Crack closure
CMOD	Crack mouth opening displacement
CTOD	Crack tip opening displacement
PCC	Partial crack closure
PICC	Plasticity induced crack closure
P_{op}	Opening load
SIF	Stress intensity factor

Introduction

More than 30 years ago, Elber [1] observed that fatigue crack faces come into contact under tensile load before the applied load reaches zero. Based on this observation he introduced the crack closure (CC) concept and postulated that the plastic deformation left at the crack wake is responsible for the closure phenomenon. Subsequently, he introduced the effective range of the stress intensity factor (SIF), ΔK_{eff}, defined as:

$$\Delta K_{eff} = K_{\max} - K_{op} \tag{1}$$

Manuscript received 3 November 2003; accepted for publication 14 September 2004; published June 2005.
Presented at ASTM Symposium on Fatigue and Fracture Mechanics: 34th Volume on 19–21 November 2003 in Tampa, FL; S.R. Daniewicz, J.C. Newman, Jr., and K-H. Schwalbe, Guest Editors.
[1] Professor, and Graduate Student, respectively, Western Michigan University, Department of Mechanical and Aeronautical Engineering, College of Engineering and Applied Sciences, Kalamazoo, MI 49008-5065.

where K_{max} and K_{op} are the SIFs calculated for the maximum load, P_{max}, and the opening load, P_{op}, respectively. This means that in order to use this model in practice, one has to find P_{op} first. It is commonly done by using the ASTM standard E 647 recommendation. According to this recommendation, P_{op} is determined as the load associated with 1, 2, or 3 % deviation of the compliance offset.

Equation 1 implies that only the load range between P_{max} and P_{op} would affect the crack tip opening displacement (CTOD) and the associated damage. The CC model (as defined by Elber) is illustrated in Fig. 1 in terms of load versus CTOD.

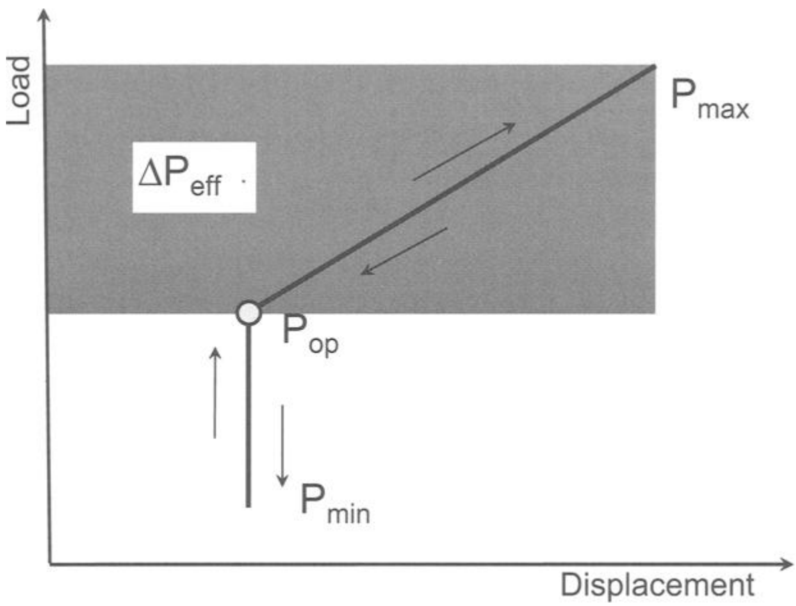

FIG. 1—*An ideal crack closure as defined by Elber.*

The Elber CC model has been widely adopted as the dominant mechanism responsible for load ratio, or in general, load history effects on fatigue crack growth behavior in metallic materials. However, despite the large amount of data generated on CC over the last 30 years, many difficulties were continuously reported in this area. As a result, the concept evolved mainly in respect of identifying additional mechanisms that may contribute to the CC phenomenon. Now it is recognized that not only the plastic deformation at the crack wake (plasticity induced crack closure - PICC), but also asperities, roughness, oxide debris, or fluids may induce CC. However, there is no general agreement on how and whether Eq 1 should be modified depending on the actual closure mechanisms involved.

In metals, in the near-threshold region, crack growth is usually associated with a single-shear mode of growth, which gives rise to a faceted fracture surface and Mode II loading. This may result in a mismatch between upper and lower fracture surfaces promoting premature contact before the crack fully closes. Thus, the rough fracture surface dominated at the near-threshold crack growth might result in isolated contact between asperities at some distance behind the crack tip (Fig. 2). Such isolated contacts would induce partial crack closure (PCC) at low rates associated with near-threshold growth. In addition to surface roughness contact, corrosion or debris-induced contact is also encountered at a very low growth rate [2]. In contrast, at higher crack propagation rates corresponding to the Paris region, the crack surface is rather 'flat' due to two intense slip systems operating simultaneously at the crack tip. Since the largest plastic stretch occurs just behind the crack tip, where the crack opening is the smallest, it can be speculated that in the Paris region the crack face contact would start from the crack tip and progress toward the crack mouth. This is so-called 'zipping' or 'peeling' closure mode (Fig. 2). These three mechanisms of crack closure have been observed experimentally for modified 1070 steel [3]. They can operate separately or together, which poses a fundamental question regarding their apparent significance on crack tip shielding.

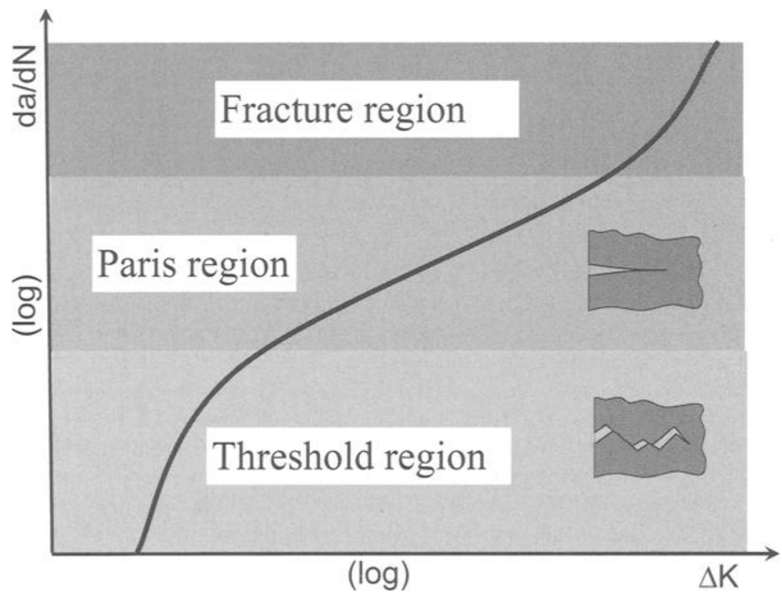

FIG. 2—*Phases of the fatigue crack growth.*

Hertzberg et al. [4] conducted experiments on artificially-induced closure in which shims were placed into the crack mouth, to wedge the crack. A compliance change was noted, but the effects on crack propagation rate and threshold were much less than what would have been predicted using Eq 1. This finding clearly indicated that the closure caused by artificial crack wedging was only partially effective. In order to achieve a more consistent and realistic estimation of the effective SIF range, some modifications of Eq 1 have been proposed.

Paris, Tada, and Donald [5] analyzed the PCC phenomena and demonstrated that interference between crack faces at a small distance behind the crack tip only partially shields the crack tip from fatigue damage. Thus, the difference between CC and PCC is that the latter recognizes that the crack tip will continue to deform below P_{op}, as illustrated in Fig. 3, and therefore will accumulate damage depending on the position and the size of the contact between the crack faces. They proposed to calculate an effective SIF range, $\Delta K_{2/PI0}$, due to partial closure as

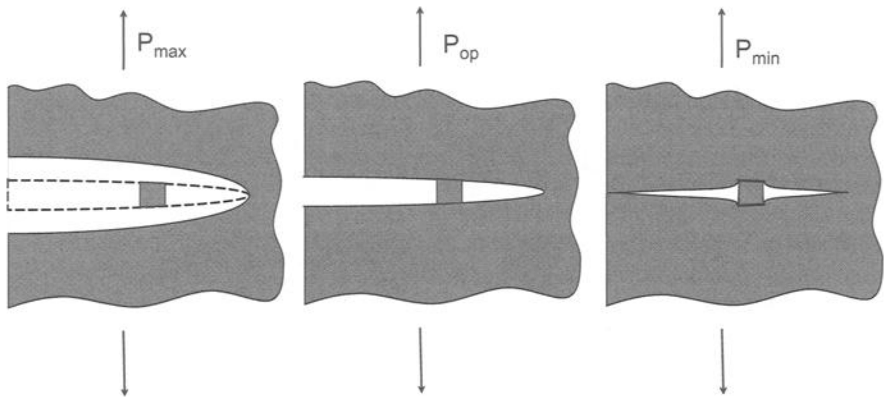

FIG. 3—*Partial crack closure.*

The above equation implies that P_{op} should be reduced approximately by $2/\pi$ in the case when PCC is present. For aluminum alloys this new effective SIF range was shown to improve significantly the correlation of FCG rates versus load ratios R, in the threshold region [5].

A similar rigid-wedge model was used earlier by Suresh, Parks, and Ritchie [2] to estimate the effect of crack tip oxide formation and its influence on the near-threshold crack closure level. Findings from the partial crack closure model concur with that of Hertzberg that closure or interference of crack faces at some distance from the crack tip only partially shields the crack tip from the damaging action due to cyclic loading.

Donald [6] addressed the PCC problem by developing the adjusted compliance ratio (ACR) method. The ACR value is determined by subtracting the compliance C_n from the secant compliance, C_s, and the compliance above the opening load, C_o, as follows:

$$ACR = \frac{C_s - C_n}{C_0 - C_n}. \tag{3}$$

The compliance C_n is an average value of two slopes, the first between 2 % and 12 % of the applied load, ΔP, and the second between 9 % and 19 %. This ratio appears to be independent of the measurement location and can be used to directly calculate the effective SIF as

$$\Delta K_{eff} = ACR \cdot \Delta K_{appl} \tag{4}$$

where $\Delta K_{appl} = K_{\max} - K_{\min}$. Equation 4 was shown to give better correlation than Eq 1 when PCC is present [6]. However, the ACR method remains mainly empirical and does not provide insight on the mechanisms of the CC. Also, it is not applicable when the crack starts to close from the tip.

Vasudevan, Sadananda, and Louat [7,8] have reconsidered fatigue crack closure and its contribution to fatigue crack growth behavior. They demonstrated that contribution to closure due to residual plastic stretch has been greatly exaggerated. Further, when asperity or roughness induced closure is present, the contribution is small and is about one quarter of that computed from the experimental compliance data.

The above discussion clearly indicates that there is a need for a more consistent and realistic estimation of the P_{op}. Therefore, the next section presents a new integration based 'Q method' for an effective determination of P_{op} based on compliance measurements.

Q Method

The ASTM standard E 647 recommended procedure for P_{op} determination from compliance measurements is based on a numerical differentiation algorithm, making the noise in the experimental data a major source of problems, especially in the threshold region [9]. This problem can be solved partially by using low pass filters or numerical algorithms for smoothing the experimental data [10]. However, the interest of the researchers is constantly shifting to smaller specimens and crack sizes, raising the expectations for more accurate crack closure determination. With this in mind, a new method for P_{op} determination was developed, based on integration rather than differentiation of the compliance data. This gives the name of the method – 'Q' (from quadrature – numerical integration). The noise resistance is improved simply because the numerical integration algorithms (like trapezoidal rule for example) are more stable and easy to implement.

Derivation

Load-displacement curves for ideal and partial crack closure are shown schematically on Figs. 4*a* and 4*b*, respectively. If there is no CC, the area A_{ABC} can be calculated using compliance C_0 when the crack is open.

$$A_{ABC} = \frac{C_0(\Delta P)^2}{2}. \tag{5}$$

The 'real' area A_Q under the load-displacement curve represents the effect of crack closure. The difference between these two areas, A_{cl}, is called 'closure area' and can be calculated as

$$A_{cl} = A_{ABC} - A_Q. \tag{6}$$

In the case of ideal CC, A_{cl} forms a right triangle ADE (Fig. 4*a*). For PCC, the associated 'closure area' (Fig. 4*b*) can be represented by the equivalent right triangle AD'E', which corresponds to an ideal CC behavior. The 'closure areas' can be calculated from

$$A_{cl} = \frac{C_0\left(P_{op} - P_{\min}\right)^2}{2} \tag{7}$$

Substituting Eqs 5 and 7 into 6, and solving for P_{op} we get

$$P_{op} = P_{\min} + \sqrt{(\Delta P)^2 - (2/C_0)A_Q} \tag{8}$$

Two limits for P_{op} can be derived from Eq 7, for $A_{cl} = 0$, $P_{op} = P_{min}$ and for $A_{cl} = A_{ABC}$, $P_{op} = P_{max}$, which corresponds to no-closure and full-closure situations, respectively.

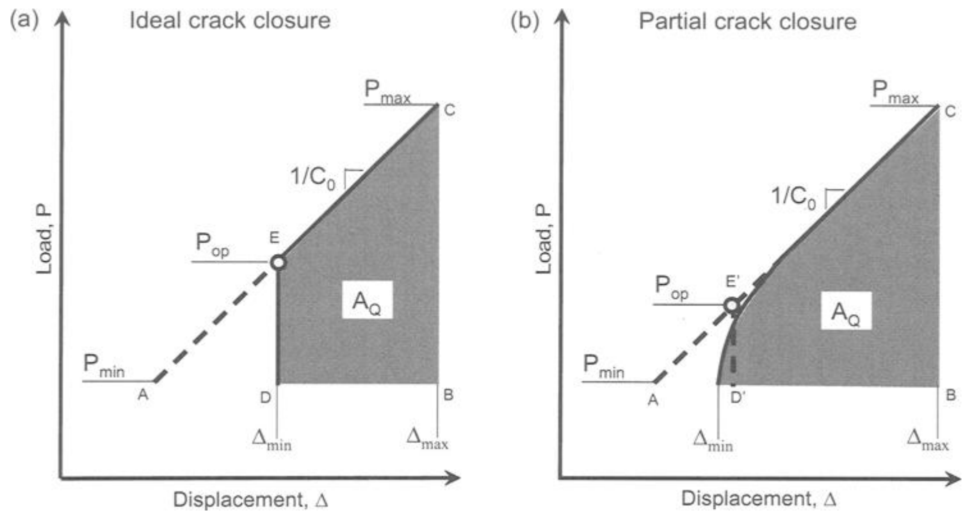

FIG. 4—*Derivation of the Q method.*

Theoretical Comparison with ASTM Method

Figure 5 shows four cases of crack closure. The crack is shown in all cases at maximum load, P_{max}. In case (a), a rigid wedge having the shape of the crack at load P_w is inserted to simulate ideal CC throughout the whole crack length. Horizontal dashed lines in Fig. 5 correspond to P_w. The other cases (b, c, and d) show the same crack containing different segments of the rigid wedge (hatched region). For all cases, the crack faces would contact the inserted wedge during unloading when $P = P_w$. The graphs on the left show P versus crack mouth opening displacement (CMOD) curves. Also on these graphs the values of P_{op} are indicated as determined using Q and ASTM methods. The graphs on the right show P versus CTOD curves together with the 'real' P_{op} values.

*An Ideal Crack Closure (Fig. 5*a*)*—The crack closes along the whole length at the same time, which corresponds to an ideal CC situation (a full shielding effect). In this case there is no difference between the CMOD and CTOD curves. Theoretically, both Q and ASTM methods should give the exact values for opening load, $P_{op} = P_w$. However, the real CMOD data contains noise, and ASTM method requires at least 1 %, 2 %, or 4 % compliance offset to occur in order to register P_{op}. This affects the accuracy of the ASTM method because P_{op} will always be somewhat lower than the real value of P_w. On the other hand, the Q method does not require any arbitrary offset and is expected to give the exact result in terms of accuracy. In terms of precision, Q method is also advantageous since the numerical integration of the whole curve is more stable than the differentiation, which is performed using small segments.

*The Crack Starts to Close from the Tip (Fig. 5*b*)*—The tip will be shielded immediately at $P_{op} = P_w$. However, the crack mouth displacement will continue to decrease with a slower rate and eventually stop before reaching P_{min}. Due to the noise in the raw data, the ASTM method will detect the first 1 %, 2 %, or 4 % compliance offset, i.e., $P_{op} \approx P_w$. The Q method will give $P_{op} < P_w$, corresponding to A_{cl} that is transformed to a right triangle (Fig. 4*b*). There are two factors that minimize the error. First, metals have significant stiffness, which makes the shape of the 'closure area' almost a right triangle (especially in the threshold region). Second, the crack can actually close at the mouth also, before the load is reduced to P_{min}.

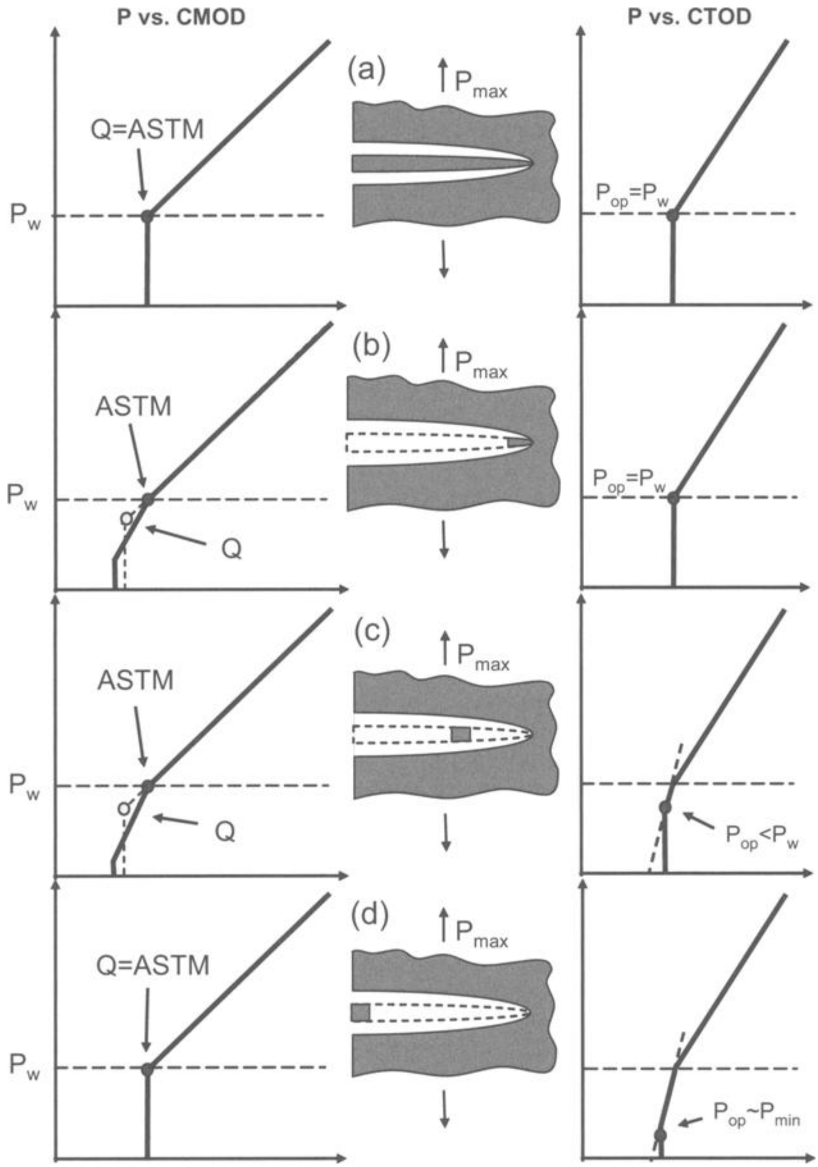

FIG. 5—*Theoretical comparison between Q an ASTM methods.*

The Crack Closure Occurs at Some Arbitrary Position along the Crack (Fig. 5c)—The ASTM method will register the load of the first contact between the crack faces as $P_{op} = P_w$. Both mouth and the tip will continue to experience deformation below P_w. The actual opening load at the crack tip will be bounded by P_{min} and P_w. The Q method will adjust the P_{op} value by transforming the 'closure area' at the crack mouth to a right triangle (Fig. 4*b*). This will result in the P_{op} value somewhere between P_{min} and P_w. In general, the Q method is sensitive to PCC, whereas the ASTM procedure is not. It is expected that the Q method will give P_{op} close to the opening load at the crack tip.

The Crack Starts to Close from the Mouth (Fig. 5d)—This is a limiting case and is not likely to be observed in the practice. Both Q and ASTM methods (and any other compliance based method) will register erroneous $P_{op} = P_w$. It will correspond to the point where the crack mouth touches the wedge. The crack tip, however, will continue to deform, causing more damage at the crack tip. Thus, both methods will give the same error in this hypothetical case.

The proposed Q method (and any other compliance based method) is phenomenological because it is impossible to relate the crack 'closure area' at the crack mouth to any of the fatigue mechanics parameters at the tip (K, G, or J) without knowing the area and the position of the contact of crack faces.

Specimen and Test Procedure

The load-displacement data were obtained from 2324-T39 and 7475-T7351 aluminum alloys. The specimen geometry is shown in Fig. 6. Specimens with the thickness of 2.54 and 5.08 mm were used to generate the data. Each specimen was precracked using compression-compression loading in order to minimize any load history effects [11]. Then, a constant load range scheme was applied in tension at a load ratio R = 0.1 or 0.9. The tension tests were started with a ΔK value somewhat smaller than the expected threshold level. If no crack propagation was observed for 10^6 cycles, then the ΔK value was increased by 0.1 $MPam^{0.5}$. Once progressive crack growth rate was achieved, the specimen was cycled at that constant ΔP value until failure.

During the test, digital pictures of the crack tip area were taken using a charge coupled device (CCD) camera with a resolution of 10^6 pixels. This allowed for 5 μm resolution in the crack length measurement. In addition, the CMOD was measured using a 'clip on' gage. Each compliance curve consists of 600 load-displacement pairs, spaced at equal load intervals. This procedure was used for both the loading and unloading compliance curves. Approximately 55 measurements were taken from each specimen at equal crack increments.

Results and Discussion

The results are depicted in Fig. 7*a*, *b*, and *c* in terms of normalized opening load, P_{op}/P_{max}, versus normalized crack length, a/w. It can be noted that the P_{op} results exhibit considerably smaller scatter when calculated using the Q method. Another important observation is that the difference between Q and ASTM increases for small crack lengths. For the particular test, this corresponds to the threshold of the fatigue crack growth. In this region, the CC is believed to be caused by asperities. This means that the crack face contact appears at some distance behind the crack tip, causing the ASTM method to register unrealistically high P_{op} in this PCC situation. In contrast, the Q method shows a gradual increase in opening load. This trend is in agreement with compression-compression pre-cracking and subsequent tensile crack growth. It is widely accepted that compression-compression pre-cracking generates a closure-free crack, which will develop closure under tensile growth from the threshold to the Paris region.

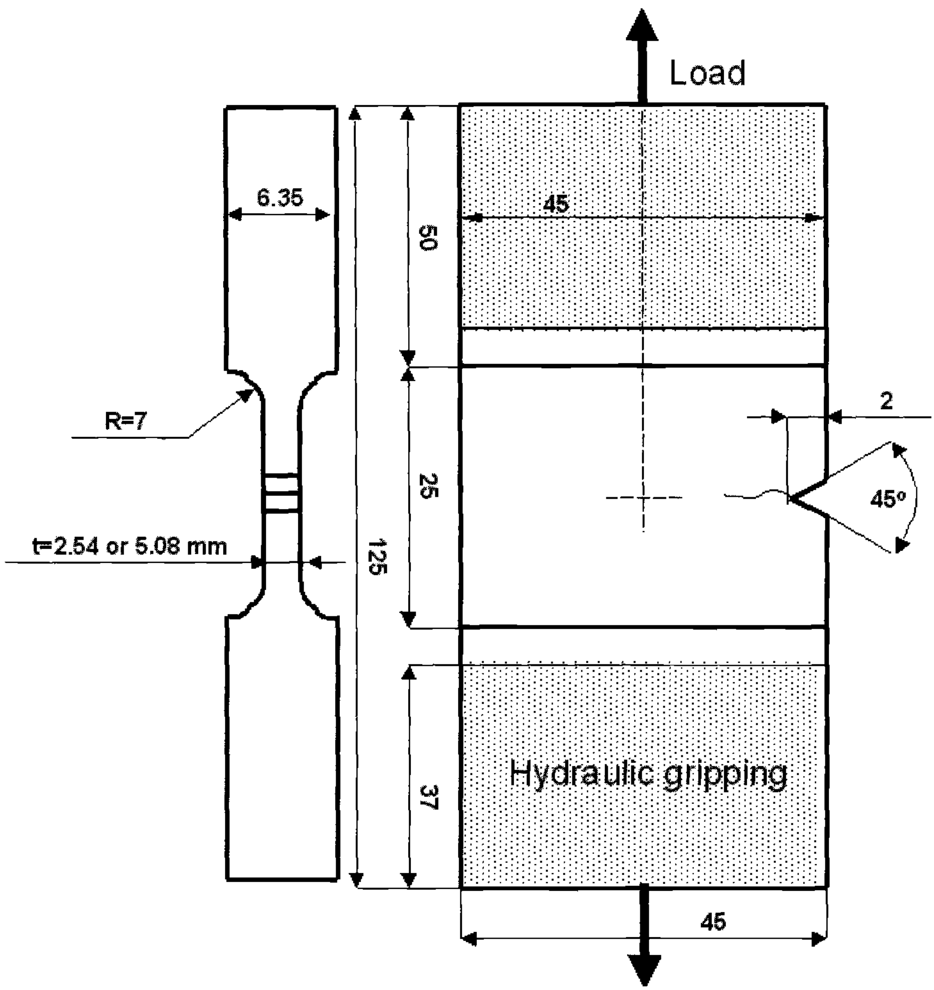

FIG. 6—*Specimen geometry and dimensions.*

Figure 7*d* shows the ratio of the opening loads determined by Q and ASTM procedures. Presented results clearly demonstrate that the Q method effectively reduces the ASTM P_{op} by a factor of $2/\pi$ as proposed by Paris et al. [5] for the PCC model.

Another comparison was made based on the correlation between da/dN vs. ΔK_{eff} data for R = 0.1 and the closure free data obtained at R = 0.9 using both the ASTM and Q methods (Fig. 8). An examination of Fig. 8 indicates that both methods do not collapse the R = 0.1 data on that of R = 0.9. This can be possibly attributed to K_{max} effects as proposed by Vasudevan and Sadananda [12]. In the near-threshold region, where Q method is expected to give better correlation than ASTM, this comparison could not be performed due to multiple crossings in the compliance offset diagram, using the ASTM procedure, which resulted in oscillating values of P_{op}/P_{max} between 0 and 1.

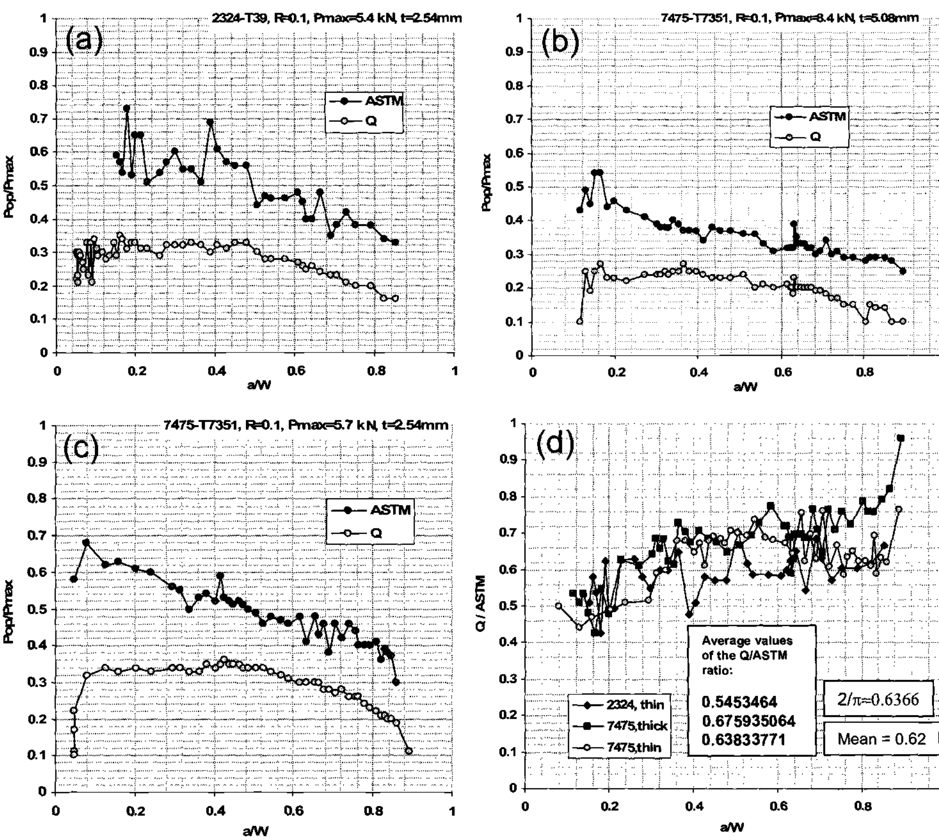

FIG. 7—*Experimental comparison between Q and ASTM methods, based on* P_{op}.

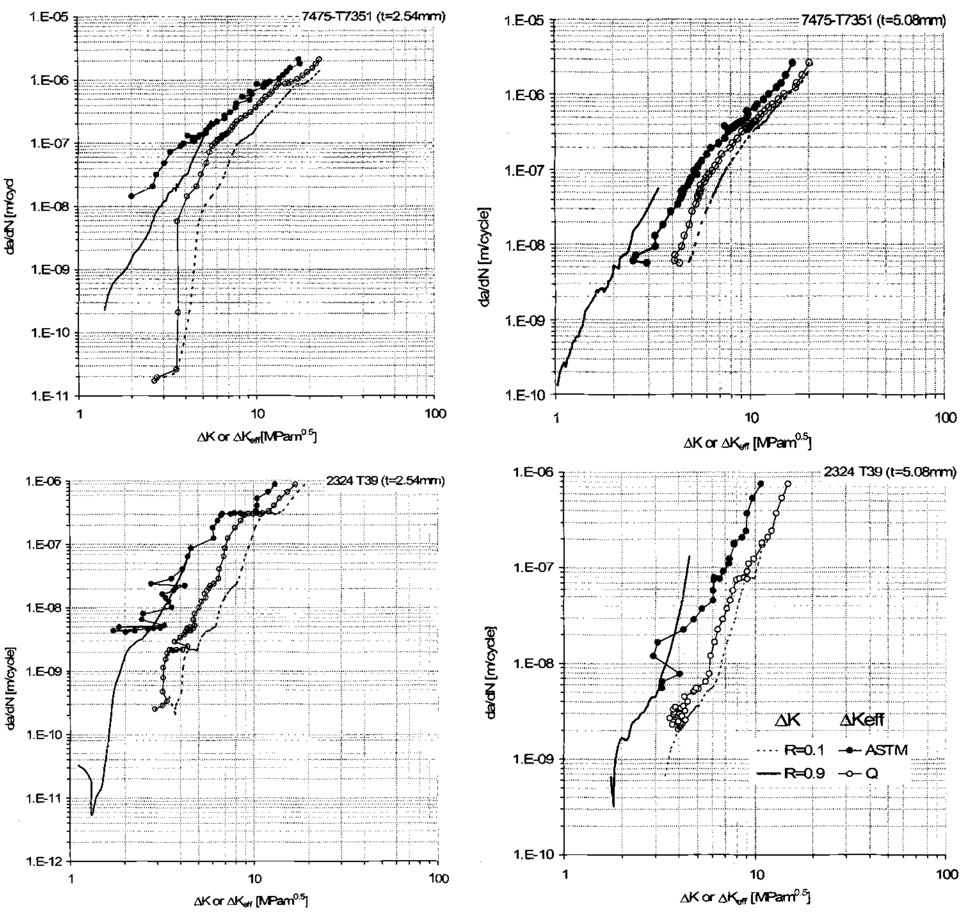

FIG. 8—*Crack growth rate in terms of ΔK or ΔK_{eff}.*

Conclusions

The following conclusions can be drawn:

- A new Q method reduces the variation in the opening load in comparison to the ASTM method. This is because the Q method uses a more stable numerical integration algorithm instead of numerical differentiation algorithm utilized in the ASTM procedure.
- The Q method allows P_{op} to be determined where multiple crossings on the compliance offset plot will invalidate ASTM results (typically in the threshold region).
- The Q method is sensitive to PCC, whereas the ASTM procedure is not. On average the P_{op} values determined using the Q method are lower by a factor of about $2/\pi$ in comparison with the values obtained utilizing the ASTM procedure.

Acknowledgments

This investigation was sponsored by the Office of Naval Research under grant N00014-01-1-0952.

References

[1] Elber, W., "The Significance of Fatigue Crack Closure," *Damage Tolerance in Aircraft Structures, ASTM STP 486*, ASTM International, West Conshohocken, PA, 1971, pp. 230–242.
[2] Suresh, S., Parks, M. D., and Ritchie, R. O., "Crack Tip Oxide Formation and Its Influence on Fatigue Crack Threshold," *Fatigue Threshold:* Fundamentals *and Engineering Applications*, Vol. 1, A. F. Blom, J. Backlund, and C. J. Beevers, Eds., Warley: Engineering Materials Advisory Services, 1982, pp. 391–408.
[3] Dougherty, J. D., Srivatsan, T. S., and Padovan, J., "Fatigue Crack Propagation and Closure Behavior of Modified 1070 Steel: Experimental Results," *Engineering Fracture Mechanics*, Vol. 56, No. 2, 1997, pp. 167–187.
[4] Hertzberg, R. W., Newton, C. H., and Jaccard, R., "Crack Closure: Correlation and Confusion," *Mechanics of Fatigue Crack Closure, ASTM STP 982*, J. C. Newman, Jr. and W. Elber, Eds., ASTM International, West Conshohocken, PA, 1988, pp. 139–148.
[5] Paris, P. C., Tada, H., and Donald, J. K, "Service Load Fatigue Damage - A Historical Perspective," *International Journal of Fatigue*, Vol. 21, 1999, pp. S35–S46.
[6] Donald, J. K., "Introducing the Compliance Ratio Concept for Determining Effective Stress Intensity," *International Journal of Fatigue*, Vol. 19, 1997, pp. S191–S195.
[7] Vasudevan, A. K., Sadananda, K., and Louat, N., "Reconsideration of Fatigue Crack Closure," *Scripta Metallurgica et Materialia*, Vol. 27, 1992, pp. 1673–1678.
[8] Vasudevan, A. K., Sadananda, K., and Louat, N., "A Review of Crack Closure, Fatigue Crack Threshold and Related Phenomena," *Materials Science and Engineering*, Vol. A188, 1994, pp. 1–22.
[9] Kujawski, D. and Stoychev, S., "Parametric Study on the Variability of Opening Load Determination," *International Journal of Fatigue*, 2003 (in press).
[10] Danievicz, S. R., "Smoothing And Differentiating Load – Displacement Data Using A Low Pass Filter For Improved Crack Opening Load Estimates," *Fatigue and Fracture of Engineering Materials and Structures*, Vol. 22, No. 4, 1999, pp. 273–280.
[11] Forth, S. C., Newman, J. C., and Forman, R. G., "On Generating Fatigue Crack Growth Thresholds," *International Journal of Fatigue*, Vol. 25, 2002, pp. S9–S15.
[12] Sadananda, K. and Vasudevan, A. K., "A Unified Framework for Fatigue Damage Analysis," *Naval Research Revue*, Vol. 50, No. 4, 1998, pp. 56–68.

SESSION 10: FATIGUE III

Journal of ASTM International, May 2005, Vol. 2, No. 5
Paper ID JAI12035
Available online at www.astm.org

Elena Paffumi,[1,2] *Karl-Fredrik Nilsson,*[1] *Nigel Taylor,*[1] *Roger Hurst,*[1] *and Martin Bache*[2]

Crack Initiation, Propagation, and Arrest in 316L Model Pipe Components under Thermal Fatigue

ABSTRACT: There is a continuing need for reliable thermal fatigue analysis tools to ensure that high safety levels are maintained in the main coolant lines of light water reactors. As a contribution to this effort, a combined experimental and numerical investigation has been conducted on cylindrical components of 316L stainless steel subjected to cyclic thermal shocks of varying intensity. It exploits a dedicated rig in which the tubular test pieces are subjected to induction heating and water quenching. Under the applied loading, a network of cracks initiates at the inner surface; some of these propagate further through the wall thickness. The number of cycles to crack initiation is estimated from surface replicas taken during intermittent stops, whereas the crack depth of fatigue cracks is measured using an ultrasound time of flight diffraction technique (TOFD). The analysis is done by a sequentially coupled thermal-stress finite element analysis using a cyclic plasticity model. Predictions of the crack initiation life (based on crack initiation curves as well as crack propagation models for microstructurally short cracks) are in good agreement with the test results. Crack propagation for small fatigue cracks was estimated by plastic strain amplitude based propagation formulas, whereas long crack propagation is analyzed by Paris law type criteria using ΔK as well as $\Delta CTOD$.

KEYWORDS: thermal fatigue, 316L, replica, TOFD, crack initiation, crack propagation, crack arrest

Introduction

The development of analysis procedures and laboratory techniques for accurate assessment of damage due to thermal fatigue is a topic of increasing importance, particularly in relation to the life assessment of main coolant lines in aging light water nuclear reactors. Thermal fatigue in a fluid mixing area (the mixing Tee problem) is a recognized problem in this respect, which due to the complex loading and effects of material degradation is still not well understood [1]. This phenomenon is linked to a turbulent mixing of two fluids at different temperatures, which induces large thermal fluctuations at the surface and associated stress and strain variations with often large plastic straining. Damage usually starts with the formation of a network of surface cracks in the region with the largest thermal fluctuations, or as discrete cracks at welds. Thermal fatigue is also a serious problem for a range of structural components in non-nuclear applications, such as boilers, heat exchangers, gun barrels, turbine rotors, and different loading situations, e.g., start-up and shutdown events.

There have been a number of studies published on the thermal fatigue problem, usually with different simplifications, often using flat plates [e.g., 2–4] or by inserting a notch starter crack [5].

The ongoing research presented in the following sections aims to advance the understanding of the basic mechanisms and loading conditions under which thermal fatigue cracks initiate and

Manuscript received 17 November 2003; accepted for publication 2 July 2004; published May 2005. Presented at ASTM Symposium on Fatigue and Fracture Mechanics: 34th Volume on 19–21 November 2003 in Tampa, FL; S.R. Daniewicz, J.C. Newman, Jr., and K-H. Schwalbe, Guest Editors.
[1] Institute for Energy, European Commission, DG-JRC, P.O. Box 2 1755 ZG Petten Netherlands.
[2] Materials Research Centre, School of Engineering, University of Wales, Swansea, SA2 8PP, UK.

propagate, and to translate this into improved practical methods for predicting thermal fatigue. Cylindrical test pieces of low-carbon austenitic steel 316L are subjected to thermal loads to initiate and propagate axial as well as circumferential cracks. The results provide a validation benchmark for the analysis procedure, based on a sequentially coupled thermal-stress finite element analysis, in which initiation and crack propagation criteria are applied.

Description of the Experimental Set-Up

The thermal shock experiments are carried out on cylindrical specimens in a special test facility previously developed for high temperature thermal cycling (Fig. 1*a*) [6,7]. The specimens are made of a low carbon 316L stainless steel with an outside diameter of 48 mm, a wall thickness of 14 mm, and a length of 224 mm (Fig. 1*b*).

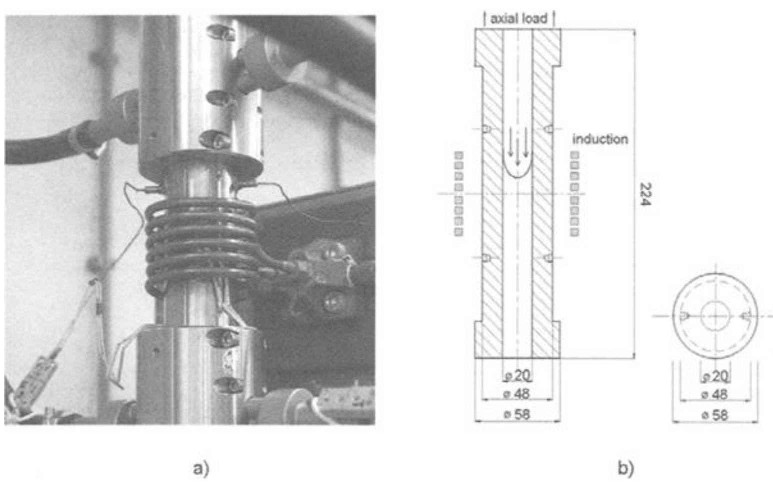

FIG. 1—*Experimental set-up:* a) *specimen with induction coil and* b) *specimen dimensions.*

The specimens are heated continuously by an external induction system. The thermal cycling is achieved by periodically injecting room temperature water through the test pieces bore (i.e., down-shock), which induces strong tensile strain variations at the inner surface. During the cycling, the test piece itself is held in a lever arm test machine, which allows application of a static axial load, but places no restraint on any global axial displacements of the test piece. Hence, the system allows the following parameters to be controlled:

- induction heating power, which determines the maximum temperature and heating rate
- duration of quenching, which controls the ΔT at the inner surface and the cycling frequency
- applied axial load

The testing procedure is outlined in Fig. 2. The test piece is first heated without the water flow in the bore of the specimen for 9 s to reach the prescribed maximum external temperature. This is followed by a 'dwell time' of 900 s at the maximum temperature to allow the temperature through the wall thickness to equalize to the maximum value. From this constant temperature distribution stage, thermal cycling starts by internally quenching the specimen with room temperature water for a prescribed time, t_{Quench}, and by heating for a certain time, t_{Heat}, when the quenching is stopped. The resulting very strong temperature variations induce transient thermal stress and strain gradients through the pipe thickness, whose intensity depends on the temperature difference between the water and the maximum temperature of the outer surface of the pipe (ΔT), the quench duration, the material properties, and the heat transfer between the pipe and the water. In designing the testing program, a compromise was sought between having a relatively low ΔT representative of the plant operating conditions and the need to apply a sufficiently severe shock to produce damage in reasonable times. This resulted in typical values for t_{Quench} and t_{Heat} of 5 and 45 s, respectively, implying an overall cyclic frequency of approximately 0.02 Hz.

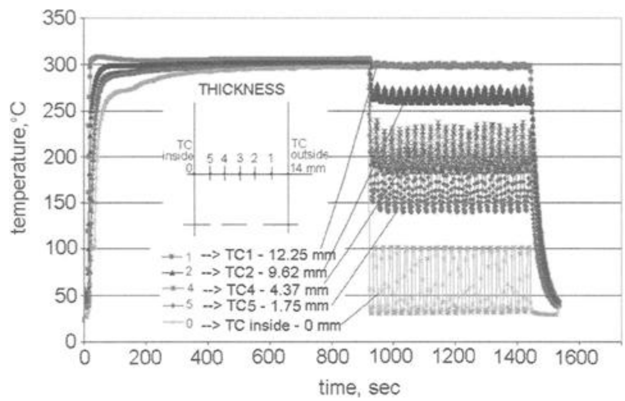

FIG. 2—*Measured temperature history at different depth locations in calibration specimen.*

The through-wall temperature variations during the cycle were measured in a specially prepared calibration specimen equipped with six thermocouples, which were connected to a computer for continuous monitoring. Figure 2 depicts typical temperature variations at different depths through the wall thickness when the external surface is kept at 300°C and the inner surface is quenched by room temperature water. The specimens used in the fatigue tests had thermocouples spot-welded on inner and outer surfaces only. The induction heating was controlled so that the outer surface temperature was kept constant.

Monitoring of the resulting fatigue damage is essential to provide data on crack initiation and propagation and to verify the analysis methods. To this end, three non-destructive techniques were employed:

- The surface replica technique was used for the multiple cracking at the quenched surface.
- Radiography with a panoramic exposure was employed to detect internal cracks for some specimens; this provided a check on the replica results and also additional information on the distribution of cracking on the bore.
- Time-of-flight-diffraction (TOFD), which is an ultrasonic technique, was adopted to monitor the location, length, and depth of cracks.

None of these methods could be used during the thermal cycling. The tests were therefore stopped at certain intervals to allow the test piece to be dismounted for the damage monitoring measurements. On-line damage monitoring methods had also been considered initially. The potential drop technique had been used in previous work on specimens with a circumferential starter notch from which a discrete crack developed rather uniformly. For the present case in which multiple cracks initiate and grow, it was judged that this would not produce meaningful data. A trial was also conducted with an acoustic emission system; in this case the overall system noise (from the induction coil's electromagnetic system and to a lesser extent the water flow during the critical quench period) made it impossible to reliably detect signals that could be related to damage development without switching off the external heating system.

Description of the Computational Model

The analysis was done by a sequentially coupled thermal-stress analysis using the commercial FE-code ABAQUS. Both cracked and un-cracked body analyses were performed using axisymmetrical eight-nodes elements. Symmetry was assumed, and only the upper half of the specimen was therefore modelled. Auxiliary software routines were developed to automatically generate finite element meshes with a progressive mesh refinement toward the inner surface to capture the large strain variations induced by the thermal shocks. For the cracked body analyses, a refined mesh was used to model the crack tip behavior and to determine crack tip fracture mechanics parameters (Fig. 3). Since the model is axisymmetric, it is implicit that such cracks are fully circumferential; to date, full 3-D modelling of partially circumferential, axial, or multiple cracks has not been considered.

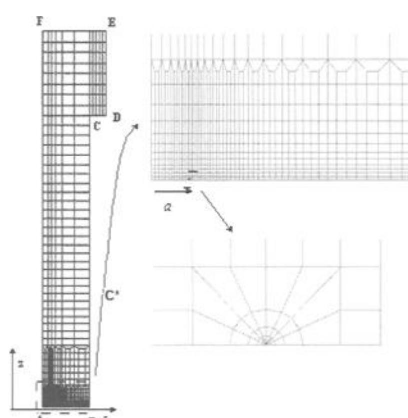

FIG. 3—*Typical FE-mesh for cracked body analysis.*

Thermal Analysis

The thermal analysis was based on Fourier heat conduction equations, with the temperature dependent properties of the steel given in Table 1 using ABAQUS heat transfer finite elements. Referring to Figs. 2 and 3, the following time dependent boundary conditions were applied. Initially, the entire specimen is at room temperature. The outer segment covered by the induction coil (BC*) was constrained to follow the experimental temperature variation of the outer surface. During the heating-up period, the temperature at the outer surface increases linearly from room temperature to the maximum temperature, T_{max}, which is then kept constant during all of the thermal cycles. The remaining part of the outer surface (C*CDE) is assumed to lose heat from free convection and radiation. The bore-hole (FA in Fig. 3) is cooled by forced convection during the quenching and by free convection and radiation when there is no quenching. Both the forced and free convection heat transfer were implemented in ABAQUS by mean of the "*FILM" option. The heat transfer coefficient increases with temperature and depends on the geometry, flow rate, and direction, and the physical properties of air and water, respectively. Temperature dependent heat transfer coefficient of $11-15$ W/m°C and 125–270 kW/m°C were used for the free, h_{free}, and forced convection, h_{force}, respectively for 50°C < T < 400°C. The adopted values have been determined from formulas based on the air/metal and water/metal surface interface [8]. Other formulas may give slightly different values, but the effect on the computed strains is small.

TABLE 1—*316 L temperature dependence of physical and mechanical properties (from the manufacturer).*

Temperature °C	20°C	300°C	500°C	700°C
Density, kg/m^3	8000	7870	7780	7680
Thermal Conductivity, W/mK	14.5	18	20	23
Specific Heat, J/kgK	480	550	580	600
Thermal Expansion, 10^{-6}/K from 20°C	15.16	18.92	20.36	21.28
Electrical Resistivity, $10^{-9}\Omega$m	760	950	1040	1120
Tensile Modulus of Elasticity, kN/mm^2	192	175	155	140

Cyclic Plasticity Model

Since the thermal cycling produces significant stresses at the inner surface, accurate modelling of the resulting plastic strains was required for the analysis. For this purpose, the stabilized non-linear kinematic hardening model proposed by Lemaitre and Chaboche [9], which is implemented in ABAQUS, was used. It is based on a von Mises flow criterion where the center of the flow surface is shifted by a back stress, $\overline{\overline{X}}$, to model the cyclic plasticity. The plasticity criterion is expressed in the form:

$$f = J_2(\overline{\overline{\sigma}} - \overline{\overline{X}}) - \sigma_Y = 0 \quad where \quad d\overline{\overline{X}} = \frac{2}{3} C d\overline{\overline{\varepsilon}}_{pl} - \gamma \overline{\overline{X}} dp. \tag{1}$$

Here, J_2 is the second stress invariant, dp is the accumulative plastic strain, σ_Y is the cyclic yield stress, C is the kinematic hardening modulus, and γ determines the rate at which the hardening decreases with increasing plastic deformation. The three parameters σ_Y, C, and γ depend on the applied strain range and need to be calibrated from uniaxial cyclic test data. In the one-dimensional case with proportional loading, the back stress relation can be integrated analytically (see Fig. 4).

$$\left.\begin{array}{l} \sigma = E\varepsilon \qquad when \quad \varepsilon \le 2\sigma_Y/E \\ \left.\begin{array}{l} \sigma = 2\sigma_Y + X \\ where \quad X = \dfrac{2C}{\gamma}\left[1 - e^{\gamma(\varepsilon-\sigma/E)}\right] \end{array}\right\} \; when\; \varepsilon > 2\sigma_Y/E \end{array}\right\} \tag{2}$$

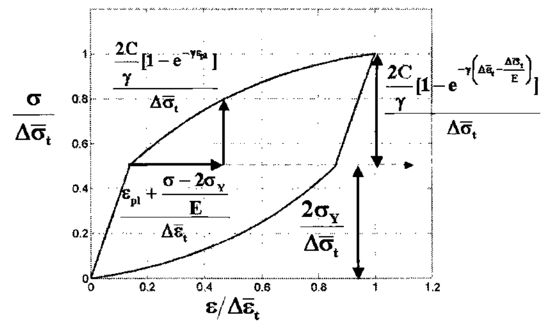

FIG. 4—*Hysteresis loop for uniaxial loading with nonlinear kinematic hardening.*

Once σ_Y and γ are known, the kinematic hardening for a given strain range can be determined directly from Eq 2 and the applied stress-strain range at the location,

$$\overline{C} = \frac{\overline{\gamma}\left(\Delta\overline{\sigma}_t - 2\overline{\sigma}_Y\right)}{2}\left[1 - e^{-\overline{\gamma}\left(\Delta\overline{\varepsilon}_t - \Delta\overline{\sigma}_t/E\right)}\right] \tag{3}$$

Low cycle fatigue data for 316L from several sources was analyzed to determine the model parameters. Figure 5 depicts the stress range, $\Delta\overline{\sigma}_t$, versus the strain range, $\Delta\overline{\varepsilon}_t$, at saturation from different strain-controlled cyclic tests [10,6], together with the curves predicted by the formula in the French RCC-MR procedure [11] for 20, 400, and 700°C, where stress is given in MPa, $\sigma_0 = 718$ MPa, m = 0.318, and the elastic modulus is as given in Table 1.

$$\Delta\overline{\varepsilon}_t = \Delta\varepsilon_{el} + \Delta\varepsilon_{pl} = \frac{2(1+\nu)\Delta\overline{\sigma}_t}{3E} + 10^{-2}\left(\frac{\Delta\overline{\sigma}_t}{\sigma_0}\right)^{1/m} \tag{4}$$

Despite some scatter, the overall consistency is good. Figure 5 also shows that there is no significant temperature dependence of the cyclic stress-strain properties. Indeed, in the RCC-MR formula, the temperature enters only through the temperature dependence of Young's modulus. The RCC-MR equation was used to estimate the three strain range dependent parameters in the cyclic-plasticity model. Firstly, the yield stress, $\overline{\sigma}_Y$, was determined by first computing the stress range, $\Delta\overline{\sigma}_t$, for a given total strain from Eq 4 and then stipulating that $\overline{\sigma}_Y = \Delta\overline{\sigma}_t(1+\nu)/3$. In the absence of full hysteresis loop data, a fixed value $\gamma = 150$ was adopted for all strain ranges. The kinematic hardening modulus $\overline{C}$ was computed from Eq 3 with stress and strain calibrated with the RCC-MR curve (Eq 4). The resulting $\overline{C}$ and $\overline{\sigma}_Y$ are plotted in Fig. 6. On account of the significant strain range dependence of $\bar{\sigma}_Y$ and $\overline{C}$ arising from the calibration, in the ABAQUS finite element analysis, these values were updated via a user subroutine. Although approximate, this procedure was considered to better represent the local cyclic plasticity effects than assuming fixed values of the Chaboche model parameters.

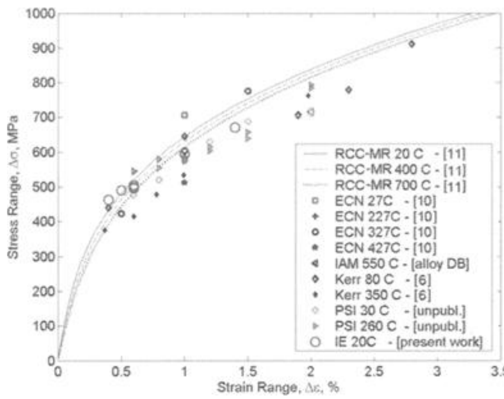

FIG. 5—*Experimental data and RCCM-curves for stress range versus strain range.*

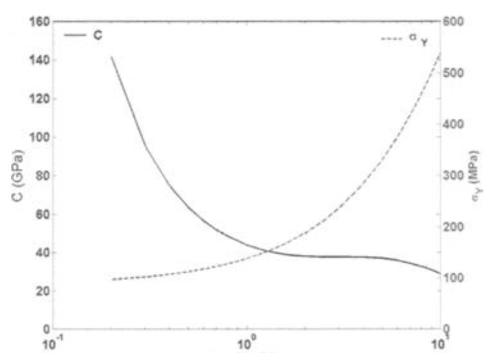

FIG. 6—*The parameters, σ_Y and, used in the analysis versus applied strain range with $\gamma = 150$.*

Thermal Stress Analysis

The computed temperature transients were read into the stress analysis as predefined fields to compute the resulting deformation and stresses in the specimen. The temperature dependent thermal expansion coefficient, α, and Young's modulus, E, as given in Table 1 were used together with the cyclic plasticity model described above. The edge ED in Fig. 3 was constrained in the radial direction ($u_r = 0$) and a symmetry condition was imposed ($u_z = 0$) along the uncracked segment of AB. All other edges were traction free. To verify the model, a test piece was prepared with special temperature resistant strain gauges on the outer surface. The measured strains were monitored during several thermal cycles and corrected for thermal mismatch effects between the gauge material and the austenitic pipe. The results were in good agreement with the FE model predictions.

Crack Propagation

The large strain variation at the inner surface implies that the propagation phase of the fatigue life will be significantly longer than the initiation phase. The crack propagation rate depends on the size of the defects and whether large-scale yielding effects need to be considered. The crack growth can be divided into three regimes: microstructurally short cracks, mechanically short cracks, and long cracks. Orblík, Polák, and Vašek [12–14] have found that the crack propagation rate of small cracks in 316L steel can be correlated to the amplitude of the plastic strain, $\Delta\varepsilon_{pl}$. For microstructurally short cracks, the growth rate is independent of the crack length, whereas for mechanically short cracks it also depends on the crack length. The relations can be written as:

$$\frac{da}{dN} = 6.4\cdot 10^{-4}\left(\Delta\varepsilon_{pl}\right)^{0.76}\cdot\left[1+\left(a/a_t\right)^{\beta}\right] \tag{5}$$

The transition crack length, a_t, depends on the plastic strain amplitude. For $\Delta\varepsilon_{pl} \approx 0.1\%$, a_t is about 100 μm [12]. The parameter, β, depends on the plastic strain amplitude and the strain history under variable loading, and values between 1 and 2 were reported in [14]. The relation with crack propagation rate proportional to the crack length ($\beta = 1$) is in agreement with the short crack equation proposed by Tomkins [15]. The validity of Eq 5 depends on the loading and material data but can typically be applied for cracks of order 1 mm [16,17,14].

For long cracks, fracture mechanics models are invoked. Under small scale yielding situations, the Paris law is conventionally used to correlate the crack growth rate with the stress intensity factor range:

$$da/dN = C_K\left(\Delta K_{eff}\right)^{m_K} \tag{6}$$

The subscript "eff" stands for "effective" and denotes that only part the variation of the crack growth parameter when the crack remains open should be accounted for as first proposed by Elber [18]. Test data for the Paris' law parameters have been reported in the literature [e.g., 19,20]. In large-scale yielding situations it has been found that crack propagation rate can be related to the energy based cyclic J-integral, ΔJ_{eff} [21], as well as the cyclic crack tip opening displacement ($\Delta CTOD_{eff}$) [22]:

$$\begin{aligned}\frac{da}{dN} &= C_{CTOD}\left(\Delta CTOD_{eff}\right)^{m_{CTOD}},\\ \frac{da}{dN} &= C_J\left(\Delta J\right)^{m_J}.\end{aligned} \tag{7}$$

Calculation of the cyclic J-integral is not straightforward for complex loadings and geometries; furthermore it is difficult to account for crack closure effects. The *CTOD* parameter requires detailed modelling of the crack tip deformation but is more straightforward to compute in more general situations. It also has the advantage that, at least theoretically, crack closure effects can be accounted for. For these reasons it is favored for the present application. To compare the large and small-scale yielding crack growth parameters, the elastic ΔK is related to

$\Delta CTOD$ as follows. Firstly, the $CTOD$ can be related to J for a power-law hardening material [23] by:

$$CTOD = \frac{d_n \cdot J}{\sigma_0} \tag{8}$$

Here, σ_0 is the yield stress, d_n depends on the hardening and the ratio E/σ_0, and $CTOD$ itself is defined as the crack opening at the 90° line [23] (Fig. 7). Secondly, under small-scale yielding and plain strain situation, the J-integral and the stress intensity factor are related through

$$J = (1-\nu^2)K^2/E \tag{9}$$

which holds for cyclic as well as monotonic loading.

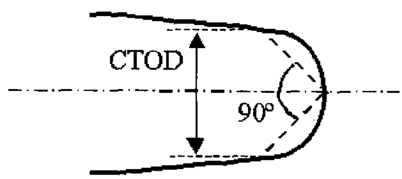

FIG. 7—*Definition of CTOD at 90° the intersection line.*

With the cyclic plasticity material model, $\Delta CTOD$ is computed directly from the crack opening profile given by the FE analysis, whereby $CTOD$ and $\Delta CTOD$ are taken as the maximum range of $CTOD$ during a cycle. In the elastic model, $\Delta CTOD$ is computed via Eq 8 with J-integral value directly from ABAQUS. Thus:

$$\begin{cases} \Delta CTOD_{EPFM} = CTOD_{EPFM}^{\max} - CTOD_{EPFM}^{\min} \\ \Delta CTOD_{LEFM} = d_n \Delta J_{LEFM}/\sigma_0 = d_n (J_{LEFM}^{\max} - J_{LEFM}^{\min})/\sigma_0 \end{cases} \tag{10}$$

For what concerns closure effects, no contact analysis is done, but the computed CTOD and J are set to zero if the computed crack opening close to the crack tip is negative. The d_n values are determined from the normalized curves given in [23] and the power-law hardening stress-strain relation (Eq 4).

Results

Test Results

Four specimens have been tested so far and are referred to as TF0, TF1, TF2, and TF3. The thermal loading and the results are summarized in Table 2. The first specimen, TF0, had a circumferential notch on the outside with a depth of 1 mm and was used as an initial exploratory test while waiting for the unnotched specimens to be machined. The other three specimens had no notch. The notched specimen was exposed to three different thermal loadings, whereas the thermal loading for each unnotched specimen was constant. The specimen TF1 was tested up to 55 600 cycles without any intermittent stops.

The surface replica technique was used to determine crack initiation. For all the specimens, cracking was obtained at the inner surface. The cracking was characterized by a large number of cracks arranged in a network. Figure 8 shows the surface replicas for the specimen TF1 before cyclic loading and after 55 600 cycles. The fourth specimen, TF3, has accumulated 20 000 cycles with evidence of surface cracking from replica and X-ray. Overall, it is noted that there is some ambiguity concerning the detection of crack initiation and its physical interpretation. In cyclic thermal shock loading, the first damage usually appears as formation of persistent slip bands from which micro-cracks are initiated. The surface replicas are taken when the specimen is unloaded. Closed surface cracks or internal cracks therefore may not be noticed.

TABLE 2—*Thermal fatigue test summary*

Test	t_{Quench} (s)	T_{Heat} (s)	T_{max} (°C)	T_{water} (°C)	Cyclic Range of First Damage (indicated by replica or X-ray)	Cycles Done	Crack Propagation
TF0	11	14	300	25	...	5000	Failure after application of external load
	6	44	300	25	...	20 000	50 kN after 52 500 cycles in total
	6	49	400	25	20 000–27 500	27 500	
TF1	6	44	300	25	0–55 600	151 000	See Table 3
TF2	6	49	400	25	14 700–20 000	47 000	Axial crack with maximum depth 5mm
TF3	6	44	350	25	15 000–20 000	25 000	Several merged shallow cracks

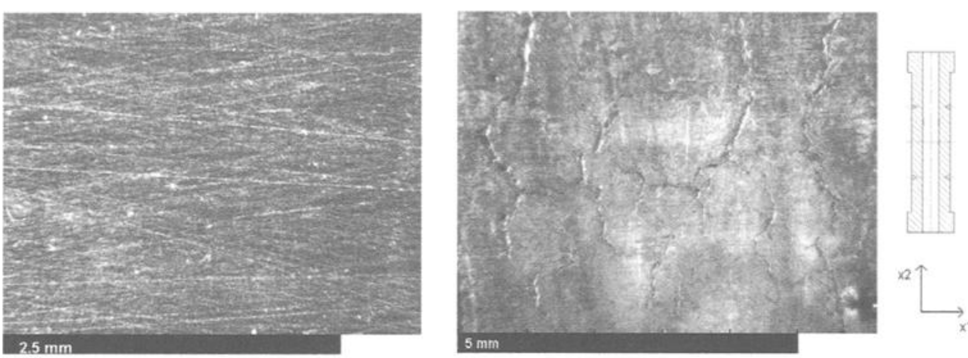

a) b)

FIG. 8—*Replicas of cracking at inner surface of specimen TF11* a) *before cycling and* b) *at 55 600 cycles.*

To assess the crack depth of specimen TF1 when first cracking was detected by the replica technique, TOFD measurements with a sizing tolerance of ±0.5 mm were made. Five cracks were found with a depth of more than 1.5 mm.

The location and direction of the cracks are given in Fig. 9, and the estimated depths after 55 600 and 70 000 cycles are given in Table 3. Only the largest circumferential one (defect ID 1) showed detectable growth, with an increase of crack depth from 2.2–3 mm but with no circumferential extension. However, a relatively large number of new small axial defects (< 1 mm) were also found. The specimen TF2 was also analyzed by the TOFD technique after 20 000 cycles. It had two cracks in the axial and one in the circumferential direction with depths of about 1 mm, but more importantly a large axial crack with an estimated maximum depth of 5 mm and length of at least 80 mm. The tests on specimens TF1, TF2, and also TF3 will be continued with intermittent TOFD measurements to follow the crack growth.

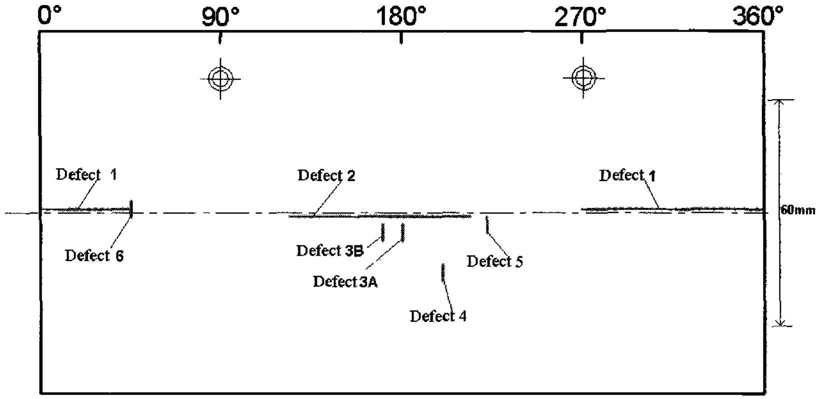

FIG. 9—*Orientation, location, and length of defects in TF1 after 55 600 from TOFD measurements.*

TABLE 3—*Crack depths on specimen TF1 from TOFD measurements.*

Defect ID	Type	Depth			Length	
		55.6 kcycles	70 kcycles	151 kcycles	55.6 kcycles	70 kcycles
1	Circumf.	2.2 mm	3 mm	3.3 mm	135°	135°
2	Circumf.	1.8 mm	1.8 mm	3.3 mm	90°	90°
3A	Axial	1.7 mm	1.7 mm	3.1 mm	5–10 mm	5–10 mm
3B	Axial	1.7 mm	1.7 mm	*	5–10 mm	5–10 mm
4	Axial	0.9 mm	0.9 mm	*	5–10 mm	5–10 mm
5	Axial	2.0 mm	2.0 mm	3.9 mm	5–10 mm	5–10 mm
6	Axial	1.7 mm	1.7 mm	3.3 mm	5–10 mm	5–10 mm

*The welded thermocouples on the specimen decrease the area to inspect.

For the notched specimen TF0, cracking was detected at the bore by replicas after 52 000 cycles (25 000 and 27 000 with T_{max} = 300°C and 400°C, respectively). An axial load (50 kN) was then applied to accelerate their propagation, and the entire specimen failed after a few more cycles. The fracture surfaces are shown in Fig. 10. There is a distinct change in the fracture surface appearance at 4 mm depth. The outer part had a much finer fracture surface than the inner. The outer also showed a pattern of striations indicating that the main crack had initiated from the notch on the outer surface and propagated toward the inner surface. But there was also the typical crack network of multiple cracks at the inner surface.

Stress and Strain Analysis

The coupled thermal-stress analysis was performed for a number of T_{max} values using both the elastic and cyclic-plasticity material models. Figure 11 shows the variation of the computed axial stress and axial plastic strain at the inner surface during several thermal cycles using the cyclic-plasticity model. The model predicts plastic shakedown, and a stabilized state is attained after seven cycles. The hoop and axial stress components are virtually identical, whereas for the plastic strain the amplitudes were essentially identical but with a slightly lower mean strain for hoop component. Figure 12 depicts the through-thickness distribution of the range and mean value of the axial plastic strain at the stabilized cycle for different T_{max} values.

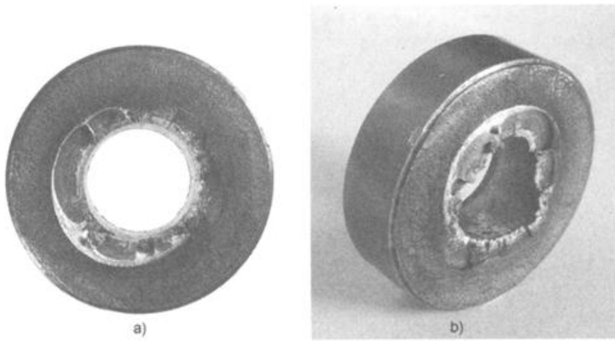

FIG. 10—*Fracture surfaces of the notched specimen, TF0, after failure.*

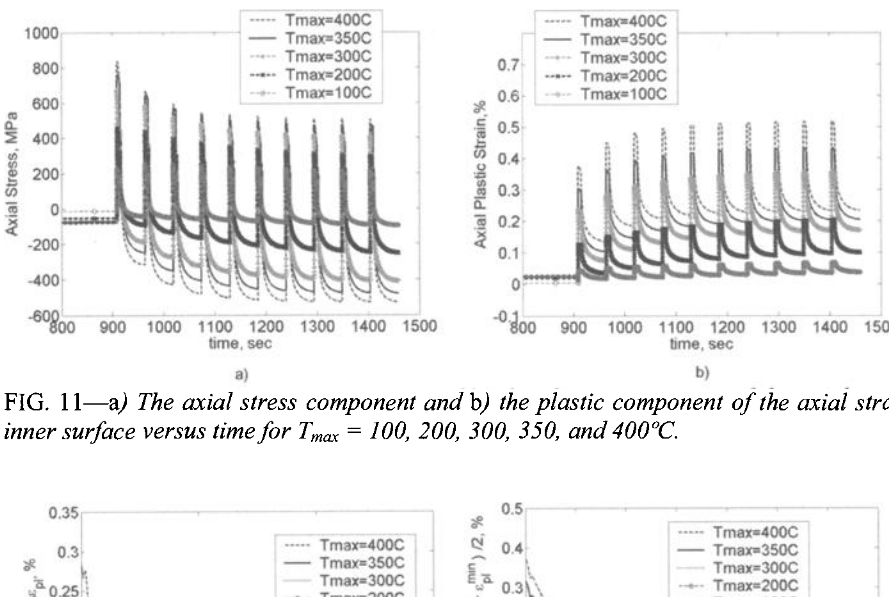

FIG. 11—a) *The axial stress component and* b) *the plastic component of the axial strain at the inner surface versus time for T_{max} = 100, 200, 300, 350, and 400°C.*

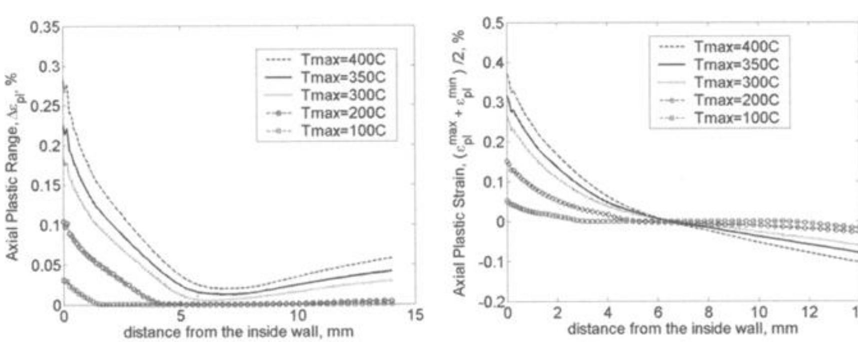

FIG. 12—*Computed distributions of* a) *the axial plastic strain range* ($\Delta\varepsilon_{pl} = \varepsilon_{pl}^{\max} - \varepsilon_{pl}^{\min}$) *and* b) *the mean value of the plastic axial strain* $\left(\varepsilon_{pl}^{\max} + \varepsilon_{pl}^{\min}\right)/2$ *for stabilized cycles at different T_{max} values.*

Crack Initiation and Propagation

Crack initiation is a very complex process, and the actual initiation can be defined in various ways. From an engineering point-of-view, the Coffin-Manson ($N \cdot \Delta\varepsilon_{pl}^{\beta} = const$) and Basquin ($N \cdot \Delta\sigma^{\alpha} = const$) laws are natural candidates for low and high cycle fatigue, respectively, using the cyclic strain and stress variation at the surface. Figure 13 compares experimental and literature data for cyclic plastic strain range versus cycles to failure. The continuous lines correspond to the RCC-MR mean curves. The fraction of the fatigue life spent in the initiation phase generally increases with lower strains. Tests on 316L indicate that the initiation phase is 5 %, 60 %, and 90 % for 10^3, 10^4, and 10^5 cycles to failure, respectively [10].

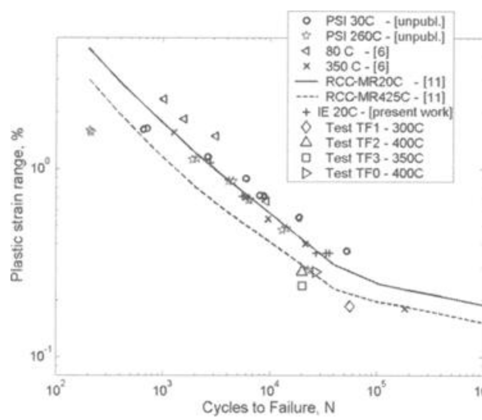

FIG. 13—*Experimental fatigue failure data, the mean RCC-MR curves, and initiation results of the present tests.*

The values from the present test series (with number of cycles to detection of surface cracking by replica and the local plastic strain range from FE-analysis) are also plotted in Fig. 13. The results indicate that the initiation life can be reasonably well predicted by the 'initiation corrected' curves for the high ΔT tests, whereas for the lower ΔT test initiation occurs earlier than expected.

If crack initiation is defined as a specific short crack length, then the short crack models given by Eq 5 can be used to determine the duration of the crack initiation phase. Figure 14*a* shows the crack depth versus the number of cycles for three different temperatures with $\beta = 1$ and 2, and $a_t = 0.1$ mm. The depth has been calculated by direct integration of Eq 5 with the axial plastic strain component as reported in Fig. 12. By virtue of the constant crack propagation rate for very short cracks, there is no need to define an initial defect size. The transition length is the natural choice to define initiation. It follows from Fig. 14*a* that the initiation phase is about 17 000, 24 000, and 37 000 cycles when $T_{max} = 400$, 300, and 200°C, respectively.

Figure 14*b* shows the computed crack depth for a circumferential and axial crack at $T_{max} =$ 400, 300, and 200°C and where the hoop component of plastic strain range has been used to describe the circumferential crack growth. The results are practically identical since the loading is equi-biaxial; this correlates well with the experimental observation of cracks in both directions.

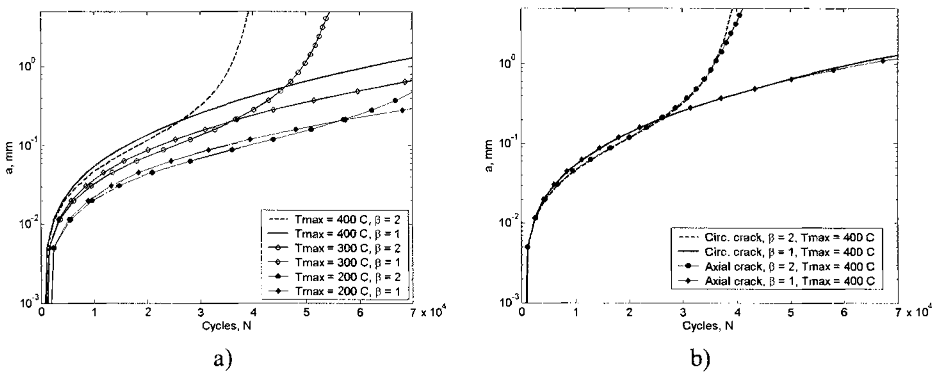

FIG. 14—*Computed crack depth versus number of cycles using short crack model with $\beta = 1$ and 2:* a) *Circumf. crack T_{max} = 200, 300, and 400°C and b) Circumf. and axial crack T_{max} = 400°C.*

Cracked body FE analyses were performed to determine propagation of long cracks following the procedure. The analyses were done for a fully circumferential crack with the mesh illustrated in Fig. 3 and with a crack depth *a* ranging from 0.5–10 mm. Both elastic and cyclic-plasticity models were considered to allow the extent of large-scale yielding effects to be assessed. Figure 15*a* shows the computed *ΔCTOD* versus crack depth for the elastic and cyclic plasticity material models and for T_{max} values of 400 and 300°C, respectively. The crack opening displacement is higher in the elastic case because the test is essentially strain controlled. As expected, the plasticity effects decrease with increasing crack length after a peak value has been attained and with the applied thermal load. In the plastic model, the crack tip remains open by virtue of crack tip blunting during the entire cycle, whereas in the elastic case it approaches zero at the end of the heating phase of the cycle when the stresses are compressive at the inner surface. The maximum *CTOD* was therefore higher for the plastic case, although the cyclic *ΔCTOD* was lower.

Figure 15*b* shows the corresponding predicted crack growth rate using a Paris law calibrated with 316L fatigue data [19,20] ($m_K = 3.89$ and $C_K = 2.67 \cdot 10^{-10}$ with *ΔK* and *da/dN* in MPa and mm/cycle, respectively). The elastic analysis used the Paris law (Eq 6) directly with *ΔK* computed from the elastic *ΔJ* as defined by Eq 9. The plastic analysis used the same growth law but with the parameter ΔK_{CTOD} from Eqs 7 and 8,

$$\Delta K_{CTOD} = \sqrt{\frac{\sigma_0 \cdot \Delta CTOD_{EPFM} \cdot E}{d_n(1-\nu^2)}} \tag{11}$$

With this approach the crack growth rate reduces to the elastic case for small-scale yielding while providing a means of extending the Paris law into the large-scale yielding regime. The crack propagation rate using the short crack formula (Eq 5) with axial plastic strain range as given in Fig. 12, with $\beta = 1$ and 2 is also shown in Fig. 15*b*. With $\beta = 1$ it predicts a crack growth rate trend, which is a factor 10 lower than that given by the axisymmetrical long crack model. Since the short crack model is empirical and relates to cracks that are small in depth and length, it is therefore not surprising that the calculated growth rate is substantially smaller than that for a complete axisymmetric crack of the same depth. Further, the present long crack model does not consider premature contact behind a propagating crack tip that may lower the effective *ΔCTOD* and hence lower the growth rate.

Concerning the experimental validation of these growth rate models, only a limited amount of data is available at this point. The TOFD analysis indicates that for specimen TF1 one crack grew from 2.2 to 3 mm in the interval from 56 000–70 000 cycles, and that in specimen TF2 an axial crack had grown to 5 mm in 20 000 cycles. The number of cycles for these crack extensions as estimated by integration of the short crack model (Eq 5) is shown in Fig. 14 for $\beta=$ 1 and 2 with $a_t = 0.1$; the results are summarized in Table 4.

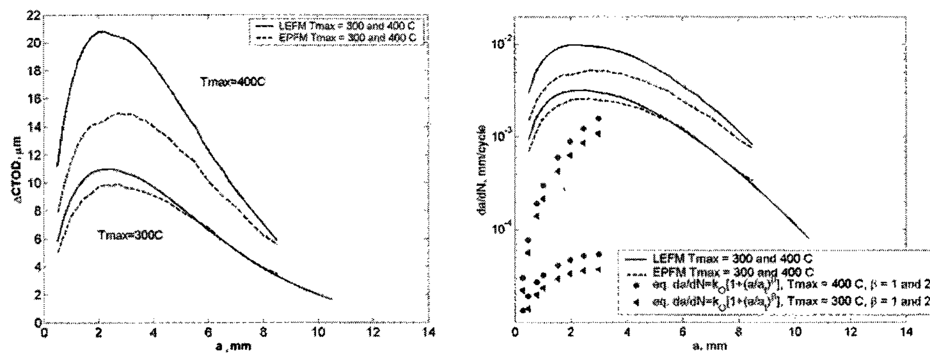

a) b)

FIG. 15—a) *Computed crack tip opening displacement at T_{max} = 300 and 400°C for an axisymmetrical defect using elastic and cyclic-plasticity model;* b) *comparison of the computed crack growth rate for axisymmetrical defect using the Paris law and that determined by short crack model given by Eq 5.*

TABLE 4—*Computed number of cycles for four crack propagation scenarios using short crack model a_t=0.1mm and β=1 and 2 and corresponding measured values.*

TEST #	a_{start} (mm)	a_{stop} (mm)	Crack Type	Predicted Cycles $a_t = 0.1$ $\beta=1$	Predicted Cycles $a_t = 0.1$ $\beta=2$	Exp. Cycles
TF1 (300°C)	0	2.2	Circ. ID 1	125 000	52 000	55 600
TF1 (300°C)	2.2	3	Circ. ID1	20 300	820	14 400
TF2 (400°C)	0	5	Axial ID 4	140 800	39 200	20 000
TF2 (400°C)*	0.1	5	Axial ID 4	123 600	21 469	20 000

*Assuming an initial crack of 0.1 mm at the start of the test.

The first phase of the crack growth follows better the $\beta=$ 2 model, whereas the subsequent growth is better described by the β=1 model. The deviation in crack growth using the upper and lower bound values of the crack model parameters are obvious in Fig. 14. The apparent inconsistency is not really unexpected since the model is being extrapolated well beyond the 1 mm for which it was originally verified.

The notched specimen, TF0, failed after application of the small 50 kN load. From the fracture surfaces (Fig. 10), the conjecture is that a crack had initiated from the notch and propagated through most of the thickness when failure occurred. It is known that cracks may initiate at notches under cyclic compressive loads due to reversed tensile stresses ahead of the notch, but then they usually arrest [24]. To assess whether crack extension could be supported by fracture analyses, elastic and cyclic-plastic models were performed with an axisymmetric crack starting from the outside. In the cyclic plastic model the crack remains closed during the entire cycle, whereas the elastic model predicts that the crack opens during the heating and ΔK increases from 5 to 10 $MPa\sqrt{m}$ when the crack depth increases from 2 to 6 mm. The corresponding crack growth rate from Paris law (Eq 6) is, however, only $1 \cdot 10^{-7}$ and $2.3 \cdot 10^{-6}$ mm/cycle. Such a model therefore cannot explain fatigue crack growth from the notch. The plastic strain variation at the outer surface is 0.06 %, which gives a crack growth rate of $2.6 \cdot 10^{-4}$ mm/cycle for a 2 mm crack for the short crack model. The short crack model, however, should not be used for compression loading.

An alternative scenario is that the cracks propagated from the inner surface until an approximately axisymmetric crack formed and the specimen failed. The border between the distinctly different fracture surfaces in Fig. 10 is about 4 mm from the inner surface. The computed maximum stress intensity factor in the elastic analysis was $73\ MPa\sqrt{m}$. In the plastic analysis, the maximum 'plastic stress intensity factor' calculated from Eq 11 using the maximum computed *CTOD* is $117\ MPa\sqrt{m}$. This should be compared with the static fracture toughness, K_{IC}, which is typically $100\ MPa\sqrt{m}$ for 316 steel [25]. Thus, from the analysis an unstable crack propagation from a circumferential crack depth of 4 mm would be possible.

Concluding Remarks

- A thermal fatigue rig has been developed to produce crack initiation and propagation at the inner surface of tubular test pieces under controlled temperature down shocks. At periodic stops, replica and X-ray measurements are made to check for crack initiation and the distribution of surface damage. The growth of such a crack is followed subsequently using ultrasound time-of-flight-diffraction measurements. The development of cracking takes place in three stages. First, a network of surface cracks develops. A few cracks (typically 10 and axial as well as circumferential) propagate to a depth of 1 mm in the tests. One or two of these become dominant and may reach sufficient depth to cause failure of the component.
- The surface replica is a good technique to map the surface cracking, but it proved difficult to detect very shallow cracks. The TOFD measurements offer significant advantages for monitoring crack propagation under complex thermal fatigue loading because it can locate and size multiple cracking sites.
- Predictions of the number of cycles to produce surface cracking detectable by replicas based on low cycle fatigue data and the FE-computed plastic strain range are in reasonable agreement with the experimental data.
- The short crack strain-based model together with a specified initiation crack depth a_i of 0.1 mm appears to predict initiation life.

- Comparison of the predicted thermal fatigue crack growth rates according to the short crack growth model and a long crack (fracture mechanics) model for a fully circumferential crack indicate up to an order of magnitude difference, with the latter the more conservative. To date, very limited TOFD crack measurement data are available for the thermal fatigue specimens. The short crack strain-based model underestimates the initial crack growth, but the subsequent development appears to follow the $\beta = 1$ model trend for cracks up to 3 mm deep. The transition between initiation, short, and long crack propagation needs to be established. Three-dimensional crack models and incorporation of crack closure effects are expected to improve understanding of thermal fatigue crack growth in this regard.

Acknowledgments

The authors would like to acknowledge the staff at the Institute of Energy that have contributed to the experimental work and Mikael Melbi, WesDyne TRC, Sweden, who performed the TOFD analyses. One of the authors (EP) gratefully acknowledges the support of European Commission for its study grant and the University of Wales, Swansea, at which she is a registered doctoral student.

References

[1] "Experience with Thermal Fatigue in LWR Piping Caused by Mixing and Stratification," *Specialist Meeting, NEA/CSNI/R(98)8,* OECD Nuclear Energy Agency, June 1998, Paris.

[2] Hayashi, M., "Thermal Fatigue Strength of Type 304 Stainless Steel in Simulated BWR Environment," *Nucl. Engng Design*, Vol. 184, 1998, pp. 135–144.

[3] Kerezi, B., Price, J. W. H., and Ibrahim, R., "A Two-Stage Model for Predicting Crack Growth Due to Repeated Thermal Shock," *Engng Fracture Mech.*, Vol. 70, 2003, pp. 721–730.

[4] Fissolo A., Marini, B., Nais, G., and Wident, P., "Thermal Fatigue Behaviour for a 316L Type Steel," *J. Nucl. Mat.*, Vols. 233–237, 1996, pp. 156–161.

[5] Skelton, R. F., "Growth of Short Cracks During High Strain Fatigue and Thermal Cycling," *Low-Cycle Fatigue and Life Prediction, ASTM STP 770*, Z. Amzallag, B. N. Neis, and P. Rabbe, Eds., ASTM International, West Conshohocken, PA, 1982, pp. 337–381.

[6] Kerr, D. C., "An Investigation of Fatigue Crack Growth in Thermally Cycled Components," *Ph.D. Thesis*, Univ. of Glasgow, 1993.

[7] Gandossi, L., "Crack Growth Behaviour in Austenitic Stainless Steel Components under Combined Thermal Fatigue and Creep Loading," *Ph.D. Thesis*, University of Swansea, 2000.

[8] Holman, J. P., *Heat Transfer*, 8th ed., McGraw-Hill Inc., 1997.

[9] Lemaitre, J. and Chaboche, J-L, *Mechanics of Solid Materials*, Cambridge University Press, Cambridge, UK, 1990.

[10] van der Schaaf, B. and van Hoepen, J., *Low-Cycle Fatigue of the European Type 316L Reference Steel for the Net First Wall and Blanket*, ECN-C-92-078, Netherlands Energy Research Foundation, 1992.

[11] "Ensemble de Caractéristiques 1S," *RCC-MR Edition*, May 1993.

[12] Obrtlík, K., Polák, J., Hájek, M., and Vašek, A., "Short Fatigue Crack Behaviour in 316L Stainless Steel," *Int. J. Fatigue*, Vol. 19, 1997, pp. 471–475.

[13] Pólak, J., Obrtlík, K., and Vašek, A., "Short Crack Growth and Fatigue Life in Variable Amplitude Loading of 316L Steel," *Fatigue Design*, VTT, G. Marquis and J. Solin, Eds., Esbo, Finland, 1998.

[14] Vasek, A., Polák, J., and Obrtlík, K., "Fatigue Damage in Two-Step Loading of 316L Steel II Sirt Crack Growth," *Fatigue Fract. Mater. Struct.*, Vol. 19, Nos. 2/3, 1996, pp. 157–163.

[15] Tomkins, B., "Fatigue Crack Propagation: An Analysis," *Phil. Mag.*, Vol. 18, 1968, pp. 1041–1066.

[16] Obrtlík, K., Polák, J., Hájek, M., and Vašek, A., "Short Fatigue Crack Behaviour in 316L Stainless Steel," *Int. J. Fatigue*, Vol. 19, 1997, pp. 471–475.

[17] Pólak, J., Obrtlík, K., and Vasek, A., "Short Crack Growth and Fatigue Life in Variable Amplitude Loading of 316L Steel," *Fatigue Design*, VTT, G. Marquis and J. Solin, Eds., Esbo, Finland, 1998.

[18] Elber W., "Fatigue Crack Closure under Cyclic Tension," *Eng. Fract. Mech.*, Vol. 2, 1970, pp. 37–45.

[19] Huthmann, H. and Picker, C., "Behaviour of Short Fatigue Cracks in Austenitic Stainless Steels," Literature Review, European Commission, Nuclear Science and Technology, EUR 15186.

[20] Maeng, W.-Y. and Kim, M.-H., "Comparative Study on the Fatigue Crack Growth Behavior of 316L and 316LN Stainless Seels; Effect of Microstructure of Cyclic-Plastic Strain Zone at Crack Tip," *J. Nuclear Mat.*, Vol. 282, 2000, pp. 32–39.

[21] Dowling, N. E and Begley, J. A., "Fatigue Crack Growth During Gross Plasticity and the J-Integral, "*Mechanics of Crack Growth, ASTM STP 590*, ASTM International, West Conshohocken, PA, 1976, pp. 82–103.

[22] Tanaka, K., Hoshide, T., Yamada, A., and Taira, S., "Fatigue Crack Propagation in Biaxial Stress Fields," *Fatigue Engng Mat. Structures*, Vol. 2, 1979, pp. 181–194.

[23] Shih, C. F., "Relationships Between the J-Integral and the Crack Opening Displacement for Stationary and Extending Cracks," *J. Mech. Phys. Solids*, Vol. 29, No. 4, 1981, pp. 305–326.

[24] Suresh, S., *Fatigue of Materials*, Cambridge University Press, Cambridge, UK, 1991.

[25] Kang, K. J., Garton, D., and Fleck, N., *Compilation of Fatigue Design Data*, Dept. of Engineering, Univ. of Cambridge, CUED/C/MATS/TR.199, 1992.

Journal of ASTM International, January 2005, Vol. 2, No. 1
Paper ID JAI12004
Available online at www.astm.org

R. Sunder[1]

Effect of Periodic Overloads on Threshold Fatigue Crack Growth in Al-Alloys

ABSTRACT: Experiments were performed on 10 mm thick C(T) specimens cut from Al-alloys to assess fatigue crack growth behavior under periodic overloads by comparison to constant amplitude loading. The tests were performed at a sufficiently high stress ratio to avoid crack closure, whose absence was confirmed from Load-COD response. ΔK_{th} values were determined under these loadings in air, salt water, and vacuum. Even though closure was absent, ΔK_{th} shows a systematic dependence on overload plastic zone ratio. Similar results were obtained in both air and salt water. In vacuum however, near threshold crack growth is accelerated by comparison to no-overload conditions, while higher growth rates see a reversal in this trend. These results appear to support the possibility that residual stress moderates crack-tip surface chemistry in near-threshold fatigue, an effect that ceases in vacuum.

KEYWORDS: crack growth mechanisms, thresholds, residual stress effect, crack closure, periodic overloads, environmental action

Introduction

The significance of near-threshold fatigue is underscored by its direct impact on durability. Predictive analyses use threshold stress intensity factor, ΔK_{th}, as a measure of near-threshold fatigue behavior. ASTM E 647 describes a recommended practice for its measurement. As explained by Miller [1], ΔK_{th} thus determined is associated with linear elastic fracture mechanics (LEFM) conditions. Conditions not covered by the standard include short crack effects and variable amplitude fatigue.

Crack growth prediction models generally assume that ΔK_{th} obtained under constant amplitude conditions may be used in fatigue crack growth predictions under spectrum loading [2]. ΔK_{th} is treated as a material constant, and it is accepted that as long as ΔK is suitably corrected for load history and stress ratio, crack extension per cycle will follow from the growth rate equation obtained from correlation of constant amplitude data.

ΔK_{th} decreases with increasing stress ratio, an effect often attributed to crack closure [3]. Another way of looking at the same relationship is in terms of the dependence of ΔK_{th} on maximum stress intensity, K_{max}. Sadananda et al. observe that there exists a certain K_{max}, beyond which ΔK_{th} will remain constant [4]. This interpretation is part of their rationale that ΔK and K_{max} are sufficient similitude criteria to cause similar crack growth rate.

Assuming that the ΔK_{th} versus K_{max} relationship is driven by crack closure, it would indeed follow that beyond a certain K_{max} (or stress ratio, R), the crack may remain fully open, thereby leading to growth rate uniquely related to ΔK. If ΔK_{th} depends on R or K_{max}, it can no longer be treated as a constant. Then, one may search for a certain "minimum" ΔK_{th}, referred to as $\Delta K_{th,min}$,

Manuscript received 17 November 2003; accepted for publication 6 April 2004; published January 2005. Presented at ASTM Symposium on Fatigue and Fracture Mechanics: 34th Volume on 19–21 November 2003 in Tampa, FL; S.R. Daniewicz, J.C. Newman, Jr., and K-H. Schwalbe, Guest Editors.
[1] BiSS Research, 41A, 1stA Cross, AECS 2nd Stage, Bangalore 560 094, India.

obviously associated with a fully open crack, to serve as a conservative material constant. A convenient experimental method to determine $\Delta K_{th,min}$ is by holding K_{max} = Const. at a value that is sufficiently high to ensure a fully open crack [5].

More recently, Lang and Marci proposed the so-called "K_{PR}" concept in an attempt to explain load interaction effects, some of which cannot be explained by crack closure [6]. K_{PR} is defined as a stress intensity level that must be exceeded for a crack to grow in fatigue. K_{PR} at a given crack size is estimated by applying fatigue cycles of $\Delta K_{th,min}$ magnitude at progressively increasing K_{min} to a point when the fatigue crack begins to grow. K_{min} at this point is treated as K_{PR}.

K_{PR} is determined on the assumption that closure-free ΔK_{th} is a material constant. This assumption is rendered questionable by evidence from different materials indicating substantive near-threshold retardation effects under closure-free conditions [7–9].

Previous work has indicated that moderation of environmental action may be a major operative mechanism of residual stress in fatigue [8,9]. Near-tip hydrostatic stress superposed on residual stress can determine the extent to which environment embrittles the fatigue crack tip. There is potential for both ΔK_{th} as well as near-threshold crack growth to be thus affected. The present study focuses on this possibility through experiments designed to avoid crack closure as a potential variable.

Experimental Procedure

Sensitivity of ΔK_{th} to load history can be investigated using periodic overloads of controlled magnitude. A systematic study using this procedure is described in [7]. Our testing was similar but restricted to higher stress ratio in order to eliminate the potential for closure related retardation. For the same reason, applied overload ratio was restricted to 50 %. This is much less than the magnitudes typically used in experiments on overload-induced retardation. Also, overload cycles carried reduced minimum load that was designed to act as a wake-suppressing under-load to preclude closure.

The experiments were performed on 10 mm thick, 40 mm wide C(T) specimens cut with L-T orientation from 7075-T7351 Al-Cu-Zn alloy plate stock. Some experiments were repeated on similar size specimens cut from Al-Cu alloy 2124-T851 (da/dN tests) and 2014-T6511 (threshold tests) cut from plate stock. Most tests were performed under uncontrolled ambient conditions with temperature varying from 23–28°C and relative humidity 72–85 %. A few threshold tests were performed with the specimen submerged in 3 % solution of NaCl (common salt) in distilled water. Also, some crack growth tests were performed in vacuum.

Two types of test programs were used. One was threshold testing at K_{max} = Const., with exponential decrease in ΔK (as described in ASTM E 647) using decay constant, α, in the range ($-0.15 < \alpha <= -0.08$ 1/mm) to estimate ΔK_{th}, and the other was to determine the da/dN versus ΔK relationship (da/dN tests). K_{max} was held constant at values ranging from 5–15 MPa$\sqrt{m}$. The threshold tests used baseline cycling at frequency ranging from 50–100 Hz with two or three periodic overload cycles applied at 1–3 Hz. During pre-cracking and in the da/dN tests, baseline cycling was in the range 30–50 Hz. Load versus COD data from clip gauge mounted on the specimen edge were recorded during the overload cycles in order to track potential non-linearity associated with crack closure.

Initial overload periodicity was set to 2000 cycles. The application software would suitably extend the baseline cycle interval up to 10 000 cycles with approaching threshold conditions.

Thus, at K_{max} = 10 MPa$\sqrt{m}$ (plastic zone size approximately 0.15 mm) and da/dN = 10^{-6} mm/cycle, overloads will repeat about seven times before the crack tip traverses a given plastic zone. As the growth rates drops further, overloads will repeat more often within a plastic zone, thereby providing the option of increasing cycle interval between overloads. The goal was to obtain sustained overload-induced near-tip residual stresses, conservative threshold estimates with negligible overload-induced crack extension. Threshold was estimated to be associated with 150 000 cycles of no detectable growth. The test software ignored computed crack increment less than 0.005 mm.

Test Automation

All the tests were performed on a 5 kN servo-hydraulic load frame equipped with a BiSS 2350 digital signal processor (DSP) control system. Adaptive control algorithm on the DSP ensured precision fatigue cycling to within 2 % of assigned range and mean. Peak-valley statistics were continuously monitored by the host application and recorded at each crack increment. The software was set to abort testing in the event of inadvertent overload exceeding 5 % of required range. Overload cycle magnitude was controlled through supervisory adaptive control implemented on the host computer. With progression of testing, overload error margins settled to within a few Newtons, or less than 0.5 % of applied range.

Uninterrupted Testing

The hydraulic pump was driven by a servo-controlled variable frequency drive to conserve energy and avoid forced oil cooling. A back-up power generator with accumulator charge on the hydraulics along with uninterrupted main power to the electronics ensured continuous and unattended testing of indefinite duration. Typical test duration was about 3–4 days, with some tests running as long as one week.

Testing in Salt Water

The tests in 3 % common salt solution were performed with the desktop load frame in a horizontal position. Water level in the bath was sufficient to submerge the specimen from crack size a/W > 0.2, but the loading pins and COD gauge were left dry. No attempt was made to circulate the water, though a cotton wick was left at the notch to wet the notch area. The solution was periodically topped off with distilled water to compensate for evaporative loss.

Vacuum Testing

Testing in vacuum was performed using a transparent Perspex cylindrical chamber capped by stainless steel disks. The lower cap is mounted through bellows to the actuator end. Vacuum induced load cell readout of about 150 N was tared at the commencement of testing. Vacuum level was maintained at 10^{-5} torr or less. In order to avoid chamber vibration leading to leakage and potential error in load readout due to inertia component, vacuum test frequency was restricted to 50 Hz. Comparative tests in air were also performed at the same frequency.

Crack Size Measurements

Crack size was estimated from unloading compliance using functions described in ASTM E 647. The procedure for crack size estimates used a statistical sample of five unloading compliance measurements from a data window covering 50–95 % of maximum load. A polynomial fit of these measurements against cycle count was used to derive weighted measurement that would account for potential growth between successive measurements as well as scatter. Estimates indicating reduction in crack size were ignored. The latest compliance measurement would replace the earliest measurement in the statistical sample. However, if the latest measurement were to be less than the previous one, it would replace the latter on the consideration that the latter may have been exaggerated.

Whenever the statistical sample indicated an increment in excess of 0.005 mm, the readout along with other relevant parameters including cycle-count, stress intensities, load error statistics, and the complete digitized Load-COD trace over the overload cycles was recorded for post processing. The latest crack estimate, updated crack size, and compliance readouts from the current statistical sample were continuously on display for visual assessment of the quality of measurements.

Repeat measurements showed a scatter of up to ±0.07 mm at $a/W \sim 0.25$, with progressive decrease in scatter down to ±0.02 mm at $a/W > 0.5$. However, crack size estimates were sometimes distorted by jumps in load level associated with switch from one step to another in threshold testing. Typically, a 50 % increase in load level would cause an immediate *reduction* of up to 0.5 mm in estimated crack size, particularly at lower a/W. This margin appeared to reduce to negligible proportions at $a/W > 0.5$. As a consequence of the above algorithm, crack growth would *appear* to be arrested for some time. This did not affect ΔK_{th} because consistency in crack size measurements is restored several millimeters before crack arrest as the effect of abrupt change in load level wears off after crack increment by a margin equal to the above mentioned error.

COD ranging and balance were unchanged from the commencement of testing, right up to failure. Also, no attempt was made to re-position the specimen or COD gauge in the course of the test, as this has been known to change crack size estimates. To keep clevis pin-induced frictional component minimal, greased undersize pins with about 1.5 mm clearance fit were used. These features, combined with CNC wire-cut knife-edge profiles on the specimens, were intended to ensure stable Load versus COD output throughout the test.

Step-to-step changes in test program starting from pre-cracking to the conclusion by crack arrest of individual threshold steps is marked on many fractures with excellent clarity of associated crack fronts on the fracture surface (see Fig. 1). Digital micrographs of such fractures permitted cross-verification of test measurements and invariably indicated that estimates were well within 0.5 mm of actually observed crack sizes. The associated deviation in K was treated as negligible. As these were systematic errors covering a large interval of crack growth, their effect on growth rate estimates also was ignored.

The above test procedure was intended to improve reproducibility of results, given the sensitivity of near-threshold fatigue crack growth data to the accuracy of fatigue loading, potential effect of even minor unintended overloads, hold times, and shut downs.

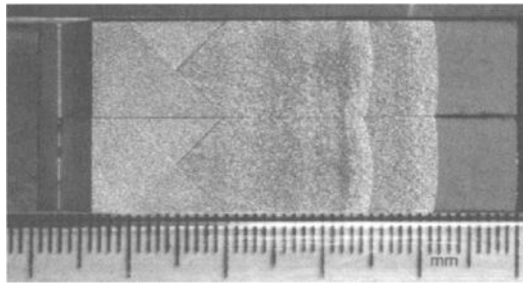

FIG. 1—*Fracture surface halves from multiple threshold test on 7075-T7351 B10/W40 C(T) specimen. Crack size estimates can be readily verified against clearly distinguishable beach marks.*

Test Results

Threshold Stress Intensity

Figure 2 summarizes baseline (no overload) threshold data from different 7075-T7351 specimens plotted against associated crack size, applied load, stress ratio, and K_{max}. Different symbols indicate different specimens. These data were obtained without application of overloads and at constant K_{max} that led to threshold at R > 0.8.

Figure 2 indicates that in ΔK_{th}, variation is random and independent of crack size, stress ratio, K_{max}, and load levels. Of particular note is the independence of ΔK_{th} from stress ratio, suggesting crack closure was indeed absent. However, a small but noticeable trend is observed in results plotted against K_{max}. It has been suggested that beyond a certain K_{max}, ΔK_{th} = Const. [4]. It is likely that a strong dependence of ΔK_{th} on K_{max} is primarily associated with closure. In the absence of closure, ΔK_{th} may indeed vary little with K_{max}. However, as K_{max} approaches K_{Ic}, an increasing fraction of fatigue may accrue from localized quasi-static crack extension. This may indeed be the trend seen when ΔK_{th} is plotted against K_{max}.

Random checks of Load versus COD data indicate that the fatigue crack was fully open during the threshold tests. It will be seen below that this was the case even when periodic overloads were applied.

The plots in Fig. 2 confirm the generally accepted trend of ΔK_{th} for long cracks being independent of crack size, applied load, K_{max}, and stress ratio (given fully open crack). Overall, the ΔK_{th} data appearing in Fig. 2 suggest that the estimated value may indeed be the lowest associated with a long and fully open crack. Further, it would appear that stringent conditions of uninterrupted testing and tight tolerance on loading error did indeed yield fairly reproducible values of ΔK_{th} ~ 1.1 MP$\sqrt{m}$ within a margin of ±10 %.

Threshold Under Periodic Overloads

Figure 3 summarizes results from threshold tests under periodic overloads. These data are from tests on 2014-T6511 and 7075-T7351. The results are plotted for the two materials as ΔK_{th} versus overload plastic zone ratio, given by the square of overload ratio. This ratio is independent of assumed stress state, and the relationship appears to be approximated by a linear trend line.

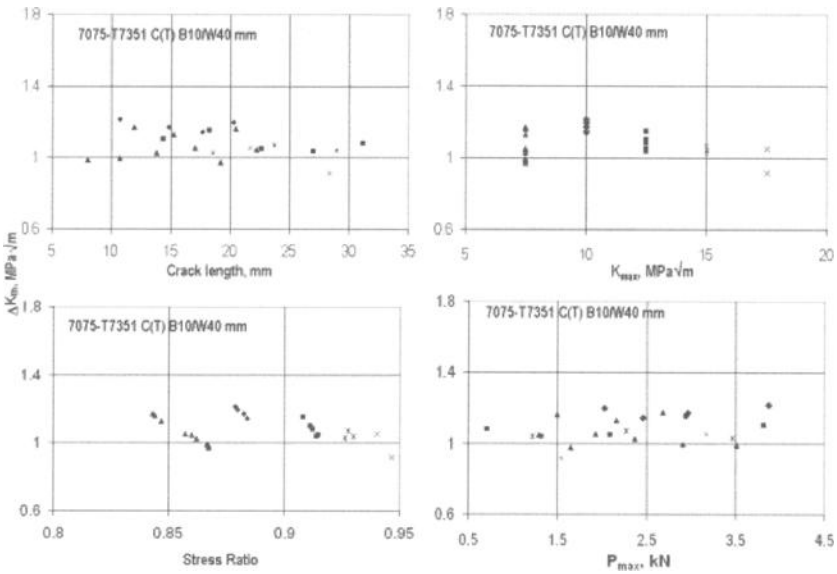

FIG. 2—*Baseline (no overload) threshold data representing 22 measurements from five specimens designated by different symbols. No result was discarded. As expected, the effect of crack size and applied load level appears negligible over the interval studied. The apparent trend when plotted against stress ratio is due to arrangement of scattered readouts obtained at same* K_{max}. *A decreasing trend appears in data plotted against* K_{max}, *suggesting a small, but noticeable effect.*

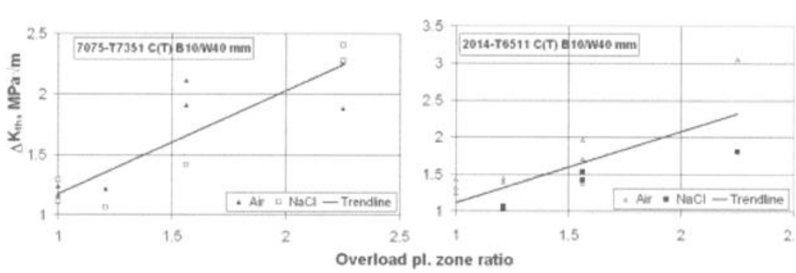

FIG. 3—*Summary of threshold data obtained under* K_{max} = *Const. With periodic application of overloads of 0, 10, 25, and 50 %. Tests on both materials were performed in both air and 3 % common salt solution. Results are plotted against ratio of overload to baseline monotonic plastic zone size. Data for both media fall in the same scatter band. Test frequency in all cases was 50–100 Hz during baseline cycling and 1–3 Hz during overloads. Systematic effect of overload is apparent even though there was no evidence of closure.*

ΔK_{th} in both the Al-Cu and as Al-Cu-Zn alloy shows similar sensitivity to periodic overloads. Further, both materials appear insensitive to the change in test medium, with data for both air and salt water falling in the same band, just as in the case of data in Fig. 2 for constant amplitude loading. This may come as a surprise particularly in the case of 7075-T7351 that is known to be susceptible to corrosion. Accelerated fatigue in these materials is attributed to hydrogen activity [10]. Both atmospheric humidity and saltwater solution serve as hydrogen sources. It has been shown [11] that for every test frequency there is a threshold partial pressure of water vapor at which crack growth rate can change by about one order of magnitude. It is likely that at the 50–100 Hz frequency used in our tests, both air and salt water induced conditions that lie on the same side of this threshold partial pressure.

Figure 4 shows fractures from 2014-T6511 tested in air and 3 % common salt solution under identical multiple threshold load programs. As already seen in Fig. 1, the fracture from testing in air (Fig. 4, top) shows individual ΔK_{th} test bands, with boundaries marking crack arrest in the previous step. As seen in the last two bands prior to fracture at the right in Fig. 4 (bottom), there is little evidence of environmental attack. The rest of the fracture surface does appear worn by corrosion, but this was clearly due to sustained exposure of the fracture surface, combined with the bearing and micro-rubbing action (due to Mode II component) during cyclic loading. The sides of the specimen submerged in the medium also carried signs of pitting corrosion from the approximately 100 h of exposure. These mechanisms along with inter-granular attack may lower fracture resistance considerably, promote inter-granular stress-corrosion cracking, and perhaps even lower frequency fatigue corrosion. However, these are obviously not the dominant mechanisms driving near-threshold fatigue at 50–100 Hz.

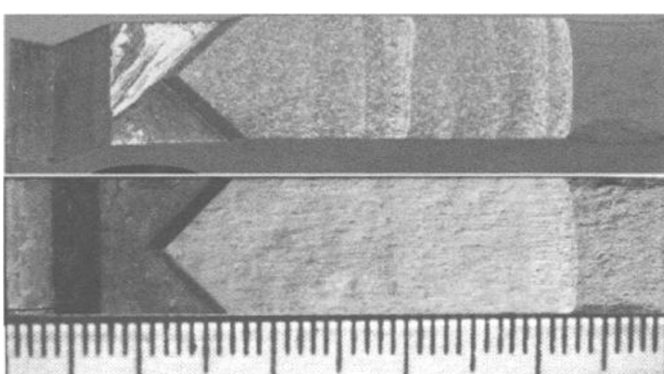

FIG. 4—*2014-T651 fractures obtained under periodic overloads of up to 50 % with decreasing ΔK at K_{max} = Const. Fracture at bottom was from test in 3 % common salt solution in distilled water. Note that the region just prior to fracture at right does not show any sign of corrosion. This suggests that the appearance of the rest of the fracture may be largely due to wear in corrosive medium of the fracture faces.*

Stress Ratio and Load Versus COD

It has been suggested that corrosion products in the wake of the crack can affect threshold through increased closure [12]. To investigate such a possibility, the linearity of Load versus COD curves was investigated by studying the last record associated with each ΔK_{th} estimate. Records for all three materials studied consistently showed no sign of non-linearity over the window of baseline loading, except when minimum load approached the 25 % mark. This should not come as a surprise, as crack arrest at threshold was always associated with high stress ratio.

Previous fractographic measurements of closure in 2014-T6511 and 2024-T351 specimens of similar thickness were of the order of 25–30 % [8,13]. Typical traces from 50 % overload tests in air appear in Fig. 5 (top). A few traces from tests in 3 % salt solution did show some non-linearity at lower load as seen in Fig. 5 (bottom). The two curves at the bottom are from the same test with the one on the left at a/W = 0.3 and the one on the right at a/W = 0.75. Both curves are associated with similar ΔK_{th}, even though they may indicate different closure levels, suggesting that the Load-COD traces were misleading, perhaps because of the influence on them of corrosion debris. When located away from the crack tip, such debris may affect the nature of the Load-COD trace without really changing crack driving force. Near-tip debris may lead to asperity-induced closure [12]. However, very high associated contact stresses may lead to their wear and break down into smaller particles that eventually "flow" to the surface to be seen as characteristic black tell-tale trails that serve airframe inspectors as signs of fatigue cracking. Corrosion products are unlikely to serve as sustained asperities, given the intense cyclic contact stresses associated with their stated action. In previous work, near crack-tip displacement measurements over a gauge length of about 0.01 mm using laser interferometry appeared to provide closure estimates consistent with fractographic measurements [13].

Overload ΔK_{th} is plotted in Fig. 6 against an "effective" stress ratio, R_{eff}. R_{eff} is determined as the ratio of baseline minimum load to overload maximum load. If closure were present, ΔK_{th} would decrease with increasing R_{eff}. Figure 6 indicates the opposite, suggesting closure was indeed absent – even under overloads.

The above evidence precludes closure as a factor in any of the threshold measurements reported above. These include ΔK_{th} estimates made under the influence of periodic overloads of up to 50 % magnitude over baseline K_{max}. Baseline ΔK_{th} values were consistent and reproducible within ±10 % over the range of variation in crack size, load level, and K_{max}. Closure-free ΔK_{th} shows a systematic and apparently linear variation with overload plastic zone ratio.

In the absence of closure, one may attribute increasing threshold fatigue resistance to near-tip residual compressive stress induced by the larger overload plastic zone. This is similar to increasing fatigue limit under the influence of tensile overloads. It has been suggested in related work that residual stresses influence fatigue crack growth by moderating crack tip environmental activity [14].

Crack Growth Rates

Two possibilities follow from the above observations. One is that even in the absence of closure, crack growth under periodic overloads will be retarded. Further, observed trends may change or even disappear in vacuum. Earlier work demonstrated both of these at the microscopic level through electron fractography of an Al-alloy and also of a nickel-base superalloy [9,15]. In an attempt to confirm these possibilities in terms of macroscopically measured growth rate that is of relevance to engineering application, tests were performed at high stress ratio with and without application of periodic overloads. Fatigue pre-cracking in these tests was under high-amplitude, low-R loading. This was followed by a decreasing K segment up to approximately a/W = 0.25, with P_{max} always dropping below the constant load level used in subsequent testing to failure. This was to preclude any transients due to retardation.

In tests on 2124-T8511, baseline data were obtained at R = 0.5. The baseline crack growth rate curve thus obtained was then compared with crack growth rates at R = 0.5 with periodic 25 % and 50 % overloads applied every 2000 cycles. Another test was performed at R = 0.7 with 50 % overloads. Figure 7 shows results from these experiments. Note that given similar overload levels, the extent of retardation does not diminish with increasing baseline stress ratio, underscoring its potential independence from closure.

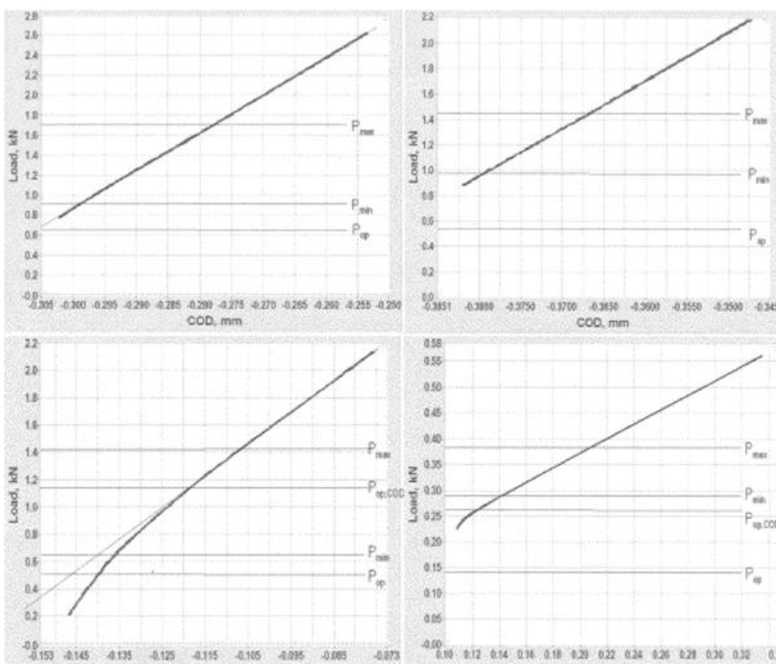

FIG. 5—*Typical Load-COD curves from tests under 7075-T7351 under periodic 50 % overload. COD was measured at crack mouth. Each curve was the last recorded in the threshold step. Curves at top are from tests in air, while those at the bottom are from tests in 3 % common salt solution. Indicated P_{op} level of 25 % corresponds to fractographic measurements on other Al-alloys. $P_{op,COD}$ corresponds to visually determined point of deviation from linear. ΔK_{th} from all four measurements were within 10 % of one another, suggesting a fully open crack in all cases. The observed non-linearity may be due to corrosion deposit on the fracture away from the crack tip.*

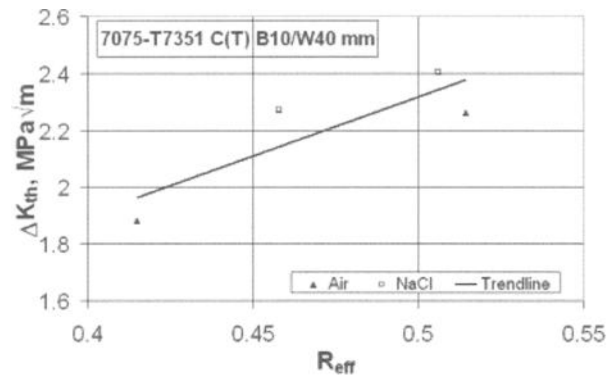

FIG. 6—*ΔK_{th} under 50 % periodic overload plotted against $R_{eff} = P_{min}/P_{ov}$. Data obtained at K_{max} values in the range of 7.5–15 MPa √m. In the event closure was involved, ΔK_{th} would decrease with increasing R_{eff}.*

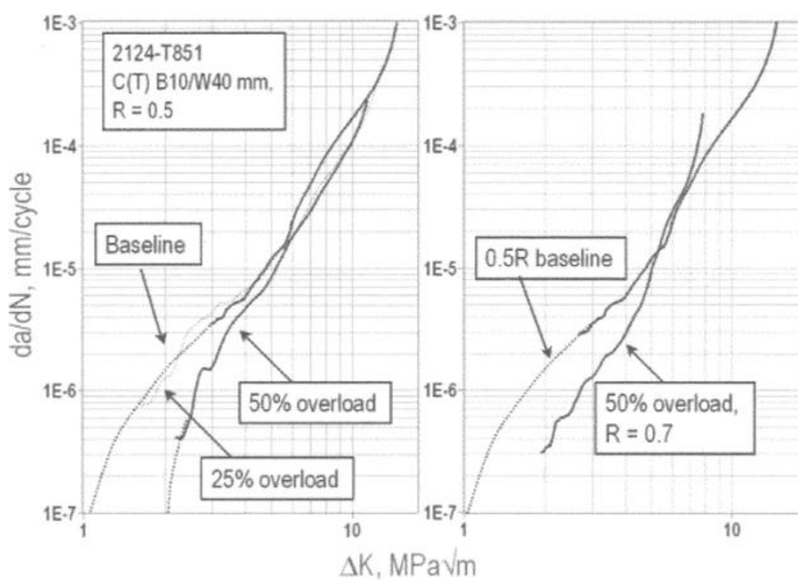

FIG. 7—*Effect of periodic overloads on da/dN in 2124-T851 at R = 0.5 and 0.7. Dotted lines indicate expected trend, based on ΔK_{th} estimates under periodic overloads as reported for 2014-T6511 and 7075-T7351 in Fig. 3.*

Near-threshold crack growth under 50 % overload is noticeably retarded as expected from earlier estimates of ΔK_{th} under periodic overloads. Dotted lines represent extrapolated trend, leading to threshold levels established in the previous tests. The retardation effect steadily diminishes with increasing crack growth rate. Retardation under 25 % overload appears negligible.

Tests on 7075-T7351 were performed at R = 0.65 in air and vacuum with and without 35 % overloads. This was to reproduce similar stress and overload ratios used in previous work on 2014-T6511 [9]. In order to confirm the somewhat surprising results in vacuum, the vacuum tests were repeated and, as shown in Fig. 8, suggest excellent reproducibility.

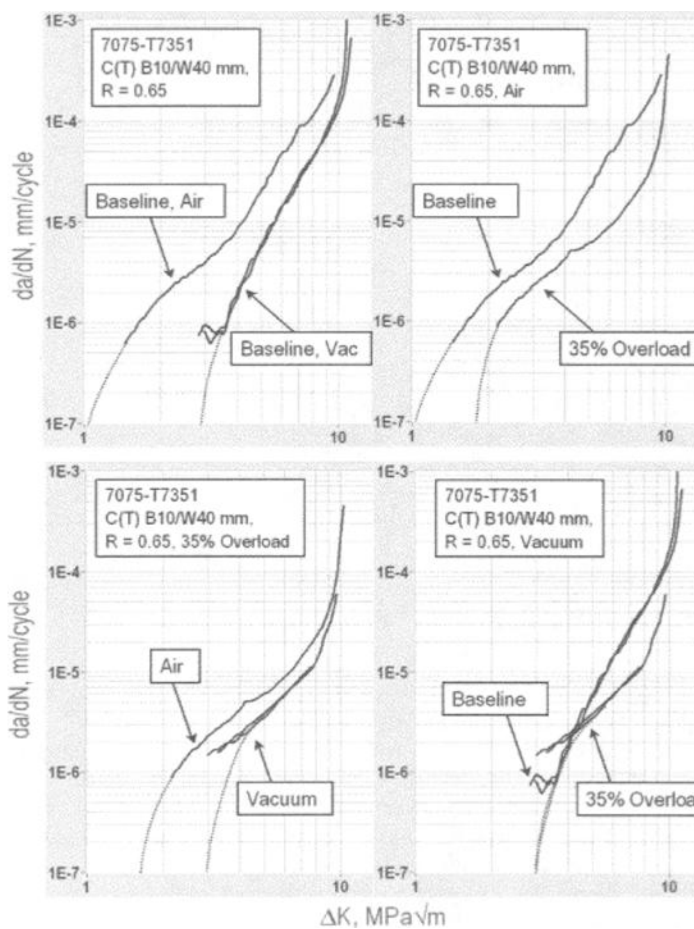

FIG. 8—*Fatigue crack growth rates in 7075-T7351 in air and vacuum with and without periodic overloads. Both baseline as well as overload tests in vacuum were repeated to confirm reproducibility of results. Extrapolated trend is indicated by dotted lines.*

Thirty-five percent periodic overloads appear to cause noticeable retardation even though baseline loading is at a high R = 0.65, which further reduces the probability of closure by comparison to the tests on 2124-T851. From earlier experience on notch root cracking in air and vacuum, we expected to observe retardation-free crack growth under 35 % periodic overloads in vacuum. Indeed, when expressed in terms of crack growth life from a/W = 0.25 to failure, all four results (two with and two without overloads) fall within 5 % of one another. It comes somewhat as a surprise that near-threshold crack growth rate under overloads in vacuum may in fact even be accelerated. This is somewhat compensated by retarded growth at higher growth rates. A discussion of this anomaly is forthcoming.

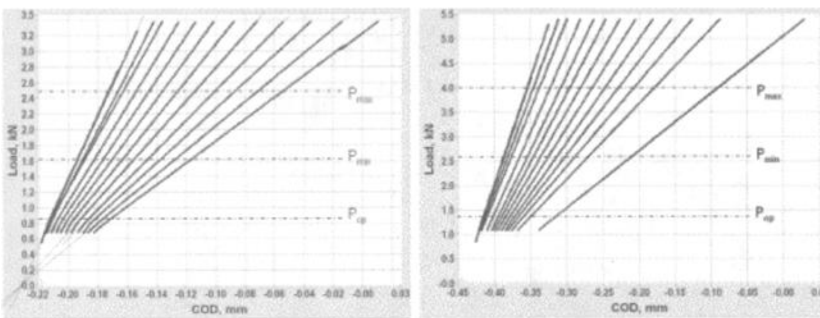

FIG. 9—*Load-COD data recorded at 1mm interval in tests on 7075-T7351 under periodic 35 % overloads. Data on left are from air, while those at right are for vacuum.* P_{op} *level at 25 % is from previous fractographic and laser IDG measurements [13].*

In order to confirm that closure was totally absent in all these tests, Load-COD data were analyzed from tests under periodic overloads in air and vacuum. These are presented in Fig. 9 as Load-COD curves recorded in air (left) as well as vacuum (right) tests at approximately 1 mm interval from a/W = 0.25 to a/W = 0.5. These traces confirm that closure was indeed absent over the entire interval of crack growth rates covered in our tests ($<10^{-7}$ to 10^{-3} mm/s).

Discussion

For over 30 years, fatigue crack closure has been used to explain the effect of stress ratio and load history on metal fatigue. Given its amenability to mechanistic modeling, it is a natural choice in attempts at predictive modeling. The experiments in this study were specifically designed to preclude crack closure. This was achieved by imposing higher stress ratio under baseline loading and also by restricting the magnitude of periodic overloads. Even though closure was absent, both threshold values as well as crack growth rates exhibited considerable sensitivity to the application of periodic overloads as illustrated in Figs. 3, 7, and 8.

Fracture mechanics similitude criteria form the basis for extrapolating laboratory constant amplitude data to other loading conditions. Enlarged plastic zone size due to overloads distorts these criteria. It enhances compressive residual stresses ahead of the crack tip, which is much similar to surface treatments like shot peening used to enhance surface residual compressive stress. The beneficial effect of reduced local mean stress in fatigue has been known from

Wohler's time. However, there hasn't been a compelling explanation for the effect, given the understanding that fatigue is driven by cyclic slip, which is mean stress-insensitive. Crack closure does explain why crack growth can be affected by stress ratio and load history, however, quantitative fractography in related work has indicated that in the cases studied, closure was able to account for only 15–25 % of observed retardation [15]. Test conditions in this study altogether precluded closure. Besides, closure cannot explain sensitivity of crack formation to load history.

Evidence from this study supports the possibility that residual stress operates quite independently of fatigue crack closure. Related work on similar materials and test conditions suggests that residual stress may operate as a "valve" to control environmental action on fatigue crack extension [8,14]. If this is in fact the case, compressive residual stress effects can at best reduce the rate of fatigue to vacuum levels. As seen in Fig. 8, overload da/dN curves in air and vacuum are closer to each other than under no-overload conditions. This was under periodic overloads of 50 % relative magnitude. Application of higher overloads will cause even greater retardation in air. However, the potential inducement of partial crack closure with increasing overload magnitude would complicate interpretation of test results.

As shown in Fig. 8, crack growth in vacuum is about one order of magnitude slower than in air, with the gap widening toward threshold, as ΔK_{th} in vacuum is about three times greater than in air. For the same reason, vacuum fatigue limit also would be considerably greater than in air. Given such material response, fatigue cracks seldom initiate on the notch surface in vacuum.

Fractographic evidence from Al-alloys shows that in vacuum fatigue is initiated at a *sub-surface* secondary particulate interface with the matrix in the form of multiple penny-shaped interfacial cracks that eventually separate the particulate from the matrix [17]. The resulting fatigue void proceeds to grow as a penny-shaped crack normal to loading direction. High cyclic triaxial stresses enhanced by local constraint cause innumerable cracks such as these to form and propagate in the notch area, with potential asymmetry in crack shape toward the notch surface, given local stress gradient. The dominant crack is formed when one of these cracks reaches the notch surface and stress intensity jumps due to the edge effect. This crack will now grow into the material and coalesce with existing internal cracks if their plane is in its proximity. This scenario may perhaps explain the reproducible ~3.5 mm segment of accelerated crack growth at the commencement of constant amplitude loading (bottom end of no-overload vacuum data in Fig. 8) to failure. This interval is several orders of magnitude greater than plastic zone size. In order to facilitate early pre-cracking of the vacuum test coupons, initial loading was about 80 % more than in air and also at low stress ratio. The associated cyclic loads may have induced internal cracks at secondary particulates, causing the initial plateau of accelerated crack growth.

Stated differently, near-threshold fatigue of Al-alloys in vacuum may be the result of interaction of two parallel processes. One is notch root crack formation or crack growth from the free edge as in air, but with the difference that much higher ΔK values are required to propagate the crack. The other is internal cracking from fatigue voids enclosing secondary particulates, driven by high cyclic triaxial stresses, enhanced by local constraint (as opposed to the free surface). Internal cracking can also occur in air, but it would be outpaced by the progress of the main crack tip that is exposed to environment.

We have thus far discussed closure and residual stress effects. The fatigue fracture surface under near-threshold conditions is usually devoid of incompatibility in crack front geometry with applied load conditions, with the exception, perhaps, of blunting. Other forms of crack front incompatibility including branching, crack front shape variation, and kinking evolve at higher growth rates, where there can be a substantial difference in preferred crack extension modes between overload and baseline cycling. This may explain why vacuum growth rates can be retarded at higher ΔK levels, even if closure is absent.

It is well known that environment accelerates fatigue crack growth by affecting the very mechanism of crack extension. Schijve and his co-workers have noted that under the same loading amplitude, crack plane rotates much earlier in vacuum from tensile to shear mode, suggesting that crack tip critical shear stress (in vacuum) takes over from critical tensile stress (in environment) as the driving parameter [18–20]. Comprehensive experiments and analysis by Bowles identified hydrogen diffusion into the crack tip and the latter's consequent embrittlement as the potential agent for local rupture by reduced critical tensile stress, thereby supporting Schijve's conclusion that environmental action cannot be attributed to closure as suggested by Buck et al. [21]. Clinching evidence may come in the form of recent work by Gach and Pippan, which shows crack-tip radius to be strongly controlled by environment [22]. Their observation that the crack tip in vacuum is the most blunted is also suggestive of greater shear activity in the absence of environment-induced embrittlement conducive to crack extension by de-cohesion. The significance of environment in determining crack extension mechanism is obvious.

Both near-tip compressive residual stress and crack closure retard fatigue crack growth, but they do so differently. The former appears to moderate environmental action at the crack tip. At the extreme, it can only enforce vacuum conditions, including crack arrest, if ΔK drops below vacuum ΔK_{th}. In contrast, closure operates by truncation of crack driving force. A fully closed crack will remain arrested, quite independent of applied ΔK. Thus, apart from macroscopic closure associated with the crack wake, one must contend with microscopic closure and opening of crack tip atomic lattice spacing that, in turn, controls the kinetics of crack-tip surface physics (diffusion) and chemistry (oxidation), and associated cyclic crack tip embrittlement. This concept is the subject of a separate paper [14].

Conclusions

Fatigue crack growth tests on Al-alloys under constant amplitude loading and under periodic overloads in air, salt water, and vacuum lead to the following conclusions:

1. ΔK_{th} estimated under closure-free conditions is insensitive to crack size, applied load level, stress ratio, and to a large extent also to K_{max}.
2. In air and salt water, closure-free ΔK_{th}, as well as crack growth rates, are sensitive to overloads as small as 35 %. ΔK_{th} more than doubles under periodic 50 % overload, and crack growth rates are retarded correspondingly.
3. In vacuum, closure-free near-threshold fatigue crack growth under periodic overloads is accelerated by comparison to no-overload conditions. This is reversed at higher growth rates, where vacuum data show retardation, like in air.
4. Near-threshold vacuum crack growth behavior may be associated with the absence of residual stress effect and also by overload-induced micro-cracking ahead of the crack tip. Vacuum retardation at higher growth rates may be due to the onset of crack front incompatibility, including blunting and branching.

Acknowledgments

The vacuum test facility was carefully designed and set up by Ramakrishna Hebbar.

References

[1] Miller, K. J., "The Three Thresholds for Fatigue Crack Propagation," *Fatigue and Fracture Mechanics: 27th Volume, ASTM STP 1296*, R. S. Piascik, J. C. Newman, and N. E. Dowling, Eds., ASTM International, West Conshohocken, PA, 1997, pp. 267–286.

[2] Newman, J. C., "A Crack-Closure Model for Predicting Fatigue Crack Growth under Aircraft Spectrum Loading," *Methods and Models for Predicting Fatigue Crack Growth under Random Loading, ASTM STP 748*, J. B. Chang and C. M. Hudson, Eds., 1981, pp. 53–84.

[3] Elber, W., "The Significance of Fatigue Crack Closure," *Damage Tolerance in Aircraft Structures, ASTM STP 486*, ASTM International, West Conshohocken, PA, 1971, pp. 230–242.

[4] Vasudevan, A. K., Sadananda, K., and Loust, N., "A Review of Crack Closure, Fatigue Crack Threshold and Related Phenomena," *Materials Science and Engineering*, A188, 1994, pp. 1–22.

[5] Marci, G. A., "A Fatigue Crack Growth Threshold," *Engineering Fracture Mechanics*, Vol. 42, 1992, pp. 367–385

[6] Lang, M. and Marci, G., "The Influence of Single and Multiple Overloads on Fatigue Crack Propagation," *Fatigue Fract. Engg. Mater, Struct.*, Vol. 22, No. 4, 1999, pp. 257–271.

[7] Hopkins, W. W., Rau, C. A., Leverant, G. R., and Yuen, A., "Effect of Various Programmed Overloads on the Threshold for High-Frequency Fatigue Crack Growth," *Fatigue Crack Growth under Spectrum Loads, ASTM STP 595*, ASTM International, West Conshohocken, PA, 1976, pp. 125–141.

[8] Sunder, R., "An Explanation for the Residual Stress Effect in Metal Fatigue," *Fatigue 2002 – Proc. 8th International Fatigue Congress*, Stockholm, 2002, EMAS, pp. 3339–3350.

[9] Sunder, R., Porter, W. J., and Ashbaugh, N. E., "The Role of Air in Fatigue Load Interaction," *Fatigue Fract Engng Mater Struct*, 26, pp. 1–16.

[10] Bowles, C. Q., "The Role of Environment, Frequency and Wave Shape During Fatigue Crack Growth in Aluminum Alloys," *Ph.D. Thesis, Report LR-270*, Delft University of Technology, Delft, The Netherlands, 1978.

[11] Bradshaw, F. J. and Wheeler, C., "The Effect of Gaseous Environment and Fatigue Frequency on the Growth of Fatigue Cracks in Some Aluminum Alloys," *Int. J. Fract. Mech.*, Vol. 5, No. 4, 1969, pp. 255–268.

[12] Suresh, S., In *Fatigue of Materials*, Cambridge University Press, Cambridge, 1991, Ch. 7.

[13] Ashbaugh, N. E., Dattaguru, B., Khobaib, M., Nicholas, T., Prakash, R. V., Ramamurthy, T. S., et al., "Experimental and Analytical Estimates of Fatigue Crack Closure in an Aluminum-Copper Alloy. Part I: Laser Interferometry and Electron Fractography," *Fatigue Fract. Engg. Mater. Struct*, Vol. 20, No. 7, 1997, pp. 951–961.

[14] Sunder, R., "Fatigue Crack Growth as a Consequence of Environment-Enhanced Brittle-Micro Fracture," *Fatigue Fract. Engng. Mater. Struct.*, Accepted for publication, 2003.

[15] Ashbaugh, N. E., Porter, W. J., Rosenberger, A. H., and Sunder, R., "Environment-Related Load History Effects in Elevated Temperature Fatigue of a Nickel-Base Super-Alloy," *Proc., Fatigue*, Stockholm, June 2–7, 2002.

[16] Sunder, R., "Fractographic Reassessment of the Significance of Fatigue Crack Closure," *Fatigue and Fracture Mechanics: 34th Volume, ASTM STP 1461*, S. R. Daniewicz, J. C. Newman, and K.-H. Schwalbe, Eds., ASTM International, West Conshohocken, PA, 2004.

[17] Sunder, R., Porter, W. J., and Ashbaugh, N. E., *Fatigue Fract Engng Mater Struct*, Vol. 25, 2002, pp. 1015–1024.
[18] Schijve, J. and Arkema, W. J., "Crack Closure and the Environmental Effect on Fatigue Crack Growth," *Report VTH-217*, Delft University of Technology, Delft, The Netherlands, 1976.
[19] Vogelesang, L. B. and Schijve, J., "Environmental Effects on Fatigue Fracture Mode Transitions Observed in Aluminum Alloys," *Report LR-289*, Delft University of Technology, Delft, The Netherlands, 1979.
[20] Vogelesang, L. B., "Some Factors Influencing the Transition from Tensile Mode Shear Mode Crack Growth under Cyclic Loading," Delft University of Technology, Report LR-222, Delft, The Netherlands, Aug. 1976.
[21] Buck, O., Frandsen, J. D., and Marcus, H. L., "Spike Overload and Humidity Effects on Fatigue Crack Delay in Al 7075-T651," *Fatigue Crack Growth Under Spectrum Loads, ASTM STP 595*, ASTM International, West Conshohocken, PA, 1976, pp. 101–112.
[22] Gach, E. and Pippan, R., "Cyclic Crack Tip Deformation – The Influence of Environment," *Proc. 10th International Conference on Fracture,* Dec. 2001, Paper ICF 100420OR.

Journal of ASTM International, June 2005, Vol. 2, No. 6
Paper ID JAI12037
Available online at www.astm.org

Gbadebo M. Owolabi[1] *and Meera N.K. Singh*[2]

Notch-Root Elastic-Plastic Strain-Stress in Particulate Metal Matrix Composites Subjected to General Loading Conditions

ABSTRACT: Determining the stress and strain history at the point of highest stress concentration in particulate metal matrix composites (PMMCs) is complicated, particularly when they have a finite concentration of inclusions, the matrix material in the vicinity of the notch is elastic-plastic, and when multiaxial cyclic loads are applied to the component. In this paper, an analytical tool is developed to approximate notch root elastic-plastic strains and stresses in PMMC components subjected to multiaxial cyclic loads. The model consists of a set of linear relations that can be solved to estimate a notch root elastic-plastic strain and stress history in PMMCs from an elastic analysis. The model is developed using assumptions about notch root behavior, the incremental mean field theory, and the endochronic theory of plasticity. The model presented provides an easy to implement approximation to the otherwise rather complex non-linear problem. The analytical results are compared to the local strains, obtained using 3D image correlation technology, at the depth of a circumferential notch in a PMMC bar subjected to proportional and non-proportionally applied monotonic and cyclic axial-torsional loads. The results of the comparison show that the proposed model works well for the geometry and load paths considered.

KEYWORDS: particulate metal matrix composites, mean field theory, endochronic theory, low cycle fatigue, Neuber's Rule

Nomenclature

C_{ijkl}	Components of a stiffness tensor
I	Identity matrix
i-l,s,t	Indices, i,j,k,l,s,t = 1,2,3 summation is implied
P	Axial Load
r	r-th component
S_{ij}	Components of deviatoric stress tensor
S_{ijkl}	Components of Eshelby's tensor
T	Torque
V	Composite volume
$V_{()}$	Volume fraction of constituent
W	Strain Energy Density
W_c	Complementary strain energy density
z, z′	Intrinsic time scale
α_r	Material constants

Manuscript received 4 November 2003; accepted for publication 7 September 2004; published June 2005. Presented at ASTM Symposium on Fatigue and Fracture Mechanics: 34th Volume on 19–21 November 2003 in Tampa, FL; S.R. Daniewicz, J.C. Newman, Jr., and K-H. Schwalbe, Guest Editors.
[1] Research Assistant, Member ASME, Department of Mechanical and Industrial Engineering, University of Manitoba, Winnipeg, Manitoba, Canada, R3T 2N2.
[2] Assistant Professor, Department of Mechanical and Industrial Engineering, University of Manitoba, Winnipeg, Manitoba, Canada, R3T 2N2.

α,β Indices, $\alpha,\beta = 1,2,3$, no summation is implied.
Δ Finite difference
ε_{ij} Components of strain tensor
$\rho(\ )$ Memory function
ρ Notch root radius
σ_{ij} Components of stress tensor
ζ Intrinsic time measure
Ω Total strain energy density
$d(.)$ Differential form of variable or constant
$(.)^e$ Elastic components of a variable
$(.)_{(f)}$ Reinforcement component of a variable or constant
$(.)^N$ Elastic-plastic components estimated by Neuber's rule
$(.)_{(m)}$ Matrix components of a variable or constant
$(.)^p$ Plastic components of a variable
$(.)_q$ q-th step component of a variable
$(.)^T$ Total components of a variable

Introduction

Due to benefits in their material properties, particulate metal matrix composites (PMMCs) are increasingly finding applications in aerospace, automotive, sports equipment, and electronic industries. In contrast to their long fiber counterparts, PMMC components generally have isotropic properties and are much easier to produce and machine by standard methods. However, since the mechanical behavior of PMMCs is still not well understood, the use of these materials in fatigue applications is still met with reluctance in practice.

Engineering components generally contain geometric discontinuities (notches), such as keyways, bolt holes, and splines. These discontinuities result in a local intensification of the stress field. In components made of PMMCs, this field may additionally be raised due to the material discontinuity at the particle-matrix interface. When the components are used in fatigue applications, these stress raisers act as perfect sites for crack initiation. Thus, if their effect on the stress field is not minimized in design, the result is often premature component failure.

In low cycle fatigue applications, although the bulk of the composite may remain elastic, the highly stressed metal matrix material in the vicinity of a notch may undergo plastic deformation. Strain based fatigue failure criterion applicable to PMMC components under multiaxial cyclic loads have only recently appeared in the literature [1,2]. In these papers, critical plane and energy-based models, developed for homogeneous materials, are shown to be applicable to PMMC components. These papers further highlight the need for both the elastic-plastic strain and stress history at a component's critical location to be known before a fatigue life prediction can be made. These values can be obtained by three methods: experimental measurements, numerical solutions, or simplified analytical techniques. Although experimental and numerical methods are the most accurate, they are expensive and time consuming, particularly when the components modeled are subjected to long histories of non-proportional cyclic loads.

For homogeneous materials, to make fatigue life prediction methods more conducive to average design environments and to shorten design lead times, there has been a great effort employed to develop simplified analytical techniques that approximate the actual elastic-plastic notch root material behavior. Neuber's rule [3] is the most frequently used approximation method used for uniaxial loading applications. Neuber's rule uses the results of an elastic notch root analysis to approximate the actual elastic-plastic notch root strains and stresses. Motivated by its simplicity in application, several researchers [4–7] have developed similar relations to address multiaxial non-proportional cyclic loading in homogeneous materials. A direct extension of Neuber's rule is found in [4,5], where a multiaxial incremental energy based form of Neuber's rule is validated against numerical and experimental data.

To benefit from the simplicity of implementation of these models, in [8], Owolabi and Singh laid out a similar methodology for approximating the notch root elastic-plastic strains in PMMC components under monotonically increasing multiaxial loads. To date, little research has been conducted on developing such simplified models for determining the elastic-plastic strain and stress history in PMMC components subjected to multiaxial cyclic loads.

It should be mentioned that all three of the aforementioned notch root elastic-plastic strain and stress history prediction methods require the adoption of a cyclic constitutive model. Inelastic constitutive models for homogeneous materials subjected to non-proportional loads are numerous and still evolving. A good review of such models is given in [9]. Only a few cyclic plasticity models applicable to PMMC components subjected to non-proportional loading have recently appeared in the literature [10,11].

This paper is an effort to develop a simplified analytical methodology for determining the notch root elastic-plastic strain and stress histories in PMMC components subjected to non-proportional cyclic loads, and to experimentally assess the solution. This methodology incorporates both a cyclic plasticity routine and a modified form of the incremental Neuber's rule given in [4,5] for homogeneous metals. All relations are developed to respect the heterogeneous nature of PMMCs and are presented first. The experimental set up and procedure is subsequently presented followed by a comparison and discussion of the results obtained. Finally, conclusions of the investigation are drawn.

Cyclic Constitutive Relations

In a composite system, the matrix follows an elastic stress-strain path until the state of stress in the matrix satisfies the yield condition. For small deformations, the components of the total incremental matrix (m) strain tensor, $d\varepsilon_{ij(m)}^{T}$, can be decomposed into its elastic, $d\varepsilon_{ij(m)}^{e}$, and plastic, $d\varepsilon_{ij(m)}^{p}$, components as:

$$d\varepsilon_{ij(m)}^{T} = d\varepsilon_{ij(m)}^{e} + d\varepsilon_{ij(m)}^{p}. \tag{1}$$

Since the reinforcement (f) remains relatively stiff, the components of the increment in the total reinforcement strain tensor, $d\varepsilon_{ij(f)}^{T}$, are comprised of only elastic parts, or:

$$d\varepsilon_{ij(f)}^{T} = d\varepsilon_{ij(f)}^{e}. \tag{2}$$

An approach to determine the elastic components of the matrix, fiber, and composite strain/stress from the applied incremental stress/strain is first described below. The plastic components of the matrix strain are subsequently presented.

Elastic Relations

The concept of average stress and strain in the composite and its constituents has been used extensively in the past to describe the effective elastic, and in some cases plastic, behavior of PMMCs. Most of the proposed models are based on Eshelby's original solution of the ellipsoidal inclusion [12]. The most frequently used of such models is the Mori-Tanaka's mean field theory [13], which was reformulated in incremental form by Li and Chen [14] to make it applicable to elastic-plastic non-proportional analysis. On the basis of this model, the approach given in [10,11] to determine the incremental elastic stress and strain components in the matrix, fibers, and composite is briefly presented.

As shown in [10,11], if an unreinforced matrix is elastic, the resulting increments in elastic stress components in the matrix, $d\sigma_{ij(m)}$, can be related to those associated with the nominally applied loads, $d\sigma_{ij}$, as:

$$d\sigma_{ij(m)} = d\sigma_{ij} - V_f C_{klst(m)} \left(S_{klst} - I\right) L^{-1} (C_{klst(f)} - C_{klst(m)}) C^{-1}_{klst(m)} d\sigma_{ij} . \tag{3}$$

In Eq (3),

$$L = [(V_f - 1) C_{ijkl(m)} (I - S_{ijkl}) + C_{ijkl(f)} [V_f (S_{ijkl} - I) - S_{ijkl}] , \tag{4}$$

where V is the volume fraction of the subscripted constituent, C_{ijkl} represents the components of the stiffness matrix of the subscripted constituent, **I** is the identity matrix, and S_{ijkl} are the components of Eshelby's tensor [12]. Eshelby's tensor can be found from the inclusions geometry and the matrix Poisson's ratio.

The components of the incremental matrix elastic strain tensor are related to the above increments in the corresponding stress tensor as:

$$d\varepsilon^{e}_{ij(m)} = C^{-1}_{ijkl(m)} d\sigma_{kl(m)} . \tag{5}$$

The components in the incremental stress and elastic strain tensors in the reinforcement can be found respectively from:

$$d\sigma_{ij(f)} = d\sigma_{ij} + V_m C_{klst(m)} \left(S_{klst} - I\right) L^{-1} (C_{klst(f)} - C_{klst(m)}) C^{-1}_{klst(m)} d\sigma_{ij} , \tag{6}$$

and

$$d\varepsilon^{e}_{ij(f)} = C^{-1}_{ijkl(f)} d\sigma_{kl(f)} . \tag{7}$$

The composite elastic mean stress can be obtained from the nominally applied loads, while the composite mean strain components can be obtained using the weighted sum of the work done by the stress increments of the constituents, or

$$d\sigma_{ij} d\varepsilon_{ij} = V_m d\sigma_{ij(m)} d\varepsilon_{ij(m)} + V_f d\sigma_{ij(f)} d\varepsilon_{ij(f)} . \tag{8}$$

It should be noted that Eq (8) applies for both elastic and elastic-plastic material behavior.

Equations (3)–(8) make it possible to determine the average components of the fiber and matrix elastic stress and strain increments knowing just the stresses associated with the applied load and the properties and volume fractions of the constituents that make up the composite.

Elastic-Plastic Cyclic Constitutive Relations

The increments in the plastic components of matrix strain, $d\varepsilon^{p}_{ij(m)}$, from Eq (1) are obtained here using a cyclic plasticity theory that is appropriate for both proportional and non-proportional loading conditions. In [11], the authors have shown that the constitutive behavior of PMMCs can be predicted using either the Mróz model [15] or the endochronic theory of plasticity [16,17] (developed for metals) in conjunction with the Mori-Tanaka's mean field theory presented above. In all the loading cases considered, both models produce a reasonable qualitative and quantitative response of the composite. The endochronic theory has the benefit of not requiring the definition of a yield surface and loading/unloading conditions. Furthermore, it has been reported in [17] that the endochronic theory is capable of predicting transient effects associated with variable amplitude non-proportional cyclic loading when applied to homogeneous materials. In this paper, the endochronic theory will be used in conjunction with the incremental mean field theory presented above to determine the elastic-plastic cyclic constitutive response of a PMMC. Since this methodology has been presented in detail by the authors in [11], only the main equations will be presented here.

In [16], the endochronic constitutive equations for plastically incompressible, rate-independent, initially isotropic materials are given by:

$$S_{ij(m)} = 2\int_0^z \rho\left(z - z'\right)\frac{d\varepsilon^{p}_{ij(m)}\left(z'\right)}{dz'}dz', \tag{9}$$

where,

$$dz = \frac{d\zeta}{f(\zeta)}, \tag{10}$$

and,

$$d\zeta = \left(d\varepsilon^{p}_{ij(m)}d\varepsilon^{p}_{ij(m)}\right)^{1/2}. \tag{11}$$

In Eqs (9)–(11), $S_{ij(m)}$ are the components of the matrix deviatoric stress tensor, $S_{ij(m)} = \sigma_{ij(m)} - \sigma_{kk(m)}\delta_{ij}/3$, where δ_{ij} is the Kroneker delta. Also, z is the intrinsic time scale, and ζ is the intrinsic time measure that defines the memory path in plastic strain space. Deformation history effects are introduced into the constitutive relations through these parameters, and $d\zeta$ is the distance between two neighboring points in plastic strain space. Also in Eqs (9)–(11), f(z) is the hardening function that can be determined from a set of transient uniaxial cyclic stress-strain tests. In this investigation, only stabilized cyclic response of PMMCs will be considered. As such, neglecting cyclic hardening (or softening), f(z) = 1 [17]. The hereditary function, $\rho(z)$, (otherwise known as kernel function) is represented by an n-order Dirichlet series:

$$\rho(z) = \sum_{r=1}^{n} C_r e^{-\alpha_r z}, \tag{12}$$

where C_r and α_r are material constants determined from the uniaxial cyclic stress-strain curve of the material.

As shown in [11] and [17], for stress-controlled simulations, dividing the loading path into q-steps and assuming a small increment, the incremental stress deviator can be calculated by:

$$\left(\Delta S_{ij}\right)_{q(m)} = 2\left[\frac{1}{\Delta z}\sum_{r=1}^{n}\frac{C_r}{\alpha_r}\left(1-e^{-\alpha_r\Delta z}\right)\right]\left(\Delta\varepsilon^{p}_{ij(m)}\right)_q + \sum_{r=1}^{n}\left(S^{r}_{ij(m)}\right)_{q-1}\left(e^{-\alpha_r\Delta z}-1\right), \tag{13}$$

from which we can obtain,

$$\Delta\varepsilon^{p}_{ij(m)} = \frac{a_{ij}\Delta z}{b}, \tag{14}$$

where,

$$a_{ij} = \frac{1}{2}\left[\left(\Delta S_{ij(m)}\right)_q + \sum_{r=1}^{n}\left(S^{r}_{ij(m)}\right)_{q-1}\left(1-e^{-\alpha_r\Delta z}\right)\right], \tag{15}$$

and,

$$b = \left[\sum_{r=1}^{n} C_r \frac{\left(1-e^{-\alpha_r\Delta z}\right)}{\alpha_r}\right]. \tag{16}$$

Rearranging and taking the inner product of Eq (13) yields:

$$b^2 - a_{ij}a_{ij} = 0 = R(\Delta z). \tag{17}$$

For a given increment of composite stress tensor, Eq (17) can be used to solve for Δz, using the Secant method to find the roots of the equation.

The matrix cyclic constitutive relation can be finalized by combining Eqs (1), (5), (14)–(17) giving:

$$\Delta\varepsilon_{ij(m)} = \frac{1+\upsilon_m}{E_m}\Delta\sigma_{ij(m)} - \frac{\upsilon_m}{E_{(m)}}\left(\Delta\sigma_{kk(m)}\right)\delta_{ij} + \frac{a_{ij(m)}\Delta z}{b}. \tag{18}$$

Incremental Neuber's Rule for Heterogeneous Materials

In the most general case, due to the traction free surface, there are seven unknown notch root parameters: three stress and four strain components. As such, an equation set aimed at defining these parameters must consist of seven independent relations. Four of these relations can be obtained from the cyclic constitutive model described above. The remaining three relations are defined in this section and are based on the incremental forms of the Neuber's rule developed for homogeneous materials in [4,5].

For homogeneous materials, it is proposed [4] that for a given increment in the external load, the corresponding increase in the total strain energy density (i.e., sum of the increment in strain energy density and complementary strain energy density) at the notch root in an elastic-plastic body can be approximated by that obtained if the body was to hypothetically remain elastic throughout the loading history. Mathematically, this can be represented as:

$$\sigma^{e}_{ij}\Delta\varepsilon^{e}_{ij} + \varepsilon^{e}_{ij}\Delta\sigma^{e}_{ij} = \sigma^{N}_{ij}\Delta\varepsilon^{N}_{ij} + \varepsilon^{N}_{ij}\Delta\sigma^{N}_{ij}, \tag{19}$$

where "e" represents notch root components that can be found from an elastic analysis, and "N" represents elastic-plastic notch root components as estimated by the incremental Neuber's rule.

This model has the benefit of predicting non-linear behavior from the results of a simple elastic analysis. Equating elastic and elastic-plastic energies at only the point of highest stress concentration is justified in [4] based on the assumption of localized plasticity. That is, the plastic zone around the notch root is small, and thus its behavior is largely controlled by that of the surrounding elastic field. Equation (19) reduces to the original form of Neuber's rule given in [3] for a body in plane stress.

The heterogeneous nature of the PMMC material can be respected in the above relationship if the total strain energy density is appropriately defined. In [18], Duva and Hutchinson formulated an expression for the macro strain energy density within a PMMC. On the basis of this definition, the weighted total strain energy density of a composite, Ω, with two phases is expressed here as:

$$\Omega=\frac{1}{V}\int_{V_f} W_f dV+\frac{1}{V}\int_{Vf} W_{c(f)}dV+\frac{1}{V}\int_{Vm} W_m dV+\frac{1}{V}\int_{Vm} W_{c(m)}dV. \tag{20}$$

In Eq (20), V is the composite material volume, W_f and W_m are the fiber and matrix strain energy densities, respectively, and $W_{c(f)}$ and $W_{c(m)}$ are the fiber and matrix complementary strain energy densities, respectively. Here, it is proposed that for an increment in load in the composite system, the corresponding increment in the constituents weighted total strain energy density at the notch root in an elastic-plastic body, Ω^N, can be approximated by that which would have been obtained if the composite system were to remain elastic through out the loading history, Ω^e. This proposed hypothesis can be expressed using Eq (20) as:

$$\Delta\Omega^e=(1-V_f)\Delta\Omega^N_{(m)}+V_f\Delta\Omega^e_{(f)}. \tag{21}$$

The formulation can be re-written as:

$$\sigma^e_{ij}\Delta\varepsilon^e_{ij}+\varepsilon^e_{ij}\Delta\sigma^e_{ij}=\left(1-V_f\right)\left(\sigma^N_{ij(m)}\Delta\varepsilon^N_{ij(m)}+\varepsilon^N_{ij(m)}\Delta\sigma^N_{ij(m)}\right)+V_f\left(\sigma^e_{ij(f)}\Delta\varepsilon^e_{ij(f)}+\varepsilon^e_{ij(f)}\Delta\sigma^e_{ij(f)}\right). \tag{22}$$

It should be emphasized here that the elastic components "e" in Eq (22) are not nominal values, but values obtained at the notch root. These values can be found using Eqs (3)–(8) and the stress concentration factors of the notched geometry modeled. If $V_f = 0$, thus indicating a homogeneous material, Eq (22), reduces to Eq (19), and for plane stress, the original form of Neuber's rule given in [3]. It should be pointed out that being based on Eq (19), Eq (22) is valid under the assumption of localized notch root plasticity.

Two additional equations are required to completely define the notch-root elastic-plastic strain and stress. Similar to that validated for homogeneous materials in [5], here it is proposed that for the composite system, the weighted contribution of each of the elastic-plastic strain-stress component to the increment in total energy density at the notch root is the same as the contribution of each stress-strain component to the increment in composite total strain energy density at the notch root when obtained from elastic analysis. The proposed formula can be expressed as:

$$\frac{\sigma^e_{\alpha\beta}\Delta\varepsilon^e_{\alpha\beta}+\varepsilon^e_{\alpha\beta}\Delta\sigma^e_{\alpha\beta}}{\sigma^e_{ij}\Delta\varepsilon^e_{ij}+\varepsilon^e_{ij}\Delta\sigma^e_{ij}}=\frac{\left(1-V_f\right)\left(\sigma^N_{\alpha\beta(m)}\Delta\varepsilon^N_{\alpha\beta(m)}+\varepsilon^N_{\alpha\beta(m)}\Delta\sigma^N_{\alpha\beta(m)}\right)+V_f\left(\sigma^e_{\alpha\beta(f)}\Delta\varepsilon^e_{\alpha\beta(f)}+\varepsilon^e_{\alpha\beta(f)}\Delta\sigma^e_{\alpha\beta(f)}\right)}{\left(1-V_f\right)\left(\sigma^N_{ij(m)}\Delta\varepsilon^N_{ij(m)}+\varepsilon^N_{ij(m)}\Delta\sigma^N_{ij(m)}\right)+V_f\left(\sigma^e_{ij(f)}\Delta\varepsilon^e_{ij(f)}+\varepsilon^e_{ij(f)}\Delta\sigma^e_{ij(f)}\right)} \tag{23}$$

In Eq (23), the indices, i, j, α, β = 1, 2, 3, and summation is assumed over i, j, while, for α, β, summation is not implied. Combining Eqs (22) and (23) yields:

$$\sigma^{e}_{\alpha\beta}\Delta\varepsilon^{e}_{\alpha\beta} + \varepsilon^{e}_{\alpha\beta}\Delta\sigma^{e}_{\alpha\beta} = \left(1 - V_f\right)\left(\sigma^{N}_{\alpha\beta(m)}\Delta\varepsilon^{N}_{\alpha\beta(m)} + \varepsilon^{N}_{\alpha\beta(m)}\Delta\sigma^{N}_{\alpha\beta(m)}\right) + V_f\left(\sigma^{e}_{\alpha\beta(f)}\Delta\varepsilon^{e}_{\alpha\beta(f)} + \varepsilon^{e}_{\alpha\beta(f)}\Delta\sigma^{e}_{\alpha\beta(f)}\right). \tag{24}$$

It should be noted that Eq (24) yields three relations, and when used in conjunction with the four relations defined by the cyclic plasticity relation (Eq (18)), they are sufficient to solve for the seven unknown notch root elastic-plastic strain and stress components.

Summary of the Simplified Methodology

In this section, the two sets of relations defined above are written fully on the notch root element of a circumferentially notched bar subjected to a tensile (P) and torsional (T) load shown in Fig. 1. Although highlighted for this case, these relations should apply for any notch root that has a traction free surface.

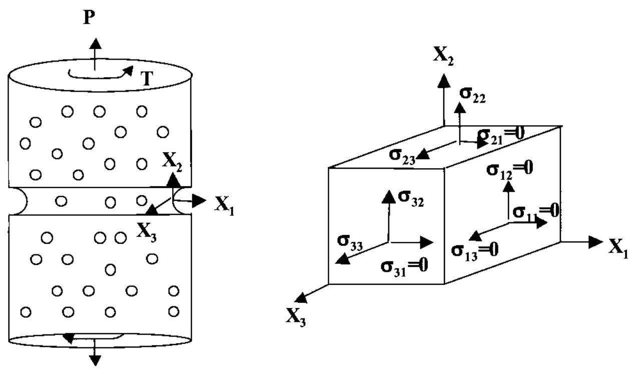

FIG. 1—*General state of stress at a notch tip.*

Elastic-Plastic Constitutive Relations (Eq (18))

$$\begin{aligned}\Delta\varepsilon^{N}_{11(m)} = {} & \left[\frac{-\upsilon_m}{E_m} + \frac{1}{6}\left(\sum_{r=1}^{3} C_r\left(\frac{1-e^{\alpha_r\Delta z}}{\alpha_r}\right)\right)^{-1}\Delta z\right]\left(\Delta\sigma^{N}_{22(m)} + \Delta\sigma^{N}_{22(m)}\right) \\ & + \frac{1}{2}\sum_{r=1}^{3}\left[\left(C_r\frac{1-e^{\alpha_r\Delta z}}{\alpha_r}\right)^{-1} S^{N(r)}_{11}\left(1-e^{-\alpha_r\Delta z}\right)\Delta z\right]\end{aligned} \tag{25}$$

$$\begin{aligned}\Delta\varepsilon^{N}_{22(m)} = {} & \left[\frac{1}{E_m} + \frac{1}{3}\left(\sum_{r=1}^{3} C_r\left(\frac{1-e^{\alpha_r\Delta z}}{\alpha_r}\right)\right)^{-1}\Delta z\right]\Delta\sigma^{N}_{22(m)} + \left[\frac{-\upsilon_m}{E_m} + \frac{1}{6}\left(\sum_{r=1}^{3} C_r\left(\frac{1-e^{\alpha_r\Delta z}}{\alpha_r}\right)\right)^{-1}\Delta z\right]\Delta\sigma^{N}_{33(m)} \\ & + \frac{1}{2}\sum_{1}^{3}\left[\left(C_r\frac{1-e^{\alpha_r\Delta z}}{\alpha_r}\right)^{-1} S^{N(r)}_{22}\left(1-e^{-\alpha_r\Delta z}\right)\Delta z\right]\end{aligned} \tag{26}$$

$$\Delta\varepsilon^{N}_{33(m)} = \left[\frac{1}{E_m} + \frac{1}{3}\left(\sum_{r=1}^{3} C_r\left(\frac{1-e^{\alpha_r\Delta z}}{\alpha_r}\right)\right)^{-1}\Delta z\right]\Delta\sigma^{N}_{33(m)} + \left[\frac{-\upsilon_m}{E_m} + \frac{1}{6}\left(\sum_{r=1}^{3} C_r\left(\frac{1-e^{\alpha_r\Delta z}}{\alpha_r}\right)\right)^{-1}\Delta z\right]\Delta\sigma^{N}_{22(m)}$$
$$+\frac{1}{2}\sum_{1}^{3}\left[\left(C_r\frac{1-e^{\alpha_r\Delta z}}{\alpha_r}\right)^{-1} S^{N(r)}_{33}\left(1-e^{-\alpha_r\Delta z}\right)\Delta z\right] \tag{27}$$

$$\Delta\varepsilon^{N}_{23(m)} = \left[\frac{1+\upsilon_m}{E_m} + \frac{1}{2}\left(\sum_{r=1}^{3} C_r\left(\frac{1-e^{\alpha_r\Delta z}}{\alpha_r}\right)\right)^{-1}\Delta z\right]\Delta\sigma^{N}_{23(m)} + \frac{1}{2}\sum_{1}^{3}\left[\left(C_r\frac{1-e^{\alpha_r\Delta z}}{\alpha_r}\right)^{-1} S^{N(r)}_{23}\left(1-e^{-\alpha_r\Delta z}\right)\Delta z\right] \tag{28}$$

Modified Incremental Neuber's Rule (Eq(24))

$$\sigma^{e}_{22}\Delta\varepsilon^{e}_{22} + \varepsilon^{e}_{22}\Delta\sigma^{e}_{22} = \left(1-V_f\right)\left(\sigma^{N}_{22(m)}\Delta\varepsilon^{N}_{22(m)} + \varepsilon^{N}_{22(m)}\Delta\sigma^{N}_{22(m)}\right) + \left(V_f\right)\left(\sigma^{e}_{22(f)}\Delta\varepsilon^{e}_{22(f)} + \varepsilon^{e}_{22(f)}\Delta\sigma^{e}_{22(f)}\right) \tag{29}$$

$$\sigma^{e}_{33}\Delta\varepsilon^{e}_{33} + \varepsilon^{e}_{33}\Delta\sigma^{e}_{33} = \left(1-V_f\right)\left(\sigma^{N}_{33(m)}\Delta\varepsilon^{N}_{33(m)} + \varepsilon^{N}_{33(m)}\Delta\sigma^{N}_{33(m)}\right) + \left(V_f\right)\left(\sigma^{e}_{33(f)}\Delta\varepsilon^{e}_{33(f)} + \varepsilon^{e}_{33(f)}\Delta\sigma^{e}_{33(f)}\right) \tag{30}$$

$$\sigma^{e}_{23}\Delta\varepsilon^{e}_{23} + \varepsilon^{e}_{23}\Delta\sigma^{e}_{23} = \left(1-V_f\right)\left(\sigma^{N}_{23(m)}\Delta\varepsilon^{N}_{23(m)} + \varepsilon^{N}_{23(m)}\Delta\sigma^{N}_{23(m)}\right) + \left(V_f\right)\left(\sigma^{e}_{23(f)}\Delta\varepsilon^{e}_{23(f)} + \varepsilon^{e}_{23(f)}\Delta\sigma^{e}_{23(f)}\right) \tag{31}$$

The modified incremental Neuber's relations (Eqs (29)–(31)) can be used in conjunction with the endochronic theory of plasticity (Eqs (25)–(28)) to define the seven relationships needed to solve for the elastic-plastic notch root strain and stress increments. In all of the above equations, only $\Delta\sigma^{N}_{ij(m)}$ and $\Delta\varepsilon^{N}_{ij(m)}$ are unknowns. All the other parameters are obtained from the elastic solutions and the stress and strain state prior to the load increment and the properties of the PMMC. All of the relations are linear, and thus they can easily be simultaneously solved. For each point in the loading history, the elastic-plastic strain and stress state at the notch root can be calculated using the elastic-plastic matrix strains and stresses calculated above, the elastic fiber strains and stresses, and Eq (8).

Experimental Set-Up and Procedure

The PMMC used was a 6061-T6 aluminum reinforced with both 10 % and 20 % volume fractions of alumina (Al_2O_3). The material properties of these materials are given in Table 1. The 25.4 mm diameter rods were both commercially extruded and heat-treated. Specimens with geometries shown in Fig. 2 were machined from the PMMCs.

TABLE 1—*Composite material properties.*

	Young Modulus, E (GPa)	Poisson Ratio, ν	Ultimate Strength (MPa)	Elongation (%)
6061-T6	69	0.33	262	20
Alumina (Al_2O_3)	399	0.25	...	...
6061/Al_2O_3/10p-T6	81	0.31	324	10
6061/Al_2O_3/20p-T6	97	0.31	344	4

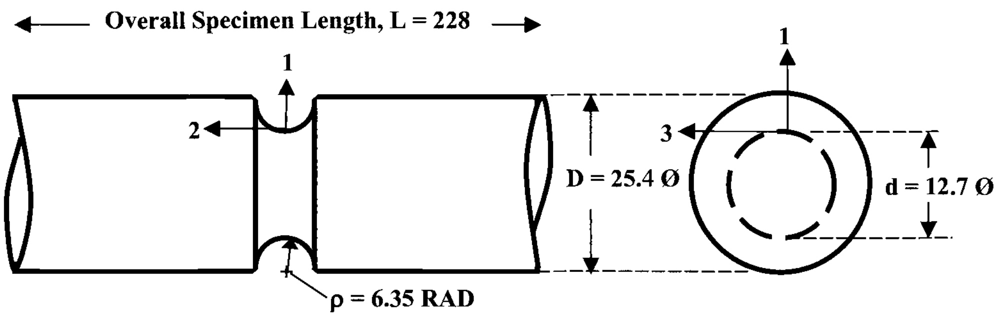

FIG. 2—*Geometry of specimen (all dimensions in mm).*

For the notch geometry shown in Fig. 2, the elastic stress concentration factors, K_t's, with respect to the coordinate system (1,2,3) shown were determined to be K_{t22} = 1.43, K_{t33} = 0.30, and K_{t23} = 1.14. These were obtained first theoretically, and then confirmed experimentally. Following the notation in Fig. 2, if a uniaxial tensile load P is applied in the axial (2) direction, the resulting elastic notch root axial, σ_{22}, and hoop, σ_{33}, stresses can be found using:

$$\sigma_{22} = \frac{4PK_{t22}}{\pi d^2}, \tag{32}$$

and

$$\sigma_{33} = \frac{4PK_{t33}}{\pi d^2}. \tag{33}$$

It should be noted that the hoop stress induced due to the notch root constraint was less than the nominal net section axial stress, and as such the stress concentration factor in the hoop direction, K_{t33}, was found to be less than unity. If a torsional load T is applied to the end of the bar, the resulting elastic notch root shear stress, σ_{23}, can be determined from:

$$\sigma_{23} = \frac{16TK_{t23}}{\pi d^3}. \tag{34}$$

The specimens were subjected to load-controlled tests conducted on a biaxial (tension-torsion) servo-hydraulic load frame. The load frame has axial and torsional load capacities of ±250 kN and ±2500 Nm, respectively. The three load paths considered are shown below in Figs. 3*a–c*. The first is a monotonic load path, and the next two are cyclic load paths. For both cyclic paths, cycles were applied until stabilized material behavior was observed. All paths were chosen to induce notch root plasticity.

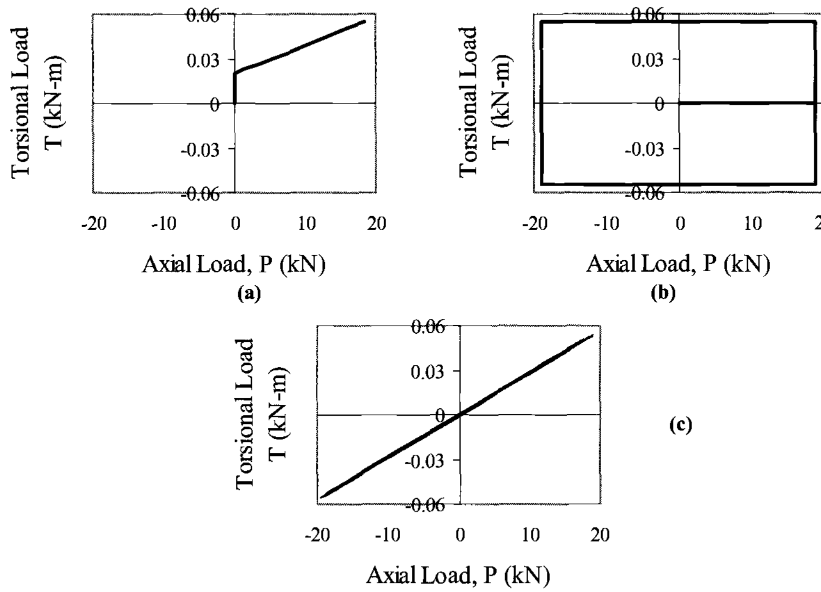

FIG. 3—a) *Monotonic torsion – combined tension-torsion,* b) *cyclic proportional tension-torsion,* c) *non-proportional cyclic box path.*

During the tests, the notch root strains were obtained using an advanced photogrammetry system that uses 3D image correlation to measure surface strain fields. To use this commercial piece of equipment [19], a random or regular pattern with a good contrast is applied to the surface of a specimen in the vicinity of the notch. This pattern deforms with the specimen as the load progresses. The deformation of the specimen under different loading conditions is recorded by two CCD cameras (Fig. 4) and is evaluated using digital image processing. Using photogrammetric principles described in [19], the specimens 3D coordinates, the 3D displacements, and surface strains are precisely calculated.

Figure 5 shows typical output from the optical strain measurement device. A section line drawn through the notch area (Fig. 5*a*) allows the surface strain distribution along the line to be recorded as the load is increased (Fig. 5*b*). It should be mentioned that the manufacturers have extensively validated this system. However, preliminary testing by the authors using the strain gauge technique and the results from the optical strain measurement device confirmed the accuracy of the system for the materials tested in this analysis.

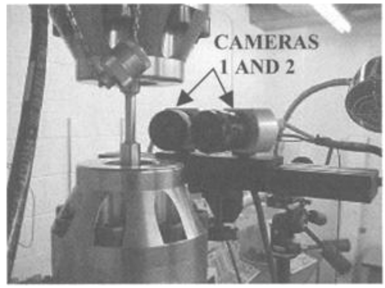

FIG. 4—*Bi-axial load frame and CCD cameras.*

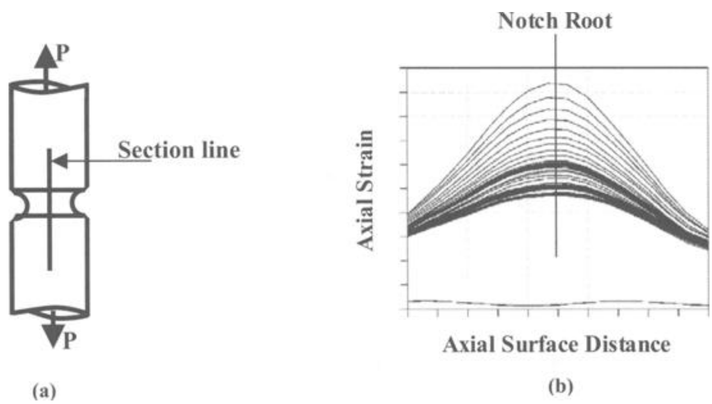

FIG. 5—*Axial strain distribution along section line for increasing loads.*

Comparison of Results

A short MATLAB [20] program was written to solve the governing equation set (Eqs (25)–(31)). This program requires as input the elastic notch root stress history. For the circumferentially notched specimen, these values were obtained on the basis of the applied load paths, the stress concentration factors, the volume fractions, material properties of the constituents, and Eqs (3)–(8). This program further requires as input the material constants for the Dirichlet function (Eq (12)) that defines the hereditary function for use in the cyclic constitutive model. These constants were obtained on the basis of a uniaxial tension test results of the 6061-T6 aluminum. For this material, three terms were found to be appropriate, and details of the extraction of these constants are given in [11]. These were determined to be $C_1 = 7841132$ MPa, $\alpha_1 = 60172$, $C_2 = 218948$ MPa, $\alpha_2 = 2097$, $C_3 = 17115$ MPa, $\alpha_2 = 348$.

The composite's notch root elastic-plastic shear strain, ε_{23}, is plotted against the axial strain, ε_{22}, for all load paths shown in Fig. 3, in Figs. 6–8. The figures show the experimental and calculated results for both the 10 % and 20 % volume fraction PMMCs. It should be mentioned that although the program calculates the full elastic-plastic stress and strain history at the notch root, for the purpose of comparison to the experimental results, only the major strains above are presented.

In general, the analytical model predicts the general trend in and all the characteristic phenomena occurring of the experimental test results. An initially elastic region is observed at the onset of loading or unloading, followed by region of elastic-plastic deformation. This confirms that the non-linear elastic-plastic behavior can be predicted from a linear elastic analysis. As the nominally applied loads increase, small differences are observed in the estimated and the measured strains. It should also be mentioned that the analytical methodology predicts the notch root strains in the materials with both volume fraction of fibers. This is a welcoming result, since the model uses only the material properties of the constituents separately.

The results from the non-proportional monotonic load path (Figs. 6*a* and *b*) show that the approximate methodology slightly over-predicts the axial strain, as the shear is kept constant. However, the differences are small, and furthermore, the slightly conservative result is advantageous in design. The results for the cyclic tests are presented for the last cycle of loading in Figs. 7 and 8. The results of the proportional loading path (Fig. 7) clearly show the model's ability to predict the elastic-plastic hysteresis loops associated with cyclic loading. The results of the box path (Fig. 8) show that the methodology is capable of predicting the elastic-plastic notch root strains for this 90° out-of-phase loading sequence. Although the results for both volume fractions of fibers indicate that the analytical methodology sometimes over-predicts, and at other points under-predicts the notch root elastic-plastic strains, the differences are small in all cases.

It is important to note that these highly supportive results are in part due to the fact that the elastic-plastic strains are relatively small in this investigation. For larger strains, it is expected that elastic-plastic subsurface strain distributions in the vicinity of the notch would violate the assumption of localized plasticity and thus lead to erroneous results using the proposed methodology. However, it should be mentioned that in [5], it was shown that the incremental Neuber's relation, developed for homogeneous materials, yielded such supportive results for much larger strains than those investigated in this study.

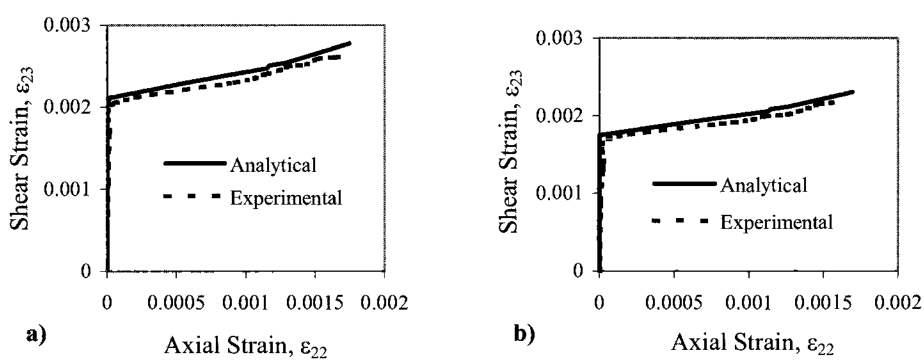

FIG. 6—*Notch root shear strains versus axial strains for torsion, combined tension-torsion monotonic loading path:* (a) *10 % volume fraction,* (b) *20 % volume fraction.*

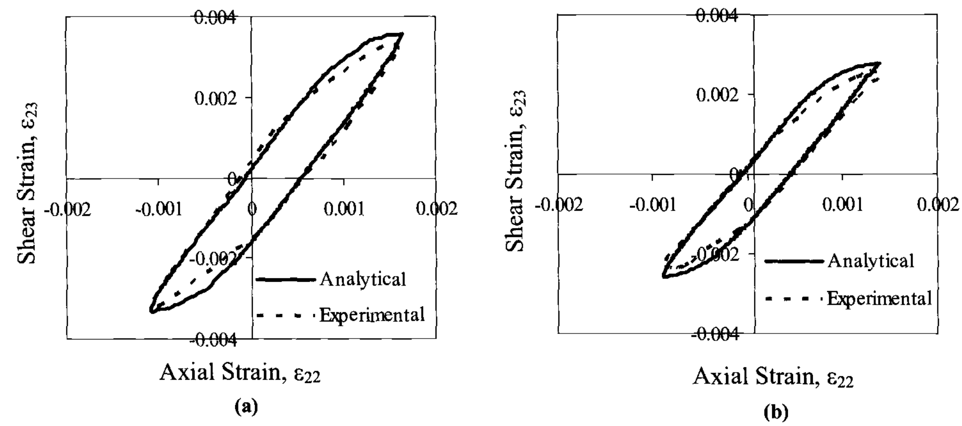

FIG. 7—*Notch root shear strains versus axial strains for torsion tension proportional cyclic loads: (a) 10 % volume fraction, (b) 20 % volume fraction.*

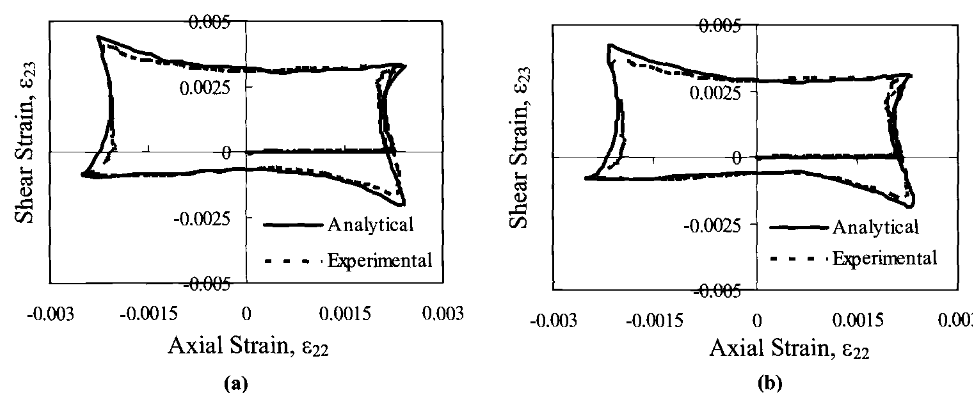

FIG. 8—*Notch root shear strains versus axial strains for box-shape loading path: (a) 10 % volume fraction, (b) 20 % volume fraction.*

Conclusions

A methodology has been presented to predict elastic-plastic notch root strains in bodies subjected to non-proportional cyclic loading sequences. The method incorporates a cyclic plasticity routine and an incremental form of Neuber's rule suitable for the analysis of heterogeneous PMMCs. The model presented provides an easy to implement linear approximation to the otherwise rather complex non-linear problem. The validity of the developed models was assessed by comparing the results obtained with experimental results for both proportional and non-proportional cyclic loading paths. The comparison indicates that the methodology is suitable for estimating the elastic-plastic strains at a notch root in PMMCs for small scale local yielding.

Acknowledgments

The authors acknowledge the grants provided by the University of Manitoba (Graduate Fellowship), Faculty of Engineering Graduate Awards, the National Sciences and Engineering Research Council of Canada (NSERC), and the Canadian Foundation for Innovation (CFI).

References

[1] Lease, K., Stephens, R., Jiang, Y., and Kurath, P., "Fatigue of a Particulate Reinforced Aluminum Metal Matrix Composite Subjected to Axial, Torsional and Combined Axial-Torsional Loading Conditions," *Int. Journal of Fatigue and Fracture of Engineering Materials and Structures*, Vol. 19, No. 8, 1996, pp.1031–1043.

[2] Zia, Z. and Ellyin, F., "Multiaxial Fatigue of an Alumina Particle Reinforced Aluminum Alloy," *Int. Journal of Fatigue*, Vol. 20, No. 1, 1998, pp. 51–56.

[3] Neuber, H., "Theory of Stress Concentration in Shear Strained Prismatic Bodies with Arbitrary Non-Linear Stress Law," *Journal of Applied Mechanics*, Vol. 28, 1961, pp. 544–550.

[4] Singh, M. N. K., Glinka, G., Dubey, R. N., "Elastic-Plastic Stress-Strain Calculation in Notched Bodies Subjected to Non-Proportional Loading," *Int. Journal of Fracture*, Vol. 76, 1996, pp. 39–60.

[5] Singh, M. N. K., "Notch Tip Stress Strain Analysis in Bodies Subjected to Non-Proportional Cyclic Loads," Ph.D. Thesis, The University of Waterloo, ON, 1998.

[6] Hoffmann, M., Amstutz, H., and Seeger, T., "Local Strain Approach in Non-Proportional Loading," *Fatigue under Biaxial and Multiaxial Loading ESIS 10*, K. Kussmaul, D. McDiarmid, and D. Socie, Eds., Mechanical Engineering Publications, 1991, pp. 357–376.

[7] Köttgen, V., Barkey, M, Socie, D., "Pseudo Stress and Strain Based Approaches to Multiaxial Notch Analysis," *Fatigue and Fracture of Engineering Materials & Structures*, Vol. 18, No. 9, 1995, pp. 981–1006.

[8] Owolabi, G. M. and Singh, M. N. K., "Elastic-Plastic Behavior of Notched PMMCs under Multiaxial Loading," *Proc. the 19th Canadian Congress of Applied Mechanics*, University of Calgary, Calgary, AB, 1–5 June 2003, Vol. 1, pp.132–133.

[9] Socie, D. and Marquis, G., *Multiaxial Fatigue*, SAE, Warrendale, PA, 2003.

[10] Lease, K. B., "Deformation and Fatigue of a Particulate Reinforced Metal Matrix Composite," Ph.D. Thesis, University of Iowa, Iowa, 1994.

[11] Owolabi, G. M, and Singh, M. N. K, "A Comparison between Two Models that Predict the Elastic-Plastic Behavior of Particulate Metal Matrix Composites under Multiaxial Fatigue Type Loading," *Proceedings. of the ASME 2003 International Mechanical Engineering Congress and Exposition*, 16–21 Nov. 2003, Washington D.C., 10 pp.

[12] Eshelby, J. B., "The Determination of the Elastic Field of an Ellipsoidal Inclusion, and Related Problems," *Proceedings of the Royal Society of London*, A241, 1959, pp. 376–396.

[13] Mori T. and Tanaka K., "Average Stress in the Matrix, and Average Elastic Energy of Materials with Misfitting Inclusions," *Acta Metallurgica*, Vol. 21, 1973, pp. 571–574.

[14] Li, Y. Y. and Chen, Y., "An Incremental Plastic Analysis of Multiphase Materials," *Journal of Applied Mechanics*, Vol. 57, 1990, pp. 562–568.

[15] Mróz, Z., "On the Description of Anisotropic Work Hardening," *Journal of the Mechanics and Physics of Solids*, Vol. 15, 1967, pp. 163–175.

[16] Valanis, K. C., "Fundamental Consequences of a New Intrinsic Time Measure: Plasticity as

a Limit of the Endochronic Theory," *Archives of Mechanics*, Vol. 32, 1980, pp.171–191.

[17] Hsu, S., Jain, S., and Griffin, O., "Verification of Endochronic Theory for Non-Proportional Loading Paths," *Journal of Engineering Mechanics*, Vol. 117, 1991, pp.110–131.

[18] Duva, J. M, and Hutchinson, J. W., "Constitutive Potentials for Dilutely Voided Nonlinear Materials," *Mechanics of Materials*, Vol. 3, 1984, pp. 41–54.

[19] *Aramis User's Manual*, Version 5, GOM Measurements, Braunschweig, Germany, 2003.

[20] *MATLAB Student Version Release 12, Learning MATLAB*, by The Math Works Inc., 2001.

Journal of ASTM International, April 2005, Vol. 2, No. 4
Paper ID JAI12002
Available online at www.astm.org

F. Mueller,[1] *A. Scholz,*[1] *and C. Berger*[1]

Influence of Crack-Surface Oxidation on Creep-Fatigue Crack Behavior of 1Cr- and 10Cr-Steels

ABSTRACT: High temperature components with notches, defects, and flaws can introduce crack initiation and crack propagation under service conditions. Fracture mechanics procedures are needed to study crack problems and to support an advanced remnant life evaluation. Since a more flexible service mode of steam power plants causes a higher number of start-up and shut-down events, creep-fatigue crack behavior is decisive for life assessment and integrity of components. Usually, fracture mechanics experiments are carried out under air conditions, although in cases of internal cracks they are not in contact with air. Therefore, it is of interest to realize the degree to which environmental conditions, e.g., crack-tip oxidation, can influence crack initiation and crack growth behavior.

In order to reveal problems related to high temperature components, the crack initiation time and crack growth rate were determined in air environment and in a gas with controlled atmosphere on 1CrMo(Ni)V- and 10CrMoWVNbN-steels. Crack initiation and propagation under creep-fatigue conditions have been described with the fracture mechanics parameters C*, K_I, and ΔK_I and C*. A modified "Two-Criteria-Diagram" was used to describe creep-fatigue crack initiation.

KEYWORDS: creep-fatigue conditions, crack propagation, crack initiation, modified Two-Criteria-Diagram, air and shielded gas, 1CrMo(Ni)V-steel, 10CrMoWVNbN-steel

Introduction

Documents on the material behavior of crack-like defects/flaws and unavoidable notches are required for the design and inspection of power plant components in high temperature long-term service. In the case of design with unavoidable notches, cracks may be initiated or propagated by creep-fatigue loading. In both cases, an experimentally safeguarded and quantitative description is required. The necessary experiments were mostly performed under normal air conditions in the laboratory. However, the locations of the stress concentrations in components under potential crack danger are often inside the material or below the surface and are consequently not affected by the environmental medium. Therefore, there is great interest to study the influence of an oxygen-free environment on the crack behavior under creep-fatigue loading.

This paper deals with results from research projects [1–3] in which the creep-fatigue crack behavior was examined. The crack initiation and crack propagation behavior under creep-fatigue loading were investigated on 1CrMo(Ni)V-steel and on 10CrMoWVNbN-steel in air and a gas under controlled atmosphere (shielded gas) on specimens of type CT. Additional results under pure fatigue and creep conditions are also included.

Manuscript received 3 November 2003; accepted for publication 15 June 2004; published April 2005. Presented at ASTM Symposium on Fatigue and Fracture Mechanics: 34th Volume on 19–21 November 2003 in Tampa, FL; S.R. Daniewicz, J.C. Newman, Jr., and K-H. Schwalbe, Guest Editors.

[1] Research Engineer, Head of Department, and Managing Director, respectively, Institute of Materials Technology, Grafenstr. 2, 64283 Darmstadt, Germany.

Materials, Specimens, and Test Procedure

The test materials were taken from industrial products before they were introduced in service. The forged steel 30CrMoNiV4-11 and the cast steel G17CrMoV5-11 are taken as reference for the well-established 1CrMo(Ni)V-power plant steels. The steels X12CrMoWVNbN10-1-1 and GX12CrMoWVNbN10-1-1 refer to the modern 10CrMoWVNbN-steels.

In this study, CT-specimens were used (Fig. 1). The specimen crack start notch was spark eroded with a notch tip radius of 0.1 mm. All CT-specimens were 20 % side-grooved in order to ensure a uniform crack growth front.

The specimens were tested under constant tensile loads (creep crack tests) and under cyclic tensile loads (fatigue and creep-fatigue crack tests). The tests under cyclic tensile loads with stress ratio R = 0.1 were performed in maximum hold times t_H of 0.3 h and 3.0 h (Fig. 2).

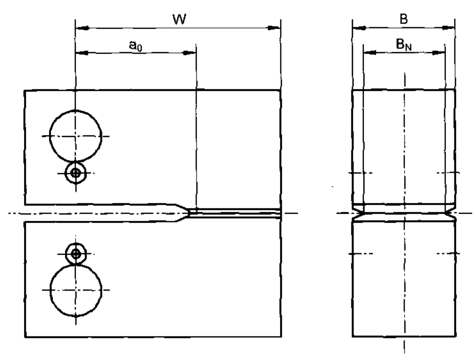

FIG. 1—*Specimen geometry.*

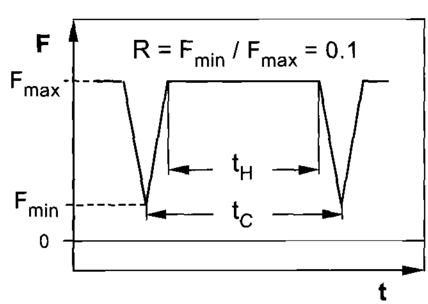

FIG. 2—*Applied load cycle for creep-fatigue tests.*

With regard to typical service temperatures, the test temperatures are as follows: 550°C for the 1CrMoNiV-forging steel, 530°C and 550°C for the 1CrMoV-cast steel, and 550°C and 600°C for the 10CrMoWVNbN-steels. The tests in controlled gas environment were performed in argon with 3 % hydrogen (Ar + 3 % H_2, shielded gas) in order to avoid crack-surface oxidation.

Parts of the tests were carried out by means of the interrupted test technique (multi specimen method), and others were carried out by means of continuous test technique (single specimen method). The interrupted test technique can be described as follows: for each stress level, a series of up to eight specimens were tested under the same loading conditions in a multi-specimen machine. After reaching time proportions from 10–80 % of predetermined test time, the row of specimens was unloaded. During each interruption, the load line displacement of all specimens was optically measured at room temperature. One specimen was fractured in brittle form at low temperature. The crack length of the specimen was determined fractographically.

By using the continuous test technique, an online measurement of the load line displacement was performed using capacitive high temperature strain gauges. The crack propagation was online-monitored with alternating current potential drop (ACPD) technique. At the end of each test, the potential drop signal was calibrated with the final crack length measured on the fractured specimens.

Test Results and Discussion

For the evaluation of the test results, the linear elastic stress intensity factor K_I [4] was used as well as the parameter C* [5]. The stress intensity factor is defined for CT-specimens as follows:

$$K_I = \frac{F}{\sqrt{B \cdot B_N \cdot W}} \cdot \frac{2 + a/W}{(1 - a/W)^{3/2}} \cdot f(a/W) \qquad (1)$$

where F is the applied load, B is the specimen thickness, B_N is the net specimen thickness, W is the specimen width, a is the current crack length, and

$$f(a/W) = 0.886 + 4.64 \cdot (a/W) - 13.32 \cdot (a/W)^2 + 14.72 \cdot (a/W)^3 - 5.6 \cdot (a/W)^4 \qquad (2)$$

The stress intensity factor is valid for linear elastic behavior only, but it can be approximated for a limited plastic zone near the crack-tip. The parameter C* is valid for stationary creep in the crack-tip environment. In [6], the parameter C* is calculated for CT-specimens, using the following formula:

$$C^* = \frac{F \cdot \dot{v}_c}{B_N \cdot (W - a)} \cdot \frac{n}{n + 1} \cdot \left(2 + 0.522 \cdot \frac{W - a}{W}\right) \qquad (3)$$

where n is the exponent in Norton's law, and $\dot{v}_c$ is the creep component of the load line displacement rate. The creep component of the load line displacement rate is given by:

$$\dot{v}_c = \dot{v}_t - (\dot{v}_e + \dot{v}_p) \qquad (4)$$

where $\dot{v}_t$, $\dot{v}_e$ and $\dot{v}_p$ are the total, elastic, and plastic load line displacement rates, respectively. This procedure only applies to the continuous test technique, where the total load line displacement rate is measured under load.

The procedure to measure load line displacement in the interrupted test technique is different, because all measurements are taken on unloaded specimens at room temperature without taking into account the elastic component v_e. By choosing relatively small test loads, the plastic part of total displacement can be neglected; therefore the measured values are used for the determination of creep displacement rate $\dot{v}_c$. Metallographical investigations on cut specimens have proven this statement. The crack-tip vicinity of Cs25-specimens taken from 1CrMoNiVsteel tested in air and shielded gas is shown in Fig. 3. Specimens were subjected to equal loads and similar test durations. The oxide layer on the crack-surface can be seen clearly (Fig. 3*b*). For the test conducted under shielded gas (Fig. 3*a*), this is not to be expected. This means that the calculated displacement rate $\dot{v}$, using measured displacements of tests under shielded gas, reflects exactly the creep component $\dot{v}_c$. For experiments in air environment conducted in this manner, the calculated rate $\dot{v}$ includes creep rate $\dot{v}_c$ and oxide layer $\dot{\delta}_{ox}$. Therefore, the oxide layer component has to be subtracted from measured displacement. The appropriate laws for oxide layer thickness as a function of time for 1CrMo(Ni)V-steel and 10CrMoWVNbN-steel are given in Fig. 4. Accordingly the 10CrMoWVNbN-steel shows favorable oxidation behavior. The laws were produced using a limited number of specimens but with test durations up to 35.000 h. With the respective equation, the calculated load line displacement rate (and/or load line displacement) can be corrected. This procedure is represented in Fig. 5 for an interrupted creep crack test at 550°C on Cs25-specimens of the steel 30CrMoNiV4-11. The correction, made in accordance to Fig. 5, was applied for the determination of the parameter C* for the interrupted tests in air. The results are described below.

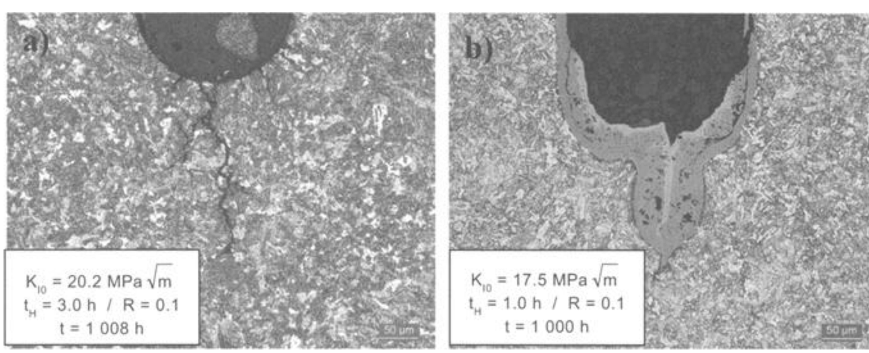

FIG. 3—*Crack-tip appearance of Cs25-specimens in creep-fatigue crack test in "Ar + 3 % H_2" (a) and "Air" (b) 30CrMoNiV4-11/AMA, 550°C.*

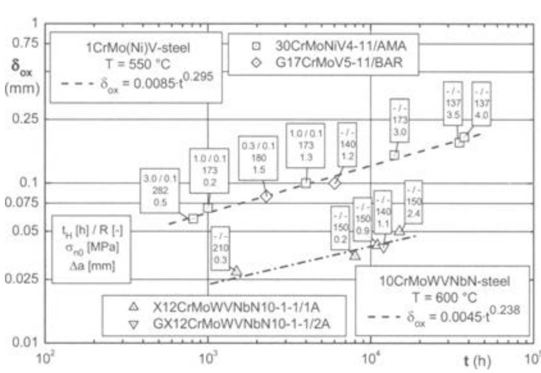

FIG. 4—*Change of oxide layer thickness on crack-surfaces on Cs25-specimens, 1CrMo(Ni)V-steel at 550°C and 10CrMoWVNbN-steel at 600°C.*

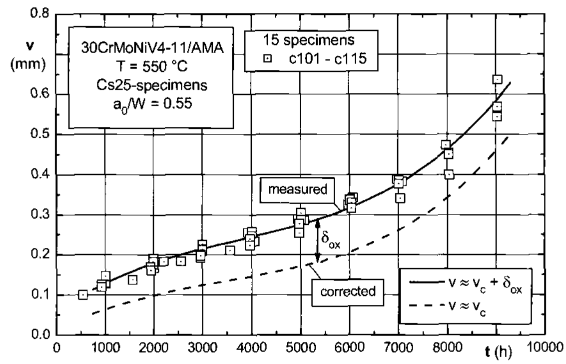

FIG. 5—*Corrected load line displacement for crack-surface oxide coating, 30CrMoNiV4-11, 550°C.*

Crack Propagation Behavior

In the following, the crack propagation under fatigue, creep, and creep-fatigue conditions in air and shielded gas will be described for crack length Δa between 0.01W and 0.05W.

Crack Growth under Pure Fatigue—Under pure fatigue conditions, the fatigue crack growth can be described by depicting the crack propagation per cycle against the range of stress intensity ΔK_I. The range of stress intensity ΔK_I is given by:

$$\Delta K_I = K_{I\,max} - K_{I\,min} \tag{5}$$

With logarithmic presentation of the fatigue crack growth rate da/dN against the cyclic stress intensity factor ΔK_I, a linear part results, which can be described by the Paris-equation [7]:

$$da/dN = c_0 \cdot \Delta K_I^{\,m} \tag{6}$$

The fatigue crack growth rates against the cyclic stress intensity factor ΔK_I for 1CrMo(Ni)V-steel and for 10CrMoWVNbN-steel in air and under shielded gas are shown in Figs. 6 and 7, respectively. In both cases, no difference between forging steel and cast steel can be observed. Shielded gas leads to lower values of fatigue crack growth rate in comparison to air conditions (Fig. 6). The results lie below the scatter band of the tests in air, but this effect is not significant for the 10CrMoWVNbN-steel (Fig. 7). This effect is caused by the different oxidation behavior, indicated in Fig. 4. The oxide layer increases relatively quickly (especially for the 1CrMo(Ni)V-steel) on the newly formed crack-surface, and it is destroyed during the following load cycle. Destruction of oxide layer takes place with small resistance. Finally, an additional part of crack propagation can be found in air.

In Figs. 6 and 7 the cyclic stress intensity factor was determined by using F_{max} and F_{min}, without including the "crack closure phenomenon." Therefore, it was of interest to consider the "crack closure" effect and attempt to make an appropriate quantification.

The cyclic stress intensity factor ΔK_I is not an appropriate parameter for the fatigue crack growth characterization, where crack closure can occur already at positive nominal stresses. In that case, the effective stress intensity factor (Fig. 8) is defined by:

$$\Delta K_{eff} = K_{I\,max} - K_{open} \tag{7}$$

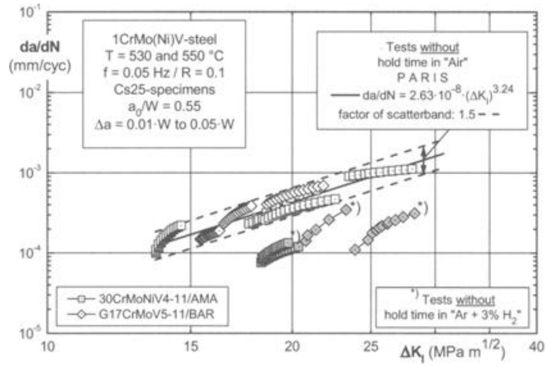

FIG. 6—*Change of crack propagation rate for fatigue tests versus parameter* ΔK_I. *1CrMo(Ni)V-steel, 530 and 550°C.*

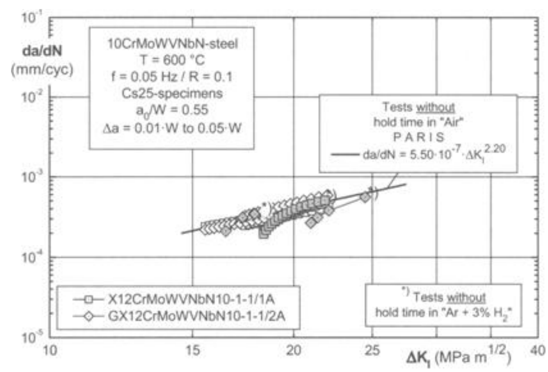

FIG. 7—*Change of crack propagation rate for fatigue tests versus parameter* ΔK_I; *10CrMoWVNbN-steel, 600°C.*

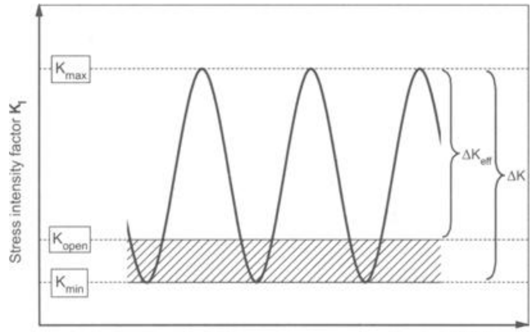

FIG. 8—*Schematic of effective stress intensity factor.*

One distinguishes different kinds of the cr ack closure, which are based on different mechanisms. The three essential crack closure mechanisms for metals [8] are:

- plastically-induced crack closing
- oxide-layer-induced crack closing
- roughness-induced crack closing

In practice, it is impossible to separate the individual influence of each mechanism on the fatigue crack growth.

Through crack closure, only a part of the applied load contributes to the crack growth. The stress intensity factor ΔK_I is introduced by a correction as effective stress intensity factor ΔK_{eff} [9] in the following form:

$$\Delta K_{eff} = U \cdot \Delta K_I \tag{8}$$

where U is the crack opening factor. There are different procedures proposed for the calculation of U. One of them is given as [9]:

$$U = 0.5 + 0.4 \cdot R \tag{9}$$

Shielded gas tests are conducted without oxidation; therefore factor U is smaller than for air tests. The statement: "fatigue crack growth rate under shielded gas is lower than in air" is still valid. A quantitative determination of the crack closure factor U for fatigue crack tests in air and under shielded gas is still under investigation.

Crack Growth under Pure Creep—The parameter C* has been chosen for the presentation of the creep crack growth rate. The above-mentioned correction for the determination of the parameter C* for creep crack tests in air was considered. The creep crack growth rate for tests in air and under shielded gas of 1CrMo(Ni)V-steel is plotted in Fig. 9 and for 10CrMoWVNbN-steel in Fig. 10. In both cases there is no difference between forged steel and cast steel. The results under shielded gas are within the scatter band of the results from air tests. This result is not surprising if the creep crack damage mechanism is considered. The formation of pores and microcracks occurs in front of the crack-tip in the ligament of the material, irrespective of the kind of surrounding medium used.

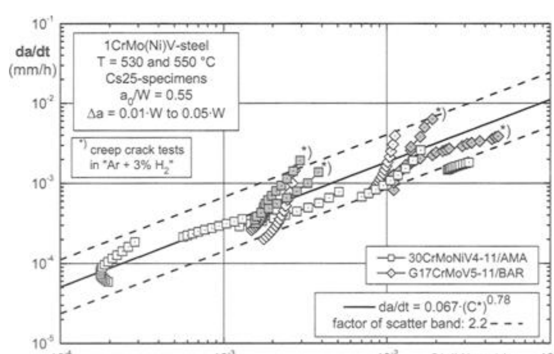

FIG. 9—*Creep crack growth rate versus parameter C*, 1CrMo(Ni)V-steel, 530 and 550°C.*

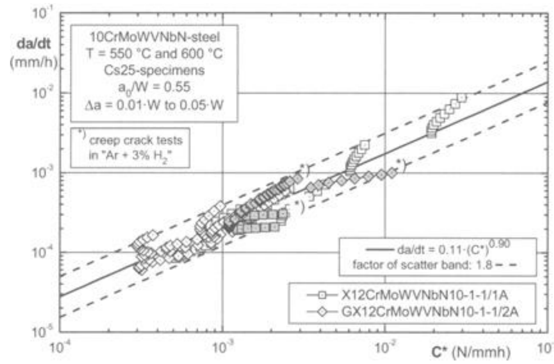

FIG. 10—*Creep crack growth rate versus parameter C*, 10CrMoWVNbN-steel, 550 and 600°C.*

Crack Growth under Creep-Fatigue Conditions—The creep-fatigue crack growth rate can be compared with the pure creep crack growth rate, as well as with the pure fatigue crack propagation rate. In Fig. 11 some results for 1CrMo(Ni)V-steels are compared with the results of the fatigue crack test. With increasing hold time, an increase of the creep crack propagation per cycle can be observed. As a result, there is no significant influence of air and shielded gas on creep-fatigue crack propagation rate. However, this crack propagation rate is achieved with a lower cyclical stress intensity factor. This is an acceleration of the creep-fatigue crack propagation rate under shielded gas.

At creep-fatigue crack experiments, crack closure effects must be considered. The oxide layer has a great influence (Fig. 3) as indicated by the assumed load process in Fig. 12. The crack will be closed earlier during the creep-fatigue crack test in air than under shielded gas. The effective load at the crack-tip under shielded gas is greater than in air. The creep-fatigue crack closure in air cannot be taken as a constant crack opening factor U, like in the fatigue crack test. The influence of the oxidation on crack closure is a function of time (Fig. 4). Future investigations are planned.

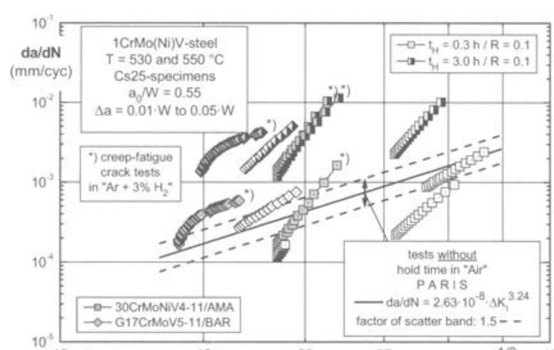

FIG. 11—*Creep-fatigue crack growth rate versus parameter ΔK_I, 1CrMo(Ni)V-steel, 530 and 550°C.*

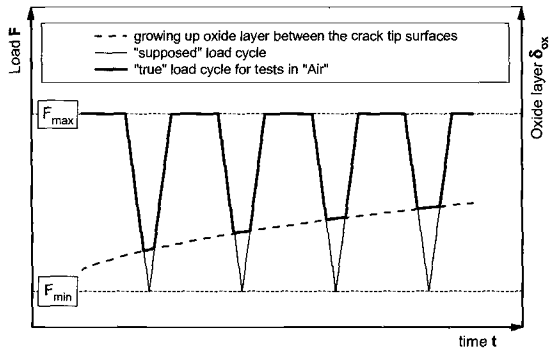

FIG. 12—*Load distribution during the creep fatigue crack test in "Air," schematically.*

Crack Initiation Behavior

A technical crack initiation length has been defined to determine the crack initiation behavior under creep and creep-fatigue conditions for tests in air and under shielded gas. This paper deals with a technical crack initiation length of $\Delta a_i = a_i - a_0 = 0.5$ mm.

Crack Initiation under Pure Creep—The creep crack initiation time $t_{i\,c}$ against the parameter C* is shown in Fig. 13 for the 1CrMo(Ni)V-steel and in Fig. 14 for the 10CrMoWVNbN-steel. No significant difference between forged and cast steel can be observed. Furthermore, there is no difference between creep crack initiation in air and under shielded gas. The solid lines correspond to the lower boundary of the scatter band, which is the worst case.

The creep crack initiation time $t_{i\,c}$ is shown as a function of K_{I0} in Figs. 15 and 16 for 1CrMo(Ni)V- and 10CrMoWVNbN-steels, respectively. For the forged and cast 10CrMoWVNbN-steels (Fig. 16), a common creep crack initiation function can be reproduced. This is not valid for the 1CrMo(Ni)V-steels. There is a difference between forged and cast steel. However, the respective shielded gas results overlapped the air results.

Using the so-called "Two-Criteria-Method" [10], it is possible to determine analytically the crack initiation of components under creep conditions. The nominal stress $\sigma_{n\,pl}$ considers the stress situation in the ligament, and the fictitious elastic parameter $K_{I\,id}$ characterizes the crack-tip situation. These loading parameters are normalized in a "Two-Criteria-Diagram" ("2CD") by the creep rupture strength $R_{u/t/T}$ and the parameter $K_{Ii\,c}$, which characterized the creep crack initiation of the material. The normalized parameters are the stress ratio $R_\sigma = \sigma_{n\,pl}/R_{u/t/T}$ for the far-field and the stress intensity ratio $R_K = K_{I\,id}/K_{Ii\,c}$ for the crack-tip. The "2CD" distinguishes three fields of damage modes. Above $R_\sigma/R_K = 2$, ligament damage is expected, below $R_\sigma/R_K = 0.5$, crack-tip damage is expected, and between these two lines a mixed damage mode is observed. Crack initiation is only expected above the boundary line. The "2CDs" are shown in Figs. 17 and 18 for 1CrMo(Ni)V- and 10CrMoWVNbN-steel, respectively. This shows that the "2CD" can also be used for creep crack initiation under shielded gas without any changes.

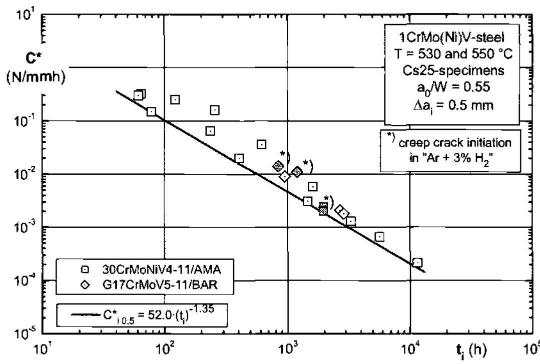

FIG. 13—*Creep crack initiation time versus parameter C*, 1CrMo(Ni)V-steel, 530 and 550 °C.*

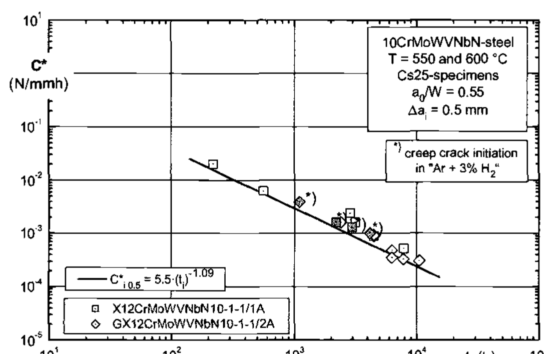

FIG. 14—*Creep crack initiation time versus parameter C*, 10CrMoWVNbN-steel, 550 and 600°C.*

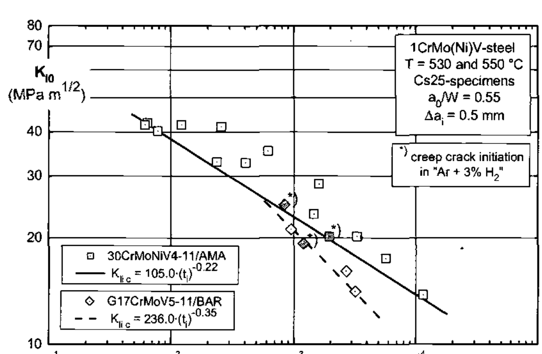

FIG. 15—*Creep crack initiation time versus parameter K_I, 1CrMo(Ni)V-steel, 530 and 550°C.*

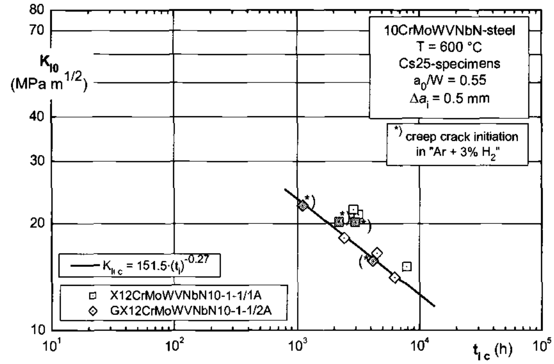

FIG. 16—*Creep crack initiation time versus parameter K_I, 10CrMoWVNbN-steel, 600°C.*

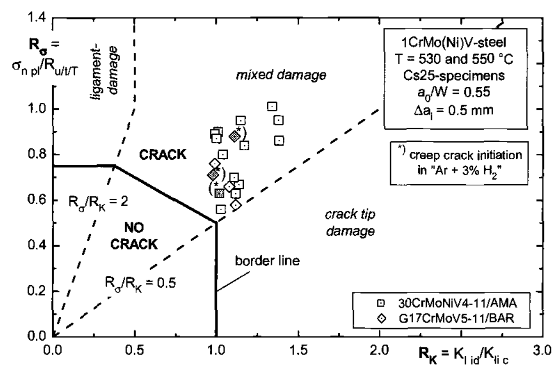

FIG. 17—*Presentation of 2CD for creep crack initiation, 1CrMo(Ni)V-steel, 530 and 550°C.*

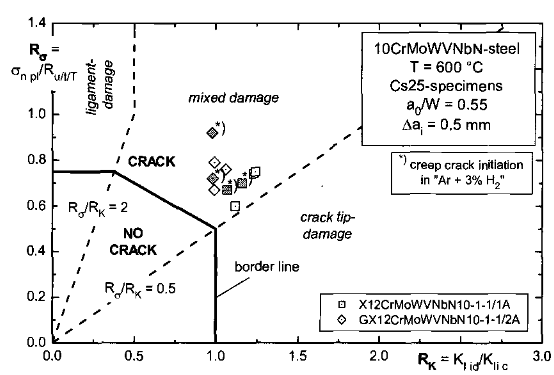

FIG. 18—*Presentation of 2CD for creep crack initiation, 10CrMoWVNbN-steel, 600°C.*

Crack Initiation under Creep-Fatigue Conditions—The crack initiation under creep-fatigue conditions is shown in Fig. 19 for the 1CrMo(Ni)V-steel and for the 10CrMoWVNbN-steel in Fig. 20 in a respective K_{I0}-$t_{i\,cf}$-diagram. A reduction in time for crack initiation time $t_{i\,cf}$ at decreasing holding times t_H could be determined. The results under shielded gas are clearly below the respective air results in some cases. The solid and dash-dotted lines are the creep crack initiation curves taken from Figs. 15 and 16. The dashed and dotted lines represent the reduced creep crack initiation curve for the modified "2CD" by the factor

$$L_{i\,c} = t_{i\,cf}/t_{i\,c} \tag{10}$$

for creep-fatigue experiments in air for hold times of $0.3 \le t_H < 3.0$ h, as assumed in [11] and [12]. In Fig. 21, the ratio $L_{i\,c}$ is represented against hold time for 1CrMo(Ni)V-steel and in Fig. 22 for 10CrMoWVNbN-steel. The line $L_{i\,c} = 1.0$ reflects the correlation for creep crack initiation, and the line $L_{i\,c} = 0.6$ gives the above described reduction for the creep-fatigue crack behavior in air. For hold times of 0.3 h, in order to stay on the conservative side, an $L_{i\,c}$ reduction to 0.25 would be necessary. The use of the engineering factor of 0.6 will result in a certain increase of the crack initiation length, but it will still be tolerable within the values of $\Delta(\Delta a_i) \le 0.5$ mm. That means that the predicted creep-fatigue crack initiation time by "2CD" is longer than the real one. For creep-fatigue crack tests with hold times of 3.0 h, a reduction is not necessary [11,12].

The modified "2CD" of 1CrMo(Ni)V-steel is shown in Fig. 23 and for 10CrMoWVNbN-steel in Fig. 24. The validity of the boundary line is confirmed by the results of creep-fatigue crack initiation tests in air and under shielded gas. No data points were found within the NO-CRACK area.

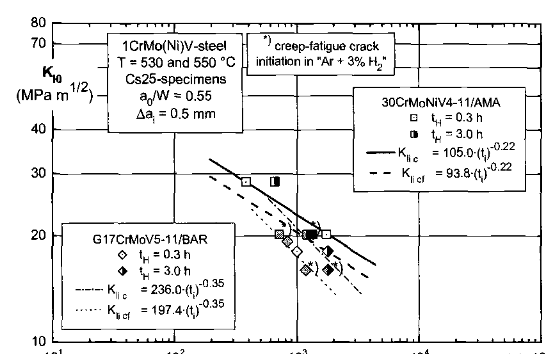

FIG. 19—*Creep-fatigue crack initiation time versus parameter K_I, 1CrMo(Ni)V-steel, 530 and 550°C.*

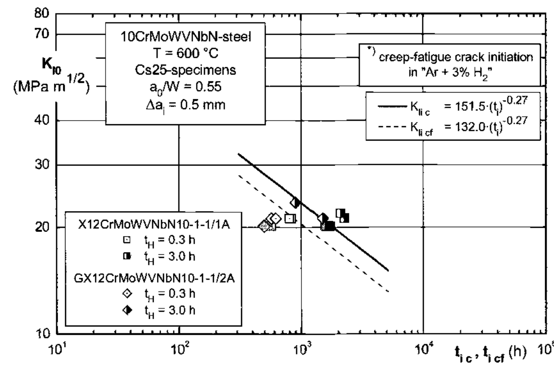

FIG. 20—*Creep-fatigue crack initiation time versus parameter* K_I, *10CrMoWVNbN-steel, 600°C.*

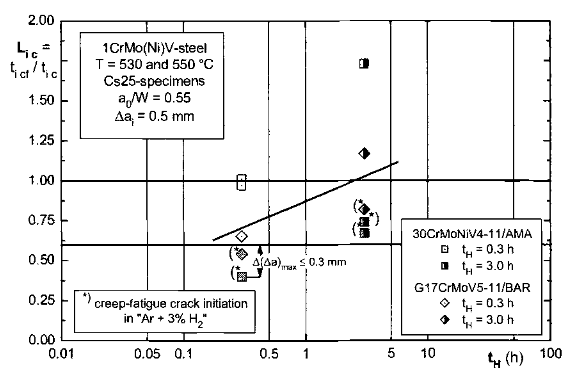

FIG. 21—*Dependence of Ratio* L_{ic} *on hold time, 1CrMo(Ni)V-steel, 530 and 550°C.*

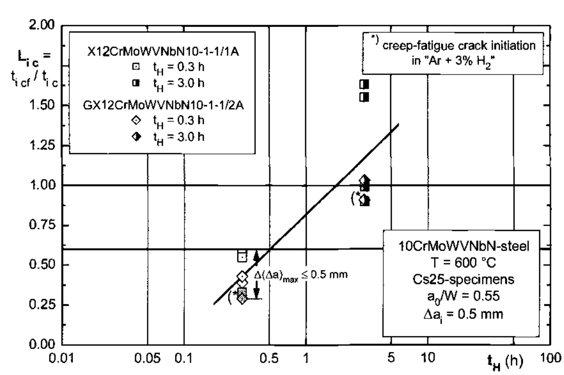

FIG. 22—*Dependence of Ratio* L_{ic} *on hold time, 10CrMoWVNbN-steel, 600°C.*

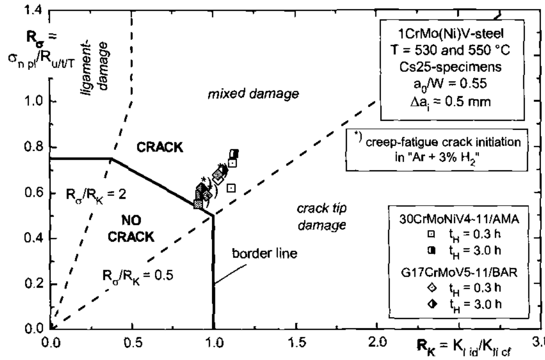

FIG. 23—*Modified 2CD for creep-fatigue crack initiation, 1CrMo(Ni)V-steel, 530 and 550°C.*

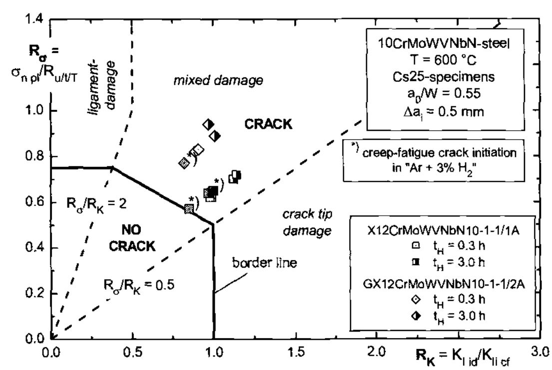

FIG. 24—*Modified 2CD for creep-fatigue crack initiation, 10CrMoWVNbN-steel, 600°C.*

Concluding Remarks

This paper describes the results of a series of creep-fatigue crack tests in air and shielded gas, performed on CT-specimens prepared from 1CrMo(Ni)V- and 10CrMoWVNbN-steels. The investigations have been carried out on forged and cast steel samples. The creep-fatigue results were supplemented by pure creep and fatigue crack tests. Crack initiation and propagation behavior were characterized by the fracture mechanics parameters C* and K_I and C*. Parameters were corrected depending on used test techniques (interrupted or continuously), test conditions (creep and/or fatigue), and the environment (air or shielded gas).

The results of crack initiation and crack propagation in air and under shielded gas can be summarized as follows:

- Under fatigue conditions, crack behavior under shielded gas show advantages.
- Under creep conditions, there are no differences between results in air and shielded gas environment.

- Under creep-fatigue conditions crack initiation time is shorter and crack propagation rate is higher for shielded gas compared to air environment.

Additionally the creep crack initiation results were evaluated with the "Two-Criteria-Diagram" ("2CD") for both environmental conditions. For creep-fatigue crack initiation, the modified "2CD" can be established. At creep-fatigue crack experiments with Short hold times, the modified "2CD" is a less conservative description.

Acknowledgments

We would like to thank the “Forschungsvereinigung der Arbeitsgemeinschaft der Eisen und Metall verarbeitenden Industrie e.V.,” the “Arbeitsgemeinschaft industrieller Forschungsvereinigung,” and the “VDEh-Gesellschaft zur Förderung der Eisenforschung mbH” for their financial and technical support. Special thanks go to C. Weichert, G. Schellenberg, and W. Stadtmueller from MPA Stuttgart and J. Ewald (head of working group) for useful discussions and joint research work.

References

[1] Berger, C., Scholz, A., Roos, E., Maile, K., Mueller, F., and Schellenberg, G., "Einfluss inerter Atmosphäre auf das Rissverhalten warmfester Stähle im Kriech- und Kriechermüdungsbereich," final report of IfW Darmstadt and MPA Stuttgart, AiF-Nr. 11722N, 2002.

[2] Mueller, F., Weichert, C., Ewald, J., "Beitrag zum Rissverhalten von niedrig legiertem Stahlguss," GIESSEREI 91, 2004, pp. 22–30.

[3] Berger, C., Scholz, A., Ross, E., Maile, K., Mueller, F., and Stadtmueller, W., "Hochtemperaturrissverhalten der 600°C-Stähle für Wellen und Gehäuse von Dampfturbinen," final report of IfWD and MPAS, AVIF Nr. A127, 2002.

[4] Irwin, G. R., "Analysis of Stresses and Strains near the End of a Crack Traversing a Plate," Trans. ASME, *J. Appl. Mech.*, 24, 1957, pp. 361–364.

[5] Landes, J. D. and Begley, J. A., "A Fracture Mechanics Approach to Creep Crack Growth," In: *Mechanics of Crack Growth, ASTM STP 590*, ASTM International, West Conshohocken, PA, 1976, pp. 128–148.

[6] ASTM Standard E 1457-00, “Standard Test Method for Measurement of Creep Crack Growth Rates in Metals,” ASTM International, West Conshohocken, PA, published November 2000.

[7] Paris, P. C., "The Fracture Mechanics Approach to Fatigue," *Proceedings of the Tenth Sagamore Army Materials Research Conference*, Syracuse University Press, 1964, pp. 107–132.

[8] Suresh, S. and Ritchie, R. O., "Propagation of Short Fatigue Cracks," *Int. Met. Rev.*, Vol. 29, 1984, pp. 445–476.

[9] Elber, W., "The Significance of Fatigue Crack Closure," *Damage Tolerance in Aircraft Structures, ASTM STP 486*, ASTM International, West Conshohocken, PA, 1971, pp. 230–242.

[10] Ewald, J., Keienburg, K.-H., "A Two-Criteria-Diagram for Creep Crack Initiation," *Int. Conf. on Creep*, Tokyo, 1986, pp. 173–78.

[11] Ewald, J., Sheng, S., Klenk, A., and Schellenberg, G., "Engineering Guide to Assessment of

Creep Crack Initiation on Components by Two-Criteria-Diagram," *International Journal of Pressure Vessels and Piping*, Vol. 78, Nos. 11–12, 2001, pp. 937–949.

[12] Granacher, J., Klenk, A., Tramer, M., Schellenberg, G., Mueller, F., and Ewald, J., "Creep Fatigue Crack Behavior of Two Power Plant Steels," *International Journal of Pressure Vessels and Piping*, Vol. 78, Nos. 11–12, 2001, pp. 909–920.

AUTHOR INDEX

SUBJECT INDEX

T

U

W

X